JUNE 2020

AJNR

VOLUME 41 • PP 943–1134

AJNR

AMERICAN JOURNAL OF NEURORADIOLOGY

JUNE 2020
VOLUME 41
NUMBER 6
WWW.AJNR.ORG

THE JOURNAL OF DIAGNOSTIC AND INTERVENTIONAL NEURORADIOLOGY

Perspectives on neuroradiology from the COVID-19 outbreak
Preoperative evaluation of craniopagus twins
Improved detection of focal cortical dysplasia
Resting-state brain activity in comatose postanoxic patients

Official Journal ASNR • ASFNR • ASHNR • ASPNR • ASSR

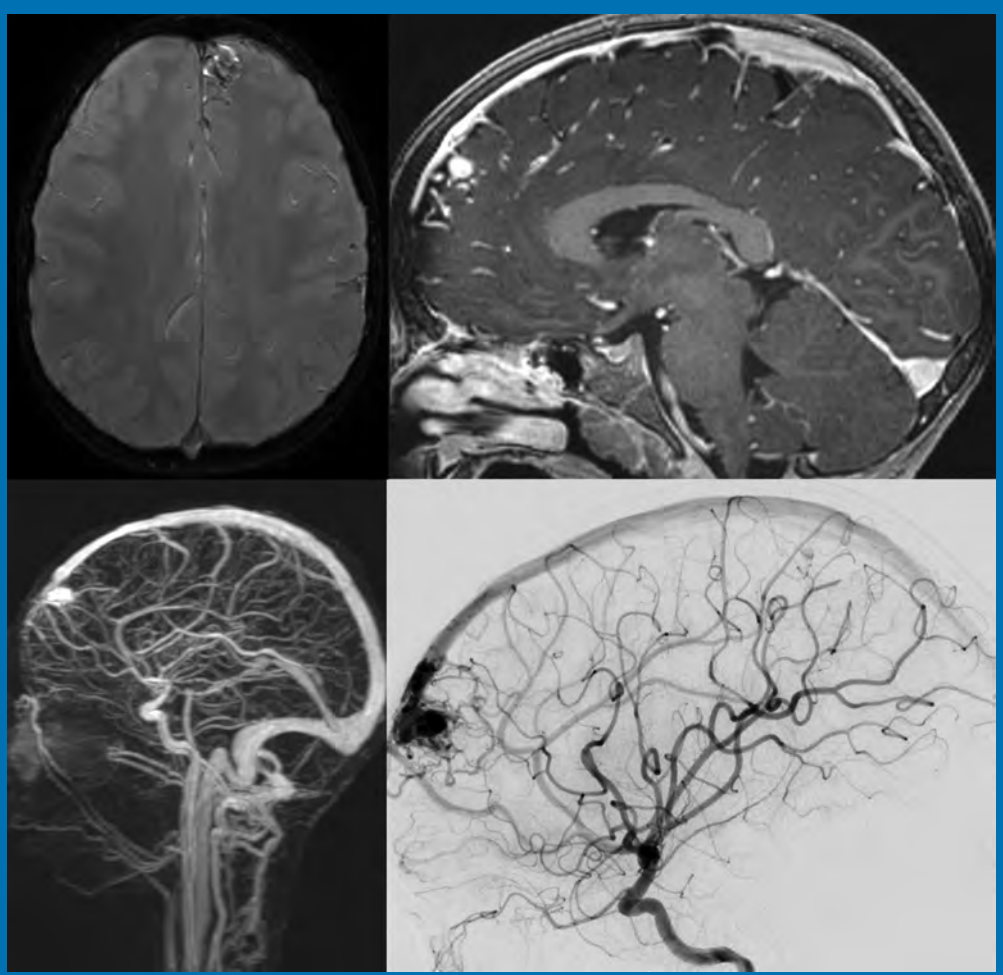

FRED™

Flow **R**e-**D**irection
Endoluminal **D**evice

FLOW DIVERSION.

SIMPLIFIED.

MicroVention™
TERUMO

MicroVention Worldwide Innovation Center
35 Enterprise
Aliso Viejo, CA 92656 USA
PH +1 714.247.8000

MicroVention UK Limted
PH +1 44 (0) 191 258 6777

MicroVention Europe S.A.R.L.
PH +33 (1) 39 21 77 46

MicroVention Deutschland GmbH
PH +49 211 210 798-0

Web
microvention.com

The New Standard of **Ease and Simplicity** in Flow Diversion Treatment.

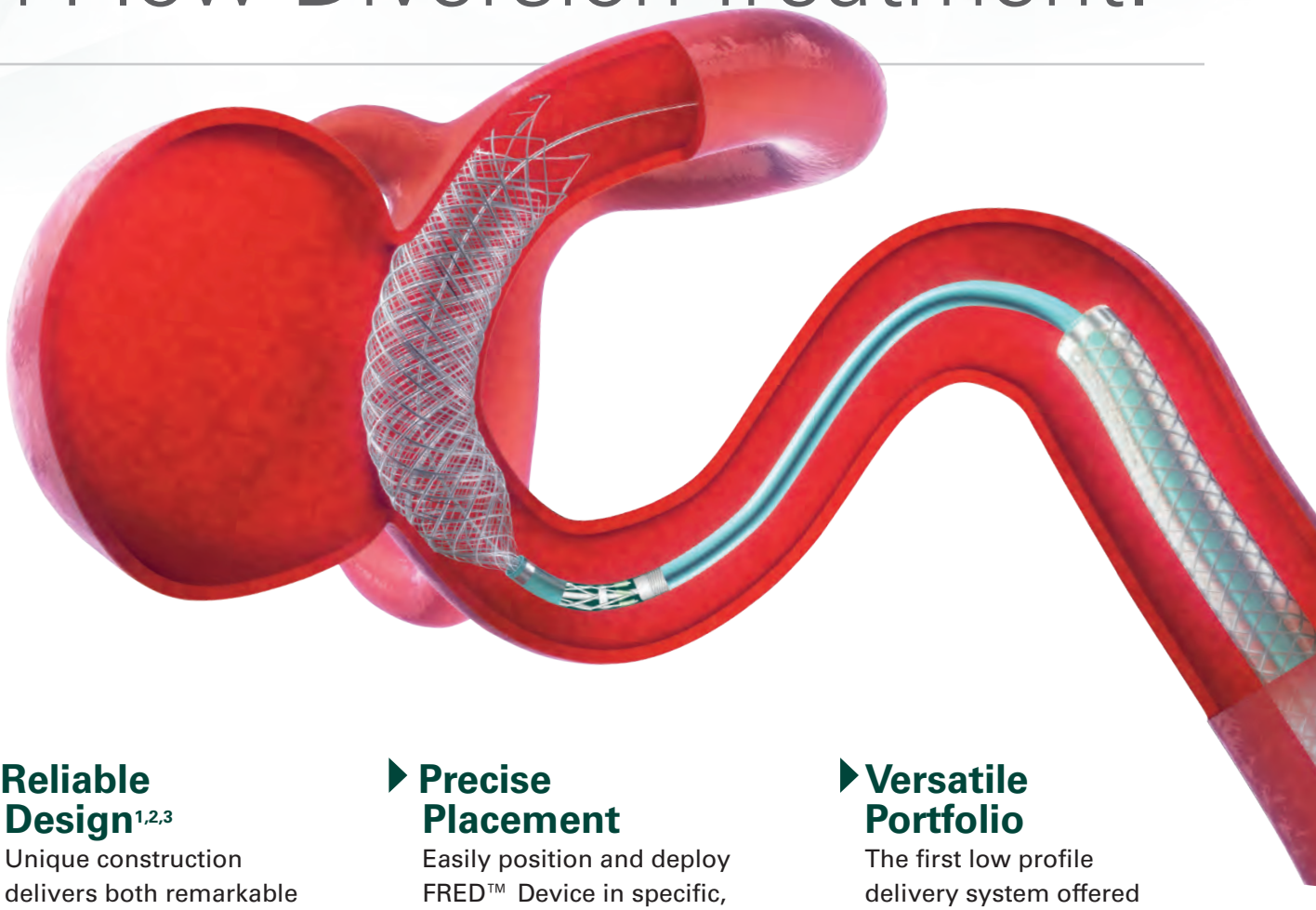

Reliable Design[1,2,3]

Unique construction delivers both remarkable ease of use and excellent flow diversion[1,2,3]

Precise Placement

Easily position and deploy FRED™ Device in specific, targeted locations[4,5,6]

Versatile Portfolio

The first low profile delivery system offered in combination with large diameter and long length options

References:
1. TR11-211 2. TR13-171 3. TR15-055 4. TR13-192 5. TR15-072 6. TR19-145

The Flow Re-Direction Endoluminal Device (FRED™) System is indicated for use in the internal carotid artery from the petrous segment to the terminus for the endovascular treatment of adult patients (22 years of age or older) with wide-necked (neck width ≥ 4 mm or dome-to-neck ratio < 2) saccular or fusiform intracranial aneurysms arising from a parent vessel with a diameter ≥ 2.0 mm and ≤ 5.0 mm.

Use of the FRED™ System is contraindicated under these circumstances: Patients in whom anticoagulant, anti-platelet therapy, or thrombolytic drugs are contraindicated. Patients with known hypersensitivity to metal such as nickel-titanium and metal jewelry. Patients with anatomy that does not permit passage or deployment of the FRED™ System. Patients with an active bacterial infection. Patients with a pre-existing stent in place at the target aneurysm. Patients in whom the parent vessel size does not fall within the indicated range. Patients who have not received dual anti-platelet agents prior to the procedure. For complete indications, contraindications, potential complications, warnings, precautions, and instructions, see instructions for use (IFU provided in the device).

RX Only: Federal (United States) law restricts this device to sale by or on the order of a physician.

We're Inside Every Great Neuroradiologist!

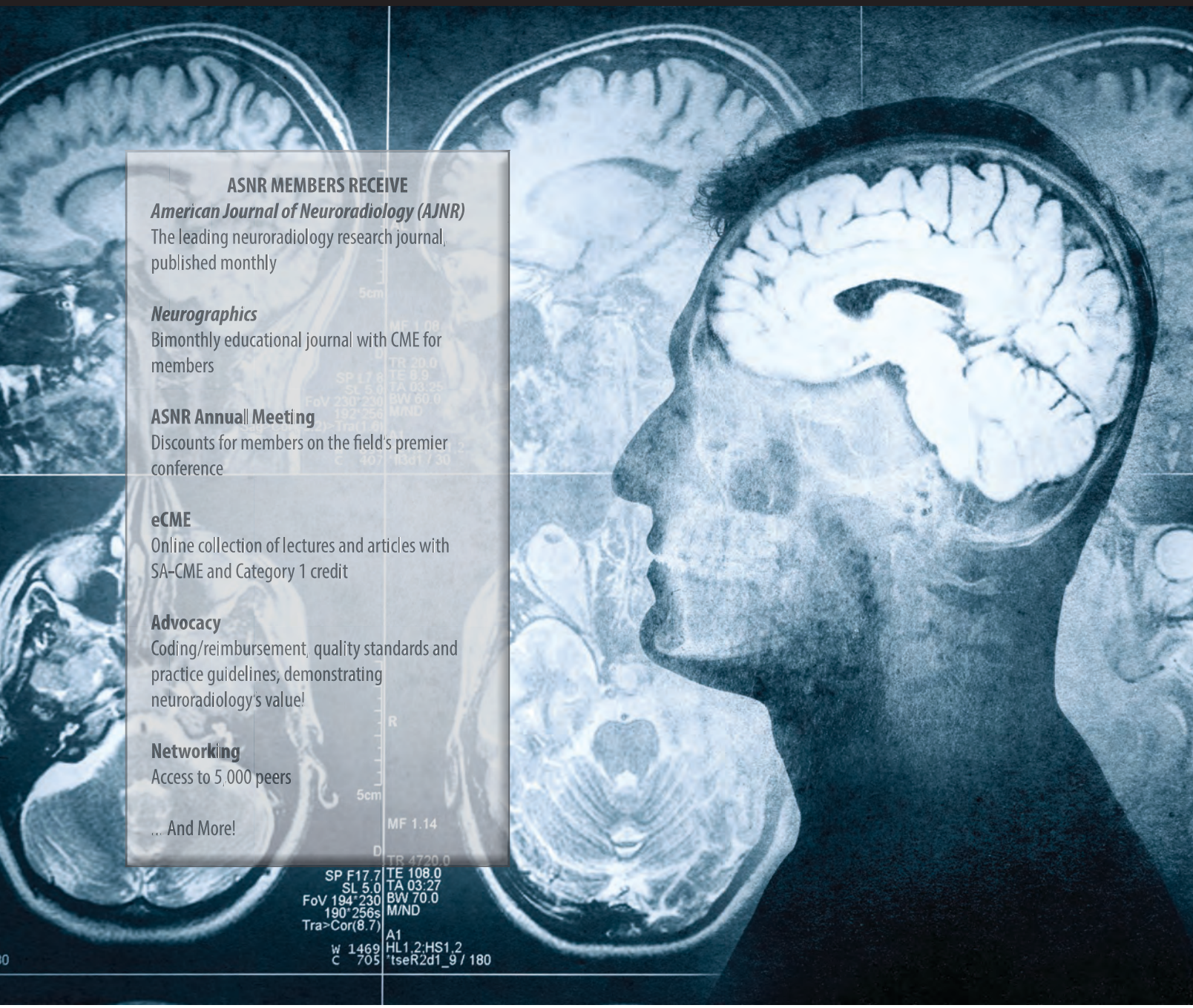

Join the leaders in neuroradiology today!
Learn more at www.asnr.org/join

ASNR
American Society of Neuroradiology

800 Enterprise Dr., Suite 205, Oak Brook, IL 60523 • (630)574-0220 • membership@asnr.org • www.asnr.org

Simplify
the MOC Process

Manage
your CME Credits Online

CMEgateway.org

Available to Members of Participating Societies

- American Board of Radiology (ABR)
- American College of Radiology (ACR)
- American Roentgen Ray Society (ARRS)
- American Society of Neuroradiology (ASNR)
- Commnission on Accreditation of Medical Physics Educational Programs, Inc. (CAMPEP)
- Radiological Society of North America (RSNA)
- Society of Interventional Radiology (SIR)
- SNM
- The Society for Pediatric Radiology (SPR)

It's Easy and Free!

Log on to CME Gateway to:

- View or print reports of your CME credits from multiple societies from a single access point.
- Print an aggregated report or certificate from each participating organization.
- Link to SAMs and other tools to help with maintenance of certification.

American Board of Radiology (ABR) participation!

By activating ABR in your organizational profile, your MOC–fulfilling CME and SAM credits can be transferred to your own personalized database on the ABR Web site.

Sign Up Today!

go to CMEgateway.org

AJNR go green

AJNR urges American Society of Neuroradiology members to reduce their environmental footprint by voluntarily suspending their print subscription.

The savings in paper, printing, transportation, and postage directly fund new electronic enhancements and expanded content.

The digital edition of *AJNR* presents the print version in its entirety, along with extra features including:

- **Publication Preview**
- **Case Collection**
- **Podcasts**
- **The *AJNR* News Digest**
- **The *AJNR* Blog**

It also reaches subscribers much faster than print. An electronic table of contents will be sent directly to your mailbox to notify you as soon as it publishes.

Readers can search, reference, and bookmark current and archived content 24 hours a day on www.ajnr.org.

ASNR members who wish to opt out of print can do so by using the AJNR Go Green link on the *AJNR* Website (http://www.ajnr.org/content/subscriber-help-and-services). Just type your name in the email form to stop print and spare our ecosystem.

AJNR

AMERICAN JOURNAL OF NEURORADIOLOGY

JUNE 2020
VOLUME 41
NUMBER 6
WWW.AJNR.ORG

Publication Preview at www.ajnr.org features articles released in advance of print. Visit www.ajnrblog.org to comment on AJNR content and chat with colleagues and AJNR's News Digest at http://ajnrdigest.org to read the stories behind the latest research in neuroimaging.

AJNR (Am J Neuroradiol ISSN 0195–6108) is a journal published monthly, owned and published by the American Society of Neuroradiology (ASNR), 800 Enterprise Drive, Suite 205, Oak Brook, IL 60523. Annual dues for the ASNR include approximately 21% for a journal subscription. The journal is printed by Cadmus Journal Services, 5457 Twin Knolls Road, Suite 200, Columbia, MD 21045; Periodicals postage paid at Oak Brook, IL and additional mailing offices. Printed in the U.S.A. POSTMASTER: Please send address changes to American Journal of Neuroradiology, P.O. Box 3000, Denville, NJ 07834, U.S.A. Subscription rates: nonmember $410 ($480 foreign) print and online, $320 online only; institutions $470 ($540 foreign) print and basic online, $935 ($1000 foreign) print and extended online, $380 online only (basic), $825 online only (extended); single copies are $35 each ($40 foreign). Indexed by PubMed/MEDLINE, BIOSIS Previews, Current Contents (Clinical Medicine and Life Sciences), EMBASE, Google Scholar, HighWire Press, Q-Sensei, RefSeek, Science Citation Index, SCI Expanded, Meta/CZI, ReadCube, and Semantic Scholar.

ONLINE FEATURES

LETTERS

BOOK REVIEWS *R.M. Quencer, Section Editor*

Please visit www.ajnrblog.org to read and comment on Book Reviews.

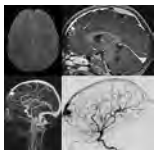

Multiple brain AVMs in HHT: SWI MR imaging (*top left*), 3D postgadolinium T1 (*top right*), time-resolved dynamic contrast-enhanced MRA (*bottom left*), and DSA (*bottom right*).

Indicates Editor's Choices selection

Indicates Fellows' Journal Club selection

Indicates open access to non-subscribers at www.ajnr.org

Indicates article with supplemental on-line table

Indicates article with supplemental on-line photo

Indicates article with supplemental on-line video

Evidence-Based Medicine Level 1

Evidence-Based Medicine Level 2

AJNR

AMERICAN JOURNAL OF NEURORADIOLOGY

Publication Preview at www.ajnr.org features articles released in advance of print. Visit www.ajnrblog.org to comment on AJNR content and chat with colleagues and AJNR's News Digest at http://ajnrdigest.org to read the stories behind the latest research in neuroimaging.

JUNE 2020 • VOLUME 41 • NUMBER 6 • WWW.AJNR.ORG

Title: Sunset in San Lorenzo–Ecuador. "San Lorenzo" is a peaceful and beautiful beach, known also as a surf spot and spectacular sunsets.

Maria Isabel Vargas, Neuroradiology Division, Geneva University Hospitals, Geneva, Switzerland

Gadolinium Deposition Safety: Seeking the Patient's Perspective

C.A. Mallio, C.C. Quattrocchi, À. Rovira, and P.M. Parizel

Gadolinium is a rare-earth metal of the lanthanide series; it is represented by the symbol Gd, and its atomic number is 64.[1,2] At room temperature, Gd is paramagnetic, meaning that it enhances nuclear relaxation rates, making it useful as a contrast agent for MR imaging. In clinical practice, Gd ions are administered to patients in the chelated form as gadolinium-based contrast agents (GBCA).[1,2]

GBCA were first introduced in the late 1980s. Because of the intrinsic toxicity of Gd salts, initial clinical trials focused on the stability of the complex between the Gd ion and the chelating agent. Early studies pointed out that the stability constant was much higher for macrocyclic (or cryptelates, as they were initially called) than for linear agents.[1,3] These concerns never received much attention because all linear and macrocyclic agents appeared to be safe and well-tolerated. Moreover, because macrocyclic GBCA were only available in Europe and not in North America, there appeared to be little scientific incentive to study these concerns further. In fact, GBCA were considered so safe that they were used in large volumes as intra-arterial contrast agents for conventional angiography in patients with iodine allergy.[4] Indeed, double-dose GBCA were also commonly applied for gadolinium-enhanced MR angiography studies. These practices all changed in 2006, when a possible causation was identified between GBCA and nephrogenic systemic fibrosis (NSF).[5] NSF is characterized by fibrosis of the skin and internal organs, and the symptoms are somewhat reminiscent of scleroderma or scleromyxedema, though the underlying pathology is different. In this respect, credit should be given to Cowper et al[6] for a very early and brilliant description of NSF.

The first cases of NSF had already been described earlier, but the possible causation between NSF and GBCA in patients with renal insufficiency was first reported in 2006.[5] Next, in 2006, the FDA restricted the use of GBCA in patients with a glomerular filtration rate of <60 mL and <15 mL/min/1.73 m^2;[7] the cutoff then proposed in 2007 was <30 mL/min/1.72 m^2.

Due to these measures, NSF has become very rare, and GBCA were, once again, considered very safe agents in patients with normal renal function.

Brain Gadolinium Deposition

New concerns have been raised in the past 5 years due to mounting evidence of unexpected central nervous system gadolinium deposition after serial administrations of GBCA.[8-11] The phenomenon was found to be greater in the dentate nucleus of the cerebellum and the globus pallidus of patients exposed to several doses of GBCA with a linear structure.[9,12,13] In fact, GBCA with a macrocyclic structure are known to have higher thermodynamic, kinetic, and conditional stability with respect to the linear ones, and these features have been suggested to mitigate the tendency of deposition.[14,15] Given that there are differences in the rates of deposition between linear and macrocyclic agents, slight differences among macrocyclic GBCA have been suggested in studies based on murine models.[13,16] Specifically, lower gadolinium concentrations were found after exposure to gadoteridol compared with gadoterate and gadobutrol, especially in the cerebellum, cerebrum, and kidneys.[16]

Despite the higher degree of gadolinium deposition, nonionic linear GBCA (eg, gadodiamide) showed the lowest rate of immediate allergic adverse events compared with ionic linear and nonionic macrocyclic GBCA.[17]

On the basis of the global use of GBCA and the concern for gadolinium deposition into brain tissue, different countries have implemented various strategies. The European Union removed the GBCA with a linear structure for general use from the market in 2017 after a 3-year multistage evaluation process.[18] In Japan, linear ligands were proposed only as an alternative when macrocyclic agents were contraindicated for clinical reasons.[19] In many other countries, such as the United States and China comprising most of the world's population, instead there have been no formal changes in the regulatory standing of the use of GBCA other than education and notices/warnings of the potential retention with unknown and unclear clinical relevance, if any, together with a call for more research on the issue.

In parallel, imaging scientists from academia and industry have developed new avenues of research, endeavoring to understand the mechanism of the phenomenon and to mitigate gadolinium deposition. Three main topics currently are the following: 1) the validation of alternative contrast molecules not containing gadolinium;[20] 2) unenhanced MR imaging techniques with quantitative image analyis, aiming to carry gadolinium-analog information;[21,22] and 3) synthetic enhanced MR imaging using very low doses of available GBCA.[23] These approaches are valid and will take brain MR imaging various steps forward in the years to come. However, the main issue is what to do about brain gadolinium deposition or, even more important, providing answers to what matters most to patients, in terms of clinical consequences on their neurologic function or the clinical effects in other sites such as skin, liver, kidney and bone.

Indeed, what remains to be proved, of great importance to patients, is whether there is any impact on cell/tissue function from the small amounts of gadolinium deposited. The current available data on clinical consequences are mainly based on clinical retrospective studies involving large cohorts (ie, 99,739 patients receiving at least 1 dose of GBCA)[24] or those including highly exposed patients (ie, 4 patients receiving at least 50 injections of GBCA).[25] These studies failed to demonstrate an association of brain gadolinium deposition with worsening of neurologic or neuropsychological status.[24,25] Also, studies applying imaging techniques to evaluate brain microstructural and functional integrity, such as sodium MR imaging,[26] resting-state functional MR imaging connectivity,[27] and

http://dx.doi.org/10.3174/ajnr.A6586

diffusion-weighted imaging,[28] showed the absence of tissue changes in the visually hyperintense dentate nuclei on unenhanced T1-weighted images after cumulative doses of GBCA. These findings were in agreement with cellular viability data obtained with histologic studies.[13,29] Thus, it seems that the gadolinium deposition observed in the brains of serially injected patients differs from that causing NSF in terms of clinical consequences.

What Matters to Patients

What matters to patients is still the main open question. Patients should be informed that there is no documented clinical risk related to gadolinium deposition in their brains and that there is substantial convergent agreement on this subject among international institutions such as the FDA,[30] European Medicines Agency (EMA),[18] and American College of Radiology, together with the American Society of Neuroradiology,[31] International Society for Magnetic Resonance in Medicine,[32] and European Society for Magnetic Resonance in Medicine and Biology–Gadolinium Research & Education Committee.[33]

Thus, by summarizing the content, interpreting the meaning of the recommendations offered by several authorities, and integrating these into clinical practice, we identified 4 major points: 1) The indication, feasibility, appropriateness, and necessity of GBCA to solve each clinical question must be investigated, controlled, and validated (including a risk-benefit analysis for each patient) by the on-site radiologist or neuroradiologist; 2) each patient should be fully informed on all relevant and updated information about GBCA safety by the on-site radiologist or neuroradiologist before undergoing the MR study; 3) GBCA should be used according to the national regulations on a local basis; and 4) as for the gadolinium deposition in the brain, there is no direct proof of a causal relationship with an impact on neurologic and neurocognitive functions.

While further research on the clinical consequences of gadolinium deposition should be promoted, it remains to be elucidated whether the presence of deposited gadolinium represents a vulnerable condition in patient groups with neurodegeneration either related to aging and/or progression of chronic diseases.

There is evidence of gadolinium deposition, with even higher concentrations, in human tissue beyond the brain, including bone,[34] skin,[35] and liver.[36] The clinical meaning of this deposition is still under scrutiny; however, no direct relationship of causality with severe adverse consequences has been reported to date. Moreover, an increased signal intensity of the anterior pituitary gland, not yet confirmed to be caused by tissue gadolinium deposition, was recently reported in patients who had undergone serial injections of gadodiamide.[37]

Last, a constellation of symptoms self-reported by patients after exposure to GBCA was identified in 2016 under the suggested definition of gadolinium deposition disease (GDD).[38] The symptoms referred to as GDD included headache, brain fog, fatigue, bone pain, central torso pain, subcutaneous tissue thickening, and tightness of hand and foot with a gloves-and-socks pattern. In this respect, a recent study showed no statistically significant different incidence of GDD symptoms between gadodiamide (linear) and gadoterate meglumine (macrocyclic).[39] Given the well-known difference in terms of deposition between linear and macrocyclic GBCA, this finding points to a different pathway between exposure to GBCA and reports of symptoms that some think should be attributed to gadolinium exposure.

CONCLUSIONS

Scientifically available information about the safety and stability constant of the compounds, together with clinical, functional, and structural data after serial GBCA injections, as well as technical development geared to dose reduction (or altogether elimination of GBCA if proved to be unnecessary in specific clinical scenarios), must be taken into account and integrated to provide an answer as to what matters most to patients.

Even if what really counts is whether retained gadolinium in the brain and body is harmful, and, to date, no proved causation with permanent severe adverse effects has been reported in patients, we should keep investigating the topic, and if the current standard practice can be outperformed using different strategies, we should definitely go for it.

Disclosures: Alex Rovira—*UNRELATED*: *Board Membership*: Bayer AG, Biogen, Novartis, Icometrix, Roche; *Payment for Lectures Including Service on Speakers Bureaus*: Sanofi Genzyme, Merck Serono, Teva Pharmaceutical Industries Ltd, Novartis, Roche, Biogen; *Payment for Development of Educational Presentations*, money was paid to defray expenses for travel, lodging and registration: Sanofi Genzyme, Merck Serono, Novartis, Roche, Biogen. Paul M. Parizel—*Other Relationships*: I have, in the past, participated as a speaker in symposia and courses that were cosponsored by the industry (Bracco, Guerbet, Schering, GE Healthcare), but not in the past 3 years, and never in relationship to the topic of this editorial.

REFERENCES

1. Parizel PM, Degryse HR, Gheuens J, et al. **Gadolinium-DOTA enhanced MR imaging of intracranial lesions.** *J Comput Assist Tomogr* 1989;13:378–85 CrossRef Medline
2. Aime S, Caravan P. **Biodistribution of gadolinium-based contrast agents, including gadolinium deposition.** *J Magn Reson Imaging* 2009;30:1259–67 CrossRef Medline
3. Knop RH, Frank JA, Dwyer AJ, et al. **Gadolinium cryptelates as MR contrast agents.** *J Comput Assist Tomogr* 1987;11:35–42 CrossRef Medline
4. Spinosa DJ, Kaufmann JA, Hartwell GD. **Gadolinium chelates in angiography and interventional radiology: a useful alternative to iodinated contrast media for angiography.** *Radiology* 2002;223:319–25 CrossRef Medline
5. Grobner T. **Gadolinium: a specific trigger for the development of nephrogenic fibrosing dermopathy and nephrogenic systemic fibrosis?** *Nephrol Dial Transplant* 2006;21:1104–08 CrossRef Medline
6. Cowper SE, Robin HS, Steinberg SM, et al. **Scleromyxoedema-like cutaneous diseases in renal-dialysis patients.** *Lancet* 2000;356:1000–01 CrossRef Medline
7. **FDA ALERT. Gadolinium-Based Contrast Agents for Magnetic Resonance Imaging Scans.** 2006. https://www.ismrm.org/special/FDA%20gadolinium1206.pdf. Accessed March 4, 2020
8. Kanda T, Ishii K, Kawaguchi H, et al. **High signal intensity in the dentate nucleus and globus pallidus on unenhanced T1-weighted MR images: relationship with increasing cumulative dose of a gadolinium-based contrast material.** *Radiology* 2014;270:834–41 CrossRef Medline
9. Quattrocchi CC, Mallio CA, Errante Y, et al. **Gadodiamide and dentate nucleus T1 hyperintensity in patients with meningioma evaluated by multiple follow-up contrast-enhanced magnetic resonance examinations with no systemic interval therapy.** *Invest Radiol* 2015;50:470–72 CrossRef Medline
10. McDonald RJ, McDonald JS, Kallmes DF, et al. **Gadolinium deposition in human brain tissues after contrast-enhanced MR imaging**

in adult patients without intracranial abnormalities. *Radiology* 2017;285:546–54 CrossRef Medline
11. Mallio CA, Ramalho J, Quattrocchi CC. **Impact of brain irradiation, chemotherapy, and presence of primary brain tumors on changes in signal intensity after exposure to gadolinium-based contrast agents.** *Radiology* 2019;290:575–76 CrossRef Medline
12. Errante Y, Cirimele V, Mallio CA, et al. **Progressive increase of T1 signal intensity of the dentate nucleus on unenhanced magnetic resonance images is associated with cumulative doses of intravenously administered gadodiamide in patients with normal renal function, suggesting dechelation.** *Invest Radiol* 2014;49:685–90 CrossRef Medline
13. Lohrke J, Frisk AL, Frenzel T, et al. **Histology and gadolinium distribution in the rodent brain after the administration of cumulative high doses of linear and macrocyclic gadolinium-based contrast agents.** *Invest Radiol* 2017;52:324–33 CrossRef Medline
14. Frenzel T, Lengsfeld P, Schirmer H, et al. **Stability of gadolinium-based magnetic resonance imaging contrast agents in human serum at 37°C.** *Invest Radiol* 2008;43:817–28 CrossRef Medline
15. Dekkers IA, Roos R, van der Molen AJ. **Gadolinium retention after administration of contrast agents based on linear chelators and the recommendations of the European Medicines Agency.** *Eur Radiol* 2018;28:1579–84 CrossRef Medline
16. Bussi S, Coppo A, Botteron C, et al. **Differences in gadolinium retention after repeated injections of macrocyclic MR contrast agents to rats.** *J Magn Reson Imaging* 2018;47:746–52 CrossRef Medline
17. Behzadi AH, Zhao Y, Farooq Z, et al. **Immediate allergic reactions to gadolinium-based contrast agents: a systematic review and meta-analysis.** *Radiology* 2018;286:471–82 CrossRef Medline
18. European Medicines Agency. **EMA's final opinion confirms restrictions on use of linear gadolinium agents in body scans (21 July 2017).** https://www.ema.europa.eu/en/documents/referral/gadolinium-article-31-referral-emas-final- opinion-confirms-restrictions-use-linear-gadolinium-agents_en-0.pdf. Accessed January 9, 2020
19. Pharmaceuticals and Medical Devices Agency. **Report on the investigation results.** Published November 11, 2017. https://www.pmda.go.jp/files/000221379.pdf. Accessed January 9, 2020
20. Shen Z, Wu A, Chen X. **Iron oxide nanoparticle-based contrast agents for magnetic resonance imaging.** *Mol Pharm* 2017;14:1352–64 CrossRef Medline
21. Amukotuwa SA, Marks MP, Zaharchuk G, et al. **Arterial spin-labeling improves detection of intracranial dural arteriovenous fistulas with MRI.** *AJNR Am J Neuroradiol* 2018;39:669–77 CrossRef Medline
22. Delgado AF, Delgado AF, De Luca F, et al. **Arterial spin-labeling in children with brain tumor: a meta-analysis.** *AJNR Am J Neuroradiol* 2018;39:1536–42 CrossRef Medline
23. Gong E, Pauly JM, Wintermark M, et al. **Deep learning enables reduced gadolinium dose for contrast-enhanced brain MRI.** *J Magn Reson Imaging* 2018;48:330–40 CrossRef Medline
24. Welk B, McArthur E, Morrow SA, et al. **Association between gadolinium contrast exposure and the risk of parkinsonism.** *JAMA* 2016;316:96–98 CrossRef Medline
25. Vymazal J, Krámská L, Brozõová H, et al. **Does serial administration of gadolinium-based contrast agents affect patient neurological and neuropsychological status? Fourteen-year follow-up of patients receiving more than fifty contrast administrations.** *J Magn Reson Imaging* 2019 Oct 30. [Epub ahead of print] CrossRef Medline
26. Eisele P, Konstandin S, Szabo K, et al. **Sodium MRI of T1 high signal intensity in the dentate nucleus due to gadolinium deposition in multiple sclerosis.** *J Neuroimaging* 2017;27:372–75 CrossRef Medline
27. Mallio CA, Piervincenzi C, Gianolio E, et al. **Absence of dentate nucleus resting-state functional connectivity changes in nonneurological patients with gadolinium-related hyperintensity on T1-weighted images.** *J Magn Reson Imaging* 2019;50:445–55 CrossRef Medline
28. Eisele P, Szabo K, Ebert A, et al. **Diffusion-weighted imaging of the dentate nucleus after repeated application of gadolinium-based contrast agents in multiple sclerosis.** *Magn Reson Imaging* 2019;58:1–5 CrossRef Medline
29. Fingerhut S, Sperling M, Holling M, et al. **Gadolinium-based contrast agents induce gadolinium deposits in cerebral vessel walls, while the neuropil is not affected: an autopsy study.** *Acta Neuropathol* 2018;136:127–38 CrossRef Medline
30. **FDA warns that gadolinium-based contrast agents (GBCA) are retained in the body; requires new class warnings.** https://www.fda.gov/drugs/drug-safety-and-availability/fda-drug-safety-communication-fda-warns-gadolinium-based-contrast-agents-gbcas-are-retained-body. Accessed January 9, 2020
31. **ACR–ASNR Position Statement on the use of gadolinium contrast agents. Manual on Contrast Media Version 10.3.** https://www.acr.org/-/media/ACR/files/clinical-resources/contrast_media.pdf. Accessed January 9, 2020
32. Gulani V, Calamante F, Shellock FG, et al; International Society for Magnetic Resonance in Medicine. **Gadolinium deposition in the brain: summary of evidence and recommendations.** *Lancet Neurol* 2017;16:564–70 CrossRef Medline
33. Quattrocchi CC, Ramalho J, van der Molen AJ, et al; GREC, European Gadolinium Retention Evaluation Consortium and the ESNR, European Society of Neuroradiology. **Standardized assessment of the signal intensity increase on unenhanced T1-weighted images in the brain: the European Gadolinium Retention Evaluation Consortium (GREC) Task Force position statement.** *Eur Radiol* 2019;29:3959–67 CrossRef Medline
34. Darrah TH, Prutsman-Pfeiffer JJ, Poreda RJ, et al. **Incorporation of excess gadolinium into human bone from medical contrast agents.** *Metallomics* 2009;1:479–88 CrossRef Medline
35. Roberts DR, Lindhorst SM, Welsh CT, et al. **High levels of gadolinium deposition in the skin of a patient with normal renal function.** *Invest Radiol* 2016;51:280–89 CrossRef Medline
36. Maximova N, Gregori M, Zennaro F, et al. **Hepatic gadolinium deposition and reversibility after contrast agent-enhanced MR imaging of pediatric hematopoietic stem cell transplant recipients.** *Radiology* 2016;281:418–26 CrossRef Medline
37. Mallio CA, Lo Vullo G, Messina L, et al. **Increased T1 signal intensity of the anterior pituitary gland on unenhanced magnetic resonance images after chronic exposure to gadodiamide.** *Invest Radiol* 2020;55:25–29 CrossRef Medline
38. Semelka RC, Ramalho J, Vakharia A, et al. **Gadolinium deposition disease: Initial description of a disease that has been around for a while.** *Magn Reson Imaging* 2016;34:1383–90 CrossRef Medline
39. Parillo M, Sapienza M, Arpaia F, et al. **A structured survey on adverse events occurring within 24 hours after intravenous exposure to gadodiamide or gadoterate meglumine: a controlled prospective comparison study.** *Invest Radiol* 2019;54:191–97 CrossRef Medline

MR-Eye: High-Resolution Microscopy Coil MRI for the Assessment of the Orbit and Periorbital Structures, Part 1: Technique and Anatomy

N.W. Dobbs, M.J. Budak, R.D. White, and I.A. Zealley

ABSTRACT

SUMMARY: Microscopy coil MR imaging of the orbits has been described previously as a technique for anatomic depiction. In the first part of this 2-part series, the improvement in spatial resolution that the technique offers compared with conventional MR imaging of the orbits is demonstrated. We provide a guide to implementing the technique, sharing pearls and pitfalls gleaned from our own practice to make implementation of microscopy coil MR imaging at your own center easy. As a quick reference guide to the small-scale structures encountered when reading the studies, a short anatomy section is included, which doubles as a showcase for the high-quality imaging that can be obtained. In the second part, our experience of microscopy coil MR imaging in day-to-day clinical practice takes it far beyond being a useful anatomic educational tool. Through a series of interesting cases, we highlight the added benefit of microscopy coil MR imaging compared with standard orbital MR imaging.

ABBREVIATION: MC-MRI = microscopy coil MR imaging

Imaging of orbital and periorbital structures and pathologies presents challenges due to the various limitations intrinsic to ultrasound, CT, and conventional MR imaging.[1,2] Management of structural pathology in and around the orbit is guided by knowledge of the compartments involved and the tissue of origin.[3] Both the initial surgical approach[4] and subsequent reconstruction techniques are influenced by factors that can only be resolved at a very small scale, sometimes at submillimeter resolution. Changes of this order cannot be resolved using CT or conventional head coil MR imaging, while ultrasound is limited to demonstration of soft tissues only and cannot demonstrate relationships with bony structures.

The use of microscopy coil MR imaging (MC-MR imaging) to depict orbital anatomy has previously been reported, generally for research studies.[5-7] In this 2-part article, we first aimed to equip the reader with an understanding of MC-MR imaging techniques to enable implementing this simple, straightforward imaging at his or her own institution. We also aimed to refresh and expand the reader's knowledge of orbital anatomy, essential for interpretation of MC-MR images. Pearls and pitfalls of the technique that we have gleaned from everyday practice are shared, to make implementation of the technique easier.

In Part 2, in addition to using MC-MR imaging as a tool for anatomic depiction, we explore the benefits of using MC-MR imaging in everyday clinical practice. We have previously described the application of MC-MR imaging in preoperative planning for Mohs micrographic surgery for nasofacial skin neoplasms.[2] Collaboration with ophthalmic surgeons has extended our practice to provide high-resolution imaging of the orbits and surrounding structures.

Figure 1 demonstrates the striking difference in image resolution between conventional head coil orbital MR imaging and MC-MR imaging. The high spatial resolution offered means that the ophthalmic surgeons at our institution believe that they can better plan surgical procedures and preserve structures that are difficult or impossible to reconstruct, while at the same time maximizing the accuracy of resection margins.

Technique

By means of a small radiofrequency receiver coil placed in close proximity to the orbit structures, a voxel size of 300 μm can be resolved with high SNR. This high SNR is maintained down to the orbital apex, beyond which signal loss becomes an issue and supplementary head coil imaging may be required. As we have previously described for the imaging of nasofacial lesions,[2] we

Received July 18, 2019; accepted after revision January 21, 2020.

From the Department of Clinical Neuroscience (N.W.D.), Western General Hospital, Edinburgh, United Kingdom; Qscan Radiology Clinics (M.J.B.), Gold Coast, Australia; Department of Clinical Radiology (R.D.W.), University Hospital of Wales, Cardiff, United Kingdom; and Department of Clinical Radiology (I.A.Z.), Ninewells Hospital, Dundee, United Kingdom.

Please address correspondence to Nicholas W. Dobbs, MBBS, Department of Clinical Neuroscience, Western General Hospital, Edinburgh, United Kingom; e-mail: nicholas.dobbs@nhs.net

Indicates open access to non-subscribers at www.ajnr.org

http://dx.doi.org/10.3174/ajnr.A6495

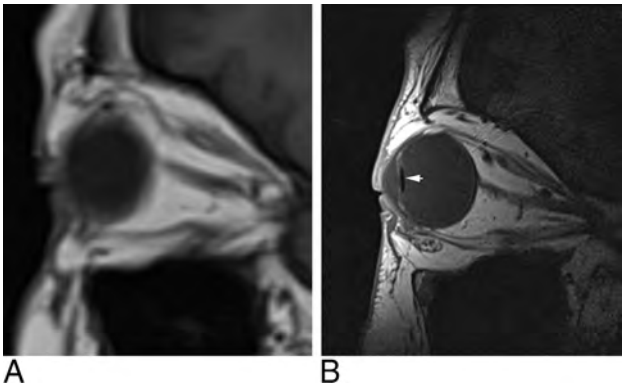

FIG 1. The difference between conventional T1-weighted sagittal imaging with a head coil (*A*) and MC-MR imaging T1-weighted sagittal imaging (*B*). In this patient, a lens prosthesis (*white arrow*) inserted during cataract surgery is demonstrated.

Sequence parameters

Parameters for MC-MR Imaging		
Parameter	T1-Weighted TSE	T2-Weighted TSE
TR (ms)	400	4000
TE (ms)	15	123
Signals averaged	2	3
FOV (mm)	80 × 70	80 × 70
Martrix	224 × 256	224 × 256
Section thickness (mm)	1	1.5
Turbo factor	3	13
Voxel size (mm)	0.3 × 0.3 × 1.5	0.3 × 0.3 × 1.5
Acquisition time	5 min, 42 sec	7 min, 6 sec

use a 40-mm-internal-diameter small-loop radiofrequency receiver coil with a 1.5T MR imaging unit (Magnetom Avanto; Siemens, Erlangen, Germany). This has 32 receiver channels and SQ-engine gradients (maximum gradient field strength, 45 mT/m; slew rate, 200 T/m/s). Sequence parameters are described in the Table.

Our standard imaging consists of optimized T1-weighted and T2-weighted TSE sequences with 0.3 × 0.3 mm pixel size and 1.5-mm section thickness acquired with no intersection gaps. Images can be acquired in any plane depending on the structures to be assessed. We have found that axial acquisitions are optimal to demonstrate the nasal bone, tarsal plate, optic nerve, and the medial and lateral rectus muscles. Sagittal acquisitions are useful for depiction of the orbital septum and the levator apparatus, as well as the superior and inferior rectus muscles. Coronal acquisitions provide an excellent overview of the extraocular muscles, the optic nerve, and any intraconal lesion extension. The presence of orbital fat around most structures means that, generally speaking, T1-weighted imaging delivers the best depiction of structural involvement, with T2-weighted and occasionally T1-weighted fat-saturation sequences used to aid lesion characterization if this is required.

With T1-weighted acquisitions taking >5 minutes, and T2-weighted acquisitions, >7 minutes, movement needs to be minimized to make the best use of the high SNR to deliver high-resolution imaging. Thus, while we make every effort to ensure

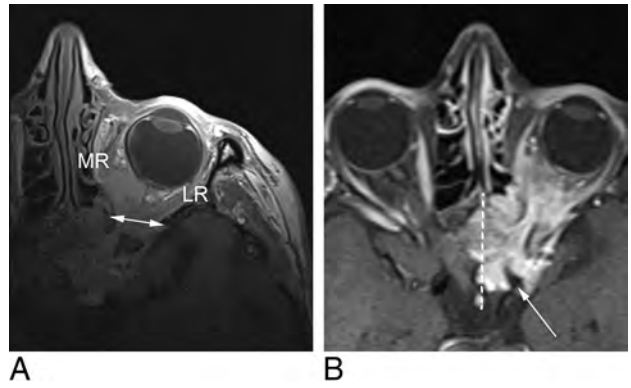

FIG 2. *A*, MC-MR imaging T1-weighted axial image demonstrates a sphenoid wing meningioma, engulfing the optic nerve as well as the medial (MR) and lateral rectus (LR) muscles. MC-MR imaging demonstrates widening of the superior orbital fissure (*double-headed arrow*), but beyond the orbital apex, the signal-to-noise ratio is low. *B*, Head coil T1-weighted fat-saturation postcontrast axial image demonstrates the lesion surrounding the left internal carotid artery (*white arrow*), infiltrating the left cavernous sinus and extending past the midline (*dotted white line*) in the intercavernous sinus.

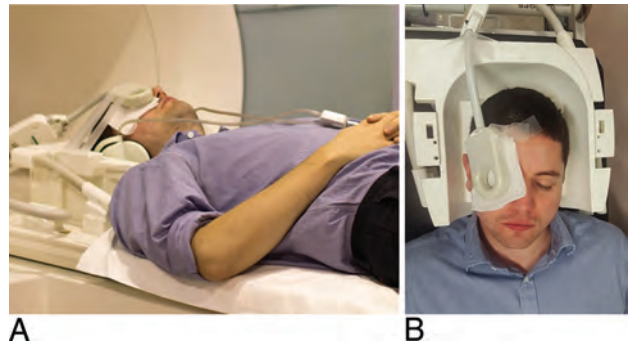

FIG 3. Correct patient and coil positioning. Photographs of the author (N.W.D.) showing final patient and coil positioning in the imaging magnet with headphones wedged against head coil for immobilization (*A*) and coil positioning over the orbit with extensive taping (*B*).

patient comfort, robust immobilization, essential for good-quality MC-MR imaging, is applied surreptitiously and with great care. The patient is positioned head first in the scanner bore with the head in the posterior portion of a head coil. In addition to offering some immobilization, this framework also allows easy transition to standard head coil imaging if required for lesions extending deep to the orbital apex (Fig 2).

Headphones are used both to help relax the patient and to minimize lateral head movement by having the headphones positioned flush against the head coil. Once the head is immobilized, gauze pads are placed over the orbit for comfort and the receiver coil is taped firmly in place on top of the gauze pads (Fig 3). When we first developed our MC-MR imaging technique for the orbits, we also used the anterior portion of the head coil to further immobilize the patient. However, doing this led to excessive eye movement, compromising image quality.

Despite the long acquisition times, unavoidable small involuntary eye movements appear to have relatively little impact on the image quality. When movement artifacts do become an

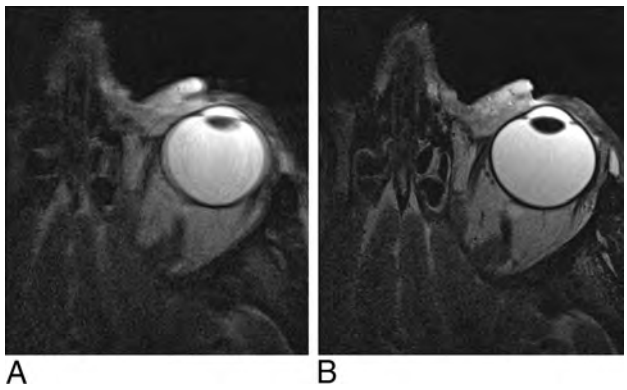

FIG 4. Persistence pays off with movement artifacts. *A*, T2-weighted axial image of the orbit with image degradation due to movement artifacts. *B*, The same patient and same imaging protocol, after ensuring patient comfort.

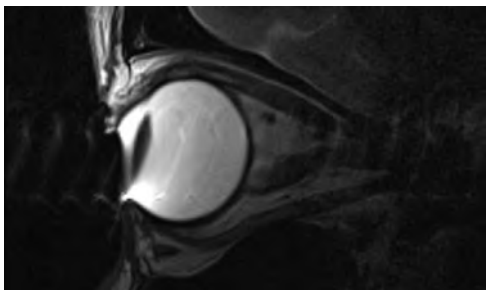

FIG 5. MC-MR imaging T2-weighted sagittal image degraded by metallic artifacts from mascara.

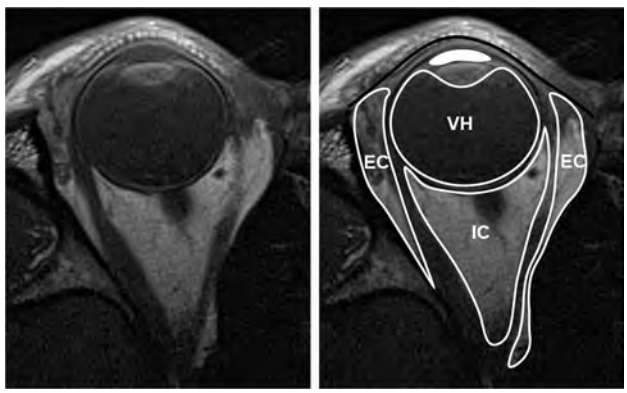

FIG 6. Compartmental anatomy shown by MC-MR imaging T1-weighted axial image, original on the left and annotated on the right. The *solid black line* indicates the orbital septum, defined by native high signal of the tarsal plate; EC, extraconal space, external to the extraocular muscles; IC, intraconal space, inside the extraocular muscles; VH, vitreous humor, behind the lens; *solid white fill*, aqueous humor, anterior to the lens and ciliary muscles.

issue, taking the time to assess any causative factor or patient discomfort is often effective (Fig 4). Most important, no cosmetics should be worn due to the artifacts arising from metallic elements in these products, particularly mascara (Fig 5).

The capital outlay required to purchase a small-loop receiver coil is small, and at Ninewells Hospital, the coil was

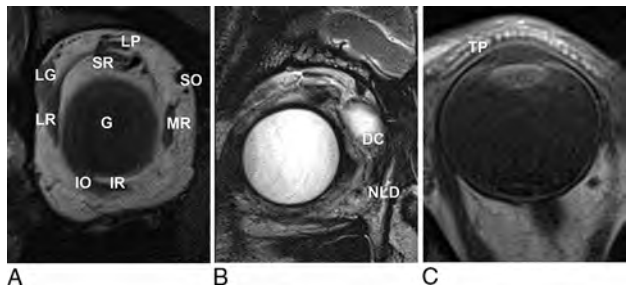

FIG 7. *A*, T1-weighted coronal MC-MR image. LG indicates the lacrimal gland, positioned superolaterally in the orbit, lying directly inferior to the orbital rim; LP, levator palpebrae superioris muscle; SR, superior rectus muscle; SO, superior oblique tendon; MR, medial rectus muscle; IR, inferior rectus muscle; IO, inferior oblique muscle; LR, lateral rectus muscle; G, globe. *B*, T2-weighted coronal MC-MR image. In this patient, a protruding dermoid cyst (DC) caused epiphora, filling the nasolacrimal duct (NLD) and allowing its demonstration with high signal on T2-weighted imaging. *C*, T1-weighted axial MC-MR image illustrates the high-signal dots of the meibomian glands within the tarsal plate (TP).

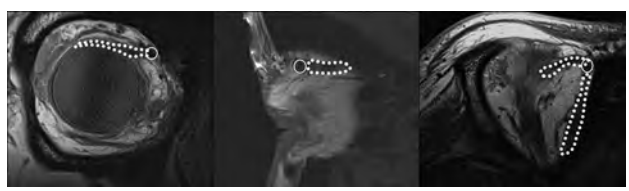

FIG 8. T1-weighted MC-MR images in the coronal, sagittal, and axial planes demonstrating the course of the superior oblique muscle and tendon (*dotted line*) through the trochlea (*circle*).

found unused on a shelf. The case-by-case cost is also low, with a scanner time for a 3-sequence examination of <20 minutes. We have found it best to use MC-MR imaging for the imaging of orbital lesions; through its high spatial and contrast resolution, MC-MR imaging can assess the relationship of a lesion to normal anatomic structures in detail sufficient to more confidently guide an appropriate clinical and surgical approach. However, the signal-to-noise ratio beyond the orbital apex is low (Fig 2). For lesions that extend beyond this point, MC-MR imaging can be used as an optional adjunct to traditional imaging if the extra-anatomic information provided stands to influence surgical options.

Orbital Anatomy

A detailed understanding of orbital anatomy is essential for describing the salient features that the ophthalmic surgeon requires for diagnosis, determining the extent of disease, and preoperative planning. MC-MR imaging allows depiction of this anatomy, from basic compartmental anatomy (Fig 6), muscular anatomy (Fig 7*A*) including the complex course of the superior oblique muscle (Fig 8), and beyond.

Vision relies on a smooth refractive surface maintained by the ocular surface system—a triple-layer tear film.[8,9] The most superficial is an oily lipid layer, produced by the meibomian glands of the tarsal plate, which reduce evaporation from the aqueous layer below, which is produced by the lacrimal gland (Fig 7).[8] Due to

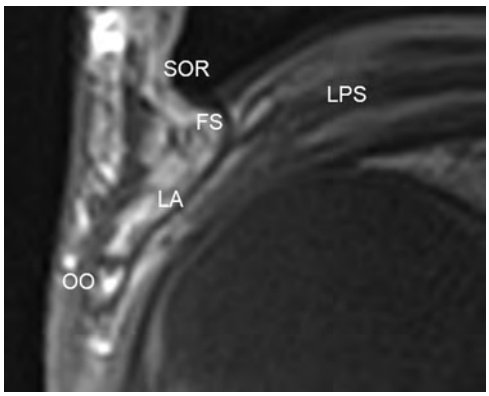

FIG 9. The levator aponeurosis shown on MC-MR imaging T1-weighted sagittal image. SOR indicates superior orbital rim; LPS, levator palpebrae superioris; FS, fibrous orbital septum; LA, levator aponeurosis; OO, orbicularis oculi.

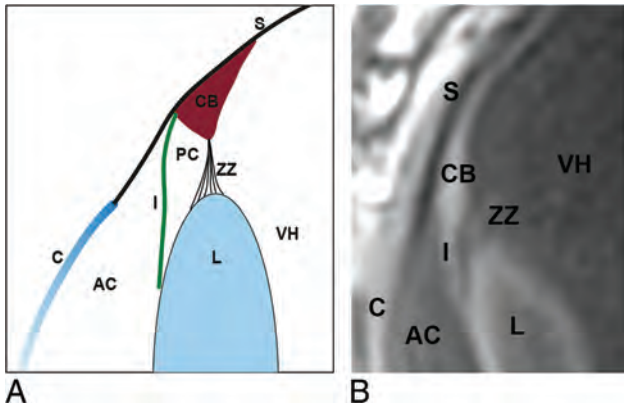

FIG 10. Diagrammatic sagittal representation of anterior segment anatomy (*A*) and its depiction on T1-weighted sagittal MC-MR imaging (*B*). S indicates sclera; CB, ciliary body; ZZ, zonule of Zinn; VH, vitreous humor; I, Iris; AC, anterior chamber; PC, posterior chamber; L, lens; C, cornea.

the lipid content, the tarsal plate is clearly depicted on T1 imaging (Fig 7), allowing localization of pre- and postseptal abnormalities.

The eyelids themselves provide protection from mechanical damage. The elevation and closure of the eyelids are undertaken by the suspensory connective tissue system of the orbit. Primarily, this consists of the levator palpebrae superioris, which traverses the orbit, in conjunction with the superior rectus muscle, before terminating as the levator aponeurosis (Fig 9).

The ring-shaped ciliary body is composed of the ciliary muscle and the ciliary epithelium. Anteriorly, the ciliary body is attached to the sclera, with the iris attaching at the anterior junction of the sclera with the ciliary body. At its most medial extent, the ciliary muscle is attached to the lens via the fibers of the zonule of Zinn (Fig 10).[10] With variable relaxation or contraction of the ciliary muscle, the zonule of Zinn alters the convexity of the lens and subsequently changes the focal point of the eye.[11,12]

Summary

The high signal-to-noise ratio of orbital MC-MR imaging facilitates high-resolution imaging, which delineates the small-scale anatomy found in and around the orbits in much greater detail than conventional MR imaging. We have described simple acquisition sequence parameters and discussed practical insights gained from our practice to aid implementation in other centers.

MC-MR imaging of the orbits and periorbital structures is straightforward and requires only a small dedicated surface coil in addition to conventional MR imaging unit equipment, keeping imaging costs low. The high-resolution imaging demonstrated has all been acquired on a 1.5T imaging unit, but the technique should apply equally to both less powerful units and, potentially more interesting, to imaging units with a field strength of ≥3T.

MC-MR imaging is most efficiently used as stand-alone imaging for lesions confined to the orbit, to help guide the best management and appropriate surgical approach. For lesions that extend beyond the orbital apex, MC-MR imaging can be used in conjunction with conventional MR imaging, which can lengthen the overall examination time but may still provide useful additional information.

In Part 2 a subsequent article, we describe MC-MR imaging findings for a range of common and less common orbital and periorbital pathologies, highlighting the value of MC-MR imaging for diagnosis, delineation of disease extent, and surgical planning.

Disclosures: Ian A. Zealley—*UNRELATED*: *Employment*: National Health Service Tayside, *Comments*: This is the health service that employs me to perform clinical duties; none directly or indirectly related to this article; *Expert Testimony*: legal firms, *Comments*: payment for providing expert witness statements unrelated to this article; *Travel/Accommodations/Meeting Expenses Unrelated to Activities Listed*: various medical education meetings, *Comments*: support from medical meeting organizers to present lectures on various topics unrelated to this article.

REFERENCES

1. Georgouli T, James T, Tanner S, et al. **High-resolution microscopy coil MR-Eye.** *Eye (Lond)* 2008;22:994–96 CrossRef Medline
2. Budak MJ, Weir-McCall JR, Yeap PM, et al. **High-resolution microscopy-coil MR imaging of skin tumors: techniques and novel clinical applications.** *Radiographics* 2015;35:1077–90 CrossRef Medline
3. Tailor TD, Gupta D, Dalley RW, et al. **Orbital neoplasms in adults: clinical, radiologic, and pathologic review.** *Radiographics* 2013;33:1739–58 CrossRef Medline
4. Paluzzi A, Gardner PA, Fernandez-Miranda JC, et al. **"Round-the-clock" surgical access to the orbit.** *J Neurol Surg B Skull Base* 2015;76:12–24 CrossRef Medline
5. Hoffmann KT, Hosten N, Lemke AJ, et al. **Septum orbitale: high-resolution MR in orbital anatomy.** *AJNR Am J Neuroradiol* 1998;19:91–94 Medline
6. Kau HC, Tsai CC, Ortube MC, et al. **High-resolution magnetic resonance imaging of the extraocular muscles and nerves demonstrates various etiologies of third nerve palsy.** *Am J Ophthalmol* 2007;143:280–87 CrossRef Medline
7. Clark RA, Demer JL. **Magnetic resonance imaging of the globe-tendon interface for extraocular muscles: is there an "arc of contact"?** *Am J Ophthalmol* 2018;194:170–81 CrossRef Medline
8. Gipson IK. **The ocular surface: the challenge to enable and protect vision: the Friedenwald lecture.** *Invest Ophthalmol Vis Sci* 2007;48:4390; 4391–98 CrossRef Medline
9. Govindarajan B, Gipson IK. **Membrane-tethered mucins have multiple functions on the ocular surface.** *Exp Eye Res* 2010;90:655–63 CrossRef Medline
10. Delamere NA. **Ciliary body and ciliary epithelium.** *Adv Organ Biol* 2005;10:127–48 CrossRef Medline
11. Perumal N, Manicam C, Steinicke M, et al. **Characterization of the human aqueous humour proteome: a comparison of the genders.** *PLoS One* 2017;12:e0172481 CrossRef Medline
12. Goel M, Picciani RG, Lee RK, et al. **Aqueous humor dynamics: a review.** *Open Ophthalmol J* 2010;4:52–59 CrossRef Medline

Preoperative Evaluation of Craniopagus Twins: Anatomy, Imaging Techniques, and Surgical Management

A.E. Goldman-Yassen, J.T. Goodrich, T.S. Miller, and J.M. Farinhas

ABSTRACT

SUMMARY: Craniopagus twins are a rare congenital malformation in which twins are conjoined at the head. Although there is high prenatal and postnatal mortality for craniopagus twins, successful separation has become more common due to advances in neuroimaging, neuroanesthesia, and neurosurgical techniques. Joined brain tissue, shared arteries and veins, and defects in the skull and dura make surgery technically challenging, and neuroimaging plays an important role in preoperative planning. Drawing on our experience from consultation for multiple successful separations of craniopagus twins, we discuss what radiologists need to know about the anatomy, classification, imaging techniques, and surgical management of craniopagus twins.

ABBREVIATIONS: CPT = craniopagus twins; CVS = circumferential venous sinus; SDVS = shared dural venous sinuses; TA = total angular; TV = total vertical

Craniopagus twins (CPT) are a rare congenital malformation in which twins are conjoined at the head. It accounts for only 2%–6% of conjoined twins, with an incidence of approximately 1 in 2.5 million lives births.[1,2] The skulls are most often joined at homologous regions on each twin in both vertical and angular orientations, with the face and foramen magnum not primarily involved.[3] CPT can manifest as total, the twins share dural venous sinuses (SDVS), and partial forms, with separate venous anatomy.[4] Although there is high prenatal and postnatal mortality for CPT, successful separation has become more common due to advances in neuroimaging, neuroanesthesia, and neurosurgical techniques.[4-20] Joined brain tissue, shared arteries and veins, and defects in the skull and dura make surgery technically challenging.[21] Separation can take place in single or multistage procedures and has evolved as the understanding of the physiology, surgical techniques, and technology of CPT have improved.[16]

Neuroimaging, including CT, MR imaging, and conventional angiography, plays an important role in mapping the shared arterial and venous structures, brain parenchyma, calvaria, and dura.[22-24] Understanding the shared vascular anatomy is important for surgical planning because separating common vessels is associated with complications such as thrombosis, air embolism, infarction, and hemorrhage.[25] Digital and physical 3D models generated from CT and MR imaging data are important tools for operative planning and as a guide in the operating room.[21] We will review the preoperative radiologic evaluation of CPT, including the anatomy, classification systems, and surgical management, that is important for the radiologist to understand. We draw on our experience in consultation for multiple successful CPT separations with an experienced neurosurgical specialist in CPT.

Embryology

The monoamniotic, monochorionic type of monozygotic twinning has the greatest potential for leading to conjoined twins.[26] The 2 main competing theories of how monoamniotic monozygotic twins conjoin are the "fission" and "fusion" theories.[27] The fission theory suggests incomplete splitting or cleavage of the embryo at the primitive streak stage, leading to conjoined fetuses. This theory explains the apparent increase in the incidence of situs inversus and mirror imaging in conjoined twins, because a dividing cell or cell mass maintains mirror imaging.[26] The fusion theory suggests that embryos rejoin at vulnerable sites after initial complete

Received November 6, 2019; accepted after revision February 10, 2020.

From the Department of Radiology (A.E.G.-Y.), Children's Hospital of Philadelphia, Philadelphia, Pennsylvania; Departments of Radiology (A.E.G.-Y., J.M.F.) and Neurosurgery (J.T.G.), Montefiore Medical Center, Bronx, New York; Department of Radiology (T.S.M.), Stamford Hospital, Stamford, Connecticut; and Department of Radiology (J.M.F.), Moffitt Cancer Center Tampa, Florida.

Paper previously presented as an educational exhibit at: Annual Meeting of the Radiological Society of North America, November 25–29, 2018; Chicago, Illinois; presentation NR274-ED-X.

Please address correspondence to Adam Goldman-Yassen, MD, MS, Children's Hospital of Philadelphia, 3401 Civic Center Blvd, Philadelphia, PA 19104; e-mail: adgoldmanyassen@gmail.com; @AdGoldmanYassen

Indicates open access to non-subscribers at www.ajnr.org

Indicates article with supplemental on-line table.

Indicates article with supplemental on-line photos.

http://dx.doi.org/10.3174/ajnr.A6571

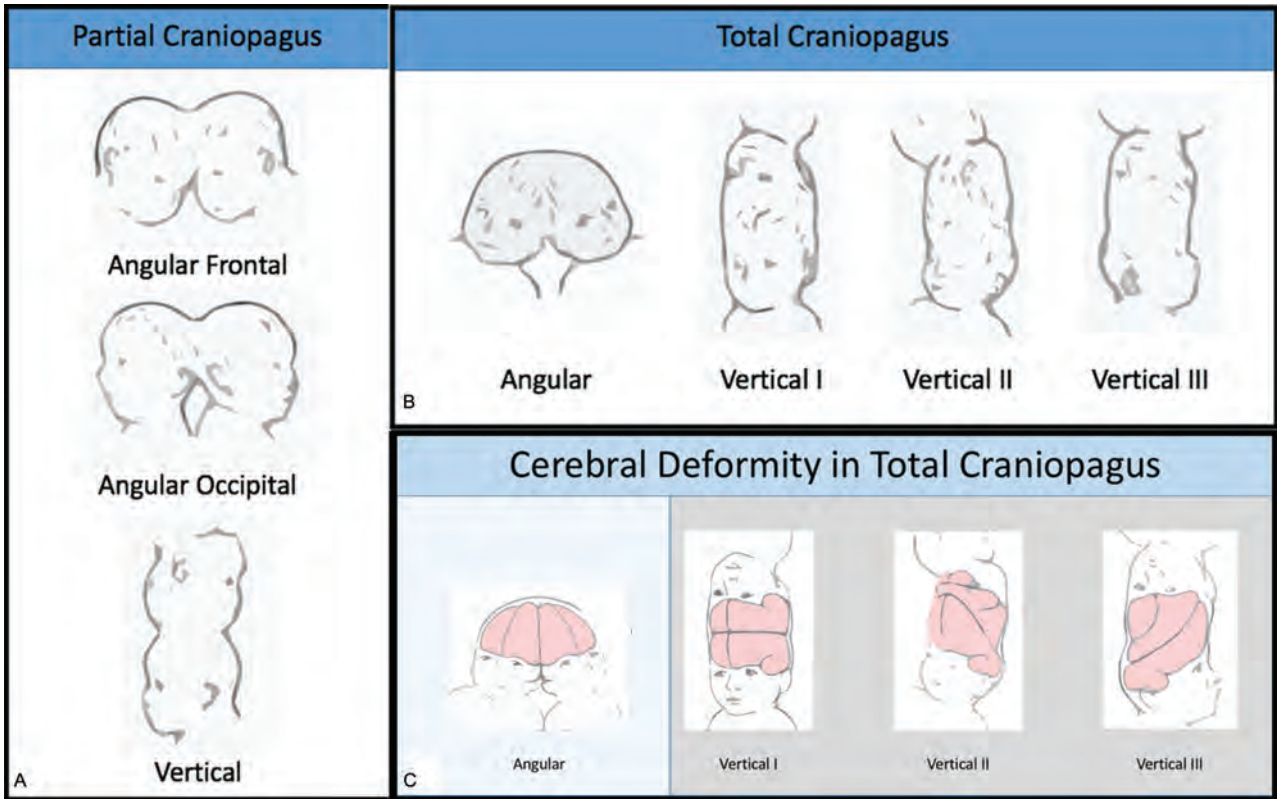

FIG 1. Stone and Goodrich[7] classification for CPT. Partial CPT lack substantial shared dural venous sinuses. Total CPT share a large portion of dural venous sinuses and present with pronounced brain compression, leading to distortion within the cranium. The 2 main subtypes are based on the long-axis angle between twins: angular and vertical. Shared calvaria causes deformity of each twin's brain. Reproduced with permission from Stone and Goodrich, 2006.[7]

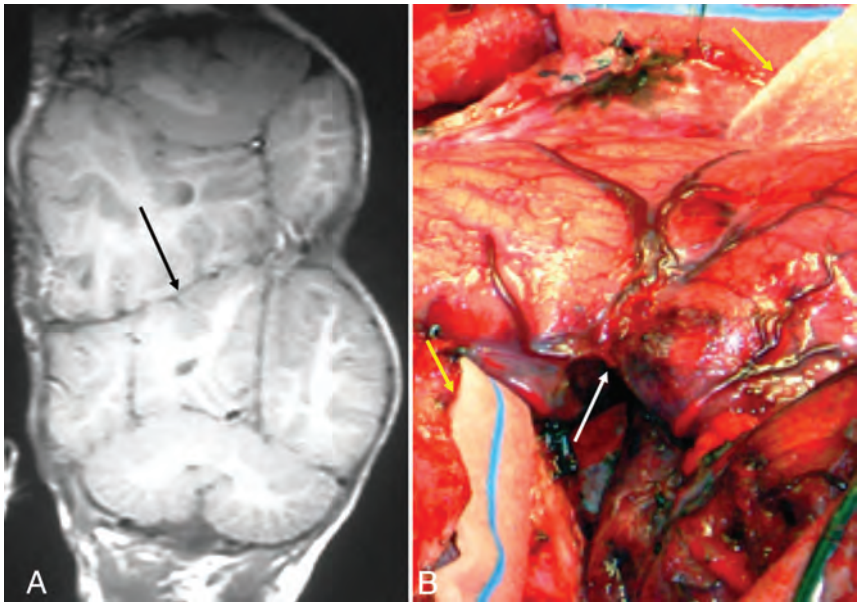

FIG 2. *A*, TI-weighted MR imaging does not clearly show conjoined brain tissue in this total CPT. However, no clear dura between cerebral hemispheres and interdigitating of gyri (*black arrow*) is seen. *B*, Intraoperative photograph from the same patient demonstrating conjoined brain tissue (*white arrow*) along the axis defined by the flanking neurosurgical sponges (*yellow arrows*).

separation. This theory accounts for the various angles at which conjoined twins can be fused, along either the dorsal-ventral axis or rostro-caudal axis.[27] The extent to which the twins are conjoined and the time of fusion during development will determine how the anatomic structures will adapt.

Classification Systems

Multiple classification systems have been proposed for CPT (On-line Table).[3,4,21,25,28] The first was developed by O'Connell,[29] in which CPT were classified as partial or total; total CPT share an extensive surface area with widely connected cranial cavities, while in partial CPT, only a limited, superficial surface area is affected. He subdivided partial craniopagus twins on the basis of the degree of rotation of one head in relation to the other, with different deformities of the brain and abnormal circulation for each. Type I vertical CPT face the same direction, type II CPT face

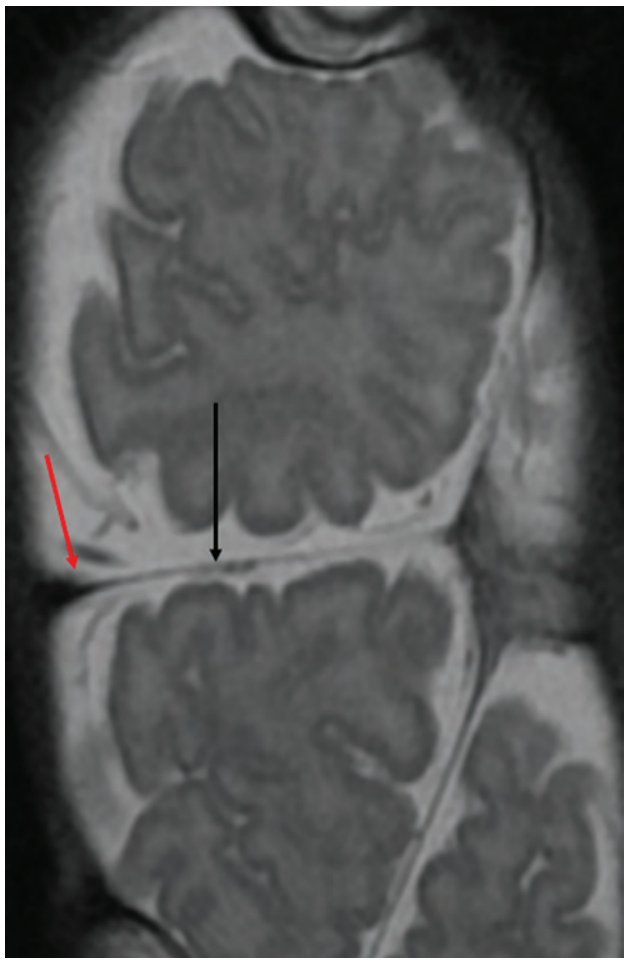

FIG 3. Coronal T2-weighted image demonstrates cerebral tissue separated by a single-layer transverse dural septum (*black arrow*). The CVS courses in the periphery of the septum (*red arrow*).

opposite sides, and type III twins have an intermediate angle of rotation.

On the basis of review of 64 cases, Stone and Goodrich[7] defined partial CPT as lacking substantial shared dural venous sinuses, whereas total CPT share a large portion of their dural venous sinuses and present with pronounced brain compression, which leads to distortion within the cranium. They defined 2 main subtypes based on the long-axis angle between twins: angular and vertical (Fig 1). Vertical craniopagus calvaria is continuous and is further subdivided on the basis of intertwin axial facial rotation, similar to the O'Connell classification. Because the Stone and Goodrich classification is most commonly used, we will use it for discussion of CPT anatomy.

Anatomy

CPT are attached only at the calvaria, without involvement of the foramen magnum, skull base, vertebrae, or face.[30] Other conjoined twinning variations involving the head include cephalopagus (involving the brain, face, thorax, and upper abdomen), parapagus diprosopus (2 faces on 1 head with 1 body), and rachipagus (joined dorsally along the vertebra and occasionally along the occiput). Conjunction is rarely symmetric and may involve any portion of the head, including underlying structures such as meninges, venous sinuses, or cortex. Configuration can vary on the basis of the attachment location and degree of rotation and angulation between the 2 twins, which will define the anatomy and difficulty of separation.

Partial CPT

Cranial unions in partial CPT are usually frontal and, less commonly, occipital or vertical biparietal.[11,17,31-40] The junctional diameter is often smaller in the partial CPT than in other types of CPT, and an incomplete layer of bone may be present between the twins.[17,34,38] In partial CPT, each child largely maintains independent calvarial convexities, except at the common area of skull junction. Cerebral deformities and compaction tend to be local and mild. The dura of each twin may be intact or deficient, and the cortical gyri may interdigitate. If the gyri do interdigitate, surgical separation is much more complex (Fig 2). Although the leptomeninges can sometimes be separable, when there is associated leptomeningeal vessel cross-over, the subsequent division will lead to some postoperative morbidity.[31,40] Dural venous cross-circulation (SDVS) is absent or negligible. Children with partial CPT undergo successful separation at an earlier age than those with total CPT, and the separation more often results in survival of both children without severe disability.[7]

Total Vertical CPT

The total vertical (TV) type of CPT consists of a longitudinal arrangement with the general appearance of 1 common continuous cranium housing 4 cerebral hemispheres.[4,29] Minor longitudinal tilting, "stove-piping," between the twins is common with a longitudinal intertwin axis or angle of 140°–180°.[29] An incomplete or complete, single-layered transverse dural septum typically separates the cerebral hemispheres deep to the conjoined region (Fig 3). The falx cerebri is usually absent or anomalous. The major cerebral arterial supply is usually confined to each respective twin. On occasion, in addition to small interconnecting leptomeningeal vessels, conjoined brain tissue may contain a larger artery requiring division at surgery.[9,41] There have been some reported cases of shared cerebral arterial supply, such as the shared middle cerebral artery circulation, which increases the complexity of a separation and may preclude safe separation.[8,42]

There are a variety of cerebral venous abnormalities associated with total CPT. Because total CPT lack 2 complete dural envelopes, the peripheral dural shelf at the conjoined cerebral hemispheric zone encloses a circumferential venous sinus (CVS) (Fig 4).[29,43-45] In TV CPT, the CVS generally traverses at least the hemicircumference of the conjoined region and replaces the absent superior sagittal sinus of both twins.[4,29] The CVS assumes an increasingly oblique configuration with increasing interaxial rotation between the TV CPT, conforming to the lateral hemispheric cleavage plane. The CVS drains the homolateral superior cerebral hemispheres of each twin, empties into a common or asymmetrically shared posterior confluence of sinuses, and may connect the lateral sinus of one twin to the lateral sinus of the other. Other types of shared venous drainage include venous sinus "lakes," a single shared superior sagittal sinus, or separate superior sagittal sinuses with variable interconnections between them.[24,29,46] The nature of the cerebral venous

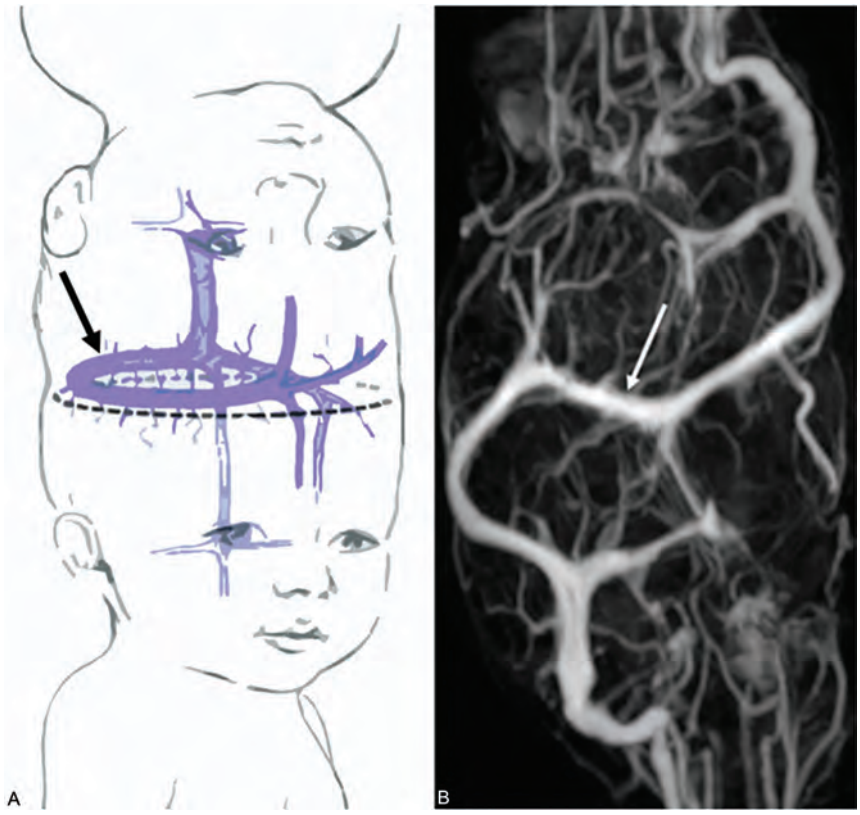

FIG 4. *A*, Surgical-separation strategy may entail sequential division of venous sinus branches from the nondominant twin (*dashed line*), allowing the anatomically predisposed dominant twin to keep the CVS (*black arrow*) and associated dura. In the nondominant twin, subsequent reversal of venous drainage to collateral basal channels may be induced (Reproduced, with permission, from Stone and Goodrich,[7] 2006). *B*, Postcontrast MR venography demonstrates the CVS (*white arrow*).

system is an important prognostic indicator of successful separation because complications during separation can lead to substantial blood loss and a catastrophic result for 1 or both children.[7] Both the CVS and SDVS are always present in TV forms of CPT, making successful surgical separation particularly hazardous.

The cerebral hemispheres in TV type I CPT demonstrate relatively symmetric superior biparietal or vertex compressive flattening. The anterior and middle fossae are spacious, while the posterior fossa tends to be small.[47] Slight tilting or intertwin axial rotation leads to facial asymmetry. Later, positional plagiocephaly is common because intertwin orientation is fixed and individual twin movement is limited by the weight and positioning of the other twin. Progressive axial rotation between the twins during development in TV types II and III produces a progressively marked obliquity of the conjoined junction. This results in oblique cerebral hemispheric compression and craniofacial and middle and posterior fossa deformities.[29] The marked bone, dural, and cerebral asymmetries in TV types II and III CPT compound the difficulties of surgical separation.[7] In addition to compressed cerebral tissue in TV CPT (Fig 1*C*), a fused cerebral cortex and underlying white mater are also found.[9,29,47]

Total Angular CPT

Total angular (TA) CPT have more acute intertwin longitudinal angulation and SDVS accompanied by complex, interconnecting venous channels (or CVS) and markedly distorted cerebral hemispheres.[48-52] One twin's brain can be inside the other twin's calvaria, adding additional to the complexity of the surgical separation. Cerebral compaction, distortion, and displacement may result in skull base deformity. Most of the TA forms of CPT are joined asymmetrically with intertwin axial rotation, but some are roughly symmetric.[10,52-55] TA CPT have shown greater extent of conjoined brain tissue, including the cerebellum, and cerebral arterial cross-filling than TV CPT (Fig 5 and On-line Fig 1).[3,25,49,55,56] TA twins are, therefore, more challenging to separate.

Anatomic Comorbidities.

CPT often present with additional comorbidities, including cardiovascular, genitourinary, craniofacial, and neurologic abnormalities.[46] Specific comorbidities include patent ductus arteriosus, aortic coarctation, hypertension, hypotension, genitourinary dysfunction and aplasia, hemiparesis, cleft lip and palate, anorectal agenesis, sirenomelia, and developmental delay. The presence of additional comorbidities increases the risk of surgery, and they are important considerations before operative management is decided. Imaging plays a key role in delineating all anatomic abnormalities present in each twin. TA CPT have a higher rate of comorbidities than TV twins, most notably genitourinary anomalies.[46]

Sedation Considerations

CT and occasionally MR imaging can be performed in neonates with a mere "feed and wrap" approach without sedation.[57] Older infants usually require general anesthesia for CT and MR imaging. Neuroanesthesia involvement is essential, using a dedicated team of anesthesiologists and equipment for each child, with closed-loop communication between teams to avoid confusion and drug errors and strict labeling of the twins to avoid confusion between them while dosing medications.[58,59] Pharmacokinetics and pharmacodynamics in CPT are altered due to circulatory mixing, and medications administered to one twin may have unexpected effects on the other.[60] Mask ventilation, access to airway, and intubation are also difficult due to the angle between the heads.[61] During imaging, it is ideal to position the twins in the position planned for surgery. This helps the surgeons become oriented to the structures as they would appear on the table during surgery.[20]

Imaging Modalities

Prenatal Imaging. Prenatal sonography (Fig 6*A*) and fetal MR imaging can be used to identify CPT in utero. The lack of

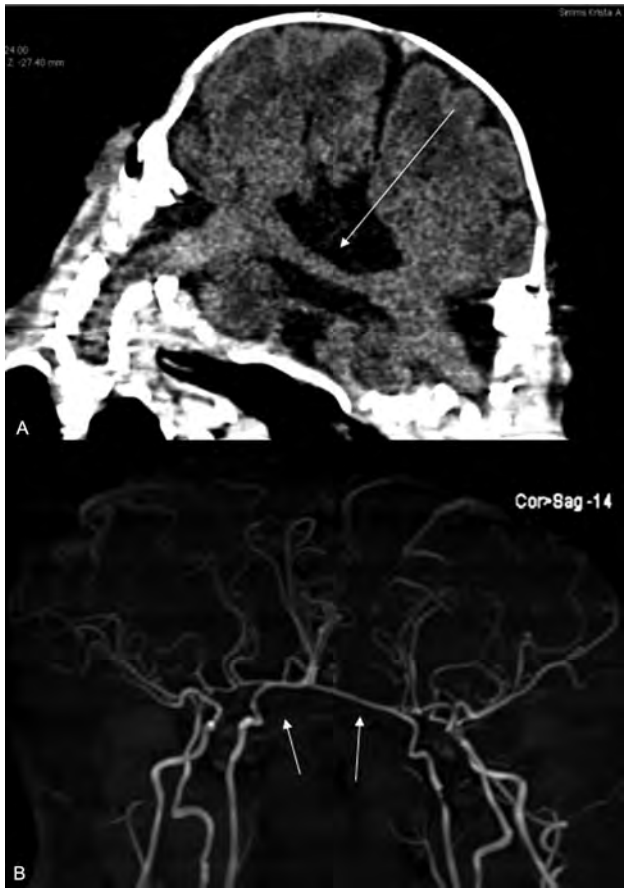

FIG 5. Coronal CT (*A*) of TA CPT shows shared brain parenchyma, including a diencephalic bridge (*arrow*). MRA of the brain (*B*) from the same patients demonstrates a shared MCA (*arrows*), with an appearance similar to that of the anterior cerebral artery. This set of twins cannot be separated.

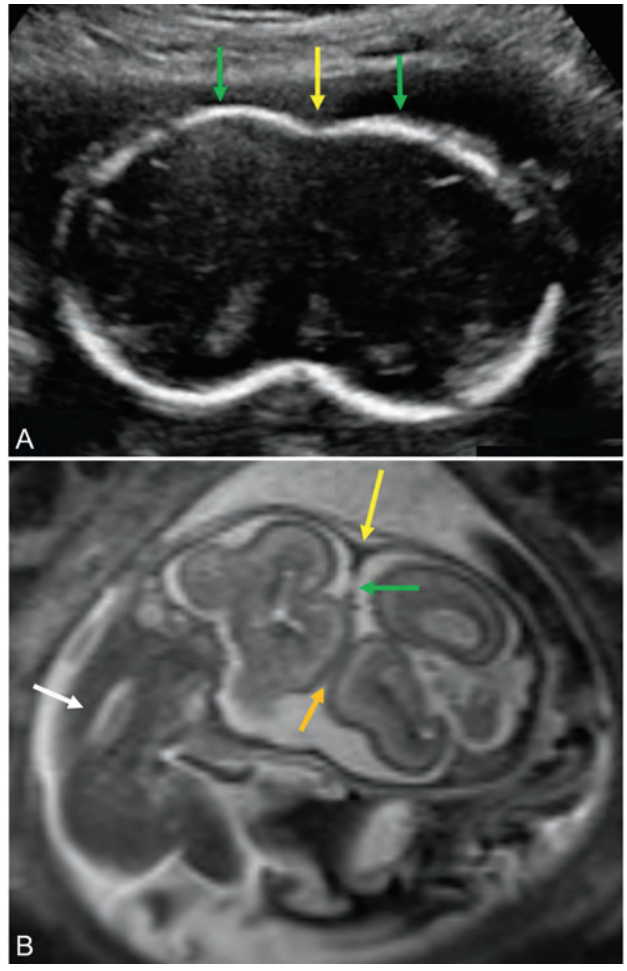

FIG 6. *A*, 2D sonogram obtained in the axial plane through the skull of the fetal CPT shows the hyperechoic joined calvaria (*green arrows*). The point of skull union between the twins is also clearly seen (*yellow arrow*). *B*, Fetal MR imaging in the coronal oblique plane through both brains of the CPT. The CVS is seen along the lateral margin of the inner calvaria at the point of bony union (*yellow arrow*), with the associated dural shelf separating the brains (*green arrow*). It is likely that the brain is fused where brain surfaces touch, and no dural or CSF cleft is seen (*orange arrow*). The torso and spine of 1 twin is also seen in this plane (*white arrow*).

ionizing radiation in both modalities makes them ideal for prenatal imaging. Antenatal diagnosis of conjoined twins can be made with ultrasonography as early as 12 weeks' gestation and is important for optimal obstetric management.[62] Prenatal diagnosis may be suspected and confirmed if 2 fetuses cannot be visualized separately in a single gestational sac. A bifid appearance of the first trimester fetal pole, presence of >3 umbilical cord vessels, persistence of heads at the same level and body plane, and failure of the fetuses to change position relative to each other with time are other sonographic features that assist in making the diagnosis.[63] 3D sonography may be more accurate than 2D sonography alone for defining the extent of the shared calvarial area and direction of the faces.[64]

Fetal MR imaging allows superior assessment of intracranial structures, including the fetal brain, vasculature, and other soft-tissue structures, and is routinely used to evaluate CPT prenatally (Fig 6*B*).[65] Fast imaging techniques are used to image the rapidly moving fetal brain for structural detail, hemorrhage, and diffusion restriction, such as HASTE (Single-shot Fast Spin Echo), EPI, true fast imaging with steady-state precession, and DWI.[66]

CT. High-resolution CT of the head with thin-section images using current pediatric, radiation dose-minimizing protocols is preferred. 3D reconstruction of the CT data is helpful to evaluate the extent of bone fusion (Fig 7*A*).[8] These data can then be reconstructed into a 3D model, which can be used by the surgeon and radiologist in preoperative planning and intraoperative reference.[42] CT angiography and venography provide adequate information related to vascularity in the conjoined area (Fig 7*B*, -7*C*), with CT venography of paramount importance in presurgical planning before each stage of separation. Thin-section, axial raw data can be segmented for vein modeling (On-line Fig 2). The resolution of CT for the evaluation of vessels is superior to contrast-enhanced MR imaging. In most cases of CPT, after the initial presentation, CTA has excluded shared arterial vessels; stage 2 and later CT scans can be protocolled as CT venograms to follow venous redistribution and evaluate veins for separation.

MR Imaging. Brain MR imaging gives a detailed assessment of the brain anatomy and development, including the shared cortex,

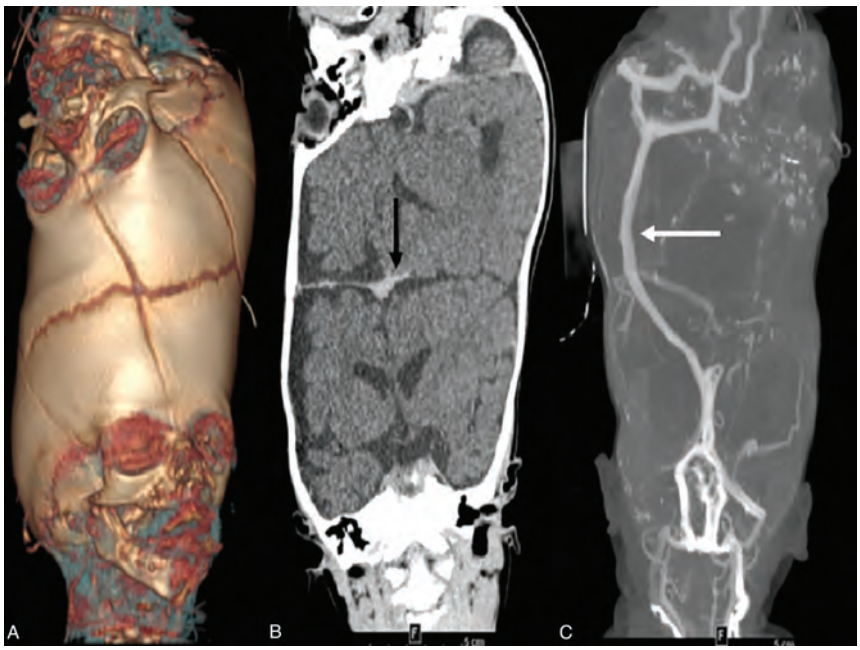

FIG 7. 3D surface rendering from CT (*A*) demonstrates suture patterns in the fused calvaria. A coronal contrast-enhanced CT venogram (*B*) demonstrates the orientation of the cerebral hemispheres and the presence of a dural septum (*arrow*). Maximum intensity projection of a CT venogram (*C*) demonstrates a shared superior sagittal sinus (*arrow*).

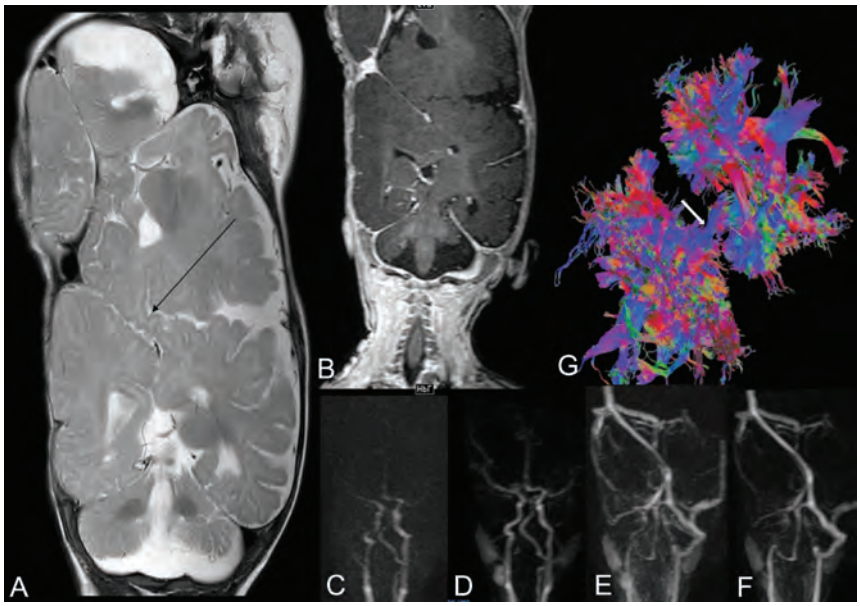

FIG 8. T2-weighted coronal image (*A*) is concerning for parenchymal bridging between the parietal lobes (*arrow*). Coronal postcontrast enhanced T1-weighted image (*B*) and dynamic MR angiography and venography (*C–F*) demonstrate a circumferential sinus communicating with both superior sagittal sinuses and dominant occipital sinuses without evidence of arterial anastomosis. Tractography (*G*) can demonstrate contiguity of white matter tracts in the cephalocaudal direction depicted in blue (*arrow*).

venous sinuses, ventricular system, dural anatomic details, and other associated anomalies (Fig 8).[8,42] MR angiography and venography can give detailed assessment of the vascular system, especially in shared areas. Time-resolved MRA (time-resolved imaging of contrast kinetics and time-resolved imaging with stochastic trajectories) helps to determine the extent of shared vasculature and the degree of vascular contribution by each twin. Just as CTA and CTV are superior for studying vessels, MR imaging is superior for studying the soft-tissue detail of the brain surface. Although the ultrafast sequences, such as single-shot T2-weighted images, have advantages in the constantly moving fetus, more conventional T1, T2, and T1-weighted images after IV gadolinium administration are used in the postnatal imaging.[57] Volumetric imaging, such as T1-weighted MPRAGE and T2 sampling perfection with application-optimized contrasts by using different flip angle evolution (SPACE sequence; Siemens), provide high-resolution anatomic detail with isotropic voxels and can be used in surgical navigation or for modeling. In addition to a standard MR imaging acquisition, high-resolution, heavily T2-weighted volumetric sequences (eg, CISS, FIESTA, and so forth) of the brain surface interface, with a slightly smaller FOV, help evaluate the degree of brain fusion (On-line Fig 3). However, from our experience, even if MR imaging does not clearly show fusion of brain parenchyma, if there is no dural shelf present, fusion may still be present at surgery. In older children or adults, functional MR imaging can be used as a noninvasive way to define hemispheric language dominance and guide surgical planning. Steady-state fMRI could be used in younger children.

Angiography

DSA can help clarify the arterial and venous anatomy accurately preoperatively.[8,20,67] Venography is performed by accessing the venous route of the child who has more fully formed sinuses. Balloon occlusion of the communication present between the venous sinuses can then show resulting hemodynamic changes that would result following surgical separation (Fig 9).[20,67] Embolization of venous structures has also been described to promote the development of collaterals and facilitate an easier surgical venous

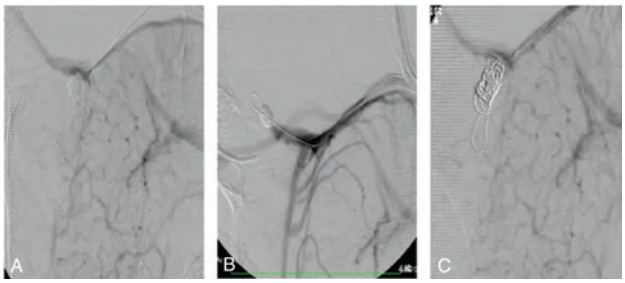

FIG 9. Multiple venous phase left ICA injections show how an occlusion balloon is used to define venous flow between twins (*A* and *B*). A coil (*C*) is then placed in a venous sinus to help promote venous collateral formation before surgery.

separation.[24,67] Coil embolization has also been used in the case of shared arterial supply.[42]

3D Models

Neuroradiologic imaging data have also produced life-sized, 3D, transparent acrylic (On-line Fig 4*A*) and ceramic (On-line Fig 5) models to better depict surgical anatomy (On-line Fig 6) and holograms depicting the complex intracranial vascular anatomy in relation to the skull and brain.[12,15,16,67-69] In the operating room, 3D models can be both physically printed for surgical reference or used in conjunction with intraoperative navigation technology.[42,69] Additionally, 3D modeling can be used to plan the craniotomies, design split-thickness bone grafts (On-line Fig 4*B*) to reconstruct cranial defects, and plan scalp tissue expander placement for adequate coverage.[67,69]

Operative Management

The goal of surgical separation of craniopagus twins involves separating shared structures, including cerebral vasculature and interdigitating brain, and reconstructing cranial structures for each twin. Single and multistage approaches have been used. In the single-stage procedure, the CVS is donated to one twin while reconstructing the sinus in the second twin. In the staged approach, one twin receives the CVS, while the other twin develops a deep venous drainage system during several months by serial ligation of draining veins (On-line Figs 7 and 8). Multistage operations are often not required for partial CPT. Reconstruction includes adequate dural, cranial, and soft-tissue coverage. The dominant twin will have a thriving and more robust clinical presentation, and the nondominant twin may experience the effects of hypotension and low cardiac output, including oliguria, lower weight, aspiration pneumonia, and failure to thrive. Most midline structures, including the CVS, will be donated to the dominant twin, with the plane of division on the side of the nondominant twin (Fig 4).

Despite multiple previous unsuccessful attempts, the first successful separation of CPT occurred in 1953, though only 1 child survived, when a multistaged approach was used.[70] As techniques improved, single-stage separations became the standard for total CPT separation, in which the surviving twin received the bulk of the superior dural venous sinuses, usually surviving with severe disability, with operations sometimes lasting as long as 22–100 hours.[3,7,11-13,15,35,52,53,71] Although surgical results for total CPT have been gradually improving across the decades, single-stage results were likely no better than the earlier developed multistaged separation procedures.[7]

Staged surgical separation is the preferred current management of choice in total CPT.[46] Gradually dividing bridging veins increases collateral formation and dilation of communicating veins in the nondominant twin, who does not receive the superior sagittal sinus. This improves venous drainage, thus reducing the risk of cerebral edema and CSF leak. Additionally, the multistage procedure allows optimal recovery between operations. The cardiac and renal issues and number of medications needed improve by the end of the third stage.

If conjoined brain tissue is present, it should be divided as early as possible to maximize cerebral plasticity.[7] Surgical separation of TV CPT should ideally be within 9–12 months of age to allow optimal psychomotor development.[7] Brain fusion of >30% bodes a very unsatisfactory outcome with very high morbidity, with a high potential of loss of 1 or both twins.

Adequate dural closure is an extremely important aspect of the operation, with the potential for CSF leakage or meningitis if not done adequately. Methods include autologous, cadaveric, or synthetic dural substitutes and scalp coverage by delayed pedicle flaps or the use of subgaleal tissue expansion.[15,25,45,47,69,72] Porcine grafts have been used successfully due to their low immune response (On-line Fig 9). CSF shunting after the operation, for hydrocephalus or to promote wound healing, may also be necessary, though the incidence of postoperative hydrocephalus is reduced in the multistage approach.[4,12,41] In a single case of TA CPT, an external distraction device was used to increase the working distance between the twins after a strip craniectomy was performed to disconnect the fused portions of the skulls.[69] The efficacy of this additional distraction technique is not clear.

CONCLUSIONS

Separation of CPT must be a well-orchestrated multidisciplinary effort. The care of these children is extremely resource-intensive, including critical care time, nursing, social support, travel, anesthesia, neurosurgery, diagnostic and interventional neuroradiology, administrative support, and the list continues. The neuroradiologist plays an important role in the care team of CPT, from initial evaluation through the operation and follow-up, using conventional imaging techniques (CT/MR imaging), angiography, and endovascular therapies and creating 3D models. Technologic advances that can greatly improve this field will include 3D virtual reality/augmented reality navigation to improve the knowledge of what lies behind a "wall" of fused brain in the operating theater, keeping loss of brain tissue to a minimum. The combination of high-resolution MR images and virtual reality 3D systems is already in use (12). Embolizing vessels will become even more precise as new endovascular devices and embolic materials become available, decreasing operative time needed for vascular ligation, providing a roadmap for surgeons when they divide veins (liquid embolic materials are clearly seen in superficial vessels with the naked eye), and further mitigating blood loss. With continued innovation, diagnostic and interventional neuroradiology plays an increasingly important role in the care of CPT.

Disclosures: James T. Goodrich—*UNRELATED*: *Royalties*: Thieme textbook.

REFERENCES

1. Edmonds LD, Layde PM. **Conjoined twins in the United States, 1970-1977.** *Teratology* 1982;25:301–08 CrossRef Medline
2. Spitz L, Kiely EM. **Conjoined twins.** *JAMA* 2003;289:1307–10 CrossRef Medline
3. Winston KR, Rockoff MA, Mullikenv JB, et al. **Surgical division of craniopagi.** *Neurosurgery* 1987;21:782–91 CrossRef Medline
4. Walker M, Browd SR. **Craniopagus twins: embryology, classification, surgical anatomy, and separation.** *Childs Nerv Syst* 2004;20:554–66 CrossRef Medline
5. Campbell S, Theile R, Stuart G, et al. **Craniopagus: second Brisbane case: case report.** *J Neurosurg* 2004;100:519–24 CrossRef Medline
6. Yang Z, Xu G. **Craniopagus twins.** *Chin Med J* 2002;115:1262–63 Medline
7. Stone JL, Goodrich JT. **The craniopagus malformation: classification and implications for surgical separation.** *Brain* 2006;129(Pt 5):1084–95 CrossRef Medline
8. Nejat F, Habibi Z, Goudarzi M, et al. **Emergency separation of craniopagus twins: case report.** *J Neurosurg Pediatr* 2017;20:307–13 CrossRef Medline
9. Hoffman HJ. **Craniopagus twins.** *Neurol Med Chir (Tokyo)* 1997;37:780 Medline
10. Cywes S, Millar AJ, Rode H, et al. **Conjoined twins: the Cape Town experience.** *Pediatr Surg Int* 1997;12:234–48 CrossRef Medline
11. Campbell S. **Separation of craniopagus twins: the Brisbane experience.** *Childs Nerv Syst* 2004;20:601–06 CrossRef Medline
12. Goh KY. **Separation surgery for total vertical craniopagus twins.** *Childs Nerv Syst* 2004;20:567–75 CrossRef Medline
13. Frazee J, Fried I, Kawamoto H, et al. **The separation of Guatemalan craniopagus twins.** *Childs Nerv Syst* 2004;20:593–600 CrossRef Medline
14. Khan ZH, Hamidi S, Miri SM. **Craniopagus, Laleh and Ladan twins, sagital sinus.** *Turk Neurosurg* 2007;17:27–32 Medline
15. Swift DM, Weprin B, Sklar F, et al. **Total vertex craniopagus with crossed venous drainage: case report of successful surgical separation.** *Childs Nerv Syst* 2004;20:607–17 CrossRef Medline
16. Staffenberg DA, Goodrich JT. **Separation of craniopagus conjoined twins with a staged approach.** *J Craniofac Surg* 2012;23:2004–10 CrossRef Medline
17. Di Rocco C, Caldarelli M, Tamburrini G, et al. **Craniopagus: the Thessaloniki-Rome experience.** *Childs Nerv Syst* 2004;20:576–86 CrossRef Medline
18. Tannuri AC, Batatinha JA, Velhote MC, et al. **Conjoined twins: twenty years' experience at a reference center in Brazil.** *Clinics (Sao Paulo)* 2013;68:371–77 CrossRef Medline
19. Ble RK, Seni K, Adjoussou S, et al. **Craniopagus conjoined twins: difficulties of management in Africa.** *Gynecol Obstet Fertil* 2008;36:56–59 Medline
20. Pai KM, Naidu RC, Raja A, et al. **Surgical nuances in the separation of craniopagus twins: our experience and a follow-up of 15 years.** *Neurol India* 2018;66:426–33 CrossRef Medline
21. Browd SR, Goodrich JT, Walker ML. **Craniopagus twins.** *J Neurosurg Pediatr* 2008;1:1–20 CrossRef Medline
22. Schindler E, Hajek P. **Craniopagus twins: neuroradiological findings (CT, angiography, MRI).** *Neuroradiology* 1988;30:11–16 CrossRef Medline
23. Sudha L, Dev B, Kamble R, et al. **Role of biplane digital subtraction angiography, and 3D rotational angiography in craniopagus twins: a case report, detailed pictorial evaluation, and review of literature.** *J Pediatr Neurosci* 2009;4:113–16 CrossRef Medline
24. Alokaili RN, Ahmed ME, Al Feryan A, et al. **Neurointerventional participation in craniopagus separation.** *Interv Neuroradiol* 2015;21:552–57 CrossRef Medline
25. Bucholz RD, Yoon KW, Shively RE. **Temporoparietal craniopagus: case report and review of the literature.** *J Neurosurg* 1987;66:72–79 CrossRef Medline
26. Kaufman MH. **The embryology of conjoined twins.** *Childs Nerv Syst* 2004;20:508–25 CrossRef Medline
27. Spencer R. **Theoretical and analytical embryology of conjoined twins, Part I: embryogenesis.** *Clin Anat* 2000;13:36–53 CrossRef Medline
28. Gaist G, Piazza G, Galassi E, et al. **Craniopagus twins: an unsuccessful separation and a clinical review of the entity.** *Childs Nerv Syst* 1987;3:327–33 CrossRef Medline
29. O'Connell JE. **Craniopagus twins: surgical anatomy and embryology and their implications.** *J Neurol Neurosurg Psychiatry* 1976;39:1–22 Medline
30. Spencer R. *Conjoined Twins: Developmental Malformations and Clinical Implications*. Johns Hopkins University Press; 2003
31. Baldwin M, Dekaban A. **Cephalopagus twins seven years after separation: follow-up of a case.** *J Neurosurg* 1965;23:199–203 CrossRef Medline
32. Wolfowitz J, Kerr EM, Levin SE, et al. **Separation of craniopagus twins.** *S Afr Med J* 1968;42:412–24 Medline
33. Lansdell H. **Intelligence test scores from infancy to adulthood for a craniopagus twin pair neurosurgically separated at 4 months of age.** *Psychol Rep* 1999;84:209–17 CrossRef Medline
34. Stanley P, Anderson FM, Segall HD. **Radiologic investigation of craniopagus twins (partial type).** *AJNR Am J Neuroradiol* 1983;4:206–08 Medline
35. Sathekge MM, Venkannagari RR, Clauss RP. **Scintigraphic evaluation of craniopagus twins.** *Br J Radiol* 1998;71:1096–99 CrossRef Medline
36. Campbell S, Theile R, Stuart G, et al. **Separation of craniopagus joined at the occiput: case report.** *J Neurosurg* 2002;97:983–87 CrossRef Medline
37. Voris HC. **Cranioplasty in a craniopagus twin.** *J Neurosurg* 1963;20:145–47 CrossRef Medline
38. Voris HC, Slaughter WB, Christian JR, et al. **Successful separation of craniopagus twins.** *J Neurosurg* 1957;14:548–60 CrossRef Medline
39. Marcinski A, Lopatec HU, Wermenski K, et al. **Angiographic evaluation of conjoined twins.** *Pediatr Radiol* 1978;6:230–32 CrossRef Medline
40. Konovalov AN, Vaĭchis ChM. **The successful separation of a craniopagus (in Russian).** *Zh Vopr Neirokhir Im N N Burdenko* 1991;3–10 Medline
41. O'Connell JE. **Surgical separation of two pairs of craniopagus twins.** *BMJ* 1964;1:1333–36 Medline
42. Rutka JT, Souweidane M, ter Brugge K, et al. **Separation of craniopagus twins in the era of modern neuroimaging, interventional neuroradiology, and frameless stereotaxy.** *Childs Nerv Syst* 2004;20:587–92 CrossRef Medline
43. Sonnenburg WM. **The blood vascular system in a parietal craniopagus.** *JAMA* 1919;73:1345–48 CrossRef
44. Grossman HJ, Sugar O, Greeley PW, et al. **Surgical separation in craniopagus.** *J Am Med Assoc* 1953;153:201–07 CrossRef Medline
45. Winston KR. **Craniopagi: anatomical characteristics and classification.** *Neurosurgery* 1987;21:769–81 CrossRef Medline
46. Harvey DJ, Totonchi A, Gosain AK. **Separation of craniopagus twins over the past 20 years: a systematic review of the variables that lead to successful separation.** *Plast Reconstr Surg* 2016;138:190–200 CrossRef Medline
47. Staffenberg DA, Goodrich JT. **Separation of craniopagus conjoined twins: an evolution in thought.** *Clin Plast Surg* 2005;32:25–34, viii CrossRef Medline
48. Wilson H, Storer EH. **Surgery in Siamese twins: a report of three sets of conjoined twins treated surgically.** *Ann Surg* 1957;145:718–25 CrossRef Medline
49. Lenard HG, Schulte FJ. **Polygraphic sleep study in craniopagus twins (where is the sleep transmitter?)** *J Neurol Neurosurg Psychiatry* 1972;35:756–62 CrossRef Medline
50. Villarejo F, Soto M, Amaya C, et al. **Total craniopagus twins.** *Childs Brain* 1981;8:149–55 CrossRef Medline

51. van Ouwerkerk WJ, van den Berg R, Allison CE, et al. **Craniopagus: the Suriname-Amsterdam conjunction.** *Childs Nerv Syst* 2004;20: 625–34 CrossRef Medline
52. Huang WQ, Fang JY, Xiao LC, et al. **Anesthetic management for separation of craniopagus twins.** *Acta Anaesthesiol Scand* 2004;48: 919–21 CrossRef Medline
53. Cameron DE, Reitz BA, Carson BS, et al. **Separation of craniopagus Siamese twins using cardiopulmonary bypass and hypothermic circulatory arrest.** *J Thorac Cardiovasc Surg* 1989;98:961–67 CrossRef Medline
54. Drummond G, Scott P, Mackay D, et al. **Separation of the Baragwanath craniopagus twins.** *Br J Plast Surg* 1991;44:49–52 CrossRef Medline
55. Jansen O, Mehrabi VA, Sartor K. **Neuroradiological findings in adult cranially conjoined twins: case report.** *J Neurosurg* 1998;89: 635–39 CrossRef Medline
56. O'Neill JA Jr, Holcomb GW 3rd, Schnaufer L, et al. **Surgical experience with thirteen conjoined twins.** *Ann Surg* 1988;208:299–312 Medline
57. McHugh K, Kiely EM, Spitz L. **Imaging of conjoined twins.** *Pediatr Radiol* 2006;36:899–910, quiz 1002–03 CrossRef Medline
58. Leelanukrom R, Somboonviboon W, Bunburaphong P, et al. **Anaesthetic experiences in three sets of conjoined twins in King Chulalongkorn Memorial Hospital.** *Paediatr Anaesth* 2004;14:176–83 CrossRef Medline
59. Vagyannavar R, Bhattacharyya A, Misra G, et al. **Craniopagus twins for magnetic resonance imaging.** *Saudi J Anaesth* 2017;11:509–10 CrossRef Medline
60. Thomas JM. **Anaesthesia for conjoined twins.** *Childs Nerv Syst* 2004;20:538–46 CrossRef Medline
61. Yadav M, Chikkala R, Kulkarni D, et al. **Anesthetic management of craniopagus conjoined twins in a remote location.** *Saudi J Anaesth* 2017;11:516–17 CrossRef Medline
62. Dasan TA, N G B, Anvekar SM. **A rare case of prenatally detected craniopagus twin.** *J Clin Diagn Res* 2015;9:TJ01–02 CrossRef Medline
63. Sharma UK, Dangol A, Chawla CD, et al. **Antenatal detection of conjoined twin.** *J Nepal Med Assoc* 2007;46:133–35 CrossRef Medline
64. Sanhal CY, Ozekinci M, Mendilcioglu I, et al. **Prenatal diagnosis of total type 1 vertical craniopagus with 3-dimensional sonography.** *J Ultrasound Med* 2014;33:179–81 CrossRef Medline
65. Rossi AC, Prefumo F. **Additional value of fetal magnetic resonance imaging in the prenatal diagnosis of central nervous system anomalies: a systematic review of the literature.** *Ultrasound Obstet Gynecol* 2014;44:388–93 CrossRef Medline
66. Saleem SN. **Fetal MRI: an approach to practice—a review.** *J Adv Res* 2014;5:507–23 CrossRef Medline
67. Harvey DJ, Vaca EE, Totonchi A, et al. **Eleven-year follow-up of craniopagus twins after unsuccessful attempt at separation: are they better off?** *Cleft Palate Craniofac J* 2019;56:817–22 CrossRef Medline
68. Goodrich JT, Staffenberg DA. **Craniopagus twins: clinical and surgical management.** *Childs Nerv Syst* 2004;20:618–24 CrossRef Medline
69. Heuer GG, Madsen PJ, Flanders TM, et al. **Separation of craniopagus twins by a multidisciplinary team.** *N Engl J Med* 2019;380:358–64 CrossRef Medline
70. Sugar O, Grossman H, Greeley P, et al. **The Brodie craniopagus twins.** *Trans Am Neurol Assoc* 1953;3:198–99 Medline
71. Todorov AB, Cohen KL, Spilotro V, et al. **Craniopagus twins.** *J Neurol Neurosurg Psychiatry* 1974;37:1291–98 CrossRef Medline
72. Piza-Katzer H. **Free allogeneic muscle transfer for cranial reconstruction.** *Br J Plast Surg* 2002;55:436–38 CrossRef Medline

From the Eye of the Storm: Multi-Institutional Practical Perspectives on Neuroradiology from the COVID-19 Outbreak in New York City

C.D. Phillips, D.R. Shatzkes, G. Moonis, K.A. Hsu, A. Doshi, and C.G. Filippi

ABSTRACT

SUMMARY: During the Severe Acute Respiratory Syndrome Coronavirus 2 (COVID-19) pandemic, neuroradiology practices have experienced a paradigm shift in practice, which affected everything from staffing, workflow, work volumes, conferences, resident and fellowship education, and research. This article highlights adaptive strategies that were undertaken at the epicenter of the outbreak in New York City during the past 4–6 weeks, as experienced by 5 large neuroradiology academic departments.

ABBREVIATIONS: ICU = intensive care unit; IT = information technology; NYC = New York City; PPE = personal protective equipment; PHI = protected health information

During the Severe Acute Respiratory Syndrome Coronavirus 2 (COVID-19) pandemic neuroradiology practices have been experiencing a paradigm shift in activities. This disruption has affected everything from staffing to workflow, work volumes, conferences, resident and fellowship education, and research. This article highlights some adaptive strategies that have been undertaken at the United States center of the outbreak in New York City during the past 4–6 weeks, as experienced by 5 large neuroradiology academic departments in New York City. The volume of COVID-19 cases seen at these institutions varies, but the numbers are staggering; while the system has not yet been overwhelmed, there are critical manpower, equipment, intensive care unit (ICU) bed, ventilator, and so forth deficiencies. The system has been taxed, and the medical community has found itself stressed to nearly the breaking point. These adaptive strategies are still relatively fluid but, in some areas, converging on consensus. As this is completed, the admission numbers at many institutions in New York City (NYC) are stabilizing and appearing to decrease, suggesting that a plateau has been reached, and if we are successful in the ongoing attempts at mitigation of the illness, the worst may be over.

Clinical Practice: Staffing

As cases of Severe Acute Respiratory Syndrome Coronavirus 2 (COVID-19) first appeared and then exponentially increased in the NYC metro area, it became clear to the population and finally to government figures that social distancing was required to "flatten the curve." Academic neuroradiology practices began to limit the number of staff in reading rooms, and as the severity of the pandemic became clearer, many staff members were quickly transitioned to work from home. Many staff members already had at-home PACS, but some neuroradiologists with no at-home PACS were actually allowed to bring their hospital PACS workstation home. This required quick acquisition of many elements of support; hospital and departmental information technology (IT) support was sought because secure data links including virtual private networks, which needed to be established, and often home network upgrades were necessary. Sites reported that they were overwhelming their IT resources to get physicians "up and running" quickly. Most have experienced minimal difficulties with bandwidths available through commercial internet providers, though some hours are very busy with subsequent decreased network speeds.

Radiologists who currently do not do remote interpretation and are anticipating doing so in the immediate future should investigate their provider bandwidth availability and be proactive at obtaining adequate network speed. Sites anticipating a surge are

Received April 15, 2020; accepted after revision April 15.

From the Department of Head and Neck Imaging (C.D.P.), Department of Radiology, Weill Cornell Medical College, NewYork-Presbyterian Hospital, New York, New York; Department of Head & Neck Imaging (D.R.S.), Department of Radiology and Otolaryngology, Zucker School of Medicine at Hofstra/Northwell, Lenox Hill Hospital, New York, New York; Department Head and Neck Imaging (G.M.), Department of Radiology, Columbia University, Columbia University Irving Medical Center, New York, New York; Department of Radiology (K.A.H.), Montefiore Medical Center and Albert Einstein College of Medicine, Bronx, New York; Departments of Radiology and Neurosurgery (A.D.), Icahn School of Medicine at Mount Sinai, New York, New York; and Departments of Biomedical Imaging and Translational Science and Radiology (C.G.F.), Zucker School of Medicine at Hofstra/Northwell, Lenox Hill Hospital and Lenox Hill-Greenwich Village, New York, New York.

Please address correspondence to Christopher G. Filippi, MD, FASFNR, Department of Biomedical Imaging and Translational Science, Zucker School of Medicine at Hofstra/Northwell, Lenox Hill Hospital and Lenox Hill-Greenwich Village, 100 East 77th St, NY, NY 10075; e-mail: cfilippi@northwell.edu; @sairaallapeikko

http://dx.doi.org/10.3174/ajnr.A6565

advised to attend to off-site reading requirements (including increasingly scarce equipment such as monitors) as quickly as possible. Conversations with hospital/departmental IT staff are also best done early. The goal has been to keep radiologists healthy and functioning as providers and viable members of the patient-care team.

The number of radiologists required in the hospital setting is based on a number of considerations, including staffing for procedures, the presence for pharmaceutical/contrast administration, overseeing trainees still in-house, and the "visibility" of a radiologist in the hospital, a feature that is uniformly of value. Radiologists remain an essential element of the health care team, and maintaining a presence in the hospital at this time is critical; Working alongside our trainees, technologists, and other staff provides moral support and some functional advantages. The institutions represented here have widely varied approaches to staffing; some divided radiology staff into 2 groups working separately and distinctly (week on, week off), and others limited exposure of older and potentially more vulnerable physicians. All the institutions have tried to ensure that minimal staff were exposed and that necessary access is maintained. When clinical care conferences have continued, video conferencing has proved very reliable and an adequate replacement for in-person meetings. Secure video conferencing methods should be routinely available for this purpose.

Procedural volumes also declined; many biopsy and other outpatient procedures were determined to be nonurgent and of too great a risk for the patient to come to a facility. The necessity for inpatient lumbar punctures, angiography, and/or neurointerventional procedures remains, and either in-house coverage or on-call staff are available for urgent procedures.

Communication is of paramount concern. Our report is our final work product, the actionable result of the study, and must be immediately available and properly delivered. In-house services maintain a normal hospital reporting system, and obviously maintain the delivery of urgent examinations through direct communication with the involved clinical services, but a mirror system of communication must be maintained for off-site interpretation. Because of social distancing, clinical services staff may not access reading rooms with the same regularity as before; many sites have posted information outside reading rooms with all contact information for the radiology staff. Particularly difficult issues have resulted from "displaced" ICU beds and the accompanying staff, often moved to different locations, including previously unused floor space and, on occasion, field hospitals. New lines of communication have been established, but urgent communications from the radiology staff to these areas has proved problematic early on.

As radiology volumes declined and intensive care physician manpower became stressed, the issue of "redeployment" was raised. Within many systems, radiology trainees and staff were reassigned to clinical areas. The wisdom and utility of this as well as the potential broad-ranging ramifications of such reassignment are clearly beyond the realm of this brief report. These staff may be truly working above and beyond their expectations or training. House staff are more likely to be redeployed to clinical services, including ICUs, than faculty. At one institution, neuroradiologists have been part of a "Patient Liaison Team," connecting with patients' families for information and support. At other sites, neuroradiologists have performed clerical work as part of clinical teams in ICUs or floors. Other redeployment activities have included participation in workplace health and safety, telemedicine, and elective examination rescheduling teams.

Challenges

1) Determination of safe and appropriate in-house staffing requirements for residents, fellows, and attending physicians.
2) Management of consults.
3) Management of multidisciplinary tumor boards and clinical conferences.
4) Facilitation of off-site reading for radiologists who were not already equipped for this.
5) Management of hospital practice committee work/administrative responsibilities.
6) Active or impending "redeployment" of radiologists.

Recommendations

1) Keep in-house coverage to an appropriate minimum.
   a) Balance concerns regarding the importance of the visibility of radiologist with the need to maintain physician health and well-being.
   b) Ensure that radiologists reading on-site have personal protective equipment (PPE) and maintain appropriate distancing.
2) Maintain prompt, appropriate communication, which is essential.
   a) Easily accessible contact information for all radiology staff, in-house and off-site.
   b) Complete lists of contact information for in-house resources for off-site staff.
3) Use Microsoft Teams, Zoom, and similar virtual or video conferencing platforms for continuation of multidisciplinary conferences.
4) Maximize IT support staffing and ensure that IT contact information is readily available.
5) Recognize that redeployment requests and mandates have been highly variable and system-dependent.

Clinical Practice: Workflow

It quickly became apparent that it was unsafe to continue elective imaging, given the risk to patients, technologists, and staff. At 4 of the included academic institutions in the NYC area, the total volume of combined CT and MR neuroimaging cases for similar periods declined by an average of 65% (range, 51%–80.9%). More specifically, neurologic CT volume declined an average of 58.6% (range, 49.3%–72.6%). Neurologic MR imaging volume declined an average of 75% (range, 56.4%–88.6%). Stroke code CT-specific cases declined by 59.7% (range, 32.2%–73.8%) (Figs 1 and 2). Coincident with the reduced elective imaging volumes, there was a need for prioritization of emergent reads to help move patients in and out of increasingly crowded emergency departments.

Elements in the workflow are worthy of individual consideration, allowing for the potential revisions by government regulators. Our reception staff, nurses, and technologists are particularly affected by patient care changes in the era of COVID-19. Redeployment of nursing personnel to clinical

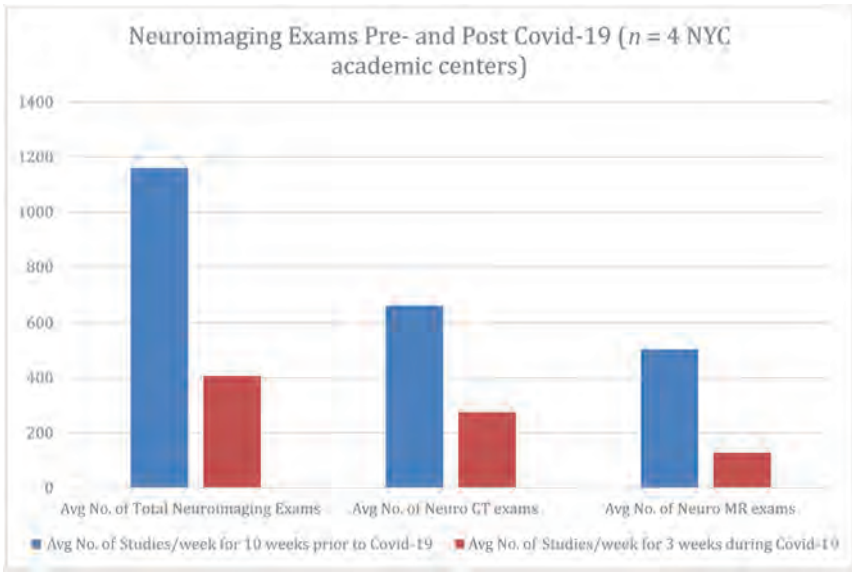

FIG 1. Chart demonstrates changes in the weekly average (Avg) of the total number of neuroimaging cases as well as changes in the weekly average of the total number of neurologic CT and MR imaging examinations. This compares weekly average volumes for 10 weeks before the NYC official shutdown to the 3 weeks following the shutdown at the height of the NYC pandemic.

units has removed nursing staff from radiology. Furloughs and layoffs have occurred. These staff can also become infected and require quarantine or hospitalization. All our institutions were aggressive early in reviewing patient examination lists and identifying and rescheduling nonurgent examinations. The radiologists' review of these requests required much time, and rescheduling remains a work-in-progress. Protocols to manage scheduled and future examinations are being created or have already been instituted. Triage requires physician input; in many cases, additional communication with referrers is necessary to gauge the urgency if not evident from requisition and electronic medical record data. We have worked to maintain safe access to imaging for patients undergoing examinations to monitor and treat oncologic diagnoses.

There have been challenging issues in designating sites for patients with known COVID-19, and other sites for noninfected patients. While there may be some benefit to designating a site for only patients with known COVID-19, the incidence of asymptomatic and afebrile patients, who unknowingly are COVID-19 positive, is problematic at sites that intend to remain for noninfected patients. All staff will be properly equipped with PPE and will practice appropriate distancing. When patients arrive for scanning deemed urgent, sites have incorporated screening before patients can access imaging suites. Social distancing in waiting areas is reinforced. The discovery of a patient with potential COVID-19 on any scanner is a major issue; the patient must be isolated, staff may require quarantine, and the scanner must be cleaned by a defined protocol.

It has been observed that turnaround time data will definitely show a unique perturbation based on the COVID-19 pandemic. Declining volumes and staff reading in real-time are the cause. These have led to issues in workflow—some are positive, but others are not. A rapid turnaround time is good for patient care and particularly positive in the emergency department. However, the "urge" of attending staff to grab an examination from a worklist and read it (the "Hungry Hippos" analogy, Fig 3) has been evident. This clearly detracts from resident/fellow education. Allowing trainees to generate preliminary interpretations is a necessary part of training programs and should continue.

Challenges

1) Triage of previously scheduled and new requests for outpatient imaging.
2) Reduction in available technologists and support staff because of illness and quarantine following exposure or redeployment.
3) Machine/room contamination by known or later-discovered patients with COVID-19.
4) Absolute decline in case volumes in neuroradiology.

Recommendations

1) Continue to prioritize reading of emergency department studies; a low emergency department turnaround time helps providers move patients from this risky setting.
2) Create a protocol to manage outpatient imaging.
   a) Every patient kept out of an imaging facility and in their homes is a potential "save" during this pandemic.
   b) Assemble a radiologist team to triage elective outpatient studies.
3) Move all outpatient imaging out of hospitals and into imaging centers; reduce the number of operating imaging centers to reduce staffing requirements.
   a) Keep technologists/other staff to a minimum and enforce appropriate quarantine practices.
   b) Maintain appropriate PPE and precautions for all staff and patients.
   c) Define protocol for machine/room cleaning after contamination by patients with COVID-19.
4) In hospital and outpatient centers, when possible, designate scanners or sites for patients under investigation.
5) Assign a smaller number of primary/backup readers and instruct others to do nonclinical (research, teaching, administrative) work.

Resident and Fellow Education

Because minimizing radiologists physically at the hospital was necessary, multiple challenges ensued regarding continuing resident and fellow education. An initial move to remove as many residents as possible from the hospital setting was followed by a "redeployment" of physicians, with residents and fellows reassigned to clinical service. This redeployment resulted in confusion and anxiety among house staff and interfered with their availability to participate in educational radiology activities. Additionally, postponement of American Board of Radiology examinations has changed the learning paradigm for senior residents.

Much of radiology learning has been "shoulder-to-shoulder" case review with an attending physician, as well as didactic teaching,

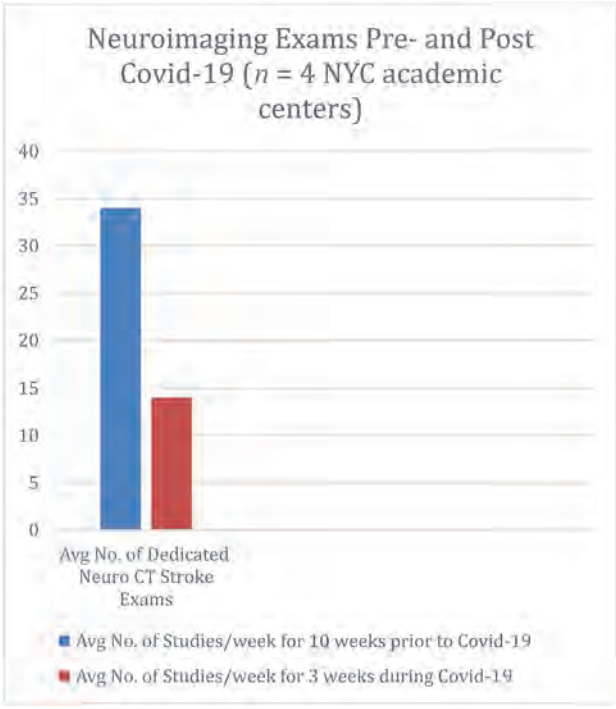

FIG 2. Chart demonstrates changes in weekly average (Avg) of the total number of designated "stroke code" cases. This compares weekly average volumes for 10 weeks before the NYC official shutdown to the 3 weeks following the shutdown at the height of the NYC pandemic.

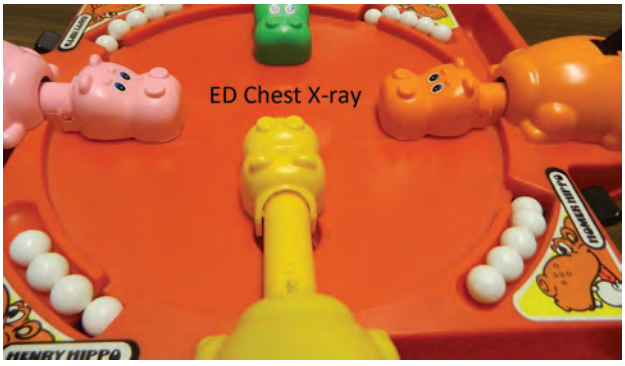

FIG 3. This analogy and tweeted image are borrowed with the courtesy of Daniel Ortiz, MD, Summit Radiology Services, Cartersville, Georgia. ED indicates emergency department.

case review, and unknown case presentations. This form of education has been largely halted. Trainee numbers in the reading rooms have diminished, and social distancing has interfered with traditional training methods. The dispersal of staff and residents necessitates video conferencing.

Staff have quickly become familiar with video conferencing for teaching. While not a perfect system, it does at least allow widely spread trainees to be involved and the educational mission of the system to continue. Trainees have also requested a more permanent archive of the material; providing a PDF or other augmented text file of lectures allows the material to be durable and residents who may be redeployed to have access to the material. Some sites have also recorded lectures. On-line teaching materials are also available.

The decrease in volume may impact resident training. As previously mentioned, staff taking cases from clinical worklists that were previously preliminarily reviewed by a trainee is an issue. Encouraging staff to allow the normal workflow in clinical areas seems an unusual problem, but clearly staff feel pressure to be active and turn examinations around quickly. Trainees benefit from case review and formulating an opinion; this system should be maintained if possible.

Challenges

1) Continuing resident/fellow conferences via online or video conferencing.
2) Providing enhanced opportunities for on-line education.
3) Mitigating the impact of reduced case volume on resident and fellow education.
4) Mitigating the impact of redeployment on resident/fellow education and well-being.

Recommendations

1) Move resident and fellow teaching conferences to on-line video conference formats (Zoom, Skype, and so forth).
2) Revise existing syllabi for continued on-line learning to maintain levels of medical student/resident/fellow training.
3) Encourage attendings to allow residents/fellows to provide standard preliminary interpretations, while facilitating turnaround times.
4) Be consistent in communication between training program directors and trainees, which is essential to ensure ongoing learning and reduce stress.

Research

In a dystopian fashion, COVID-19 has presented a research opportunity for imaging physicians and a huge roadblock to ongoing or planned research. Institutional review boards have typically been receptive to COVID-19 research (active clinical outcomes practices that combine "learning" as well as "doing" treatments), advocated data collection for subsequent retrospective analyses, and are remaining active during this time to allow researchers the opportunity to begin studies. On the other hand, institutional review boards have prohibited other unrelated ongoing research protocols that involve healthy controls in the hospital/clinic setting from continuing. Clinical trials that involve administration of drugs on a defined schedule, particularly in oncologic care, have largely continued.

Many institutions have moratoriums on sharing electronic medical records with other institutions. This policy clearly stems from the past inadvertent release of PHI and existing legislation to protect confidential patient data, but the restriction can also have deleterious effects. For example, if all NYC academic centers wanted to share the electronic medical records of patients with COVID-19 for the development of artificial intelligence (AI) algorithm tools for triage or outcomes research, this collaboration would be highly restricted at present.

Some centers have instituted special review institutional review board panels to handle any COVID-19–related research in an effort to centralize the process and avoid repetition (and potentially link up like-minded projects), to prevent overwhelming institutional review boards. At least 2 institutions are using an expedited process for any clinical or translational research related to COVID-19, particularly drug trials. Some institutions have also used a blanket

institutional review board for data collection on all patients with COVID-19 performed across their network to ease collaboration and reduce the workload on institutional review boards.

It is impossible to over emphasize the value of ongoing communications among providers, researchers, associated staff, and patients and research subjects during this time. A clear discussion among those involved with ongoing research during a potential hiatus is a necessity. Departments are also in a position to leverage downtime from clinical activities to the benefit of research; additional academic and/or nonclinical time that can be used to complete research, apply for grants, and so forth is of immense value to academic physicians.

Challenges

1) Handling enormous volumes of data that are being generated on patients with COVID-19.
2) Avoiding potential exposures of research subjects.
3) Maintaining viability of ongoing research work.

Recommendations

1) Departments and organizations must collect a wide range of data on patients with COVID-19 in a systematic data-mineable fashion.
2) Ongoing clinical trials using imaging should ideally be segregated from interaction with potentially infected outpatients or hospitalized patients.
3) Organize/communicate with other institutions with experience with the disease to pool findings.
4) Communicate with patients in active studies to keep them enrolled.
5) Avoid loss of data in longitudinal studies as practicable.
6) Use downtime to complete ongoing projects to the extent possible and increase academic productivity.

Conferences and Meetings

As expected, during the pandemic, many planned meetings have been cancelled, postponed, or are being held in a "virtual" format. Most health care networks have restricted travel related to business. Several institutions ruled that physicians with scheduled time away for meetings that were canceled were unable to reschedule the time as work time and were bound to take the time off though travel was prohibited; this ruling was to avoid the expected backlog of travel and conference time when meetings are again scheduled and may overlap with the expected volume rebound of imaging studies that have been postponed. There is discussion of continued restrictions on vacation and meeting time allowances at some institutions after the "curve is flattened," again because of the expected rebound. These restrictions may impact attendance at future meetings. If restrictions to travel remain in place, neither speakers nor participants may be able to attend. It is not possible for large meetings to nimbly change venues in response to a rapidly changing pandemic, and there is no guarantee that air travel will resume with normal schedules.

The disruption of academic meetings is a small part of this problem, but one that may have real economic repercussions. Attendance at and involvement in large medical meetings are an important element in academic advancement and promotion and tenure. The potential economic benefit to cities hosting meetings is also considerable. A large number of medical meetings (American Roentgen Ray Society, American Society of Neuroradiology, European Society of Head and Neck Radiology, among others) have either canceled their planned physical meetings, are attempting virtual meetings, or are postponing their meetings until later and hopefully achievable dates.

The virtual meeting plan has had numerous advocates, but issues remain with nondedicated time to attend a virtual meeting while still working on a clinical service. Data security and privacy are concerns with virtual meetings. The infamous "Zoom bomb" has been widely reported in the press and can be disruptive as well as a security concern. Prerecorded lectures as well as conferencing platforms are means of carrying out the educational mission of a meeting, and discussions can be via on-line platforms. Interruptions obviously occur and can be catastrophic, depending on where in the chain they occur, but are fortunately relatively uncommon. Some organizations have relied on podcasts and other digital formats to perform their academic missions, some with relative success. Canceled meetings are an anathema to organizations that benefit from the interactions and activities of these meetings, to say nothing of the potential loss of revenue. Postponing a meeting can lead to a less-than-optimal rescheduling, overlap with other meetings also being rescheduled, and pose the additional risk of a second or third wave of COVID-19.

Challenges

1) Planning in advance to attend meetings in late summer or fall that are in jeopardy of cancellation.
2) Scheduling future time away, which will be difficult with multiple other staff similarly looking at future meeting times, work volume rebounds, manpower requirements, and so forth.
3) Planning future meetings given the new COVID-19 reality.
4) Maintaining security with virtual meeting content.

Recommendations

1) Be proactive and plan a virtual meeting backup in anticipation of disruptions from local disease outbreaks, economic impact, and work-related restrictions on employee movement.
2) Condense meetings to a 1-day virtual workshop/on-line forum with restricted participation or make meeting lectures available on-line.
3) Provide security for virtual meeting content.

Physician Well-Being

There is omnipresent stress in an environment where an unseen pathogen is seemingly "stalking" you. Radiologists are often tagged as "loners" but, in fact, practice in constant communication with others: staff, technologists, nurses, and trainees. Staff who have typically been close to one another, surrounded by other staff and trainees, interacting with these individuals as a part of their practice, now find themselves sheltered in place at home, reading remotely. There are no lunch breaks, no shared time for coffee, and minimal interactions with anyone. Limited hospital manpower reserves also added another stress to radiologists: the uncertainty of being "redeployed" or reassigned to an

area of medicine where they are minimally competent or untrained. Morale has definitely declined.

Physicians previously proud of their clinical volumes may be "out of the loop" and acutely aware of the lack of productivity forced on them. Many of us have seen an aggressive approach to worklists: taking cases from lists when the examinations were not completed and staff taking cases before trainees have an opportunity to review them.

The issue of ego and well-being is personal. Finding a way to keep in touch with friends, colleagues, and acquaintances during this period requires effort. How one chooses to engage with others is not the issue; remained engaged with others is the issue. Phone, e-mail, texts, video chats, and so forth are viable. It is a good time to refresh old friendships. If you are a social media fan, the platforms are varied and can be useful, but clearly using social media to air issues with hospital administration, fellow staff, or others can be a potential landmine. A few moments to review hospital or system policies regarding social media can be valuable, particularly if one is frustrated and irritated. Outlets to reduce stress are also a personal issue, but as long as the outlet is not ultimately deleterious, whatever works for you is likely good. A widely held opinion echoed recently is that a crisis serves to pinpoint many hidden system problems. A useful means to handle that stress is to identify those problems and work to find solutions. An administration that openly and frequently communicates with the physicians contributes to a more positive view of the situation, reduces uncertainty, and lessens stress.

Stress that seems unbearable needs to be recognized as a problem, and help should be sought. Many of our systems have engaged support services and mental health professionals and made them available. There is no shame in seeking help for an issue that is so widely disruptive to society as we have known it.

Challenges

1) Lack of social interactions.
2) Stress and anxiety over work, health, and society.
3) Loss of productivity in the workplace.
4) Guilt.

Recommendations

1) Find ways to interact.
2) Know your institutional policies regarding media when discussing or providing opinions on administration decisions or practices.
3) Find useful/creative/constructive outlets to reduce stress.
4) Alert staff to signs of excessive stress and anxiety; facilitate access to behavioral health services when they are needed.
5) Work locally to address shortcomings in pandemic re-sponses. Some have advocated a "postpandemic" committee to review concerns and provide recommendations. Well-conceived and organized plans may move beyond local or regional to national significance. A "pandemic panel" to address all issues identified for improving the ability of physicians to express concerns through the American College of Radiology, Radiological Society of North America, American Society of Neuroradiology, or other organizations may be a useful outcome of this event.
6) Keep open communication lines between administration to staff. This is of paramount importance.

Long-Term Plan (Aftermath)

The isolation and its consequences will clearly end, and a return to normalcy in work and life will occur, though with differences, both expected and unexpected. Gearing up the medical imaging world will take time but is expected to return to prepandemic levels with a significant pent-up demand that could generate considerably increased short-term volumes. Social distancing and other factors may influence our practices for some time. The other mitigating factor here is the increase in unemployment, with loss of medical benefits that some may encounter. With the pandemic having exposed some weaknesses in the current imaging methodology, changes can be expected in the way we work. Off-site imaging has clearly proved its efficacy.

Challenges

1) Anticipated increase in workload when imaging returns.
2) Expected period when no/minimal travel or meetings will be allowed, given this potential period of increased volumes.

Recommendations

1) Sites may contemplate extended hours and increased availability for imaging services after restrictions are lifted.
2) Practices will likely increase access to PACS resources in-home and off-site.
3) Physicians will need to have flexibility in time-off schedules

Conclusions

Dealing with COVID-19 remains a work in progress, but there is a consensus that during surge periods, radiology departments will need to keep most staff off-site working from remote workstations, maintain but minimize their presence at hospitals for procedures and consults, minimize outpatient imaging for safety, maintain education of trainees, gather data on the disease to hopefully facilitate treatment of this ongoing episode or future pandemics, and enhance connectivity within the neuroradiology department and with neurologists, neurosurgeons, and head and neck surgeons by all means available to maintain patient care. When the pandemic worsened, systems have not hesitated to use deployment to either remote or clinical work as the volume of work in the more seriously affected areas reached a threshold by which staffing and subsequently patient care were challenged. We acknowledge our clinical colleagues who have faced this pandemic directly; they are truly performing a service that is of astounding risk and scope. We also acknowledge our radiology colleagues who have been reassigned to clinical areas to provide, in some cases, direct care to patients with this disease. Neuroradiology remains a critical support service for our clinical colleagues and for patients hospitalized with COVID-19.

ACKNOWLEDGMENTS

We extend special thanks to Keith Hentel, MD (Weill Cornell Medical College, NewYork-Presbyterian Hospital, New York City).

Asymptomatic COVID-19: What the Neuroradiologist Needs to Know about Pulmonary Manifestations

R.F. Barajas, Jr, G. Rufener, J. Starkey, T. Duncan, and C. Fuss

ABSTRACT

SUMMARY: Coronavirus disease 2019 (COVID-19) is an infectious disease with a high asymptomatic incidence. Asymptomatic infections within a population will inevitably lead to diagnosis via unrelated medical imaging. We report the case of an asymptomatic patient undergoing a spine CT examination for trauma who was incidentally found to have lung abnormalities later confirmed to be COVID-19. We aim to familiarize neuroradiologists with the spectrum of COVID-19 pulmonary manifestations that are likely to be observed on neck and spine CT imaging.

ABBREVIATIONS: COVID-19 = coronavirus disease 2019; GGO = ground glass opacities; SARS-CoV-2 = Severe Acute Respiratory Syndrome–coronavirus 2

A novel coronavirus, Severe Acute Respiratory Syndrome–coronavirus 2 (SARS-CoV-2) or World Health Organization designated coronavirus disease 2019 (COVID-19) has developed into a pandemic.[1,2] Initial reports suggest that COVID-19 is a highly infectious disease transmitted through respiratory droplets and fomites, resembling the spread of influenza.[3] Unlike influenza, COVID-19 appears to have a prolonged incubation period with a median of 5.1 days but up to 14 days from exposure.[4] The transmission rate is likely heightened by infected patients demonstrating little or no respiratory symptoms. The rate of asymptomatic infections remains unknown; however, data from the Diamond Princess Cruise Ship and Washington State Skilled Nursing Facility cohorts suggest that approximately 50% of the patients with confirmed COVID-19 were asymptomatic at the time of diagnosis.[4,5]

The potential of a highly infectious disease spreading via asymptomatic carriers poses unique challenges in the radiologic setting because risk stratification and isolation protocols depend on a suggestive clinical history. Likewise, the presence of a large, asymptomatic cohort will inevitably lead to incidental diagnoses. We report the case of an asymptomatic patient undergoing a cervical spine CT examination for trauma who was incidentally found to have lung abnormalities, later confirmed to be COVID-19. Given the escalating incidence, the aim of this report is to familiarize neuroradiologists with the spectrum of COVID-19 pulmonary manifestations that are likely to be observed on neck and spine CT examinations.

Brief Report

An 83-year-old man with a history of chronic obstructive pulmonary disease and diabetes mellitus type 2 presented to our institution with 3 days of progressive altered mental status culminating in a fall from standing. A chronic infrequent dry cough was reported, but acute respiratory symptoms were denied. Initial physical examination and vital sign assessment were unremarkable. CT of the cervical spine for suspected traumatic injury showed incidental lung findings of peripheral bilateral apical ground glass opacities (GGO) with a crazy paving appearance (Figure). The reporting neuroradiologist (R.F.B., Jr) consulted the cardiothoracic radiology section chief (C.F.) regarding possible COVID-19 infection. It was agreed that the recently published Radiological Society of North America (RSNA) Expert Consensus Statement on Reporting Chest CT Findings Related to COVID-19 should be used.[6] The treating emergency medicine physician was notified of the high suspicion for

Received April 4, 2020; accepted after revision April 9.

From the Departments of Radiology (R.F.B., Jr, G.R., J.S., C.F.); Advanced Imaging Research Center (R.F.B., Jr); and Knight Cancer Institute, Translational Oncology Research Program (R.F.B., Jr), Oregon Health & Science University, Portland, Oregon; and Departments of Radiology (T.D.), Portland Veterans Affairs Medical Center, Portland, Oregon.

This material is the result of work supported by resources and the use of facilities at the Portland Veterans Affairs Medical Center.

The content does not represent the views of the United States Department of Veterans Affairs or the United States Government.

This work was supported, in part, by National Institutes of Health grant KL2TR002370 (R.F.B., Jr).

Please address correspondence to Ramon F. Barajas, Jr, MD, Department of Radiology, Neuroradiology Section, Oregon Health & Science University, L340 3181 S.W. Sam Jackson Park Rd., Portland, OR 97239; e-mail: barajaslab@ohsu.edu; @OHSURadiology

http://dx.doi.org/10.3174/ajnr.A6561

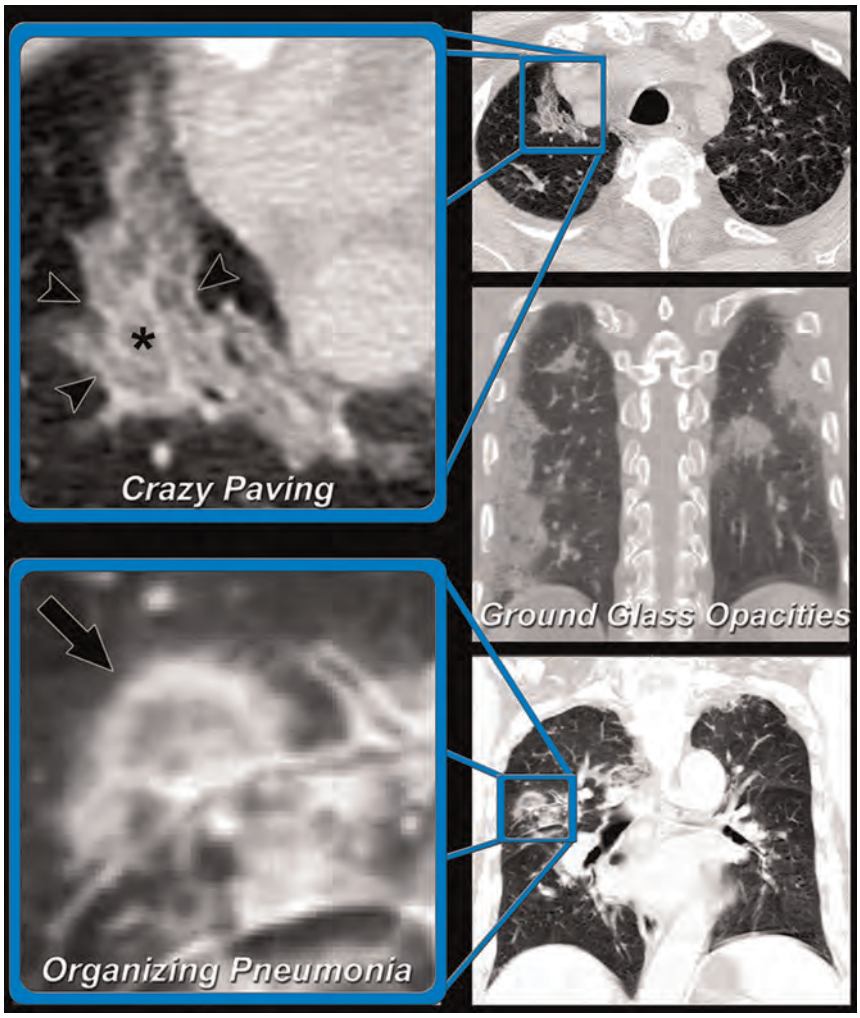

FIGURE. Pulmonary manifestations of asymptomatic COVID-19 Infection. An 83-year-old man without acute respiratory symptoms presented to our institution for CT of the cervical spine following a fall from standing. Limited evaluation of the lung apex on the cervical spine CT (*upper row*) demonstrated bilateral GGO (*asterisk*) with associated interlobular septal thickening (*arrowheads*, crazy paving), a typical appearance for COVID-19 infection. After consultation with the treating emergency department physician, the patient was placed on droplet precautions, a COVID-19 viral test was obtained, and CT of the chest was performed to assess the extent of disease. Bilateral peripheral GGO (*middle row*) and organizing pneumonia (*arrow*) were observed (*lower row*). The patient's GeneXpert COVID-19 test subsequently had positive findings, and the patient was admitted to the medical intensive care unit for observation. This case highlights the importance of familiarity with the pulmonary manifestations of COVID-19 and current expert consensus reporting recommendations. This familiarity will ensure timely, optimal patient care in the current pandemic setting.

COVID-19 viral pneumonia, and standard protocols for infection and exposure control were initiated.

On the same day, a GeneXpert test (Cepheid) was reported positive for COVID-19 (SARS-CoV-2). The patient was admitted to the medical intensive care unit because of age and comorbidities. Findings of a standard viral panel were negative, including influenza A and B. Labs were notable for thrombocytopenia, mild leukopenia, and mildly elevated D-dimer levels. An experimental course of hydroxychloroquine was initiated. On hospital day 3, the patient experienced a fever of 38.9°C with waxing and waning delirium. Nevertheless, the patient remained on room air without shortness of breath or progressive respiratory symptoms. The patient remains in the medical intensive care unit at the time of this writing.

DISCUSSION

Our case highlights the importance of the neuroradiologist being familiar with pulmonary CT findings associated with COVID-19. The neuroradiologist may be the first provider to recognize the possibility of a COVID-19 infection. This role places the responsibility of alerting the treating physician so that standard operating procedures for infection and exposure control can be initiated.

The RSNA Expert Consensus Statement on Reporting Chest CT Findings Related to COVID-19 has recently provided an up-to-date summary of published literature.[6] Patients with symptomatic COVID-19 infections typically present with GGO with or without superimposed consolidations. Pulmonary consolidation has been reported as peripheral, posterior, and diffuse with a predominate lower lung zone distribution. The GGO can have a rounded morphology with superimposed inter- or intralobular septal thickening, termed "crazy paving." The GGO associated with COVID-19 do not seem to follow a perihilar pattern. Later stages of the disease can demonstrate an organizing pneumonia manifested by a "reversed halo sign" or "atoll sign." The aforementioned pulmonary CT findings are neither sensitive nor specific. Indeed, GGO and crazy paving are observed in many viral lung infections and inflammatory diseases.

The RSNA Expert Consensus Statement on Reporting Chest CT Findings Related to COVID-19 has provided structured language to assist radiologists in reducing reporting variability and uncertainty (Table).[6] While focused on the reporting of chest CT findings, it could also be useful to the neuroradiologist in describing incidentally observed pulmonary abnormalities. Four reporting categories based on pulmonary CT findings have been proposed, and reporting language is suggested. We propose, in the context of the ongoing pandemic, that the presence of typical and indeterminate pulmonary imaging findings on neck or spine CT examinations should prompt the neuroradiologist to discuss the possibility of COVID-19 infection with the treating physician in an expedited manner. Pulmonary manifestations of COVID-19 seem to be dependent on the patient's disease state at the time of imaging. A comprehensive study of pulmonary findings in asymptomatic patients with COVID-19 has not been reported.

Adapted RSNA consensus guidelines for reporting CT findings related to COVID-19[a]

CT Imaging Appearance	Pulmonary CT Findings	Suggested Reporting Language
Typical	Crazy paving Bilateral Peripheral GGO Bilateral Peripheral Multifocal Rounded Organizing pneumonia	"Commonly reported imaging features of (COVID-19) pneumonia are present. Other processes such as influenza pneumonia and organizing pneumonia, as can be seen with drug toxicity and connective tissue disease, can cause a similar imaging pattern."
Indeterminate	No typical features and GGO Multifocal Diffuse Perihilar Unilateral Nonrounded	"Imaging features can be seen with (COVID-19) pneumonia, though are nonspecific and can occur with a variety of infectious and noninfectious processes."
Atypical	No typical or indeterminate features and Isolated lobar or segmental consolidation without GGO Centrilobular nodules Cavitation Smooth interlobular septal thickening with pleural effusion	"Imaging features are atypical or uncommonly reported for (COVID-19) pneumonia. Alternative diagnosis should be considered."
Negative	No CT features of pneumonia	"No CT findings present to indicate pneumonia. (Note: CT may be negative in the early stages of COVID-19.)"

[a] This table was adapted from Simpson et al.[6] Crazy paving is rounded ground glass opacification associated with inter- and intralobular septal thickening. Organizing pneumonia is a focus of GGO with peripheral consolidation previously described as "atoll sign" or "reverse halo sign."

As of April 2020, the RSNA, Society of Thoracic Radiology, and the American College of Radiology (ACR) recommend against CT imaging being used to screen for or as a first-line test to diagnose COVID-19.[6] The ACR highlights the limitations of using CT for COVID-19 diagnosis. Normal findings on chest CT do not mean that an individual does not have a COVID-19 infection. Likewise, abnormal CT findings are not sufficiently specific to establish the diagnosis.

In conclusion, ground glass opacities, crazy paving, and organizing pneumonia encountered on pulmonary CT scans should prompt consideration of COVID-19 infection in the current pandemic, with expedited communication with the referring providers and follow-up testing as appropriate.

ACKNOWLEDGMENTS

The first author thanks Bethany Barajas, MSN, for her helpful comments regarding this article, the clinical colleagues who are risking their health to treat patients with COVID-19, and the many patients who are confronting a deadly disease.

Disclosures: Ramon F. Barajas—*RELATED*: *Grant*: National Institutes of Health, *Comments*: National Institutes of Health Career Training Grant KL2TR002370.* Timothy Duncan—*UNRELATED*: *Employment*: Portland Veterans Affairs Medical Center, *Comments*: I am a VA staff physician. Cristina Fuss—*OTHER RELATIONSHIPS*: My husband is a shareholder at ViewRay Inc, which specializes in the Magnetic Resonance Imaging Guided Linear Accelerator. *Money paid to the institution.

REFERENCES

1. World Health Organization. **Novel coronavirus (2019-nCoV) situation report-15.** February 4, 2020. https://www.who.int/docs/default-source/coronaviruse/situation-reports/20200204-sitrep-15-ncov.pdf?sfvrsn=88fe8ad6_2. Accessed April 3, 2020
2. World Health Organization. **WHO Director-General's opening remarks at the media briefing on COVID-19.** March 11, 2020. https://www.who.int/dg/speeches/detail/who-director-general-s-opening-remarks-at-the-media-briefing-on-covid-19—11-march-2020. Accessed April 3, 2020
3. Lauer SA, Grantz KH, Bi Q, et al. **The incubation period of coronavirus disease 2019 (COVID-19) from publicly reported confirmed cases: estimation and application.** *Ann Intern Med* 2020 Mar 10. [Epub ahead of print] CrossRef Medline
4. Japanese National Institute of Infectious Diseases. **Field Briefing: Diamond Princess COVID-19 Cases. 20 Feb Update.** https://www.niid.go.jp/niid/en/2019-ncov-e/9417-covid-dp-fe-02.html. Accessed April 3, 2020
5. Kimball A, Hatfield KM, Arons M, et al. **Asymptomatic and Presymptomatic SARS-CoV-2 Infections in Residents of a Long-Term Care Skilled Nursing Facility—King County, Washington, March 2020.** Morbidity and Mortality Weekly Report (MMWR). https://www.cdc.gov/mmwr/volumes/69/wr/mm6913e1.htm. Accessed April 3, 2020
6. Simpson S, Kay FU, Abbara S, et al. **Radiological Society of North America Expert Consensus Statement on Reporting Chest CT Findings Related to COVID-19: Endorsed by the Society of Thoracic Radiology, the American College of Radiology, and RSNA.** *Radiology: Cardiothoracic Imaging* 2020;2:e200152 CrossRef

Comparison of MRI, MRA, and DSA for Detection of Cerebral Arteriovenous Malformations in Hereditary Hemorrhagic Telangiectasia

M. Vella, M.D. Alexander, M.C. Mabray, D.L. Cooke, M.R. Amans, C.M. Glastonbury, H. Kim, M.W. Wilson, D.E. Langston, M.B. Conrad, and S.W. Hetts

ABSTRACT

BACKGROUND AND PURPOSE: Patients with hereditary hemorrhagic telangiectasia (HHT) have a high prevalence of brain vascular malformations, putting them at risk for brain hemorrhage and other complications. Our aim was to evaluate the relative utility of MR imaging and MRA compared with DSA in detecting cerebral AVMs in the HHT population.

MATERIALS AND METHODS: Of 343 consecutive patients evaluated at the University of California, San Francisco HTT Center of Excellence, 63 met the study inclusion criteria: definite or probable hereditary hemorrhagic telangiectasia defined by meeting at least 2 Curacao criteria or positive genetic testing, as well as having at least 1 brain MR imaging and 1 DSA. MRIs were retrospectively reviewed, and the number of AVMs identified was compared with the number of AVMs identified on DSA.

RESULTS: Of 63 patients, 45 (71%) had AVMs on DSA with a total of 92 AVMs identified. Of those, 24 (26%) were seen only on DSA; 68 (74%), on both DSA and MR imaging; and 5 additional lesions were seen only on MR imaging. Of the 92 lesions confirmed on DSA, 49 (53.3%) were seen on the 3D-T1 postgadolinium sequence, 52 (56.5%) were seen on the 2D-T1 postgadolinium sequence, 35 (38.0%) were seen on the SWI sequence, 24 (26.1%) were seen on T2 sequence, and 25 (27.2%) were seen on MRA. The sensitivity and specificity of MR imaging as a whole in detecting AVMs then confirmed on DSA were 80.0% and 94.4%, respectively, and the positive and negative predictive values were 97.3% and 65.4%, respectively.

CONCLUSIONS: This study reinforces the use of MR imaging as a primary screening tool for cerebral AVMs in patients with hereditary hemorrhagic telangiectasia and suggests that 3D-T1 postgadolinium and 2D-T1 postgadolinium performed at 3T are the highest yield sequences.

ABBREVIATION: HHT = hereditary hemorrhagic telangiectasia

Hereditary hemorrhagic telangiectasia (HHT) is a rare, autosomal dominant disease characterized by the formation of mucocutaneous, lung, brain, and visceral organ vascular malformations.[1] Diagnosis of probable or definite HHT is defined by meeting ≥2 of the Curacao criteria or testing positive for known disease-causing mutations, including those in the *endoglin* (*ENG*), *activin A receptor like type 1* (*ACVRL1*), and *SMAD family member* 4 (*SMAD4*) genes.[1,2] Up to 23% of patients with HHT develop cerebral vascular malformations, including brain arteriovenous malformations, cavernous malformations, developmental venous anomalies, capillary telangiectasias, vein of Galen malformations, arteriovenous fistulas, capillary vascular malformations, and transitional or mixed malformations.[3-6] Most of these lesions are cerebral AVMs, which have the risk of potential rupture.[4] Studies have reported the risk of rupture in patients with HHT from 0.4% to 1.3% per year per patient or 0.3%–0.7% per year per lesion.[7,8] Given this risk, current guidelines recommend screening with cerebral MR imaging for all adults with possible or definite HHT and all children with possible or definite HHT within the first 6 months of life.[1,9] These same guidelines suggest using sequences with and without contrast as well as blood-sensitive sequences but provide no further specific recommendations as to which sequences are of the greatest utility.[1,9]

Received January 30, 2020; accepted after revision March 26.

From the Departments of Radiology and Biomedical Imaging (M.V.), Division of Neurointerventional Radiology (D.L.C., M.R.A., D.E.L., S.W.H.), Division of Diagnostic Neuroradiology (C.M.G.), Division of Interventional Radiology (M.W.W., M.B.C.), Hereditary Hemorrhagic Telangiectasia Center of Excellence (H.K., D.E.L., M.B.C., S.W.H.), and Anesthesia and Perioperative Care (H.K.), University of California, San Francisco, San Francisco, California; Department of Radiology, Division of Interventional Neuroradiology (M.D.A.), University of Utah, Salt Lake City, Utah; and Department of Radiology, Division of Neuroradiology (M.C.M.), University of New Mexico, Albuquerque, New Mexico.

This investigation was supported by the National Institutes of Health under the Ruth L. Kirschstein National Research Service Award T32EB001631 from the National Institute of Biomedical Imaging and Bioengineering, as well as R01EB012031.

Please address correspondence to Steven W. Hetts, MD, Division of Neurointerventional Radiology and HHT Center of Excellence, Department of Radiology and Biomedical Imaging, 505 Parnassus Ave, L-351, San Francisco, CA 94143-0628; e-mail: steven.hetts@ucsf.edu

http://dx.doi.org/10.3174/ajnr.A6549

While studies have proposed that specific MR images may be beneficial in evaluating the presence of AVMs in non-HHT populations, there are limited data demonstrating the specific utility of these sequences in screening for AVMs in patients with HHT.[10-12] Because the HHT population is undergoing screening to detect AVMs before they become clinically apparent, the AVMs this screening test seeks to find may often be smaller or have different characteristics compared with those seen on diagnostic examinations of symptomatic patients with AVMs in the general population.[1,4] We, therefore, sought to evaluate the relative utility of diagnostic screening MR imaging and MRA as well as the utility of specific MR imaging sequences compared with the criterion standard of DSA in detecting cerebral AVMs within the HHT population.

Table 1: Demographics of patients included in the study

Demographics	
Total No. of patients	$n = 63$
Female sex	41/63 (65%)
Age at time of MR imaging (mean) (yr)	36 ± 20
Curacao score	
1	1/63 (2%)[a]
2	18/63 (29%)
3	20/63 (32%)
4	24/63 (38%)
HHT-causing mutation	
ENG	23/63 (37%)
ACVRL1	5/63 (8%)
Variant of unknown significance	2/63 (3%)
Family member positive	6/63 (10%)
Negative genetic testing	9/63 (14%)
No genetic testing available	18/63 (29%)
Neurologic symptoms	
Present	50/63 (79%)
Absent	13/63 (21%)

[a] Genetically confirmed HHT.

MATERIALS AND METHODS

This retrospective study was approved by the institutional review board and performed in compliance with Health Insurance Portability and Accountability Act. All patients evaluated at the University of California, San Francisco HHT Center of Excellence as of January 2017 were screened for inclusion in this study ($n = 343$). The medical charts of these patients were retrospectively reviewed, and demographic data including age, sex, Curacao criteria, genetic testing results, and the presence of patient-reported neurologic symptoms were collected, along with information on cerebral imaging to evaluate inclusion in this study.

Inclusion criteria for the study were probable or definite HHT as defined by meeting at least 2 Curacao criteria or positive genetic testing as well as having at least 1 brain MR imaging and 1 cerebral DSA with images available for viewing on our PACS. Of the 343 patients reviewed, 246 met the study definition of probable or definite HHT, and of those, 63 patients had both sets of imaging available for our review and therefore met the full inclusion criteria.

All available MR imaging and MRA images for these 63 patients were retrospectively reviewed by a fellowship-trained neuroradiologist (M.D.A.), a subset of the studies (38 total) was reviewed by a second fellowship-trained neuroradiologist (M.C.M.), and any discrepancies between the 2 readers were adjudicated by a third fellowship-trained neuroradiologist (S.W.H.). All readers were blinded to the official reports. These readers evaluated each MR imaging study as a whole and recorded the total number of AVMs identified for each patient as well as on which sequences the AVMs were visible (3D-T1-weighted postgadolinium, 2D-T1-weighted postgadolinium, MRA, T2-weighted, SWI). Because these MRIs were performed at many different institutions (with patients later being referred to University of California, San Francisco) and on different types and field strengths (0.7T, 1.16T, 1.5T, and 3T) of MR imaging machines, there was no standardized set of sequences for the evaluated MRIs and MRAs. The cerebral DSA

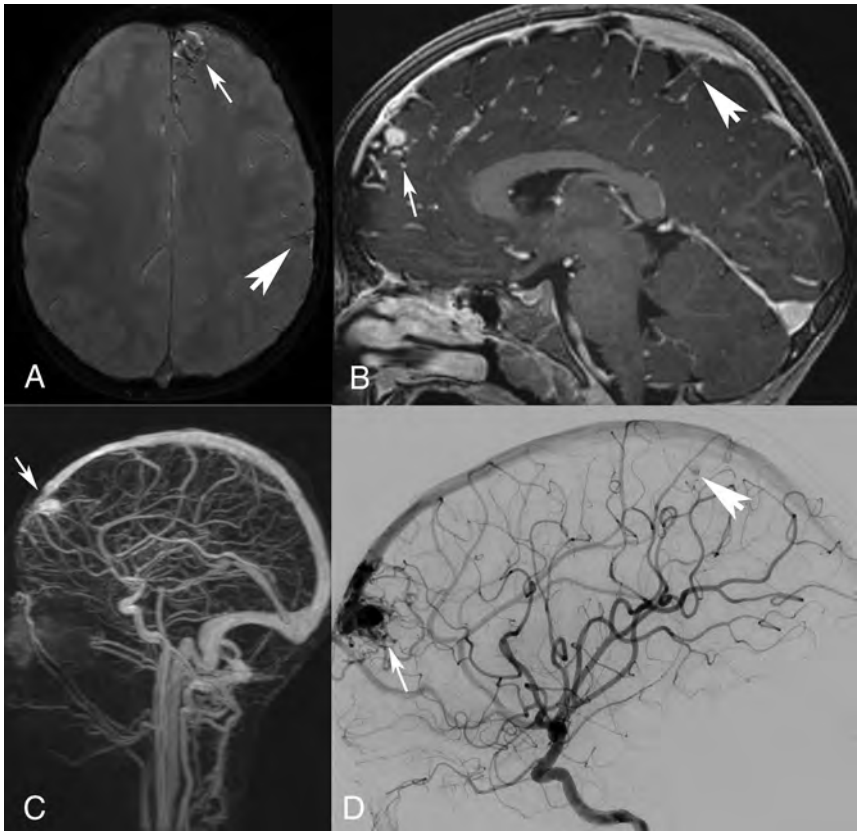

FIG 1. Multiple brain AVMs in HHT: positive on MR imaging, MRA, and DSA. A 5-year-old boy with a frontopolar cerebral AVM (*white arrow*) demonstrated on SWI MR imaging (*A*), 3D postgadolinium T1 (*B*), time-resolved dynamic contrast-enhanced MRA (*C*), and DSA (*D*). A smaller AVM (*white arrowhead*) is suggested by hypointensity on SWI (*A*), enhancement on 3D postgadolinium T1 (*B*), and enhancement and subtle arteriovenous shunting on DSA (*D*). The smaller AVM is not seen on MRA (*C*).

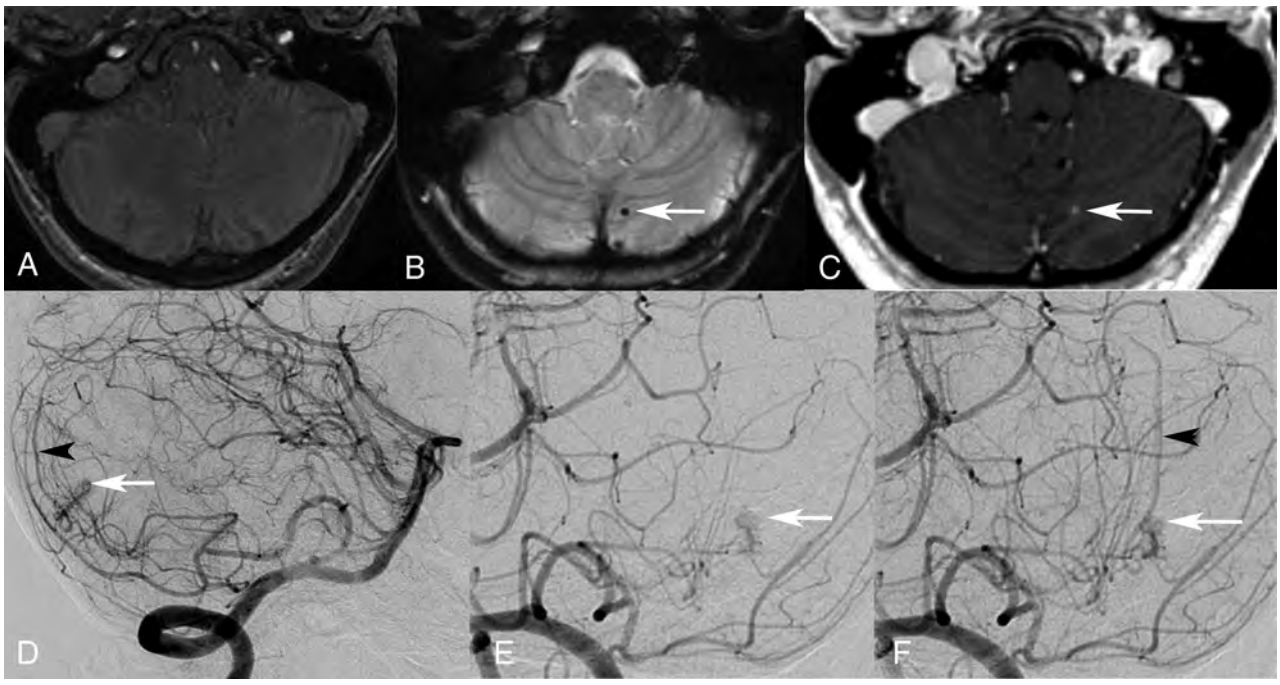

FIG 2. Small cerebellar AVM in HHT: positive on MR imaging, negative on MRA, and positive on DSA. A 49-year-old woman with a cerebellar hemispheric AVM (*white arrow*) not apparent on TOF-MRA (*A*) but apparent with microhemorrhage on SWI (*B*), on 3D postgadolinium T1 (*C*), and on DSA (*D–F*). DSA (*D* and *F*) additionally distinguishes the AVM nidus (*white arrow*) from the AVM draining vein (*black arrowhead*).

images for all 63 cases were reviewed by a fellowship-trained neurointerventional radiologist (S.W.H.) who determined and recorded the total numbers of cerebral AVMs visible on DSA.

Once the totals were compiled, true- and false-positive rates of cerebral AVM detection were determined for each identified lesion, with DSA being used as the criterion standard. These data were then used to determine which MR imaging sequences had the highest rates of true-positive cerebral AVM detection. In addition, the sensitivity, specificity, and positive and negative predictive values of MR imaging as a whole (including all available sequences with and without gadolinium and including MRA if available) and each sequence individually were calculated. For these calculations, a true-positive screening MR imaging or sequence was considered to be one that showed any possible AVM even if the exact number of AVMs did not match the number seen on cerebral DSA.

RESULTS

Of the 63 patients evaluated, 65% were women, and the average age at the time of the evaluated MR imaging was 36 ± 20 years, with a range of 1–77 years (Table 1). The Curacao scores ranged from 1 to 4 because some included patients meeting only a single criterion had positive genetic testing. A total of 39 of the 63 patients underwent genetic testing for known HHT-causing gene mutations, the results of which are listed in Table 1. A total of 24 patients had not undergone genetic testing at the time of the study, 6 (9%) of whom had family members who tested positive for known disease-causing mutations. Self-reported neurologic symptoms ranging from headaches, dizziness, and paresthesias to syncope, seizures, transient ischemic attacks, and strokes were seen in 79% of patients. Two patients had clinically evident AVM rupture on presentation, both of whom were younger than 12 years of age.

Of the 63 patients whose imaging was evaluated, a total of 45 (71%) were found to have at least 1 cerebral AVM on criterion standard DSA imaging. A total of 92 individual cerebral AVM lesions were identified in these patients' cerebral DSAs. Of the identified lesions, 24 (26%) were seen only on cerebral DSA, 68 (74%) were seen on MR imaging and cerebral DSA, and 5 additional lesions were identified only on MR imaging. Examples of these lesions can be seen in Figs 1–4. Table 2 describes the percentage of total lesions seen on MR imaging as a whole as well as each evaluated sequence compared with the total number of lesions seen on MR imaging ($n = 73$) and DSA ($n = 92$). The lesions seen on MR imaging ranged from 2 to 55 mm. The sensitivity and specificity of MR imaging (including all available sequences with and without gadolinium) as a screening technique used to detect at least 1 cerebral AVM, which was then confirmed on criterion standard cerebral DSA, were 80.0% and 94.4%, respectively, and the positive and negative predictive values were 97.3% and 65.4%, respectively (Table 3).

Of the 63 MRIs evaluated, 54 (86%) included postgadolinium imaging, while the other 9 (14%) were noncontrast only. Table 4 describes additional characteristics of the MRIs performed, including the field strength and frequency of each type of sequence as well as the spatial resolution ranges for each sequence type. Of the 3 studies not performed on a 1.5T or 3T magnet, 1 was performed on a 0.7T magnet, 1 was listed as a 1.16T magnet, and 1 had the magnet strength information missing from the DICOM data. The sensitivity, specificity, and positive and negative predictive values of each of the sequences evaluated as well as MR imaging as a whole and MR imaging based on magnet strength are shown in Table 3.

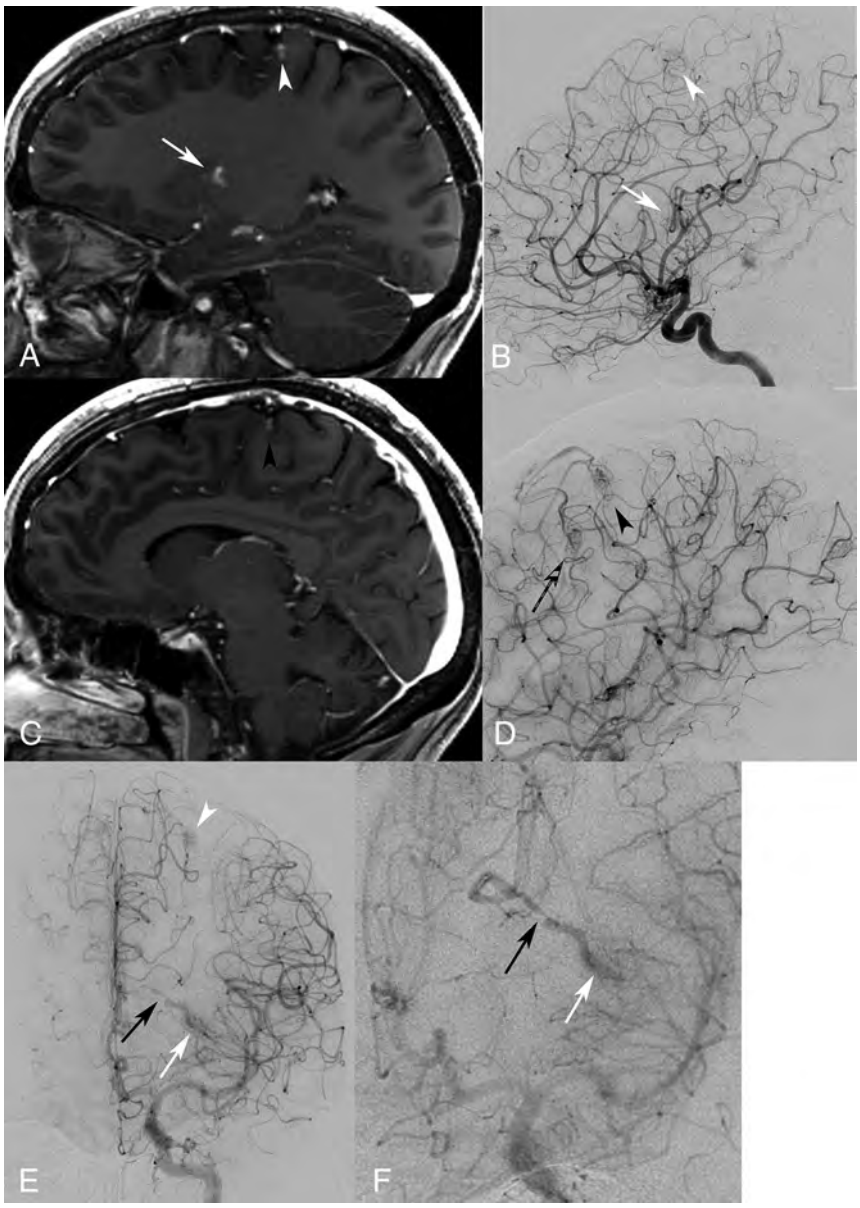

FIG 3. Multiple brain AVMs in HHT: positive on MR imaging, MRA, and DSA. A 23-year-old woman with 2 brain AVMs identified on MRA, 7 brain AVMs identified on MR imaging, and 11 identified on DSA. Selected images demonstrate a left basal ganglia AVM (*white arrow*) on 3D-postgadolinium T1 (*A*), left ICA lateral DSA (*B*), left ICA anterior-posterior arterial phase DSA (*E*), and magnified left ICA anterior-posterior capillary phase DSA (*F*). Note that the angioarchitecture of the basal ganglia AVM is best seen on DSA (*E* and *F*), including a high-grade stenosis of the deep draining vein of the AVM (*black arrow*). Although 3D-postgadolinium T1 image of the right hemisphere (*C*) demonstrates 1 cortical AVM (*black arrowhead*), right ICA lateral DSA (*D*) demonstrates 2 cortical AVMs; the more anterior of these lesions (*hashed arrow*) was only apparent on DSA.

Of the patients evaluated, 50 had MRAs performed as part of their overall MR imaging examinations. Of these 50 MRAs, 26 (52%) were performed on a 1.5T magnet, 23 (46%) were performed on a 3T magnet, and 1 was reported as being performed on a 1.16T magnet. The sensitivity and specificity of MRA alone as a screening technique used to detect at least 1 cerebral AVM, which was then confirmed on criterion standard cerebral DSA, were 50.0% and 92.9%, respectively, and the positive and negative predictive values were 94.7% and 41.9%, respectively (Table 3). The sensitivity, specificity, and positive and negative predictive values of each type of MRA can also be found in Table 3. Of note, the 2 postgadolinium-only MRA studies both yielded false-negative results, though the statistical significance of this finding is unclear, given the paucity of this type of case. In none of the 50 cases in which MRA was performed were there AVMs that were seen only on the MRA sequence and not on at least 1 additional sequence.

DISCUSSION

While current guidelines suggest that MR imaging be used as a screening tool for cerebral AVMs in patients with HHT, there are limited data on the accuracy of MR imaging in screening this particular patient population. Our study demonstrates that compared with the criterion standard DSA, MR imaging is relatively sensitive and specific when used to find cerebral AVMs in this population, with a sensitivity of 80.0%, specificity of 94.4%, and a negative predictive value of 65.4%. These data reflect the overall sensitivity and specificity of MR imaging as a screening technique, including all MR imaging sequences evaluated with and without gadolinium. This finding is similar to the reported 80%–95% sensitivity of MR imaging in detecting medium-to-large cerebral AVMs in the non-HHT population reported in the literature.[11-13] Our data, on the other hand, suggest that MRA alone (either TOF, postgadolinium, or a combination) as a screening technique is less optimal in the HHT population, with a sensitivity and specificity of 50.0% and 92.9%, respectively, and a negative predictive value of 41.9%. This finding is further supported by the fact that there were no cases in which a lesion was detected only on an MRA sequence and not on other sequences as well, suggesting that the addition of MRA to the overall MR imaging did not affect the sensitivity and specificity of MR imaging as a whole. This study supports MR imaging performing well as a screening tool for brain AVMs in the HHT population seen at our Center of Excellence, while MRA should not be used as a sole screening tool for cerebral AVMs in this population.

Our data also suggest that of the MR imaging sequences analyzed, postcontrast imaging sequences were the most useful in detecting cerebral AVMs with 3D-T1 postgadolinium and 2D-T1

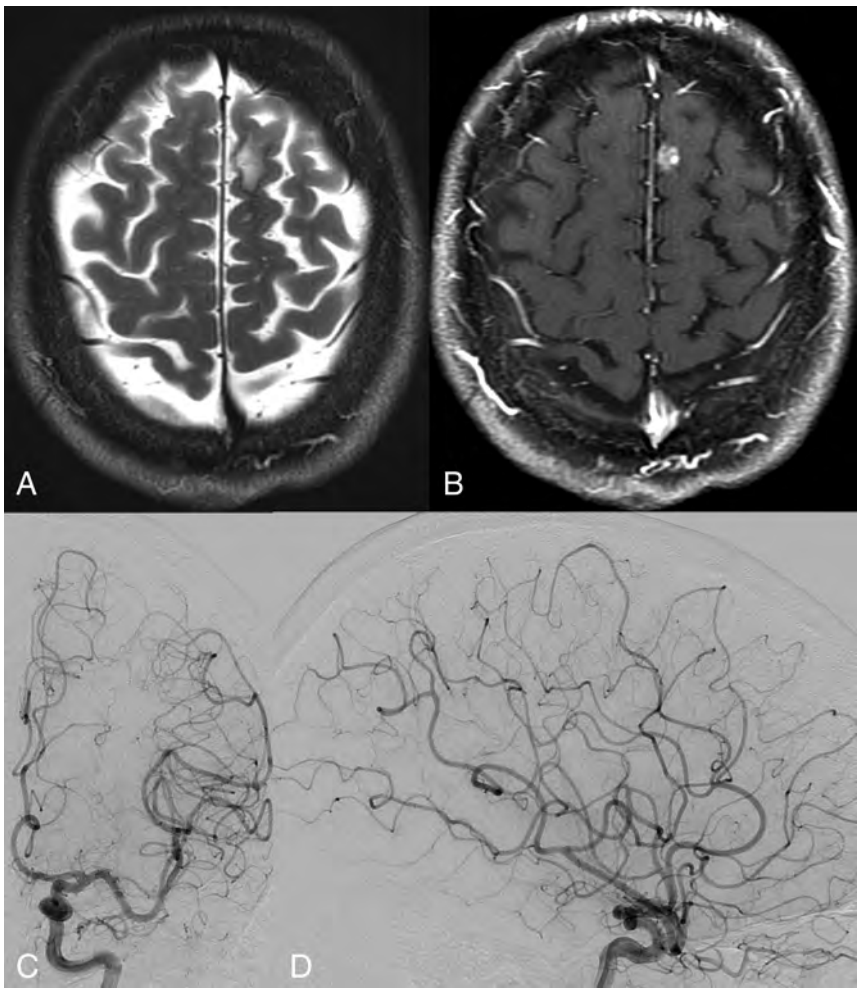

FIG 4. Cerebral vascular lesion in HHT: positive on MR imaging and negative on MRA and DSA. A 72-year-old man previously treated with gamma knife radiosurgery for a left frontal AVM. T2 MR imaging (*A*) demonstrates gliosis in the superior frontal gyrus but no apparent AVM vessels, postgadolinium 2D-T1 MR imaging (*B*) demonstrates an enhancing lesion in the superior frontal gyrus, and left ICA anterior-posterior (*C*) and lateral (*D*) DSA demonstrate no AVM.

Table 2: Number of AVMs seen on each evaluated MR image compared with the total number seen on each technique

Sequence	Total No. of AVMs Seen on Given Sequence	Percentage of all AVMs Seen on MR Imaging ($n = 73$)	Percentage of all AVMs Seen on DSA ($n = 92$)
Total AVMs seen on MR imaging	73	100.0%	79.3%
3D-T1 Postgad	49	67.1%	53.3%
2D-T1 Postgad	52	71.2%	56.5%
SWI	35	47.9%	38.0%
T2	24	32.9%	26.1%
MRA	25	34.2%	27.2%

Note:—Postgad indicates postgadolinium.

postgadolinium sequences showing up to 56.5% of lesions later confirmed on cerebral DSA and 71.2% of those seen on MR imaging. These postgadolinium MR imaging sequences also showed good sensitivity and negative predictive values (86.2% and 69.2%, respectively, for 3D-T1 postgadolinium and 75.0% and 60.9% respectively, for 2D-T1 postgadolinium), which are desirable in a good screening test. While MRA on its own and more specifically TOF-MRA alone showed poor sensitivity and negative predictive values, suggesting that these sequences would be poor screening tests, the studies that included both TOF and postcontrast MRA showed improved sensitivity and negative predictive values (70.0% and 75.0%, respectively, for the combination of TOF and postgadolinium MRA compared with 47.8% and 25.0%, respectively, for TOF-MRA alone), suggesting that the addition of postgadolinium MRA may improve the utility of this sequence.

In addition, our study suggests that 3T MR imaging is superior to 1.5T MR imaging, with a sensitivity of 85.7% and specificity of 100.0% compared with 72.7% and 92.9% in 3T versus 1.5T, respectively. While the MRIs performed on other field strengths also appeared to have high sensitivity and specificity, there were too few of these cases to draw firm conclusions.

Our study obviously has several limitations, the most important of which is the heterogeneity of the MR imaging studies that were evaluated. Because these studies came from many different sites, there was variation in the MR imaging magnet strength and the exact sequences performed; thus, we chose to stratify the sequences in the most general way possible rather than by individual manufacturer's sequence type. This heterogeneity of scanners and sequences may, therefore, lead our data to somewhat underestimate the true detection capability of these sequences. Additional studies evaluating a prospective cohort of patients with HHT all scanned on the same scanners with the same standardized protocol of imaging sequences may help to confirm the true sensitivity of each of these sequences in this population.

Whereas MR imaging is a noninvasive test used to screen patients with HHT for brain AVMs, DSA is an invasive test used to confirm findings on MR imaging and go beyond those findings to risk-stratify patients. Predicting the likelihood of future brain AVM rupture is the focus of many academic studies and is of paramount importance to individual patients and their physicians as they decide whether to treat any particular brain AVM. Susceptibility-weighted MR imaging sequences have demonstrated utility in detecting microhemorrhage within sporadic brain AVMs; this

Table 3: Sensitivity, specificity, and positive and negative predictive values of MR imaging as a whole, individual MR imaging sequences, and MR imaging as a whole at different given magnet strengths for the presence of cerebral AVM[a]

	No. of Positive Studies	Sensitivity	Specificity	Positive Predictive Value	Negative Predictive Value
Sequence					
MR imaging as a whole[b]	37	80.0%	94.4%	97.3%	65.4%
3D-T1 postgadolinium	25	86.2%	100.0%	100.0%	69.2%
2D-T1 postgadolinium	27	75.0%	100.0%	100.0%	60.9%
T2	20	54.1%	94.4%	95.2%	50.0%
SWI	23	51.2%	93.8%	95.7%	41.7%
MRA (any)[c]	19	50.0%	92.9%	94.7%	41.9%
TOF-MRA only	11	47.8%	100.0%	100%	25.0%
Postgadolinium MRA only	2	0.0%	NA	NA	0.0%
TOF and postgadolinium MRA	8	70.0%	90.0%	87.5%	75.0%
Magnet strength					
1.5T	17	72.7%	92.9%	94.1%	68.4%
3T	18	85.7%	100.0%	100.0%	50.0%
Other	2	100.0%	100.0%	100.0%	100.0%

Note:—NA indicates not applicable.

[a] A sequence (or MR imaging as a whole) was considered positive if it showed any number of AVMs even if the number did not ultimately match that seen on DSA.

[b] MR imaging as a whole included all available sequences with and without gadolinium evaluated for all patients.

[c] MRA (any) calculations included TOF and postgadolinium MRA either alone or in combination, depending on what was available for a given study.

Table 4: Characteristics of evaluated MRIs

Strength/Sequence	No. of Cases with Given Strength or Sequence (% of 63 Total Cases)	Range of Spatial Resolution
Magnet strength		
1.5T	36 (57.1%)	
3T	24 (38.1%)	
Other magnet strength	3 (4.8%)	
Sequence		
3D-T1 Postgadolinium	38 (60.3%)	0.4–5 mm
2D-T1 Postgadolinium	50 (79.4%)	1–5 mm
SWI	59 (93.7%)	1.6–6 mm
T2	53 (84.1%)	1–7.5 mm
MRA (any)	50 (79.4%)	0.5–2.6 mm
TOF-MRA only	28 (44.4%)	0.5–2.6 mm
Postgadolinium MRA only	2 (3.2%)	1–1.2 mm
TOF and postgadolinium MRA	20 (31.7%)	1–1.4 mm

finding is a predictor of future AVM rupture.[14] DSA can demonstrate detailed angioarchitectural features of AVMs that connote a higher risk of future rupture that are often not discernable on MR imaging, including feeding artery aneurysms, nidal aneurysms, and venous outflow stenosis.[15,16]

Our practice has been to perform DSA on patients with HHT who have either a brain hemorrhage or a potential brain AVM identified on screening MR imaging. Thus, another fundamental limitation of our study is that DSA is typically performed on patients who have a suspicious finding on MR imaging or MRA, not on patients who have normal MR imaging and MRA findings, thus likely undercounting the number of potential cerebral vascular malformations identifiable by DSA. There are, of course, small neurovascular lesions that may not be apparent on brain MR imaging but can be detected on DSA. In the HHT population, it would be expected that many of these very small malformations would be capillary vascular malformations that do not have arteriovenous shunting as opposed to nidus-type AVMs that do, by definition, have arteriovenous shunting. Although capillary lesions likely have a lower risk of hemorrhage than shunting lesions, the rupture rate of small shunting AVMs remains unknown. Detection of such lesions, thus, remains important for clinical decision-making. Some patients and physicians choose treatment even of small unruptured brain AVMs to prevent future cerebral hemorrhage, particularly if there are angioarchitectural high-risk features, lesional microhemorrhage, genetic predisposition, or a family history of brain AVM hemorrhage.

CONCLUSIONS

This study reinforces the use of MR imaging as a primary screening tool for cerebral AVMs in patients with HHT and suggests that a combination of postgadolinium sequences, specifically 3D-T1 postgadolinium and 2D-T1 postgadolinium, has the highest yield for brain AVM detection in patients with HHT and that MRA, and in particular TOF-MRA, alone is not sensitive enough to be used as a sole screening tool.

Disclosures: Maya Vella—*RELATED*: *Grant*: Ruth L. Kirschstein National Research Service Award T32EB001631, *Comments*: I am currently pursuing a T32 Research Fellowship year; therefore, any work I publish this year is funded by my salary provided by the T32 grant; *UNRELATED*: *Employment*: Radiology Resident Physician at University of California, San Francisco. Marc C. Mabray—*UNRELATED*: *Grants/Grants Pending*: National Institutes of Health/NIH.* Matthew R. Amans—*UNRELATED*: *Consultancy*: Covidien, *Comments*: Pipeline proctor. Christine M. Glastonbury—*UNRELATED*: *Royalties*: Amirsys-Elsevier, Comments: royalties from books and book chapters. Helen Kim—*RELATED*: *Grant*: National Institutes of Health; *UNRELATED*: *Consultancy*: Recursion Pharmaceuticals; *Grants/Grants Pending*: National Institutes of Health. Steven W. Hetts—*RELATED*: *Grant*: National Institute of Biomedical Imaging and Bioengineering*; *UNRELATED*: *Consultancy*, MicroVention Terumo, Route 92 Medical, and Imperative Medical Comments: CEC member for unrelated stroke treatment clinical trials; Core imaging laboratory for clinical trials: Stryker Neurovascular.* *Money paid to the institution.

REFERENCES

1. Faughnan ME, Palda VA, Garcia-Tsao G, et al; HHT Foundation International Guidelines Working Group. **International guidelines**

for the diagnosis and management of hereditary haemorrhagic telangiectasia. *J Med Genet* 2011;48:73–87 CrossRef Medline
2. Shovlin CL, Guttmacher AE, Buscarini E, et al. **Diagnostic criteria for hereditary hemorrhagic telangiectasia (Rendu-Osler-Weber syndrome).** *Am J Med Genet* 2000;91:66–67 CrossRef Medline
3. Maher CO, Piepgras DG, Brown RD Jr, et al. **Cerebrovascular manifestations in 321 cases of hereditary hemorrhagic telangiectasia.** *Stroke* 2001;32:877–82 CrossRef Medline
4. Fulbright RK, Chaloupka JC, Putman CM, et al. **MR of hereditary hemorrhagic telangiectasia: prevalence and spectrum of cerebrovascular malformations** *AJNR Am J Neuroradiol* 1998;19:477–84 Medline
5. Krings T, Kim H, Power S, et al; Brain Vascular Malformation Consortium HHT Investigator Group. **Neurovascular manifestations in hereditary hemorrhagic telangiectasia: imaging features and genotype-phenotype correlations.** *AJNR Am J Neuroradiol* 2015;36:863–70 CrossRef Medline
6. Brinjikji W, Iyer VN, Lanzino G, et al. **Natural history of brain capillary vascular malformations in hereditary hemorrhagic telangiectasia patients.** *J Neurointerv Surg* 2017;9:26–28 CrossRef Medline
7. Yang W, Liu A, Hung AL, et al. **Lower risk of intracranial arteriovenous malformation hemorrhage in patients with hereditary hemorrhagic telangiectasia.** *Neurosurgery* 2016;78:684–93 CrossRef Medline
8. Willemse RB, Mager JJ, Westermann CJ, et al. **Bleeding risk of cerebrovascular malformations in hereditary hemorrhagic telangiectasia.** *J Neurosurg* 2000;92:779–84 CrossRef Medline
9. Easey AJ, Wallace GM, Hughes JM, et al. **Should asymptomatic patients with hereditary haemorrhagic telangiectasia (HHT) be screened for cerebral vascular malformations? Data from 22,061 years of HHT patient life.** *J Neurol Neurosurg Psychiatry* 2003;74:743–48 CrossRef Medline
10. Sommer C, Mullges W, Ringelstein EB. **Noninvasive assessment of intracranial fistulas and other small arteriovenous malformations.** *Neurosurgery* 1992;30:522–28 CrossRef Medline
11. Mori H, Aoki S, Okubo T, et al. **Two-dimensional thick-slice MR digital subtraction angiography in the assessment of small to medium-size intracranial arteriovenous malformations.** *Neuroradiology* 2003;45:27–33 CrossRef Medline
12. Mukherji SK, Quisling RG, Kubilis PS, et al. **Intracranial arteriovenous malformations: quantitative analysis of magnitude contrast MR angiography versus gradient-echo MR imaging versus conventional angiography.** *Radiology* 1995;196:187–93 CrossRef Medline
13. Gauvrit JY, Oppenheim C, Nataf F, et al. **Three-dimensional dynamic magnetic resonance angiography for the evaluation of radiosurgically treated cerebral arteriovenous malformations.** *Eur Radiology* 2006;16:583–91 CrossRef Medline
14. Guo Y, Saunders T, Su H, et al. **Silent intralesional microhemorrhage as a risk factor for brain arteriovenous malformation rupture.** *Stroke* 2012;43:1240–46 CrossRef Medline
15. Hetts SW, Cooke DL, Nelson J, et al. **Influence of patient age on angioarchitecture of brain arteriovenous malformations.** *AJNR Am J Neuroradiol* 2014;35:1376–80 CrossRef Medline
16. Alexander MD, Cooke DL, Nelson J, et al. **Association between venous angioarchitectural features of sporadic brain arteriovenous malformations and intracranial hemorrhage.** *AJNR Am J Neuroradiol* 2015;36:949–52 CrossRef Medline

4D Flat Panel Conebeam CTA for In Vivo Imaging of the Microvasculature of the Human Cortex with a Novel Software Prototype

N. Huizinga, F. Keil, A. Birkhold, M. Kowarschik, S. Tritt, and J. Berkefeld

ABSTRACT

SUMMARY: It was the aim of our pilot study to investigate whether time-resolved flat panel conebeam CTA is able to demonstrate small cortical vessels in vivo. In 8 patients with small AVMs, time-resolved coronal MPRs of the vasculature of the frontal cortex were recalculated from 3D rotational angiography datasets with the use of a novel software prototype. 4D flat panel conebeam CTA demonstrated the course of the cortical arteries with small perpendicular side branches to the underlying cortex. Pial arterial and venous networks could also be identified, corresponding to findings in injection specimens. Reasonable image quality was achieved in 6 of 8 cases. In this small study, in vivo display of the cortical microvasculature with 4D flat panel conebeam CTA was feasible and superior to other angiographic imaging modalities.

ABBREVIATIONS: 3DRA = 3D rotational angiography; FPCBCTA = flat panel conebeam CTA

In the past, the vascular supply of the human cortex has been described according to findings from ex vivo injection specimens. The cortical arteries follow the course of the sulci as a source of a pial network of anastomoses and small direct branches to the cortex. Cortical draining veins are also collected by a venous network with further connections into superficially located cortical veins.[1] Beyond the level of pre- and postcapillary vessels, the vascular ultrastructure was investigated further by means of scanning electron microscopy, which was able to detect capillary networks within the cortical layers.[2] In vivo vascular imaging with DSA is widely limited to the display of larger branches. Small arterial and venous networks of the cortex are frequently obscured by the overlay of vessels on projection images. The resolution of other, less invasive angiographic modalities such as CTA or MRA is even worse, and reliable display of submillimeter structures cannot be achieved with routine acquisitions. SWI has the potential to show the microvasculature at 7T or with the use of iron-based contrast agents.[3] Until now, the clinical interest in imaging of the microvasculature of the human cortex was limited, but this may change due to research demonstrating the importance of the microcirculation in patients with cerebral ischemia or small-vessel disease.[4-7]

Received December 30, 2019; accepted after revision March 28, 2020.

From the Institute of Neuroradiology (N.H., F.K., J.B.), University Hospital of Frankfurt, Frankfurt, Germany; Siemens Healthcare GmbH (A.B., M.K.), Forchheim, Germany; and Helios Dr. Horst Schmidt Kliniken Wiesbaden (S.T.), Wiesbaden, Germany.

The concepts and information presented in this article are based on research and are not commercially available.

Please address correspondence to Joachim Berkefeld, MD, Institute of Neuroradiology, University Hospital of Frankfurt, Schleusenweg 2–16, D-60528 Frankfurt am Main, Germany; e-mail: Berkefeld@em.uni-frankfurt.de

http://dx.doi.org/10.3174/ajnr.A6574

It was shown that flat panel conebeam CTA (FPCBCTA) derived from 3D rotational angiography (3DRA) datasets is able to demonstrate small perforating branches of proximal parts of the cerebral arteries.[8,9]

Recent technical advances have led to a more refined technique, with the possibility of using the temporal information of 3DRA to reconstruct time-resolved 3D volumes and CT-like images.[10] It was the purpose of our pilot study to determine whether in vivo imaging of the cortical microvasculature is feasible with the use of 4D-FPCBCTA. The 4D option was chosen due to the advantage to select and demonstrate the proper angiographic phase with the best filling of the vessels. The use of a novel software prototype facilitated the visualization of the consecutive filling of small arteries and veins.

MATERIALS AND METHODS

Time-resolved coronal MPRs of the vasculature of the frontal cortex were recalculated from routinely acquired 3DRA datasets. The patients had justifying indications for a 3DRA protocol with a prolonged scan time of 12 seconds for treatment planning of AVMs.

For evaluation of the normal microvasculature, we selected 8 consecutive patients with small supratentorial AVMs with a nidus size of <3 cm and without major compromise of hemodynamics in the frontal cortex. Proceedings were approved by the local ethics committee at the University Hospital of Frankfurt, Germany.

All patients had selective transfemoral catheterization of the ICA under local anesthesia. DSA projection images and 3DRA datasets were obtained using modified Artis zee biplane neuroangiography equipment (Siemens). For 3DRA, the rotation angle was 260° with 2 runs (a native run without contrast and a fill run with contrast, 304 projections each) of 12 seconds each. The acquisition protocol is based on 2×2 binning of the

detector pixels of 154 × 154 μm each (0.308 × 0.308 mm effective pixel size). The FOV of the reconstructions was 238 × 184 mm with an isotropic voxel size of 0.46 mm^3 and a 512^2 matrix. After an x-ray delay of 2 seconds in the fill run, 20 mL of nonionic contrast with 300 mg of iodine/mL was automatically injected with a flow rate of 3 mL/s. For 2D-DSA, we used a protocol with a variable frame rate with up to 2 frames/s after hand injection of contrast.

For the reconstruction of 4D volumes and corresponding MPRs, the projection images were transferred to a dedicated workstation (syngo X Workplace VD20; Siemens) equipped with a software prototype as an extension of the currently available syngo Dyna4D software (Siemens). The prototype reduces streak artifacts, and the reconstruction algorithm should improve the recognition of consecutive filling of arteries and veins. We evaluated the cortical microvasculature, according to 4D-FPCBCTA MPRs in a coronal plane perpendicular to the course of the frontal gyri and sulci. The MPR with the best filling of small vessels was selected according to a cine display of the sequence of time-resolved MPRs, which is available at any time point during the scan time of 12 seconds. Usually the best filling of the microvasculature was visible after two-thirds of the scan time and at the end of the scan. We also tried MIPs or cuts from volume rendering data, which were found to be inferior to MPRs. The best visualization of the tubular character of small vessels occurred from section thicknesses between 6 and 9.5 mm. The findings from the reconstructions were compared with corresponding DSA images in a posterior-anterior projection and with findings in the literature.

Identification of vascular structures and image documentation was by consensus of 2 reviewers.

RESULTS

Eight consecutive patients (7 men and 1 woman, with a mean age of 45 years) met the inclusion criteria. Two datasets were only partly evaluable due to incomplete filling of the anterior cerebral artery due to hypoplasia of the A1 segment or movement artifacts.

In 6 fully evaluable cases, 4D-MPRs demonstrated the main branches of the cortical arteries following the course of the gyri into the depth of the sulci. From these main branches, small perpendicular arteries were visible, which could be followed for a few millimeters in the direction of the cortex. Intracortical networks were not detectable. Beneath these direct cortical branches, we found network-like anastomoses of small arteries above the surface of the cortex (Fig 1). In the venous phase, cortical draining veins could be identified perpendicular to larger collecting veins with network-like structures draining further into straight veins toward superficial cortical veins (Fig 2). The findings on MPRs were confirmed on corresponding DSA images with their sharper separation of the angiographic phases. Comparisons with drawings derived from illustrations from the literature[1,2] also confirmed our main findings.

DISCUSSION

Our casuistic pilot study showed the feasibility of in vivo imaging of the cortical microvasculature with the use of 4D-FPCBCTA and a novel software prototype. Compared with conventional reconstructions from 3D volume data, time-resolved MPRs are advantageous because they enable selection of the proper volume in the angiographic phases with the best filling of small arteries or veins. As is known from previous studies, temporal resolution of 4D-FPCBCTA and derived reconstructions is limited by overlapping of the arterial and venous phases.[11]

The filling of smaller vessels with slower flow demands a prolonged contrast bolus covering larger parts of the scan time compared with the shorter and sharper bolus of 2D-DSA. Even with the use of the software prototype, the overlapping angiographic phases led to difficulties in differentiating arteries and veins. Therefore, we selected reconstructions with typical anatomic patterns described for the course of arteries following the gyri and sulci, pial networks, and veins. The veins could be identified due to enhanced filling at the end of the scan and due to their straight course and connections to cortical veins, which could easily be detected. Correct assignment of arteries and veins was confirmed by comparison with DSA images showing the main structures. The display of fine details, such as pial or venous networks, was disadvantageous on DSA projection images due to the overlay of adjacent cortical vessels and their territories. In the current prototype implementation, the same threshold is used for segmentation of arteries and veins. Future implementations may investigate a thresholding technique for distinguishing arteries and veins.

The spatial resolution of 4D-FPCBCTA is limited; thus, we were unable to demonstrate intracortical vessels and vascular networks with vessels smaller than 100 μm, which have been previously described in scanning electron microscopy studies.[2] Only stump-like proximal parts of intracortical arteries and veins could be visualized. The vessel sizes we could display ranged between 150 and 750 μm, according to descriptions in the literature.[1,2] In animal experiments, MR imaging with SWI and iron-based contrast agents could visualize intracortical vessels of >10 μm.[3] For optimal display of vessels, section thicknesses between 6 and 9.5 mm were chosen. Thinner slices could improve the detection of small branches. The tubular character and branching of the vessels are better displayed on thick-section MPRs.

For our study, we used an Artis zee system (Siemens), which is not the latest technology. The visualization of vessels smaller than the voxel size of 0.5 mm^3 may be challenging, even with the latest generations of neuroangiography systems. Secondary reconstructions with smaller voxel sizes may improve the visualization of small vessels.

Based on our experience with the software prototype, further improvement of image quality in the display of small vessels can be expected and may become the subject of future studies.

Suboptimal image quality was caused by incomplete filling of the anterior cerebral territory in a patient with a hypoplastic A1 segment. FPCBCTA after IV contrast could avoid this problem of selective injections. In tentative reconstructions, the opacification of small vessels after IV contrast was much weaker and hardly evaluable.

Movement artifacts caused image degradation in another patient. General anesthesia, which could further improve image quality, is not adequate for a purely diagnostic procedure for treatment planning of an AVM. We tried reconstructions of

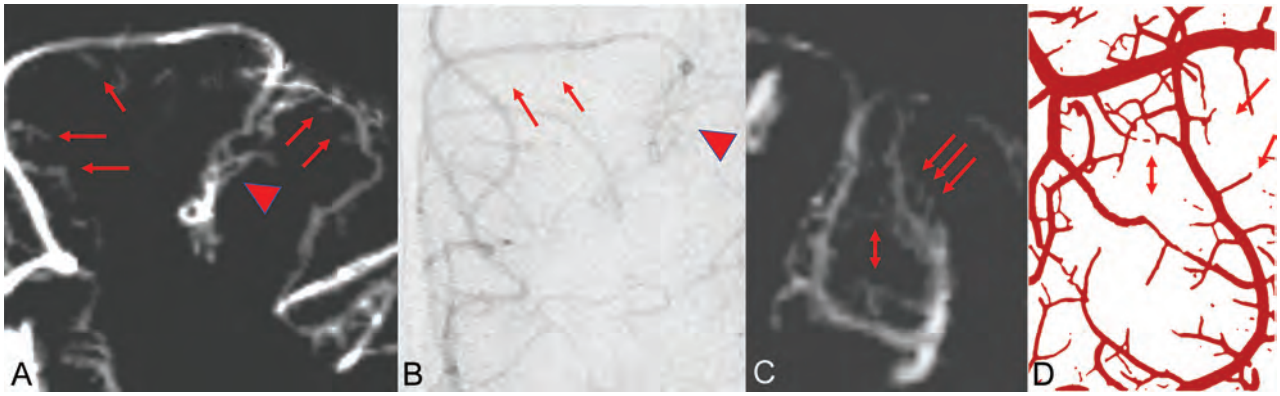

FIG 1. Coronal 4D-FPCBCTA reconstruction of the arterial microvasculature at the superior and middle frontal gyri and the superior frontal sulcus (*A*) and the corresponding DSA image, late arterial phase (*B*). Main arterial branches (*red arrows*) and the sulcal pial arterial network (*red arrowhead*) can be identified. Perpendicular branches to the cortex are difficult to see on DSA. *C*, A more detailed view shows arteries bending from the cortical surface into the depth the superior frontal sulcus. Perpendicular branches can be followed in the direction of the cortex of the adjacent middle frontal gyrus (*red arrows*). Note network-like intra-arterial connections (*double red arrow*). *D*, Similar findings are detected in injection specimens of cortical arteries (*corresponding arrows*). Drawing reprinted with permission from Duvernoy et al.[1]

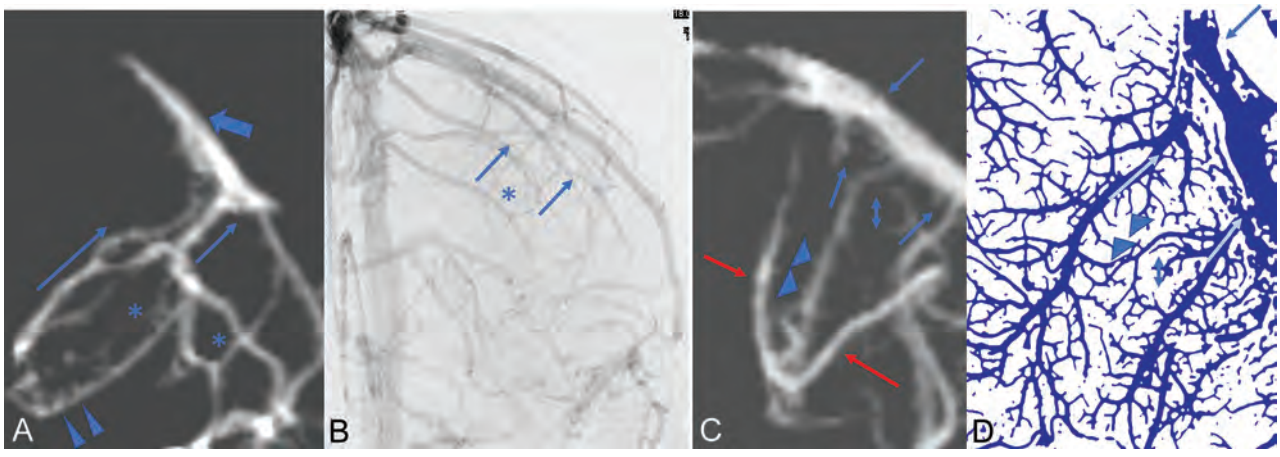

FIG 2. Coronal 4D-FPCBCTA reconstruction of veins in the middle frontal sulcus (*A*) and corresponding DSA image, late venous phase (*B*). Collecting veins (*thin blue arrows*) and the sulcal venous network (*asterisks*) can be identified on DSA. Small veins draining into the collecting veins are only partly visible (*blue arrowheads*). Further drainage of the collecting veins into a superficial cortical vein (*thick blue arrow*). Note considerable overlay of venous structures in the DSA projection image. *C*, Cortical veins are also fed by perpendicular branches from the cortex (*blue arrowheads*). Collecting veins show a straight course toward a larger cortical vein (*blue arrows*). Network-like connections are weakly accentuated (*blue double arrow*). Note the overlay by a sulcal artery (*red arrows*). *D*, Corresponding findings on a drawing from an injection specimen with small cortical draining veins (*blue arrowheads*) perpendicular to straight collecting veins to a cortical vein (*thin blue arrows*). Drawing reprinted with permission from Duvernoy et al.[1]

3DRA data from patients with aneurysms under general anesthesia with scan times of 5 seconds. Display of the microvasculature was clearly inferior, probably due to incomplete filling of small vessels and a lack of temporal resolution.

A disadvantage of 4D-FPCBCTA is its invasiveness, with potential risks of arterial catheterization. Until now, selective angiography with 4D-FPCBCTA provides the best contrast resolution for small vessels compared with less invasive imaging modalities.[12,13] One reason is the ability to obtain secondary reconstructions from the raw data without any loss of spatial resolution.

SWI after administration of iron-based contrast material may be further developed as a less invasive alternative. The first published images of the cerebral microvasculature with the use of this technique are promising but still inferior regarding the details seen on our reconstructions.[3]

Another disadvantage of 4D-FPCBCTA is the increased radiation exposure of 3DRA, with a prolonged scan time of 12 seconds. Effective dosage, according to the International Commission on Radiological Protection 103 (ATOM Phantom; CIRS; mobile MOSFET dosimetry system, Best Medical Canada), of 0.94 mSv for the 12-second 4D-FPCBCTA acquisition is lower than the reported doses of time-resolved CTA with the use of multislice CT[14] but higher than actual published doses of 3DRA with shorter scan times.[15] For 2D-DSA with 2 frames/s (Plane A - Posterior-Anterior, Plane B – 90° to plane A), an effective dose of 0.41 mSv (for 20 seconds) was determined.

Prolonged scan time and temporal resolution are key factors for successful display of small vessels. One main limitation of our study is the small number of cases due to time-consuming post-processing with manual window settings to enhance the vessels at the limits of the spatial resolution. The evaluation of a larger and more representative sample demands a standardization of the generation of 4D-MPRs, including further software improvement for tracking arteries and veins, which is challenging due to the close proximity of the arterial and venous parts of the cortical microvasculature. A more detailed comparison of the data with anatomic specimens, including measurements of vessel sizes, is also desirable.

Potential clinical applications of imaging of small cortical vessels are improved anatomic visualization of leptomeningeal anastomoses in patients with obstructions of cerebral arteries or in the surroundings of vascular malformations. Imaging of the normal microvasculature may also enhance our understanding of the angioarchitecture of pial AVMs.[11] Current imaging studies in patients with small-vessel disease are focused on MR imaging at high field strengths to show subcortical microinfarcts or microbleeds.[4,16] Visualization of small vessels is still based on postmortem studies.[17] It would be interesting to know whether direct visualization of cortical vessels in vivo could contribute to assessment of vascular density or other pathologic changes in patients with degenerative or inflammatory small-vessel disease.

CONCLUSIONS

In this small study, in vivo imaging of the cortical microvasculature with 4D-FPCBCTA and the use of a novel software prototype were feasible. Spatial resolution is currently superior to other angiographic imaging modalities.

Disclosures: Fee Keil—*RELATED*: *Payment for Writing or Reviewing the Manuscript*: funding by Siemens, €750/publication paid to the university*; *OTHER RELATIONSHIPS*: The Workstation used for analyzing the data belongs to Siemens and was only given as a loan to our institution; cooperation between Siemens and the Institution of Neuroradiology Frankfurt with external funding of €750/publication for open access. Annette Birkhold—*UNRELATED*: *Employment*: Siemens Healthcare AG. Markus Kowarschik—*UNRELATED*: *Employment*: Siemens Healthineers AG, *Comments*: full-time employee. Stephanie Tritt—*RELATED*: *Support for Travel to Meetings for the study or Other Purposes*: There is a permanent scientific cooperation between Siemens and the Institute of Neuroradiology, Frankfurt, and travel fees to meetings were paid by the company.* Joachim Berkefeld—*RELATED*: *Consulting Fee or Honorarium*: scientific cooperation with Siemens Healthineers, *Comments*: 2.500,_ €posterior-anterior paid to the university.* The dedicated workstation for 4D reconstructions and the software prototype were provided by Siemens Healthineers*; *UNRELATED*: *Consultancy*: MicroVention; proctoring for endovascular treatment of intracranial aneurysms with the Woven Endo-Bridge (WEB)-device, *Comments*: 3000,_ posterior-anterior honorarium. *Money paid to the institution.

REFERENCES

1. Duvernoy HM, Delon S, Vannson L. **Cortical blood vessels of the human brain.** *Brain Res Bull* 1981;7:519–79 CrossRef Medline
2. Reina-De La Torre F, Rodriguez-Baeza A, Sahuquillo-Barris J. **Morphological characteristics and distribution pattern of the arterial vessels in human cerebral cortex: a scanning electron microscope study.** *Anat Rec* 1998;251:87–96 CrossRef Medline
3. Wang H, Jiang Q, Shen Y, et al. **The capability of detecting small vessels beyond the conventional MRI sensitivity using iron-based contrast agent enhanced susceptibility weighted imaging.** *NMR Biomed* 2020;33:e4256 CrossRef Medline
4. Wardlaw JM, Smith EE, Biessels GJ, et al; STandards for ReportIng Vascular changes on nEuroimaging (STRIVE v1). **Neuroimaging standards for research into small vessel disease and its contribution to ageing and neurodegeneration.** *Lancet Neurol* 2013;12:822–38 CrossRef Medline
5. Kremer PH, Jolink WM, Kappelle LJ, et al; SMART and ESPRIT Study Groups. **Risk factors for lobar and non-lobar intracerebral hemorrhage in patients with vascular disease.** *PLoS One* 2015;10:e0142338 CrossRef Medline
6. Shi Y, Wardlaw JM. **Update on cerebral small vessel disease: a dynamic whole-brain disease.** *Stroke Vasc Neurol* 2016;1:83–92 CrossRef Medline
7. Shibuya M, da Costa Leite C, Lucato LT. **Neuroimaging in cerebral small vessel disease: update and new concepts.** *Dement Neuropsychol* 2017;11:336–42 CrossRef Medline
8. Lescher S, Samaan T, Berkefeld J. **Evaluation of the pontine perforators of the basilar artery using digital subtraction angiography in high resolution and 3D rotation technique.** *AJNR Am J Neuroradiol* 2014;35:1942–47 CrossRef Medline
9. Lescher S, Zimmermann M, Konczalla J, et al. **Evaluation of the perforators of the anterior communicating artery (AComA) using routine cerebral 3D rotational angiography.** *J Neurointerv Surg* 2016;8:1061–66 CrossRef Medline
10. Lang S, Gölitz P, Struffert T, et al. **4D DSA for dynamic visualization of cerebral vasculature: a single-center experience in 26 cases.** *AJNR Am J Neuroradiol* 2017;38:1169–76 CrossRef Medline
11. Lescher S, Gehrisch S, Klein S, et al. **Time-resolved 3D rotational angiography: display of detailed neurovascular anatomy in patients with intracranial vascular malformations.** *J Neurointerv Surg* 2017;9:887–94 CrossRef Medline
12. Zhang Z, Fan Z, Kong Q, et al. **Visualization of the lenticulostriate arteries at 3T using black-blood T1-weighted intracranial vessel wall imaging: comparison with 7T TOF-MRA.** *Eur Radiol* 2019;29:1452–59 CrossRef Medline
13. Nagata H, Murayama K, Suzuki S, et al. **Initial clinical experience of a prototype ultra-high-resolution CT for assessment of small intracranial arteries.** *Jpn J Radiol* 2019;37:283–91 CrossRef Medline
14. Radon MR, Chandran A, Bhojak M, et al. **Radiation dose reduction in 4D cerebral CT angiography by individualized estimation of cerebral circulation time.** *AJNR Am J Neuroradiol* 2016;37:2189–94 CrossRef Medline
15. Guberina N, Lechel U, Forsting M, et al. **Dose comparison of classical 2-plane DSA and 3D rotational angiography for the assessment of intracranial aneurysms.** *Neuroradiology* 2016;58:673–78 CrossRef Medline
16. Banerjee G, Wilson D, Jäger HR, et al. **Novel imaging techniques in cerebral small vessel diseases and vascular cognitive impairment.** *Biochim Biophys Acta* 2016;1862:926–38 CrossRef Medline
17. Kövari E, Herrmann FR, Gold G, et al. **Association of cortical microinfarcts and cerebral small vessel pathology in the ageing brain.** *Neuropathol Appl Neurobiol* 2017;43:505–13 CrossRef Medline

Application of Deep Learning to Predict Standardized Uptake Value Ratio and Amyloid Status on ^{18}F-Florbetapir PET Using ADNI Data

F. Reith, M.E. Koran, G. Davidzon, and G. Zaharchuk, for the Alzheimer's Disease Neuroimaging Initiative

ABSTRACT

BACKGROUND AND PURPOSE: Cortical amyloid quantification on PET by using the standardized uptake value ratio is valuable for research studies and clinical trials in Alzheimer disease. However, it is resource intensive, requiring co-registered MR imaging data and specialized segmentation software. We investigated the use of deep learning to automatically quantify standardized uptake value ratio and used this for classification.

MATERIALS AND METHODS: Using the Alzheimer's Disease Neuroimaging Initiative dataset, we identified 2582 ^{18}F-florbetapir PET scans, which were separated into positive and negative cases by using a standardized uptake value ratio threshold of 1.1. We trained convolutional neural networks (ResNet-50 and ResNet-152) to predict standardized uptake value ratio and classify amyloid status. We assessed performance based on network depth, number of PET input slices, and use of ImageNet pretraining. We also assessed human performance with 3 readers in a subset of 100 randomly selected cases.

RESULTS: We have found that 48% of cases were amyloid positive. The best performance was seen for ResNet-50 by using regression before classification, 3 input PET slices, and pretraining, with a standardized uptake value ratio root-mean-square error of 0.054, corresponding to 95.1% correct amyloid status prediction. Using more than 3 slices did not improve performance, but ImageNet initialization did. The best trained network was more accurate than humans (96% versus a mean of 88%, respectively).

CONCLUSIONS: Deep learning algorithms can estimate standardized uptake value ratio and use this to classify ^{18}F-florbetapir PET scans. Such methods have promise to automate this laborious calculation, enabling quantitative measurements rapidly and in settings without extensive image processing manpower and expertise.

ABBREVIATIONS: AD = Alzheimer disease; ADNI = Alzheimer's Disease Neuroimaging Initiative; AUC = area under the curve; ROC = receiver operating characteristic; SUVR = standardized uptake ratio value; SPM = Statistical Parametric Mapping; RMSE = root-mean-square error; PPV = positive predictive value; NPV = negative predictive value

Alzheimer disease (AD) has a large clinical impact and continues to increase in prevalence.[1] While clinical judgment is essential to make the diagnosis of AD, the use of physiologic biomarkers can play an important role in ambiguous cases or to track the status of disease over time. One hallmark pathology of AD is the deposition of amyloid beta.[2-4] Besides the measurement of biomarkers in CSF,[5] a widespread method to detect amyloid plaques is the use of PET. Recent studies[6,7] have shown that the radiopharmaceutical ^{18}F-AV-45 (florbetapir) can be used to detect amyloid beta deposition in PET scans in vivo and noninvasively, as it exhibits high affinity-specific binding to amyloid plaques.

PET imaging assessment is often performed solely in a qualitative fashion, where scans are classified as positive or negative depending on whether there is visual uptake of amyloid tracer in the cerebral cortex. However, if quantification is desired, several steps of processing are usually needed. For example, co-registered MR imaging scans may be used to identify relevant brain regions for the purposes of segmentation. One popular method for quantitatively assessing amyloid is based on cortical amyloid beta load in 4 regions (frontal, anterior/posterior cingulate, lateral parietal, and lateral temporal cortex), normalized by uptake in the whole cerebellum, a metric known as the standardized uptake value ratio

Received December 13, 2019; accepted after revision March 21, 2020.

From the Departments of Radiology (F.R., M.E.K., G.D., G.Z.) and Nuclear Medicine (M.E.K., G.D.), Stanford University, Stanford, California.

Data used in the preparation of this article were obtained from the Alzheimer's Disease Neuroimaging Initiative (ADNI) database (adni.loni.usc.edu). As such, the investigators within the ADNI contributed to the design and implementation of ADNI and/or provided data but did not participate in analysis or writing of this report. A complete listing of ADNI investigators can be found at: http://adni.loni.usc.edu/wp-content/uploads/how_to_apply/ADNI_Acknowledgement_List.pdf.

Please address correspondence to Greg Zaharchuk, MD, PhD, Stanford University, 1201 Welch Rd, MC5488, Stanford, CA 94305; e-mail: gregz@stanford.edu; @GregZ_MD

Indicates article with supplemental on-line tables.

http://dx.doi.org/10.3174/ajnr.A6573

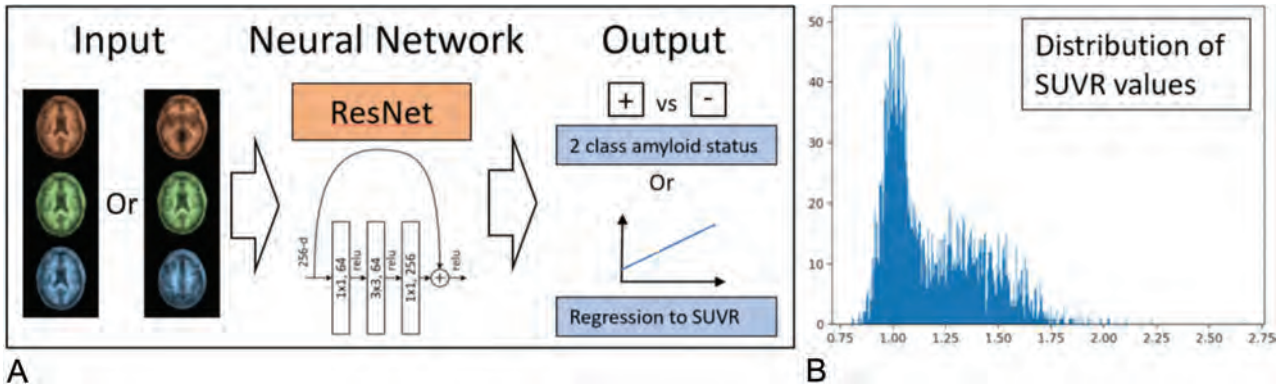

FIG 1. *A*, The input to ResNet consists of 3 or more input channels. In the case of 1 section prediction, the section is copied to all 3 color channels. If 3 slices are used as input, each color channel has an individual section. The input layer can be modified to include more slices as well. The convultional neural network can be used to predict amyloid status directly or to measure SUVR (regression). *B*, Histogram of all SUVR values from the cases included in this study ($n = 2582$).

(SUVR).[8,9] While straightforward conceptually, in practice this is a laborious task, requiring precise co-registration, segmentation, and intensive quality control that can take many hours per case, and which is prone to errors.

We show that we can automate amyloid SUVR measurement by using a deep network and then use this to perform classification. Our approach does not require MR imaging, by using data from the PET scan only. We show that the performance is comparable to more complicated current state-of-the-art methods[10,11] with an accuracy of over 95%, and we explore the importance of the number of input PET slices and pretraining with ImageNet. Finally, we show that while this task is feasible for human readers, the trained network is more accurate.

MATERIALS AND METHODS

Patient Data

We obtained all available ^{18}F-AV-45 (florbetapir) PET scans from the Alzheimer's Disease Neuroimaging Initiative (ADNI) as of August 2019. From the available data, we used the "advanced search" function to select the following data ("AV45 Coreg, Avg, Std Img and Vox Siz, Uniform Resolution"), which represents the co-registered average of the 20 minute acquisition that was then resized to have a uniform voxel size, with a uniform size of 160 × 160 in-plane and 96 axial slices. We downloaded all available scans in Neuroimaging Informatics Technology Initiative file format, as well as the UC Berkeley AV45 analysis to obtain SUVR ("SUMMARYSUVR_WHOLECEREBNORM") for each case, a number which ranged roughly between 0.8 and 2.0.[10,11] This calculation for each case requires many separate postprocessing steps, including registration to the patient's MR imaging by using Statistical Parametric Mapping (SPM; http://www.fil.ion.ucl.ac.uk/spm/) software, skull-stripping, and cortical and subcortical ROI segmentation by using FreeSurfer (http://surfer.nmr.mgh.harvard.edu), and then the use of a weighted mean to calculate the final SUVR value with respect to a specific reference region. A histogram of distribution values can be viewed in Fig 1. Joshi et al[12] proposed that a cutoff of 1.11 can be used to classify scans into amyloid positive and negative cases, because this value exceeds the upper 95% confidence interval for healthy subjects.

Deep Learning Implementation

Our code was implemented in Python by using PyTorchr (https://pytorch.org/).[13] We chose a residual neural network[14] as our deep learning architecture. We chose a neural network depth of 50 layers, also referred to as ResNet-50. To identify whether a deeper network could improve performance, we also assessed performance by using a deeper convultional neural network with 152 layers (ResNet-152). The standard ResNet architecture ends with a layer for distinguishing 1000 differing classes. We changed this number to 2 classes when our aim was to predict amyloid status (classification), and used a log softmax activation function with a loss function based on negative log likelihood:

$$L = -\frac{1}{n}\sum_{i=1}^{n} \log\left(\hat{y}^{(i)}\right)$$

To modify ResNet for prediction of the SUVR (regression), the last, fully connected layer was changed to a single output only that is linear without any subsequent activation function. This output was then used to calculate a mean squared error loss:

$$L = \frac{1}{n}\sum_{i=1}^{n} \left(y^{(i)} - \hat{y}^{(i)}\right)^2$$

During training, Adam[15] was used to optimize the neural network's parameters based on its loss via back propagation. We investigated various hyper-parameters for training and settled on an initial learning rate of 0.0001, 30 epochs, and a 10x decrease of learning rate every 10 epochs. The batch size was set to 32. Based on our data, 1 epoch resulted in 65 iterations. Experiments were run on a Stanford high-performance computing server with 32 CPU cores and 6 Nvidia GK210 graphics processors. Training ResNet-50 and ResNet-152 with the use of 1 graphics processor took 22 and 38 minutes, respectively. We additionally researched the potential benefits of transfer learning[16,17] by fine-tuning ResNet weights that were pretrained by using the ImageNet dataset of natural images.[18] When using ImageNet weights, we adjusted the standard deviation and mean of each channel to match the distribution of ImageNet data.

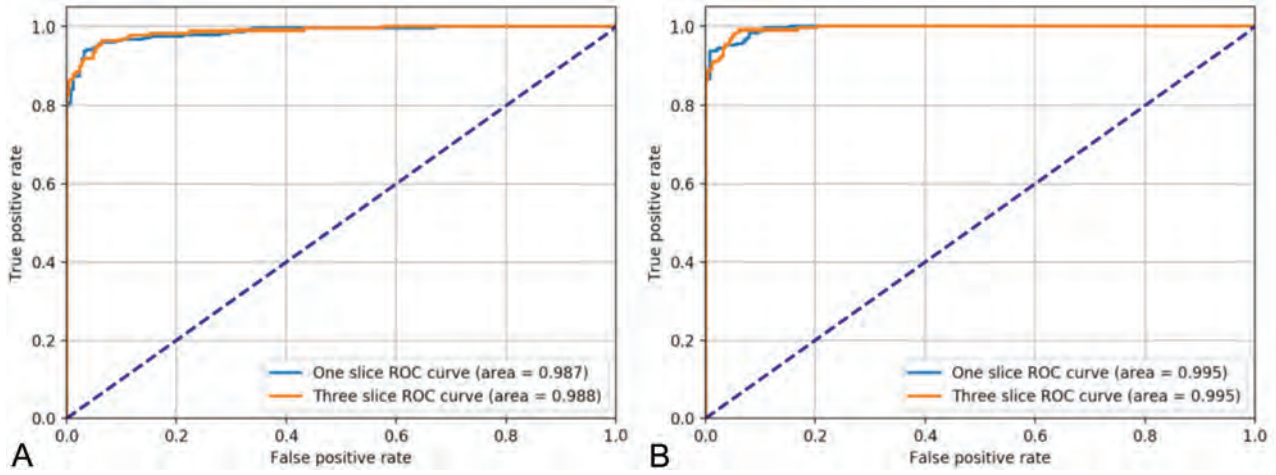

FIG 2. ROC curves test results. *A*, shows performance for 1-section and 3-section input data for binary classification. *B*, displays performance for 1- and 3-section classification via regression. All configurations use pretrained ImageNet weights.

We also modified the ResNet architecture to accept a higher number of slices for input by altering the first convolutional layer. The original first layer transforms 3 input channels into 64 feature channels via 7 × 7 convolutional filters. We adjusted this layer to accommodate the number of input channels we desired. When using randomly initialized weights, we followed the standard PyTorch initialization routine for ResNet.[13] When using pretrained ImageNet weights, we copied the 3-channel weights to the multiple of input channels we created. Because activations get added up, we divided the copied channel weights by number of copies created. When extending from 3 to 9 channels for example, we would divide the weights of all input channels by 3 because the activations of all input layers get added up for 1 convolution. This way, simply copying the 3-channel input to the additional channels added would result in the same activation map. We did not use 3D convolutions, as the selected slices were not adjacent and as we wanted to compare pretrained ImageNet weights.

We split the data into random subsets for training (80%, $n = 2066$) and testing (20%, $n = 516$), ensuring that all samples of 1 specific subject are in 1 subset only to avoid training and testing on the same individuals. We normalized the data before we fed it into the neural network as follows: we subtracted the mean and divided by the standard deviation of each channel individually. When using 1 section only, we chose section 50 out of 96 (slices are zero indexed). Section 50 was chosen as it is a central brain section covering the deep gray regions and cortex of many different brain lobes, ideal for assessing amyloid uptake in cortex. When training ResNet with 3 slices, we chose slices with a distance of 10 to the original section, in our case slices 40, 50, and 60. We also tested a distance of 20, as well as a distance of 40. In this preliminary test, a distance of 10 yielded the best result. For an input of 9 slices, we sampled linearly spaced slices from the entire PET scan. To this end, slices 10, 20, 30, 40, 50, 60, 70, 80 and 90 were selected. For 27-section input, the slices used were: 0, 3, 7, 10, 14, 17, 21, 25, 28, 32, 35, 39, 42, 46, 50, 53, 57, 60, 64, 67, 71, 75, 78, 82, 85, 89 and 93. Training was performed 5 times with different "seeds," meaning that each distinct experiment varies with respect to train/test splits, initializations, and the order of training batches, to allow us to understand variability in the network.

Comparison with Human Readers

To establish the accuracy of expert human readers on this task, we enlisted 3 readers (neuroradiologist, joint nuclear medicine/radiology resident, and nuclear medicine physician), all of whom have been certified to read amyloid PET scans. They were asked to read 100 randomly selected cases from the test set as positive or negative, based only on the single gray-scale center section image as described previously. They were also timed on this task. We then compared the human readers' performance with respect to the ground truth by using the binarized SUVR threshold method. Additionally, human performance was compared with ResNet-50, initialized via ImageNet weights, and by using the regression approach.

Statistical Analysis

The metrics for each experiment are an average over 5 seeded runs. If not stated otherwise, we calculate metrics based on test set prediction performance. Accuracy is calculated based on the standard threshold of 0.5 for binary classification, and at an SUVR threshold of 1.11 for regression. Calculation of sensitivity, specificity, positive predictive value (PPV), and negative predictive value (NPV) are calculated based on the stated thresholds. To statistically compare the different models on accuracy, sensitivity, and specificity, we constructed a linear mixed-effects model to determine the effects of model type (binary classification directly or with regression), depth of network (ResNet-50 versus ResNet-152), use of ImageNet pretraining (yes, no), and number of input slices (1, 3, 9, and 27).

RESULTS

In the 2582 ^{18}F-florbetapir PET scans, the mean SUVR value was 1.19 [IQR 1.01–1.36] (Fig 2). When differentiated by amyloid status by using the SUVR 1.11 threshold, 49.8% of samples were amyloid positive. The samples were acquired from 62 different sites and 40 different types of scanners.

Table 1: Various test metrics for binary classification. Performance reflects mean of 5 separate seeded runs

Binary Classification	Accuracy	Sensitivity	Specificity	PPV	NPV	ROC AUC
1 section, random initialization	92.83% (1.16%)	89.76% (2.11%)	95.87% (0.43%)	95.61% (0.68%)	90.34% (1.69%)	0.9735 (0.0095)
1 section, pretrained	93.41% (1.13%)	91.07% (2.39%)	95.69% (0.72%)	95.55% (0.46%)	91.48% (2.00%)	0.9815 (0.0059)
3 sections, random initialization	92.40% (0.86%)	90.24% (1.05%)	94.56% (0.92%)	94.32% (1.17%)	90.59% (0.82%)	0.9782 (0.0072)
3 sections, pretrained	93.88% (0.78%)	91.52% (1.40%)	96.23% (0.94%)	96.14% (0.64%)	91.80% (1.71%)	0.9850 (0.0044)
9 sections, random initialization	93.14% (0.95%)	90.79% (2.19%)	95.39% (1.77%)	95.26% (1.81%)	91.28% (1.12%)	0.9821 (0.0064)
9 sections, pretrained	93.14% (0.69%)	91.75% (1.77%)	94.43% (1.85%)	94.43% (1.62%)	92.01% (1.18%)	0.9843 (0.0038)
27 sections, random initialization	93.84% (1.04%)	92.23% (1.88%)	95.40% (1.54%)	95.31% (1.48%)	92.49% (1.46%)	0.9831 (0.0062)
27 sections, pretrained	93.45% (0.64%)	90.67% (1.58%)	96.17% (1.19%)	96.01% (1.15%)	91.17% (0.86%)	0.9858 (0.0041)

The numbers in parentheses represent SD.

Table 2: Linear mixed-effects model analysis of different methods for classifying amyloid PET imaging

	Accuracy		Sensitivity		Specificity	
Factor	Odds Ratio	*P* Value	Odds Ratio	*P* Value	Odds Ratio	*P* Value
Type (ResNet-50 vs. -152)	0.96 (0.89–1.03)	.258	0.916 (0.82–1.02)	.112	1.00 (0.89-1.11)	.944
Method (binary classification vs. regression first)	0.79 (0.70–0.89)	<.001	0.54 (0.45–0.63)	<.001	1.24 (1.03–1.50)	.024
Initialization (random vs. pretrained)	0.33 (0.30–0.37)	<.001	0.45 (0.38–0.53)	<.001	0.22 (0.19–0.26)	<.001
Slices (1 vs. 3)	1.17 (1.08–1.26)	<.001	1.15 (1.03-1.28)	.012	1.22 (1.10–1.36)	<.001

Parenthesis refer to 95% confidence intervals for odds ratios.

Single Section Prediction: Binary Amyloid Status Classification

Instead of using regression, in this section we present results of training simply on the binarized categories (positive/negative) based on SUVR (Table 1). Using ResNet-50 with random weights and a single section as input, we achieved a training set accuracy of 99.95% (0.05% SD) and a test set accuracy of 92.8% (1.2% SD). Maximizing Youden J statistic yields an index of 0.865. The mean sensitivity and specificity are 89.8% and 95.9%, respectively. The area under the receiver operating characteristic curve (AUC ROC) is 0.974. Using ImageNet pretrained weights slightly improved results, achieving an accuracy of 93.4%. AUC ROC increased to 0.982, while the Youden J statistic slightly increased to 0.876. Sensitivity increased from 89.8% to 91.2%. Specificity was essentially unchanged by pretraining: 95.7% versus 95.9%.

Single Section Prediction: Regression for Amyloid Classification

For random weight initialization, regression converges to a root-mean-square error (RMSE) for SUVR prediction of 0.108 (0.014 SD). Translating this performance into amyloid status prediction by using the 1.11 cutoff value, we achieve a test set accuracy of 85.7% (2.2% SD), with Youden J statistic of 0.775 (0.044 SD). Significantly better results were achieved by using ImageNet initialization: an RMSE of 0.059 (0.005 SD) and a test accuracy of 93.8% (1.0% SD). The Youden J statistic reaches 0.896 (0.017 SD) and the AUC is 0.986 (0.007 SD). Details are found in Online Table 1.

At best performance, we misclassified approximately 25 of the 516 amyloid scans that were evaluated in the test set. For the method with best prediction (ie, regression, pretrained weights, 3 slices), we evaluated the errors in these cases and found that SUVR value predictions were generally very close to the SUVR 1.11 threshold cutoff and that the predictions of the model were still very close to ground truth. This may reflect the inherent noise in the measurement to some extent. We found that the highest RMSE (worst regression predictions) appeared in high SUVR ground truth values (>1.6). Looking at the amyloid status positive data in the test set, we find that 12% have SUVR greater than 1.6. A higher RMSE (0.117) was seen in these cases. We furthermore find that the top 10% largest RMSE regression errors had an average ground truth SUVR of 1.40. This lower accuracy for high SUVR values is not relevant to amyloid status prediction as all these cases are well over the binarization threshold.

Comparison of Different Models

Details of the mixed-effects model are shown in Table 2. There was no effect of a deeper network (152 versus 50 layers). However, there was an effect of the classification method (with regression being superior to direct binarization), pretraining (superior by using initialization with ImageNet weights), and number of input slices (see below). The ResNet-50 model by using regression, pretraining, and 3 slices as input was the best model. The analysis on input slices showed no differences among the different cases (1, 3, 9, or 27 slices) for specificity. For accuracy and sensitivity, there were significant differences between 1 and 9 or 27 slices, but no differences between 3 and 9 or 27 slices, making 3 section input the optimal choice. This is detailed in Online Table 2. Figure 3 shows performance for different combinations of pre-training, input slices, and tasks (binary classification vs. regression). Online Table 3 shows the

performance of the ResNet-152 network in detail. Online Table 4 shows details of the linear mixed-effects model related to the number of input slices.

Human Reader Evaluation

An example of 10 of the 100 randomly selected reader cases is shown in Fig 4 to give a sense of the data that are being input to the network and that the human readers had available for analysis. The 3 readers performed well on the task, with accuracy of 86%, 89%, and 90%, respectively (Table 3). This compared with an accuracy of 96% for the ResNet-50, single section input, pretrained, regression model. All 4 deep network "misses" in this dataset were cases where the ground truth SUVR was very close to the 1.11 cutoff value, within 0.03 U in all cases. There were 8/100 cases in which all 3 readers classified the case opposite to the ground truth SUVR classification (6 positive and 2 negative cases based on SUVR ground truth). In these cases, the network classified them correctly 87.5% of the time (7/8 cases). The mean time for the humans to assess the 100 cases was 8.2 minutes.

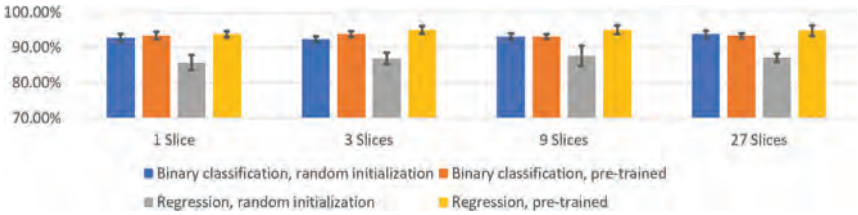

FIG 3. Classification performance as a function of number of input slices. All results reflect the average of 5 seeded runs.

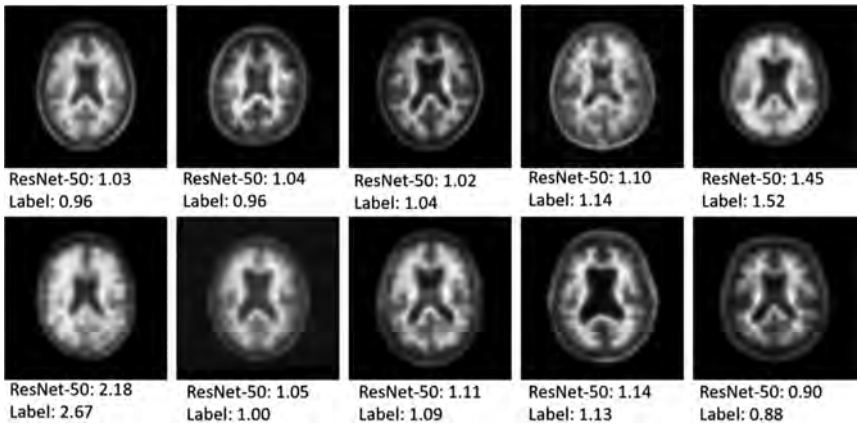

FIG 4. Examples of PET scans used for single section prediction. The top number represents the prediction of the network while the bottom number is the ground truth manual SUVR measurement from the ADNI data base.

DISCUSSION

In this work, we demonstrate that the use of deep learning has tremendous potential to simplify analysis of ^{18}F-florbetapir PET scans, with the best models yielding greater than 95% accuracy on a large, balanced collection of studies collected at multiple sites and on multiple scanners. This is of value because it can help inform visual readings, allowing a fairly accurate assessment in the absence of human expertise. It should also enable more rapid quantitative assessment, which is useful for large-scale studies and longitudinal analysis. We have shown that a single central section is sufficient for high performance and that increasing the number of slices used as inputs to the model accrues only modest improvements. We demonstrated that if the network is set up as a regression task (ie, predicting SUVR and then from that classifying into positive and negative cases), that pretraining with ImageNet natural images can improve performance and improve training stability. Envisioning this as a regression task also allows a quantitative measure of error to ground truth, allowing the network to be more accurate across a wide range of SUVR values, not just those near the SUVR threshold that separates positive and negative cases. As such, it can be applied to cases across the severity spectrum, where classification may not change but quantitative variation in cortical amyloid uptake is present. Lastly, we found that increasing the capacity of the network from 50 to 152 layers did not appreciably improve performance, making this a memory efficient process. It is possible that if more data become available, a more complex model might show benefits, a common trend in deep learning classification tasks.[19]

Measurement of quantitative cortical amyloid uptake is important to both validate visual reads as well as to assess longitudinal changes over time. Currently, this requires a laborious process that includes MR imaging-based cortical and cerebellar segmentation by using FreeSurfer, typically requiring hours to days of processing time and human interaction, followed by co-registration of PET images into the MR imaging native space. Direct prediction is much more efficient, as evidenced by our network requiring

Table 3: Comparison of prediction performance for 100 randomly selected test set samples

Clinical Evaluation	ResNet-50	Reader 1	Reader 2	Reader 3	All Readers
Accuracy	96.00%	90.00%	86.00%	89.00%	90.00%
Sensitivity	95.83%	85.42%	77.08%	87.50%	85.42%
Specificity	96.15%	94.23%	94.23%	90.38%	94.23%
PPV	95.83%	93.18%	92.50%	89.36%	93.18%
NPV	96.15%	87.50%	81.67%	88.68%	87.50%
Time	0:03 min	8:00 min	9:30 min	6:58 min	24:28 min

3 seconds to process 100 cases. As larger AD trials become the norm, this improved efficiency should be of benefit to rapidly assess outcomes and to reduce the costs of clinical trials.

It was surprising to us that adding more PET slices did not significantly improve performance. This suggests there is information on a single axial section located near the middle of the brain that enables the prediction of SUVR (which requires information from outside this section). This has the advantage of reducing the storage needs and preprocessing of PET, while also limiting the amount of data required by the model for training. It might even allow for thin-ring detectors that are being developed as MR imaging inserts for PET/MR imaging to be used.[20] Our clinical reader study suggests that humans were not as good at extracting this information from a single section, with even consensus reads showing inferior performance compared with the model. Of interest, there were 8 cases in which all 3 readers disagreed with the ground truth SUVR classification; in 7 of these, the model classified the case correctly. The human readers tended to call positive cases with atrophy as negative, a known challenge with amyloid interpretation. The model could therefore be useful to support and potentially improve expert decisions with regard to binary amyloid reading, though this would require more study.

Only limited prior literature exists demonstrating deep learning performance for this task, in much smaller datasets. For example, Kang et al[21] showed in a small cohort of 176 patients that they could train a VGG network to classify amyloid status with 89%–92% accuracy, though the ground truth in these cases was determined by a (single) visual read by using the brain amyloid plaque load criteria. Cattell et al[22] showed 96% accuracy in a group of 264 studies by using predefined image intensity gradients combined with a support vector machine with the ground truth defined visually by 3 readers. Most other studies applying deep learning to the ADNI data base have focused on using PET imaging (FDG and amyloid) to predict clinical categories (normal, mild cognitive impairment, AD, etc.).[23-26] While this is surely interesting, clinical assessments are known to be subjective, as evidenced by the recent results of the Imaging Dementia-Evidence for Amyloid Scanning (IDEAS) trial.[27] Predicting a relevant quantitative feature such as SUVR is objective and could find use in data mining, clinical trial assessments, and longitudinal analysis.

There are several limitations to this work. While it is by far the largest study of this task, it is unclear whether the conclusions of the paper might change as more data become available (ie, deeper networks may in fact perform better given enough data). Also, the network here is not predicting a clinical judgment, but rather information that could be obtained analytically from the data itself, begging the question of whether a deep learning–based method is required for this task. The analytic process is extremely time-consuming and requires considerable expertise in image processing; the current method could be immediately used by sites without these capabilities. Furthermore, many research centers do not routinely acquire MR imaging scans and there may be challenges in co-registering PET images to older MR imaging scans of the patient, because there may be interval changes, particularly in brain atrophy. Finally, we cannot determine precisely why the performance is so good and what the remaining limitations might be; this is a problem inherent to deep learning, where visualization of the network's inner workings is a known challenge.[28] Some preliminary work we did looking at saliency maps showed that the network broadly uses the entire image, rather than focusing on the cortical ribbon as might be expected. However, given that the estimates of errors in SUVR due to the co-registration step in the traditional postprocessing methods (0.03–0.07) is on the same level of that found by using the pretrained deep learning method (0.04–0.06), showing any improvement on this metric might be limited by the ground truth accuracy.[29]

CONCLUSIONS

We have trained multiple deep networks showing the ability to classify and estimate SUVR on ^{18}F-florbetapir PET imaging with good accuracy by using the large ADNI dataset. Such methods have promise for automating this laborious calculation, enabling quantitative measurements rapidly and in settings without extensive image processing manpower and expertise.

ACKNOWLEDGMENTS

Data collection and sharing for this project was funded by the Alzheimer's Disease Neuroimaging Initiative (ADNI) (National Institutes of Health Grant U01 AG024904) and DOD ADNI (Department of Defense award number W81XWH-12–2-0012). ADNI is funded by the National Institute on Aging, the National Institute of Biomedical Imaging and Bioengineering, and through generous contributions from the following: AbbVie, Alzheimer's Association; Alzheimer's Drug Discovery Foundation; Araclon Biotech; BioClinica, Inc.; Biogen; Bristol-Myers Squibb Company; CereSpir, Inc.; Cogstate; Eisai Inc.; Elan Pharmaceuticals, Inc.; Eli Lilly and Company; EuroImmun; F. Hoffmann-La Roche Ltd and its affiliated company Genentech, Inc.; Fujirebio; GE Healthcare; IXICO Ltd.; Janssen Alzheimer Immunotherapy Research & Development, LLC.; Johnson & Johnson Pharmaceutical Research & Development LLC.; Lumosity; Lundbeck; Merck & Co., Inc.; Meso Scale Diagnostics, LLC.; NeuroRx Research; Neurotrack Technologies; Novartis Pharmaceuticals Corporation; Pfizer Inc.; Piramal Imaging; Servier; Takeda Pharmaceutical Company; and Transition Therapeutics. The Canadian Institutes of Health Research is providing funds to support ADNI clinical sites in Canada. Private sector contributions are facilitated by the Foundation for the National Institutes of Health (www.fnih.org). The grantee organization is the Northern California Institute for Research and Education, and the study is coordinated by the Alzheimer's Therapeutic Research Institute at the University of Southern California. ADNI data are disseminated by the Laboratory for Neuro Imaging at the University of Southern California.

Disclosures: Greg Zaharchuk—*RELATED: Grant:* Stanford ADRC, Human-centered AI program*; *Provision of Writing Assistance, Medicines, Equipment, or Administrative Support:* Nvidia, *Comments:* GPU donation*; *UNRELATED: Grants/Grants Pending:* various NIH projects, GE Healthcare, Bayer Healthcare*; *Payment for Development of Educational Presentations:* GE Healthcare; *Stock/Stock Options:* Equity, Subtle Medical. *Money paid to institution.

REFERENCES

1. Mayeux R, Stern Y. **Epidemiology of Alzheimer disease.** *Cold Spring Harbor Perspectives in Medicine* 2012;2:a006239 CrossRef

2. Hyman B. **The neuropathological diagnosis of Alzheimer's disease: clinical-pathological studies.** *Neurobiol Aging* 1997;18:S27–32 CrossRef Medline
3. Braak H, Braak E. **Diagnostic criteria for neuropathologic assessment of Alzheimer's disease.** *Neurobiol Aging* 1997;18:S85–88 CrossRef Medline
4. Cummings BJ, Pike CJ, Shankle R, et al. **β-amyloid deposition and other measures of neuropathology predict cognitive status in Alzheimer's disease.** *Neurobiol Aging* 1996;17:921–33 CrossRef Medline
5. Palmqvist S, Zetterberg H, Blennow K, et al. **Accuracy of brain amyloid detection in clinical practice using cerebrospinal fluid β-amyloid 42: a cross-validation study against amyloid positron emission tomography.** *JAMA Neurol* 2014;71:1282–89 CrossRef Medline
6. Johnson KA, Sperling RA, Gidicsin CM, et al. **Florbetapir (F18-AV-45) PET to assess amyloid burden in Alzheimer's disease dementia, mild cognitive impairment, and normal aging.** *Alzheimers Dement* 2013;9:S72–83 CrossRef Medline
7. Camus V, Payoux P, Barré L, et al. **Using PET with 18 F-AV-45 (florbetapir) to quantify brain amyloid load in a clinical environment.** *Eur J Nucl Med Mol Imaging* 2012;39:621–31 CrossRef Medline
8. Landau SM, Mintun MA, Joshi AD; Alzheimer's Disease Neuroimaging Initiative. **Amyloid deposition, hypometabolism, and longitudinal cognitive decline.** *Ann Neurol* 2012;72:578–86 CrossRef Medline
9. Landau SM, Lu M, Joshi AD, et al. **Comparing positron emission tomography imaging and cerebrospinal fluid measurements of β-amyloid.** *Ann Neurol* 2013;74:826–36 CrossRef Medline
10. Mormino EC, Kluth JT, Madison CM, et al. **Episodic memory loss is related to hippocampal-mediated β-amyloid deposition in elderly subjects.** *Brain* 2009;132:1310–23 CrossRef Medline
11. Jagust WJ, Landau SM, Shaw LM, et al. **Relationships between biomarkers in aging and dementia.** *Neurology* 2009;73:1193–99 CrossRef Medline
12. Landau S, Jagust W. **Florbetapir processing methods. Alzheimer's Disease Neuroimaging Initiative**; 2015. https://adni.bitbucket.io/reference/docs/UCBERKELEYAV45/ADNI_AV45_Methods_JagustLab_06.25.15.pdf
13. Paszke A, Gross S, Chintala S, et al. **Automatic Differentiation in PyTorch.** In: NIPS Autodiff Workshop; 2017
14. He K, Zhang X, Ren S, et al. **Deep residual learning for image recognition.** In: *Proceedings of the IEEE Conference on Computer Vision and Pattern Recognition*; 2016;770–78
15. Kingma DP, Ba J, Adam A. **Method for stochastic optimization.** arXiv preprint arXiv:14126980; 2014
16. Yosinski J, Clune J, Bengio Y, et al. **How transferable are features in deep neural networks?** *Advances in Neural Information Processing Systems* 2014;27:3320–28
17. Shin HC, Roth HR, Gao M, et al. **Deep convolutional neural networks for computer-aided detection: CNN architectures, dataset characteristics and transfer learning.** *IEEE Trans Med Imaging* 2016;35:1285–98 CrossRef Medline
18. Deng J, Dong W, Socher R, et al. **Imagenet: A large-scale hierarchical image database.** *In: 2009 IEEE Conference on Computer Vision and Pattern Recognition IEEE* 2009;248–55
19. Krizhevsky A, Sutskever I, Hinton GE. **Imagenet classification with deep convolutional neural networks.** *Advances in Neural Information Processing Systems* 2012;25:1097–1105
20. Levin CS. **Promising new photon detection concepts for high-resolution clinical and preclinical PET.** *J Nucl Med* 2012;53:167–70 CrossRef Medline
21. Kang H, Kim WG, Yang GS, et al. **VGG-based BAPL score classification of 18F-florbetaben amyloid brain PET.** *BSL* 2018;24:418–25 CrossRef
22. Cattell L, Platsch G, Pfeiffer R, et al. **Classification of amyloid status using machine learning with histograms of oriented 3D gradients.** *Neuroimage Clin* 2016;12:990–1003 CrossRef Medline
23. Choi H, Jin KH. **Predicting cognitive decline with deep learning of brain metabolism and amyloid imaging.** *Behavioural Brain Research* 2018;344:103–09 CrossRef
24. Ding Y, Sohn JH, Kawczynski MG, et al. **A deep learning model to predict a diagnosis of Alzheimer disease by using 18F-FDG PET of the brain.** *Radiology* 2018;290:456–64 CrossRef
25. Singh S, Srivastava A, Mi L, et al. **Deep-learning-based classification of FDG-PET data for Alzheimer's disease categories.** In: 13th International Conference on Medical Information Processing and Analysis. *International Society for Optics and Photonics* 2017;10572:105720J
26. Lu D, Popuri K, Ding GW, et al. **Multiscale deep neural network based analysis of FDG-PET images for the early diagnosis of Alzheimer's disease.** *Med Image Anal* 2018;46:26–34 CrossRef Medline
27. Rabinovici GD, Gatsonis C, Apgar C, et al. **Association of amyloid positron emission tomography with subsequent change in clinical management among Medicare beneficiaries with mild cognitive impairment or dementia.** *JAMA* 2019;321:1286–94 CrossRef
28. Adebayo J, Gilmer J, Muelly M, et al. **Sanity checks for saliency maps.** *Advances in Neural Information Processing Systems* 2018;31:9505–15
29. Schwarz CG, Jones DT, Gunter JL, et al. **Contributions of imprecision in PET/MRI rigid registration to imprecision in amyloid PET SUVR measurements.** *Hum Brain Mapp* 2017;38:3323–36

Voxel-Based Morphometry—from Hype to Hope. A Study on Hippocampal Atrophy in Mesial Temporal Lobe Epilepsy

F. Riederer, R. Seiger, R. Lanzenberger, E. Pataraia, G. Kasprian, L. Michels, J. Beiersdorf, S. Kollias, T. Czech, J. Hainfellner, and C. Baumgartner

ABSTRACT

BACKGROUND AND PURPOSE: Automated volumetry of the hippocampus is considered useful to assist the diagnosis of hippocampal sclerosis in temporal lobe epilepsy. However, voxel-based morphometry is rarely used for individual subjects because of high rates of false-positives. We investigated whether an approach with high dimensional warping to the template and nonparametric statistics would be useful to detect hippocampal atrophy in patients with hippocampal sclerosis.

MATERIALS AND METHODS: We performed single-subject voxel-based morphometry with nonparametric statistics within the framework of Statistical Parametric Mapping to compare MRI from 26 well-characterized patients with temporal lobe epilepsy individually against a group of 110 healthy controls. The following statistical threshold was used: $P < .05$ corrected for multiple comparisons with family-wise error over the region of interest right and left hippocampus.

RESULTS: The sensitivity for the detection of atrophy related to hippocampal sclerosis was 0.92 (95% CI, 0.67–0.99) for the right hippocampus and 0.60 (0.31–0.83) for the left, and the specificity for volume changes was 0.98 (0.93–0.99). All clusters of decreased hippocampal volumes were correctly lateralized to the seizure focus. Hippocampal volume decrease was in accordance with neuronal cell loss on histology reports.

CONCLUSIONS: Nonparametric voxel-based morphometry is sensitive and specific for hippocampal atrophy in patients with mesial temporal lobe epilepsy and may be useful in clinical practice.

ABBREVIATIONS: TLE = temporal lobe epilepsy; VBM = voxel-based morphometry; TIV = total intracranial volume; ILAE = International League Against Epilepsy; DARTEL = Diffeomorphic Anatomical Registration Through Exponentiated Lie Algebra; MAP = Morphometric Analysis Program; ROC = Receiver operating characteristic curves; AUC = area under the curve; SnPM = Statistical non Parametric Mapping; HS = hippocampal sclerosis; FLAIR = fluid attenuated inversion recovery; EEG = electroencephalography

Voxel-based morphometry (VBM) is a powerful automated tool to investigate cerebral gray matter changes, based on high-resolution structural MR imaging.[1] It has been used to demonstrate network atrophy in temporal lobe epilepsy (TLE)[2-4] and neuroplasticity in pain conditions, such as medication-overuse headache,[5] and in learning.[6]

While inference from VBM studies is mostly based on group comparisons, information for the individual subject would be of great clinical value. The use of VBM for single subjects however is limited by a high rate of false-positive findings.[7] Recent studies demonstrate that this problem can be overcome with the use of nonparametric statistics.[8]

TLE is the most frequent among the focal epilepsies. The most common underlying pathology in patients with temporal lobe epilepsy is mesial temporal sclerosis characterized by selective hippocampal neuronal loss and gliosis.[9] In medically refractory TLE, hippocampal atrophy is associated with a favorable

Received October 18, 2019; accepted after revision March 18, 2020.

From the Hietzing Hospital with Neurological Center Rosenhügel & Karl Landsteiner Institute for Clinical Epilepsy Research and Cognitive Neurology (F.R., J.B., C.B.), Vienna, Austria; Neuroimaging Labs, Department of Psychiatry and Psychotherapy (R.S., R.L.); Departments of Neurology (E.P.), Radiology and Nuclear Medicine (G.K.), and Neurosurgery (T.C.); and Institute of Neurology (J.H.), Medical University of Vienna, Vienna, Austria; Clinic of Neuroradiology (L.M., S.K.), University Hospital Zurich, Zurich, Switzerland; Faculty of Medicine (F.R.), University of Zurich, Zurich, Switzerland; and Medical Faculty (C.B.), Sigmund Freud Private University, Vienna, Austria.

This work was kindly supported by the Scientific Fund of the Major of the Capital Vienna (Medizinisch Wissenschaftlicher Fonds des Bürgermeisters der Bundeshauptstadt Wien), Project number 17111. The funding source had no influence on the conduct of the study or interpretation of the results.

Previously presented in abstract form at: Congress of the Austrian Neurological Association, March 20-22, 2019; Eisenstadt, Austria.

Please address correspondence to Franz Riederer, MD, Neurological Center Rosenhügel & Karl Landsteiner Institute for Clinical Epilepsy Research and Cognitive Neurology, Riedelgasse 5, A-1130 Vienna, Austria; e-mail: franz.riederer@uzh.ch

Indicates open access to non-subscribers at www.ajnr.org
Indicates article with supplemental on-line appendix and table.
Indicates article with supplemental on-line photos.
http://dx.doi.org/10.3174/ajnr.A6545

outcome after epilepsy surgery[10] and in a large epilepsy surgery series, hippocampal sclerosis was the most frequent finding.[9] Thus, identification of hippocampal sclerosis (HC) is of high clinical relevance during presurgical evaluation. A previous study found that VBM was not sensitive to cortical neuronal loss and hippocampal sclerosis in individual patients.[11] Voxel-based automated analyses have rarely been used for the detection of hippocampal sclerosis in the individual.[12-14] Recent methodologic advances, such as the use of a high-dimensional warping to the template brain, are likely to improve sensitivity of VBM.[15]

The aim of our study was to evaluate the potential role of VBM for the detection of hippocampal atrophy in individual epilepsy patients, by using high-dimensional warping and nonparametric statistics in a clinical setting. This was done by comparing well-characterized individual patients with known hippocampal sclerosis against a large normal data base from healthy controls, estimating sensitivity and specificity. Specifically, we studied whether subjects with known hippocampal atrophy and healthy controls were correctly assigned by the automated algorithm.

MATERIALS AND METHODS

Overview

The study was approved by the ethics committee of the Medical University of Vienna. The conduct of the study is in accordance with the Declaration of Helsinki. In brief, hippocampal volumes were estimated automatically, based on high-resolution 3D structural MR imaging scans. Hippocampal volumes were assessed by 1) comparing individual MR imaging scans against a large normal data base from healthy controls, by using VBM and nonparametric statistics that automatically detect voxels with gray matter changes; 2) plotting estimates of extracted hippocampal volumes from individual patients with temporal lobe epilepsy against the healthy control data base.

Patients with Epilepsy and Healthy Control MR Imaging Data Base

The present retrospective analysis includes high-resolution MR imaging scans from 26 patients with TLE (5 patients from the Karl Landsteiner Institute of Clinical Epilepsy Research, acquired on a 3T Achieva scanner (Philips), termed "3T VIE," and 21 patients from the Medical University Vienna, acquired on a 1.5T Gyroscan (Philps), termed "1.5T VIE" from a previous study that are fully described therein),[2] fulfilling the following criteria (all inclusion criteria and none of the exclusion criteria): 1) Patients with drug-resistant epilepsy, ie, those who had a failure of adequate trials of 2 tolerated, appropriately chosen and used antiepileptic drug schedules (monotherapy or combination) to achieve persistent seizure freedom.[16] 2) Diagnosis of TLE defined by typical clinical seizure semiology, interictal and ictal EEG findings documented during video-EEG monitoring. 3) Patients had undergone high-resolution T1-weighted volume MR imaging sequences of the brain (eg, MPRAGE). Exclusion criteria: 1) Lesions in the brain, except hippocampal sclerosis. 2) Significant vascular comorbidity or vascular risk factors such as uncontrolled hypertension. Demographic and clinical data including MR imaging findings are summarized in the On-line Table. Mean age was 38.2 ± 13.0 years (range 18–60), 13 were women. Definition of the criterion standard (hippocampal sclerosis, side) was based on the following: An expert panel consisting of neurologists, neuroradiologists, and neurosurgeons reached a consensus on the diagnosis and the side of seizure focus, based on clinical semiology, ictal and interictal electroencephalography (EEG), and a dedicated MR imaging epilepsy protocol. Histology data and postsurgical outcome were available in the 20/26 patients who had had an operation.

Healthy controls were recruited by using local advertisements at the research sites and screened by senior neurologists. Our healthy control data base comprised high-resolution 3D T1-weighted sequences from the Karl Landsteiner Institute of Clinical Epilepsy Research and Cognitive Neurology, Vienna (acquired on "3T VIE," $n = 44$) and from previous studies at the Institute for Biomedical Engineering, University and ETH Zurich (acquired on a 3T Achieva scanner, termed "3T ZH," $n = 66$).[17,18] In addition, high-resolution MR imaging scans acquired on "1.5T VIE" from the previous epilepsy study[2] were available, $n = 12$. Thus, the healthy control data base comprised a total of 122 subjects (71 women, 41 men; mean age 36.2 ± 12.5 years, range 22–62). The size of the control group was based on previous work on nonparametric single-subject VBM.[7,8]

Details of the scanning protocols are given in the On-line Appendix. All images were examined by a senior neuroradiologist and only participants without structural abnormalities or motion artifacts were included. The inclusion of data from different scanners was considered helpful for the evaluation of the method in a real-world setting, where scanners may occasionally be replaced.

Demographic, Clinical, and Follow-Up Data

Demographic and clinical data and radiologic MR imaging reports were acquired from electronic charts. Follow-up data from the patients from the previous epilepsy study[2] were collected if available, by using electronic charts from the Medical University of Vienna, including histology (if the patient had undergone epilepsy surgery) and seizure outcome according to the International League Against Epilepsy (ILAE) classification,[19] considering seizure control during the last available 12 months. Mean follow-up duration of operated patients was 9.6 ± 4.1 years. Detailed histologic reports were collected from operated patients and retrospectively assigned according to the ILAE classification scheme for hippocampal sclerosis (HS)[20] based on description of cell loss in the respective subfields.

VBM and Estimation of Hippocampal Gray Matter Volumes

Images were segmented into gray matter, white matter, and cerebrospinal fluid with the VBM8 toolbox (http://dbm.neuro.uni-jena.de/wordpress/vbm/download/), incorporated in the SPM8 (http://www.fil.ion.ucl.ac.uk/spm/software/spm8/) software running on Matlab R2008b (MathWorks). The VBM8 toolbox uses a high-dimensional Diffeomorphic Anatomical Registration Through Exponentiated Lie Algebra (DARTEL) for optimized registration of different brains[15] to the template brain as a default setting. The basic idea behind DARTEL is to increase the accuracy

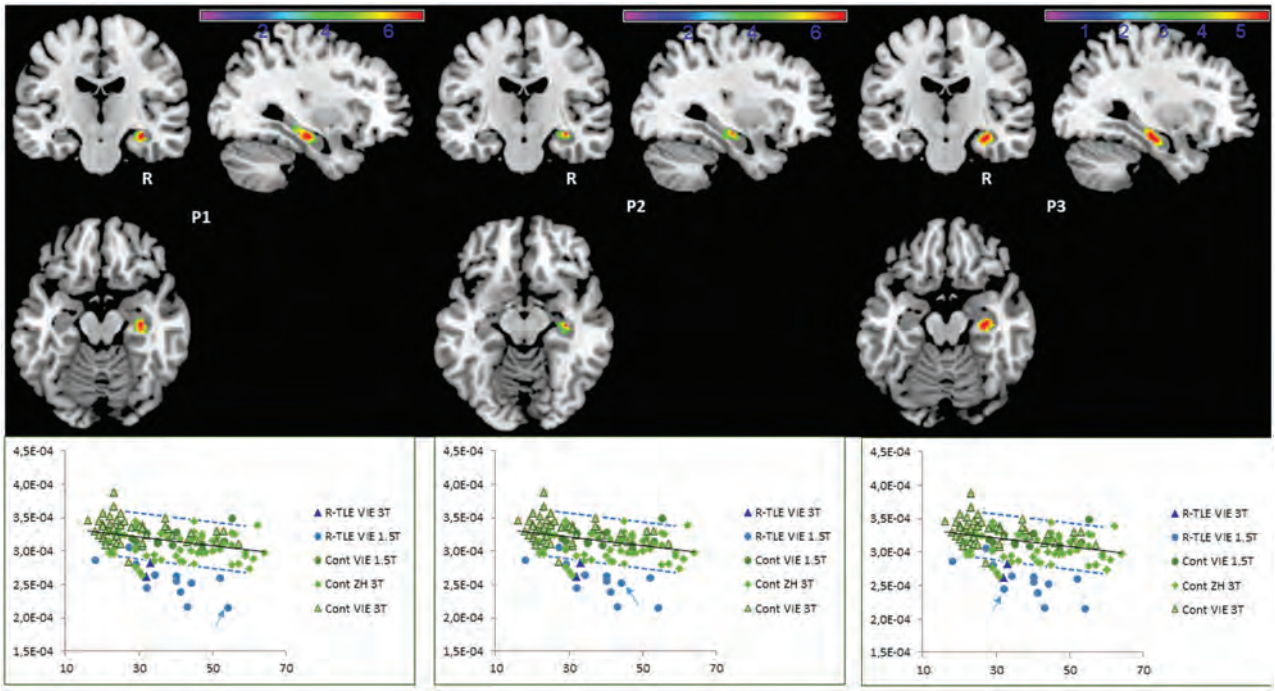

FIG 1. Comparison of representative individual patients with right-sided TLE against a normal data base of 110 healthy controls. The color scale indicates the nonparametric *t*-value. Results are displayed at $P < .05$ corrected for multiple comparisons with family-wise error across the ROI. The scatterplot shows extracted hippocampal volumes/total intracranial volume for controls and patients (y-axis, institutionary units), where the individual patient is indicated with a blue arrow. Different symbols indicate the control cohorts. The x-axis indicates the age. Blue dotted lines show percentiles 5 and 95, respectively.

of intersubject alignment by modeling the shape of each scan by using millions of parameters (3 per voxel).[15] The default DARTEL-template in VBM8 was used to keep the analysis pipeline identical for all subjects, independent from the scanner site. The sampling distance was set to 1 and the bias regularization to extremely light, expecting high-intensity nonuniformity artifact; otherwise default settings were used. The "modulation" procedure ensures the preservation of volume information after normalization to the template. The normalized GM segments were smoothed by using a 6-mm full width at half maximum Gaussian kernel. Individual MR imaging scans of patients were compared against the healthy controls from "3T ZH" and "3T VIE" ($n = 110$), by using Statistical non Parametric Mapping[21] (SnPM, http://www2.warwick.ac.uk/fac/sci/statistics/staff/academic-research/nichols/software/snpm), as this approach is less dependent on normality of data and is less likely to yield false-positives. SnPM is a toolbox for SPM based on nonparametric permutation testing[21] where normality of data and equal variance are not required. This should be an advantage in unbalanced statistical designs such as single-case VBM where one subject is compared against a control group.[8] Age, sex, and total intracranial volume (TIV), which is calculated as the sum of GM, white matter, and cerebrospinal fluid by the VBM toolbox, were used as nuisance variables.

Only voxels in the right or left hippocampus (as defined by the MarsBaR toolbox http://marsbar.sourceforge.net/about.html) were considered. The following threshold was defined a priori: $P < .05$, corrected for multiple comparisons with family-wise error, across the ROI right + left hippocampus (small volume correction).

The proportion of patients with known hippocampal atrophy who had clusters of decreased GM in the respective hippocampus was calculated (sensitivity). In a second step, in an identical way, individual MRI of the healthy control group ($n = 122$) was successively compared against the healthy controls from "3T ZH" and "3T VIE" ($n = 110$), to determine specificity (true-negative rate = 1 – false-positive rate). Thus, sensitivity and specificity of the volumetric approach for the detection of hippocampal atrophy was calculated with 95% Wilson confidence intervals.

Subsequently, GM of the right and left hippocampus was extracted automatically from individual normalized and smoothed GM segments by using the MarsBaR toolbox (http://marsbar.sourceforge.net/). Individual hippocampal volumes for the right and left sides divided by TIV were plotted against the data from healthy controls, from which percentiles 5 and 95 were estimated. The hippocampal volumes in subjects with known hippocampal sclerosis would be expected to be below percentile 5 of controls, based on pilot data.

Finally, for quality control, test-retest reliability for extracted hippocampal volumes was calculated based on scans of healthy controls who were scanned twice at "3T ZH." Possible interscanner differences were estimated, comparing right and left hippocampal volumes of healthy controls between the 3 scanners by using MarsBaR.

RESULTS

VBM in Individual Patients and Specificity of Findings

Significant volume decreases are shown in Fig 1 and On-line Fig 1. Results for individual patients including nonparametric *t*-

Sensitivity and specificity of single-subject VBM for the detection of hippocampal atrophy

Sensitivity for the detection of hippocampal atrophy in patients with mesial temporal lobe epilepsy[a]				
	R Hippocampus decrease	L Hippocampus decrease		
	0.92 (0.67–0.99)	0.60 (0.31–0.83)		
Specificity of hippocampal volume changes				
	R Hippocampus		L Hippocampus	
	Decrease	Increase	Decrease	Increase
Specificity	0.99 (0.96–1.00)	1.00 (0.97–1.00)	0.99 (0.96–1.00)	0.99 (0.96–1.00)
	Decrease or increase in R or L Hippocampus			
Specificity	0.98 (0.93–0.99)			

[a]Wilson 95% CI is given in brackets.

scores are given in the On-line Table. The sensitivity for the detection of hippocampal sclerosis was 0.92 for the right side and 0.60 for the left, with a high specificity of 0.98 (Table). Importantly, right-sided hippocampal atrophy could be detected in 1 patient (P13) in whom routine MR imaging was considered normal (only fluid attenuated inversion recovery [FLAIR] hyperintensity was detected with the automated Morphometric Analysis Program [MAP]).[22] In 4 patients with left-sided hippocampal sclerosis, no atrophy could be detected automatically at this threshold, and 2 of them had only very mild signs of hippocampal sclerosis on MR imaging (On-line Table, clinical data). All clusters of decreased hippocampal volumes were on the side of the seizure focus.

Extracted Hippocampal Volumes in Patients with Temporal Lobe Epilepsy

In 12/13 patients with hippocampal sclerosis/atrophy on the right side, extracted hippocampal volumes/TIV were below percentile 5 ipsilaterally (Fig 1), corresponding to a sensitivity of 0.92 (95% Wilson CI, 0.67–0.99). The patient with a normal MR imaging report (P13) and FLAIR hyperintensity in automated postprocessing on the right side had a hippocampal volume/TIV just below percentile 5. Conversely, in 8/10 patients with hippocampal sclerosis/atrophy on the left side, hippocampal volumes/TIV were below percentile 5, corresponding to a sensitivity of 0.80 (0.49–0.94). The 3 cases with left hippocampal volumes/TIV above percentile 5 had no or only very discrete signs of atrophy in radiologic reports. Lateralization was correct in all cases (with low hippocampal volume), ie, the side of low hippocampal volume/TIV always corresponded to the side of seizure onset. Receiver operating characteristic curves (ROC) for the detection of hippocampal atrophy based on extracted hippocampal volumes for the right and left hippocampus are shown in On-line Fig 2. The area under the curve (AUC) was 0.964 for the right hippocampus and 0.900 for the left hippocampus, indicating excellent accuracy. ROC analyses including only subjects from the scanner 1.5T VIE showed similar AUC values (right hippocampus 0.993; left hippocampus 0.898).

Histology from Resected Hippocampal Specimens and Postsurgical Outcome

Histopathologic results and postsurgical outcome according to the ILAE classification[19] were available in all patients who underwent epilepsy surgery ($n = 20$; On-line Table). Radiologic findings of hippocampal sclerosis were confirmed in all operated cases histologically (On-line Table) as a finding of partial HS (type 1 in most cases). One case with FLAIR hyperintensity in the hippocampus and signs of volume increase in automated volumetry (P25) had no hippocampal sclerosis, but did have discrete dispersion of granular cells and reactive oligodendral hyperplasia. Seventeen out of 19 cases with hippocampal sclerosis on histology showed decreased hippocampal volume on automated volumetry. Outcome was favorable in most cases (On-line Table), in accordance with the literature.[10]

Hippocampal Volumes in Healthy Controls

Left hippocampal volumes were significantly larger compared with right hippocampal volumes (0.47 ± 0.046 versus 0.44 ± 0.046; $P < .001$, paired t-test). Left and right hippocampal volumes/TIV (ratio) showed a significant negative correlation with age (left: $r = -0.196$, $P = .031$; right: $r = -0.361$, $P < .001$).

Test-Retest Reliability

Thirty-seven healthy controls were scanned twice at the 3T ZH, with a mean time interval of 166.4 ± 27.9 days. Extracted hippocampal volumes/TIV were stable between time points, as evidenced by good correlations for right ($r = 0.95$) and left hippocampal volumes ($r = 0.96$; On-line Fig 3). In addition, hippocampal volumes were compared between time points on a voxel basis, by using a paired t-test design within SPM. At the whole brain level, corrected for multiple comparisons with family-wise error, no significant differences were found. In ROI analyses, a few voxels showed decreased gray matter in the region of the right hippocampal tail at the later time point (5 voxels at $x = 26$, $y = -36$, $z = 7$ and 1 voxel at $x = 23$, $y = -36$, $z = 4$; On-line Fig 3).

Comparisons between Scanners

Hippocampal volumes were compared between healthy controls scanned with the scanners 3T VIE, 3T ZH, and 1.5T VIE, by using an ANOVA model within SPM and the MarsBar toolbox, with the covariates age, sex, and TIV. The Bonferroni correction for multiple testing was applied. For the left hippocampus, no significant differences were found between the scanners. Right hippocampal volumes from the 3T ZH were significantly lower compared with those from the 3T VIE ($P < .001$, corrected) and 1.5T VIE ($P = .001$, corrected). In age- and sex-matched healthy controls, right hippocampal volume was 7.1% lower on data from 3T ZH as compared with 3T VIE. However, these between scanner effects for the right hippocampus were considerably lower than the differences related to hippocampal atrophy in patients (On-line Fig 4).

DISCUSSION

Various VBM techniques have been evaluated for the detection of occult brain lesions in focal epilepsy.[23] The present study focuses on the detection of hippocampal atrophy based on automated analyses of T1-weighted MR imaging of the brain. Our study demonstrates that hippocampal atrophy related to mesial temporal sclerosis can be automatically detected in individual patients by VBM by using nonparametric statistics with high sensitivity and specificity. Using small volume correction for multiple comparisons, the finding of atrophy was highly specific (0.99), indicating that this procedure adequately minimizes false-positives. Furthermore, VBM always correctly lateralized the epileptogenic zone. Our data indicate that this technique should be useful in clinical practice, because it enables an objective user-independent measurement of individual atrophy and is less time-consuming than manual volumetric methods. Likewise, various automated hippocampal volumetry techniques including the use of FreeSurfer (http://surfer.nmr.mgh.harvard.edu) and NeuroQuant (CorTech Labs, San Diego, California) have been proposed to increase the diagnostic sensitivity for hippocampal sclerosis.[24-30] In one using NeuroQuant, hippocampal asymmetry *z* scores had the best sensitivity (86.7%–89.5%) and specificity (92.2%–94.1%) to discriminate patients with TLE from healthy controls with AUC values ranging from 0.915–0.939.[27] In another study, the combination of automated hippocampal T2-relaxometry techniques with volumetry has been shown to improve separation of patients with HS from healthy controls.[31] Similarly, an automated volumetry and FLAIR analysis tool improved the diagnosis of ambiguous HS.[32] Huppertz et al[33] showed that an automated quantitative FLAIR analysis in SPM could assist the diagnosis of hippocampal sclerosis with high sensitivity (97.1%) and specificity (95.4%).

In contrast to these studies that primarily analyzed estimates of hippocampal volumes, the present work is focused on automated voxel-based analyses, providing topographic information on atrophy patterns. Voxel-based techniques have rarely been used for the individual diagnosis of hippocampal sclerosis. Bonilha et al[12] demonstrated voxelwise standardized *z* scores to be helpful for the detection of hippocampal sclerosis (with an AUC of 0.973) and more recently, machine-learning techniques have been used to discriminate right or left mesial TLE from healthy controls.[13,14] Our findings contrast with one previous study that found VBM not to be sensitive for the detection of hippocampal sclerosis and neuronal loss in individual patients.[11] Methodologic issues such as improved preprocessing by using high-dimensional warping, the use of nonparametric statistics, and a large control group probably can explain this discrepancy. One previous study on healthy controls showed that the high rate of false-positives frequently observed in single-subject VBM studies[7] can be minimized by using nonparametric statistics, which is not based on the assumption of normal distribution and equal variance.[8] By comparing 122 individual healthy controls successively against the healthy control group, we confirmed a low false-positive rate (2%), ie, high specificity (0.98), as long as correction for multiple testing was applied. Conversely, correction for multiple comparisons across the whole brain may be too conservative, when the main interest lies on hippocampal structures and we propose an a priori-defined small volume correction to be optimal in this case. Extracting hippocampal volumes and comparing these to normal values can further strengthen the detection of atrophy in individual patients.

As right and left hippocampal volumes significantly differed in favor of the left side in healthy controls, it is mandatory to estimate normal ranges separately for both sides. Asymmetry of mesial temporal lobe structures (left > right), including the hippocampal formation, has been found in an earlier VBM study on a large group of healthy controls.[34] Although, this may depend on analysis techniques, because the reverse asymmetry has also been reported by using NeuroQuant[27] or FreeSurfer.[24] Right and left hippocampus showed only a slight decrease with age in contrast to an obvious total gray matter volume loss (data not shown), corroborating previous findings indicating that the hippocampus may be relatively spared from volume loss over a wide age range in healthy controls.[35]

For quality control, additional analyses in healthy controls were conducted, considering reproducibility of volumetric measurements and possible variability between MR imaging scanners. As 37 healthy controls were scanned twice with the 3T ZH, test-retest reliability could be calculated and was considered excellent, with *r*-values ranging from 0.95–0.96 for extracted hippocampal volumes. Voxel-based comparisons between time points showed no significant differences between time points at whole brain level; however, ROI analyses for the right and left hippocampus revealed a few voxels with reduced gray matter in the region of the right hippocampal tail at the later time point. These were considered unlikely to have an influence on the results because of the distinct anatomic localization.

The present study used MR imaging data from 3 different scanners, two 3T scanners of the same type (3T VIE and 3T ZH, both Achieva) and one 1.5T scanner from the same manufacturer (1.5T VIE, Gyroscan). Motivation for this approach was the assumption that a large control group would ultimately increase the sensitivity for alterations in individual patients. In addition, a large control group of $n = 198$ was also used in the study of Scarpazza et al[8] on nonparametric VBM. Furthermore, MR imaging scanners are being replaced from time to time, so that data from different machines may be collected when a rare condition is to be studied over a longer time period. Finally, multicenter MR imaging studies may be an emerging strategy in the study of rare disorders. In our study, a scanner effect was seen only for the right hippocampus with decreased volume estimates for data from 3T ZH. This possibly decreased the sensitivity for the detection of right HS, because a large portion of the healthy controls was investigated at this site. Ultimately, interscanner effects could not be exactly determined, because different subjects were scanned in Vienna and in Zurich. However, in the between-scanners analyses, sex and age were used as nuisance variables, so that these finding should not be confounded by demographic variability. Age- and sex-matched comparisons of mean hippocampal volumes confirmed lower hippocampal volumes in subjects scanned with 3T ZH compared with 3T VIE (7.1% lower); whereas comparisons with 1.5T VIE were not significant after correction for multiple comparisons, but this sample was rather small ($n = 11$, data not shown).

The variability of automated volumetric measurements between scanners has previously been estimated to range up to 14.7%

(coefficient of variation) depending on the structures studied.[36] Our data indicate, however, that the volumetric changes detected in hippocampal sclerosis clearly outweigh interscanner differences (Online Fig 4). Thus, combining data from different scanners may be feasible when the expected disease-related effects are expected to exceed the interscanner variability. Interestingly, intersite effects for various MR imaging measures including gray matter volume have been observed even after harmonizing imaging protocols.[37] Nevertheless, harmonization of scanning protocols and equipment should be attempted whenever possible.

In the present study, hippocampal sclerosis could be verified by histology in most cases. This suggests in vivo determined volume decrease to be associated with cell loss in the case of hippocampal sclerosis, though this could not be shown directly in our study. Histologic sections were not available for quantitative analysis and thus, no correlations between MR imaging derived hippocampal volume and histologic measures such as cell size or attenuation could be performed. Hippocampal subfield volumes estimated by a manual segmentation approach have been shown to correlate with neural attenuation and size derived from histology.[38] Likewise, automatically estimated total hippocampal volumes were correlated with histopathologic neural attenuation in the hippocampus and its subfields.[39]

Most of the operated cases were considered to have type 1 HS, which is the most abundant form with good prognosis.[20,40] Our data indicate that automated detection of volume decrease related to HS is probably not confined to this subtype as a few subjects with type 2 or 3 HS also showed significant atrophy.

Previous studies have consistently shown atrophy in patients with mesial TLE beyond the hippocampus in regions anatomically and functionally related, such as thalamus and cingulum, ie, network atrophy,[2-4,41] based on group comparisons. The nonparametric approach of the present study may have the potential to identify network atrophy on an individual level though sensitivity and specificity of findings would have to be thoroughly assessed across regions. Thus, the prevalence of atrophy in particular regions could be estimated, which is probably of interest for our understanding of TLE.[42] This was, however, beyond the scope of our study, and further work on this issue will be necessary.

As a limitation of the present study, it has to be mentioned that the sensitivity and specificity of findings apply exclusively to the hippocampus that has been analyzed; findings may differ for other regions in terms of false-positives,[7] depending also on region-specific smoothness of data. The present study did not evaluate the proposed analysis pipeline for discrimination between mesial TLE and other forms of epilepsy. Another limitation is the pooling of MR imaging data from different sites without harmonization of study protocols and equipment, inherent in the retrospective design. Further, in the present study, no direct comparisons between hippocampal volume and histologic measures could be performed. Finally, it has to be acknowledged that hippocampal volume loss is only one of the hallmarks of hippocampal sclerosis, where hyperintensity on FLAIR and T2-weighted images, loss of internal structure, as well as changes on diffusion tensor imaging may also be considered.[25,43] It should also be emphasized that the presented analysis pipeline is meant to assist neuroradiologists¨ and clinicians¨ work in the context of dedicated radiologic and clinical evaluation.

Strengths of the present study include the well-characterized group of patients with epilepsy with histologic and long-term follow-up data and the large number of healthy controls being subsequently and individually compared with the control group. SPM and its toolboxes are freely available, which could encourage the clinical application of VBM for volumetry. Required computational resources were considered within acceptable limits because processing time per image was approximately 50 minutes.

CONCLUSIONS

Although reproducibility and specificity of findings from VBM studies have been a matter of debate, our findings show that nonparametric VBM is sensitive and specific for hippocampal atrophy in patients with mesial TLE, and we encourage its use in clinical practice. Further, we provide evidence that MR imaging data from different centers may be combined for morphometric studies if gross structural abnormalities are expected. The importance of harmonization of MR imaging scanning protocols and equipment should be considered in future prospective studies. Lastly, because VBM can provide information on whole-brain topographic changes, future studies could investigate individual atrophy patterns in TLE.

ACKNOWLEDGMENTS

The authors express their gratitude to the developers of Statistical Parametric Mapping at the Wellcome Trust Center for Neuroimaging, United Kingdom, and Statistical non Parametric Mapping, at the University of Warwick, United Kingdom, for distributing their software packages to the community.

Disclosures: Franz Riederer—*RELATED: Grant:* Scientific grant from the Major of the Capital of Vienna, Comments: https://www.wien.gv.at/gesundheit/einrichtungen/med-wiss-fonds/.* Rupert Lanzenberger—*RELATED: Grant:* Scientific Fund of the Major of the Capital Vienna*; *UNRELATED: Grants/Grants Pending:* Siemens Healthcare regarding clinical research using PET/MR; *Speakers Bureaus/Travel/Accommodations/Meeting Expenses Unrelated to Activities Listed:* Bruker BioSpin MR, Heel; *Other:* I am shareholder of BM Health GmbH, Austria, since 2019; Ekaterina Pataraia—*UNRELATED: Employment:* Medizinische Universität Wien. Gregor Kasprian—*UNRELATED: Consultancy:* Bellaria Diagnose, Vienna; *Employment:* Medical University of Vienna; *Grants/Grants Pending:* Austrian Research Fund.* Spyros Kollias—*UNRELATED: Employment:* University hospital of Zurich, Comments: My salary; *Travel/Accommodations/Meeting Expenses Unrelated to Activities Listed:* University Hospital of Zurich, Comments: Traveling allowances for scientific meetings. *Money paid to institution.

REFERENCES

1. Ashburner J, Friston KJ. **Voxel-based morphometry–the methods.** *NeuroImage* 2000;11:805–21 CrossRef Medline
2. Riederer F, Lanzenberger R, Kaya M, et al. **Network atrophy in temporal lobe epilepsy: a voxel-based morphometry study.** *Neurology* 2008;71:419–25 CrossRef Medline
3. Bonilha L, Rorden C, Castellano G, et al. **Voxel-based morphometry reveals gray matter network atrophy in refractory medial temporal lobe epilepsy.** *Arch Neurol* 2004;61:1379–84 CrossRef Medline
4. Mueller SG, Laxer KD, Cashdollar N, et al. **Voxel-based optimized morphometry (VBM) of gray and white matter in temporal lobe epilepsy (TLE) with and without mesial temporal sclerosis.** *Epilepsia* 2006;47:900–07 CrossRef Medline
5. Riederer F, Gantenbein AR, Marti M, et al. **Decrease of gray matter volume in the midbrain is associated with treatment response in medication-overuse headache: possible influence of orbitofrontal cortex.** *J Neurosci* 2013;33:15343–49 CrossRef Medline

6. Draganski B, Gaser C, Busch V, et al. **Neuroplasticity: changes in grey matter induced by training.** *Nature* 2004;427:311–12 CrossRef Medline
7. Scarpazza C, Sartori G, De Simone MS, et al. **When the single matters more than the group: very high false positive rates in single case voxel based morphometry.** *NeuroImage* 2013;70:175–88 CrossRef
8. Scarpazza C, Nichols TE, Seramondi D, et al. **When the single matters more than the group (ii): addressing the problem of high false positive rates in single case voxel based morphometry using non-parametric statistics.** *Front Neurosci* 2016;10:6 CrossRef Medline
9. Blumcke I, Spreafico R, Haaker G, et al; EEBB Consortium. **Histopathological findings in brain tissue obtained during epilepsy surgery.** *N Engl J Med* 2017;377:1648–56 CrossRef Medline
10. Jones AL, Cascino GD. **Evidence on use of neuroimaging for surgical treatment of temporal lobe epilepsy: a systematic review.** *JAMA Neurol* 2016;73:464–70 CrossRef Medline
11. Eriksson SH, Thom M, Symms MR, et al. **Cortical neuronal loss and hippocampal sclerosis are not detected by voxel-based morphometry in individual epilepsy surgery patients.** *Hum Brain Mapp* 2009;30:3351–60 CrossRef Medline
12. Bonilha L, Halford JJ, Rorden C, et al. **Automated MRI analysis for identification of hippocampal atrophy in temporal lobe epilepsy.** *Epilepsia* 2009;50:228–33 CrossRef
13. Focke NK, Yogarajah M, Symms MR, et al. **Automated MR image classification in temporal lobe epilepsy.** *NeuroImage* 2012;59:356–62 CrossRef Medline
14. Chen S, Zhang J, Ruan X, et al. **Voxel-based morphometry analysis and machine learning based classification in pediatric mesial temporal lobe epilepsy with hippocampal sclerosis.** *Brain Imaging Behav* 2019. [Online ahead of print] CrossRef Medline
15. Ashburner J. **A fast diffeomorphic image registration algorithm.** *NeuroImage* 2007;38:95–13 CrossRef Medline
16. Kwan P, Arzimanoglou A, Berg AT, et al. **Definition of drug resistant epilepsy: consensus proposal by the ad hoc Task Force of the ILAE Commission on Therapeutic Strategies.** *Epilepsia* 2010;51:1069–77 CrossRef Medline
17. Riederer F, Marti M, Luechinger R, et al. **Grey matter changes associated with medication-overuse headache: correlations with disease related disability and anxiety.** *World J Biol Psychiatry* 2012;13:517–25 CrossRef Medline
18. Riederer F, Landmann G, Gantenbein AR, et al. **Nondermatomal somatosensory deficits in chronic pain are associated with cerebral grey matter changes.** *World J Biol Psychiatry* 2017;18:227–38 CrossRef
19. Wieser HG, Blume WT, Fish D, et al; Commission on Neurosurgery of the International League Against Epilepsy. **ILAE Commission Report. Proposal for a new classification of outcome with respect to epileptic seizures following epilepsy surgery.** *Epilepsia* 2001;42:282–86 Medline
20. Blumcke I, Thom M, Aronica E, et al. **International consensus classification of hippocampal sclerosis in temporal lobe epilepsy: a task force report from the ILAE Commission on Diagnostic Methods.** *Epilepsia* 2013;54:1315–29 CrossRef Medline
21. Nichols TE, Holmes AP. **Nonparametric permutation tests for functional neuroimaging: a primer with examples.** *Hum Brain Mapp* 2002;15:1–25 CrossRef Medline
22. Wagner J, Weber B, Urbach H, et al. **Morphometric MRI analysis improves detection of focal cortical dysplasia type II.** *Brain* 2011;134:2844–54 CrossRef Medline
23. Martin P, Winston GP, Bartlett P, et al. **Voxel-based magnetic resonance image postprocessing in epilepsy.** *Epilepsia* 2017;58:1653–64 CrossRef
24. McDonald CR, Hagler DJ Jr., Ahmadi ME, et al. **Subcortical and cerebellar atrophy in mesial temporal lobe epilepsy revealed by automatic segmentation.** *Epilepsy Res* 2008;79:130–38 CrossRef Medline
25. Sidhu MK, Duncan JS, Sander JW. **Neuroimaging in epilepsy.** *Curr Opin Neurol* 2018;31:371–78 CrossRef Medline
26. Azab M, Carone M, Ying SH, et al. **Mesial temporal sclerosis: accuracy of NeuroQuant versus neuroradiologist.** *AJNR Am J Neuroradiol* 2015;36:1400–06 CrossRef Medline
27. Farid N, Girard HM, Kemmotsu N, et al. **Temporal lobe epilepsy: quantitative MR volumetry in detection of hippocampal atrophy.** *Radiology* 2012;264:542–50 CrossRef Medline
28. Winston GP, Cardoso MJ, Williams EJ, et al. **Automated hippocampal segmentation in patients with epilepsy: available free online.** *Epilepsia* 2013;54:2166–73 CrossRef Medline
29. Coan AC, Kubota B, Bergo FP, et al. **3T MRI quantification of hippocampal volume and signal in mesial temporal lobe epilepsy improves detection of hippocampal sclerosis.** *AJNR Am J Neuroradiol* 2014;35:77–83 CrossRef Medline
30. Hammers A, Heckemann R, Koepp MJ, et al. **Automatic detection and quantification of hippocampal atrophy on MRI in temporal lobe epilepsy: a proof-of-principle study.** *NeuroImage* 2007;36:38–47 CrossRef Medline
31. Winston GP, Vos SB, Burdett JL, et al. **Automated T2 relaxometry of the hippocampus for temporal lobe epilepsy.** *Epilepsia* 2017;58:1645–52 CrossRef
32. Vasta R, Caligiuri ME, Labate A, et al. **3T magnetic resonance imaging simultaneous automated multimodal approach improves detection of ambiguous visual hippocampal sclerosis.** *Eur J Neurol* 2015;22:725–47 CrossRef Medline
33. Huppertz HJ, Wagner J, Weber B, et al. **Automated quantitative FLAIR analysis in hippocampal sclerosis.** *Epilepsy Res* 2011;97:146–56 CrossRef Medline
34. Good CD, Johnsrude I, Ashburner J, et al. **Cerebral asymmetry and the effects of sex and handedness on brain structure: a voxel-based morphometric analysis of 465 normal adult human brains.** *NeuroImage* 2001;14:685–700 CrossRef Medline
35. Good CD, Johnsrude IS, Ashburner J, et al. **A voxel-based morphometric study of ageing in 465 normal adult human brains.** *NeuroImage* 2001;14:21–36 CrossRef Medline
36. Huppertz HJ, Kroll-Seger J, Kloppel S, et al. **Intra- and interscanner variability of automated voxel-based volumetry based on a 3D probabilistic atlas of human cerebral structures.** *NeuroImage* 2010;49:2216–24 CrossRef Medline
37. Shinohara RT, the NAIMS Cooperative, Oh J, Nair G, et al. **Volumetric analysis from a harmonized multisite brain mri study of a single subject with multiple sclerosis.** *AJNR Am J Neuroradiol* 2017;38:1501–09 CrossRef Medline
38. Goubran M, Bernhardt BC, Cantor-Rivera D, et al. **In vivo MRI signatures of hippocampal subfield pathology in intractable epilepsy.** *Hum Brain Mapp* 2016;37:1103–19 CrossRef Medline
39. Jardim AP, Corso JT, Garcia MT, et al. **Hippocampal atrophy on MRI is predictive of histopathological patterns and surgical prognosis in mesial temporal lobe epilepsy with hippocampal sclerosis.** *Epilepsy Res* 2016;128:169–75 CrossRef Medline
40. Blumcke I, Pauli E, Clusmann H, et al. **A new clinico-pathological classification system for mesial temporal sclerosis.** *Acta Neuropathol* 2007;113:235–44 CrossRef Medline
41. Bonilha L, Edwards JC, Kinsman SL, et al. **Extrahippocampal gray matter loss and hippocampal deafferentation in patients with temporal lobe epilepsy.** *Epilepsia* 2010;51:519–28 CrossRef Medline
42. Bonilha L, Elm JJ, Edwards JC, et al. **How common is brain atrophy in patients with medial temporal lobe epilepsy?** *Epilepsia* 2010;51:1774–79 CrossRef Medline
43. Lee DH, Gao FQ, Rogers JM, et al. **MR in temporal lobe epilepsy: analysis with pathologic confirmation.** *AJNR Am J Neuroradiol* 1998;19:19–27 Medline

Brain Network Disruption in Whiplash

J.P. Higgins, J.M. Elliott, and T.B. Parrish

ABSTRACT

BACKGROUND AND PURPOSE: Whiplash-associated disorders frequently develop following motor vehicle collisions and often involve a range of cognitive and affective symptoms, though the neural correlates of the disorder are largely unknown. In this study, a sample of participants with chronic whiplash injuries were scanned by using resting-state fMRI to assess brain network changes associated with long-term outcome metrics.

MATERIALS AND METHODS: Resting-state fMRI was collected for 23 participants and used to calculate network modularity, a quantitative measure of the functional segregation of brain region communities. This was analyzed for associations with whiplash-associated disorder outcome metrics, including scales of neck disability, traumatic distress, depression, and pain. In addition to these clinical scales, cervical muscle fat infiltration was quantified by using Dixon fat-water imaging, which has shown promise as a biomarker for assessing disorder severity and predicting recovery in chronic whiplash.

RESULTS: An association was found between brain network structure and muscle fat infiltration, wherein lower network modularity was associated with larger amounts of cervical muscle fat infiltration after controlling for age, sex, body mass index, and scan motion ($t = -4.02$, partial $R^2 = 0.49$, $P < .001$).

CONCLUSIONS: This work contributes to the existing whiplash literature by examining a sample of participants with whiplash-associated disorder by using resting-state fMRI. Less modular brain networks were found to be associated with greater amounts of cervical muscle fat infiltration suggesting a connection between disorder severity and neurologic changes, and a potential role for neuroimaging in understanding the pathophysiology of chronic whiplash-associated disorders.

ABBREVIATIONS: rs-fMRI = resting-state fMRI; MFI = muscle fat infiltration; WAD = whiplash-associated disorder(s); MVC = motor vehicle collision

The term "whiplash" refers to the transfer of force to the cervical spine via rapid acceleration-deceleration of the head. It is often associated with a motor vehicle collision (MVC) whereby some patients (about 20%) develop a complex array of persistent physiologic and psychological sequelae, collectively known as whiplash-associated disorders (WAD).[1] In addition to neck pain, headache, limited neck range of motion, and bodily pain, patients with persistent WAD may exhibit decreased performance on neuropsychological tests involving attention and working memory.[2,3]

There remains little available literature toward identifying a single salient structural lesion to help explain the disparate signs and symptoms in WAD.[4-6] Recent work, however, has reported that qualitative and quantitative measures of muscle fat infiltration (MFI) in the cervical spine can be useful for differentiating patients with severe WAD, mild WAD symptoms, idiopathic neck pain, those that have "recovered," and healthy controls.[7-11] In addition, it has shown early promise as a prognostic marker for recovery trajectories.[12] The mechanisms underlying the development of MFI remain elusive, but could include disuse, denervation, altered activation of the sympathetic nervous system, stress system dysregulation, and neuroinflammation.[13,14]

Received November 25, 2019; accepted after revision April 14, 2020.

From the Departments of Radiology (J.P.H., T.B.P.) and Physical Therapy and Human Movement Sciences (J.M.E.), Feinberg School of Medicine, Northwestern University, Chicago, Illinois; Discipline of Physiotherapy, Faculty of Health Sciences (J.M.E.), The University of Sydney and the Northern Sydney Local Health District; and The Kolling Research Institute, St. Leonards, NSW, Australia.

The project described originated at Northwestern University, Feinberg School of Medicine, Department of Physical Therapy and Human Movement Sciences, and was supported by the National Institutes of Health (NIH) through Grant Number R01HD079076: Eunice Kennedy Shriver National Institute of Child Health & Human Development; National Center for Medical Rehabilitation Research (J.M.E., T.B.P.). The content is solely the responsibility of the authors and does not necessarily represent the official views of the NIH.

Please address correspondence to Todd B. Parrish, PhD, Department of Radiology, Feinberg School of Medicine, Northwestern University, 737 N Michigan Ave, Suite 1600, Chicago, IL 60611; email: toddp@northwestern.edu; @ElliottJSyd

Indicates open access to non-subscribers at www.ajnr.org

Indicates article with supplemental on-line photos.

http://dx.doi.org/10.3174/ajnr.A6569

Demographic and clinical details[a]

Group/Measure	Recovered		Moderate		Severe	
	Current Study ($n = 5$)	Entire Study ($n = 30$)	Current Study ($n = 10$)	Entire Study ($n = 33$)	Current Study ($n = 8$)	Entire Study ($n = 15$)
Sex (M/F)	3/2	13/17	8/2	4/29	6/2	3/12
BMI	23.5 (3.8)	24.9 (3.9)	24.5 (5.6)	24.4 (4.4)	25.3 (3.8)	27.6 (5.6)
Age	35.3 (12.8)	33.1 (10.2)	35.7 (13.8)	35.3 (12.1)	36.1 (13.2)	36.8 (11.3)
Days since MVC	349.6 (149.3)	383.3 (35.7)	273 (137.3)	385.9 (20.4)	385 (141.3)	420.3 (79.7)
NDI[b]	4.8 (4.6)	5.5 (6.4)	17 (9.7)	18.9 (10.2)	38.5 (13.1)	30.9 (13.9)
MFI	18.6 (5.5)	17.1 (4.9)	21.6 (6.6)	20.8 (6.9)	21.9 (7.2)	23.3 (6.8)
TIDS Total[b]	3.4 (4.9)	3.0 (4.2)	6.3 (5.3)	8.4 (5.1)	15.1 (8.3)	11.0 (6.3)
PDS Arousal Symptom Severity[b]	0.4 (0.9)	0.8 (1.5)	3.1 (2.7)	3.9 (2.8)	8 (3.6)	5.3 (4.2)
Pain[b]	1.2 (2.2)	1.2 (1.6)	3.1 (2.7)	3.8 (2.6)	6 (1.8)	5.1 (2.7)
HADS Depression[b]	0.8 (1.3)	1.6 (2.6)	2.6 (2.4)	2.7 (2.2)	8.2 (4.9)	5.8 (4.5)
Modularity[b]	0.55 (0.04)	n/a	0.47 (0.07)	n/a	0.46 (0.10)	n/a

Note:—BMI indicates body mass index; NDI, Neck Disability Index; MFI, muscle fat infiltration; TIDS, Traumatic Injury Distress Scale; PDS, Posttraumatic Diagnostic Scale; HADS, Hospital Anxiety and Depression Scale.

[a] Presented as counts or mean (SD).

[b] Significant pair-wise comparisons of groups within this study. NDI: Recovered versus moderate ($P = .005$), recovered versus severe ($P < .001$), moderate versus severe ($P = .002$); TIDS: Recovered versus severe ($P = .01$), moderate versus severe ($P = .02$); PDS: Moderate versus severe ($P = .007$), recovered versus severe ($P < .001$), recovered versus moderate ($P = .01$); pain: Recovered versus severe ($P = .003$), moderate versus severe ($P = .02$); HADS depression: Recovered versus severe ($P = .003$), moderate versus severe ($P = .01$); modularity: Recovered versus moderate ($P = .02$), recovered versus severe ($P = .05$).

Neuroimaging findings in WAD have been mixed, with some studies reporting changes in cerebral perfusion[15,16] and white matter tract integrity,[17] and others failing to find associations by using functional or morphologic imaging.[18,19] Resting-state-fMRI (rs-fMRI) is a rapidly growing tool and has been widely applied to the investigation of abnormal brain activity in clinical populations. While several studies have revealed connections between rs-fMRI and mild-to-severe traumatic brain injury,[20,21] none thus far have identified similar associations within the WAD population.

Analysis of large-scale networks by using graph theoretical approaches has recently gained traction as a method for the characterization of brain networks observed by using rs-fMRI. Within a graph theoretical framework, brain regions can be considered nodes that are linked by edges defined by the strength of pair-wise correlations between pairs of nodes. This topologic arrangement of nodes and edges can be described as a graph, which may be divided into interconnected subnetworks referred to as modules. Modularity has been found to arise in many complex systems,[22] and advances in neuroimaging have led to the characterization of brain networks as being hierarchically organized and modular systems.[23,24] Modularity as a quantitative measure can be considered as the ratio between the number of connections (edges), which are located within modules, to the number of connections occurring between modules.

In this preliminary study, we investigated potential links between network modularity and symptom metrics in a sample of 23 patients with chronic WAD. Modularity was chosen because it provides a metric of whole-brain network organization that has shown promise as a marker of brain plasticity and has been applied in the study of a range of clinical conditions, some of which may be superficially similar to WAD, such as mild traumatic brain injury and PTSD.[25-30] Along with standard clinical scales for assessment of WAD, such as the Neck Disability Index[31] and the Traumatic Injury Distress Scale,[32] measures of MFI were included as an outcome metric.

MATERIALS AND METHODS

Participants

This is a secondary ancillary study of participants drawn from a prospective study investigating the neuromuscular mechanisms underlying poor recovery following a whiplash injury (ClinicalTrials.gov Identifier: NCT02157038). In the main study, 97 participants were recruited (19 lost to attrition), consented, and enrolled via an urban academic emergency medicine department and were eligible provided they both reported MVC-related neck pain and were within the Quebec Task Force Classification category of WAD grade II (movement restriction with no radicular symptoms).[1] Participants were eligible provided they consented and enrolled in the parent study and agreed to undergo imaging of the brain.

Volunteers were not considered if they had a spinal fracture (from the current MVC), radiologic evidence of a spinal cord lesion, or implants contraindicated for MR safety. Participants were not considered if they were pregnant or if, in the absence of an effective form of contraception, they could possibly have conceived since the first day of their last menstrual period.

The study was approved by the relevant Institutional Review Board. The 23 participants (17 female, average age of 35.8 ± 12.8 years) participated in the additional data collection during their regular study visit. Participants were recruited for imaging at least 3 months following their motor vehicle collision (mean 328 ± 133.16 days), and were categorized as recovered (5), moderate (10), or severe (8) in symptoms at the time of imaging. Participant characteristics are summarized in the Table.

MR Imaging Data

MR imaging data were collected by using a 3 T Prisma (Siemens) scanner with a 64-channel head-neck coil. Structural images were collected by using a 3D T1-weighted scan (TR = 2.17 seconds, TE = 1.69 ms, FOV = 256 × 224, 1 mm isotropic voxel size) of the brain, and a T2-weighted sagittal turbo spin-echo sequence of the cervical spine. A 3D multi-echo

gradient-echo scan (FOV = 190 × 320 mm, 0.7 × 0.7 × 3 mm voxel size) was collected for the quantification of MFI by acquiring images at echo times where water and fat are in phase and out of phase ($TR/TE_1/TE_2 = 6.59/2.45/3.68$ ms) to produce water-fat ratio images. rs-fMRI was acquired with a whole-brain multiband T2*-weighted sequence (TR = 613 ms, TE = 22 ms, 2 mm voxel size, multiband factor = 8, and 800 volumes).

Preprocessing

Muscle Fat Infiltration. MFI scores were calculated by using the Dixon water-fat scan as previously described.[12] Briefly, fat and water compartments of the bilateral multifidi and semispinalis muscles from C3-C7 were manually segmented by a rater blinded to the status of the participant. The mean voxel intensity within each compartment was extracted and MFI was then calculated to generate a percentage of neck muscle fat present for each subject by using the following equation:

$$MFI\ (\%) = \frac{Fat}{(Fat + Water)} * 100$$

Brain Imaging. Quality control metrics were extracted for T1 and BOLD images by using MRIQC (https://mriqc.readthedocs.io/en/stable/index.html).[33] Preprocessing was accomplished by using the Nipype (https://nipype.readthedocs.io/en/latest/)[34]-based tool fMRIPrep version 1.3.2 (https://fmriprep.readthedocs.io/en/stable/)[35] and AFNI version 19.2.04 (http://afni.nimh.nih.gov/afni).[36]

T1 images were bias-corrected by using ANTs (http://stnava.github.io/ANTs/) N4BiasFieldCorrection,[37] and skull stripped by using ANTs ants-BrainExtraction. Brain tissue compartments (white matter/gray matter/cerebrospinal fluid) were segmented by using FMRIB Automated Segmentation Tool (FAST; http://fsl.fmrib.ox.ac.uk/fsl/fslwiki/fast) in native space.[38] Finally, brain-extracted T1 images were transformed to the Montreal Neurological Institute 152 Nonlinear Asymmetric template version 2009c by using ANTs AntsRegistration tool.[39]

Functional data were section-timing corrected by using AFNI 3dTshift and motion corrected by using FMRIB Intramodal Motion Correction tool (MCFLIRT; http://fsl.fmrib.ox.ac.uk/fsl/fslwiki/MCFLIRT) before co-registration to the T1 by using FMRIB Linear Image Registration Tool (FLIRT; https://fsl.fmrib.ox.ac.uk/fsl/fslwiki/FLIRT).[40] The resulting transforms were concatenated with the T1-to-Montreal Neurological Institute warp and applied in 1 step by using antsApplyTransforms. Framewise displacement was used to exclude high-motion (framewise displacement > 0.5) frames of the time-series, along with 1 subsequent volume. This procedure resulted in an exclusion of between 0.5%–25.8% of data, with a minimum residual time-series of 6.5 minutes (mean 9.09 ± 1.5 min). To remove physiologic noise, 6 principal components of white matter/CSF signals were extracted to create aCompCor (https://nipype.readthedocs.io/en/0.13.1/interfaces/generated/nipype.algorithms.confounds.html) nuisance regressors.[41] Motion estimates along with aCompcor regressors and low frequency cosine basis regressors were removed via linear regression; regression, censoring, and smoothing (6 mm full width at half maximum) were performed by using AFNI 3dTproject.

Network Modularity Calculation

Regions of interest were defined as 5 mm-spheres by using the Power 264 coordinates.[42] Temporal signal-to-noise ratios were calculated for each node/participant, and the average and standard deviation were calculated across all regions (34.0 ± 10.1). ROIs were excluded if they were more than 2 SD below the mean in any participant (30 regions). Mean time course signals within the remaining ROIs were used to create a 234 × 234 Pearson correlation matrix for each participant, which were converted to z scores. Thresholds were used to minimize the number of node pairs considered to constitute edges to a percentage of the strongest connections. To reduce the dependence of results on specific threshold selection, the connection densities used ranged from the top 2%–10% in increments of 1%, and an average across this range was taken for use in subsequent analysis, though results across specific thresholds showed similar effects (On-line Figures). This range was chosen because it was used in the construction of the Power 264 region atlas and has been utilized in previous work.[42,43]

The resulting undirected weighted correlation matrices were input to the Brain Connectivity Toolbox (version 2019–03-03)[44] in Matlab 2016b (MathWorks) to estimate the optimal community structure and calculate modularity. The network was divided into communities by using the Newman spectral algorithm, with the goal of maximizing within-community connections while minimizing connections between communities.[45-47] Modularity (Q) is then calculated to quantify the extent to which the network is amenable to such subdivision, with higher values of Q representing networks with a relatively high proportion of within-community connections to connections between communities. This form of weighted modularity was calculated as:

$$Q^w = \frac{1}{l^w} \sum_{i,j \in N} \left[w_{i,j} - \frac{k_i^w k_j^w}{l^w} \right] \delta_{m_i,m_j}$$

where i and j are connections between nodes, l^w is the sum of all weights in the graph, k_i is the weighted degree of a node, m_i is the module containing node i, and $\delta_{m_i,m_j=1}$ if $m_i = m_j$, and 0 otherwise.

Statistical Analysis

Potential associations were investigated with multiple linear regression by using R version 3.4.4 (http://www.r-project.org/) function lm in package stats v3.6.1.[48] Covariates in all models included age, body mass index, sex (coded as 0/1 for male/female), and mean framewise-displacement (fMRI time-series motion). Clinical metrics included Neck Disability Index,[31,49] MFI, CES-D Depression Scale,[50] Traumatic Injuries Distress Scale total, Posttraumatic Diagnostic Scale hyperarousal symptom severity,[51] numeric pain rating scale (0–10), and the Hospital Anxiety and Depression Scale Depression.[52] Associations were considered significant if they passed Bonferroni correction (P .05/7; $P \leq .007$).

RESULTS

Initial tests for assumptions of linear modeling did not find evidence of collinearity among predictors or extreme non-normality in clinical variables. Among models including only the covariates, the only significant effect observed was of age on MFI, with

greater age being associated with larger amounts of fat infiltration ($t = 3.17$, $P = .005$). In the full models, network modularity was found to be negatively associated with MFI ($t = -4.02$, partial $R^2 = 0.49$, $P < .001$; Fig 1) and was not found to be associated with any other clinical metrics. Figure 2 shows the network structure for the participants with the highest and lowest MFI scores. No correlation was found between mean scan motion (framewise displacement) and modularity across participants (Pearson $r = -0.21$, $P = .34$).

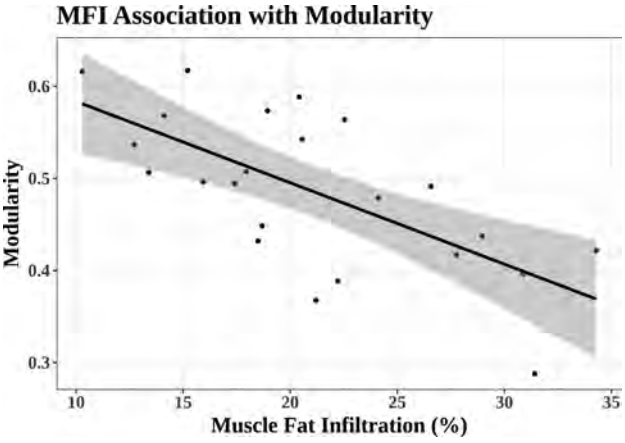

FIG 1. Plot of average modularity (Q) versus MFI (%) in the cervical spine. Range represents 95% confidence interval via R function im (ggplot2).

DISCUSSION

This study is an investigation of whether rs-fMRI network measures can characterize the clinical status of a heterogeneous group of patients with persistent WAD. While previous research in WAD has yet to accurately and consistently identify markers of structural cervical spine pathology with conventional imaging, this study has found promising results of altered network structure in the brain by using more advanced imaging techniques. Such techniques have potential to influence our mechanistic understanding of WAD and other common yet enigmatic neuromusculoskeletal conditions, such as low back pain, fibromyalgia, osteoarthritis, and rotator cuff pathology.

The rationale for modularity as a chosen measure is 2-fold. First, modularity is a global metric capable of assessing whole-brain network organization without the need for defining a priori regions. This makes it an appropriate target for initial investigation given the lack of existing research into the neural correlates of WAD, as well as the modest sample size of the current ancillary study. In addition, modularity has been implicated in several

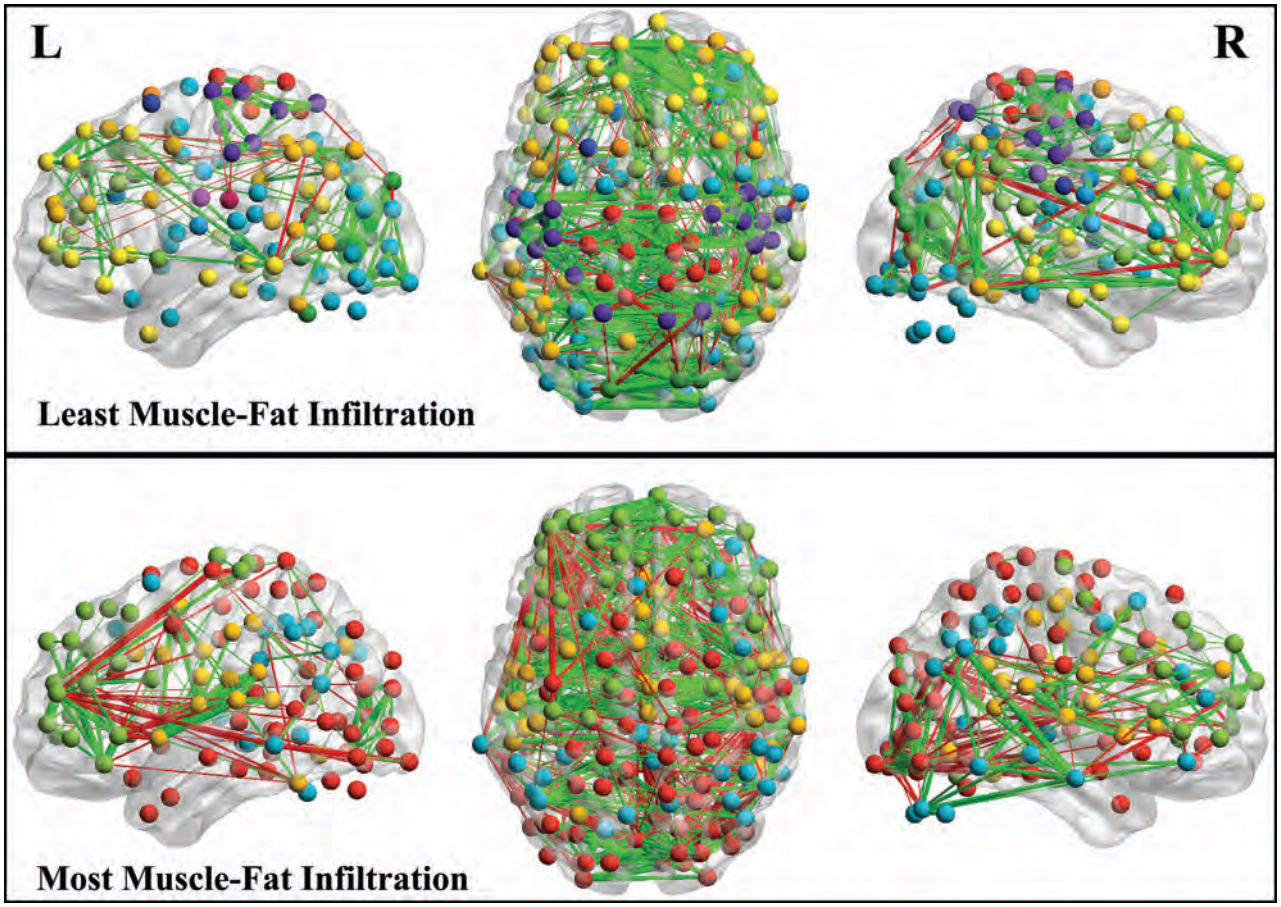

FIG 2. Network structure in the patients with lowest and highest MFI scores. Node colors show communities, *green lines* show edges within communities, *red lines* show edges between. The top row exhibits a high level of modularity (high within community connectivity), while the bottom row demonstrates a low level of modularity (fewer communities and more between community connections).

neurologic conditions that share similarities with the clinical course of WAD, primarily posttraumatic stress disorder[29] and traumatic brain injury.[53,54]

The prospect of anticipating the directionality of associations with modularity is not straightforward. While work in aging has suggested lower modularity may be detrimental,[55] research in psychiatric illnesses has reported deleterious effects of modularity bidirectionally, and researchers in traumatic brain injury have reported increases in the acute phase,[53] yet, the opposite in patients with persistent postconcussive syndrome.[54] While some work has suggested a possible role of mild traumatic brain injury following whiplash both from kinematic modeling[56] and observations of symptom similarities,[3] the prevalence of brain injury in WAD remains largely unknown.

Given the complexities of psychosocial, traumatic, and physical components of WAD, further research is needed to determine how this finding causally relates to the condition. While there is reason to believe network changes may be related to concussive forces, it is also possible that such changes are concurrent with alterations in mood associated with trauma,[29,57] connected to symptoms of chronic pain,[58] or related to changes in a neuroimmune network,[13] in which case, the finding of disrupted modularity may not be specific to WAD but present in posttraumatic stress disorder and traumatic brain injury, for example.

The possibility of altered brain network structure in WAD raises interesting considerations for future research and clinical practice. While most patients who experience an initial whiplash injury go on to make a full recovery, many continue to exhibit symptoms for years following the event, and few quantitative tools are available for differentiating these groups in the acute stage.[59,60] However, previous work has suggested cervical spine measures of MFI $>$ 20.5% (range for those with slow recovery was 6.2–40.6% and rapid recovery was 7.2–22.9%) within the first 2 weeks following the MVC resulted in a sensitivity of 87.5% (true-positive rate) and a specificity of 92.9% (true-negative rate) for predicting outcomes at 3 months post MVC.[12] The use of brain network modularity in WAD has the potential to capture a wide range of diverse network connectivity variations in a global metric that may increase prediction when used in conjunction with estimates of MFI and other clinical risk factors.

In addition to the potential diagnostic value, modularity has been shown to be predictive of treatment outcomes in contexts with potential relevance to WAD. High modularity scores have been shown to be associated with greater treatment success by using cognitive training for traumatic brain injury.[61] In a similar fashion, high baseline modularity has been used to predict larger cognitive gains in response to an exercise intervention in healthy older adults.[62] In light of these findings and with an ongoing trial investigating the effects of exercise on WAD (which includes fMRI),[63] network modularity presents a promising marker for treatment prediction.

This study has several limitations. As a global network measure, modularity does not carry explicit information about which sub-networks are disrupted and in what ways. This finding represents a first attempt at applying graph theoretical analysis to a sample of participants with WAD and suggests the need for additional investigation into the types of network reorganization underlying the observed change in modularity. Because no neuropsychological testing was performed, we were unable to investigate these differences in relation to cognitive outcomes such as working memory, executive function, attention, etc.

Furthermore, the intention of this work is not to suggest "we need more imaging" in clinical practice. In purest terms, judicious and informed use of advanced neuroimaging in tandem with other known risk factors may increase confidence of the primary driver of a patient's recovery trajectory, which should ultimately inform a plan of care.[64,65] The work offers new directions for research in the field to consider multivariate and multisystem pre- and post-collision factors in establishing prognostic phenotypes, leading to new and more informed clinical trials.

Finally, the lack of an association between modularity and the other clinical measures is surprising and could reflect the ancillary nature of this study in that we were not powered to detect differences related to low resolution self-report measures. However, the full sample reflects the known heterogeneity of the WAD condition and provides a foundation for further mechanistic work investigating the bi-directionality of pathways linking peripheral inflammation with neural circuitries sub-serving pain, emotions, muscle structure and function, and outcomes following whiplash injury.

CONCLUSIONS

Despite evidence for the presence of cognitive symptoms, little is known about the neurobiological correlates of WAD. The discovered association between global brain network organization and a metric of WAD severity highlights the need for further advanced imaging investigations.

ACKNOWLEDGMENTS

The authors wish to thank the Emergency Medicine Department at Northwestern Memorial Hospital and Marie Wasielewski Chicago, Illinois, for their assistance in the recruitment of acutely injured participants. We also wish to thank all participants for their involvement.

Disclosures: James Elliott—*RELATED: Grant:* National Institutes of Health, *Comments:* R01HD079076*; *UNRELATED: Board membership:* JOSPT, *Comments:* Accommodation/travel to professional conference; *Consultancy:* Kaiser Permanente, *Comments:* Professional development workshops; *Employment:* University of Sydney, *Comments:* Professor. Todd Parrish—*RELATED: Grant:* NIH*; *UNRELATED: Grants/Grants Pending:* NIH renewal.* *Money paid to institution.

REFERENCES

1. Spitzer WO, Skovron ML, Salmi LR, et al. **Scientific monograph of the Quebec Task Force on Whiplash-Associated Disorders: redefining "whiplash" and its management.** *Spine (Phila Pa 1976)* 1995;20(8 Suppl):1S–73S Medline
2. Beeckmans K, Crunelle C, Van Ingelgom S, et al. **Persistent cognitive deficits after whiplash injury: a comparative study with mild traumatic brain injury patients and healthy volunteers.** *Acta Neurol Belg* 2017;117:493–500 CrossRef Medline
3. Ettlin TM, Kischka U, Reichmann S, et al. **Cerebral symptoms after whiplash injury of the neck: a prospective clinical and neuropsychological study of whiplash injury.** *J Neurol Neurosurg Psychiatry* 1992;55:943–48 CrossRef Medline

4. Matsumoto M, Ichihara D, Okada E, et al. **Cross-sectional area of the posterior extensor muscles of the cervical spine in whiplash injury patients versus healthy volunteers–10 year follow-up MR study.** *Injury* 2012;43:912–16 CrossRef Medline
5. Ronnen HR, de Korte PJ, Brink PR, et al. **Acute whiplash injury: is there a role for MR imaging?–a prospective study of 100 patients.** *Radiology* 1996;201:93–96 CrossRef Medline
6. Matsumoto M, Ichihara D, Okada E, et al. **Modic changes of the cervical spine in patients with whiplash injury: a prospective 11-year follow-up study.** *Injury* 2013;44:819–24 CrossRef Medline
7. Elliott J, Jull G, Noteboom JT, et al. **Fatty infiltration in the cervical extensor muscles in persistent whiplash-associated disorders: a magnetic resonance imaging analysis.** *Spine (Phila Pa 1976)* 2006;31:E847–55 CrossRef
8. Elliott JM, O'Leary S, Sterling M, et al. **G. Magnetic resonance imaging findings of fatty infiltrate in the cervical flexors in chronic whiplash.** *Spine (Phila Pa 1976)* 2010;35:948–54
9. Karlsson A, Leinhard OD, Åslund U, et al. **An investigation of fat infiltration of the multifidus muscle in patients with severe neck symptoms associated with chronic whiplash-associated disorder.** *J Orthop Sports Phys Ther* 2016;46:886–93 CrossRef Medline
10. Abbott R, Peolsson A, West J, et al. **The qualitative grading of muscle fat infiltration in whiplash using fat and water magnetic resonance imaging.** *Spine J* 2018;18:717–25 CrossRef
11. Elliott J, Sterling M, Noteboom JT, et al. **Fatty infiltrate in the cervical extensor muscles is not a feature of chronic, insidious-onset neck pain.** *Clin Radiology* 2008;63:681–87 CrossRef
12. Elliott JM, Courtney DM, Rademaker A, et al. **The rapid and progressive degeneration of the cervical multifidus in whiplash: an MRI study of fatty infiltration.** *Spine (Phila Pa 1976)* 2015;40:E694–700 CrossRef Medline
13. Nusslock R, Brody GH, Armstrong CC, et al. **Higher peripheral inflammatory signaling associated with lower resting-state functional brain connectivity in emotion regulation and central executive networks.** *Biol Psychiatry* 2019;86:153–62 CrossRef Medline
14. Passatore M, Roatta S. **Influence of sympathetic nervous system on sensorimotor function: whiplash associated disorders (WAD) as a model.** *Eur J Appl Physiol* 2006;98:423–49 CrossRef Medline
15. Linnman C, Appel L, Söderlund A, et al. **Chronic whiplash symptoms are related to altered regional cerebral blood flow in the resting state.** *Eur J Pain* 2009;13:65–70 CrossRef Medline
16. Vállez García D, Doorduin J, Willemsen AT, et al. **Altered regional cerebral blood flow in chronic whiplash associated disorders.** *EBioMedicine* 2016;10:249–57 CrossRef Medline
17. Jang SH, Kwon YH. **A review of traumatic axonal injury following whiplash injury as demonstrated by diffusion tensor tractography.** *Front Neurol* 2018;9:57 CrossRef Medline
18. Sturzenegger M, Radanov BP, Winter P, et al. **MRI-based brain volumetry in chronic whiplash patients: no evidence for traumatic brain injury.** *Acta Neurol Scand* 2008;117:49–54 CrossRef Medline
19. Radanov BP, Bicik I, Dvorak J, et al. **Relation between neuropsychological and neuroimaging findings in patients with late whiplash syndrome.** *J Neurol Neurosurg Psychiatry* 1999;66:485–89 CrossRef Medline
20. Churchill NW, Hutchison MG, Graham SJ, et al. **Connectomic markers of symptom severity in sport-related concussion: Whole-brain analysis of resting-state fMRI.** *Neuroimage Clin* 2018;18:518–26 CrossRef Medline
21. Konstantinou N, Pettemeridou E, Stamatakis EA, et al. **Altered resting functional connectivity is related to cognitive outcome in males with moderate-severe traumatic brain injury.** *Front Neurol* 2019;9:1163 CrossRef Medline
22. Newman MEJ. **The structure and function of networks.** *Computer Physics Communications* 2002;147:40–45 CrossRef
23. Sporns O, Betzel RF. **Modular brain networks.** *Annu Rev Psychol* 2016;67:613–40 CrossRef Medline
24. Wig GS. **Segregated systems of human brain networks.** *Trends Cogn Sci (Regul Ed)* 2017;21:981–96 CrossRef Medline
25. Rudie JD, Brown JA, Beck-Pancer D, et al. **Altered functional and structural brain network organization in autism.** *Neuroimage Clin* 2012;2:79–94 CrossRef Medline
26. Gratton C, Nomura EM, Pérez F, et al. **Focal brain lesions to critical locations cause widespread disruption of the modular organization of the brain.** *J Cogn Neurosci* 2012;24:1275–85 CrossRef Medline
27. Alexander-Bloch A, Gogtay N, Meunier D, et al. **Disrupted modularity and local connectivity of brain functional networks in childhood-onset schizophrenia.** *Front Syst Neurosci* 2010;4:147 CrossRef Medline
28. Ye M, Yang T, Qing P, et al. **Changes of functional brain networks in major depressive disorder: a graph theoretical analysis of resting-state fMRI.** *PloS One* 2015;10:e0133775–e0133775 CrossRef Medline
29. Akiki TJ, Averill CL, Wrocklage KM, et al. **Default mode network abnormalities in posttraumatic stress disorder: A novel network-restricted topology approach.** *Neuroimage* 2018;176:489–98 CrossRef Medline
30. de Haan W, van der Flier WM, Koene T, et al. **Disrupted modular brain dynamics reflect cognitive dysfunction in Alzheimer's disease.** *Neuroimage* 2012;59:3085–93 CrossRef Medline
31. Vernon H, Mior S. **The Neck Disability Index: a study of reliability and validity.** *J Manipulative Physiol Ther* 1991;14:409–15 Medline
32. Walton DM, Krebs d, moulden d, et al. **The Traumatic Injuries Distress scale: A new tool that quantifies distress and has predictive validity with patient-reported outcomes.** *J Orthop Sports Phys Ther* 2016;46:920–28 CrossRef Medline
33. Esteban O, Birman D, Schaer M, et al. **MRIQC: Advancing the automatic prediction of image quality in MRI from unseen sites.** *PLoS One* 2017;12:e0184661 CrossRef Medline
34. Gorgolewski K, Burns CD, Madison C, et al. **Nipype: a flexible, lightweight and extensible neuroimaging data processing framework in python.** *Front Neuroinform* 2011;5:13 CrossRef Medline
35. Esteban O, Markiewicz CJ, Blair RW, et al. **fMRIPrep: a robust preprocessing pipeline for functional MRI.** *Nat Methods* 2019;16:111–16 CrossRef Medline
36. Cox RW. **AFNI: software for analysis and visualization of functional magnetic resonance neuroimages.** *Comput Biomed Res* 1996;29:162–73 CrossRef Medline
37. Tustison NJ, Avants BB, Cook PA, et al. **N4ITK: improved N3 bias correction.** *IEEE Trans Med Imaging* 2010;29:1310–20 CrossRef Medline
38. Zhang Y, Brady M, Smith S. **Segmentation of brain MR images through a hidden Markov random field model and the expectation-maximization algorithm.** *IEEE Trans Med Imaging* 2001;20:45–57 CrossRef Medline
39. Fonov V, Evans AC, Botteron K; Brain Development Cooperative Group, et al. **Unbiased average age-appropriate atlases for pediatric studies.** *NeuroImage* 2011;54:313–27 CrossRef Medline
40. Jenkinson M, Smith S. **A global optimisation method for robust affine registration of brain images.** *Med Image Anal* 2001;5:143–56 CrossRef Medline
41. Behzadi Y, Restom K, Liau J, et al. **A component based noise correction method (CompCor) for BOLD and perfusion based fMRI.** *Neuroimage* 2007;37:90–101 CrossRef Medline
42. Power JD, Cohen AL, Nelson SM, et al. **Functional network organization of the human brain.** *Neuron* 2011;72:665–78 CrossRef Medline
43. Gallen CL, Baniqued PL, Chapman SB, et al. **Modular brain network organization predicts response to cognitive training in older adults.** *PLoS One* 2016;11:e0169015 CrossRef Medline
44. Rubinov M, Sporns O. **Complex network measures of brain connectivity: uses and interpretations.** *Neuroimage* 2010;52:1059–69 CrossRef Medline
45. Newman ME. **Modularity and community structure in networks.** *Proc Natl Acad Sci USA* 2006;103:8577–82 CrossRef Medline

46. Reichardt J, Bornholdt S. **Statistical mechanics of community detection.** *Phys Rev E Stat Nonlin Soft Matter Phys* 2006;74:016110 Pt 2 CrossRef Medline
47. Newman MEJ. **Finding community structure in networks using the eigenvectors of matrices.** *Physical Review* 2006;74:036104 CrossRef
48. R Core Team. **R: A language and environment for statistical computing [computer program].** *Vienna, Austria: R Foundation for Statistical Computing* 2018 https://www.R-project.org/
49. Vernon H. **The Neck Disability Index: state-of-the-art, 1991-2008.** *J Manipulative Physiol Ther* 2008;31:491–502 CrossRef Medline
50. Andresen EM, Malmgren JA, Carter WB, et al. **Screening for depression in well older adults: evaluation of a short form of the CES-D.** *Am J Prev Med* 1994;10:77–84 CrossRef
51. McCarthy S. **Post-Traumatic Stress Diagnostic Scale (PDS).** *Occup Med (Lond)* 2008;58:379 CrossRef Medline
52. Zigmond AS, Snaith RP. **The hospital anxiety and depression scale.** *Acta Psychiatr Scand* 1983;67:361–70 CrossRef Medline
53. Han K, Mac Donald CL, Johnson AM, et al. **Disrupted modular organization of resting-state cortical functional connectivity in U.S. military personnel following concussive 'mild' blast-related traumatic brain injury.** *Neuroimage* 2014;84:76–96 CrossRef
54. Messé A, Caplain S, Pélégrini-Issac M, et al. **Specific and evolving resting-state network alterations in post-concussion syndrome following mild traumatic brain injury.** *PLoS One* 2013;8:e65470 CrossRef
55. Song J, Birn RM, Boly M, et al. **Age-related reorganizational changes in modularity and functional connectivity of human brain networks.** *Brain Connect* 2014;4:662–76 CrossRef Medline
56. Elkin BS, Elliott JM, Siegmund GP. **Whiplash injury or concussion? A possible biomechanical explanation for concussion symptoms in some individuals following a rear-end collision.** *J Orthop Sports Phys Ther* 2016;46:874–85 CrossRef Medline
57. Sartin-Tarm A, Cisler J, Ross M. **Resting state functional neural network modularity among adult women with PTSD.** *Biological Psychiatry* 2018;83:S137 CrossRef
58. Mano H, Kotecha G, Leibnitz K, et al. **Classification and characterisation of brain network changes in chronic back pain: A multicenter study.** *Wellcome Open Res* 2018;3:19 CrossRef Medline
59. Gargan MF, Bannister GC. **The rate of recovery following whiplash injury.** *Eur Spine J* 1994;3:162–64 CrossRef Medline
60. Carroll LJ, Hogg-Johnson S, Cote P, et al. **Course and prognostic factors for neck pain in workers: results of the Bone and Joint Decade 2000-2010 Task Force on Neck Pain and Its Associated Disorders.** *Spine (Phila Pa 1976)* 2008;33:S93–100 CrossRef Medline
61. Arnemann KL, Chen AJW, Novakovic-Agopian T, et al. **Functional brain network modularity predicts response to cognitive training after brain injury.** *Neurology* 2015;84:1568–74 CrossRef Medline
62. Baniqued PL, Gallen CL, Voss MW, et al. **Brain network modularity predicts exercise-related executive function gains in older adults.** *Front Aging Neurosci* 2017;9:426 CrossRef Medline
63. Peolsson A, Karlsson A, Ghafouri B, et al. **Pathophysiology behind prolonged whiplash associated disorders: study protocol for an experimental study.** *BMC Musculoskelet Disord* 2019;20:51 CrossRef Medline
64. Walton DM, Elliott JM. **A new clinical model for facilitating the development of pattern recognition skills in clinical pain assessment.** *Musculoskelet Sci Pract* 2018;36:17–24 CrossRef Medline
65. Walton DM, Elliott JM. **An integrated model of chronic whiplash-associated disorder.** *J Orthop Sports Phys Ther* 2017;47:462–71 CrossRef Medline

Value of 3T Susceptibility-Weighted Imaging in the Diagnosis of Multiple Sclerosis

M.A. Clarke, D. Pareto, L. Pessini-Ferreira, G. Arrambide, M. Alberich, F. Crescenzo, S. Cappelle, M. Tintoré, J. Sastre-Garriga, C. Auger, X. Montalban, N. Evangelou, and À. Rovira

ABSTRACT

BACKGROUND AND PURPOSE: Previous studies have suggested that the central vein sign and iron rims are specific features of MS lesions. Using 3T SWI, we aimed to compare the frequency of lesions with central veins and iron rims in patients with clinically isolated syndrome and MS-mimicking disorders and test their diagnostic value in predicting conversion from clinically isolated syndrome to MS.

MATERIALS AND METHODS: For each patient, we calculated the number of brain lesions with central veins and iron rims. We then identified a simple rule involving an absolute number of lesions with central veins and iron rims to predict conversion from clinically isolated syndrome to MS. Additionally, we tested the diagnostic performance of central veins and iron rims when combined with evidence of dissemination in space.

RESULTS: We included 112 patients with clinically isolated syndrome and 35 patients with MS-mimicking conditions. At follow-up, 94 patients with clinically isolated syndrome developed MS according to the 2017 McDonald criteria. Patients with clinically isolated syndrome had a median of 2 central veins (range, 0–19), while the non-MS group had a median of 1 central vein (range, 0–6). Fifty-six percent of patients who developed MS had ≥1 iron rim, and none of the patients without MS had iron rims. The sensitivity and specificity of finding ≥3 central veins and/or ≥1 iron rim were 70% and 86%, respectively. In combination with evidence of dissemination in space, the 2 imaging markers had higher specificity than dissemination in space and positive findings of oligoclonal bands currently used to support the diagnosis of MS.

CONCLUSIONS: A single 3T SWI scan offers valuable diagnostic information, which has the potential to prevent MS misdiagnosis.

ABBREVIATIONS: CDMS = clinically definite MS; CIS = clinically isolated syndrome; CV = central vein; DIS = dissemination in space; DIT = dissemination in time; IR = iron rim; NPV = negative predictive value; OCB = oligoclonal band; PPV = positive predictive value

MS diagnosis is based on typical clinical symptoms and radiologic findings, and it incorporates the principles of demonstration of demyelinating lesions disseminated in space (DIS) and time (DIT). Radiologically, DIS is demonstrated by the presence of ≥1 T2-hyperintense lesion characteristic of MS in ≥2 of the following CNS topographies: periventricular, cortical, or juxtacortical; infratentorial; and spinal cord; and DIT is demonstrated by the simultaneous presence of gadolinium-enhancing and nonenhancing lesions on a single scan or by a new T2 lesion compared with a previous MR imaging scan. Following the 2017 revisions to the McDonald criteria, a positive finding on lumbar

Received December 19, 2019; accepted after revision March 19, 2020.

From the Vall d'Hebron Research Institute (M.A.C., D.P., M.A., M.T., J.S.-G., C.A., X.M., A.R.), Barcelona, Spain; Section of Neuroradiology, Department of Radiology (D.P., L.P.-F., C.A., A.R.), Hospital Universitari Vall d'Hebron, Universitat Autònoma de Barcelona, Barcelona, Spain; Department of Neurology-Neuroimmunology (G.A., M.T., J.S.-G., X.M.), Centre d'Esclerosi Múltiple de Catalunya (Cemcat), Hospital Universitari Vall d'Hebron, Universitat Autònoma de Barcelona, Barcelona, Spain; Department of Neurosciences, Biomedicine and Movement Sciences (F.C.), University of Verona, Verona, Italy; Division of Radiology (S.C.), University Hospital Leuven, Leuven, Belgium; Division of Neurology (X.M.), St. Michael's Hospital, University of Toronto, Toronto, Ontario, Canada; and Division of Clinical Neuroscience (N.E.), University of Nottingham, Nottingham, UK.

The European Center for Treatment and Research in Multiple Sclerosis and Magnetic Resonance Imaging in Multiple Sclerosis provided funding for M.A.C.'s fellowship. Furthermore, we acknowledge the "Red Española de Esclerosis Múltiple" (RD07/0060; RD12/0032) and the project PI18/00823, which are sponsored by the Fondo de Investigación Sanitaria, the Instituto de Salud Carlos III, the Ministry of Economy and Competitiveness in Spain, and the "Ajuts per donar Suport als Grups de Recerca de Catalunya (2009 SGR 0793)," which is sponsored by the "Agència de Gestió d'Ajuts Universitaris i de Recerca" of the Generalitat de Catalunya in Spain.

Paper previously presented at: Annual Congress of the European Committee for Treatment and Research in Multiple Sclerosis, September 11–13, 2019; Stockholm, Sweden; and Annual Meeting of the European Society of Neuroradiology, September 18–22, 2019; Oslo, Norway.

Please address correspondence to Àlex Rovira, MD, Servei de Radiologia, Hospital Universitari Vall d'Hebron, Psg. Vall d'Hebron 119-129, 08035 Barcelona, Spain; e-mail: alex.rovira@idi.gencat.cat

Indicates open access to non-subscribers at www.ajnr.org
Indicates article with supplemental on-line table.

http://dx.doi.org/10.3174/ajnr.A6547

puncture can be used to diagnose MS in the absence of DIT.[1] This has led to an increase in sensitivity but a decrease in specificity, compared with the 2010 criteria.[2,3] As a result, MS-specific imaging markers are needed to improve the diagnostic process and prevent overdiagnosis.

SWI is an MR imaging technique sensitive to paramagnetic compounds that distort the local magnetic field, such as deoxyhemoglobin and iron.[4,5] Recently, the role of SWI in MS has gained attention because it offers additional information about MS WM lesions, which cannot be appreciated on conventional T1- and T2-weighted images currently used to diagnose and monitor patients.[6,7]

Evidence from 7T studies and recently from 3T and 1.5T studies[8-13] shows that MS lesions form around small veins, a phenomenon termed "the central vein (CV) sign." Studies of patients with established disease have proposed a 40% threshold of WM lesions with CVs to differentiate MS and other disorders that can mimic MS on MR imaging.[14-16] Similarly, lesions with hypointense rims, likely reflecting iron deposition within the microglia and macrophagic cells at the edge of some chronic MS lesions, the so-called iron rims (IRs), have been identified on SWI in all subtypes of MS.[7,17] However, this imaging feature seems to be absent in other diseases such as neuromyelitis optica spectrum disorder,[18] Susac syndrome,[19] and ischemic lesions.[20] This finding suggests that both CVs and IRs might be specific features of MS lesions, which could be applied diagnostically.

However, most studies have assessed the CV sign and the IRs separately and, so far, have mainly been performed on small populations of patients with already-established diagnoses, using 7T scanners and/or sequences not commonly used in clinical practice. In this study, we aimed to assess the frequency of CVs and IRs detected on unenhanced SWI acquired on a clinical 3T scanner in patients with typical clinically isolated syndrome (CIS) and MS-mimicking disorders. Additionally, we aimed to test their usefulness as diagnostic imaging markers of MS lesions in patients at the earliest stages of the disease. We hypothesized that patients who went on to develop MS would have a higher number of lesions with CVs and IRs compared with patients who did not.

MATERIALS AND METHODS

Ethics

This study received approval from the Clinical Research Ethics Committee at the Vall d'Hebron University Hospital (PR(AG) 302/2018). All patients signed written informed consent.

Patients

We recruited patients between October 2010 and February 2019. All scans were acquired as part of routine, clinical assessment.

Two groups of patients were recruited using consecutive sampling. The first one is part of an ongoing cohort study described previously[21,22] and included a prospective cohort of patients younger than 50 years of age with a typical CIS suggestive of CNS demyelination, scanned within 3–5 months of the first clinical attack (CIS group). Sixteen patients with CIS included in this study have been previously reported in a cross-sectional study of the CV sign.[23] The second group comprised patients with WM multifocal abnormalities not attributed to MS scanned either before or after being formally given a non-MS diagnosis (non-MS group). We excluded any patients without SWI or T2-weighted FLAIR images, with images acquired using a different set of SWI and/or FLAIR protocols, and with scans of insufficient quality for analysis. Neurologists and/or radiologists independently provided the clinical diagnoses for the patients included in this study and were blinded to any study results reported here.

Immunoglobulin G Oligoclonal Bands

Intrathecal immunoglobulin oligoclonal band (OCB) testing was performed in patients with CIS within 3 months of the first clinical attack and in some of the non-MS group (if requested by the patient's neurologist as part of the clinical work-up). OCBs were determined using agarose isoelectric focusing combined with immunoblotting in the CSF and serum.[24]

MR Imaging Acquisition

All MR images were acquired on a 3T Magnetom Trio MR imaging system (Siemens) with a 12-channel phased array head coil and a whole-body transmit coil. The following sequences were obtained in all the patients: 3D axial gradient-echo SWI without contrast (TR = 33 ms, TE1 = 6.08 ms, TE2 = 24.6 ms, flip angle = 15°, matrix size = 288 × 384 × 104, voxel size = 0.65 × 0.65 × 3.0 mm); and transverse 2D-T2-FLAIR (TR = 9000 ms, TE = 87 ms, TI = 2500 ms, flip angle = 119°, matrix size = 412 × 512 × 46, voxel size = 0.49 × 0.49 × 3.0 mm) or sagittal 3D-FLAIR (TR = 5000 ms, TE = 394 ms, TI = 1800 ms, flip angle = 120°, matrix size = 240 × 256 × 176, voxel size = 1.0 × 1.0 × 1.0 mm). 3D-FLAIR sequences were reconstructed in the axial plane using 3-mm-thickness contiguous slices.

Image Processing and Analysis

Each patient's FLAIR and susceptibility-weighted images were coregistered using SPM12 software (http://www.fil.ion.ucl.ac.uk/spm/software/spm12), and 3D Slicer, Version 4.10.0[25] (http://www.slicer.org), was used to assess the images. Brain lesions were identified on the T2-FLAIR images and were analyzed for the presence of both CVs and IRs on the axial plane of the SWI.

For the analysis of CVs, we followed the guidelines described by the North American Imaging in Multiple Sclerosis Cooperative;[11] however, we included confluent lesions in our analysis to assess both CVs and IRs in all the analyzable lesions and to calculate their combined frequency. If a confluent lesion had a single CV or its "fingers" had CVs, we classed that lesion as positive for a CV. IRs were identified as areas of hypointense ringlike signal, which corresponded to the edge of the lesion, encircling it fully or partially. We also recorded information about lesions with scattered iron deposition in the form of hypointense iron "dots" on SWI, described previously.[26] We excluded lesions that were <3 mm in their shortest axis, lesions located infratentorially, and lesions that were not fully visible on the SWI. For each lesion, we recorded the topography: juxtacortical, periventricular, subcortical, or deep gray matter.

Image analysis was performed by M.A.C. (with 5 years' experience in MS lesion analysis). A subset of 25 randomly selected scans was analyzed by a second rater (F.C.) to calculate interrater

agreement and determine the effect of rater experience on identifying the lesion features of interest. The second rater (a neurology resident with 4 years' experience) had no previous experience in identifying CVs and IRs and underwent training under the supervision of M.A.C. before analysis. Both raters were blinded to all clinical information at the time of the analysis.

Study Design

Our study included 3 main analyses. Data from both patients with CIS and non-MS were used in the first part of the analysis, and we subsequently focused on the CIS population only (Parts 2 and 3).

Part 1: Frequency of CVs and IRs in Patients with CIS and Non-MS. First, we compared the number of lesions with IRs, iron dots, and CVs between the CIS and non-MS groups to quantify the frequency of these lesion features in the 2 populations.

Part 2: Diagnostic Value of CVs and IRs. We used information about the frequency of IRs, iron dots, and CVs in the CIS group to perform an exploratory analysis of the diagnostic value of using an absolute number of lesions with IRs and CVs to predict conversion to MS. We included only patients with a minimum of 3 years of follow-up or a confirmed diagnosis of MS according to the 2017 McDonald criteria.

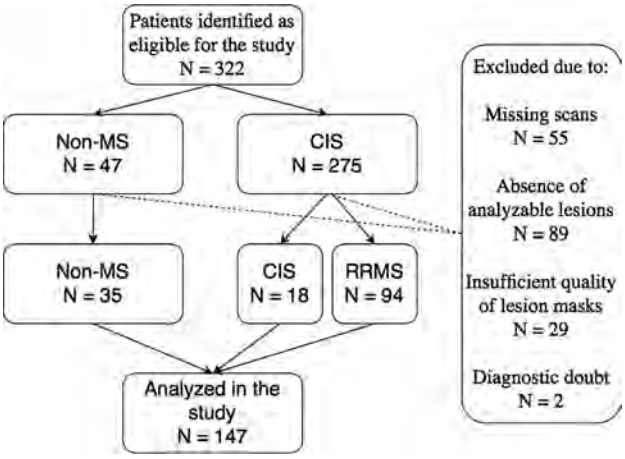

FIG 1. Patient flow diagram showing how patients were selected for the study and the reasons for exclusion. We excluded patients for the following reasons: 1) missing either their SWI or T2-FLAIR scan; 2) lesions <3 mm or infratentorial lesions that could not be identified on the SWI due to artifacts; 3) automated lesion masks not passing quality checks; and 4) diagnostic doubt by the end of the study follow-up. RRMS indicates relapsing-remitting multiple sclerosis.

Part 3: Dissemination in Space + Analysis. We assessed the diagnostic value of IRs, iron dots, and CVs in combination with evidence of dissemination in space (DIS) by testing the following proposed criteria:

- DIS + IR: evidence of DIS and simultaneous presence of rim + and rim – lesions
- DIS + iron: evidence of DIS, and rim + and rim – lesions or iron dots
- DIS + CVs: evidence of DIS and lesions with central veins

We compared the results with the performance of baseline DIS and positive OCBs (DIS + OCB), the simultaneous presence of gadolinium-enhancing and nonenhancing lesions (DIS + gadolinium Gadobutrol [Gadovist, Bayer]), and DIS + any of the above (IR, iron, 2 CVs, OCBs, and/or gadolinium). We assessed the diagnostic value of the DIS + criteria compared with the following outcomes: radiologic conversion to MS (at baseline or during follow-up) and the Poser criteria (clinically definite MS [CDMS] with evidence of 2 clinical attacks separated in time and in space). We included only patients with a minimum of 3 years of follow-up or with a positive outcome (DIS + DIT or Poser criteria).

Statistical Analysis

Statistical analysis was performed using SPSS, Version 24, and the diagnostic performance was assessed using MedCalc for Windows, Version 15.0 (MedCalc Software). $P < .05$ was used to indicate statistically significant results.

Interrater agreement was calculated separately for lesions with CVs and IRs using the intraclass correlation coefficient (2-way mix model, single measures, absolute agreement) in a small sample of randomly chosen scans.

We selected the minimum number of lesions with CVs and IRs for a diagnosis to ensure high specificity. The sensitivity, specificity, accuracy, positive predictive value (PPV), and negative predictive value (NPV) with 95% confidence intervals were calculated for each proposed index test. We also tested for the location preference of lesions with CVs and IRs using a chi-square test. A Cox regression was used to calculate the risk of conversion to MS for each of the proposed DIS+ criteria. We used patients with CIS not fulfilling the given criteria as the reference group.

Demographic and clinical data of the patients included in the study

	CIS Group ($n = 112$)	Non-MS Group ($n = 35$)
Mean age (SD, range) (yr)	35.4 (7.9, 19–49)	41.7 (11.5, 20–67)
Sex, female No. (%)	70 (70.5%)	23 (65.7%)
Clinical diagnosis at the end of the study No. (%)	MS = 94 (83.9%) (including CDMS = 42 [37.5%]) CIS = 18 (16.1%)	Autoimmune disease = 13 (37.1%) Vascular disease = 8 (22.9%) Incidental findings = 1 (2.9%) Infectious disease = 1 (2.9%) Headache = 3 (8.6%) Other = 9 (25.7%)
+/− OCBs No. (not performed)	80/21 (11)	2/15 (18)
Median EDSS (range)	1.5 (0–4.5)	NA
Median WM lesion No. (range)	4 (1–31)	7 (1–31)

Note:—EDSS indicates Expanded Disability Status Scale; NA, not available.

RESULTS

Patients

One hundred twelve patients with CIS and 35 in the non-MS group were included in the study. A patient flow diagram can be seen in Fig 1. Demographic and clinical data are shown in the Table. In the CIS group, the mean follow-up

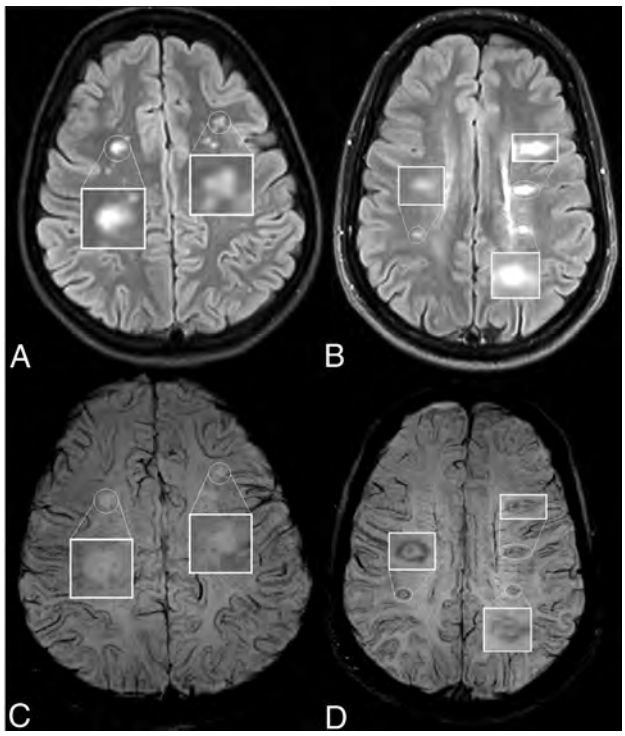

FIG 2. Lesion appearance on axial T2-FLAIR (*upper row*) and the corresponding susceptibility-weighted (*lower row*) images in patients with Sjögren disease (*A* and *C*) and MS (*B* and *D*). The patient with Sjögren disease has no visible CVs or IRs on the SWI. The patient with MS has clearly visible IRs, which correspond to the lesion edges visible on the T2-FLAIR. CVs are also visible inside the lesions as *hypointense dots* or *lines*.

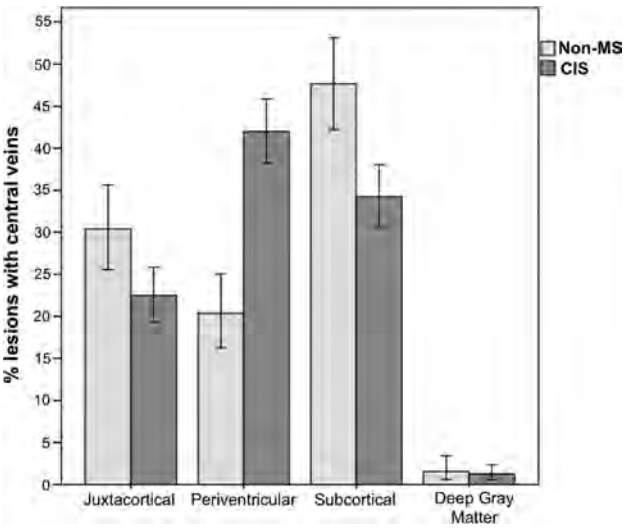

FIG 3. The location of lesions with central veins in the CIS and non-MS groups. *Error bars* represent standard error.

time was 4.6 ± 2 years. During that period, 94 patients (84%) received a diagnosis of MS according to the 2017 McDonald criteria, including 42 (37.5%) who converted to CDMS (Poser criteria).[27] During the follow-up, 24 patients with CIS did not undergo disease-modifying therapy and 84 did, with data missing for 4 patients. In the non-MS group, 19 individuals (54%) did not have an established diagnosis at the time of the scan, and the mean follow-up of that group of patients was 4.7 ± 2 years. For the non-MS group with an already-established diagnosis before the scan ($n = 16$), the median disease duration was 2 years (range, 0–49 years).

The non-MS diagnoses included the following groups of diseases: autoimmune (anti-myelin oligodendrocyte glycoprotein–associated disease, Susac syndrome, anti-aquaporin-4 + neuromyelitis optica spectrum disorder, primary antiphospholipid syndrome, CNS vasculitis, Sjögren, Sjogren's syndrome, neurosarcoidosis), small vessel vascular disease, infectious disease (human T-cell leukemia virus, type 1–associated myelopathy), headache (including migraine), nonspecific leukoencephalopathy, and incidental white matter findings in healthy subjects or unrelated to clinical symptoms (nonspecific paresthesias or visual symptoms, cranial nerve palsy, or neuralgia). A diagnosis of MS had been explicitly excluded by their neurologists in all these cases.

Lesion Analysis

In total, we analyzed 955 focal WM lesions; 636 in the CIS group and 319 in the non-MS group. Figure 2 shows sample lesions with CVs and IRs and without them.

Regarding the interrater agreement, the intraclass correlation coefficient based on the number of lesions with CVs was 0.84 (95% CI, 0.67–0.93), and for the number of lesions with IRs, it was 0.84 (95% CI, 0.64–0.93).

Part 1: Frequency of CVs and IRs in Patients with CIS and Non-MS. In the CIS group, 410 lesions (64.5%) had a CV, while only 53 (16.6%) had a CV in the non-MS group. Fifty-six (50%) patients with CIS had ≥3 lesions with CV versus seven (20%) in the non-MS group. Figure 3 shows the location of lesions with CVs in the CIS and non-MS groups. The difference in the distribution of lesions with CVs in the CIS group, assessed by a chi-square test, was significant ($X^2(3) = 169.805$, $P < .001$), showing preference for periventricular and subcortical locations. Figure 4 shows the differences in the proportions and number of lesions with CVs between the 2 groups. None of the non-MS group reached the previously proposed 40% threshold of WM lesions with CVs (range, 0%–37.5%).

One hundred twenty-seven lesions (19.9%) in the CIS group had an IR, while none of the lesions in the non-MS group had one. Of all patients with CIS, 47.3% had at least 1 lesion with an IR and none of the patients who remained with CIS at the end of the study both according to the 2017 McDonald criteria and the Poser criteria had any lesions with IRs. Of patients without IRs, 63.6% subsequently initiated disease-modifying therapies compared with 94.3% of patients with IRs.

More than half of all the lesions with IRs were located periventricularly, demonstrating a significant location preference ($\chi^2(3) = 86.4$, $P < .001$), and three-quarters of all the patients with IRs had at least 1 periventricular lesion with an IR; 13.2% of all CIS lesions had both a CV and an IR. See Fig 5 for a summary of the incidence and location of lesions with IRs in our study.

Forty-six CIS lesions (7.2%) and 16 non-MS lesions (5%) had an iron dot. For both the CIS and non-MS groups, the median number of lesions with iron dots was 0 (range, 0–3). Twenty-four patients with CIS and 8 with non-MS had at least 1 lesion with an iron dot.

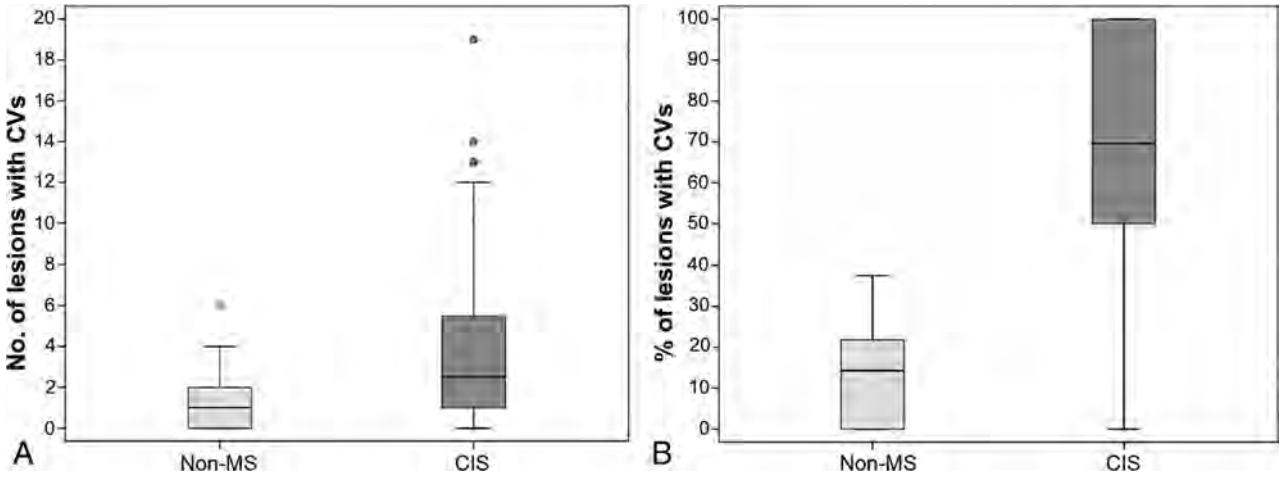

FIG 4. Summary of the incidence of lesions with CVs in the CIS and non-MS groups. *A*, The number of lesions with CVs (per patient) in the 2 groups. *B*, The percentage of lesions with CVs (per patient) in the 2 groups.

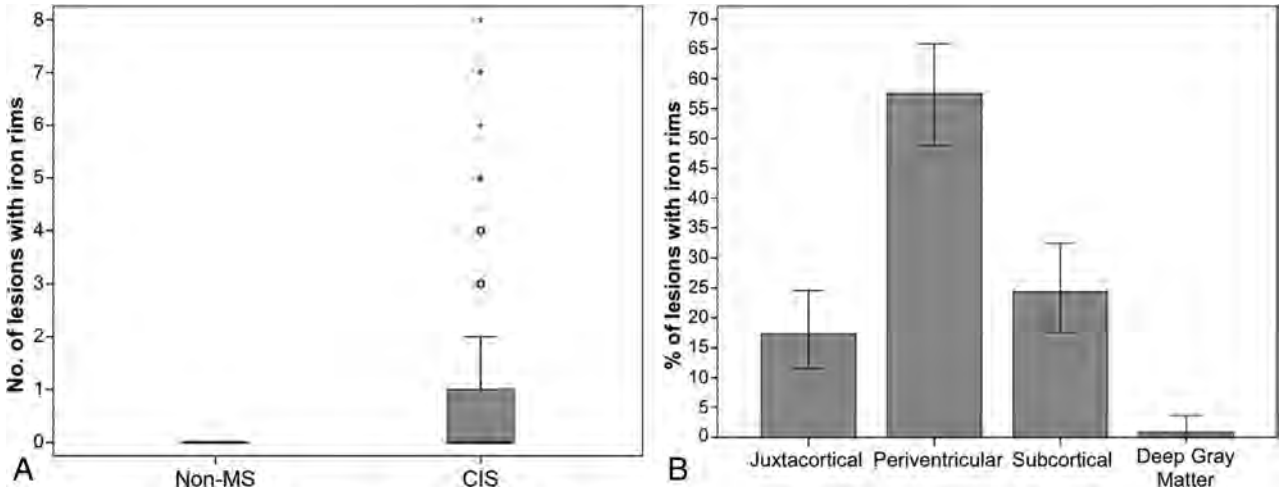

FIG 5. Summary of the incidence of lesions with iron rings in the CIS and non-MS groups. *A*, The number of lesions with iron rings (per patient) in the 2 groups. *B*, The location of lesions with iron rings in the CIS group.

For analyses presented in Parts 2 and 3, we excluded 4 patients with CIS who did not have a minimum of 3 years of follow-up or a confirmed diagnosis of MS according to the 2017 McDonald criteria.

Part 2: Diagnostic Value of CVs and IRs. The presence of 3 lesions with CVs and/or 1 lesion with an IR on the baseline SWI scan resulted in 70.2% sensitivity (95% CI, 59.9%–79.2%) and 85.7% specificity (95% CI, 57.2%–98.2%) in predicting conversion to MS. The PPV and NPV were 97.1% (95% CI, 90.1%–99.2%) and 30.0% (95% CI, 22.7%–38.5%), respectively. Using the 40% threshold of lesions with CVs and/or 1 lesion with an IR, we achieved 90.4% sensitivity (95% CI, 82.6%–95.5%) and 35.7% specificity (95% CI, 12.8%–64.9%), and PPV and NPV were 90.4% (95% CI, 86.4%–93.4%) and 35.7% (95% CI, 17.9%–58.7%), respectively.

Part 3: DIS+ Analysis. The On-line Table shows the sensitivity, specificity, PPV, and NPV, and hazard ratios for DIS + DIT criteria and DIS + DIT alternatives. For DIS + CVs, we selected 2 CVs (rather than 3) to classify patients as having MS because this increased the number of patients who could be diagnosed at baseline, while still ensuring high specificity. Each of the proposed tests resulted in the following number of patients receiving a diagnosis at baseline: DIS + OCB ($n = 69$), DIS + gadolinium ($n = 55$), DIS + IR ($n = 48$), DIS + iron ($n = 55$), DIS + 2 CVs ($n = 64$), and DIS + any ($n = 83$).

DISCUSSION

In our study, we compared the frequency of lesions with CVs and IRs in patients with CIS and MS-mimicking disorders and tested the diagnostic value of these 2 imaging markers using a 3T SWI protocol. We report that clinically acquired SWI can successfully detect CVs and IRs with high interrater agreement.

In our study, the frequency of CVs was notably lower in the non-MS group, and finding at least 1 lesion with an IR achieved 100% specificity when used to differentiate CIS and non-MS groups. Moreover, finding at least 3 lesions with CVs or 1 lesion

with an IR on a baseline SWI scan demonstrated high sensitivity and specificity (70% and 86%, respectively) in predicting conversion to MS in patients with typical CIS followed up for an average of 4 and a half years. Moreover, combining evidence of DIS and the simultaneous presence of iron-positive and iron-negative lesions or the presence of at least 2 lesions with CVs predicted a 2- to 3-fold increased risk of a subsequent MS diagnosis (irrespective of using the radiologic or clinical criteria) and demonstrated increased diagnostic specificity compared with using DIS and positive OCBs, currently used to support the diagnosis of MS in clinical practice.

The International Panel on Diagnosis of MS has identified the study of the CV sign and IRs as a high-priority research area.[1] The CV sign has been previously studied using a variety of MR imaging protocols. Some of them, such as FLAIR*,[28] require extra postprocessing steps, while others have used a 3D echo-planar sequence with a gadolinium-based contrast agent.[13] Our protocol used a widely available 3D gradient-echo sequence without contrast, a strategy that follows the recommendations made by different organizations on the restrictive use of gadolinium-based contrast agents due to convincing evidence indicating the deposition of gadolinium in certain regions of the CNS after repeat administrations.[29]

The use of 3 lesions with CVs for MS diagnosis has previously demonstrated high specificity values of >90%,[13,30] including in the largest multicenter study of the CV sign, which reported high specificity (89%) when 3 lesions with CVs were used to distinguish MS (including CIS) and non-MS, though the patients with CIS were not followed up longitudinally.[23] The only previous, prospective study of the CV sign using 3T SWI involved 14 patients and concluded that the CV sign was useful in differentiating MS and non-MS lesions.[31] In our study of >100 patients with CIS, we confirm that an unenhanced SWI sequence, which can be easily implemented in a clinical MR imaging protocol, can offer valuable diagnostic information at the earliest stages of MS.

Similarly, most of the studies that assessed the presence of IRs have been performed using 7T quantitative susceptibility mapping and phase imaging.[17,18,32-36] Recently, Absinta et al[37] compared 7T and 3T phase images and found that almost all 7T rings were also visible at 3T. However, quantitative susceptibility mapping and phase imaging are not typically used, or even available, for diagnostic purposes in clinical practice. In our study using SWI sequences, IRs were completely absent in patients who did not have an MS diagnosis, whereas 56% of patients who fulfilled the 2017 McDonald criteria had at least 1 lesion with an IR.

Moreover, because lesions with IRs are thought to represent the chronic, active stage of lesion evolution,[7,37] we could speculate that the simultaneous presence of iron-positive and -negative lesions on a single scan provides objective evidence of DIT, similar to the way the simultaneous presence of gadolinium-enhancing and nonenhancing lesions on a single MR imaging scan is used in the McDonald criteria. Iron dots, on the other hand, were rare, comprising <10% of all the lesions. This hypointense signal on SWI might indicate iron aggregates within lesions;[38] however, it is also possible that in small lesions, IRs appear dotlike due to partial volume effects. Future follow-up of patients included in this study will help us understand the temporal evolution of these lesions in MS.

In our study, when combined with evidence of DIS, the presence of iron-positive and -negative lesions or 2 lesions with CVs had higher specificity compared with OCBs, which had the lowest specificity of all the tests. Although useful diagnostically as an alternative to DIT, OCB testing is invasive and can result in adverse effects,[39] which cause some patients to refuse to have a lumbar puncture. Specific, noninvasive MR imaging markers have the potential to help diagnose MS without exposing patients to unnecessary risks. Moreover, from the patient perspective, a short (in our study, <5 minutes), additional MR imaging sequence would be far more convenient than OCB testing.

One of the strengths of our study is that our patients were scanned before a final diagnosis was reached, reflecting the way the CV sign and IRs would be applied in clinical practice. So far, few studies of the CV sign at 3T have tested its diagnostic value in patients with CIS with follow-up.[31,40,41] We are not aware of any studies of the diagnostic value of IRs at 3T. Another strength of our study is the easy implementation of our diagnostic criteria in a clinical setting, even by relatively inexperienced raters. Finding a fixed number of lesions with CVs and/or IRs is more practical than using a proportion-based approach, which requires the analysis of all the lesions. Moreover, the low number of lesions required for a diagnosis means this approach can be applied even in patients with a small lesion load.

Our study also had limitations. Our non-MS group was relatively small, and we analyzed only scans from 1 center using a single scanner and protocol. These features mean that our results cannot be generalized to other centers or scanners. We excluded a large proportion of patients from the study, largely due to lack of eligible lesions (supratentorial, >3 mm), which could likely have led to an overestimation of the true frequency of lesions with CVs and IRs in this patient population. Moreover, the use of absolute numbers of lesions with CVs should be further tested in future studies of patients with a full spectrum of MS mimics. This is an important issue, considering that many studies have primarily reported proportion-based diagnostic cut offs and studies comparing the use of absolute lesion numbers versus proportion-based approaches remain inconclusive.[13,23]

It remains to be determined which, if any, gradient-echo sequence would be optimal for the detection of CVs and IRs on the same scan. While the Magnetic Resonance Imaging in Multiple Sclerosis study found that an optimized T2*-weighted protocol led to increased diagnostic sensitivity in a small number of patients compared with SWI,[23] a further evaluation of clinically available 3T imaging protocols is needed. Finally, even with a mean follow-up period of 4 and a half years, some patients did not develop CDMS; only long-term follow-up of these patients will demonstrate the usefulness of SWI in MS diagnosis.

CONCLUSIONS

Clinically available, 3T susceptibility-weighted MR imaging can successfully visualize CVs and IRs, which appear to be highly specific features of early MS lesions. Our easy-to-implement proposed criteria could be applied in a clinical setting without the need for postprocessing and could be a good alternative to gadolinium for demonstrating DIT or to OCB testing. Future prospective, multicenter studies are needed to confirm our findings of the diagnostic role of the CV sign and IRs in MS.

ACKNOWLEDGMENTS

We wish to thank Aran Garcia-Vidal (Vall d'Hebron Research Institute, Barcelona, Spain) for assistance with data organization for this project.

Disclosures: Margareta A. Clarke—*RELATED*: *Grant*: European Center For Treatment and Research In Multiple Sclerosis–Magnetic Resonance Imaging in Multiple Sclerosis Fellowship, *Comments*: 2018 European Center For Treatment and Research in Multiple Sclerosis–Magnetic Resonance Imaging in Multiple Sclerosis Fellow stipend; *Consulting Fee or Honorarium*: Novartis Pharmaceuticals UK, *Comments*: speaker honorarium for a talk at a the Novartis-sponsored research meeting. The talk was not related to any research or activities carried out/supported by Novartis; *Support for Travel to Meetings for the Study or Other Purposes*: European Center for Treatment and Research in Multiple Sclerosis travel grant, paid to the individual, *Comments*: a young investigators travel grant to attend and present this work at the 35th Congress for the Treatment and Research in Multiple Sclerosis. Deborah Pareto—*UNRELATED*: *Other*: teaching honoraria from Novartis and Sanofi-Genzyme. Lucas Pessini-Ferreira—*UNRELATED*: *Employment*: Hospital Vall d'Hebrón. Georgina Arrambide—*UNRELATED*: *Consultancy*: Sanofi Genzyme, Merck, and Roche, *Comments*: compensation for consulting services or participation in advisory boards*; *Grants/Grants Pending*: Instituto de Salud Carlos III, *Comments*: Proyectos de Investigación en Salud, grant PI19/01590, Neurofilament light chain levels as a prognostic biomarker of disease evolution and of treatment response in multiple sclerosis*; *Payment for Lectures Including Service on Speakers Bureaus*: Sanofi Genzyme, Merck, and Novartis, *Comments*: speaking honoraria*; *Travel/Accommodations/Meeting Expenses Unrelated to Activities Listed*: Novartis, Roche, Stendhal, and European Center for Treatment and Research in Multiple Sclerosis, *Comments*: travel expenses for scientific meetings; *Other*: Novartis, *Comments*: research support.* Mar Tintoré—*UNRELATED*: *Board Membership*: Almirall, Bayer, Biogen-Idec, Genzyme, Merck Serono, Novartis, Roche, Sanofi-Aventis, and Teva Pharmaceuticals; *Consultancy*: Almirall, Bayer, Biogen Idec, Genzyme, Merck Serono, Novartis, Roche, Sanofi-Aventis, and Teva Pharmaceuticals; *Grants/Grants Pending*: Biogen Idec, Genzyme, Novartis*; *Payment for Lectures Including Service on Speakers Bureaus*: Almirall, Bayer, Biogen Idec, Genzyme, Merck Serono, Novartis, Roche, Viela Bio, Sanofi-Aventis, and Teva Pharmaceuticals; *Payment for Development of Educational Presentations*: Biogen, Merck; *Travel/Accommodations/Meeting Expenses Unrelated to Activities Listed*: Almirall, Bayer, Biogen Idec, Genzyme, Merck Serono, Novartis, Roche, Sanofi-Aventis, and Teva Pharmaceuticals. Jaume Sastre-Garriga—*RELATED*: *Grant*: European Center for Treatment and Research in Multiple Sclerosis, *Comments*: European Center for Treatment and Research in Multiple Sclerosis—Magnetic Resonance Imaging in Multiple Sclerosis fellowship*; *UNRELATED*: *Payment for Lectures Including Service on Speakers Bureaus:* Genzyme, Biogen, Bayer, Merck, Biopass, Bial Pharmaceuticals, Novartis, Roche, Teva Pharmaceutical Industries, Celgene. Xavier Montalban—*UNRELATED*: *Consultancy*: Actelion Pharmaceuticals, Alexion Pharmaceuticals, Bayer, Biogen, Celgene, EMD Serono, Genzyme, Immunic Therapeutics, MedDay Pharma, Merck, Nervgen Pharma, Novartis, Roche, Sanofi Genzyme, Teva Pharmaceutical Industries, TG Therapeutics, EXCEMED, Multiple Sclerosis International Federation and National MS Society. Nikos Evangelou—*UNRELATED*: *Consultancy*: Biogen, Roche, *Comments*: member of advisory board; *Grants/Grants Pending*: Media Research Center, Patient-Centered Outcomes Research Institute, National Institute for Health Research*; *Payment for Lectures Including Service on Speakers Bureaus*: Biogen, Roche; *Payment for Development of Educational Presentations:* Biogen, *Comments*: educational material for use of MRI in MS; *Travel/Accommodations/Meeting Expenses Unrelated to Activities Listed*: Biogen, *Comments*: attendance at European Center For Treatment and Research in Multiple Sclerosis. Àlex Rovira—*UNRELATED*: *Board Membership*: Novartis, Sanofi-Genzyme, Bayer, Roche, Biogen; *Payment for Lectures Including Service on Speakers Bureaus*: Bayer, Sanofi-Genzyme, Bracco, Merck Serono, Teva Pharmaceutical Industries, Novartis, Roche, and Biogen; *Payment for Development of Educational Presentations*: Bayer, Sanofi-Genzyme, Bracco, Merck Serono, Teva Pharmaceutical Industries, Novartis, Roche, and Biogen. *Money paid to the institution.

REFERENCES

1. Thompson AJ, Banwell BL, Barkhof F, et al. **Diagnosis of multiple sclerosis: 2017 revisions of the McDonald criteria.** *Lancet Neurol* 2018;17:162–73 CrossRef Medline
2. Hyun JW, Kim W, Huh SY, et al. **Application of the 2017 McDonald diagnostic criteria for multiple sclerosis in Korean patients with clinically isolated syndrome.** *Mult Scler* 2019;25:1488–95 CrossRef Medline
3. Gobbin F, Zanoni M, Marangi A, et al. **2017 McDonald criteria for multiple sclerosis: earlier diagnosis with reduced specificity?** *Mult Scler Relat Disord* 2019;29:23–25 CrossRef Medline
4. Reichenbach JR, Venkatesan R, Schillinger DJ, et al. **Small vessels in the human brain: MR venography with deoxyhemoglobin as an intrinsic contrast agent.** *Radiology* 1997;204:272–77 CrossRef Medline
5. Haacke EM, Xu Y, Cheng YC, et al. **Susceptibility weighted imaging (SWI).** *Magn Reson Med* 2004;52:612–18 CrossRef Medline
6. Haacke EM, Makki M, Ge Y, et al. **Characterizing iron deposition in multiple sclerosis lesions using susceptibility weighted imaging.** *J Magn Reson Imaging* 2009;29:537–44 CrossRef Medline
7. Dal-Bianco A, Grabner G, Kronnerwetter C, et al. **Slow expansion of multiple sclerosis iron rim lesions: pathology and 7 T magnetic resonance imaging.** *Acta Neuropathol* 2017;133:25–42 CrossRef Medline
8. Tallantyre E, Brookes M, Dixon J, et al. **Demonstrating the perivascular distribution of MS lesions in vivo with 7-Tesla MRI.** *Neurology* 2008;70:2076–78 CrossRef Medline
9. Tallantyre EC, Morgan PS, Dixon JE, et al. **A comparison of 3T and 7T in the detection of small parenchymal veins within MS lesions.** *Investigative Radiol* 2009;44:491–94 CrossRef Medline
10. Mistry N, Abdel-Fahim R, Samaraweera A, et al. **Imaging central veins in brain lesions with 3-T T2*-weighted magnetic resonance imaging differentiates multiple sclerosis from microangiopathic brain lesions.** *Mult Scler* 2016;22:1289–96 CrossRef Medline
11. Sati P, Oh J, Constable RT, et al; NAIMS Cooperative. **The central vein sign and its clinical evaluation for the diagnosis of multiple sclerosis: a consensus statement from the North American Imaging in Multiple Sclerosis Cooperative.** *Nat Rev Neurol* 2016;12:714–22 CrossRef Medline
12. Samaraweera AP, Clarke MA, Whitehead A, et al. **The central vein sign in multiple sclerosis lesions is present irrespective of the T2* sequence at 3 T.** *J Neuroimaging* 2017;27:114–21 CrossRef Medline
13. Maggi P, Absinta M, Grammatico M, et al. **The central vein sign differentiates MS from CNS inflammatory vasculopathies.** *Ann Neurol* 2018;83:283–94 CrossRef Medline
14. Tallantyre EC, Dixon JE, Donaldson I, et al. **Ultra-high-field imaging distinguishes MS lesions from asymptomatic white matter lesions.** *Neurology* 2011;76:534–39 CrossRef Medline
15. Campion T, Smith P, Turner B, et al. **FLAIR* for the non-invasive histological diagnosis of multiple sclerosis (S29.003).** *Neurology* 2015;84:(14 Suppl)S29.003
16. Mistry N, Dixon J, Tallantyre E, et al. **Central veins in brain lesions visualized with high-field magnetic resonance imaging: a pathologically specific diagnostic biomarker for inflammatory demyelination in the brain.** *JAMA Neurol* 2013;70:623–28 CrossRef Medline
17. Harrison DM, Li X, Liu H, et al. **Lesion heterogeneity on high-field susceptibility MRI is associated with multiple sclerosis severity.** *AJNR Am J Neuroradiol* 2016;37:1447–53 CrossRef Medline
18. Chawla S, Kister I, Wuerfel J, et al. **Iron and non-iron-related characteristics of multiple sclerosis and neuromyelitis optica lesions at 7T MRI.** *AJNR Am J Neuroradiol* 2016;37:1223–30 CrossRef Medline
19. Wuerfel J, Sinnecker T, Ringelstein EB, et al. **Lesion morphology at 7 Tesla MRI differentiates Susac syndrome from multiple sclerosis.** *Mult Scler* 2012;18:1592–99 CrossRef Medline
20. Hosseini Z, Matusinec J, Rudko DA, et al. **Morphology-specific discrimination between MS white matter lesions and benign white matter hyperintensities using ultra-high-field MRI.** *AJNR Am J Neuroradiol* 2018;39:1473–79 CrossRef Medline
21. Tintore M, Rovira A, Rio J, et al. **Defining high, medium and low impact prognostic factors for developing multiple sclerosis.** *Brain* 2015;138:1863–74 CrossRef Medline
22. Arrambide G, Tintore M, Espejo C, et al. **The value of oligoclonal bands in the multiple sclerosis diagnostic criteria.** *Brain* 2018;141:1075–84 CrossRef Medline
23. Sinnecker T, Clarke MA, Meier D, et al; for the MAGNIMS Study Group. **Evaluation of the central vein sign as a diagnostic imaging biomarker in multiple sclerosis.** *JAMA Neurol* 2019 Aug 19. [Epub ahead of print] CrossRef Medline

24. Freedman MS, Thompson EJ, Deisenhammer F, et al. **Recommended standard of cerebrospinal fluid analysis in the diagnosis of multiple sclerosis: a consensus statement.** *Arch Neurol* 2005;62:865–70 CrossRef Medline
25. Fedorov A, Beichel R, Kalpathy-Cramer J, et al. **3D Slicer as an image computing platform for the Quantitative Imaging Network.** *Magn Reson Imaging* 2012;30:1323–41 CrossRef Medline
26. Hagemeier J, Heininen-Brown M, Poloni GU, et al. **Iron deposition in multiple sclerosis lesions measured by susceptibility-weighted imaging filtered phase: a case control study.** *J Magn Reson Imaging* 2012;36:73–83 CrossRef Medline
27. Poser CM, Paty DW, Scheinberg L, et al. **New diagnostic criteria for multiple sclerosis: guidelines for research protocols.** *Ann Neurol* 1983;13:227–31 CrossRef Medline
28. Campion T, Smith RJ, Altmann DR, et al. **FLAIR* to visualize veins in white matter lesions: a new tool for the diagnosis of multiple sclerosis?** *Eur Radiol* 2017;27:4257–63 CrossRef Medline
29. Guo BJ, Yang ZL, Zhang LJ. **Gadolinium deposition in brain: current scientific evidence and future perspectives.** *Front Mol Neurosci* 2018;11:335–35 CrossRef Medline
30. Solomon AJ, Watts R, Ontaneda D, et al. **Diagnostic performance of central vein sign for multiple sclerosis with a simplified three-lesion algorithm.** *Mult Scler* 2018;24:750–57 CrossRef Medline
31. Kau T, Taschwer M, Deutschmann H, et al. **The "central vein sign": is there a place for susceptibility weighted imaging in possible multiple sclerosis?** *Eur Radiol* 2013;23:1956–62 CrossRef Medline
32. Absinta M, Sati P, Gaitan MI, et al. **Seven-Tesla phase imaging of acute multiple sclerosis lesions: a new window into the inflammatory process.** *Ann Neurol* 2013;74:669–78 CrossRef Medline
33. Yao B, Bagnato F, Matsuura E, et al. **Chronic multiple sclerosis lesions: characterization with high-field-strength MR imaging.** *Radiology* 2012;262:206–15 CrossRef Medline
34. Bagnato F, Hametner S, Yao B, et al. **Tracking iron in multiple sclerosis: a combined imaging and histopathological study at 7 Tesla.** *Brain* 2011;134:3602–15 CrossRef Medline
35. Bian W, Harter K, Hammond-Rosenbluth KE, et al. **A serial in vivo 7T magnetic resonance phase imaging study of white matter lesions in multiple sclerosis.** *Mult Scler* 2013;19:69–75 CrossRef Medline
36. Hammond KE, Metcalf M, Carvajal L, et al. **Quantitative in vivo magnetic resonance imaging of multiple sclerosis at 7 Tesla with sensitivity to iron.** *Ann Neurol* 2008;64:707–13 CrossRef Medline
37. Absinta M, Sati P, Fechner A, et al. **Identification of chronic active multiple sclerosis lesions on 3T MRI.** *AJNR Am J Neuroradiol* 2018;39:1233–38 CrossRef Medline
38. Hametner S, Wimmer I, Haider L, et al. **Iron and neurodegeneration in the multiple sclerosis brain.** *Ann Neurol* 2013;74:848–61 CrossRef Medline
39. Engelborghs S, Niemantsverdriet E, Struyfs H, et al. **Consensus guidelines for lumbar puncture in patients with neurological diseases.** *Alzheimers Dement (Amst)* 2017;8:111–26 CrossRef Medline
40. Clarke MA, Samaraweera AP, Falah Y, et al. **Single Test to ARrive at Multiple Sclerosis (STAR-MS) diagnosis: a prospective pilot study assessing the accuracy of the central vein sign in predicting multiple sclerosis in cases of diagnostic uncertainty.** *Mult Scler* 2020;26:433–41 CrossRef
41. Maggi P, Absinta M, Sati P, et al. **The "central vein sign" in patients with diagnostic "red flags" for multiple sclerosis: a prospective multicenter 3T study.** *Mult Scler* 2020;26:421–32 CrossRef Medline

Morphometric MRI Analysis: Improved Detection of Focal Cortical Dysplasia Using the MP2RAGE Sequence

T. Demerath, L. Rubensdörfer, R. Schwarzwald, A. Schulze-Bonhage, D.-M. Altenmüller, C. Kaller, T. Kober, H.-J. Huppertz, and H. Urbach

ABSTRACT

BACKGROUND AND PURPOSE: Focal cortical dysplasias are the most common resected epileptogenic lesions in children and the third most common lesion in adults, but they are often subtle and frequently overlooked on MR imaging. The purpose of this study was to evaluate whether MP2RAGE-based morphometric MR imaging analysis is superior to MPRAGE-based analysis in the detection of focal cortical dysplasia.

MATERIALS AND METHODS: MPRAGE and MP2RAGE datasets were acquired in a consecutive series of 640 patients with epilepsy. Datasets were postprocessed using the Morphometric Analysis Program to generate morphometric *z* score maps such as junction, extension, and thickness images based on both MPRAGE and MP2RAGE images. Focal cortical dysplasia lesions were manually segmented in the junction images, and volumes and mean *z* scores of the lesions were measured.

RESULTS: Of 21 focal cortical dysplasias discovered, all were clearly visible on MP2RAGE junction images, whereas 2 were not visible on MPRAGE junction images. In all except 4 patients, the volume of the focal cortical dysplasia was larger and mean lesion *z* scores were higher on MP2RAGE junction images compared with the MPRAGE-based images ($P = .005$, $P = .013$).

CONCLUSIONS: In this study, MP2RAGE-based morphometric analysis created clearer output maps with larger lesion volumes and higher *z* scores than the MPRAGE-based analysis. This new approach may improve the detection of subtle, otherwise overlooked focal cortical dysplasia.

ABBREVIATIONS: FCD = focal cortical dysplasia; MAP = Morphometric Analysis Program

Focal cortical dysplasias (FCDs) are the most common epileptogenic lesions in children undergoing epilepsy surgery and the third most common cause in adults.[1] They encompass a broad spectrum of histopathologic abnormalities and have recently been classified in a 3-tiered system, in which FCD type I has abnormal radial and/or tangential laminations and FCD type II is composed of dysmorphic neurons either without (FCD IIa) or with (FCD IIb) balloon cells. FCD type III lesions are dysplastic lesions occurring alongside other lesions, eg, hippocampal sclerosis or tumors.[2]

Whether a dysplastic lesion is detected on MR imaging depends on the degree of histopathologic abnormality and on the quality of the MR imaging examination.[3] The impact of the MR imaging quality can be derived from the increasing proportions of FCD type II in cohorts of patients undergoing epilepsy surgery.[4] Many of these FCDs were detected following postprocessing of an MPRAGE sequence, which highlighted subtle and thus equivocal findings on conventional, mostly FLAIR, sequences.[5,6] For MR imaging postprocessing, several epilepsy centers use the Morphometric Analysis Program (MAP), which is based on algorithms of the freely available Statistical Parametric Mapping (SPM; http://www.fil.ion.ucl.ac.uk/spm/software/spm12) software. By comparison with a normal data base, 3 different morphometric maps are generated that highlight suspicious brain regions characterized by subtle blurring of the gray-white junction, abnormal cortical gyration, or abnormal cortical thickness.[7,8]

The MP2RAGE sequence is a refinement of the MPRAGE sequence. It combines 2 MPRAGE datasets acquired, interleaved at different TIs, and creates a homogeneous T1-weighted contrast

Received January 23, 2020; accepted after revision March 24.

From the Departments of Neuroradiology (T.D., L.R., R.S., C.K., H.U.) and Epileptology (A.S.-B., D.-M.A.), Faculty of Medicine, Medical Center–University of Freiburg, Freiburg, Germany; Advanced Clinical Imaging Technology (T.K.), Siemens Healthcare AG, Lausanne, Switzerland; and Swiss Epilepsy Clinic (H.-J.H.), Klinik Lengg AG, Zurich, Switzerland.

Paper previously presented as a poster at: Annual Meeting of the German Society of Neuroradiology, October 3–6, 2018; Frankfurt, Germany.

Please address correspondence to Horst Urbach, MD, Department of Neuroradiology, University Medical Center Freiburg, Breisacher Str 64, 79106 Freiburg, Germany; e-mail: horst.urbach@uniklinik-freiburg.de

Indicates article with supplemental on-line table.

http://dx.doi.org/10.3174/ajnr.A6579

Epilepsy-dedicated MR imaging protocol[a]

MR Imaging Sequence	No. of Slices/Thickness (mm)	Voxel Size (mm^3)	TI/TR/TE/α (ms/ms/ms/degree)	Acquisition Time (Min:Sec)
Sag 3D-MPRAGE	160/1	1 × 1 × 1	900/2000/2.26/12	4:40
Sag 3D-FLAIR-SPACE	160/1	1 × 1 × 1	1800/5000/388/var	6:52
Ax 2D-T2-TSE	42/3	0.4 × 0.4 × 3	5040/102/150	4:34
Ax 2D-T2*	23/5	0.7 × 0.7 × 5	639/19.9/20	2:33
Cor 2D-T2-STIR	40/2	0.4 × 0.4 × 2	100/5390/25/140	8:07
Cor 2D FLAIR	68/2	0.7 × 0.7 × 0.2	2500/9000/87/150	4:14
Ax 2D-DWI-SE EPI	23/5	0.6 × 0.6 × 5	3400/85	0:46
Sag 3D-MP2RAGE	192/1	1 × 1 × 1	700, 2200/2000/2.26/12	8:52

Note:—SPACE indicates sampling perfection with application-optimized contrasts by using flip angle evolution; SE, spin-echo; α, flip angle; Sag, sagittal; Ax, axial; Cor, coronal; var, variable flip angle.

[a] 3T Magnetom Prisma (Siemens).

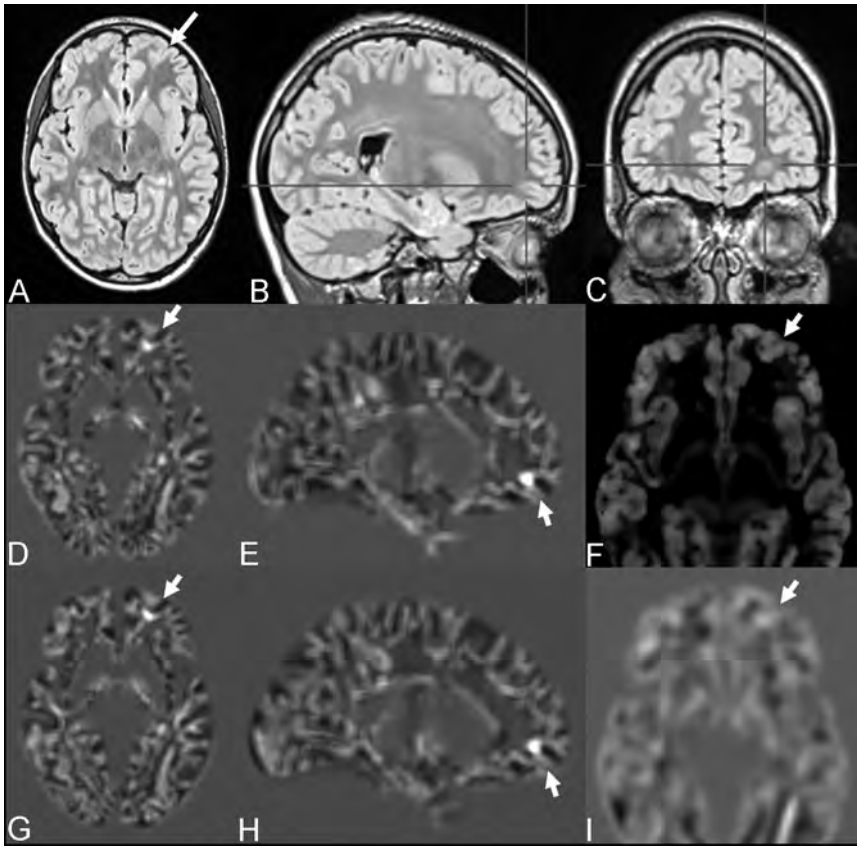

FIG 1. FCD with the transmantle sign of the left medial fronto-orbital gyrus (bottom-of-sulcus dysplasia) in a 12-year-old girl with seizures (patient 1). The lesion was overlooked on visual inspection (*A–C*) but was highlighted with MPRAGE-based (*D* and *E*) and MP2RAGE-based (*G–H*) junction images. MP2RAGE-based thickness (*F*) and extension (*I*) maps were considered to have negative findings.

with an intrinsic correction of B_1 inhomogeneities and reduced residual proton density and T2* weighting. T1 relaxation times can be derived from the MP2RAGE contrast, which has been shown to be highly reproducible both across subjects and within the same subject using different scanning parameters.[9] We conducted this prospective study because we hypothesized that due to higher B_1 homogeneity, the MP2RAGE sequence is better suited for morphometric MR imaging analysis and the resulting FCD detection than the traditionally used MPRAGE sequence.

MATERIALS AND METHODS

Within a 4-year period (July 1, 2015–June 30, 2019), 640 patients with epilepsy were studied with an epilepsy-dedicated protocol[10] and an additional MP2RAGE sequence on a 3T scanner (Magnetom Prisma; Siemens) (Table).

The study was in accordance with the 1964 Helsinki Declaration and its later amendments and was approved by the local ethics committee (University Medical Center Freiburg).

Morphometric MR Imaging Analysis

Morphometric MR imaging analysis was performed on MPRAGE and MP2RAGE images using a fully automated script, MAP, running in Matlab, Version R2014b (MathWorks). The current version of the program (MAP18) corresponds to previous implementations known as MAP07[6,11,12] but now uses algorithms of SPM12, eg, the algorithm for normalization into Montreal Neurological Institute space known as "unified segmentation" (with small modifications in SPM12 compared with SPM5; see SPM12 Manual, page 51f, www.fil.ion.ucl.ac.uk) and the recently improved segmentation into 5 tissue classes instead of 3 as in SPM5. The creation of the morphometric maps has been described in detail in previous publications.[7,8,13,14] Briefly, each T1 input image is normalized to Montreal Neurological Institute space, simultaneously corrected for intensity inhomogeneities and segmented in different tissue compartments. The distribution of gray and white matter is analyzed on a voxelwise basis and compared with a normal data base. On the basis of this analysis, 3D morphometric maps, called extension image, junction image, and thickness image, are generated. These are *z* score maps in which brain regions that deviate from the normal data base have

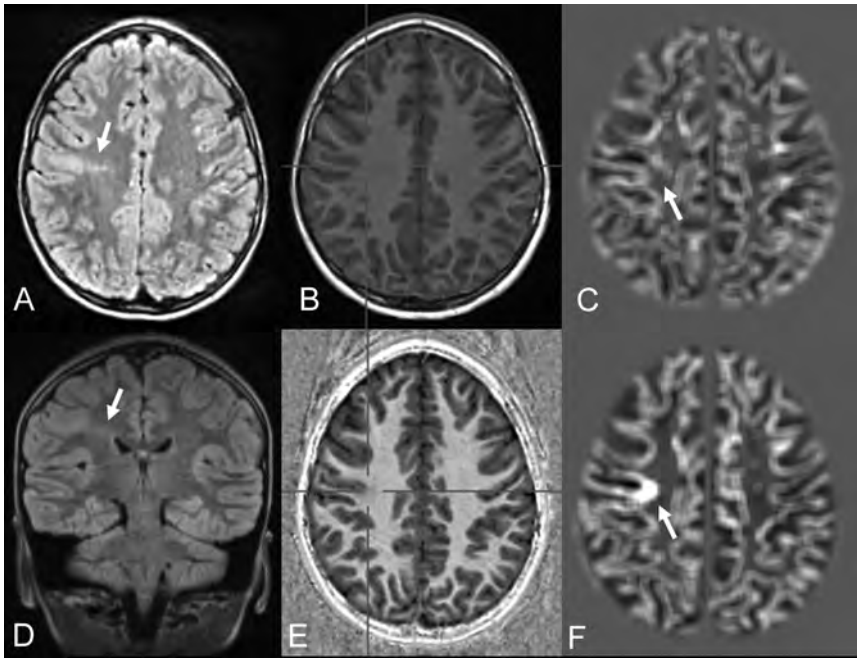

FIG 2. FCD with the transmantle sign of the right precentral gyrus in a 7-year-old girl with seizures (patient 18). Despite movement artifacts, the lesion is clearly visible on FLAIR (*A* and *D*) and MP2RAGE-based junction images (*F*). In an MPRAGE-based junction image (*C*) for comparison, the lesion is not clearly distinguishable. Strong T1WI contrast is seen in a uniform MP2RAGE image (*E*) compared with MPRAGE (*B*).

higher *z* scores and appear bright, thereby highlighting typical MR imaging features of FCDs, such as abnormal gyration and abnormal extension of gray matter into white matter (extension image), blurring of the gray-white matter junction (junction image), and abnormal cortical thickness (thickness image).

Because the junction image is the most sensitive of these maps, it was the focus of this study, and its creation will be described in more detail here:

Means and SDs of the voxel intensities in the gray and white matter compartments are used to determine individual lower (mean gray matter signal intensity + one-half gray matter SD) and upper (mean white matter signal intensity – one-half white matter SD) intensity thresholds for filtering and conversion of the normalized and intensity-corrected input image to a binary image. Each voxel with a gray value between these thresholds is set to 1 in the resulting binary image, and the other voxels are set to zero. The resulting binary image is then smoothed by a 3D convolution filter and compared with a normal data base. The datasets forming the normal database have been processed in the same way as described above and then used to create an average image and an image providing SDs for all voxel positions. These are used to transform the smoothed binary image into the final junction image with *z* score normalized data. Bright regions in the junction image correspond to cortical areas with a less defined border between gray and white matter and a broader transition zone compared with the normal data base.[8]

For the present study, 2 different normal data bases of healthy controls have been used, one for MPRAGE data and the other for MP2RAGE data. They consist of MPRAGE and MP2RAGE datasets, respectively, of the same cohort of 154 persons (88 women, 66 men) with a mean age of 33.9 years (range, 20–64 years), measured on a 3T Magnetom Prisma scanner.

Evaluation

All morphometric maps (ie, junction, extension, and thickness images) were displayed in MRIcro (https://people.cas.sc.edu/rorden/mricro/mricro.html) in the full-range contrast setting and screened alongside coregistered 3D-FLAIR sequences for dysplastic lesions. An FCD was diagnosed when the typical radiologic criteria were clearly identifiable on either T1 or FLAIR images. In such cases, lesions were manually segmented on axial slices of the junction images generated from MPRAGE and MP2RAGE sequences, respectively, according to the extent of the bright area highlighting the blurring of the gray-white matter junction. All segmentation results were stored as ROIs, and volumes and *z* scores were measured.

Thickness and extension images were evaluated only for positive or negative findings in a consensus reading by 2 readers with >3 and >20 years' experience in clinical neuroimaging. In this context, MPRAGE and MP2RAGE junction images were also examined for false-positive lesions, ie, findings without correlation in the FLAIR sequences.

Statistics

The Wilcoxon signed rank test was used to compare the volumes and *z* scores of the FCDs obtained with MPRAGE- versus MP2RAGE-based junction images. Statistical analysis and graphic representation were performed with SPSS 22 (IBM) and R (https://www.R-project.org).

RESULTS

Twenty-one lesions with MR imaging characteristics of FCD type II were identified in 20 patients (mean age, 27 ± 14.9 years; range, 7–60 years). An operation has been performed in only 7 patients so far (2 with FCD IIa, 4 with FCD IIb, and in 1 patient [patient 9] in whom only ectopic neurons were found). Seizure outcome has been available in 6 patients so far and was Engel Epilepsy Surgery Outcome Scale IA in 4 patients and IVB in 2 patients (patients 1 and 17; On-line Table).

Postprocessing of the MPRAGE and MP2RAGE sequences helped to detect 2 FCD IIa lesions, which were overlooked on conventional MR images (patients 1, 2; Fig 1). Two lesions (patients 14, 18; Fig 2) were invisible on MPRAGE-based junction images but clearly identified on MP2RAGE-based images. In 20 patients, we detected, in total, 34 (MPRAGE junction) and 32 (MP2RAGE junction) false-positive lesions, respectively (for individual values, see

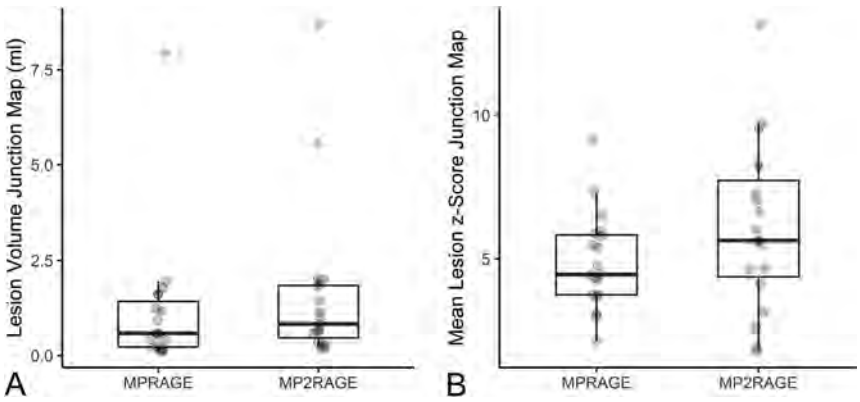

FIG 3. Lesion volumes (*A*, in milliliters) and mean lesion z scores (*B*) in MPRAGE- and MP2RAGE-based junction maps.

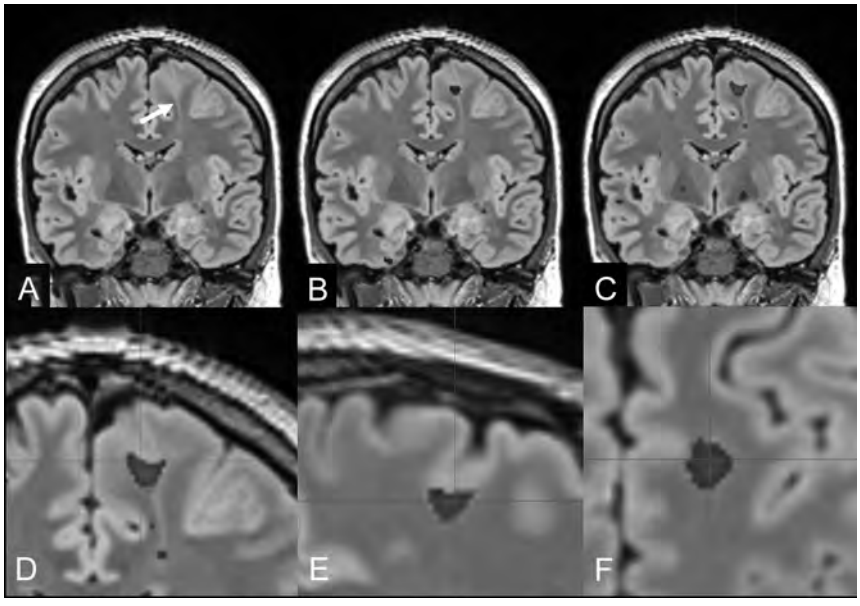

FIG 4. FCD IIb with a transmantle sign of the left superior frontal gyrus (bottom-of-sulcus dysplasia) in a 27-year-old man with right-sided sensory-motor seizures (patient 5). *A*, Reformatted 1-mm-thick coronal FLAIR section (*arrow*: transmantle sign of the FCD). *B*, Overlay of MPRAGE-based junction image abnormalities with *z* scores of >4. *C*, Overlay of MP2RAGE-based junction image abnormalities with *z* scores of >4. The MP2RAGE-based junction image matches the signal abnormalities at the gray matter junction as a characteristic feature of FCD type II (*D–F*, magnified coronal, sagittal, and axial views).

On-line Table). Distribution of false-positive findings was similar between both techniques, with no false-positives in 3 MPRAGE/6 MP2RAGE datasets, 1 false-positive in 7/6, two false-positives in 7/2, three in 1/4, four in 2/1, and 5 false-positive findings in 1 MP2RAGE dataset.

The median volumes of true-positive lesions, manually segmented on junction images, were 0.586 mL (range, 0.114–7.946 mL; standard error of the mean, 0.403 mL) for the MPRAGE-based junction images and 0.829 mL (range, 0.182–8.690 mL; standard error of the mean, 0.441 mL) for the MP2RAGE- based junction images, respectively ($P = .005$). The median *z* scores on full-range contrast junction images were 4.452 (range, 2.111–9.125; standard error of the mean, 0.381) for MPRAGE and 5.643 (range, 1.762–13.176; standard error of the mean, 0.654) for the MP2RAGE-based analysis, respectively ($P = .013$). The distribution of volumes and *z* scores, including median values, are presented in Fig 3.

A comparative analysis showed that MAP-junction was the most sensitive morphometric map (Figs 2, 4, and 5). Evidence of disturbed GM-WM differentiation was found in the MP2RAGE-based junction images of all 21 FCDs in 20 patients (On-line Table and Figs 1, 2, 4, and 5). In contrast, abnormalities in the thickness and extension images were only present in 13/21 and 16/21 lesions for the MPRAGE- and 13/21 and 18/21 lesions for the MP2RAGE-based analysis.

DISCUSSION

In the present study, postprocessing of an MP2RAGE sequence yielded larger lesion volumes and lesion *z* scores of the junction images compared with the MPRAGE sequence. In addition, it helped to detect 2 FCDs that were not highlighted on MPRAGE-based junction images.

The junction images display the abnormal transition of the gray-white matter junction. Blurring of the gray-white matter transition is a common feature in type I and II FCDs. The prevalence of transition zone abnormalities on structural (nonpostprocessed) MR imaging ranges between 53% (FCD Ia) and 79% (FCD IIb).[15] The sensitivity and specificity of MAP junction maps in histology-proved FCDs, based on T1WI, have been reported as 64% and 96%.[16]

Displaying larger and brighter lesions, the MP2RAGE sequence likely increases the sensitivity and diagnostic confidence, which may have an impact on the decision to proceed with invasive electroencephalography recordings or epilepsy surgery.

The abnormal cortical morphology as reflected by an increased cortical thickness and abnormal extension of gray matter into white matter is common in FCD II but is typically absent in FCD I and III. However, abnormal cortical morphology is more difficult to identify on the extension and thickness images than the abnormal transition of the gray-white matter junction on the corresponding junction images. In most cases, the lesions were detected with the aid of the junction images. However, there was a tendency for better detection of FCDs on MP2RAGE-based extension images (positive findings in 18/21 versus 16/21 lesions), whereas

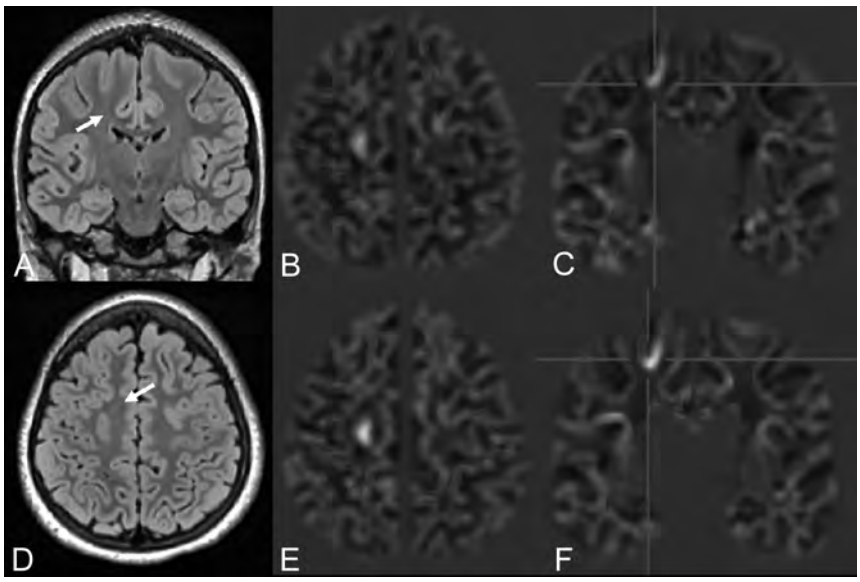

FIG 5. FCD with a transmantle sign of the right superior frontal gyrus (bottom-of-sulcus dysplasia) (FLAIR *A* and *D*) in an 11-year-old girl with left upper and lower limb somatosensoric aura and motor seizures (patient 20). The MPRAGE- (*B* and *C*) and MP2RAGE-based junction images (*E* and *F*) match the signal abnormalities at the gray matter junction as a characteristic feature of FCD type II. MP2RAGE delivers, in this case, higher contrast junction images and better lesion definition compared with MPRAGE.

thickness images only had positive findings in 13/21 lesions in both techniques.

Our finding of larger lesion sizes in MP2RAGE-based MAP analysis raises the question about the real size of a lesion. By demonstrating larger lesion volumes, MP2RAGE-based junction maps may be superior in defining peripheral lesion components. Furthermore, positive findings on extension and thickness images suggest that an integrated definition and lesion detection in an automated approach represent the next step in MAP-based FCD postprocessing. Even if the resection of the subcortical component does not seem to improve the outcome, an integrative definition of the lesion component at the cortico-medullary junction should be sought.

Recently, a modification of the MP2RAGE sequence with altered TIs to null CSF and white matter in the 2 respectively acquired TI images has been published.[17] The fluid and white matter suppression sequence appears ideally suited to search for FCD, but its use for morphometric analysis again requires the buildup of a sequence-specific normal data base of healthy controls.

A limitation of this study is the difficulty of evaluating whether in light of a higher sensitivity of MP2RAGE-based junction images, there are also more false-positive findings. In this study, we performed a qualitative visual evaluation with the aid of the results of the morphometric analysis. We did not use a specific threshold value for an automated detection of FCD, but re-assessed the "bright spots" on the morphometric analyses on FLAIR sequences to discover subtle lesions with abnormalities at the gray-white matter interface. Therefore, a further quantification and assessment of false-positive findings in patients or healthy controls is simply not possible. To at least estimate false-positive findings in patients, we visually compared MPRAGE- and MP2RAGE-based junction images using the full-range contrast setting of MRIcro. We found 34 and 32 false-positives in 20 patients on MPRAGE- and MP2RAGE-based images, respectively, with a similar distribution between both techniques. No differences with regard to the cluster size or the *z* scores of false-positives were found.

To estimate false-positive findings in healthy controls, we analyzed 70 healthy controls, assuming that they did not have FCD. With a general linear model and a leave-one-out strategy, each voxel was compared with the corresponding voxel of the remainder. Number and *z* scores of false-positive voxels ($P < .001$, $P < .05$ family-wise error–corrected) were not different between MPRAGE and MP2RAGE datasets (unpublished data).

However, at this point, for the detection of FCD in an epileptologic setting, sensitivity is more important than specificity or the number of false-positive findings because an undetected or overlooked lesion may prevent the patient from accessing an epilepsy surgery program. Conversely, no putative FCD would undergo an operation directly, but first the epileptogenic potential of a possible lesion would always have to be verified using electrophysiologic methods. Therefore, a high sensitivity is more crucial for this type of clinical situation than a high specificity.

Another limitation is the relatively low number of FCDs and the fact that histopathologic proof has been obtained in only 7 patients so far. In 1 patient (patient 9), only ectopic neurons but no FCD were encountered. However, because the patient was seizure-free 3 months after the operation, a neuropathologic sampling error should also be taken into consideration.

Recently, a modification of the MP2RAGE sequence with inversion pulses to suppress CSF and white matter has been published.[15] The fluid and white matter suppression sequence appears ideally suited to search for FCD but again requires the buildup of a data base of healthy controls and a larger number of patients with FCD.

CONCLUSIONS

MP2RAGE compared with MPRAGE produced junction images with larger FCD lesion volumes and higher lesion *z* scores, which may improve the detection of FCD in patients with focal epilepsy.

Disclosures: Andreas Schulze-Bonhage—*UNRELATED*: *Board Membership*: advisory boards on antiepileptic drugs of pharmaceutical companies; *Consultancy*: pharmaceutical and medical device consulting; *Grants/Grants Pending*: research on seizure detection and neurophysiologic correlates of cognition*; *Payment for Lectures Including Service on Speakers Bureaus*: lectures on epileptology. Tobias Kober—*UNRELATED*: *Employment*: Siemens Healthcare AG Switzerland,

Comments: full employment. Horst Urbach—*UNRELATED*: *Board Membership*: coeditor *Clinical Neuroradiology*; *Payment for Lectures Including Service on Speakers Bureaus*: Bayer AG, Stryker, UCB, Eisei Co, Bracco; *OTHER RELATIONSHIPS*: shareholder of VEObrain GmbH. *Money paid to the institution.

REFERENCES

1. Blumcke I, Spreafico R, Haaker G, et al; EEBB Consortium. **Histopathological findings in brain tissue obtained during epilepsy surgery.** *N Engl J Med* 2017;377:1648–56 CrossRef Medline
2. Blümcke I, Thom M, Aronica E, et al. **The clinicopathologic spectrum of focal cortical dysplasias: a consensus classification proposed by an ad hoc Task Force of the ILAE Diagnostic Methods Commission.** *Epilepsia* 2011;52:158–74 CrossRef Medline
3. Von Oertzen J, Urbach H, Jungbluth S, et al. **Standard magnetic resonance imaging is inadequate for patients with refractory focal epilepsy.** *J Neurol Neurosurg Psychiatry* 2002;73:643–47 CrossRef Medline
4. Bien CG, Raabe AL, Schramm J, et al. **Trends in presurgical evaluation and surgical treatment of epilepsy at one centre from 1988–2009.** *J Neurol Neurosurg Psychiatry* 2013;84:54–61 CrossRef Medline
5. Wagner J, Weber B, Urbach H, et al. **Morphometric MRI analysis improves detection of focal cortical dysplasia type II.** *Brain* 2011;134:2844–54 CrossRef Medline
6. Wang ZI, Jones SE, Jaisani Z, et al. **Voxel-based morphometric magnetic resonance imaging (MRI) postprocessing in MRI-negative epilepsies.** *Ann Neurol* 2015;77:1060–75 CrossRef Medline
7. Huppertz HJ, Grimm C, Fauser S, et al. **Enhanced visualization of blurred gray-white matter junctions in focal cortical dysplasia by voxel-based 3D MRI analysis.** *Epilepsy Res* 2005;67:35–50 CrossRef Medline
8. Huppertz HJ. Morphometric MRI analysis. In: Urbach H, ed. *MRI in Epilepsy*. Springer-Verlag; 2013:73–84
9. Marques JP, Kober T, Krueger G, et al. **MP2RAGE, a self bias-field corrected sequence for improved segmentation and T1-mapping at high field.** *Neuroimage* 2010;49:1271–81 CrossRef Medline
10. Urbach H, Mast H, Egger K, et al. **Presurgical MR imaging in epilepsy.** *Clin Neuroradiol* 2015;25(Suppl 2):151–55 CrossRef Medline
11. Wang S, Jin B, Aung T, et al. **Application of MRI post-processing in presurgical evaluation of non-lesional cingulate epilepsy.** *Front Neurol* 2018;9:1–7 CrossRef Medline
12. Wang W, Lin Y, Wang S, et al; Pediatric Imaging, Neurocognition and Genetics Study. **Voxel-based morphometric magnetic resonance imaging postprocessing in non-lesional pediatric epilepsy patients using pediatric normal databases.** *Eur J Neurol* 2019;26:969–71 CrossRef Medline
13. Kassubek J, Huppertz HJ, Spreer J, et al. **Detection and localization of focal cortical dysplasia by voxel-based 3-D MRI analysis.** *Epilepsia* 2002;43:596–602 CrossRef Medline
14. Huppertz HJ, Wellmer J, Staack AM, et al. **Voxel-based 3D MRI analysis helps to detect subtle forms of subcortical band heterotopia.** *Epilepsia* 2008;49:772–85 CrossRef Medline
15. Krsek P, Maton B, Korman B, et al. **Different features of histopathological subtypes of pediatric focal cortical dysplasia.** *Ann Neurol* 2008;63:758–69 CrossRef Medline
16. Wong-Kisiel LC, Tovar Quiroga DF, Kenney-Jung DL, et al. **Morphometric analysis on T1-weighted MRI complements visual MRI review in focal cortical dysplasia.** *Epilepsy Res* 2018;140:184–91 CrossRef Medline
17. Chen X, Qian T, Kober T, et al. **Gray-matter-specific MR imaging improves the detection of epileptogenic zones in focal cortical dysplasia: a new sequence called fluid and white matter suppression (FLAWS).** *Neuroimage Clin* 2018;20:388–97 CrossRef Medline

Prediction of Outcome Using Quantified Blood Volume in Aneurysmal SAH

W.E. van der Steen, H.A. Marquering, L.A. Ramos, R. van den Berg, B.A. Coert, A.M.M. Boers, M.D.I. Vergouwen, G.J.E. Rinkel, B.K. Velthuis, Y.B.W.E.M. Roos, C.B.L.M. Majoie, W.P. Vandertop, and D. Verbaan

ABSTRACT

BACKGROUND AND PURPOSE: In patients with SAH, the amount of blood is strongly associated with clinical outcome. However, it is commonly estimated with a coarse grading scale, potentially limiting its predictive value. Therefore, we aimed to develop and externally validate prediction models for clinical outcome, including quantified blood volumes, as candidate predictors.

MATERIALS AND METHODS: Clinical and radiologic candidate predictors were included in a logistic regression model. Unfavorable outcome was defined as a modified Rankin Scale score of 4–6. An automatic hemorrhage-quantification algorithm calculated the total blood volume. Blood was manually classified as cisternal, intraventricular, or intraparenchymal. The model was selected with bootstrapped backward selection and validated with the R^2, C-statistic, and calibration plots. If total blood volume remained in the final model, its performance was compared with models including location-specific blood volumes or the modified Fisher scale.

RESULTS: The total blood volume, neurologic condition, age, aneurysm size, and history of cardiovascular disease remained in the final models after selection. The externally validated predictive accuracy and discriminative power were high (R^2 = 56% ± 1.8%; mean C-statistic = 0.89 ± 0.01). The location-specific volume models showed a similar performance (R^2 = 56% ± 1%, P = .8; mean C-statistic = 0.89 ± 0.00, P = .4). The modified Fisher models were significantly less accurate (R^2 = 45% ± 3%, P < .001; mean C-statistic = 0.85 ± 0.01, P = .03).

CONCLUSIONS: The total blood volume–based prediction model for clinical outcome in patients with SAH showed a high predictive accuracy, higher than a prediction model including the commonly used modified Fisher scale.

ABBREVIATIONS: aSAH = aneurysmal subarachnoid hemorrhage; IPH = intraparenchymal hemorrhage; IQR = interquartile range; IVH = intraventricular hemorrhage; TBV = total blood volume; WFNS = World Federation of Neurosurgical Societies

Aneurysmal subarachnoid hemorrhage (aSAH) is a severe form of stroke caused by the rupture of an intracranial aneurysm.[1] The in-hospital case-fatality rate is approximately 30%, and a large proportion of patients have a poor clinical outcome.[2] Known predictors of outcome are age, neurologic condition at admission, aneurysm size, and hemorrhage volume.[3]

A prediction model including predictors that are quickly and easily available after admission of the patient to the emergency department could assist physicians in making treatment decisions and counseling patients and their families. Such a model including the age, World Federation of Neurosurgical Societies (WFNS) grade on admission, and premorbid history of hypertension, was recently published.[4] Adding the amount of blood, as assessed on the Fisher scale, to their model did not substantially increase the predictive value. This finding is remarkable because the amount of blood has been strongly associated with poor outcome in previous studies.[5,6]

The hemorrhage volume in patients with aSAH is frequently estimated using the Fisher scale, which grades the amount of

Received December 28, 2019; accepted after revision March 26, 2020.

From the Departments of Biomedical Engineering and Physics (W.E.v.d.S., H.A.M., L.A.R., A.M.M.B.), Radiology and Nuclear Medicine (W.E.v.d.S., H.A.M., R.v.d.B., C.B.L.M.M.), Neurology (W.E.v.d.S., Y.B.W.E.M.R.), and Clinical Epidemiology, Biostatistics and Bioinformatics (L.A.R.); and Neurosurgical Center Amsterdam (W.E.v.d.S., B.A.C., W.P.V., D.V.), Amsterdam University Medical Center, University of Amsterdam, Amsterdam, the Netherlands; and Departments of Neurology and Neurosurgery, Brain Center Rudolf Magnus (M.D.I.V., G.J.E.R.) and Radiology (B.K.V.), University Medical Center, Utrecht University, Utrecht, the Netherlands.

This work was supported by NutsOhra (FNO grant 1403-023) from the NutsOhra Fund.

Previously presented as an abstract at: International Subarachnoid Hemorrhage Conference, June 25–28, 2019; Amsterdam, the Netherlands.

Please address correspondence to Wessel E. van der Steen, MD, Department of Neurology, Room L0-148, Amsterdam UMC, University of Amsterdam, Meibergdreef 9, 1105AZ, Amsterdam, the Netherlands; e-mail: w.e.vandersteen@amc.uva.nl

http://dx.doi.org/10.3174/ajnr.A6575

blood in both the cisterns and the ventricles.[7] This 4-category radiologic scale is coarse and has only moderate interobserver agreement.[5] An extensive grading scale, such as the Hijdra sum score, has shown a stronger association with outcome. However, its extensiveness makes it less suitable for use in daily practice.[8] Currently, automated quantitative and observer-independent measures are available to determine the hemorrhage volume.[9]

We aimed to develop and validate a prediction model that estimates the risk of poor clinical outcome, including predictors available at admission, using automated quantified total blood volume (TBV) as one of the candidate predictors. Furthermore, we aimed to develop secondary models, including the cisternal, intraventricular (IVH), and intraparenchymal (IPH) blood volumes separately, and a model including the modified Fisher scale and to compare their performances with that of the TBV models.

MATERIALS AND METHODS

Development and Validation Cohort

Patients for the development and validation cohort were collected from the prospective aSAH registries of the Amsterdam University Medical Center and the University Medical Center Utrecht in the Netherlands, respectively. The development cohort consisted of all patients with aSAH admitted to the Amsterdam University Medical Center between December 2011 and December 2016. The validation cohort consisted of patients admitted to the University Medical Center Utrecht between 2013 and 2015. We used the following inclusion criteria: 1) SAH with subarachnoid blood on first admission NCCT or confirmed by xantochromic CSF after lumbar puncture; 2) confirmation of a ruptured aneurysm, diagnosed by either CTA, MRA, or DSA; and 3) 18 years of age or older. We excluded patients for whom the hemorrhage volume could not be segmented due to large movement and/or metal artifacts on admission NCCT. Finally, patients participating in the Ultra-Early Tranexamic Acid After Subarachnoid Hemorrhage (ULTRA) trial (clinicaltrials.gov No. NCT02684812) were excluded.[10] For the retrospective analysis of this registry, the need for informed consent was waived by the local medical ethics committees.

Collected Candidate Predictor Variables

We collected the following clinical candidate predictor variables: age, sex, history of hypertension, history of diabetes, history of cardiovascular disease, and neurologic condition on first admission assessed by the WFNS scale. Collected radiologic candidate predictor variables were the TBV and location-specific blood volumes, including cisternal, IVH, and IPH blood volumes; the modified Fisher grade; aneurysm size (defined as the maximum width or length of the aneurysm suspected of rupture); and aneurysm location (anterior or posterior circulation). The TBV was measured on admission NCCT using a fully automatic hemorrhage-quantification algorithm. The method was based on relative density increases due to the presence of blood. The analysis started by classification of different brain structures by atlas-based segmentation. Thereafter, the density was evaluated to set a tissue-specific threshold for segmentation of blood. Finally, a region-growing algorithm included subtle attenuated parts of the hemorrhagic areas. The TBV was calculated by multiplying the voxels that were classified as blood by the voxel size and was expressed in centiliters.[9] Most scans were performed on a Somatom AS+ (Ultra-fast Ceramic Detector; Siemens) or Brilliance iCT (solid state detector; Phillips Healthcare). For the analysis, 5- or 3-mm section thickness scans were used. The TBV consisted of all extravasated blood visible on NCCT after ictus, including cisternal, IVH, and IPH blood volumes. The TBV was classified as cisternal, IVH, or IPH by manually outlining the ventricular or intraparenchymal part of the segmented total hemorrhage. In case the patient had recurrent bleeding before treatment, the CT scan after the recurrent bleeding was used instead of the baseline scan to determine the blood volumes. All segmentations were checked and, if necessary, corrected by an experienced radiologist (R.v.d.B.), who was blinded to all clinical data and outcome. The modified Fisher scale was administered by an experienced neurosurgeon.[11]

Outcomes

The clinical outcome was assessed using the mRS in the development cohort and on the Glasgow Outcome Scale in the validation set. The clinical outcome was assessed at 6 months after the SAH in the development cohort and at 3 months in the validation set. A neurovascular research nurse assessed the mRS using a structured interview, either during a visit to the outpatient clinic or by telephone interview. The neurovascular research nurse was blinded to the TBV at admission. Delayed cerebral ischemia was considered as clinical deterioration, defined as the occurrence of new focal neurologic impairment or a decrease of $\geq$2 points on the Glasgow Coma Scale (with or without new hypodensity on CT) that could not be attributed to other causes, in accordance with the definition proposed by a multidisciplinary research group.[12] The primary outcome was an unfavorable clinical outcome and was defined as an mRS score of 4–6 in the development cohort and as a Glasgow Outcome Scale score of 1–3 in the validation cohort. The secondary outcome was death after the SAH during the observation period.

Statistical Analysis

Baseline variables were compared between the development and validation cohorts using the Fisher exact test for dichotomous and categoric variables, the independent-samples *t* test for normally distributed continuous variables, and the Mann-Whitney *U* test for non-normally distributed continuous variables.

Missing Data. In the development set, 22% of the cases had $\geq$1 missing variable, with a maximum of 11% missing per variable. In the validation set, 28% of the cases had >1 missing variable, with a maximum of 16% missing per variable. We assumed data to be missing at random. Missing values were imputed with multiple imputation.[13] Using multiple imputation, we created 20 complete imputed datasets of both the development and the validation sets.

Model Development. All candidate predictor variables were included in logistic regression models. Variables with limited predictive value, according to the Akaike information criterion, were stepwise-backward removed until a final model with the lowest

Table 1: Characteristics of the development and validation cohorts[a]

	Development (n = 409)	Validation (n = 317)	P Value
Age (mean) (SD) (yr)	57 (13)	59 (14)	.05
Female sex	277 (68)	222 (70)	.5
History of hypertension	131 (35)	96 (31)	.2
History of cardiovascular disease	75 (20)	61 (20)	1
History of diabetes	25 (7)	18 (6)	.6
WFNS score			.04
I	182 (46)	106 (39)	
II	51 (13)	37 (14)	
III	12 (3)	9 (3)	
IV	68 (17)	40 (15)	
V	81 (21)	74 (27)	
Aneurysm location			.44
Anterior circulation	324 (79)	243 (82)	
Posterior circulation	85 (21)	54 (18)	
Aneurysm size (median) (IQR) (mm)	6 (4–9)	5 (4–8)	.96
Aneurysm treatment			<.001
Coiling	273 (67)	153 (48)	
Clipping	64 (16)	95 (30)	
No treatment	72 (18)	69 (22)	
Total blood volume (median) (IQR) (mL)	29 (12–60)	26 (9–51)	.36
Cisternal blood volume (median) (IQR) (mL)	20 (8–41)	18 (6–34)	.1
Intraventricular blood volume (median) (IQR) (mL)	0.5 (0–2)	0.3 (0–2)	.1
Intraparenchymal blood volume (median) (IQR) (mL)	0 (0–3)	0 (0–3)	.8
Modified Fisher grade			.15
0	20 (5)	12 (4)	
1	26 (6)	9 (3)	
2	7 (2)	8(3)	
3	92 (23)	83 (27)	
4	262 (64)	201 (64)	
Clinical DCI	109 (27)	61 (29)	.6

Note:—DCI indicates delayed cerebral ischemia.
[a] All values are in No. (%) unless otherwise indicated.

Akaike information criterion was defined. The backward selection procedure was repeated in 100 randomly drawn samples of each of the 20 imputed development datasets using bootstrap resampling, creating 2000 models.[14] Candidate predictors that remained in >50% of these models were included as predictors in our final models.

Model Performance and Internal Validation. The explained variance of the models was evaluated with R^2. The ability to discriminate between patients with or without a poor outcome was assessed with the C-statistic. The agreement between the observed and the predicted outcomes was assessed with a calibration curve. Model performance was internally validated by calculating the optimism-corrected R^2 and C-statistic.[14] These optimism-corrected performance measures were calculated in each of the 20 imputed development sets, and the performance measures were averaged using mean ± SD.

External Validation. The performance of the models in the validation set was evaluated with R^2, the C-statistic, a calibration curve, the calibration slope, and the intercept (calibration-in-the-large). The calibration slope reflects the average strength of the predictor effects. A calibration slope of 1 indicates perfect agreement between the average predictor effects in the development and validation sets. The intercept reflects the difference between the average of the predicted outcome and the average of the observed outcome. An intercept of zero indicates perfect calibration. The external validation was performed in each of the 20 imputed validation sets, and the performance measures were averaged using the mean (± SD).

Secondary Models. If the TBV remained in the final model, the performance of this model was compared with a location-specific volume model in which the TBV was replaced with the cisternal, IVH, and IPH blood volumes. Furthermore, we created a model in which the TBV was replaced with the modified Fisher scale. The performances of these secondary models were compared with the TBV model by comparing the mean R^2 values in the imputed datasets with the independent-samples t test. The C-statistics of the models were compared using the DeLong test.

Sensitivity Analyses. Because not treating a patient has a strong effect on outcome, the inclusion of patients who were not treated may have biased the model. To determine the predictive value of the model on treated patients, we performed a sensitivity analysis including only patients who received aneurysm treatment. Because the predictive value of the amount of blood may decrease with increasing time between the initial hemorrhage and the admission CT scan, the performance of the TBV model was tested on a subset including only patients who underwent CT within 48 hours after symptom onset. Finally, to determine the effect of the manual corrections of the TBV, a sensitivity analysis including uncorrected TBV instead of corrected TBV was performed.

Analyses were performed using SPSS, Version 24.0.0.1 (IBM); R, Version 3.3.2 (http://www.r-project.org/); and R packages Hmisc, bootstepAIC, rms, pROC, and calibration curves.

RESULTS

The development cohort consisted of 409 patients, of whom 154 (38%) had a poor outcome (including patients who died) and 110 (27%) died within 6 months. The validation cohort consisted of 317 patients, of whom 140 (44%) had a poor outcome (including patients who died) and 80 (28%) died. Eight patients in the development cohort and 2 patients from the validation cohort were excluded due to movement and/or metal artifacts. Characteristics of patients in the development and validation cohorts are shown in Table 1. Patients in the validation cohort more often had a WFNS V grade on admission and more often underwent clipping as aneurysm treatment than patients in the development cohort. No other differences between the development and validation cohorts were found. For the whole group, the median time

Table 2: Model validation

	Internal		External	
	R^2, % (SD)	C-statistic (SD)	R^2, % (SD)	C-statistic (SD)
Unfavorable outcome				
TBV model	52 (0.6)	0.88 (0.01)	56 (1.8)	0.89 (0.01)
mFisher model	43 (0.9)	0.84 (0.01)	45 (3)	0.85 (0.01)
Location-specific model	50 (0.8)	0.88 (0.01)	56 (1)	0.89 (0.00)
Death				
TBV model	48 (0.8)	0.87 (0.01)	50 (1.2)	0.89 (0.00)
mFisher model	42 (1.4)	0.85 (0.01)	42 (2.6)	0.85 (0.01)
Location-specific mode	47 (1.0)	0.87 (0.01)	49 (1.3)	0.88 (0.01)

Note:—mFisher indicates modified Fisher scale.

between the onset of symptoms and CT used for volume measurement was 2.5 hours (interquartile range [IQR] = 1.1–14 hours). For the patients who had recurrent bleeding, the median time between the onset of symptoms and CT was 2.3 hours (IQR = 1.0–12.0 hours).

Model Selection and Performance

The following variables remained in the models after selection: TBV at first admission, WFNS grade at first admission, age, aneurysm size, and history of cardiovascular disease. The mean R^2 of the model was 54% ± 0.5% for poor outcome and 50% ± 1% for death. The mean R^2 values of the included variables were 35% ± 0% for TBV, 29% ± 0.7% for WFNS, 13% ± 0.7% for aneurysm size, 11% ± 0% for age, and 6% ± 1% for a history of cardiovascular disease. The models discriminated well between patients with and without a poor outcome (mean C-statistic = 0.89 ± 0.01) and mortality (mean C-statistic = 0.88 ± 0.01).

Model Validation

Internal validation showed that the optimism of the models was low for both poor outcome and death groups (Table 2). The predictive accuracy and discriminative power of the models in the external validation cohort for both outcome and death were comparable with those of the development cohort (Table 2).

The calibration plot showed a good correlation between predicted and observed outcomes in the validation set, though the models somewhat underestimated the risk of poor outcome (Fig 1*A*, -*B*). The mean slope was 1.1 ± 0.5 for poor outcome and 0.97 ± 0.03 for death. The calibration-in-the-large was 0.58 ± 0.03 for poor outcome and 0.12 ± 0.03 for death.

Secondary Models

The location-specific blood volume models showed a comparable explained variance to the TBV model for both poor outcome (mean R^2 = 56% ± 1% versus 56% ± 2%, P = .8) and death (mean R^2 = 49% ± 1% versus 50% ± 1%, P = .1). The mean R^2 values of the individual compartments were 17% ± 0% for cisternal volume, 12% ± 0% for IVH volume, and 14% ± 0% for IPH volume. The discriminative power was also similar for outcome (mean C-statistic = 0.89 ± 0.00 versus 0.89 ± 0.01, P = .4) and death (mean C-statistic = 0.88 ± 0.01 versus 0.89 ± 0.00, P = .66) (Table 2). The calibration plots of the location-specific models showed a comparable calibration for both outcome and death with the TBV models. (Fig 1*C*, -*D*).

The explained variance of the models including the modified Fisher scale in the validation set was significantly lower than the models including the TBV for both poor outcome (R^2 = 45% ± 3% versus 56% ± 2%, P < .001) and death (R^2 = 42% ± 3% versus 50% ± 1%, P < .001). These models showed less accurate discrimination between patients with and without a poor outcome (mean C-statistic = 0.85 ± 0.01 versus 0.89 ± 0.01, P = .03) and death (mean C-statistic = 0.85 ± 0.01 versus 0.89 ± 0.00, P = .01) (Table 2). Calibration plots of the modified Fisher models showed a comparable calibration for outcome and a poorer calibration for death (Fig 1*E*, -*F*).

Sensitivity Analyses

After we included only patients who underwent aneurysm treatment, 337 patients remained in the development cohort and 248 patients remained in the validation cohort. Both the explained variance and the discriminative power were lower compared with the whole group (R^2 = 41% ± 1%; mean C-statistic = 0.84 ± 0.01).

After including only patients who had a brain CT within 48 hours after the initial bleeding, 340 and 281 patients remained in the development and validation cohorts, respectively. The explained variance increased (R^2 = 60% ± 1%), while the discriminative power did not change (mean C-statistic = 0.91 ± 0.00).

A sensitivity analysis including uncorrected TBV showed a slightly lower explained variance and discriminative power (R^2 = 49% ± 1%; mean C-statistic = 0.87 ± 0.01) compared with the corrected TBV.

DISCUSSION

The developed prediction models in patients with aSAH including quantified hemorrhage accurately discriminated patients with a favorable outcome from those with an unfavorable clinical outcome. The model including location-specific blood volumes showed similar results compared with the TBV model. Including the TBV in the model resulted in a higher predictive accuracy than including the modified Fisher scale instead.

One previous study also developed an outcome-prediction model including TBV.[15] In that study, various prognostic models for outcome were developed; the model including WFNS grade, age, and total bleeding volume (as continuous variables) had the highest predictive value. The internal performance of this model was similar to that of our models. Aneurysm size and a history of cardiovascular disease were not assessed in that study. An important difference between the previous and current study is the external validation of the developed models. External validation of prediction models is important because developing and validating a model on the same cohort may result in overly optimistic performance estimates.[16] Therefore, our models were validated on a registry of patients with SAH from a different center.

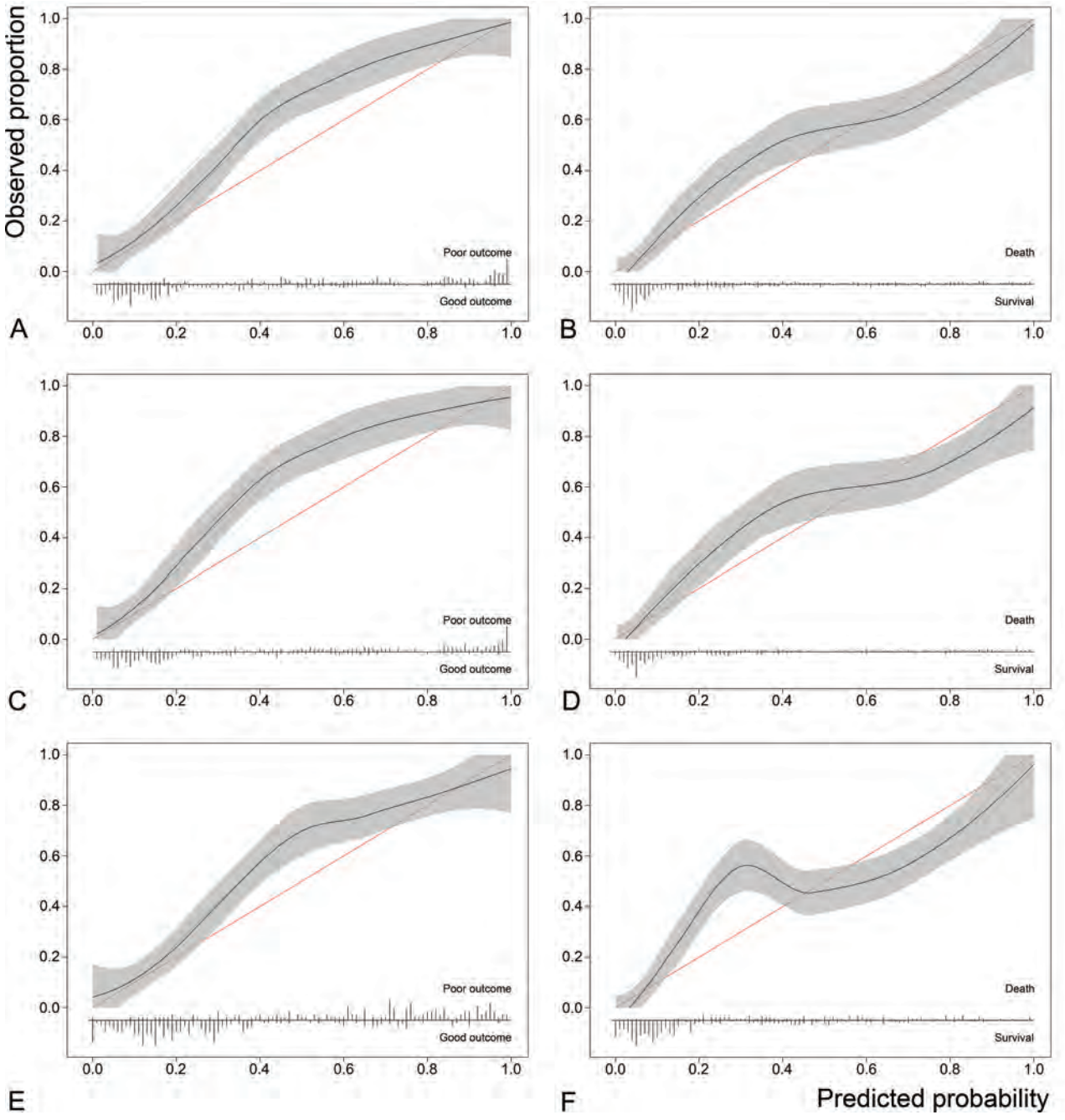

FIG 1. Calibration plots of the TBV model for poor outcome (*A*), the TBV model for death (*B*), the location-specific model for poor outcome (*C*), the location-specific model for death (*D*), the modified Fisher model for poor outcome (*E*), and the modified Fisher model for death (*F*).

The variables that remained in our models after bootstrapped backward selection are comparable with the variables included in previously developed models. A systematic review showed that previously developed models most frequently included age, neurologic condition (assessed with WFNS or Hunt and Hess grade), amount of bleeding (assessed with the Fisher or modified Fisher grade), and aneurysm size.[3] These are all variables that are available shortly after admission to the hospital. These factors not only directly determine the risk of poor outcome but could also increase the risk of the occurrence of late complications like delayed cerebral ischemia and hydrocephalus, which may further determine a patient's risk of poor outcome.[2,17] However, these late complications are less suitable for early prediction of aSAH outcome.

The prognostic value of imaging variables in patients with aSAH has been debatable. The predictive accuracy of the amount of blood, assessed with the Fisher scale, was low in a large cohort of patients in an SAH trial.[18] Furthermore, in a recently published prediction model derived from that cohort, the addition of the amount of blood to a prediction model did not increase its predictive value.[4] The externally validated explained variance and predictive accuracy of our models were larger than those of previously published models that included a radiologic scale to assess the amount of blood.[3,4,19] One reason for this difference may be that categorization of a

continuous variable leads to loss of information.[20] Furthermore, the Fisher scale and modified Fisher scale have shown only moderate interobserver agreement.[6,21] Automatically quantified TBV is less observer-dependent; this feature may contribute to its higher predictive value.

Considering the cisternal, IVH, and IPH volumes instead of TBV in the model separately did not improve the predictive value of the model. Of these compartments, the amount of blood in the cisterns had the highest explained variance, followed by IPH and IVH volume. From the literature, it is known that the amount of blood in the cisterns is associated with outcome.[5,8,22] Several studies have found an association between IVH and/or IPH volume and poor outcome.[23-25] On the contrary, another study found that a large IPH volume was not associated with poor outcome. All patients included in this study were treated with surgical decompression. In this study, a large number of patients with small IPH volumes also had a poor outcome.[26] As for IVH, it may be that a relatively large blood clot in the ventricles results in less increase in intracranial pressure compared with an equal amount of blood in the subarachnoid space, which may result in a relatively better outcome.

After we included only patients who received treatment, the predictive value was lower compared with the whole group. Currently, the decision not to treat the aneurysm of a patient is based on a variety of factors such as the neurologic status, age, comorbidities, and aneurysm configuration. Patients who are not treated are most likely in poor condition and are estimated to have a very poor prognosis. Therefore, when we excluded those patients from the analysis, only patients with a relatively better prognosis remained. This finding may explain why the predictive value was somewhat lower in treated patients. Nevertheless, the model still showed a high discrimination between patients with and without a poor outcome who were treated. Including nontreated patients in the analyses may introduce some bias because not treating a patient itself will likely lead to a poor outcome. However, information about treatment is frequently not available at admission, and by including both treated and nontreated patients, the model can be applied to all patients who arrive at the emergency department.

An important strength of this study is the use of prospectively collected patient data, which were collected for observational studies in patients with SAH and thoroughly checked by trial nurses and treating clinicians. Furthermore, validation of the prediction model on an external cohort shows that the predictions made by the model are robust and that the model makes accurate predictions for new patients. Only variables that are quickly and easily obtainable after the patient's admission to the hospital were used. This step is necessary because quick decision-making in patients with aSAH is required. Thus, including factors that take considerable time to obtain would limit the clinical applicability of a model. The use of automatic hemorrhage-segmentation techniques to assess the TBV resulted in a more precise measurement of the blood volume compared with coarse grading scales.

On the contrary, the use of automatic hemorrhage-segmentation techniques can also be regarded as a weakness of this study. Hemorrhage-segmentation software needs to be available to apply these models to a hospital population. Furthermore, the currently used automated method required manual correction, which may limit its present usefulness in a clinical setting. However, increasingly more (machine learning) methods to segment structures in CT images are available.[27] The segmentations were corrected by only a single radiologist, which may have introduced some observer bias. Nevertheless, in the sensitivity analysis, we have shown that the influence of the observer on the results was minimal, suggesting that the effect of this single radiologist is modest at most. If a patient had a rebleed, the CT scans after the rebleed were used to determine the TBV. However, no WFNS scores after rebleed were systematically registered, so only admission WFNS scores were used. This use may have led to some limiting of the predictive value of the WFNS grade compared with the TBV. In future studies, use of the modified WFNS scale may further improve the predictive accuracy.[28] A more extensive assessment of the patients' comorbidities, for example using the Charlson Comorbidity Index, could further improve the model.[29] The sample size used for developing and validating these models was relatively small; however, a minimum of 10 cases of poor outcome per variable was still met.[14]

Accurate prediction can assist clinicians in decision-making and improve communication with patients and their families. Furthermore, it may reduce costs by allocating patients to the right intensity of treatment at admission. However, determining whether a model performs well enough to be applied in daily practice is difficult. A C-statistic of 0.89, indicating that the probability that a patient with a poor outcome is given a higher probability of a poor outcome than a patient without a poor outcome, is 0.89, is considered a reliable model.[14,30] A perfectly discriminative model would have a C-statistic of 1.00.

Thus, our model can, with a fairly high amount of certainty, predict which patients with aSAH will have a poor outcome. This study does not show whether clinical decisions based on our models actually improve patient outcome. Furthermore, it does not show whether statistically significant more accurate outcome prediction is also clinically relevant. To assess this question, an impact study that quantifies the effect of using a prognostic model on patient outcome and/or cost-effectiveness in a randomized trial is required.[31] Furthermore, a software package integrating automatic hemorrhage segmentation and clinical values needs to be developed before these models can be more broadly used.

CONCLUSIONS

The TBV-based prediction models for clinical outcome in patients with aSAH have a high predictive accuracy, higher than prediction models including the more commonly used modified Fisher scale. Including location-specific volumes did not improve the quality of the prediction models. The TBV models can accurately predict which patients will have a poor outcome early in the disease process and may aid clinicians in clinical decision-making.

Disclosures: Henk A. Marquering—*OTHER RELATIONSHIPS*: cofounder and shareholder of Nico.lab. Lucas Alexandre Ramos—*RELATED*: *Grant*: ITEA3.* René van den Berg—*UNRELATED*: *Consultancy*: Cerenovus.* Anna M. M. Boers—*UNRELATED*: *Stock/Stock Options*: Nico.lab. Yvo B.W.E.M. Roos—*UNRELATED*: *Stock/Stock Options*: minor stock holder of Nico.Lab. Charles B.L.M. Majoie—*UNRELATED*: *Grants/Grants Pending*: Netherlands CardioVascular Research

Initiative/Dutch Heart Foundation, European Commission, TWIN Foundation, Stryker*; *Stock/Stock Options*: Nico.lab (modest), *Comments*: a company that focuses on the use of artificial intelligence for medical image analysis. *Money paid to the institution.

REFERENCES

1. van Gijn J, Kerr RS, Rinkel GJ. **Subarachnoid haemorrhage.** *Lancet* 2007;369:306–18 CrossRef Medline
2. Vergouwen MD, Jong-Tjien-Fa AV, Algra A, et al. **Time trends in causes of death after aneurysmal subarachnoid hemorrhage: a hospital-based study.** *Neurology* 2016;86:59–63 CrossRef Medline
3. Jaja BN, Cusimano MD, Etminan N, et al. **Clinical prediction models for aneurysmal subarachnoid hemorrhage: a systematic review.** *Neurocrit Care* 2013;18:143–53 CrossRef Medline
4. Jaja BN, Saposnik G, Lingsma HF, et al; SAHIT oration. **Development and validation of outcome prediction models for aneurysmal subarachnoid haemorrhage: the SAHIT multinational cohort study.** *BMJ* 2018;360:j5745 CrossRef Medline
5. Kramer AH, Hehir M, Nathan B, et al. **A comparison of 3 radiographic scales for the prediction of delayed ischemia and prognosis following subarachnoid hemorrhage.** *J Neurosurg* 2008;109:199–207 CrossRef Medline
6. Woo PY, Tse TP, Chan RS, et al. **Computed tomography interobserver agreement in the assessment of aneurysmal subarachnoid hemorrhage and predictors for clinical outcome.** *J Neurointerv Surg* 2017;9:1118–24 CrossRef Medline
7. Fisher CM, Kistler JP, Davis JM. **Relation of cerebral vasospasm to subarachnoid hemorrhage visualized by computerized tomographic scanning.** *Neurosurgery* 1980;6:1–9 CrossRef Medline
8. Hijdra A, van Gijn J, Nagelkerke NJ, et al. **Prediction of delayed cerebral ischemia, rebleeding, and outcome after aneurysmal subarachnoid hemorrhage.** *Stroke* 1988;19:1250–56 CrossRef Medline
9. Boers AM, Zijlstra IA, Gathier CS, et al. **Automatic quantification after subarachnoid hemorrhage on non-contrast computed tomography.** *AJNR Am J Neuroradiol* 2014;35:2279–86 CrossRef Medline
10. Germans MR, Post R, Coert BA, et al. **Ultra-early tranexamic acid after subarachnoid hemorrhage (ULTRA): study protocol for a randomized controlled trial.** *Trials* 2013;14:143 CrossRef Medline
11. Frontera JA, Claassen J, Schmidt JM, et al. **Prediction of symptomatic vasospasm after subarachnoid hemorrhage: the modified Fisher scale.** *Neurosurgery* 2006;59:21–27 CrossRef Medline
12. Vergouwen MD, Vermeulen M, van Gijn J, et al. **Definition of delayed cerebral ischemia after aneurysmal subarachnoid hemorrhage as an outcome event in clinical trials and observational studies: proposal of a multidisciplinary research group.** *Stroke* 2010;41:2391–95 CrossRef Medline
13. Little R, An H. **Robust likelihood-based analysis of multivariate data with missing values.** *Statistica Sinica* 2004;14:949–68
14. Steyerberg EW. *Clinical Prediction Models: A Practical Approach to Development, Validation, and Updating.* Springer-Verlag; 2009
15. Lagares A, Jiménez-Roldán L, Gomez PA, et al. **Prognostic value of the amount of bleeding after aneurysmal subarachnoid hemorrhage.** *Neurosurgery* 2015;77:898–907 CrossRef Medline
16. Bleeker SE, Moll HA, Steyerberg EW, et al. **External validation is necessary in prediction research: a clinical example.** *J Clin Epidemiol* 2003;56:826–32 CrossRef Medline
17. De Oliveira Manoel AL, Jaja BN, Germans MR, et al. **The VASOGRADE: a simple grading scale for prediction of delayed cerebral ischemia after subarachnoid hemorrhage.** *Stroke* 2015;46:1826–31 CrossRef Medline
18. Jaja BN, Lingsma H, Steyerberg EW, et al; on behalf of SAHIT investigators. **Neuroimaging characteristics of ruptured aneurysm as predictors of outcome after aneurysmal subarachnoid hemorrhage: pooled analyses of the SAHIT cohort.** *J Neurosurg* 2016;124:1703–11 CrossRef Medline
19. van Donkelaar CE, Bakker NA, Birks J, et al. **Prediction of outcome after aneurysmal development.** *Stroke* 2019;50:837–44 CrossRef
20. Altman DG, Royston P. **The cost of dichotomising continuous variables.** *BMJ* 2006;332:1080 CrossRef Medline
21. van der Jagt M, Hasan D, Bijvoet HW, et al. **Interobserver variability of cisternal blood on CT after aneurysmal subarachnoid hemorrhage.** *Neurology* 2000;54:2156–58 CrossRef Medline
22. Dengler NF, Diesing D, Sarrafzadeh A, et al. **The Barrow Neurological Institute Scale revisited: predictive capabilities for cerebral infarction and clinical outcome in patients with aneurysmal subarachnoid hemorrhage.** *Neurosurgery* 2017;81:341–49 CrossRef Medline
23. Jabbarli R, Reinhard M, Roelz R, et al. **Intracerebral hematoma due to aneurysm rupture: are there risk factors beyond aneurysm location?** *Neurosurgery* 2016;78:813–20 CrossRef
24. Kramer AH, Mikolaenko I, Deis N, et al. **Intraventricular hemorrhage volume predicts poor outcomes but not delayed ischemic neurological deficits among patients with ruptured cerebral aneurysms.** *Neurosurgery* 2010;67:1044–52 CrossRef Medline
25. Jabbarli R, Reinhard M, Roelz R, et al. **The predictors and clinical impact of intraventricular hemorrhage in patients with aneurysmal subarachnoid hemorrhage.** *Int J Stroke* 2016;11:68–76 CrossRef Medline
26. Zijlstra IA, van der Steen WE, Verbaan D, et al. **Ruptured middle cerebral artery aneurysms with a concomitant intraparenchymal hematoma: the role of hematoma volume.** *Neuroradiology* 2018;60:335–42 CrossRef Medline
27. Litjens G, Kooi T, Bejnordi BE, et al. **A survey on deep learning in medical image analysis.** *Med Image Anal* 2017;42:60–88 CrossRef Medline
28. Sano H, Satoh A, Murayama Y, et al; members of the 38 registered institutions and WFNS Cerebrovascular Disease & Treatment Committee. **Modified World Federation of Neurosurgical Societies subarachnoid hemorrhage grading system.** *World Neurosurg* 2015;83:801–07 CrossRef Medline
29. Bar B, Hemphill JC. **Charlson comorbidity index adjustment in intracerebral hemorrhage.** *Stroke* 2011;42:2944–46 CrossRef Medline
30. Altman DG, Vergouwe Y, Royston P, et al. **Prognosis and prognostic research: validating a prognostic model.** *BMJ* 2009;338:b605 CrossRef Medline
31. Moons KGM, Altman DG, Vergouwe Y, et al. **Prognosis and prognostic research: application and impact of prognostic models in clinical practice.** *BMJ* 2009;338:b606 CrossRef Medline

Resting-State Brain Activity for Early Prediction Outcome in Postanoxic Patients in a Coma with Indeterminate Clinical Prognosis

D. Pugin, J. Hofmeister, Y. Gasche, S. Vulliemoz, K.-O. Lövblad, D. Van De Ville, and S. Haller

ABSTRACT

BACKGROUND AND PURPOSE: Early outcome prediction of postanoxic patients in a coma after cardiac arrest proves challenging. Current prognostication relies on multimodal testing, using clinical examination, electrophysiologic testing, biomarkers, and structural MR imaging. While this multimodal prognostication is accurate for predicting poor outcome (ie, death), it is not sensitive enough to identify good outcome (ie, consciousness recovery), thus leaving many patients with indeterminate prognosis. We specifically assessed whether resting-state fMRI provides prognostic information, notably in postanoxic patients in a coma with indeterminate prognosis early after cardiac arrest, specifically for good outcome.

MATERIALS AND METHODS: We used resting-state fMRI in a prospective study to compare whole-brain functional connectivity between patients with good and poor outcomes, implementing support vector machine learning. Then, we automatically predicted coma outcome using resting-state fMRI and also compared the prediction based on resting-state fMRI with the outcome prediction based on DWI.

RESULTS: Of 17 eligible patients who completed the study procedure (among 351 patients screened), 9 regained consciousness and 8 remained comatose. We found higher functional connectivity in patients recovering consciousness, with greater changes occurring within and between the occipitoparietal and temporofrontal regions. Coma outcome prognostication based on resting-state fMRI machine learning was very accurate, notably for identifying patients with good outcome (accuracy, 94.4%; area under the receiver operating curve, 0.94). Outcome predictors using resting-state fMRI performed significantly better ($P < .05$) than DWI (accuracy, 60.0%; area under the receiver operating curve, 0.63).

CONCLUSIONS: Indeterminate prognosis might lead to major clinical uncertainty and significant variations in life-sustaining treatments. Resting-state fMRI might bridge the gap left in early prognostication of postanoxic patients in a coma by identifying those with both good and poor outcomes.

ABBREVIATIONS: CA = cardiac arrest; EEG = electroencephalography; FC = functional connectivity; ICU = intensive care unit; LOOCV = leave-one-out cross-validation; NPV = negative predictive value; PPV = positive predictive value; rs-fMRI = resting-state fMRI

Cardiac arrest (CA) is an important cause of death in the United States and Europe, with an annual incidence of 110/100,000.[1,2] Only 7.6% of patients treated for out-of-hospital cardiac arrest survive to hospital discharge. In Europe, 128,000–275,000 individuals per year are treated for out-of-hospital cardiac arrest, and 10% survive.[2,3] Due to improvements made in prehospital and intrahospital CA management, a growing number of patients survive the first days following CA, yet can remain unconscious. The main factor determining death in patients with out-of-hospital cardiac arrest admitted to the intensive care unit (ICU), accounting for two-thirds of deaths, is postanoxic brain injury, which leads to a withdrawal of care. Prognostication of patients in a coma can be performed soon after CA (approximately 3 days) and relies on

Received August 13, 2019; accepted after revision March 21, 2020.

From the Departments of Intensive Care (D.P., Y.G.), Radiology (J.H.), Neurology (S.V.), and Neuroradiology (K.-O.L.), Geneva University Hospitals, Geneva, Switzerland; Geneva Neuroscience Center (J.H., D.V.D.V.); Radiology and Medical Informatics (J.H., D.V.D.V.); and Faculty of Medicine (S.H.), University of Geneva, Geneva, Switzerland; Institute of Bioengineering (D.V.D.V.), Ecole Polytechnique Fédérale de Lausanne (EPFL), Lausanne, Switzerland; Centre d'Imagerie Rive Droite (S.H.), Geneva, Switzerland; and Department of Surgical Sciences, Radiology (S.H.), Uppsala University, Uppsala, Sweden.

D. Pugin is funded by a research fellowship of the Faculty of Medicine of Geneva University and by a Templin grant. J. Hofmeister is supported by a Research and Development fund by Geneva University Hospitals. S. Vulliemoz is funded by Swiss National Science Foundation grants 169198 and CRSII5_170873, and K.O. Lövblad, by a Swiss National Science Foundation grant 32003B_160222/1.

Please address correspondence to Deborah Pugin, MD, NeuroIntensive Care Unit, Department of Intensive Care Medicine, Geneva University Hospitals, rue Gabrielle Perret Gentil 4, CH-1205 Geneva, Switzerland; e-mail: Deborah.pugin@hcuge.ch

Indicates open access to non-subscribers at www.ajnr.org
Indicates article with supplemental on-line appendix and table.
http://dx.doi.org/10.3174/ajnr.A6572

multimodal testing, using clinical examination, electrophysiologic testing, structural and diffusion neuroimaging, and biomarkers.[4-6] While this multimodal prognostication is accurate for predicting poor outcome (ie, death), it is not sensitive enough to identify patients with good outcome (ie, consciousness recovery). Thus, even after current multimodal testing, a subset of patients is left with indeterminate prognosis (ie, all patients not identified as having poor outcome).[7]

Several neuroimaging studies have shown that changes on DWI within 5 days after CA predicted poor outcome.[8-15] Yet the timing of DWI analysis is crucial because diffusion values vary soon after anoxia.[10] Moreover, while DWI is a strong predictor of poor outcome, it is not sensitive enough to identify patients with good outcomes.

The spontaneous activity of the brain is not random, but rather organized in functional networks.[16] Resting-state fMRI (rs-fMRI) is a powerful tool for mapping the brain functional connectivity (FC) of patients and healthy volunteers.[17] Several studies have reported that rs-fMRI could differentiate between states of consciousness in patients with chronic brain damage, with decreased FC correlating with the degree of consciousness impairment.[18] It has been recently shown that fMRI could detect early signs of consciousness in response to passive stimulation in comatose patients following traumatic brain injury[19] and that FC strength correlated with favorable long-term outcome in postanoxic patients in a coma.[20] However, rs-fMRI has yet to be systematically assessed for the early prognostication of the postanoxic patient in a coma.

Our study aimed to predict coma outcome (ie, consciousness recovery versus remaining comatose; namely good-versus-poor outcome) using rs-fMRI and machine learning methods. We focused on cases of particular clinical interest, notably early postanoxic patients in a coma and patients left with indeterminate prognosis after standard multimodal testing.

MATERIALS AND METHODS

Subjects and Protocol

The study took place at the Geneva University Hospitals, approved by the local ethics committee for research on human subjects and performed in accordance with the Declaration of Helsinki. We screened all patients comatose following CA admitted to the Geneva University Hospitals' ICU during 4 years ending September 2016.

On admittance, patients comatose following CA were assessed by the ICU team. Those fulfilling the inclusion criteria (see below) and with legal representatives to provide written informed consent were scheduled for early MR imaging (intended to be performed 4 days after CA). All patients still comatose 3 days after CA were considered for inclusion. Patients in a coma were defined as those who did not respond to commands, with Glasgow Coma Scale scores of $\leq$8 not related to sedation. Patients identified with poor outcome after standard multimodal testing according to the American Academy of Neurology guidelines (generalized myoclonic jerks and bilateral N20 wave abolition or flat electroencephalography [EEG]) were excluded.[4,21,22] Patients with MR imaging contraindications like pacemakers or extracorporeal membrane oxygenation were excluded. Moreover, major sedation is required for cardiogenic shock treated with extracorporeal membrane oxygenation. This sedation then prevents reliable neuroprognostication in patients. Patients who were conscious and receptive to commands before day 3 or with a history of brain injury were also excluded. Thus, we included only patients whose outcome was left uncertain after current standard multimodal testing. The standard multimodal testing included clinical examination, and particularly pupillary and corneal reflexes, electrophysiologic testing including EEG and somatosensory-evoked potentials, and neuroimaging (mainly MR imaging).[21,22] Poor outcome was defined as Glasgow Pittsburgh Cerebral Performance Category scale of 4–5 (persistent vegetative state or death). Patients with a good outcome were patients with Glasgow Pittsburgh Cerebral Performance Category of 1–3 (absent, mild, moderate, or severe neurologic disabilities).[6,21] All patients were treated with normothermia (36°) for the first 24 hours.

MRIs were performed at the radiology department of the Geneva University Hospitals, with patients positioned in the scanner while still intubated. The whole MR imaging scanning session was supervised by a neurointensivist from the ICU team (D.P.) involved in the study; all fMRI sessions were recorded without sedation. If the patient was uncomfortable or moving during imaging, propofol was added after fMRI sequences were recorded. Surviving patients were followed up at 3, 6, and 12 months with the mRS, Glasgow Outcome Scale, Cerebral Performance Category scale, and Disability Rating Scale. Information was gathered by physicians blinded to the fMRI results. This process was undertaken either by the physician in charge of inpatients or by phone interview for patients who were discharged.

MR Imaging Acquisition and Analysis

All patients included underwent MR imaging with a protocol including a 3D-T1 image, DWI, and a blood oxygen level–dependent resting-state sequence (On-line Appendix).

DWI derived from DTI with 30 directions plus the B_0 of each patient were analyzed to predict coma outcome, as per the description of Wijman et al,[9] by computing the percentage of brain volume with an ADC value of $<650 \times 10^{-6}$ mm^2/s. Patients with >10% brain volume with abnormal ADC values were assigned to the poor outcome group, while the others were assigned to the good outcome group, as proposed by Wijman et al. fMRI and 3D-T1 images were preprocessed for each subject independently, following standard protocol[23,24] (On-line Appendix), including normalization into Montreal Neurological Institute space, to assess whole-brain resting-state activity of each comatose patient and to compare the brain network topology of patients with good and poor outcomes. Thus, we statistically compared brain-network activity derived from fMRI between groups with good and poor outcomes, following standard procedure[25] (On-line Appendix).

Coma Outcome Prediction

We ultimately aimed to base predictions of coma outcome on resting-brain activity measured with fMRI. Thus, we trained a machine learning classifier to identify patients with good and poor outcomes based on brain network topology derived from fMRI (On-line Appendix). Classification performance was assessed using leave-one-out cross-validation (LOOCV) methods, because our sample size was relatively small, allowing computing prediction-accuracy measures (overall accuracy, sensitivity, specificity, positive prediction value [PPV], and negative predictive value [NPV]). Finally, we

statistically compared the prediction accuracy based on resting-brain activity with that using DWI (On-line Appendix).

RESULTS

Demographic Data

We screened 351 patients comatose following CA, 17 of whom underwent the whole protocol and were included in the final analysis (Fig 1). At admission, 7/17 patients had areactive mydriasis, 1 had reactive mydriasis, and 9 had a reactive miosis. At day 3, three patients had reactive mydriasis and 14 had reactive miosis. All patients had controlled normothermia (36°) for the first 24 hours. Of these 17, nine regained consciousness (mean, 4 ± 7.8 days after the MR imaging session; good outcome group); the remaining 8 did not and finally died (poor outcome group). Both groups were similar in terms of demographic data, apart from the time until the return of spontaneous circulation, which was 50% longer in the poor outcome group (Table 1). Both groups were scanned in the same time window after hospital admission, when no survival prognosis could be made on the basis of their clinical status or standard multimodal testing (Table 2). No sedation was used during fMRI. If the patient was uncomfortable or moving during imaging, propofol was added after fMRI sequences were recorded. The mean delay between propofol cessation and MR imaging was 41 hours (minimum, 24 hours; maximum, 120 hours) and 82 hours for midazolam (minimum, 19 hours; maximum, 264 hours).

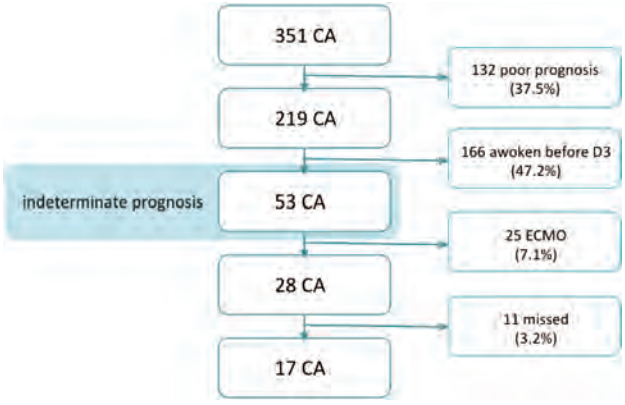

FIG 1. Inclusion flow chart. D indicates day; ECMO, extracorporeal membrane oxygenation.

At 1 year, 5 patients with good outcome had Disability Rating Scale scores of ≤1, eight had Glasgow Outcome Scale scores of ≥4 and a Cerebral Performance Category score of ≤ 2, and 7 had mRS ≤1 (ie, they were almost completely independent). Two patients remained partially or totally dependent, essentially due to cognitive disorders. Of the patients who died, 1 patient had a second CA, 5 remained in a persistent comatose state leading to care withdrawal, and 2 had adverse outcomes following extubation.

Network Topology

We initially compared network topology between the good and poor outcome groups at each individual functional connection (ie, edge weight). We first visually inspected the mean whole-brain network of each group, observing much better–preserved network architecture in patients with good outcomes than in those with poor outcomes. We then statistically compared network topology between groups (Fig 2). We observed a significant increase in connectivity between many brain regions in the good outcome group (Fig 3). The strongest and most extensive increased connectivity in the good outcome group (versus poor outcome) occurred within and between the occipital, parietal, temporal, and frontal regions. We observed significant changes within the occipital nodes and between the fronto-occipital, temporo-occipital, and occipitolimbic nodes. We also observed increased connectivity within the parietal nodes and among the parietofrontal, parietocentral, and parietotemporal nodes. The temporal lobe showed increased connectivity within the temporo-medial nodes and among the temporofrontal, temporocentral,

Table 1: Demographic and clinical characteristics of patients

	All (*n* = 17)	Good Outcome (*n* = 9)	Poor Outcome (*n* = 8)	*P* Value
Male	14 (82.4%)	7 (77.8%)	7 (87.5%)	.6
Age (yr)	57.5 ± 15.6	52.2 ± 13.2	63.4 ± 16.9	.07
CA witnessed	17 (100%)	9 (100%)	8 (100%)	NA
CA outside hospital	13 (76.5%)	8 (88.9%)	5 (62.5%)	.2
Time to ROSC (min)	23.4 ± 15.9	17 ± 10.2	30.62 ± 18.6	.03
First monitored rhythm				
VF/VT	10 (58.6%)	7 (77.8%)	3 (37.5%)	
PEA	2 (11.7%)	1 (11.1%)	1 (12.5%)	
Asystole	5 (29.3%)	1 (11.1%)	4 (50%)	
Hospital stay (days)	19 ± 20	28 ± 23.9	9 d ± 6.2	.97
ICU stay (days)	9 ± 5.4	10 ± 5.1	8 ± 6.1	.71
ETT length (days)	7 ± 4.3	8 ± 4.9	7 ± 3.8	.65
Time before fMRI (days)	4 ± 2.9	5 ± 3.4	4 ± 2.2	.72
Myoclonia	2 (11.8%)	1 (11.1%)	1 (12.5%)	.92
Lactate (mmol/L)	7.2 ± 4.1	7.1 ± 3.7	7.36 ± 4.8	.43
First GCS				
3	14 (82.4%)	7 (77.8%)	6 (87.5%)	
6	1 (5.9%)	1 (11.1%)		
7	2 (11.7%)	1 (11.1%)	1 (12.5%)	

Note:—ROSC indicates return of spontaneous circulation; VF/VT, ventricular fibrillation/tachycardia; PEA, pulseless electrical activity; ETT, endotracheal intubation; GCS, Glasgow Coma Scale; NA, not applicable.

temporoparietal, and temporo-occipital nodes. Finally, we observed significant increased connectivity among the frontoparietal, frontocentral, frontotemporal, and fronto-occipital nodes.

We also observed a less significant increase in focal connectivity in the poor outcome group (versus good outcome). The poor outcome group exhibited higher focal activity within the temporosuperior and temporopolar regions, as well as between these temporosuperior and temporopolar regions and occipital areas.

Taken together, these results suggest that patients who eventually recover consciousness (ie, the good outcome group) initially exhibit higher activity within the occipital areas and between these areas and widely distributed cortical regions, except for the temporosuperior and temporopolar regions. Conversely, patients who ultimately die (ie, poor outcome) initially show higher activity focally, among the occipital, temporosuperior, and temporopolar regions, as well as within these areas.

Table 2: EEG pattern

	Good Outcome ($n = 9$)	Poor Outcome ($n = 8$)
Malignant EEG pattern	0/9	0/8
Periodic features	5/9 none, 4/9 RDA	5/8 none; 2/8 LPDs, 1/8 RDA
Unreactive EEG	2/9 unreactive, 7/9 reactive	6/8 unreactive, 2/8 reactive
Seizure	0/9	0/8
Disorganized background	1/9	4/8

Note:—Malignant EEG pattern indicates suppressed background with or without continuous periodic discharges, burst-suppression, abundant periodic discharges, or rhythmic epileptiform transients, electrographic seizure, discontinuous or low-voltage background, reversed anterior-posterior gradient; Unreactive EEG, absence of background reactivity or only stimulus-induced discharges; LPDs, lateralized periodic discharges; RDA. rhythmic Δ activity.

Coma Outcome Prediction

Diffusion Imaging. The percentage of brain volume with ADC values of $<650 \times 10^{-6}$ mm^2/s was used to predict coma outcome, with a threshold set at 10% as proposed by Wijman et al.[9] The model achieved 64.7% accuracy in discriminating good and poor coma outcomes (poor outcome prediction sensitivity, 25.0%; specificity, 100.0%; PPV, 100%; NPV 60.0%; area under the receiver operating characteristic curve, 0.625).

Resting-State fMRI. We then used rs-fMRI to train a machine learning

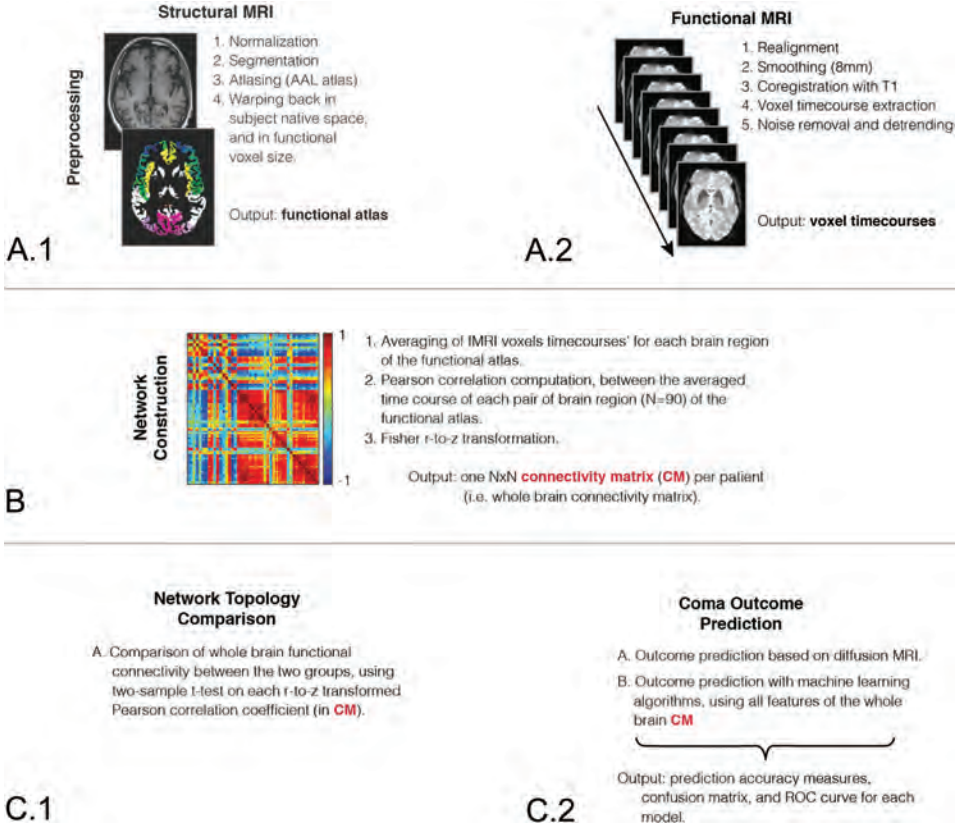

FIG 2. Analysis pipeline. Structural (*A.1*) and functional (*A.2*) MRIs of each patient are first preprocessed to extract time courses of each brain voxel. *B*, An averaged time course is then computed for each of 90 brain regions of the Automated Anatomical Labeling atlas, and recursive Pearson correlations are computed between each brain region pair, to obtain a whole-brain connectivity network for each patient. *C.1*, Networks of patients with good and poor outcomes are compared using a 2-sample *t* test corrected for multiple comparisons. *C.2*, A support vector machine classifier is also trained on the connectivity networks of each patient to discriminate patients with good and poor outcomes. N indicates brain regions; CM, connectivity matrix; ROC, receiver operating characteristic; AAL, Automated Anatomical Labeling.

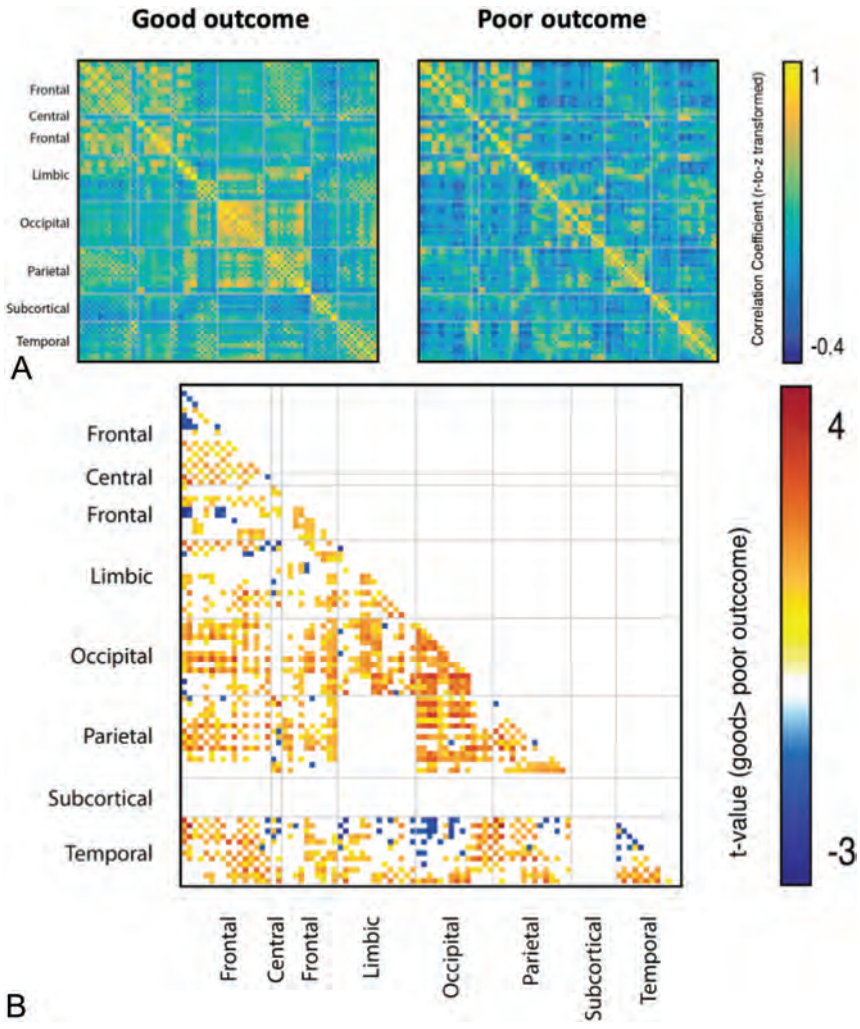

FIG 3. Statistical analysis of the functional network topology of good and poor outcome groups. *A*, Mean functional connectivity matrices of good and poor outcome groups. *B*, Statistical comparison of functional connectivity among all 90 brain regions of the Automated Anatomical Labeling atlas, with a *t*-score given only for significant comparisons ($P < .05$ after correction for multiple comparisons).

algorithm in automatic prediction of coma outcome. We used all the features derived from connectivity matrices of all patients (4005 features × 17 subject matrices) to predict coma outcome using a machine learning classifier (see above) and LOOCV, with and without dimension reduction (using principal component analysis). Without dimension reduction, our linear support vector machine classifier achieved 66.7% overall prediction accuracy. With dimension reduction applied during LOOCV, we achieved 94.4% overall prediction accuracy using a linear support vector machine classifier ($C = 0.1$). This model achieved 100% sensitivity in predicting poor outcome, 87.5% specificity, 100% PPV, and 90% NPV, for an area under the curve of 0.938. Adding a DWI feature (ie, the percentage of brain volume with abnormal ADC values) to the classification model did not change the prediction accuracy.

Finally, we compared automatic outcome prediction based on rs-fMRI and machine learning with prediction based on DWI following the method proposed by Wijman et al.[9] We found that the machine learning classifier trained on rs-fMRI features yielded significantly better prediction accuracy than the DWI method ($P = .025$, two-sided; Fig 4).

DISCUSSION

We wanted to take advantage of the advances in machine learning to assess how functional neuroimaging can improve early prognostication of postanoxic patients in a coma left with an indeterminate prognosis after standard multimodal testing. To this end, we trained and assessed the performance of a machine learning classifier in discriminating between patients with good and poor outcomes based on FC patterns derived from rs-fMRI. We found that automatic prediction based on functional neuroimaging coupled with machine learning methods yielded better prognostication compared with current diffusion neuroimaging methods, especially in terms of identifying patients who would subsequently recover consciousness (ie, good outcome). Additionally, we report on the early changes observed in cortico-cortical FC between good and poor outcome groups in a very difficult group of patients with indeterminate outcome following standard clinical and electrophysiologic tests.

Whole-Brain Functional Connectivity Predicts Coma Outcome

Postanoxic patients in a coma very often undergo MR imaging to identify potential brain lesions and determine neurologic outcome. Conventional MR imaging based solely on structural images was found to underestimate the severity of lesions, notably when performed soon after CA.[26] More recently, DWI was proposed to overcome these failings. It proved sensitive in detecting ischemic lesions soon after CA (2–5 days).[27] It was thus proposed as a neuroimaging tool for early prognostication of postanoxic patients in a coma, because the extent of lesions observed on DWI correlates with neurologic outcome.[9,26,28-30] Recent studies have reported that quantitative DWI based on the extent of impaired brain volume (with a threshold set at 10%, as in our study) offers high specificity for predicting poor outcome in postanoxic patients in a coma, with PPVs between 96%[29] and 100%.[9] However, it was less sensitive in identifying patients with good outcome, with NPVs for poor outcome of between 54%[31] and 73%.[9] Similarly, in our study, we found that quantitative DWI offered very high specificity for predicting poor outcome (100% PPV), yet lower

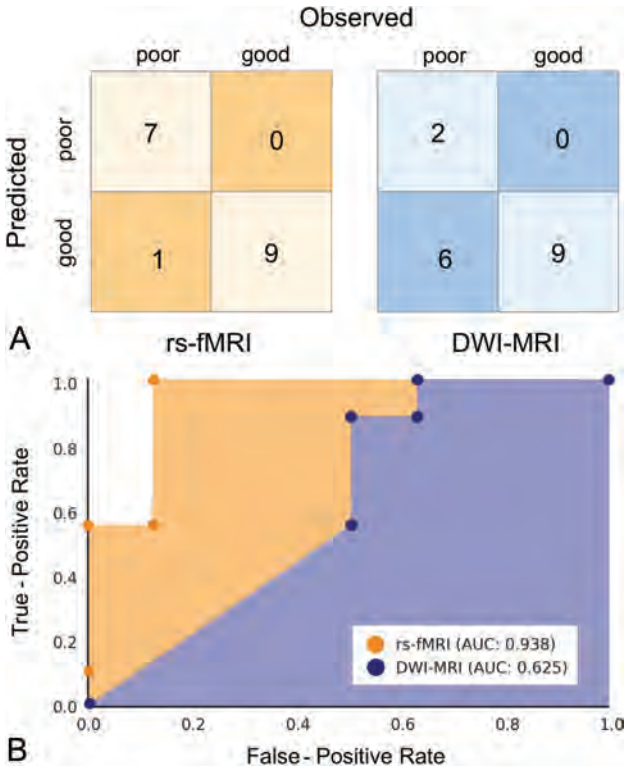

FIG 4. Outcome classification using rs-fMRI and DWI. *A*, Confusion matrix for the rs-fMRI classification using support vector machine (*left*, in orange) and DWI classifications using the model proposed by Wijman et al,[9] 2009 (*right*, in blue). *B*, Receiver operating characteristic curves for rs-fMRI and DWI classification models. AUC indicates area under the curve.

performance for predicting good outcome (60.0% NPV). Thus, both our results and those of recent studies demonstrate that all patients not identified as having poor outcome retain indeterminate prognosis following quantitative DWI analysis. These findings might lead to substantial clinical uncertainty and significant variations in life-sustaining treatments.[7]

Rs-fMRI is available in most specialized large hospitals and has been used successfully to evaluate the state of consciousness of patients with chronic disorders of consciousness or traumatic brain injuries.[18] Here, we used rs-fMRI for early prediction of postanoxic coma outcome in patients left with indeterminate prognosis after standard multimodal testing. We accurately predicted the outcome of 16/17 (94.1%) patients in a coma based on their whole-brain FC at rest. Using a support vector machine classifier with LOOCV was found to offer very high accuracy (100% PPV) for identifying patients with poor outcome, similar to quantitative DWI. However, much higher accuracy for predicting consciousness recovery (ie, NPV for predicting poor outcome) was achievable using rs-fMRI (90%) compared with quantitative DWI (60.0%). This outcome is particularly interesting because there is a critical need to test for predicting good outcome but no widespread and well-accepted tool.

A recent study by Sair et al[20] also evaluated postanoxic patients in a coma, finding that higher default mode network connectivity assessed soon after CA using rs-fMRI correlates with favorable outcome at 1 year, compared with patients with unfavorable outcome. Although the author investigated the long-term neurologic outcome, these results are in line with ours because they also demonstrate that whole-brain FC correlates with outcome in postanoxic patients in a coma. Here, we provide further evidence that rs-fMRI could be used in patients comatose soon after CA. The mean time between CA and fMRI in our cohort was 4 ± 2.9 days versus 12.6 ± 5.6 days for Sair et al. All our patients underwent fMRI between 2 and 8 days after CA, except one who underwent fMRI 13 days after CA due to prior treatment with extracorporeal membrane oxygenation. Despite the delay in recording fMRI, this patient's whole-brain FC was extremely similar to that of the others in the good outcome group. Moreover, our study specifically focused on a group of patients left with indeterminate prognosis after current multimodal testing, excluding patients with catastrophic outcome or patients already conscious, and revealed that automatic outcome prognostication using machine learning based on rs-fMRI outperforms current state-of-the-art DWI methods. Finally, the study by Sair et al did not test whole-brain FC as in the current study. Rather it tested within and between standard topographic network connectivity in terms of the relationship to the outcome.

Overall, our results demonstrate that rs-fMRI achieves significantly better prognostication of postanoxic patients in a coma left with an indeterminate prognosis after standard multimodal testing than DWI, notably with very high accuracy and higher specificity in predicting good outcome. This finding could have a great impact on the identification and clinical management of patients with good outcome, reducing the uncertainty that remains after current multimodal prognostication.

Higher Whole-Brain Functional Connectivity in Patients Recovering from Coma

Whole-brain activity varies greatly depending on states of consciousness, both in healthy volunteers (eg, during sleep or sedation)[31,32] and in patients with disorders of consciousness.[33] Most neuroimaging studies investigating disorders of consciousness have focused on patients with chronic impaired consciousness or compared them with healthy volunteers.[18,34,35] Here, we investigated changes in brain activity in postanoxic patients comatose shortly after CA and found differences in whole-brain FC observable early on between patients with good and poor outcomes, even in the absence of extended lesions on morphologic MR imaging.

Patients with good-versus-poor outcome exhibited higher FC strength between widely distributed cortical areas, especially in the occipital, frontal, parietal, and inferior temporal cortices. This suggests that patients who subsequently recover from comas have better preserved cortico-cortical connectivity, similar to the higher cortico-cortical connectivity in higher states of consciousness observed in patients with chronic disorders of consciousness[18,36] and healthy volunteers under sedation.[37,38] In our study, we could not identify significant connections between the cortex and subcortical regions despite the known role of thalamocortical and other cortical-subcortical connections in consciousness. We reason that this issue is because those connections tend to be weak in states of reduced consciousness, and the patients in our studies were indeed unconscious.

Our results also suggest that recovery from coma relies on better preserved whole-brain cortico-cortical connectivity, plausibly between the frontal and parietal areas, as shown by Crone et al[39] in patients with chronic disorders of consciousness. In our study, the most extensive changes were observed in visual areas (ie, occipital and inferior temporal regions), with higher brain FC exhibited by patients with good outcome, even if they kept their eyes closed in the scanner. Our results are thus in line with the finding of an increased connectivity of visual areas with increased levels of consciousness when comparing chronic comatose patients and healthy volunteers.[40] This is also congruent with the preserved ability for sensory processing[41] and mental imaging[42] observed in patients with a minimal conscious state compared with a vegetative state. Studies assessing brain dynamic FC activity could bring further insight into how the functional brain networks of these patients are reorganized.

Patients with poor outcomes had few higher FC strengths among the focal cortical areas, notably in the temporopolar regions. Given the close link between the temporopolar regions and other limbic areas,[43] these findings might relate to limbic hyperconnectivity observed in patients in chronic comatose and vegetative states.[44]

Overall, we found much higher cortico-cortical connectivity in patients with good outcome, consistent with the findings of higher cortico-cortical connectivity with higher levels of consciousness in both patients and healthy volunteers in other studies. Most interesting, the changes observed in acute postanoxic patients in a coma resemble those reported in patients with chronic consciousness disorders, notably concerning the global higher whole-brain FC found in patients who subsequently recover consciousness.[35] This finding suggests that the changes in whole-brain connectivity observed in chronic disorders of consciousness may develop soon after loss of consciousness. Future studies should, however, repeatedly investigate comatose patients to find further evidence supporting whole-brain FC changes persisting from acute-to-chronic disorders of consciousness.

In our study, we could not identify significant connections between the cortex and subcortical regions despite the known role of thalamocortical and other cortical-subcortical connections in consciousness. We reason that this issue is because those connections tend to be weak in states of reduced consciousness, and the patients in our study were indeed unconscious.

Limitations

Although our results appear promising, they need to be further validated in a larger prospective cohort study, notably using independent training and testing samples to prove the accuracy of rs-fMRI for early outcome prognostication in postanoxic patients in a coma. A major limitation of our study is the small number of patients included, despite screening 351 consecutive patients and identifying 28/351 (8%) eligible ones (increasing to 53/351 [15%] patients if adding the 25 patients with an extracorporeal membrane oxygenation procedure, limiting MR imaging use). We excluded all patients conscious before day 3 or identified with poor prognosis using multimodal testing according to the American Academy of Neurology guidelines.[4] Moreover, we included only patients who were sedation-free during the fMRI session, to avoid drug-induced changes in brain activity. Concerning DWI, previous studies specifically assessed the impact of timing on DWI accuracy. This has not yet been done with fMRI. The essential point of the current study was to perform fMRI early after cardiac arrest and to focus on those cases with uncertain outcome because this scenario is, in our opinion, the most challenging yet, at the same time, clinically most relevant one. The effect of timing of fMRI assessment with respect to coma onset should be specifically assessed, yet this is beyond the scope of our current article. The current investigation did not include a healthy control group because the objective of the current study was to discriminate patients with good-versus-poor outcomes. An additional control group is not necessary for this objective. Although scientifically interesting, the discrimination of patients versus controls is irrelevant from a clinical perspective. Our strict selection of only patients left with indeterminate prognosis after standard multimodal testing soon after CA represents a population in which such diagnostic tests would be crucial for clinical decision-making. On the basis of our inclusion rate, we anticipate that rs-fMRI-based prognostication could be valuable for around 8%–15% of patients in a postanoxic comatose state.

CONCLUSIONS

Using machine learning classification methods, we found that rs-fMRI yields a valuable contribution in the prognostication of postanoxic patients in a coma left with an indeterminate prognosis after standard multimodal testing, notably offering high accuracy for identifying patients with both good (ie, patients who will regain consciousness) and poor (ie, patients who will evolve poorly) outcomes. Our results might thus bridge the gap left in early prognostication of postanoxic patients in a coma by achieving significantly better outcome prediction than current DWI methods. Moreover, our study may contribute to improving understanding of brain FC changes occurring after loss of consciousness, with the early changes reported here mirroring changes observed in chronic comatose patients.

ACKNOWLEDGMENTS

The authors thank Dr Gabrielle Cremer from Cremer Consulting SARL for expert English editing.

Disclosures: Sven Haller—*UNRELATED*: *Payment for Lectures Including Service on Speakers Bureaus*: GE Healthcare. Serge Vulliemoz—*RELATED*: *Grant*: Swiss National Research Foundation, *Comments*: Principal Investigator of 1 current grant and co-Principal Investigator of another*; *Support for Travel to Meetings for the Study or Other Purposes*: Swiss National Research Foundation, *Comments*: travel funding in the context of the grant*; *UNRELATED*: *Stock/Stock Options*: Epilog, Belgium, *Comments*: shareholder of Epilog, a start-up providing electroencephalogram analysis for clinical and research groups. *Money paid to the institution.

REFERENCES

1. Mozaffarian D, Benjamin EJ, Go AS, et al; American Heart Association Statistics Committee and Stroke Statistics Subcommittee. **Heart disease and stroke statistics–2015 update: a report from the American Heart Association.** *Circulation* 2015;131:e29–322 CrossRef Medline

2. Atwood C, Eisenberg MS, Herlitz J, et al. **Incidence of EMS-treated out-of-hospital cardiac arrest in Europe.** *Resuscitation* 2005;67:75–80 CrossRef Medline
3. Grasner JT, Lefering R, Koster RW, et al. **EuReCa ONE-27 Nations, ONE Europe, ONE Registry: a prospective one-month analysis of out-of-hospital cardiac arrest outcomes in 27 countries in Europe.** *Resuscitation* 2016;105:188–95 CrossRef Medline
4. Wijdicks EF, Hijdra A, Young GB, et al; Quality Standards Subcommittee of the American Academy of Neurology. **Practice parameter: prediction of outcome in comatose survivors after cardiopulmonary resuscitation (an evidence-based review)—report of the Quality Standards Subcommittee of the American Academy of Neurology.** *Neurology* 2006;67:203–10 CrossRef Medline
5. Sandroni C, Cavallaro F, Callaway CW, et al. **Predictors of poor neurological outcome in adult comatose survivors of cardiac arrest: a systematic review and meta-analysis, Part 2: patients treated with therapeutic hypothermia.** *Resuscitation* 2013;84:1324–38 CrossRef Medline
6. Sandroni C, Cavallaro F, Callaway CW, et al. **Predictors of poor neurological outcome in adult comatose survivors of cardiac arrest: a systematic review and meta-analysis, Part 1: patients not treated with therapeutic hypothermia.** *Resuscitation* 2013;84:1310–23 CrossRef Medline
7. Weijer C, Bruni T, Gofton T, et al. **Ethical considerations in functional magnetic resonance imaging research in acutely comatose patients.** *Brain* 2016;139:292–99 CrossRef Medline
8. Mlynash M, Campbell DM, Leproust EM, et al. **Temporal and spatial profile of brain diffusion-weighted MRI after cardiac arrest.** *Stroke* 2010;41:1665–72 CrossRef Medline
9. Wijman CA, Mlynash M, Caulfield AF, et al. **Prognostic value of brain diffusion-weighted imaging after cardiac arrest.** *Ann Neurol* 2009;65:394–402 CrossRef Medline
10. Choi SP, Park KN, Park HK, et al. **Diffusion-weighted magnetic resonance imaging for predicting the clinical outcome of comatose survivors after cardiac arrest: a cohort study.** *Crit Care* 2010;14:R17 CrossRef Medline
11. Rossetti AO, Oddo M, Logroscino G, et al. **Prognostication after cardiac arrest and hypothermia: a prospective study.** *Ann Neurol* 2010;67:301–07 CrossRef Medline
12. Stevens RD, Hannawi Y, Puybasset L. **MRI for coma emergence and recovery.** *Curr Opin Crit Care* 2014;20:168–73 CrossRef Medline
13. Park JS, Lee SW, Kim H, et al. **Efficacy of diffusion-weighted magnetic resonance imaging performed before therapeutic hypothermia in predicting clinical outcome in comatose cardiopulmonary arrest survivors.** *Resuscitation* 2015;88:132–37 CrossRef Medline
14. Hirsch KG, Mlynash M, Jansen S, et al. **Prognostic value of a qualitative brain MRI scoring system after cardiac arrest.** *J Neuroimaging* 2015;25:430–37 CrossRef Medline
15. Keijzer HM, Hoedemaekers CW, Meijer FJ, et al. **Brain imaging in comatose survivors of cardiac arrest: pathophysiological correlates and prognostic properties.** *Resuscitation* 2018;133:124–36 CrossRef Medline
16. Shehzad Z, Kelly AM, Reiss PT, et al. **The resting brain: unconstrained yet reliable.** *Cereb Cortex* 2009;19:2209–29 CrossRef Medline
17. Sharp DJ, Scott G, Leech R. **Network dysfunction after traumatic brain injury.** *Nat Rev Neurol* 2014;10:156–66 CrossRef Medline
18. Vanhaudenhuyse A, Noirhomme Q, Tshibanda LJ, et al. **Default network connectivity reflects the level of consciousness in non-communicative brain-damaged patients.** *Brain* 2010;133:161–71 CrossRef Medline
19. Edlow BL, Chatelle C, Spencer CA, et al. **Early detection of consciousness in patients with acute severe traumatic brain injury.** *Brain* 2017;140:2399–2414 CrossRef Medline
20. Sair H, Hannawi Y, Li S, et al; For the Neuroimaging for Coma Emergence and Recovery (NICER) Consortium. **Early functional connectome integrity and 1-year recovery in comatose survivors of cardiac arrest.** *Radiology* 2018;287:247–55 CrossRef Medline
21. Callaway CW, Donnino MW, Fink EL, et al. **Part 8: Post-Cardiac Arrest Care:—2015 American Heart Association Guidelines Update for Cardiopulmonary Resuscitation and Emergency Cardiovascular Care.** *Circulation* 2015;132:S465–82 CrossRef Medline
22. Nolan JP, Soar J, Cariou A, et al. **European Resuscitation Council and European Society of Intensive Care Medicine Guidelines for Post-resuscitation Care 2015: Section 5 of the European Resuscitation Council Guidelines for Resuscitation 2015.** *Resuscitation* 2015;95:202–22 CrossRef Medline
23. Leonardi N, Richiardi J, Gschwind M, et al. **Principal components of functional connectivity: a new approach to study dynamic brain connectivity during rest.** *Neuroimage* 2013;83:937–50 CrossRef Medline
24. Richiardi J, Eryilmaz H, Schwartz S, et al. **Decoding brain states from fMRI connectivity graphs.** *Neuroimage* 2011;56:616–26 CrossRef Medline
25. Meskaldji DE, Fischi-Gomez E, Griffa A, et al. **Comparing connectomes across subjects and populations at different scales.** *Neuroimage* 2013;80:416–25 CrossRef Medline
26. Wijdicks EF, Campeau NG, Miller GM. **MR imaging in comatose survivors of cardiac resuscitation.** *AJNR Am J Neuroradiol* 2001;22:1561–65 CrossRef Medline
27. Mintorovitch J, Moseley ME, Chileuitt L, et al. **Comparison of diffusion- and T2-weighted MRI for the early detection of cerebral ischemia and reperfusion in rats.** *Magn Reson Med* 1991;18:39–50 CrossRef Medline
28. Hastie T, Tibshirani R, Friedman J. *The Elements of Statistical Learning: Data Mining, Inference, and Prediction*. Springer; 2009
29. Hirsch KG, Mlynash M, Eyngorn I, et al. **Multi-center study of diffusion-weighted imaging in coma after cardiac arrest.** *Neurocrit Care* 2016;24:82–89 CrossRef Medline
30. Wu X, Zou Q, Hu J, et al. **Intrinsic functional connectivity patterns predict consciousness level and recovery outcome in acquired brain injury.** *J Neurosci* 2015;35:12932–46 CrossRef Medline
31. Boveroux P, Vanhaudenhuyse A, Bruno MA, et al. **Breakdown of within- and between-network resting state functional magnetic resonance imaging connectivity during propofol-induced loss of consciousness.** *Anesthesiology* 2010;113:1038–53 CrossRef Medline
32. Peltier SJ, Kerssens C, Hamann SB, et al. **Functional connectivity changes with concentration of sevoflurane anesthesia.** *Neuroreport* 2005;16:285–88 CrossRef Medline
33. Laureys S, Schiff ND. **Coma and consciousness: paradigms (re)framed by neuroimaging.** *Neuroimage* 2012;61:478–91 CrossRef Medline
34. Owen AM, Coleman MR. **Functional neuroimaging of the vegetative state.** *Nat Rev Neurosci* 2008;9:235–43 CrossRef Medline
35. Hannawi Y, Lindquist MA, Caffo BS, et al. **Resting brain activity in disorders of consciousness: a systematic review and meta-analysis.** *Neurology* 2015;84:1272–80 CrossRef Medline
36. Boly M, Tshibanda L, Vanhaudenhuyse A, et al. **Functional connectivity in the default network during resting state is preserved in a vegetative but not in a brain dead patient.** *Hum Brain Mapp* 2009;30:2393–2400 CrossRef Medline
37. Greicius MD, Kiviniemi V, Tervonen O, et al. **Persistent default-mode network connectivity during light sedation.** *Hum Brain Mapp* 2008;29:839–47 CrossRef Medline
38. Noirhomme Q, Soddu A, Lehembre R, et al. **Brain connectivity in pathological and pharmacological coma.** *Front Syst Neurosci* 2010;4:160 CrossRef Medline

39. Crone JS, Soddu A, Holler Y, et al. **Altered network properties of the fronto-parietal network and the thalamus in impaired consciousness.** *Neuroimage Clin* 2014;4:240–48 CrossRef Medline
40. Achard S, Delon-Martin C, Vertes PE, et al. **Hubs of brain functional networks are radically reorganized in comatose patients.** *Proc Natl Acad Sci USA* 2012;109:20608–13 CrossRef Medline
41. Demertzi A, Antonopoulos G, Heine L, et al. **Intrinsic functional connectivity differentiates minimally conscious from unresponsive patients.** *Brain* 2015;138:2619–31 CrossRef Medline
42. Monti MM, Vanhaudenhuyse A, Coleman MR, et al. **Willful modulation of brain activity in disorders of consciousness.** *N Engl J Med* 2010;362:579–89 CrossRef Medline
43. Chabardes S, Kahane P, Minotti L, et al. **Anatomy of the temporal pole region.** *Epileptic Disord* 2002;4(Suppl 1):S9–15 Medline
44. Di Perri C, Bastianello S, Bartsch AJ, et al. **Limbic hyperconnectivity in the vegetative state.** *Neurology* 2013;81:1417–24 CrossRef Medline

Long-Term Outcomes of the WEB Device for Treatment of Wide-Neck Bifurcation Aneurysms

M. Fujimoto, I. Lylyk, C. Bleise, P. Albiña, J. Chudyk, and P. Lylyk

ABSTRACT

BACKGROUND AND PURPOSE: Treatment of wide-neck bifurcation aneurysms using endovascular therapy is still challenging even with the development of treatment devices. The purpose of this investigation was to assess the safety and efficacy of treatment with a Woven EndoBridge (WEB) device for wide-neck bifurcation aneurysms.

MATERIALS AND METHODS: All patients treated with a WEB device at our institution between May 2009 and November 2016 were retrospectively evaluated. Clinical and imaging evaluation, aneurysm occlusion status, and modified Rankin scale score were analyzed 1 day after treatment and in the short- (<6 months), mid- (<24 months), and long-term (>24 months) follow-up periods.

RESULTS: Forty-one cases of wide-neck aneurysms were analyzed in this study. Overall, 78.8% of the aneurysms had complete occlusion in the last follow-up, and 19.5% required retreatment with additional endovascular devices. A good clinical outcome (modified Rankin scale: 0–2) was obtained in 95.1% of the patients, and the overall treatment-related morbidity and mortality rates were 2.4% and 0.0%, respectively. The mean follow-up time was 15.3 ± 13.5 months.

CONCLUSIONS: The results obtained in this study suggest that treatment of wide-neck bifurcation aneurysms with a WEB device is feasible with an acceptable safety and efficacy rate.

ABBREVIATIONS: IA = intracranial aneurysm; WEB = Woven EndoBridge; WEB-DL = Woven EndoBridge Dual-Layer; WEB-SL/SLS = Woven EndoBridge Single-Layer and Single-Layer Sphere; AcomA = anterior communicating artery

In recent years, an improvement in devices and techniques has resulted in an increase in endovascular treatment of intracranial aneurysms (IAs). Although the efficacy of endovascular therapy has been recognized widely, wide-neck bifurcation aneurysms still are considered unsuitable for endovascular therapy because of unfavorable geometry or daughter-vessel involvement.[1-4] Recently, the promising efficacy and safety profile of the novel Woven EndoBridge (WEB) device (Sequent Medical) for wide-neck bifurcation aneurysm treatment has been published in major clinical studies.[5,6] However, only a few case series have reported the long-term follow-up results for this device; therefore, the long-term results still remain to be determined.[7]

The purpose of this study was to analyze the mid- and long-term results of wide-neck bifurcation aneurysms treated with the WEB device and assess its safety and efficacy profile.

MATERIALS AND METHODS

Patient Population

Approval from the ethics committee was obtained before this study was conducted, and all patients gave written informed consent. A total of 39 patients with unruptured wide-necked IAs who were admitted to our institution and treated with the WEB device between May 2009 and November 2016 were retrospectively reviewed in this study. Indications for treatment of an aneurysm with this device were decided independently by 2 interventional neuroradiologists according to particular aneurysm characteristics.

Device

The WEB device is a self-expanding flow disruption device for the treatment of wide-neck and bifurcation IAs. The original WEB device, WEB Dual-Layer (WEB-DL), was a dual-layer nitinol braided intravascular device containing 2 components. The WEB Single-Layer (WEB-SL) and WEB Single-Layer-Sphere

Received January 6, 2020; accepted after revision March 30.

From the Department of Neurosurgery (M.F.), Shin-Yurigaoka General Hospital, Kawasaki, Japan; Clinica Sagrada Familia (M.F., I.L., C.B., J.C., P.L.), ENERI, Buenos Aires, Argentina; and Department of Neurosurgery (P.A.), Hospital Barros Luco Trudeau, University of Santiago, Santiago, Chile.

Please address correspondence to Michio Fujimoto, MD, PhD, 255 Furusawa, Asao-Ku, Kawasaki-Shi, Kanagawa, 215-0026, Japan; e-mail: michio19741111@gmail.com

http://dx.doi.org/10.3174/ajnr.A6548

(WEB-SLS) devices, each consisting of 1 component, were released after WEB-DL. The patients in this study were treated with WEB-DL devices until June 2014 and then with WEB-SL or WEB-SLS devices, according to the surgical decision.

Antiplatelet Therapy

For unruptured IAs, antiplatelet therapy pre- and posttreatment was given according to our institutional protocol, with 100 mg of aspirin daily and 75 mg of clopidogrel daily 7 days before treatment. Systemic heparinization was adjusted to be 2–3 times the normal activated clotting time during the procedure. Clopidogrel was stopped in most patients, depending on the result of the treatment. However, aspirin was continued at least until the first angiographic control.

Aneurysm Characteristics

Suitable aneurysms for using the WEB device included those with wide-neck morphology, located at bifurcations at the or middle cerebral artery, anterior communicating artery (AcomA), internal carotid artery, or basilar artery. Aneurysm size of those included in the study ranged between 4 and 11 mm in diameter because this was the recommended size for using the WEB device by the manufacturer. Wide-neck morphology was defined as a neck width $\geq$4 mm or a dome-to-neck ratio $<$2.

Data Collection

Clinical data were collected for each patient including the following factors: age, sex, history of hypertension, family history of subarachnoid hemorrhage, aneurysm location, aneurysm size (height and width), neck size, type and size of device used, complications during and after the procedure, additional devices used during the procedure, and mRS score both at discharge and in the last follow-up.

Data Analysis

Clinical and imaging evaluation was performed 1 day after treatment and in the short-, mid-, and long-term follow-up periods. Short-term follow-up was defined as the examination performed within 6 months after the procedure, midterm follow-up as within 2 years, and long-term follow-up as $>$2 years after treatment. Anatomic results in each follow-up period were evaluated in all aneurysms using DSA. Occlusion status was assessed by Raymond-Roy occlusion classification (complete occlusion, residual neck, and residual aneurysm).[8] The opacification of the proximal recess of the WEB device was considered complete occlusion in this scale.[7] Good clinical outcome was defined as an mRS score of 0–2.[9] Treatment-related morbidity in the last follow-up was defined as an mRS score $>$2 or an increase of more than 1 point in the mRS score compared with pretreatment status. In addition, we calculated the difference between the size of the aneurysm and the WEB device used in each procedure. Angiographic evaluation of occlusion status was analyzed independently by an interventional neuroradiologist and a neurosurgeon, and clinical status, including mRS score, was assessed by a neurologist.

Statistical Analysis

Descriptive data were expressed as the mean $\pm$ SD for quantitative variables and as the frequency with percentage for qualitative variables. Qualitative variables were compared using the Fisher exact test, and quantitative variables were evaluated by the Mann-Whitney *U* test with GraphPad Prism 6 (GraphPad Software). Differences were deemed statistically significant at $P < .05$.

RESULTS

Patients

A total of 47 patients (40 women and 7 men) with 49 aneurysms were enrolled in this study. The patients who did not undergo follow-up and who had an SAH were excluded from the evaluation (8 patients). Hence, a total of 39 patients (32 women and 7 men) with 41 unruptured aneurysms were analyzed in this study. Multiple procedures were necessary because of multiple aneurysms (2 patients). The mean age was 63.5 $\pm$ 7.8 years.

Aneurysms and Devices

Twenty-nine aneurysms were located at the MCA bifurcation (29/41, 70.0%), 9 at the AcomA (9/41, 21.9%), 1 at the ICA terminus (1/41, 2.4%), and 2 at the tip of the basilar artery (2/41, 4.8%).

Forty-one aneurysms were unruptured (100%). The mean aneurysm size was 7.6 $\pm$ 1.9 (4.4–11.0) mm, and the mean aneurysm neck size was 5.5 $\pm$ 1.6 (3.5–8.0) mm. Five aneurysms were considered large ($<$25 mm) (5/41, 12.1%). The mean dome-to-neck ratio was 1.3 $\pm$ 0.25 (0.8–1.6). Thirty-one aneurysms were treated with the WEB-DL device (75.6%), 9 with the WEB-SL device (21.9%), and 1 with the WEB-SLS device (2.4%). Technical success was achieved in 39 (95.1%) cases, and technical failure caused by the inappropriate size of the WEB device was recognized in 2 cases. In these 2 cases, another size of the WEB device was placed successfully. Additional intracranial stent placement was required in 2 cases because of device protrusion into the parent artery (Fig 1).

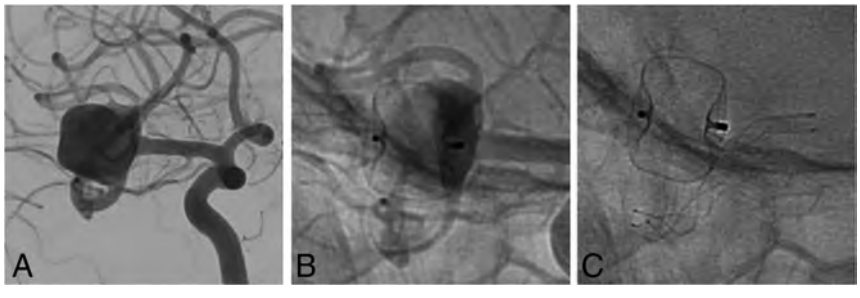

FIG 1. *A*, Angiogram shows right MCA bifurcation aneurysm with a wide neck. *B*, The WEB device protruding into the parent artery is causing flow reduction in the M2 segment. *C*, Radiograph demonstrating an LVIS stent (MicroVention) placed in the MCA elevates the distal edge of the WEB device.

Aneurysm Follow-Up

The overall mean follow-up time was 15.4 $\pm$ 13.4 (2–67) months. The angiographic results for each follow-up are summarized in Table 1. Twenty-one of 41 (51.2%) aneurysms were evaluated the following day. Complete occlusion

Table 1: Results of treatment at each follow-up

	Initial Follow-Up % (n = 21)	Short-Term (<6 Months) % (n = 24)	Midterm (6–24 Months) % (n =28)	Long-Term (>24 Months) % (n = 8)
Complete occlusion	71.4 (15)	62.5 (15)	57.1 (16)	62.5 (5)
Residual neck	28.5 (6)	16.8 (4)	17.8 (5)	25.0 (2)
Residual aneurysm	0.0 (0)	20.8 (5)	25.0 (7)	12.5 (1)
Retreatment	0.0 (0)	0.0 (0)	17.8 (6)	25.0 (2)

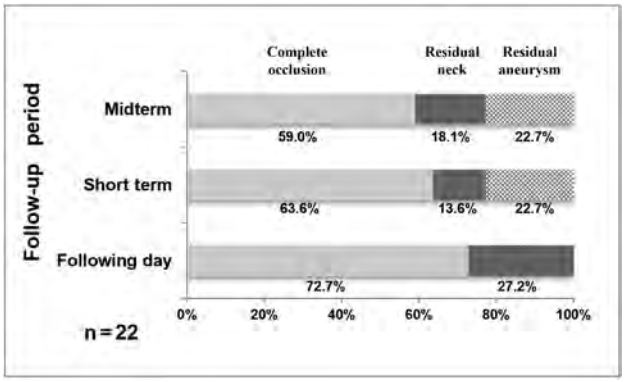

FIG 2. Occlusion state at each period in the midterm follow-up group.

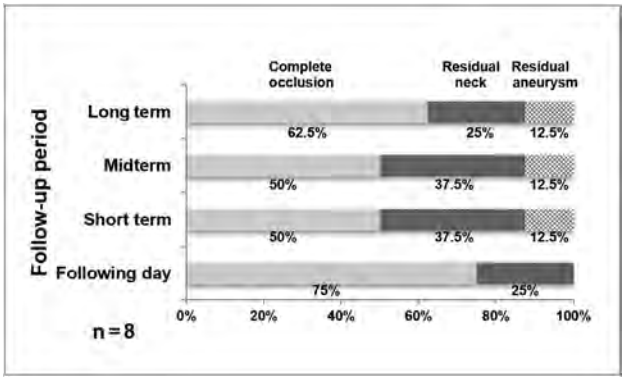

FIG 3. Occlusion state at each period in the long-term follow-up group.

was seen in 15/21 (71.4%) and residual neck in 6/21 (28.5%). Short-term follow-up (4.1 ± 1.0 months) was obtained in 24 aneurysms. Complete occlusion was seen in 15/24 (62.5%), residual neck in 4/24 (16.8%), and residual aneurysm in 5/24 (20.8%). No patient required retreatment. Midterm follow-up (12.8 ± 6.3 months) was obtained in 28 aneurysms. Complete occlusion was seen in 16/28 (57.1%), residual neck in 5/28 (17.8%), and residual aneurysm in 7/28 (25.0%). Six aneurysms required additional devices (coiling, stent-assisted coiling, pCONus, or pCANvas device [phenox]) during this period. Twenty-two of 28 aneurysms of the midterm group had angiographic images in all follow-up periods (the following day, short-term, and midterm) (Fig 2). Complete occlusion, residual neck, and residual aneurysm in the short-term period were 63.6%, 13.6%, and 22.7%, respectively, and in the midterm period were 59.0%, 18.1%, and 22.7%, respectively. Long-term follow-up (35.8 ± 13.1 months) was obtained for 8 patients, excluding 6 patients who were retreated with additional devices during the midterm follow-up period. All patients of the long-term group achieved angiographic follow-up in all periods. Complete occlusion was seen in 5/8 (62.5%), residual neck in 2/8 (25.0%), and residual aneurysm in 1/8 (12.5%) (Fig 3). In this group, 2 patients required additional stent-assisted coiling in the long-term period. Overall aneurysm anatomic outcome without retreatment in the last follow-up was as follows: complete occlusion was achieved in 26/33 aneurysms (78.8%), residual neck in 5/33 (15.1%), and residual aneurysm in 2/33 (6.0%). Retreatment for residual aneurysm or neck within the follow-up was required for 8/41 (19.5%) (Table 2). One aneurysm (2.4%) with residual neck in the midterm follow-up left untreated spontaneously occluded in the long-term follow-up. Two aneurysms (4.8%) with residual neck in the short-term follow-up worsened when reaching the midterm follow-up. All occluded aneurysms in the midterm follow-up were stable and continued to be occluded in the long-term follow-up. To clarify the potential factors affecting retreatment, all aneurysms except for those in the patients evaluated only in the short-term period (31 aneurysms) were divided into 2 groups: patients who required retreatment and patients who did not. The characteristics of each group are shown in Table 3. There were no statistically significant differences between the 2 groups in patient characteristics of age, sex, history of hypertension, and family history of SAH. Additionally, neck size, aneurysm location (MCA or AcomA), dome-to-neck ratio, and type of WEB device (DL or SL/SLS) were not associated with retreatment. However, the aneurysm height (P = .026), the aneurysm width (P = .029), and the height difference between the aneurysm and the WEB device (P = .038) were significantly greater in the retreatment group than in the group without retreatment.

Complications

No intraoperative rupture was observed. Periprocedural thromboembolic events were observed in 5/41 (12.1%) cases. Among these, thrombus formation at the aneurysm neck was observed in 3 cases, and additional treatment, such as mechanical thrombectomy (in 1 patient) or additional intracranial stent placement (in 2 patients), was required. Nevertheless, the 3 patients recovered without neurologic deficit. After the procedure, a transient ischemic attack occurred in 1 patient within the first 24 hours. Cerebral infarction caused by occlusion of the distal portion of the anterior cerebral artery was observed in 1 patient with an AcomA aneurysm 4 days later. This patient developed lower limb palsy remaining until the last clinical follow-up.

Clinical Follow-Up

All enrolled patients were evaluated before treatment and at their last angiographic follow-up. Overall, a good clinical outcome (mRS score: 0–2) was observed in 39/41patients (95.1%). Clinical worsening related to an ischemic complication was observed in only 1 patient (2.4%) in our entire series. One patient died during

Table 2: Characteristics of patients and aneurysms of retreatment cases

Patient No.	Sex	Age (yr)	Location	W (mm)	H (mm)	D/N Ratio	WEB Type	Follow-Up Period of Retreatment	Additional Device
1	F	54	MCA	10.1	10.5	1.7	DL	Midterm	Y stent and coils
2	F	62	MCA	5.4	5.6	1.2	DL	Midterm	Stent and coils
3	F	65	AcomA	11	10	1.5	DL	Midterm	Stent and coils
4	F	71	AcomA	9	8	1.3	DL	Midterm	Stent and coils
5	F	63	MCA	10	9	1.7	DL	Long-term	pCONus and coils
6	F	67	AcomA	9	8	1.5	DL	Midterm	Stent and coils
7	F	67	AcomA	11	8	1.3	DL	Midterm	pCANvas
8	F	55	MCA	5	6	1.3	DL	Long-term	Stent and coils

Note:—D/N ratio indicates dome-to-neck ratio; H, aneurysm height; W, aneurysm width.

Table 3: Comparison of patients, aneurysms, and device characteristics according to the presence of retreatment

	Retreatment		
	Present	Absent	*P* Value
Number of patients (n)	8	23	
Patient characteristics			
Age, y (average ± SD)	63.0 ± 5.9	62.2 ± 8.0	.929
Male/female	0/8	7/28	.31
Hypertension	4/8 (50%)	16/33 (48%)	.938
Family history	1/8 (12.5%)	2/33 (6%)	.488
Aneurysm characteristics			
Height (mm)	8.13 ± 1.72	6.36 ± 1.85	.026
Width (mm)	8.81 ± 2.35	6.73 ± 1.83	.029
Neck (mm)	6.03 ± 1.36	5.34 ± 1.36	.112
Dome-to-neck ratio	1.44 ± 0.19	1.28 ± 0.19	.132
Aneurysm location			
AcomA	4/8 (50%)	5/33 (15%)	.054
MCA	4/8 (50%)	25/33 (75%)	.202
Device characteristics			
Height difference from the aneurysm	−2.39 ± 0.86	−1.40 ± 1.20	.038
Width difference from the aneurysm	−0.69 ± 1.35	0.36 ± 0.92	.055
DL/SL&SLS	8/0	23/10	.162

the midterm follow-up as a consequence of an uncontrolled disease unrelated to the treatment. Overall, treatment-related morbidity and mortality rates were 2.4% and 0.0%, respectively.

DISCUSSION

Treatment of wide-neck bifurcation aneurysms using endovascular therapy is still challenging even with the development of devices. Therefore, the purpose of this study was to evaluate the safety and efficacy of the WEB device in the treatment of patients with wide-neck bifurcation IAs. Forty-one cases of wide-neck aneurysms were analyzed in this study. Overall, 78.8% of aneurysms had complete occlusion in the last follow-up, and 19.5% required retreatment with additional endovascular devices. A good clinical outcome (mRS score: 0–2) was obtained in 95.1% of the patients, and overall treatment-related morbidity and mortality rates were 2.4% and 0.0%, respectively (mean follow-up time: 15.4 ± 13.4 months). The results exhibited by this study indicate that treatment for this kind of aneurysm with the WEB device is feasible with an acceptable safety and efficacy rate.

Device

The WEB device is a flow disruption device developed for the treatment of wide-neck and bifurcation IAs, which are unfavorable to treat with conventional coiling or with adjunctive techniques such as balloon-assisted coiling or stent-assisted coiling. In other words, this device may be helpful for the treatment of complex aneurysms, such as MCA bifurcation, AcomA, basilar artery, and ICA terminus. In fact, among the population analyzed in this study, the MCA bifurcation and the AcomA were the most common locations, involving 71.4% and 21.4% of the aneurysms treated, respectively.

Angiographic Outcome

Several multicenter studies have showed the effectiveness and safety of the WEB device in the treatment of IAs. The WEB Clinical Assessment of Intrasaccular Aneurysm Therapy (WEBCAST) study, which evaluated 51 aneurysms, including 3 ruptured aneurysms (5.9%), treated with the WEB DL device, demonstrated an 85.4% adequate occlusion rate in the 6-month follow-up and showed low morbidity (2.0%) and mortality (0.0%) rates in the last follow-up.[5] Recently, a few studies have demonstrated the mid- and long-term results for IAs treated with the WEB device.[10-13] Mine et al[14] demonstrated rates of 72.3% complete occlusion and 27.2% neck remnant at the long-term follow-up (median: 24 months). The former study included a patient who was retreated when calculating the angiographic outcome; our analysis, however, excluded patients who were not treated exclusively with the WEB device to demonstrate the true effectiveness of the device. In the following study, Pierot et al[7] published the long-term (median: 27.4 months) result for the WEB-DL device; they reported complete occlusion in 68.4%,

neck remnant in 15.8%, and aneurysm remnant in 15.8%. Despite the large proportion of MCA bifurcation and AcomA aneurysms in the former study, their outcome results were equivalent to a recent meta-analysis regarding the treatment of wide-neck aneurysms using conventional endovascular modalities (coiling or stent-assisted coiling), which showed a complete or near-complete occlusion rate of 71.9%.[15] Compared with the current literature, our results may be considered at least equal (complete occlusion rate in 79.4%).[5,7,10,12,16] However, in the mid- and long-term groups with data obtained in all observation periods (ie, except cases observed only for the short-term period), complete occlusions were achieved in 59.0% in the midterm group and 62.5% in the long-term group; the results are lower than the overall outcome. These results are considered as a result of the complete occlusion obtained in the short-term period, and the following observation was interrupted in some cases. Our study had a relatively high proportion of MCA bifurcation IAs (71.4%) compared with the WEBCAST2 study (45.5%), a currently controversial aneurysmal location considered difficult for endovascular treatment in general, further emphasizing the efficacy of this device.[10]

Complications

Thromboembolic complications are some of the main concerns in treatment with the WEB device. Large aneurysm size, wide-neck morphology, and coil protrusion are considered risk factors for thromboembolic complications in conventional endovascular therapy.[17,18] The thromboembolic complication rate related to conventional endovascular therapy, including assisted-coiling techniques, has been reported in several studies (4.3%–20.8%).[2,3,19-21] On the other hand, the thromboembolic complication rate related to WEB device treatment has been considered to be higher than conventional endovascular therapy (9.0%–23.5%).[5,7,10,16,22] Our results concerning thromboembolic complications (11.9%) were in line with previously published data, which is probably related to the high proportion of aneurysms considered high risk included in this series. Thrombus formation was observed at the neck level in 4 cases; in all of these cases, a WEB device protrusion into the parent artery was previously recognized. Thrombus formation at the aneurysm neck has already been reported in other studies.[6,16,22] Consequently, a WEB device protrusion into the parent artery, causing luminal narrowing and blood flow focal slowing, was considered as a risk factor for thrombus formation. Hence, an appropriate device and aneurysm selection are considered to be crucial for reducing this kind of complication.

Retreatment

Of the study patients, 19.5% (8/41) required retreatment (Table 3). The retreatment rate was relatively high compared with previous long-term series (11.5%–16.3%).[7,14] Proper indications and timing for retreatment have not been established yet. The uncertainty for this decision among different endovascular teams could be one of the reasons for our high retreatment rate. In the WEBCAST2 study, all the patients who required retreatment had it between the short- (4.8 ± 2.5 months) and midterm follow-up (14.9 ± 8.3 months) periods, with no retreatment performed between the mid- and long-term follow-up (27.9 ± 13.7 months) periods. Furthermore, spontaneous improvement in occlusion was not recognized in their study.[10] On the other hand, in the present study, retreatment was performed in the mid- (12.8 ± 6.3 months) or long-term (35.8 ± 13.1 months) follow-up periods when the aneurysm status was angiographically diagnosed as a residual aneurysm. Among all cases, the occlusion state improved spontaneously during follow-up in only 1 case with a residual neck in the midterm period, and no spontaneous improvement from a state of residual aneurysm was observed over the whole follow-up period. Therefore, the retreatment was carried out, especially in the case in which the residual aneurysm state continued in the short- and midterm follow-up periods or in the case in which the obstruction state worsened at the midterm period.

Our higher retreatment rate compared with the former could be related, at least partially, to our long period of observation, highlighting the importance of further studies with longer angiographic and clinical follow-up.

As shown in 2 cases from our study, even if complete occlusion has been achieved in the short-term follow-up, a worsening in the occlusion status could happen on further angiographic evaluation. Our team concluded that when residual neck or aneurysm is recognized in the first 6 months since treatment, it is recommended to propose a new treatment in the following period.

Factors Affecting Retreatment and Occlusion

Although several studies presented the usefulness of the WEB device, retreatment was needed in some cases. A small number of studies reported the factors associated with retreatment. Unruptured aneurysms, anterior circulation, and aneurysm neck size of 4–10 mm were shown in a meta-analysis as proper conditions for treatment with the WEB device.[23] In addition, Herbreteau et al[24] analyzed WEB shape modification due to WEB compression. According to their study, the results implied association between the WEB shape modification and adequate occlusion. However, there was no difference between WEB sizing and occlusion status.

In the present study, we found that the aneurysm height, width, and height difference between the aneurysm and the WEB device were significantly greater in the retreatment group than in the group without retreatment. From these results, the risk of retreatment was considered to increase in the case of larger aneurysms or when the aneurysm was treated with undersized WEB. Whenever we choose any size of the WEB for treatment, especially in the case of a vertically long aneurysm, the size of the WEB could be relatively small. The factors related to the aneurysm occlusion status were also investigated. All aneurysms were divided into 2 groups: complete and incomplete occlusion (residual neck and residual aneurysm). As a result, aneurysm height ($P = .008$), width ($P = .003$), and neck size ($P = .004$) and the height difference between the aneurysm and the WEB device ($P = .003$) were significantly greater in the incomplete occlusion group than in the complete occlusion group. Furthermore, the type of WEB device showed no significant difference between the 2 groups. This result matched a recent long-term follow-up study, indicating a similar complete occlusion rate in both types of devices (WEB-DL: 50.8%; WEB-SL/SLS: 51.7%).[25]

Limitations

This study has several limitations. First, it has a limited number of patients, and only 8 patients had long-term angiographic follow-

up after being treated exclusively with the WEB device (6 patients were excluded because of retreatment). Nonetheless, this study gave us important information regarding the course of aneurysm occlusion and the timing for retreatment. Another limitation may be represented by a selection bias toward aneurysm location, with MCA bifurcation IAs accounting for 71.4% of the entire series. However, given that this location is considered one of the most challenging for endovascular treatment, the data obtained here allow us to further consider the WEB device as a feasible option for the treatment of MCA bifurcation IAs.

CONCLUSIONS

This study shows the safety and efficacy of the WEB device for the treatment of wide-neck bifurcation IAs in a long-term follow-up. The WEB device should be considered a valuable option for the treatment of aneurysms deemed unsafe to treat with other endovascular modalities. Further studies are needed to establish the appropriate indications for this device.

ACKNOWLEDGMENTS

We would like to thank Editage (www.editage.com) for English language editing.

Disclosures: Carlos Bleise—*UNRELATED: Employment:* ENERI-Sagrada Familia.

REFERENCES

1. Chalouhi N, Jabbour P, Singhal S, et al. **Stent-assisted coiling of intracranial aneurysms: predictors of complications, recanalization, and outcome in 508 cases.** *Stroke* 2013;44:1348–53 CrossRef Medline
2. Blackburn SL, Abdelazim AM, Cutler AB, et al. **Endovascular and surgical treatment of unruptured MCA aneurysms: meta-analysis and review of the literature.** *Stroke Res Treat* 2014;2014:1–11 CrossRef
3. De Leacy RA, Fargen KM, Mascitelli JR, et al. **Wide-neck bifurcation aneurysms of the middle cerebral artery and basilar apex treated by endovascular techniques: a multicentre, core lab adjudicated study evaluating safety and durability of occlusion (BRANCH).** *J NeuroIntervent Surg* 2019;11:31–36 CrossRef
4. Lylyk P, Chudyk J, Bleise C, et al. **Treatment of wide-necked bifurcation aneurysms: initial results with the pCANvas neck bridging device.** *Clin Neuroradiol* 2019;29:467–77 CrossRef Medline
5. Pierot L, Costalat V, Moret J, et al. **Safety and efficacy of aneurysm treatment with WEB: results of the WEBCAST study.** *J Neurosurg* 2016;124:1250–56 CrossRef Medline
6. Pierot L, Moret J, Turjman F, et al. **WEB treatment of intracranial aneurysms: feasibility, complications, and 1-month safety results with the WEB DL and WEB SL/SLS in the French observatory.** *AJNR Am J Neuroradiol* 2015;36:922–97 CrossRef
7. Pierot L, Klisch J, Liebig T, et al. **WEB-DL endovascular treatment of wide-neck bifurcation aneurysms: long-term results in a European series.** *AJNR Am J Neuroradiol* 2015;36:2314–19 CrossRef Medline
8. Roy D, Milot G, Raymond J. **Endovascular treatment of unruptured aneurysms.** *Stroke* 2001;32:1998–2004 CrossRef Medline
9. Weisscher N, Vermeulen M, Roos YB, et al. **What should be defined as good outcome in stroke trials; a modified Rankin score of 0-1 or 0-2?** *J Neurol* 2008;255:867–74 CrossRef Medline
10. Pierot L, Gubucz I, Buhk JH, et al. **Safety and efficacy of aneurysm treatment with the WEB: results of the WEBCAST 2 study.** *AJNR Am J Neuroradiol* 2017;38:1151–55 CrossRef Medline
11. Sivan-Hoffmann R, Gory B, Riva R, et al. **One-year angiographic follow-up after WEB-SL endovascular treatment of wide-neck bifurcation intracranial aneurysms.** *AJNR Am J Neuroradiol* 2015;36:2320–24 CrossRef Medline
12. Armoiry X, Turjman F, Hartmann DJ, et al. **Endovascular treatment of intracranial aneurysms with the WEB device: a systematic review of clinical outcomes.** *AJNR Am J Neuroradiol* 2016;37:868–72 CrossRef Medline
13. Lubicz B, Mine B, Collignon L, et al. **WEB device for endovascular treatment of wide-neck bifurcation aneurysms.** *AJNR Am J Neuroradiol* 2013;34:1209–14 CrossRef Medline
14. Mine B, Goutte A, Brisbois D, et al. **Endovascular treatment of intracranial aneurysms with the Woven EndoBridge device: mid term and long term results.** *J Neurointerv Surg* 2018;10:127–32 CrossRef Medline
15. Zhao B, Yin R, Lanzino G, et al. **Endovascular coiling of wide-neck and wide-neck bifurcation aneurysms: a systematic review and meta-analysis.** *AJNR Am J Neuroradiol* 2016;37:1700–05 CrossRef Medline
16. van Rooij SBT, van Rooij WJ, Peluso JP, et al. **WEB treatment of ruptured intracranial aneurysms: a single-center cohort of 100 patients.** *AJNR Am J Neuroradiol* 2017;38:2282–87 CrossRef Medline
17. Soeda A, Sakai N, Sakai H, et al. **Thromboembolic events associated with Guglielmi detachable coil embolization of asymptomatic cerebral aneurysms: evaluation of 66 consecutive cases with use of diffusion-weighted MR imaging.** *AJNR Am J Neuroradiol* 2003;24:127–32
18. Doerfler A, Wanke I, Goericke SL, et al. **Endovascular treatment of middle cerebral artery aneurysms with electrolytically detachable coils.** *AJNR Am J Neuroradiol* 2006;27:513–20 Medline
19. Pierot L, Spelle L, Vitry F; ATENA Investigators. **Immediate clinical outcome of patients harboring unruptured intracranial aneurysms treated by endovascular approach: results of the ATENA study.** *Stroke* 2008;39:2497–2504 CrossRef Medline
20. Vendrell JF, Costalat V, Riquelme C, et al. **Stent-assisted coiling of complex middle cerebral artery aneurysms: initial and midterm results.** *AJNR Am J Neuroradiol* 2011;32:259–63 CrossRef Medline
21. Pierot L, Cognard C, Anxionnat R, for the CLARITY Investigators. **Factors affecting the rate and outcome of endovascular treatment complications in a series of 782 patients (CLARITY study).** *Radiology* 2010;256:916–23 CrossRef
22. Papagiannaki C, Spelle L, Januel AC, et al. **WEB intrasaccular flow disruptor—prospective, multicenter experience in 83 patients with 85 aneurysms.** *AJNR Am J Neuroradiol* 2014;35:2106–11 CrossRef Medline
23. Zhang SM, Liu LX, Ren PW, et al. **Effectiveness, safety and risk factors of Woven EndoBridge device in the treatment of wide-neck intracranial aneurysms: systematic review and meta-analysis.** *World Neurosurg* 2019Aug 13. Pii: S1878-8750(19)32175-8 CrossRef
24. Herbreteau D, Bibi R, Narata AP, et al. **Are anatomic results influenced by web shape modification? analysis in a prospective, single-center series of 39 patients with aneurysms treated with the WEB.** *AJNR Am J Neuroradiol* 2016;37:2280–86 CrossRef Medline
25. Pierot L, Moret J, Barreau X, et al. **Aneurysm treatment with Woven Endobridge in the cumulative population of three prospective, multicenter series: 2-year follow-up.** *Neurosurgery* 2020 Jan 20. Pii:nyz557 CrossRef

Multicenter Postmarket Analysis of the Neuroform Atlas Stent for Stent-Assisted Coil Embolization of Intracranial Aneurysms

J.-K. Burkhardt, V. Srinivasan, A. Srivatsan, F. Albuquerque, A.F. Ducruet, B. Hendricks, B.A. Gross, B.T. Jankowitz, A.J. Thomas, C.S. Ogilvy, G.A. Maragkos, A. Enriquez-Marulanda, R.W. Crowley, M.R. Levitt, L.J. Kim, C.J. Griessenauer, C.M. Schirmer, S. Dalal, K. Piper, M. Mokin, E.A. Winkler, A.A. Abla, C. McDougall, L. Birnbaum, J. Mascitelli, M. Litao, O. Tanweer, H. Riina, J. Johnson, S. Chen, and P. Kan

ABSTRACT

BACKGROUND AND PURPOSE: The Neuroform Atlas is a new microstent to assist coil embolization of intracranial aneurysms that recently gained FDA approval. We present a postmarket multicenter analysis of the Neuroform Atlas stent.

MATERIALS AND METHODS: On the basis of retrospective chart review from 11 academic centers, we analyzed patients treated with the Neuroform Atlas after FDA exemption from January 2018 to June 2019. Clinical and radiologic parameters included patient demographics, aneurysm characteristics, stent parameters, complications, and outcomes at discharge and last follow-up.

RESULTS: Overall, 128 aneurysms in 128 patients (median age, 62 years) were treated with 138 stents. Risk factors included smoking (59.4%), multiple aneurysms (27.3%), and family history of aneurysms (16.4%). Most patients were treated electively (93.7%), and 8 (6.3%) underwent treatment within 2 weeks of subarachnoid hemorrhage. Previous aneurysm treatment failure was present in 21% of cases. Wide-neck aneurysms (80.5%), small aneurysm size (<7 mm, 76.6%), and bifurcation aneurysm location (basilar apex, 28.9%; anterior communicating artery, 27.3%; and middle cerebral artery bifurcation, 12.5%) were common. A single stent was used in 92.2% of cases, and a single catheter for both stent placement and coiling was used in 59.4% of cases. Technical complications during stent deployment occurred in 4.7% of cases; symptomatic thromboembolic stroke, in 2.3%; and symptomatic hemorrhage, in 0.8%. Favorable Raymond grades (Raymond-Roy occlusion classification) I and II were achieved in 82.9% at discharge and 89.5% at last follow-up. mRS ≤2 was determined in 96.9% of patients at last follow-up. The immediate Raymond-Roy occlusion classification grade correlated with aneurysm location ($P < .0001$) and rupture status during treatment ($P = .03$).

CONCLUSIONS: This multicenter analysis provides a real-world safety and efficacy profile for the treatment of intracranial aneurysms with the Neuroform Atlas stent.

ABBREVIATIONS: AcomA = anterior communicating artery; RROC = Raymond-Roy occlusion classification

The recently FDA-approved Neuroform Atlas (Stryker) stent is a new microstent to assist coil embolization of intracranial aneurysms. Gaining CE marking in Europe in May 2015, this device was just recently approved in the United States (Humanitarian Device Exemption approval in January 2018 and premarket approval in May 2019). Therefore, large clinical experience with this device and published case series are not available in the literature.

Received February 13, 2020; accepted after revision March 29.

From the Department of Neurosurgery (J.-K.B., V.S., A.S., O.T., J.J., S.C., P.K.), Baylor College of Medicine, Houston, Texas; Department of Neurosurgery (F.A., A.F.D., B.H.), Barrow Neurological Institute, Phoenix, Arizona; Department of Neurological Surgery (B.A.G.), University of Pittsburgh Medical Center Presbyterian, Pittsburgh, Pennsylvania; Department of Neurosurgery (B.T.J.), Cooper University, Camden, New Jersey; Beth Israel Deaconess Medical Center (A.J.T., C.S.O., G.A.M.), Harvard Medical School, Boston, Massachusetts; Boston Medical Center (A.E.-M.), Boston, Massachusetts; Department of Neurosurgery (R.W.C.), Rush Medical College, Chicago, Illinois; Department of Neurological Surgery (M.R.L., L.J.K.), University of Washington, Seattle, Washington; Department of Neurosurgery (C.J.G., C.M.S., S.D.), Geisinger Health, Danville, Pennsylvania; Research Institute of Neurointervention (C.J.G., C.M.S.), Paracelsus Medical University, Salzburg, Austria; Department of Neurosurgery (K.P., M.M.), University of Southern Florida College of Public Health, Tampa, Florida; Department of Neurological Surgery (E.A.W., A.A.A.), University of California, San Francisco, San Francisco, California; Department of Neurosurgery (C.M., L.B., J.M.), University of Texas Health San Antonio, San Antonio, Texas; and Department of Neurosurgery (M.L., O.T., H.R.), NYU Langone Medical Center, New York, New York.

Paper previously presented at: Congress of Neurological Surgeons, July 30, 2019; Schaumburg, Illinois.

Please address correspondence to Jan-Karl Burkhardt, MD, Department of Neurosurgery, Baylor College of Medicine Medical Center, 7200 Cambridge St, Suite 9B, Houston, TX 77030; e-mail: Jan-Karl.Burkhardt@bcm.edu; @JanKarlBurkhar1

Indicates article with supplemental on-line tables.

http://dx.doi.org/10.3174/ajnr.A6581

Meant to treat wide-neck aneurysms and aneurysms located at vessel bifurcations in the anterior circulation, the Atlas stent aims to further improve aneurysm coiling through its application in small-diameter parent vessels. The exact approved FDA indications include the use of the Neuroform Atlas stent with neurovascular embolization coils in the anterior circulation of the neurovasculature for the endovascular treatment of patients 18 years of age or older with saccular wide-neck (neck width ≥4 mm or a dome-to-neck ratio of <2) intracranial aneurysms arising from a parent vessel with diameters of ≥2.0 and ≤4.5 mm. Therefore, posterior circulation aneurysms are "off-label." The Atlas stent can be delivered through a standard coiling (0.017-inch) catheter, thus making the procedure simpler and possibly safer than earlier-generation stents. The same microcatheter can deploy the Atlas stent in the parent vessel and then be navigated through the stent struts into the aneurysm for coiling (re-probing or re-crossing). Another option is to leave 1 microcatheter in the aneurysm for eventual coiling and deploy the stent with a second microcatheter (jailing technique). This technique is usually not needed with the Atlas device but may be required on the basis of aneurysm and parent vessel anatomy. It can also be used as a rescue stent procedure by deploying a stent after coiling is initiated and the coils are extruded.

Previous studies have demonstrated that stent-assisted coiling with this device is feasible and safe for the patient in a clinical trial setting,[1-4] but a postmarket analysis from daily clinical practice is not available in the literature. The aim of this study was to analyze the efficacy and safety of the device in the postmarket approval period in the United States.

MATERIALS AND METHODS

Study Design, Participating Centers, and Inclusion Criteria

This multicenter retrospective cohort study included all consecutive patients of the participating centers with intracranial aneurysms treated with the Neuroform Atlas stent after the FDA Humanitarian Device Exemption approval from January 2018 until June 2019. The following US academic neurosurgical centers participated in this study: Baylor College of Medicine Medical Center ($n = 10$), New York University Langone Medical Center ($n = 13$), Geisinger Medical Center ($n = 7$), Beth Israel Medical Center ($n = 20$), University of Southern Florida ($n = 11$), University of Texas San Antonio ($n = 12$), University of California, San Francisco ($n = 8$), University of Pittsburgh Medical Center ($n = 15$), University of Washington Seattle ($n = 4$), Rush University Chicago ($n = 3$), and Barrow Neurological Institute ($n = 25$).

Aneurysms were included in this study if they had wide-neck characteristics or because the operator thought that it was appropriate to use the Atlas stent. Posterior circulation aneurysms were included in this study as well, though they were treated as off-label.

The study was approved by the local institutional review board at each participating center for retrospective data collection and review after approval at Baylor College of Medicine, serving as the primary site for de-identified data analysis. The following information was then collected at each center and sent to Baylor College of Medicine without patient identification for analysis: patient demographics, aneurysm and parent vessel characteristics, antiplatelet regimen and platelet function test results if obtained, and procedural details on the Atlas stent. Data on complications as well as patient outcomes were collected on the basis of angiographic data for radiologic outcome, mRS score, symptoms details, and NIHSS for clinical outcome immediately after the procedure and at last follow-up as available.

Neuroform Atlas Stent and Procedure Details

The self-expanding nitinol Neuroform Atlas stent is characterized by its mixed open-cell and closed-cell design, and cell size has been reduced compared with the previous generation of the Neuroform stents. The stent is available in diameters between 3 and 4.5 mm with lengths of 15, 21, 24, and 30 mm; has 3 radiopaque markers; and can be deployed through a 0.017-inch microcatheter such as an Excelsior SL-10 (Stryker).[1]

The procedure itself, including dose and type of antiplatelet management, was under the discretion of the participating neurointerventionalist with the choice of a jailed or re-probed technique. The choice of coils was left to the discretion of the treating neurointerventionalist. Antiplatelet management was also left to the discretion of the treating neurointerventionalist and mainly consisted of dual-antiplatelet medication with aspirin and clopidogrel or ticagrelor at least 5 days before and up to 3 months after the procedure with continuation of aspirin monotherapy after 3 months.

Radiographic and Clinical Outcome

Radiographic outcome was measured using DSA or MRA according to institution-specific follow-up protocol. The degree of aneurysm treatment success was assessed according to the revised Raymond-Roy occlusion classification (RROC) immediately after the procedure and at last follow-up by each center.[5] Clinical outcome was measured with the mRS before and immediately after the procedure and at last follow-up by each center. In patients with SAH, the Hunt and Hess grade and Fisher scales were used to grade the severity of the SAH.

Clinical and radiologic complications were defined as any deviation from expectation during or after the procedure.

Literature Review and Statistical Analysis

All available clinical case series that used Atlas stent-assisted coiling were searched on PubMed, and the data provided were compared with our results. Data were presented as a median with interquartile range for continuous variables and proportions for categoric variables. The Pearson χ^2 test and ANOVA were used to assess differences between groups for categoric and continuous variables, respectively. Significance was assessed at $P < .05$. All analyses were performed using the Statistical Package for the Social Sciences, Version 24 (IBM).

RESULTS

Patient Characteristics

Overall, 128 patients were treated with Atlas stent-assisted coiling for 128 aneurysms in 11 academic neurovascular centers (On-line Table 1). Female sex was more common in this cohort (71.1%, $n = 91$), with an overall median age of 62 years (range, 16–84 years). Multiple aneurysms were present in 27.3% ($n = 35$) of the cases, with a family history for aneurysms found in 16.4% ($n = 21$). Smoking as a risk factor was present in 76 patients, including active

smokers ($n = 69$, 53.9%) and former smokers ($n = 7$, 5.5%). Most of the treated aneurysms presented as unruptured (86.7%, $n = 111$), but 9 patients (7%) had an SAH >2 weeks, and 8 patients (6.3%), <2 weeks before treatment.

Aneurysm Characteristics

Most treated aneurysms were <7 mm ($n = 98$, 76.6%), with a median neck size of 3.9 mm (range, 2–14 mm) and a median dome-to-neck ratio of 1.6 (0.6–5) (On-line Table 1). Wide-neck aneurysms were present in 80.5% ($n = 103$) and 49.2% ($n = 63$) based on a dome-to-neck ratio of <2 and an aneurysm neck size of >4 mm, respectively. The most common aneurysm locations were the apex of the basilar artery ($n = 37$, 28.9%), followed by the anterior communicating artery (AcomA) ($n = 35$, 27.3%) and the MCA ($n = 19$, 14.8%) (On-line Table 1). In 76.6% of cases ($n = 98$), the decision for Atlas stent-assisted coiling was made by the treating neurointerventionalist due to a large aneurysm neck. In 21% ($n = 27$) of the cases, the decision was made on the basis of a failed previous treatment, including both open microsurgical clipping ($n = 4$) and endovascular coiling ($n = 23$).

Procedure Details

In most the cases, only 1 Atlas stent was used to treat the aneurysm (92.2%, $n = 118$). A single catheter for stent deployment followed by re-probing the stent for coiling was used in 59.4% ($n = 76$) of cases (On-line Table 1). The most common stent size used in this cohort was 3 mm, including 3 × 21 mm (25%, $n = 32$), 3 × 24 (25.9%, $n = 33$), and 3 × 15 mm (18%, $n = 23$). Most patients were tested for platelet function before the procedure (P2Y12 testing in 67.2%, $n = 86$), and the most common combination of periprocedural antiplatelet drug regimen was aspirin, 325 mg, plus clopidogrel, 75 mg, daily 5–7 days before the procedure (83.6%, $n = 107$) (On-line Table 1). A small subset of patients had a vessel diameter of <1.5 mm (23 of 128 patients, 18%), and stent-assisted coiling was still feasible in this subset of patients.

Complications

Technical complications occurred in 6 cases (4.7%), including stent-deployment failure ($n = 3$), failure of re-probing to coil the aneurysm after stent deployment requiring placement of a flow diverter over the Atlas stent ($n = 1$), stent migration after deployment ($n = 1$), and coil protrusion through stent struts ($n = 1$). Thromboembolic complications were observed in 6 cases (4.7%) during the procedure and were treated with intra-arterial thrombolysis. Three of the 6 cases were asymptomatic after the procedure ($n = 3/128$, 2.3%). All 6 patients were on aspirin, 325 mg, and clopidogrel, 75 mg, daily before the procedure, and the P2Y12 showed clopidogrel response in all patients. All patients received an intra-arterial glycoprotein IIb/IIIa inhibitor in addition to heparin during thrombosis. One patient also received intra-arterial tPA. Hemorrhagic complications occurred in 2 patients (1.6%), including one during the procedure and the second during postoperative follow-up. The intraoperative hemorrhagic complication occurred during coiling of the aneurysm after stent placement was already performed, and aneurysm rupture was controlled by deploying additional coils. The second hemorrhagic complication occurred during follow-up, and aneurysm re-rupture (SAH) occurred in this patient at day 30 after treatment of a ruptured pericallosal artery aneurysm. Additional coiling was performed by re-probing the aneurysm through the stent without additional complications. The complication rate was not higher in the subset of patients with small parent vessel diameters (<1.5 mm). Only 1 of 23 patients (4.3%) had a complication (stent migration) in this subset.

Outcome

Immediate radiologic outcome ($n = 123$) showed RROC grades I and II in 43.9% and 39.0% of the cases, which improved at last follow-up (median, 3.6 months; $n = 38$) to 76.3% for grade I and 13.2% for grade II, respectively (On-line Table 1). Clinical outcome at last follow-up was favorable with an mRS of 0–2 in 96.9% of the patients ($n = 124$) compared with the clinical status before the procedure ($n = 123$, 96.1%). The immediate RROC grade correlated with aneurysm location ($P < .0001$) and rupture status during treatment ($P = .03$) (Figure) but not with aneurysm size ($P = .25$) or wide-neck aneurysm status (dome-to-neck ratio of <2, $P = .12$; aneurysm neck size of >4 mm, $P = .70$).

DISCUSSION

This multicenter postmarket analysis on the clinical use of the Atlas stent for stent-assisted coiling includes a post-FDA-approval experience with this novel device in the United States. On the basis of the early experience across academic neurovascular centers in the United States, we were able to show, in 128, patients, that the device was safe and efficient as a new aneurysm treatment tool. This provides an alternative to other stents for stent-assisted coiling such as the LEO Baby (Balt Extrusion) and LVIS Jr (MicroVention).[2,6,7]

Recently, several other groups reported their experiences with the Atlas stent; however, our study is the largest to date with 128 in patients and aneurysms (111 unruptured and 17 ruptured). Our study population has an age distribution, female-to-male ratio, RROC I and II occlusion rate, and average number of stents per aneurysm similar to those of most other studies (On-line Table 2 and Table). The mRS at last follow-up and retreatment rate were favorable in all studies using the Atlas stent for stent-assisted coiling. All studies as well as ours showed low rates of hemorrhagic complications and permanent neurologic deficits and a mortality rate of <5%. Besides the study by ten Brinck et al,[1] all studies had low rates of deployment failure and thromboembolic complications and procedure-related clinical complications below 7%.[6,8-13]

The advantage of the Atlas stent is its reach in parent vessels with smaller diameters; therefore, this stent widens the endovascular treatment indication to aneurysms previously not considered candidates for stent-assisted coiling. Our results of parent vessel size measurements, stent diameter, and number of stents per aneurysm are used to confirm this: The average proximal and distal vessel sizes during stent deployment were 2.75 and 2 mm, with a range of 1.1–4.7 and 0.7–4.2 mm, respectively, and in 68.9% of cases, the smallest available stent (3 mm) was used. Furthermore, in most cases (92.2%), only 1 stent was needed to achieve a favorable stent-assisted coiling result. More than 75% of

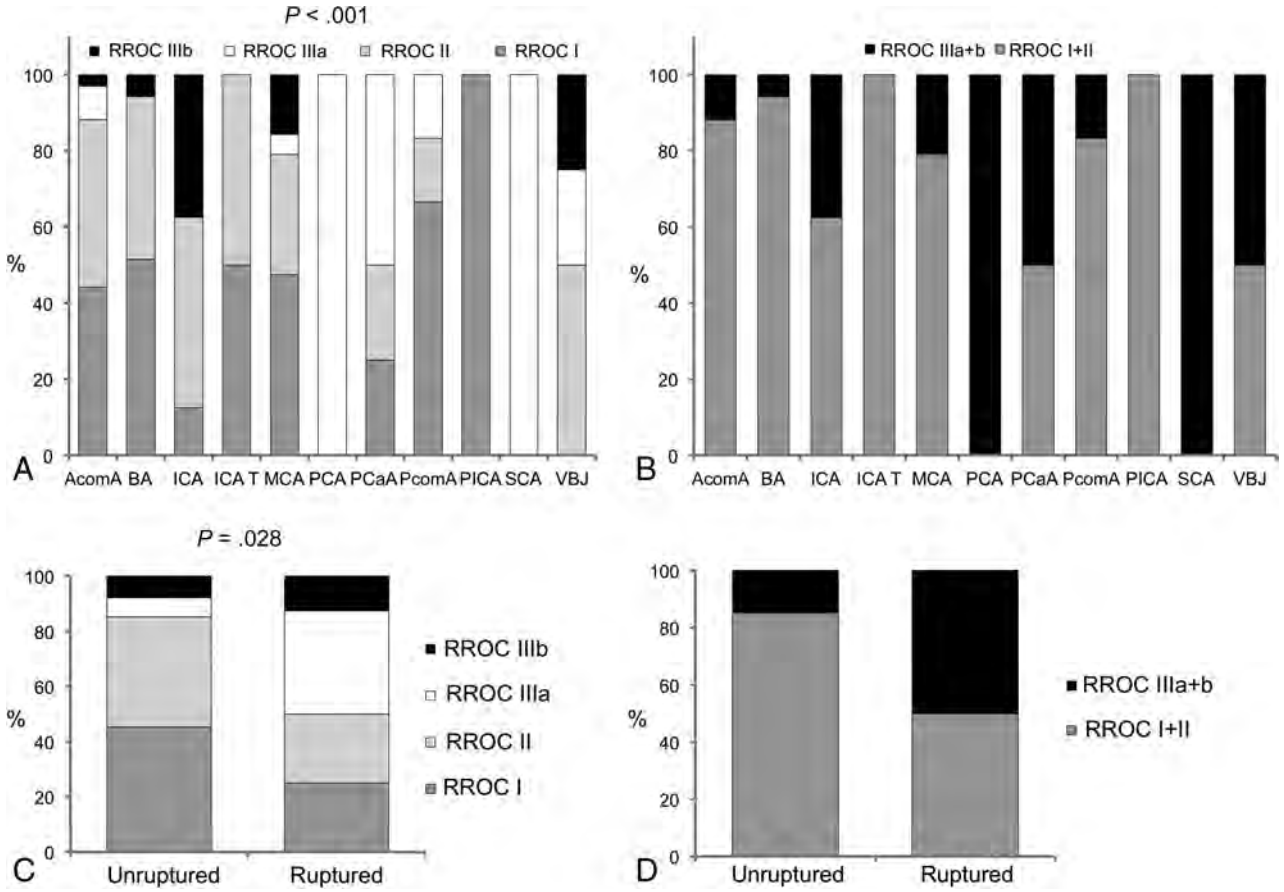

FIGURE. Immediate RROC grade (*A*) compared with aneurysm location and dichotomized into RROC grades I + II and IIIa + IIIb (*B*). Immediate RROC grade (*C*) compared with ruptured or unruptured aneurysm status before treatment and dichotomized into RROC grades I + II and IIIa + IIIb (*D*). BA indicates basilar artery apex; ICA, supraclinoid internal carotid artery, including the ophthalmic/paraclinoid segment and anterior choroidal artery; ICA T, internal carotid artery terminus; PCA, posterior cerebral artery; PCaA, pericallosal artery; PcomA, posterior communicating artery; VBJ, vertebrobasilar junction; SCA, superior cerebellar artery.

Comparison of clinical complications with previous studies

Study	Deployment Failure (%)	Hemorrhagic Complications (%)	Thromboembolic Complications (%)	Procedure-Related Clinical Complications (%)	Permanent Neurologic Deficit (%)	Mortality (%)
Caragliano et al[8] (2019)	0	2.65	3.5	6.2	–	2.65
Tsai et al[12] (2019)	0	1.7	5.2	6.9	0	0
Cay et al[9] (2018)	0	0	0	0	0	0
Gross et al[6] (2019)	3	0	3	3	1	0
Ulfert et al[13] (2018)	0	0	2.7	2.7	0	0
Quintana et al[11] (2019)	3.3	3.3	3.3	3.3	0	0
Jankowitz et al[10] (2019)	0	3.3	3.3	6.6	0	0
ten Brinck et al[1] (2019)	11.1	0	14.8	18.5	3	0
Current study	2.3	1.6	4.7	3.1	–	0.8

Note:— – indicates not reported.

our treated aneurysms were <7 mm, again confirming the ability of the Atlas stent to treat smaller aneurysms in smaller parent vessels. As with other available stents for stent-assisted coiling, aneurysms treated with this technique are usually wide-neck. We found that 80.5% of patients had a wide-neck aneurysm based on a dome-to-neck ratio of <2, with a median dome-to-neck ratio of 1.6. Neck size >4 mm, another classic wide-neck aneurysm definition, was present in only 49.2% of the cases. This is not surprising because most of the aneurysms were small to begin with. Therefore, the dome-to-neck ratio is a more reliable metric to capture wide-neck aneurysms in the specific patient population with distal small wide-neck aneurysms. A subset of patients with a small parent vessel diameter (<1.5 mm) underwent stent-assisted coiling, and we were able to show that this is feasible, with comparable results and complication rates compared with a larger (>1.5 mm) parent vessel size.

Although we had only a short-term follow-up in our patient cohort, our complete aneurysm occlusion rate at last follow-up of 76.3% (RROC I) is getting close to that of surgical clipping results in classic aneurysm bifurcation locations in historical studies with comparable complication rates and outcomes.[14,15] Additionally, if we counted small-neck residual occlusion results (RROC II) as favorable increases, the favorable occlusion rate would be 89.5% (RROC I and II) at last follow-up. It will be interesting to see how the RROC grade will change with time in patients with longer follow-up and whether the results of RROC grade I can then be comparable with microsurgical clipping results in the future. It was also an interesting finding that aneurysm location and ruptured aneurysm status correlated with immediate RROC grade results (Fig 1). This correlation underlines the indication of this device leading to the best angiographic results in patients with unruptured aneurysms in bifurcational locations.

The low-profile Acclino stent (Acandis; https://www.acandis.com/acclino-flex-stent-67-en) has also been reported to show results similar to those of our Atlas stent-assisted coiling study.[16] However, this device is not FDA-approved, and its use in the United States is limited. The recently published study on 131 procedures with this device showed results and complication rates comparable with those in our study.[17]

Another advantage of the small size of the Atlas stent is that it can be deployed by the same coiling catheter, thus simplifying the coiling procedure. Because this is a new device, we still observed a high rate of using 2 separate microcatheters, one for deploying the stent and one jailed in the aneurysm to coil after stent deployment (40.6%). In 59.4% of the cases, the same microcatheter was used, and after stent deployment, the struts of the stent were crossed into the aneurysm for coiling. This re-probing was successful in all except of 1 case. Clearly, the advantage of jailing a second catheter is to secure the catheter position within the aneurysm, especially in challenging aneurysm neck directions off the parent vessel. On the other hand, re-probing the stent enables the coiling catheter to be free within the aneurysm and paint the only coil as with standalone coiling, along with the advantage of securing the coils within the aneurysm sac. It will be interesting to see whether the proportion of re-probing increases with time as more experience is gained with the Atlas stent.

All patients received antiplatelet medications before stent deployment, with aspirin, 325 mg, plus clopidogrel, 75 mg, daily being the most common regimen. All patients also underwent P2Y12 testing. Although unruptured aneurysms were mainly selected for the procedure, 6.3% of the patients were treated with Atlas stent coiling within 2 weeks of aneurysm rupture. Some of these aneurysms were coiled alone with only coil migration, and the Atlas stent was used as a salvage technique to reposition the coils and keep the parent vessel open. In 13.6% of patients, coils were first deployed before the stent, thus showing the ability of the Atlas stent to be used in coil migration as well as in acutely ruptured aneurysms.

There are several limitations to this study. Besides the retrospective data collection and analysis, we had only short clinical and radiologic follow-up data. Furthermore, complications and anatomic results were not independently evaluated.

CONCLUSIONS

This multicenter analysis provides a real-world safety and efficacy profile for the treatment of intracranial aneurysms with the Neuroform Atlas stent, and our excellent radiologic and clinical results are promising for future studies.

Disclosures: Jan-Karl Burkhardt—*UNRELATED*: *Board Membership*: Advisory Board, Longeviti Neuro Solutions. Visish Srinivasan—*UNRELATED*: *Employment*: Baylor College of Medicine. Andrew Ducruet—*UNRELATED*: *Consultancy*: Penumbra, Stryker, Medtronic, Cerenovus, Koswire. Bradley A. Gross—*UNRELATED*: *Consultancy*: Medtronic and MicroVention (no payment received at this point). Ajith J. Thomas—*UNRELATED*: *Consultancy*: Stryker, *Comments*: Data Safety Monitoring Board of SCENT Trial*; *Expert Testimony*: CRICO, *Comments*: cerebrovascular cases. Georgios A. Maragkos—*UNRELATED*: *Grants/Grants Pending*: Medtronic Neurovascular Group, *Comments*: Neurovascular Research Fellowship Grant.* R. Webster Crowley—*UNRELATED*: *Consultancy*: Cerenovus, Medtronic, *Comments*: I have proctored physicians for the PulseRider device from Cerenovus and Pipeline flow-diverting stent from Medtronic. Michael R. Levitt—*UNRELATED*: *Consultancy*: Minnetronix*; *Grants/Grants Pending*: Stryker, Covidien, Volcano Corporation, Philips Healthcare, *Comments*: unrestricted educational grants*; *Stock/Stock Options*: eLoupes, Synchrotron, Cerebrotech Medical Systems, *Comments*: stock in each of these private companies. Louis J. Kim—*UNRELATED*: *Stock/Stock Options*: SPI Surgical. Justin Mascitelli—*UNRELATED*: *Payment for Lectures Including Service on Speakers Bureaus*: Penumbra, PMI.* Maxim Mokin—*UNRELATED*: *Consultancy*: Cerenovus, Canon Medical; *Grants/Grants Pending*: National Institutes of Health R21NS109575*; *Travel/Accommodations/Meeting Expenses Unrelated to Activities Listed*: Serenity Medical, Synchron, EndoStream, VICIS.* Howard Riina—*UNRELATED*: *Consultancy*: Medtronic, Stryker; *Grants/Grants Pending*: Medtronic, fellowship funding*; *Payment for Lectures Including Service on Speakers Bureaus*: Medtronic, Stryker. *Money paid to the institution.

REFERENCES

1. ten Brinck MF, de Vries J, Bartels R, et al. **NeuroForm Atlas stent-assisted coiling: preliminary results.** *Neurosurgery* 2019;84:179–89 CrossRef Medline
2. Aydin K, Arat A, Sencer S, et al. **Stent-assisted coiling of wide-neck intracranial aneurysms using low-profile LEO Baby stents: initial and midterm results.** *AJNR Am J Neuroradiol* 2015;36:1934–41 CrossRef Medline
3. Sedat J, Chau Y, Gaudart J, et al. **Stent-assisted coiling of intracranial aneurysms using LEO stents: long-term follow-up in 153 patients.** *Neuroradiology* 2018;60:211–19 CrossRef Medline
4. Wang F, Chen X, Wang Y, et al. **Stent-assisted coiling and balloon-assisted coiling in the management of intracranial aneurysms: a systematic review and meta-analysis.** *J Neurol Sci* 2016;364:160–66 CrossRef Medline
5. Mascitelli JR, Moyle H, Oermann EK, et al. **An update to the Raymond-Roy occlusion classification of intracranial aneurysms treated with coil embolization.** *J NeuroIntervent Surg* 2015;7:496–502 CrossRef Medline
6. Gross BA, Ares WJ, Ducruet AF, et al. **A clinical comparison of Atlas and LVIS Jr stent-assisted aneurysm coiling.** *J Neurointerv Surg* 2019;11:171–74 CrossRef Medline
7. Akmangit I, Aydin K, Sencer S, et al. **Dual stenting using low-profile LEO Baby stents for the endovascular management of challenging intracranial aneurysms.** *AJNR Am J Neuroradiol* 2015;36:323–29 CrossRef Medline
8. Caragliano AA, Papa R, Pitrone A, et al. **The low-profile Neuroform Atlas stent in the treatment of wide-necked intracranial aneurysms: immediate and midterm results: an Italian multicenter registry.** *J Neuroradiol* 2019 Apr 2. [Epub ahead of print] CrossRef Medline
9. Cay F, Peker A, Arat A. **Stent-assisted coiling of cerebral aneurysms with the Neuroform Atlas stent.** *Interv Neuroradiol* 2018;24:263–69 CrossRef Medline
10. Jankowitz BT, Hanel R, Jadhav AP, et al. **Neuroform Atlas stent system for the treatment of intracranial aneurysm: primary results of the Atlas humanitarian device exemption cohort.** *J Neurointerv Surg* 2019;11:801–06 CrossRef Medline
11. Quintana EM, Valdes PV, Deza EM, et al. **Initial experience and one-year follow-up with Neuroform Atlas stent system for the**

treatment of brain aneurysms. *Interv Neuroradiol* 2019;25:521–29 CrossRef Medline
12. Tsai JP, Hardman J, Moore NZ, et al. **Early post-Humanitarian Device Exemption experience with the Neuroform Atlas stent.** *J Neurointerv Surg* 2019;11:1141–44 CrossRef Medline
13. Ulfert C, Pham M, Sonnberger M, et al. **The Neuroform Atlas stent to assist coil embolization of intracranial aneurysms: a multicentre experience.** *J Neuronterv Surg* 2018;10:1192–96 CrossRef Medline
14. Mooney MA, Simon ED, Brigeman S, et al. **Long-term results of middle cerebral artery aneurysm clipping in the Barrow Ruptured Aneurysm Trial.** *J Neurosurg* 2018;130:895–901 CrossRef Medline
15. Rodríguez-Hernández A, Sughrue ME, Akhavan S, et al. **Current management of middle cerebral artery aneurysms: surgical results with a "clip first" policy.** *Neurosurgery* 2013;72:415–27 CrossRef Medline
16. Brassel F, Grieb D, Meila D, et al. **Endovascular treatment of complex intracranial aneurysms using Acandis Acclino stents.** *J Neurointerv Surg* 2017;9:854–59 CrossRef Medline
17. Goertz L, Smyk MA, Siebert E, et al. **Low-profile laser-cut stents for endovascular treatment of intracranial aneurysms: incidence, clinical presentation and risk factors of thromboembolic events.** *Clin Neuroradiol* 2020 Jan 22. [Epub ahead of print] CrossRef Medline

Long-Term Rupture Risk in Patients with Unruptured Intracranial Aneurysms Treated with Endovascular Therapy: A Systematic Review and Meta-Analysis

A. Rizvi, S.M. Seyedsaadat, M. Alzuabi, M.H. Murad, R. Kadirvel, W. Brinjikji, and D.F. Kallmes

ABSTRACT

BACKGROUND: Surveillance imaging of previously unruptured, coiled aneurysms remains routine even though reports of rupture of these aneurysms are extremely rare.

PURPOSE: We performed meta-analysis to examine long-term rupture risk over ≥1-year follow-up duration in patients with unruptured intracranial aneurysm who underwent endovascular therapy.

DATA SOURCES: Multiple databases were searched for relevant publications between 1995 and 2018.

STUDY SELECTION: Studies reporting outcome of long-term rupture risk over ≥1-year follow-up in treated patients with unruptured intracranial aneurysms were included.

DATA ANALYSIS: Random effects meta-analysis was used, and results were expressed as long-term rupture rate per 100 patient-year with respective 95% CIs. For ruptured aneurysms during follow-up, data were collected on size and completeness of initial Treatment.

DATA SYNTHESIS: Twenty-four studies were identified. Among 4842 patients with a mean follow-up duration of 3.2 years, a total of 12 patients (0.25%) experienced rupture of previous unruptured intracranial aneurysms after endovascular treatment. Nine of these 12 patients harbored aneurysms that were large, incompletely treated, or both. A total of 2 anterior circulation, small, completely coiled aneurysms subsequently ruptured. The long-term rupture rate per 100 patient-year for unruptured intracranial aneurysms treated with endovascular therapy was 0.48 (95% CI, 0.45–0.51). Retreatment was carried out in 236 (4.9%) of these 4842 patients.

LIMITATIONS: A limitation of the study is that a lack of systematic nature of follow-up and mean follow-up duration of 3.2 years are not sufficient to make general recommendations about aneurysm followup paradigms.

CONCLUSIONS: Given a 5% retreatment rate, postcoil embolization spontaneous rupture of previously unruptured, small- and medium-sized, well-treated aneurysms is exceedingly rare.

ABBREVIATIONS: CI = confidence interval; PRISMA = Preferred Reporting Items for Systematic Reviews and Meta-Analyses; PY = patient-year; UIA = unruptured intracranial aneurysm

The advent and popularization of endovascular techniques have led to a growing paradigm shift in coil embolization and decline in historical microsurgical clipping techniques for the treatment of unruptured intracranial aneurysms (UIAs) over the past 20 years or so. Multiple studies have emphasized the follow-up imaging of patients treated with endovascular therapy due to concerns for its long-term durability and increased recurrence rates coupled with greater need for retreatment compared with microsurgical clipping.[1-3] However, even though recurrences after endovascular therapy are reported in up to 30% of treated aneurysms, reports of spontaneous rupture of previously unruptured, coiled aneurysms have been unusual. Even though such spontaneous ruptures are rare, most practitioners carry out long-term surveillance imaging and offer retreatment for previously unruptured, coiled aneurysms.[4,5] Surveillance imaging carries substantial cost and may cause ongoing anxiety, and retreatment

Received November 17, 2019; accepted after revision March 19, 2020.

From the Department of Radiology (A.R., S.M.S., M.A., R.K., W.B., D.F.K.) and Evidence-Based Practice Center (M.H.M.), Mayo Clinic, Rochester, Minnesota; Department of Medicine (A.R.), University of Texas Medical Branch, Galveston, Texas; and Joint Department of Medical Imaging (W.B.), Toronto Western Hospital, Toronto, Ontario, Canada.

Grant support: This research was supported by AHA postdoctoral fellowship award # 19POST34381068 and NIH grant # NS076491.

Please address correspondence to Asim Rizvi, MD, Department of Radiology, Mayo Clinic, 200 First St SW, Rochester, MN 55905; e-mail: drasimrizvi@gmail.com; @Crabalian

Indicates open access to non-subscribers at www.ajnr.org

Indicates article with supplemental on-line appendix and tables.

http://dx.doi.org/10.3174/ajnr.A6568

carries risk of stroke.[6] Thus, it would benefit the community to better understand the rate of spontaneous rupture of coiled, unruptured aneurysms.

To date, there is lack of randomized controlled trials as well as a paucity of aggregated data regarding rupture risk for both small and large UIAs treated with endovascular techniques. We therefore performed a systematic review and meta-analysis of studies to examine the long-term risk of rupture over a follow-up duration of ≥1 year in patients with UIA who underwent endovascular therapy.

MATERIALS AND METHODS

Literature Search

The current study adheres to PRISMA (Preferred Reporting Items for Systematic Reviews and Meta-Analyses) guidelines. The electronic databases Ovid MEDLINE, Ovid EMBASE, and Scopus were systematically examined to locate relevant studies by using predefined search criteria. The search strategy was designed and conducted by a medical reference librarian with input from the authors. Controlled terminology supplemented with keywords was used to search for unruptured cerebral aneurysm, unruptured brain aneurysm, unruptured intracranial aneurysm AND endovascular treatment of aneurysm, coiling of aneurysm, endovascular coiling, endovascular embolization, elective coil treatment AND long-term follow-up, long-term results, aneurysm rupture, rupture of aneurysm. The search was confined to investigations that were published between January 1995 and December 2018. The search strategy is available in the On-line Appendix.

Three independent investigators scanned all manuscripts and performed data extraction. Abstracts or conference papers were excluded because of insufficient data. All retrieved studies were examined, and any potential overlapping data were omitted. Three reviewers performed the final screening of reports for inclusion in the meta-analysis. In the event of any disagreement, a general consensus was met between reviewers after further extensive review of the full-text articles. In addition, all references cited in the identified articles were manually searched for potentially relevant studies.

Study Eligibility

The inclusion criteria for studies in the analysis were 1) studies assessing long-term risk of rupture in patients with UIA who underwent endovascular therapy, 2) studies examining previously unruptured small (<10 mm) and large (>10 mm) intracranial aneurysms that underwent endovascular treatment, and 3) studies reporting mean follow-up duration of ≥1 year after endovascular therapy. Studies published before 1995 were excluded from this meta-analysis. Studies or patients in the included studies were also excluded if they reported giant (>25 mm) or ruptured aneurysm at initial presentation. Additionally, animal or in vitro studies as well as studies with ≤10 patients were excluded as were studies published in languages other than English without any available translation.

Data Collection

Three independent investigators (A.R., S.M.S., and M.A.) extracted data with subsequent verification. The following data were collected for each eligible investigation: year of publication, patient demographics, aneurysm location, mean follow-up duration, and number of patients with ruptures. For documented ruptured aneurysms during follow-up, we collected data on size and completeness of initial treatment (On-line Table 2).

Methodologic Quality

Because the studies were uncontrolled (case series), the methodologic quality of these series (ie, risk of bias) was analyzed by using a modified tool suggested by Murad et al.[7] Each study was judged on 5 items categorized into 4 groups: 1) selection bias (whole experience of the treating center, ie, the study reporting consecutive patients at the recruiting center and therefore less likelihood of selective reporting of the patients who had better outcomes), 2) ascertainment bias (ascertainment of exposure and outcome of interest), 3) causality bias (adequate follow-up period for outcomes to occur), and 4) reporting bias (sufficient details to allow for replication of research). For the purposes of the current study, we determined that the risk of bias depended mainly on 2 factors: selection domain and the independent or blinded assessment of outcomes.

Outcome Variables

For the current study purposes, the following outcome was assessed: long-term rupture of UIA following endovascular treatment over a follow-up duration of ≥1 year.

Statistical Analysis

From each eligible study, data were extracted for the number of patients with UIA and rupture after endovascular therapy during a follow-up duration of ≥1 year. Event rates were expressed as long-term (≥1 year) rupture rate per 100 patient-year (PY) with respective 95% confidence intervals (95% CIs) that were derived from the Poisson distribution. A continuity correction factor of 0.001 was used to address studies with zero event rates. Random effects meta-analysis was used for pooling across studies.[8] The I^2 statistic was used to express the proportion of heterogeneity that is not attributable to chance.[9] Meta-analysis was conducted by using STATA Version 15 (StataCorp).

RESULTS

Literature Search

We identified 438 articles from the literature search. After removing duplicates, 433 articles were screened by title and abstract. Of these, 122 articles were read full-text. A total of 24 studies met the eligibility criteria and were included in the meta-analysis. A PRISMA flow chart of the search and selection process of the articles is shown in Fig 1.

Baseline characteristics of each study are listed in On-line Table 2. A total of 5309 patients were included who were followed-up for ≥1 year after endovascular therapy. The mean age within studies was 55.0 ± 6.0 years, and the mean follow-up duration was 3.2 years. The largest study had 2035 patients,[10] and the smallest study had 13 patients.[11] Four studies were multicenter,[10,12-14] and 20 were single-center studies.[11,15-33] Among all included studies, the longest mean follow-up duration was 15.5 years,[14] and the

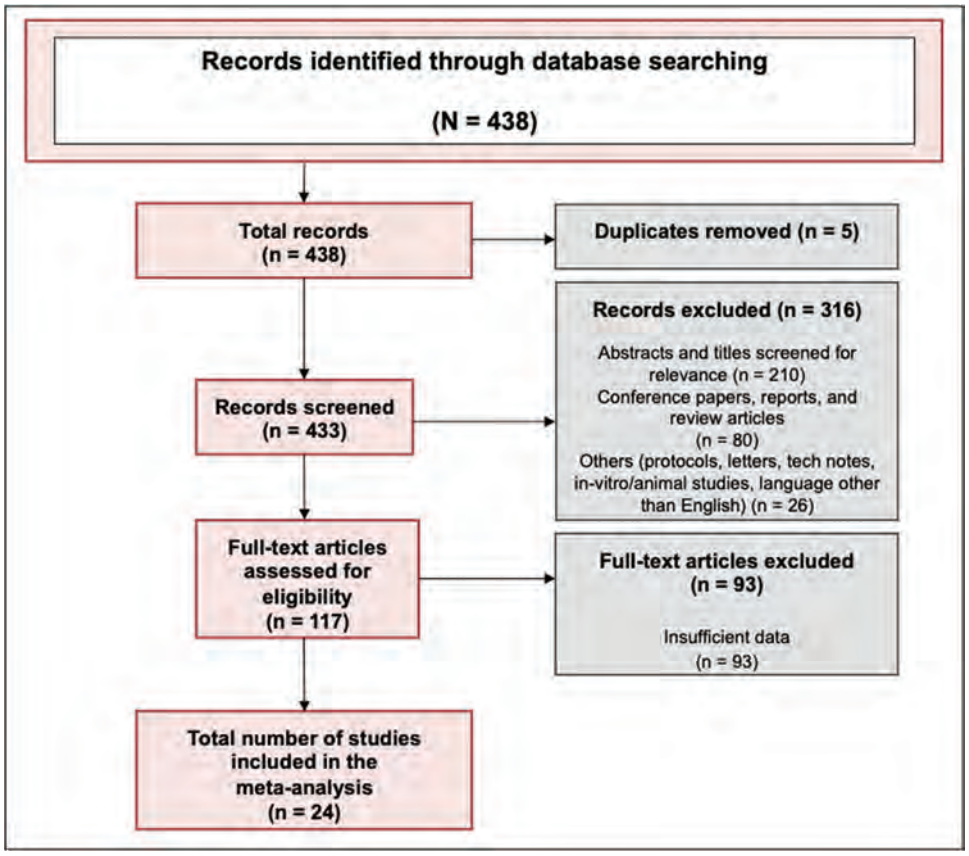

FIG 1. PRISMA (Preferred Reporting Items for Systematic Reviews and Meta-Analyses) flow diagram.

shortest follow-up duration was 1 year.[24,27,30] Methodologic quality was moderate to high in all included studies (On-line Table 3).

Long-Term Rupture Risk with Unruptured Aneurysms Treated with Endovascular Therapy

Among 4842 patients with a mean follow-up duration of 3.2 years, a total of 12 patients (0.25%) experienced rupture of previously unruptured aneurysms following endovascular treatment. Nine of these 12 patients harbored aneurysms that were either large, incompletely treated, or both. A total of 2 anterior circulation, small, completely coiled aneurysms subsequently ruptured. All these ruptures of previous UIAs were reported more than 1 year after the initial endovascular treatment (Table). The long-term rupture rate per 100 PY for UIAs treated with endovascular therapy was 0.48 (95% CI, 0.45–0.51) (Fig 2). In particular, 4.9% of these patients (236 among 4842 patients) underwent retreatments for previously treated UIAs (On-line Table 1).

Heterogeneity

The I^2 value was 98.8% for long-term rupture rate per 100 PY, suggesting high heterogeneity. The low numbers precluded analysis of the reasons for this apparent heterogeneity.

DISCUSSION

This systematic review and meta-analysis revealed that the subsequent rupture of treated UIAs is extremely unusual and was nearly nonexistent among well-treated, small aneurysms. Overall, we noted that about 1 aneurysm ruptured every 200 PY, and most of those few cases represented either small or initially incompletely treated aneurysms. It is potentially notable that the 12 ruptures were spread out over case series published between 1999 and 2018. We fully acknowledge that the true rupture rate of coiled aneurysms remains unknown because about 5% of the patients in this meta-analysis underwent retreatment. Furthermore, it is plausible that these 5% were a high-risk group that may have gone on to rupture. We also acknowledge that a mean follow-up of 3.2 years is not sufficient to make general recommendations about aneurysm surveillance imaging, and a MR angiography every 5 years is not a big request among patients who have a propensity to form life-threatening brain aneurysms. To this end, prior studies have also reported predisposing factors that may predict aneurysm recurrence, which is essentially the biggest risk factor for posttreatment rupture.[34] Even so, the data contained herein should prompt additional discussion and scrutiny regarding the routine use of surveillance imaging and retreatment in patients with previously treated UIA.

In particular, most reports of rupture of aneurysms previously treated with endovascular therapy were in large,[14,20,32] suboptimally coiled aneurysms,[16,29] or both.[28] Further still, the rates of rupture of UIA may vary widely depending on aneurysm location, size, history of other (ruptured) aneurysms, positive family history, and/or smoking history. The current study brings robust meta-analytic techniques to further underscore the significance of low rupture rates among UIAs

Studies that reported long-term aneurysm rupture following endovascular therapy

Author, Year	Number of Patients with Long-Term Aneurysm Rupture Posttreatment	Location of Long-Term Aneurysm Rupture Posttreatment	Reason for Rupture
Kaku et al, 1999[15]	1	Anterior ($n = 1$)	Incomplete occlusion followed by aneurysmal recanalization and regrowth 15 months after IDC embolization on carotid angiogram. Patient had subarachnoid hemorrhage at 15 months after treatment and died.
Johnston et al, 2000[16]	3	Not explicitly reported ($n = 3$)	Rupture caused by incomplete occlusion for technical reasons leading to delayed subarachnoid or intracranial hemorrhage during a mean follow-up duration of 3.8 years. Two patients refused follow-up angiography despite new compressive symptoms. In the third patient, only a small portion of the aneurysm could be treated, and surgical clipping was refused.
Terada et al, 2005[20]	1	Posterior ($n = 1$)	Bilateral posterior cerebral arteries were left patent after aneurysm embolization. Fatal rupture of large basilar tip aneurysm at 28 months due to no follow-up visits and died the day before admission from a massive subarachnoid hemorrhage.
Im et al, 2009[12]	1	Anterior ($n = 1$)	Rupture occurred 18 months after complete coil embolization of a 5-mm MCA bifurcation aneurysm. The patient was lost to clinical follow-up after initial coil embolization, which was later on completely occluded by second coil embolization. The patient had a good recovery without neurologic deficits.
Pyysalo et al, 2013[28]	3	Anterior ($n = 2$) Not explicitly reported ($n = 1$)	Delayed ruptures during mean follow-up duration of 13 years. First patient with 20-mm, incompletely coiled MCA aneurysm with no follow-up due to age of 65 years. Second patient with 4-mm, completely coiled MCA aneurysm with some follow-up and rupture a couple of years later. The data were not found for the third patient.
Mine et al, 2014[29]	1	Not explicitly reported ($n = 1$)	Delayed rupture during mean follow-up duration of 2.2 years because of incomplete coiling and refusal of further treatment.
Petr et al, 2016[32]	1	Anterior ($n = 1$)	Delayed rupture of large MCA aneurysm and death during a mean follow-up duration of 1.7 years.
Koyanagi et al, 2018[14]	1	Posterior ($n = 1$)	Rupture of a large (14-mm) basilar bifurcation aneurysm at 21 months.
Total	12		

Note:—IDC indicates interlocking detachable coils.

previously treated by endovascular therapy and represents a systematic aggregation of long-term rupture rate after endovascular therapy during a follow-up duration of ≥1 year. It extends the findings of smaller studies, which may be limited by factors such as small sample size or single-center design, and it broadens generalizability.

The extremely low rate of posttreatment rupture is not at all surprising, given the low rates of spontaneous rupture of untreated UIA. Based on outcomes from ruptured aneurysm case series, it is clear that coil embolization is highly protective of rerupture, diminishing rerupture rates from about 50% for untreated aneurysms to <2% for coiled aneurysms. A similar relative decrease in rupture rate for UIA would bring down an already low rate to a vanishingly low rate, rendering routine surveillance imaging, at least in small, completely coiled aneurysms, potentially unnecessary. Our study carried out a complete analysis of the best existing data on rupture of previously unruptured, coiled aneurysms and has shown that rupture is extremely rare. It will hopefully prompt future researchers to catalog all relevant data, including reasons for retreatment, in future publications. We acknowledge that noninvasive imaging with MR angiography at extended intervals would not be unreasonable until further data are available.

This study has limitations. There was lack of a systematic nature of follow-up among included studies with imaging modalities such as digital subtraction angiography and MR angiography. We were unable to stratify outcome of long-term rupture by size of

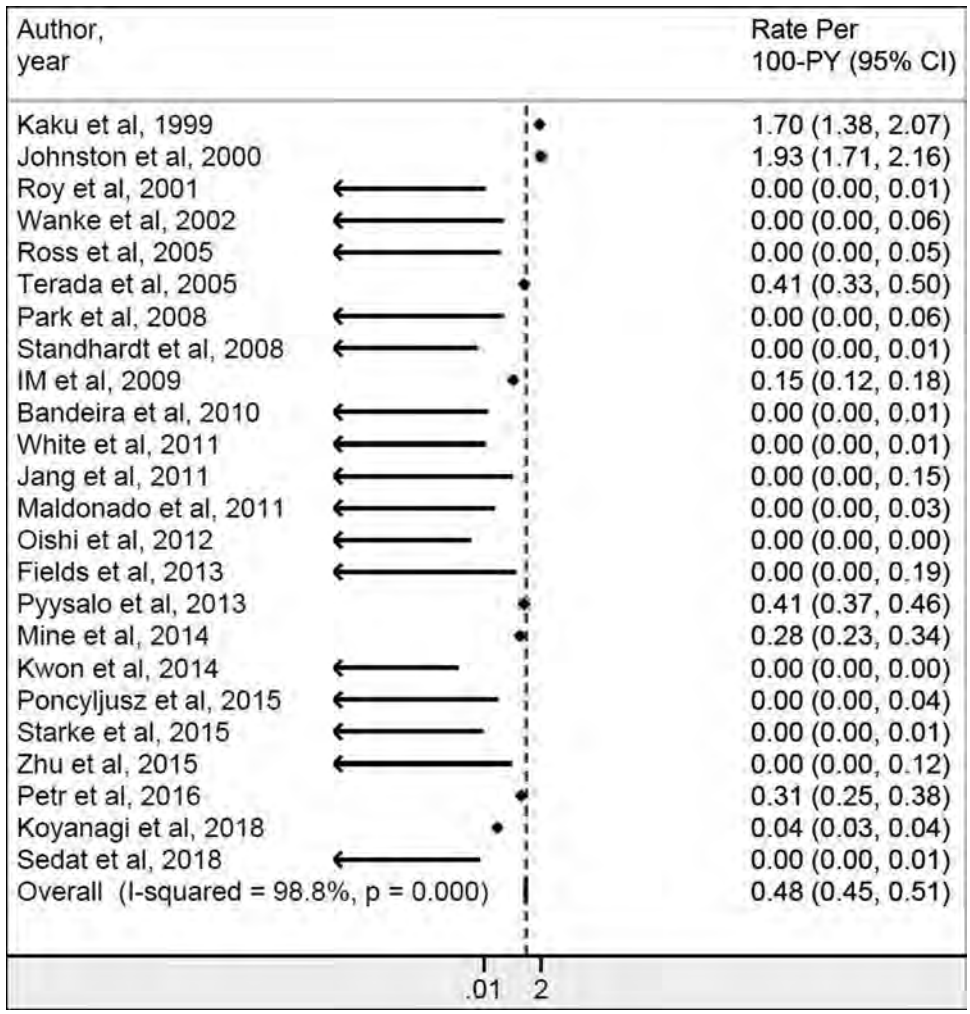

FIG 2. Forest plot for long-term (≥1 year) rupture rate per 100 patient-year (PY) with respective 95% confidence intervals (95% CIs).

aneurysms because specific data from most of the studies cannot be used because of a lack of detailed information for statistical analysis purposes. Additionally, a mean follow-up duration of 3.2 years is not sufficient to make general recommendations about aneurysm follow-up paradigms. As noted, about 5% of aneurysms underwent retreatment, so we cannot exclude the possibility that some of these retreated aneurysms would have gone on to rupture without retreatment. Further still, specific reasons for retreatment were not provided in the available studies, though we can surmise that recanalization likely was the most common cause. For this reason, our study can be best applied in the setting of patients who were not subsequently retreated, for any reason, which remains most patients. There is a lack of a core laboratory and lack of standardization in reporting specific data, such as size criteria defining an aneurysm as "large," what constitutes a suboptimally coiled aneurysm, or even agreement in how to measure a complex-shaped aneurysm. Furthermore, variability exists in the type (MR angiography vs digital subtraction angiography) and intervals of surveillance imaging. Techniques and technology also dramatically changed during the study period, which may affect results, as well as the applicability of the practices and rupture rate in the 1990s to today's practices and surveillance philosophies. We also acknowledge that correlation of rupture with myriad demographic features would be instructive. However, the vanishingly rare event rate (12 cases among almost 5000 aneurysms) renders any such subanalysis or correlative study impossible. Another limitation is that particularly in large metropolitan medical centers, the ability to reliably track for subsequent hemorrhage may be susceptible to underreporting, and given that this is a literature review, we do not have access to systematic databases such as the Veterans Affairs system. Last, this review includes studies of various designs, each of which may have its own set of limitations.

CONCLUSIONS

Given a 5% retreatment rate, post–coil embolization spontaneous rupture of previously unruptured, small- and medium-sized, well-treated aneurysms is exceedingly rare. Future studies are warranted with complete follow-up reporting to address the basic question about the risk of hemorrhage.

Disclosures: Asim Rizvi—*RELATED: Grant:* 19POST34381068, *Comments:* American Heart Association Grant, AHA postdoctoral fellowship award*; *Support for Travel to Meetings for the Study or Other Purposes:* 19POST34381068, *Comments:* American Heart Association Grant, AHA postdoctoral fellowship award*; *Other:* NS076491, *Comments:* NIH grant*; *UNRELATED: Grants/Grants Pending:* 19POST34381068, *Comments:* This research was supported by AHA postdoctoral fellowship award # 19POST34381068 and NIH grant # NS076491.* Seyed Mohammad

Seyedsaadat—*RELATED: Grant:* AHA 2 years postdoctoral research fellowship. Ram Kadirvel—*RELATED: Grant:* NIH, *Comments:* R01 NS076491 and R43 NS110114; *Other:* Cerenovus, Insera Therapeutics LLC, Marblehead Medical LLC, Microvention Inc, MIVI Neuroscience Inc, Neurogami Medical Inc, Triticum Inc, *Comments:* Research contracts; *UNRELATED: Stock/Stock Options:* Neurosigma Inc.* David Kallmes—*UNRELATED: Grants/Grants Pending:* Medtronic, Microvention, NeuroSigma, Neurogami, General Electric, *Comments:* Research support*; *Stock/Stock Options:* Superior Medical Experts, *Comments:* Founder/stockholder. *Money paid to institution.

REFERENCES

1. Byrne JV, Sohn MJ, Molyneux AJ, et al. **Five-year experience in using coil embolization for ruptured intracranial aneurysms: outcomes and incidence of late rebleeding.** *J Neurosurg* 1999;90:656–63 CrossRef Medline
2. Campi A, Ramzi N, Molyneux AJ, et al. **Retreatment of ruptured cerebral aneurysms in patients randomized by coiling or clipping in the International Subarachnoid Aneurysm Trial (ISAT).** *Stroke* 2007;38:1538–44 CrossRef
3. Plowman RS, Clarke A, Clarke M, et al. **Sixteen-year single-surgeon experience with coil embolization for ruptured intracranial aneurysms: recurrence rates and incidence of late rebleeding. Clinical article.** *J Neurosurg* 2011;114:863–74 CrossRef Medline
4. Soize S, Gawlitza M, Raoult H, et al. **Imaging follow-up of intracranial aneurysms treated by endovascular means: why, when, and how?** *Stroke* 2016;47:1407–12 CrossRef Medline
5. Wallace RC, Karis JP, Partovi S, et al. **Noninvasive imaging of treated cerebral aneurysms, part I: MR angiographic follow-up of coiled aneurysms.** *AJNR Am J Neuroradiol* 2007;28:1001–18 CrossRef Medline
6. Thompson BG, Brown RD, Amin-Hanjani S, et al; American Heart Association Stroke Council, Council on Cardiovascular and Stroke Nursing, and Council on Epidemiology and Prevention; American Heart Association; American Stroke Association. **Guidelines for the Management of Patients With Unruptured Intracranial Aneurysms: A Guideline for Healthcare Professionals From the American Heart Association/American Stroke Association.** *Stroke* 2015;46:2368–400 CrossRef Medline
7. Murad MH, Sultan S, Haffar S, et al. **Methodological quality and synthesis of case series and case reports.** *BMJ Evid Based Med* 2018;23:60–63 CrossRef Medline
8. DerSimonian R, Laird N. **Meta-analysis in clinical trials.** *Control Clin Trials* 1986;7:177–88 CrossRef
9. Higgins JP, Thompson SG, Deeks JJ, et al. **Measuring inconsistency in meta-analyses.** *BMJ* 2003;327:557–60 CrossRef Medline
10. Kwon SC, Kwon O-K; Korean Unruptured Cerebral Aneurysm Coiling (KUCAC) Investigators. **Endovascular coil embolization of unruptured intracranial aneurysms: a Korean multicenter study.** *Acta Neurochir (Wien)* 2014;156:847–54 CrossRef Medline
11. Zhu Y, Pan J, Shen J, et al. **Clinical and radiological outcomes after treatment of unruptured paraophthalmic internal carotid artery aneurysms: a comparative and pooled analysis of single-center experiences.** *World Neurosurg* 2015;84:1726–38 CrossRef
12. Im SH, Han MH, Kwon OK, et al. **Endovascular coil embolization of 435 small asymptomatic unruptured intracranial aneurysms: procedural morbidity and patient outcome.** *AJNR Am J Neuroradiol* 2009;30:79–84 CrossRef
13. White PM, Lewis SC, Gholkar A, et al; HELPS trial collaborators. **Hydrogel-coated coils versus bare platinum coils for the endovascular treatment of intracranial aneurysms (HELPS): a randomised controlled trial.** *Lancet* 2011;377:1655–62 CrossRef Medline
14. Koyanagi M, Ishii A, Imamura H, et al. **Long-term outcomes of coil embolization of unruptured intracranial aneurysms.** *J Neurosurg* 2018;129:1492–98 CrossRef Medline
15. Kaku Y, Yoshimura S, Hayashi K, et al. **Follow-up study on intraaneurysmal embolization for unruptured cerebral aneurysms.** *Interv Neuroradiol* 1999;5(suppl 5):89–92 CrossRef Medline
16. Johnston SC, Wilson CB, Halbach VV, et al. **Endovascular and surgical treatment of unruptured cerebral aneurysms: comparison of risks.** *Ann Neurol* 2000;48:11–19 CrossRef
17. Roy D, Milot G, Raymond J. **Endovascular treatment of unruptured aneurysms.** *Stroke* 2001;32:1998–2004 CrossRef Medline
18. Wanke I, Doerfler A, Dietrich U, et al. **Endovascular treatment of unruptured intracranial aneurysms.** *AJNR Am J Neuroradiol* 2002;23:756–61
19. Ross IB, Dhillon GS. **Complications of endovascular treatment of cerebral aneurysms.** *Surg Neurol* 2005;64:12–18 discussion 18-19 CrossRef Medline
20. Terada T, Tsuura M, Matsumoto H, et al. **Endovascular treatment of unruptured cerebral aneurysms.** *Acta Neurochir Suppl* 2005;94:87–91 CrossRef Medline
21. Park SH, Lee CY, Yim MB. **The merits of endovascular coil surgery for patients with unruptured intracranial aneurysms.** *J Korean Neurosurg Soc* 2008;43:270–74 CrossRef Medline
22. Standhardt H, Boecher-Schwarz H, Gruber A, et al. **Endovascular treatment of unruptured intracranial aneurysms with Guglielmi detachable coils: short- and long-term results of a single-centre series.** *Stroke* 2008;39:899–904 CrossRef Medline
23. Bandeira A, Raphaeli G, Baleriaux D, et al. **Selective embolization of unruptured intracranial aneurysms is associated with low retreatment rate.** *Neuroradiology* 2010;52:141–46 CrossRef
24. Jang EW, Jung JY, Hong CK, et al. **Benefits of surgical treatment for unruptured intracranial aneurysms in elderly patients.** *J Korean Neurosurg Soc* 2011;49:20–25 CrossRef Medline
25. Maldonado IL, Machi P, Costalat V, et al. **Neuroform stent-assisted coiling of unruptured intracranial aneurysms: short- and midterm results from a single-center experience with 68 patients.** *AJNR Am J Neuroradiol* 2011;32:131–36 CrossRef Medline
26. Oishi H, Yamamoto M, Shimizu T, et al. **Endovascular therapy of 500 small asymptomatic unruptured intracranial aneurysms.** *AJNR Am J Neuroradiol* 2012;33:958–64 CrossRef
27. Fields JD, Brambrink L, Dogan A, et al. **Stent assisted coil embolization of unruptured middle cerebral artery aneurysms.** *J NeuroIntervent Surg* 2013;5:15–19 CrossRef
28. Pyysalo L, Luostarinen T, Keski-Nisula L, et al. **Long-term excess mortality of patients with treated and untreated unruptured intracranial aneurysms.** *J Neurol Neurosurg Psychiatry* 2013;84:888–92 CrossRef Medline
29. Mine B, Aljishi A, D'Harcour J-B, et al. **Stent-assisted coiling of unruptured intracranial aneurysms: long-term follow-up in 164 patients with 183 aneurysms.** *J Neuroradiol* 2014;41:322–28 CrossRef Medline
30. Poncyljusz W, Zarzycki A, Zwarzany L, et al. **Bare platinum coils vs. HydroCoil in the treatment of unruptured intracranial aneurysms—a single center randomized controlled study.** *Eur J Radiology* 2015;84:261–65 CrossRef Medline
31. Starke RM, Durst CR, Evans A, et al. **Endovascular treatment of unruptured wide-necked intracranial aneurysms: comparison of dual microcatheter technique and stent-assisted coil embolization.** *J Neurointerv Surg* 2015;7:256–61 CrossRef Medline
32. Petr O, Brinjikji W, Cloft H, et al. **Current trends and results of endovascular treatment of unruptured intracranial aneurysms at a single institution in the flow-diverter era.** *AJNR Am J Neuroradiol* 2016;37:1106–13 CrossRef
33. Sedat J, Chau Y, Gaudart J, et al. **Stent-assisted coiling of intracranial aneurysms using LEO stents: long-term follow-up in 153 patients.** *Neuroradiology* 2018;60:211–19 CrossRef Medline
34. Zhang Q, Jing L, Liu J, et al. **Predisposing factors for recanalization of cerebral aneurysms after endovascular embolization: a multivariate study.** *J Neurointerv Surg* 2018;10:252–57 CrossRef Medline

Fast Stent Retrieval Improves Recanalization Rates of Thrombectomy: Experimental Study on Different Thrombi

S. Soize, L. Pierot, M. Mirza, G. Gunning, M. Gilvarry, M. Gawlitza, D. Vivien, M. Zuber, and E. Touzé

ABSTRACT

BACKGROUND AND PURPOSE: About 20% of patients with acute ischemic stroke due to large-artery occlusion do not achieve recanalization with mechanical thrombectomy. We aimed to determine whether the speed of retrieval of the stent retriever influences the efficacy in removing different clot types.

MATERIALS AND METHODS: Sixty mechanical thrombectomies were performed using an in vitro pulsatile cerebrovascular circulation model with controlled pressure and flow rate. Experiments were dichotomized into fast and slow retrieval using a wedging technique, in which the stent retriever and distal catheter are retrieved together. We used 3 different clot types: erythrocyte-rich, fibrin-rich, and friable clots. Primary end points were complete (TICI 3) and successful (TICI 2b–3) recanalizations. Secondary measures were distal and new territory embolizations.

RESULTS: Fast retrieval was more frequently associated with complete (RR = 1.83; 95% CI, 1.12–2.99) and successful recanalization (RR = 1.50; 95% CI, 1.03–2.19) than slow retrieval, without a difference in distal embolization (RR = 0.75; 95% CI, 0.29–1.90). There were no emboli in a new territory. The advantage of fast retrieval over slow retrieval differed according to the clot composition, with a stronger effect with fibrin-rich clots with regard to complete (RR = 4.00; 95% CI, 1.11–14.35; *P*int = .04) and successful (*P*int = .10) recanalization.

CONCLUSIONS: In our experimental model, a fast removal improved recanalization rates of mechanical thrombectomy, especially in the case of fibrin-rich clots. An in vivo confirmation is warranted to see whether our findings can have an impact in clinical practice.

ABBREVIATIONS: DC = distal catheter; MT = mechanical thrombectomy; RR = relative risk; *P*int = *P* interaction; RBC = red blood cell; SR = stent retriever

Mechanical thrombectomy (MT) is considered the first-line therapy for selected patients with acute ischemic stroke with a proximal cerebral artery occlusion.[1-3] The dramatic technological improvements, such as the combined use of stent retrievers (SRs) and distal catheters (DCs), have led to recanalization rates unreached before.[4,5] With the goal of increasing clot entrapment, techniques in which the thrombus is wedged between the SR and DC have become more popular.[6-8] Nevertheless, a successful recanalization is still not obtained in around 20% of patients.[9] Potential issues may arise from the retrieval technique itself, the interactions between device-thrombus, and the clot composition.[9,10] To date, only a few experimental studies have investigated th1053e interaction of the SR with artificial thrombi,[11-18] and the influence of the retrieval speed on MT success has never been explored. The most instinctive approach to remove an SR is to pull it back slowly to save the vessel from potential damage and the clot from breaking.[5,9] However, a fast removal can mobilize the clot suddenly and allow application of higher pulling force to enhance wedging. We aimed to determine whether the speed of retrieval influences the efficacy in removing clots.

Received January 17, 2020; accepted after revision March 2.

From the Department of Neuroradiology (S.S., L.P., M. Gawlitza), Hôpital Maison Blanche, Champagne-Ardenne University, Reims, France; Unité Mixte de Recherche (UMR)-S 1237 Physiopathology and Imaging of Neurological Disorders (S.S., D.V., E.T.), National Institute for Health and Medical Research, Normandie University, Université Caen Normandie, Cyceron, Caen, France; Neuravi/Cerenovus (M.M., G.G., M. Gilvarry), Galway, Ireland; and Department of Neurology (M.Z.), Hôpital Saint-Joseph, Paris Descartes University, Paris, France.

Please address correspondence to Sebastien Soize, MD, Department of Neuroradiology, Hôpital Maison Blanche, 45 Rue Cognacq-Jay, Reims 51092, France; e-mail: ssoize@chu-reims.fr

Indicates article with supplemental on-line video.

http://dx.doi.org/10.3174/ajnr.A6559

MATERIALS AND METHODS

Study Setting

Using an in vitro model of cerebrovascular occlusion, we performed a total of 60 thrombectomy experiments (1 pass only for each), dichotomized into 2 groups according to the speed of retrieval of the SR-DC unit (fast or slow retrieval). The experiments were

performed with 3 types of clots. Half of the tests were performed with Solitaire 2 (4 × 20 mm) (Medtronic) and half with Embotrap II (5 × 21 mm) (Neuravi/Cerenovus). Consequently, there were 2 speeds × 3 types of clots × 5 maneuvers each × 2 devices, corresponding to 60 MTs in total.

Flow Model

In brief, the model is made of silicone channels (Elastrat) mimicking the human anterior intracranial circulation. The flow model had sharp angles and large perforator diameters to create challenging conditions, and a posterior flow was also added for complete circle of Willis flow. A saline solution at 37°C was pumped through the model with a 430-mL/min flow rate and 110/60 mm Hg pulsatile pressure. A fresh clot was introduced into the model to simulate the vessel occlusion (Fig 1).

Clots Types

We used 3 different types of clot depending on their composition (Fig 2): red blood cell (RBC)-rich, fibrin-rich, and hybrid clots (representing the challenges of a friable clot). The RBC-rich clots were formed from whole ovine blood by allowing the blood to clot spontaneously. The fibrin-rich clots were prepared by first spinning down the blood sample in a centrifuge and recombining 5% RBCs with 95% plasma to produce a fibrin-rich clot.[19] Hybrid clots were prepared specifically to represent the challenges of friable clots. They were prepared by cutting spontaneously formed clot (RBC-rich) into 1- to 1.5-mm cubes. Ten of these cubes were inserted into a 2.5-mm diameter silicone tube where they were lightly glued together with a mixture of blood and thrombin. Once the mixture was fully set (30 minutes), the hybrid clot was carefully removed from the silicone tube. The size of all clot types was standardized at a 2.5- mm diameter by 10-mm length. Clots were introduced into the model and navigated into the M1 or M2 MCA segment using the anterograde flow of the circulating fluid. A 3-minute embedding time was respected.

Thrombectomy Technique

MT consisted of a microcatheter (Rebar-18; Medtronic) navigated through a distal catheter (Sofia Plus; MicroVention), which was advanced into a guide catheter (Neuron Max; Penumbra). We used 0.014-inch microwires (Traxcess 14; MicroVention) to cross the thrombus. The proximal third to half of the stent retriever was deployed across the clot. Thereafter, the DC was advanced into the proximal M1, and the microcatheter was withdrawn inside the DC. After 3 minutes, the SR was retrieved until half was inside the DC or until resistance was felt. Then, the system was retrieved completely as a single unit (SR + DC + microcatheter) with a continuous movement.[7,8] No suction was applied during removal. A fast retrieval was performed in 5 seconds maximum, and a slow retrieval, in 15 seconds minimum. To ensure reproducibility, we performed 10 training experiments before starting the study. The speed was calculated by dividing the time (measured by an assistant with a stopwatch) by the distance (measured from the guide catheter tip to the proximal limit of the thrombus with a flexible meter). The MT result was instantly graded by the performing physician according to an adapted TICI score: complete recanalization (TICI 3), recanalization with small emboli exceeding the model limits (TICI 2b), recanalization but emboli blocked distally (TICI 2a), a piece of thrombus removed but persistent occlusion (TICI 1), and no recanalization (TICI 0). Distal emboli

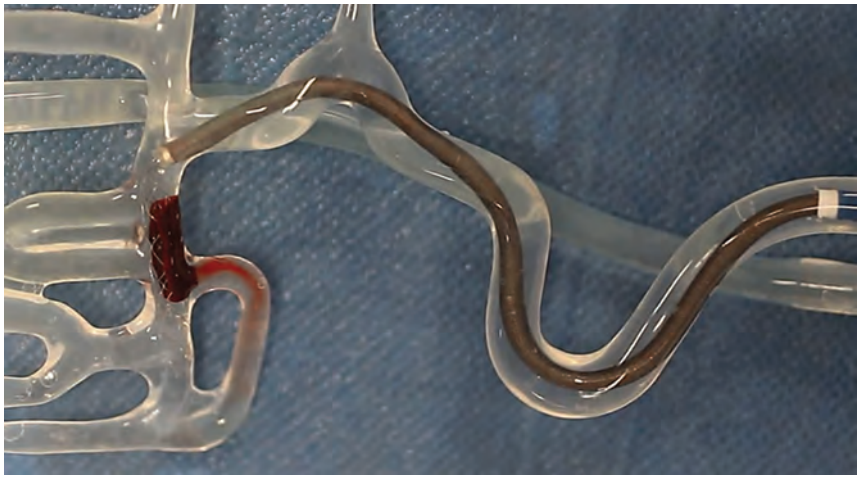

FIG 1. Flow model.

FIG 2. Clot types. The figure shows the 3 types of clot during MT inside the model: RBC-rich (left), fibrin-rich (middle), and hybrid friable clot (right).

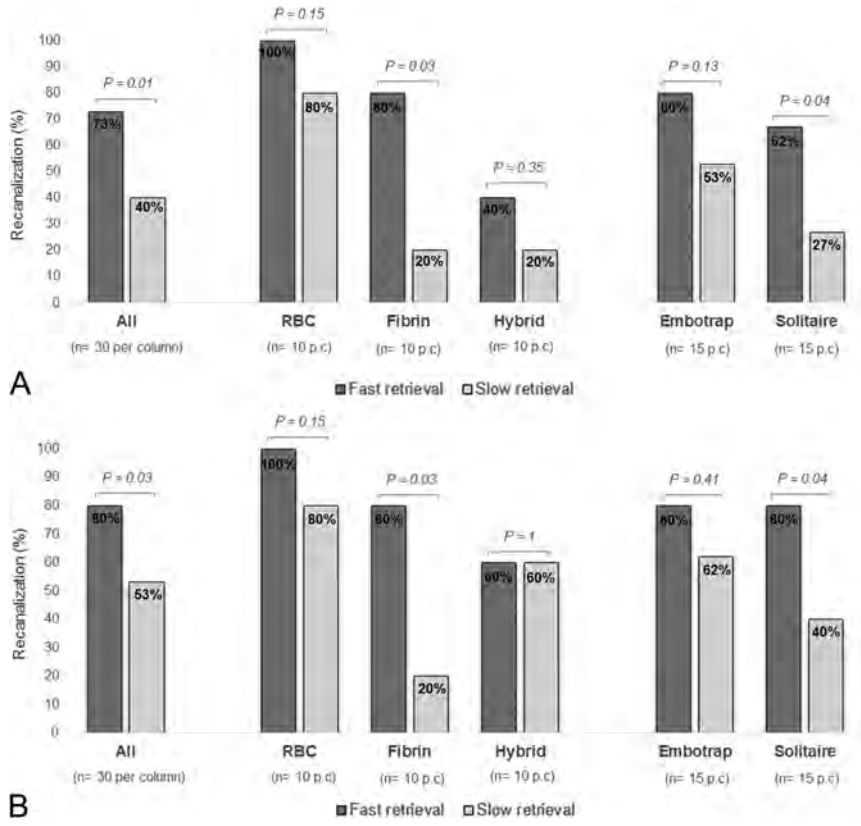

FIG 3. Complete (*A*) and successful (*B*) recanalization rates.

corresponded to part of the initial thrombus migrating in the MCA territory farther than the distal limit of the model (ie, <1.5 mm in diameter). Emboli in a new territory were any clots migrating into another area. Primary outcome measures were complete (TICI 3) and successful recanalization (TICI 2b–3). Secondary measures were distal and new territory emboli. All experiments were recorded and reviewed for verification purposes (On-line Videos).

Statistical Analyses

Distribution normality was assessed using the Kolmogorov-Smirnov test. Continuous variables were described as mean ± SD or median and interquartile range and were compared using the Student *t* test or Mann-Whitney *U* test. Categoric variables were presented as counts and compared using the χ^2 or Fisher exact test. Relative risks and their 95% confidence intervals were calculated. Interaction analyses were performed using the Cochran-Mantel-Haenszel test. Analyses were performed using STATA software (Realease 15.0; StataCorp).

RESULTS

Fast-versus-Slow Retrieval

The mean time of retrieval was 2.4 ± 1.2 seconds in the fast group and 27.3 ± 6.8 seconds in the slow group ($P < .001$). Overall, fast retrieval led to higher rates of complete (73% versus 40%, $P = .01$) and successful (80% versus 53%, $P = .03$) first-pass recanalization than slow retrieval. Fast retrieval was more frequently associated with complete (Relative Risk = 1.83; 95% CI, 1.12–2.99) and successful first-pass recanalization (RR = 1.50; 95% CI, 1.03–2.19) than slow retrieval. Recanalization rates in the whole experiment as well as according to clot type and SR type are shown in Fig 3.

Clot Composition

The advantage of fast retrieval over slow retrieval differed according to the clot composition (Fig 4), with a stronger effect obtained with fibrin-rich clots (RR = 4.00; 95% CI, 1.11–14.35) than with RBC-rich (RR = 1.25; 95% CI, 0.92–1.70) and hybrid friable (RR = 2.00; 95% CI, 0.47–8.56) clots with regard to complete recanalization (*P*int = .04). This result was similar when considering successful recanalization instead (*P*int = .10) (Fig 2).

SR Type

The advantage of fast retrieval over slow retrieval did not differ according to the SR type (Fig 2) with regard to complete recanalization (*P*int = .32) or successful recanalization (*P*int = .19) (Fig 4).

Distal Embolization

Distal embolization occurred only with hybrid friable clots and was not different between fast (20.0%) and slow (26.7%) retrieval groups (RR = 0.75; 95% CI, 0.29–1.90). There were no emboli in a new territory.

DISCUSSION

Our experimental study showed that a fast retrieval improves recanalization rates, without increasing the rate of distal embolization. It was all the more important that we measured the achievement of complete/successful revascularization after 1 pass, which is associated with significantly higher rates of good clinical outcome.[20-22] In this experimental study, we reached 73% and 80% of complete and successful recanalization with 1 pass, while in clinical routine, current thrombectomy techniques yield around 30% and 50% complete and successful recanalization, respectively.[20-22] Although not instinctive, a fast removal can mobilize the clot suddenly, allow application of higher pulling force, enhance clot wedging, and minimize loss of apposition during the path of retrieval. Also, it may leave less time for variations of the pulling force, hence avoiding undesired loss of contact between SR and DC. A fast removal did not modify the rate of distal embolization, probably because of an active pinning of the whole thrombus length.

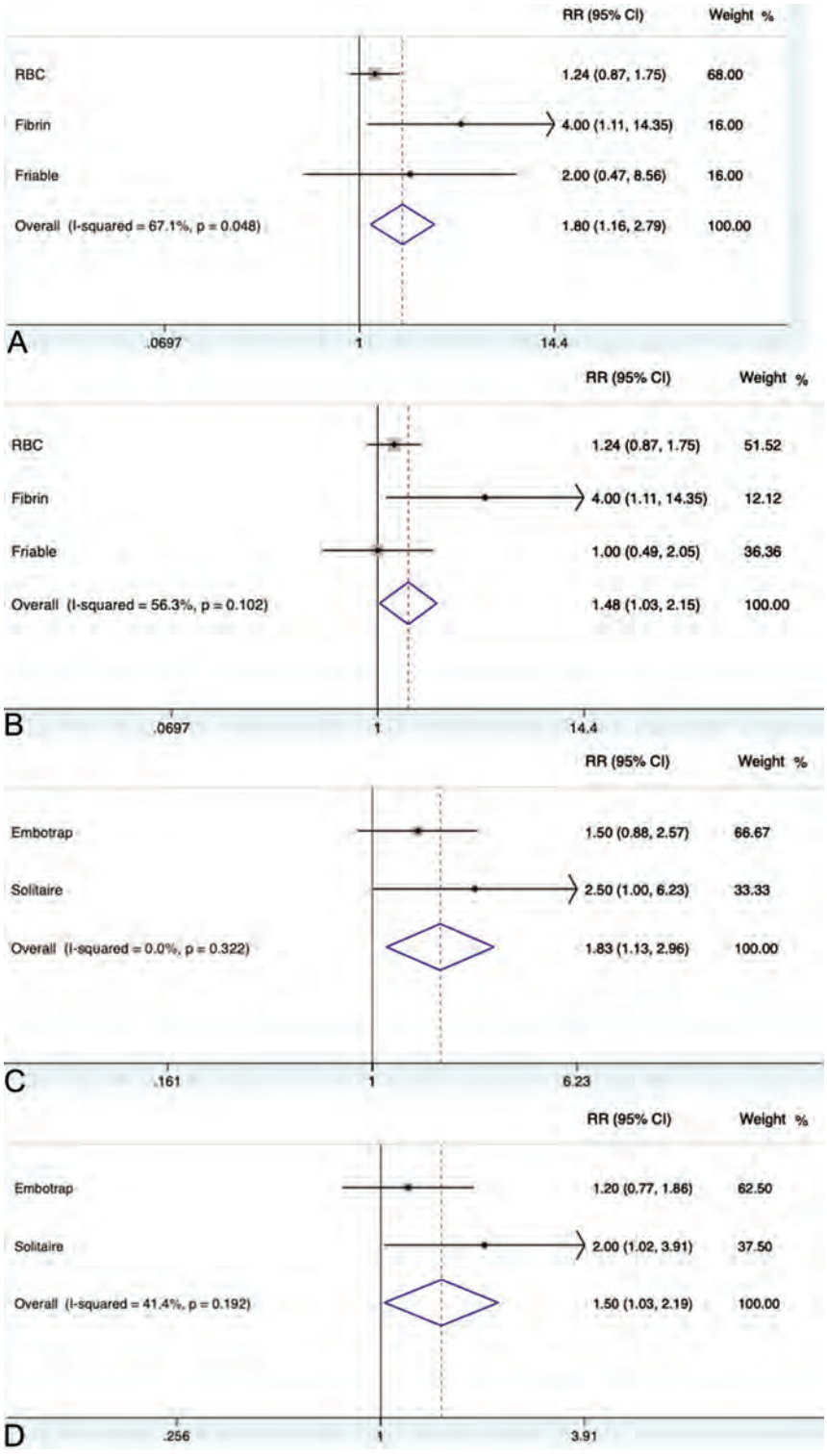

FIG 4. Interactions analyses. Interaction between the speed of retrieval and the clot type with regard to complete (*A*) and successful (*B*) recanalization. Interaction between the speed of retrieval and stent retriever type with regard to complete (*C*) and successful (*D*) recanalization.

While fast retrieval seems promising in terms of recanalization, an important concern is the clinical safety of this technique. Indeed, human perforating arteries cannot be modeled accurately, and the risk of injury remains unknown. The manufacturers recommend slowly withdrawing the SR as a precaution for safety. When one performs a mechanical retrieval, the perforators may be exposed to excessive force due to stretching and may be rarely sheared off, leading to extravasation. A sudden mobilization of the clot may enhance its retrieval, but the effect on the lenticulostriate arteries is unknown. Thus, the safety of fast retrieval needs to be evaluated in vivo.

The composition and physical properties of the clot can play a key role in the response to MT.[9,23-25] We observed a stronger advantage of fast over slow retrieval with fibrin-rich clots. These clots probably account for a large part of MT failures because they are firm and sticky.[9,23,24] Fast retrieval, by mobilizing the clot suddenly, may have contributed to better clot trapping. Because imaging features of fibrin-rich thrombi are correlated with decreased revascularization rates,[25,26] a fast retrieval might be recommended in such cases, to enhance first-pass revascularization. This is all the more important in that there is the potential for thrombus compression and increasing difficulty of subsequent retrieval after each thrombectomy attempt.[9]

Our study has potential limitations. First, the model and clots were more representative of embolic stroke types (not atherosclerosis). The circulation model does not fully simulate the human artery, and further in vivo studies are mandatory to confirm our results and evaluate the clinical safety. Also, tortuous anatomy probably has an impact that cannot be measured with our model.[22] Second, because we aimed to analyze only factors attributable to the SR, we did not apply aspiration. In all the in vitro attempts, the DC was always in the M1 proximal part, covering the anterior cerebral artery and in the same axis as the clot. In such cases, the need for proximal aspiration was probably less important than when clot and DC are far away from each other (eg, distal M2 clot, or DC still in the ICA) or in a very tortuous M1. Because only 1 specific procedural setup was simulated, it may not translate to other procedures (longer clots, techniques not similar to Aspiration-Retriever Technique for Stroke or stent-assisted vacuum-locked extraction (SAVE

technique), and use of a baloon guide catheter). Such setups remain to be tested.

CONCLUSIONS

In our experimental model, a fast removal improved recanalization rates of MT, especially in case of fibrin-rich clots, which are known to be challenging to remove. An in vivo confirmation is warranted to see whether our findings can impact clinical practice.

Disclosures: Laurent Pierot—*UNRELATED*: *Consultancy*: Balt, MicroVention, phenox, Vesalio. Mahmood Mirza—*UNRELATED*: *Employment*: Cerenovus; *Stock/Stock Options*: Cerenovus. Matthias Gawlitza—*UNRELATED*: *Expert Testimony*: MicroVention, *Comments*: member of the Clinical Event Committee for a company-initiated study on a neurovascular device; *Travel/Accommodations/Meeting Expenses Unrelated to Activities Listed*: Neuravi/Cerenovus, phenox, MicroVention, *Comments*: travel and accommodations for training workshops of the respective companies; *Other*: Lin. Michael Gilvarry—*UNRELATED*: *Employment*: Cerenovus; *Stock/Stock Options*: Cerenovus.

REFERENCES

1. Powers WJ, Rabinstein AA, Ackerson T, et al; American Heart Association Stroke Council. **2018 Guidelines for the Early Management of Patients with Acute Ischemic Stroke: a Guideline for Healthcare Professionals From the American Heart Association/American Stroke Association.** *Stroke* 2018;49:e46–10 CrossRef Medline
2. Mokin M, Ansari SA, McTaggart RA, et al; Society of NeuroInterventional Surgery. **Indications for thrombectomy in acute ischemic stroke from emergent large vessel occlusion (ELVO): report of the SNIS Standards and Guidelines Committee.** *J Neurointerv Surg* 2019;11:215–20 CrossRef Medline
3. Gandhi CD, Al Mufti F, Singh IP, et al; Standards and Guidelines committee of the Society of NeuroInterventional Surgery (SNIS). **Neuroendovascular management of emergent large vessel occlusion: update on the technical aspects and standards of practice by the Standards and Guidelines Committee of the Society of NeuroInterventional Surgery.** *J Neurointerv Surg* 2018;10:315–20 CrossRef Medline
4. Goyal M, Menon BK, van Zwam WH, et al. **Endovascular thrombectomy after large-vessel ischaemic stroke: a meta-analysis of individual patient data from five randomised trials.** *Lancet* 2016;387:1723–31 CrossRef Medline
5. Pierot L, Soize S, Benaissa A, et al. **Techniques for endovascular treatment of acute ischemic stroke: from intra-arterial fibrinolytics to stent-retrievers.** *Stroke* 2015;46:909–14 CrossRef Medline
6. Mokin M, Ionita CN, Nagesh SV, et al. **Primary stentriever versus combined stentriever plus aspiration thrombectomy approaches: in vitro stroke model comparison.** *J Neurointerv Surg* 2015;7:453–57 CrossRef Medline
7. Massari F, Henninger N, Lozano JD, et al. **ARTS (Aspiration-Retriever Technique for Stroke): initial clinical experience.** *Interv Neuroradiol* 2016;22:325–32 CrossRef Medline
8. Maus V, Behme D, Kabbasch C, et al. **Maximizing first-pass complete reperfusion with SAVE.** *Clin Neuroradiol* 2018;28:327–38 CrossRef Medline
9. Yoo AJ, Andersson T. **Thrombectomy in acute ischemic stroke: challenges to procedural success.** *J Stroke* 2017;19:121–30 CrossRef Medline
10. Kaesmacher J, Gralla J, Mosimann PJ, et al. **Reasons for reperfusion failures in stent-retriever-based thrombectomy: registry analysis and proposal of a classification system.** *AJNR Am J Neuroradiol* 2018;39:1848–53 CrossRef Medline
11. Gralla J, Schroth G, Remonda L, et al. **Mechanical thrombectomy for acute ischemic stroke thrombus-device interaction, efficiency, and complications in vivo.** *Stroke* 2006;37:3019–24 CrossRef Medline
12. Chueh JY, Wakhloo AK, Gounis MJ. **Effectiveness of mechanical endovascular thrombectomy in a model system of cerebrovascular occlusion.** *AJNR Am J Neuroradiol* 2012;33:1998–2003 CrossRef Medline
13. Wenger KJ, Nagl F, Wagner M, et al. **Improvement of stent retriever design and efficacy of mechanical thrombectomy in a flow model.** *Cardiovasc Intervent Radiol* 2013;36:192–97 CrossRef Medline
14. Mordasini P, Brekenfeld C, Byrne J, et al. **Experimental evaluation of immediate recanalization effect and recanalization efficacy of a new thrombus retriever for acute stroke treatment in vivo.** *AJNR Am J Neuroradiol* 2013;34:153–58 CrossRef Medline
15. Mokin M, Setlur Nagesh SV, Ionita CN, et al. **Comparison of modern stroke thrombectomy approaches using an in vitro cerebrovascular occlusion model.** *AJNR Am J Neuroradiol* 2015;36:547–51 CrossRef Medline
16. Madjidyar J, Hermes J, Freitag-Wolf S, et al. **Stent-thrombus interaction and the influence of the aspiration on mechanical thrombectomy: evaluation of different stent retrievers in a circulation model.** *Neuroradiology* 2015;57:791–97 CrossRef Medline
17. van der Marel K, Chueh JY, Brooks OW, et al. **Quantitative assessment of device-clot interaction for stent retriever thrombectomy.** *J Neurointerv Surg* 2016;8:1278–82 CrossRef Medline
18. Machi P, Jourdan F, Ambard D, et al. **Experimental evaluation of stent retrievers' mechanical properties and effectiveness.** *J Neurointerv Surg* 2017;9:257–63 CrossRef Medline
19. Duffy S, Farrell M, McArdle K, et al. **Novel methodology to replicate clot analogs with diverse composition in acute ischemic stroke.** *J Neurointerv Surg* 2017;9:486–91 CrossRef Medline
20. Zaidat OO, Castonguay AC, Linfante I, et al. **First pass effect: a new measure for stroke thrombectomy devices.** *Stroke* 2018;49:660–66 CrossRef Medline
21. Ducroux C, Piotin M, Gory B, et al. **First pass effect with contact aspiration and stent retrievers in the Aspiration versus Stent Retriever (ASTER) trial.** *J Neurointerv Surg* 2020;12:386–91 CrossRef Medline
22. Srivatsa S, Duan Y, Sheppard JP, et al. **Cerebral vessel anatomy as a predictor of first-pass effect in mechanical thrombectomy for emergent large-vessel occlusion.** *J Neurosurg* 2020 Jan 24. [Epub ahead of print] CrossRef Medline
23. Yuki I, Kan I, Vinters HV, et al. **The impact of thromboemboli histology on the performance of a mechanical thrombectomy device.** *AJNR Am J Neuroradiol* 2012;33:643–48 CrossRef Medline
24. Gunning GM, McArdle K, Mirza M, et al. **Clot friction variation with fibrin content; implications for resistance to thrombectomy.** *J NeuroIntervent Surg* 2018;10:34–38 CrossRef Medline
25. Lövblad KO. **Targeting the clot in acute stroke.** *AJNR Am J Neuroradiol* 2018;39:E77 CrossRef Medline
26. Brinjikji W, Duffy S, Burrows A, et al. **Correlation of imaging and histopathology of thrombi in acute ischemic stroke with etiology and outcome: a systematic review.** *J Neurointerv Surg* 2017;9:529–34 CrossRef Medline

Relevance of Distal Arterial Collapse in Stenting of Atherosclerotic Near-Occlusion of the Carotid Artery

F. Cay, B.E. Cil, S. Balcı, E.M. Arsava, M.A. Topçuoğlu, and A. Arat

ABSTRACT

BACKGROUND AND PURPOSE: Carotid near-occlusion has been subclassified into near-occlusion with and without collapse. We aimed to compare the technical success and perioperative complication rates of carotid artery stent placement with special attention to these subtypes to see whether there is a clinical relevance of this subclassification.

MATERIALS AND METHODS: From January 2014 to January 2018, we retrospectively evaluated all patients with atherosclerotic extracranial carotid stenosis treated by carotid artery stent placement. Patients with near-occlusion were identified based on DSA findings. Patient characteristics, the presence of criteria for near-occlusion and collapse, arterial diameters, technical success rate, and perioperative (≤30 days) complications were analyzed.

RESULTS: We identified 59 near-occlusions in 58 (46 men, 11 with collapse) patients. Forty-one patients (70.7%) were symptomatic. Technical success rate was 98.3% (58 of 59 procedures). In 1 case of near-occlusion with collapse, we were not able to pass through the stenosis. Compared with patients without collapse (4.2% of 48 cases), those with collapse (30% of 10 stented patients) had significantly higher rates of postintervention hyperperfusion syndrome ($P = .032$). In the whole cohort, the permanent morbidity and mortality rate was 3.4% (1.7% permanent morbidity and 1.7% mortality). For asymptomatic and symptomatic near-occlusion groups, the rates were 0% and 4.9%, respectively. The composite risk of stroke, death, and myocardial infarction was similar between the groups with and without collapse ($P = .682$). Rate of hyperperfusion syndrome (with or without permanent deficit) was similar ($P = 1$) in preoperatively symptomatic patients versus asymptomatic patients (9.8% vs 5.9%). Internal carotid artery diameter consistently increased after carotid artery stent placement in patients with collapse and was not related to the development of hyperperfusion syndrome.

CONCLUSIONS: Care should be taken to minimize hyperperfusion risk in patients with near-occlusion undergoing CAS, especially in the subgroup of patients with collapse and in patients with both symptomatic and asymptomatic carotid stenosis.

ABBREVIATIONS: CEA = carotid endarterectomy; CAS = carotid artery stent placement; ECA = external carotid artery; TCD = transcranial Doppler

Carotid near-occlusion is defined as very severe carotid artery stenosis with a reduced lumen diameter distal to the stenotic segment. Ischemic stroke is one of the leading causes of morbidity and mortality worldwide. Carotid artery stenosis is responsible for 18%–29% of these cases[1]. It has been well demonstrated that stroke risk increases with an escalating degree of carotid stenosis.[2,3] Therefore, it would be expected that carotid near-occlusion would be associated with the greatest stroke risk. However, stroke risk in carotid near-occlusion is not well defined. The post hoc analyses of the North American Symptomatic Carotid Endarterectomy Trial (NASCET) and European Carotid Surgery Trial (ECST) reported a low stroke risk with medical therapy in near-occlusion compared with severe carotid artery stenosis without near-occlusion.[2,3] In contrast, some authors have reported that symptomatic patients with near-occlusion have a high stroke risk with medical treatment,[4-7] and one of the latest publications on carotid near-occlusion treatment suggests that there is a higher 30-day stroke and death rate after medical therapy than after carotid endarterectomy (CEA) or carotid artery stent placement (CAS) because the 1-year stroke-free or death-free survival rates were 96.1% for CEA, 94.4% for CAS, and 81.2% for medical therapy.[8] Thus, these results favor carotid revascularization in this subset of patients with severe carotid stenosis.

Received December 2, 2019; accepted after revision March 24, 2020.

From the Departments of Radiology (F.C., S.B., A.A.) and Neurology (E.M.A., M.A.T.), Hacettepe University Hospital, Ankara, Turkey; and Department of Radiology (B.E.C.), Koç University Hospital, Istanbul, Turkey.

Paper previously presented at: 104th Meeting of the Radiological Society of North America, November 28, 2018; Chicago, Illinois.

Please address correspondence to Anil Arat, Department of Radiology, Hacettepe University Hospital, Sihhiye 06100, Ankara, Turkey; e-mail: anilarat@hotmail.com

http://dx.doi.org/10.3174/ajnr.A6570

One would assume that the presence of a collapsed distal carotid artery is a major risk for CAS. Whether near-occlusion with collapse is associated with a higher risk of failure or complications compared with near-occlusion without collapse remains to be shown.[9,10] We aimed to compare the technical success and perioperative (≤30 days) complication rates of CAS for the 2 near-occlusion subtypes to determine whether there is a clinical relevance of this subclassification in endovascular treatment.

MATERIALS AND METHODS

After ethical approval was obtained from our institutional review board, we retrospectively evaluated all patients with atherosclerotic extracranial ICA stenosis treated with CAS in a single medical institution between January 2014 and January 2018. Patients with near-occlusion were identified based on cerebral DSA findings. The DSA images were evaluated by 2 interventional radiologists independently based on the DSA criteria; in case of disagreement, consensus was reached. Two of the 4 following criteria described by Fox et al[11] were sought for a near-occlusion diagnosis: 1) delayed arrival of contrast medium in the distal ICA, 2) evidence of intracranial collaterals, 3) reduced ICA diameter compared with the contralateral ICA diameter, and 4) reduced ICA diameter compared with the ipsilateral external carotid artery (ECA) diameter. Collapse was defined as a stringlike lumen distal to the stenotic segment. Patients who were unable or unwilling to stay on antiplatelet agents, those with total occlusion of the cervical carotid artery on the initial diagnostic angiogram, patients with occlusion of the intracranial carotid artery, and patients with suspected vasculitic involvement of the cervical carotid artery were not offered CAS as a treatment technique. Patient characteristics, the presence of criteria for near-occlusion and collapse, arterial diameters, technical success rate, and perioperative (≤30 days) complications were analyzed.

Before carotid revascularization was performed, all patients were evaluated by 2 stroke neurologists. Baseline neurologic status was evaluated based on the modified Rankin scale before the procedure. Patients were defined as symptomatic if they had a transient ischemic attack (ocular or hemispheric) or stroke without severe disability (mRS score ≤3) up to 6 months before the procedure. Disabled patients (mRS of 4 or more) were not treated except for a single patient with a baseline mRS score of 4. This patient was treated because the patient also had contralateral ICA occlusion and insufficient collateral flow from the posterior circulation. Hyperperfusion syndrome was diagnosed based on clinical findings, which included seizures, focal neurologic deficits, or a deterioration of consciousness without evidence of a new stroke on cross-sectional imaging. In patients with subtle or equivocal findings, the presence of cerebral edema, hemorrhage, or both in the ipsilateral carotid territory without an acute territorial stroke led to the diagnosis of hyperperfusion syndrome.

The angiograms of the patients with collapse were evaluated for pre- and postprocedure ICA diameters. The measurement was made at the same level based on bony landmarks. We assumed the diameter of the ECA was constant during the procedure, and the ratio of the postprocedure diameter of the ICA over the preprocedure diameter was calculated with the following formula: (postprocedure ICA diameter/postprocedure ECA diameter) divided by (preprocedure ICA diameter/preprocedure ECA diameter). Angiograms were also scrutinized for dissection, thrombus formation, and intracranial embolization.

All of the patients referred for treatment of carotid stenosis by stent placement were initially evaluated by CTA. Those who had an ultrasound evaluation as an initial diagnostic technique were also verified by CTA. In case of equipoise, a contrast-enhanced head and neck MRA was performed. All patients who had noninvasive confirmation of the stenosis first underwent a cerebral DSA. None of the patients were denied CAS based on anatomy of the aortic arch on CTA or plaque morphology on ultrasound imaging. Stent placement was universally performed in a second session.

Interventional Procedure

Written informed consent was obtained from all patients before the procedure. Dual antiplatelet therapy (75 mg of clopidogrel and 300 mg of aspirin per day) was orally initiated at least 5 days before the procedure for elective cases. For acute cases, patients were preloaded with 6 tablets of clopidogrel. Although the value of intraprocedural monitoring studies such as transcranial Doppler sonography (TCD) during CAS has been delineated well in the literature,[12] we were unable to use this technique intraprocedurally in our major tertiary referral center, because of logistical reasons such as scheduling issues and unavailability of a full-time specialist dedicated to TCD in the angiography suite. After insertion of the femoral vascular sheath under monitored anesthesia, common carotid artery catheterization was performed with a long sheath. The stenosis was crossed with a microguidewire. When a distal protection device was used, it was either advanced directly over this guidewire, or alternatively, a small-bore microcatheter was used to cross the stenosis, and it was exchanged with the protection device. Then, under distal protection (Spider FX, Medtronic or Emboshield, Abbott Vascular), proximal protection (Mo.Ma system, Medtronic), or dual (proximal and distal) cerebral protection, angioplasty was performed with a 2- to 3-mm balloon catheter to dilate the stenotic segment. Then, a self-expandable stent (Protégé, Medtronic) was deployed. If there was suspicion for suboptimal plaque coverage, a second stent was deployed telescopically. Postdilation was performed with a monorail angioplasty balloon catheter after stent deployment.

Blood pressure and heart and expiratory rates were continuously monitored during the procedure by anesthesiologists. After the procedure, all patients were admitted to an intensive care unit for at least 24 hours. During the procedure and the postoperative period, the mean blood pressure was kept at around 100 mm Hg, preferably by using esmolol or nitroglycerin infusion as needed for 24–48 hours.

Patients were advised to use 300 mg/day of aspirin and 75 mg/day of clopidogrel for at least 6 months after the procedure and were asked to return for a 1-month clinical follow-up and a 6-month cervical Doppler sonography study.

Statistical Analysis

The SPSS 20.0 (IBM) program was used for statistical analysis. Continuous data were presented as mean ± SD and categoric data as frequency and percentage. Categoric variables compared were with use of the χ-square test (Fisher exact test if required), and mean values were compared with use of the independent-samples *t*

Table 1: Angiographic findings in carotid near-occlusion

Findings	*n* (%)
Near-occlusion with collapse	11 (18.6)
Delayed arrival of contrast medium in the distal ICA	53 (89.8)
Evidence of intracranial collateral	47 (79.7)
Reduced ICA diameter compared with the contralateral ICA diameter[a]	56 (100)
Reduced ICA diameter compared with the ipsilateral ECA diameter	53 (89.8)

[a]Not applicable in 3 patients because of contralateral total occlusion or near-occlusion with collapse.

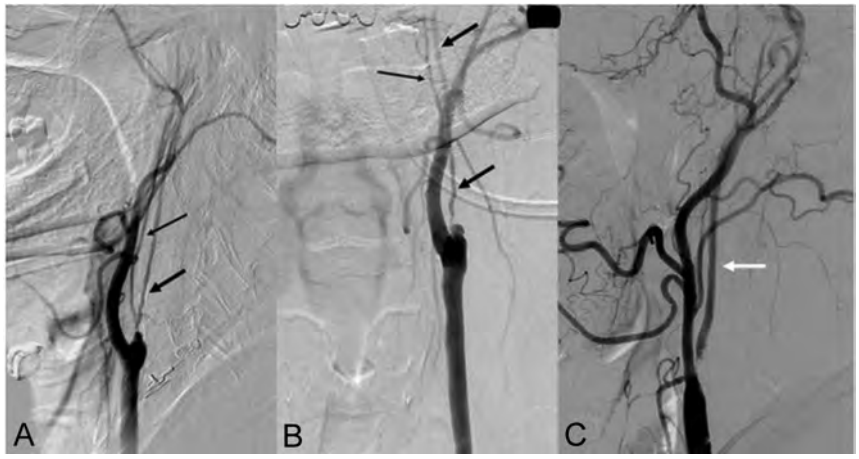

FIG 1. *A* and *B*, Near-occlusion with collapse. Cervical angiograms in lateral and anteroposterior projections, respectively. *Thick black arrows* indicate the string sign in near-occlusion with collapse. *Thin black arrows* indicate ascending pharyngeal artery. The ascending pharyngeal artery should not be confused with near-occlusion with collapse, especially in the setting of total ICA occlusion. *C*, Near-occlusion without collapse. Lateral cervical angiogram shows tight stenosis of ICA origin and diameter reduction in distal cervical ICA (*white arrow*) compared with the ipsilateral external carotid artery.

Table 2: Patient characteristics

Characteristics	Near-Occlusion with Collapse (*n* = 11) (%)	Near-Occlusion without Collapse (*n* = 47) (%)	*P* Value
Age (mean)	65.73 ± 11.6	67.81 ± 8.7	.509
Male sex	9 (81.8)	37 (78.7)	1
Left side	6 (54.5)	29 (60.4)	.745
Symptomatic	8 (72.7)	33 (70.2)	1
Hypertension	7 (63.6)	36 (76.6)	.450
Diabetes	6 (54.5)	26 (53.3)	1
Active smoker	4 (36.4)	24 (51.1)	.380
Hypercholesterolemia	5 (45.5)	25 (53.2)	.644
Coronary heart disease	4 (36.4)	15 (31.9)	1
Contralateral severe stenosis (≥70)/ near-occlusion/total occlusion)	1[a] (9.1)	8[b] (16.7)	1

[a]Near-occlusion without collapse.
[b]One near-occlusion with collapse, 2 total occlusions, and 5 severe stenoses.

test (Mann-Whitney *U* test if required). Statistical significance was set at $P = .05$.

RESULTS

A total of 58 patients (46 men, mean age 67.41 ± 9.2 years) with 59 near-occlusions were treated with CAS. One patient had bilateral near-occlusion. Near-occlusion with collapse was diagnosed in 12 cases by the first interventional radiologist and in 11 by the second interventional radiologist. In 11 of these, the final diagnosis was near-occlusion with collapse. By consensus, the last patient was finally diagnosed with near-occlusion without collapse.

The angiographic findings in the patients with near-occlusion are listed in Table 1. Angiographic examples of near-occlusions with and without collapse are demonstrated in Fig 1. There was no significant difference between the near-occlusion with collapse and near-occlusion without collapse groups based on patient characteristics (Table 2). The near-occlusions were symptomatic in 41 patients (70.7%, including 23 patients with stroke, 16 patients with TIA, and 2 patients with acute ICA occlusion after the diagnosis of near-occlusion) and asymptomatic in 17 patients (29.3%). Two patients (1 with collapse and 1 without collapse) were treated emergently for acute ICA occlusion, which developed as the patient was waiting for a CAS procedure after the elective cerebral DSA. Otherwise, CAS was performed electively.

Fifty-eight of the 59 CAS procedures were successful. In 1 case of near-occlusion with collapse, we were not able to pass through the stenosis because of patient motion under conscious sedation; the patient was advised to undergo stent placement under general anesthesia during the procedure, but he refused to have any type of procedure under general anesthesia. Examples of the procedures in 2 patients with and without collapse are provided in Figs 2 and 3. Additional stents were used in 12 of the 58 cases. In 10 cases, the second stent was deployed because the operator's threshold to deploy a second stent in case of the slightest suspicion of plaque prolapse is low. In 2 cases, the second stent was deployed as the position of the first stent was deemed to be less than ideal by the operator. Overall, 17 patients were asymptomatic, and the permanent morbidity and mortality rate, excluding transient symptoms related to hyperperfusion syndrome, in this group was 0%. One patient of 17 in this group had an episode of a seizure related to hyperperfusion syndrome and was treated with antiepileptics promptly and without any clinical consequences. Forty-one patients were symptomatic. Of these, 1 died as a result of stent occlusion, and 1 had residual

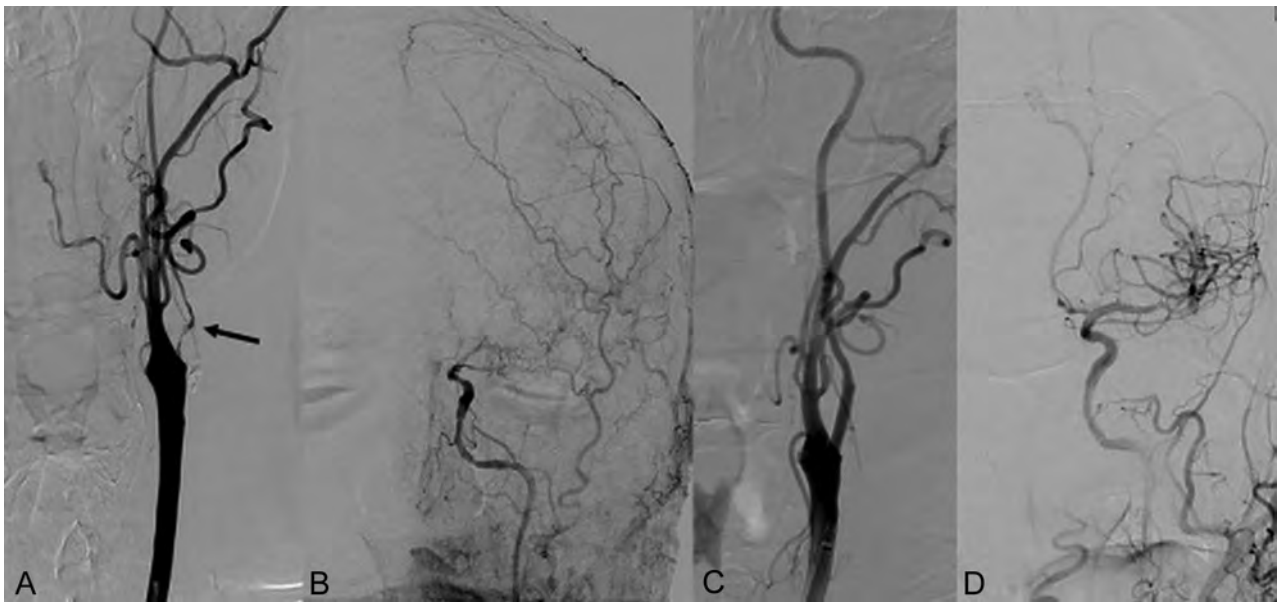

FIG 2. *A* and *B*, Preoperative cervical and cranial angiograms in patient with near-occlusion with collapse (*arrow* in *A*), respectively. *C* and *D*, Postoperative cervical and cranial angiograms show improvement of diameter of ICA and restoration intracranial blood flow, respectively.

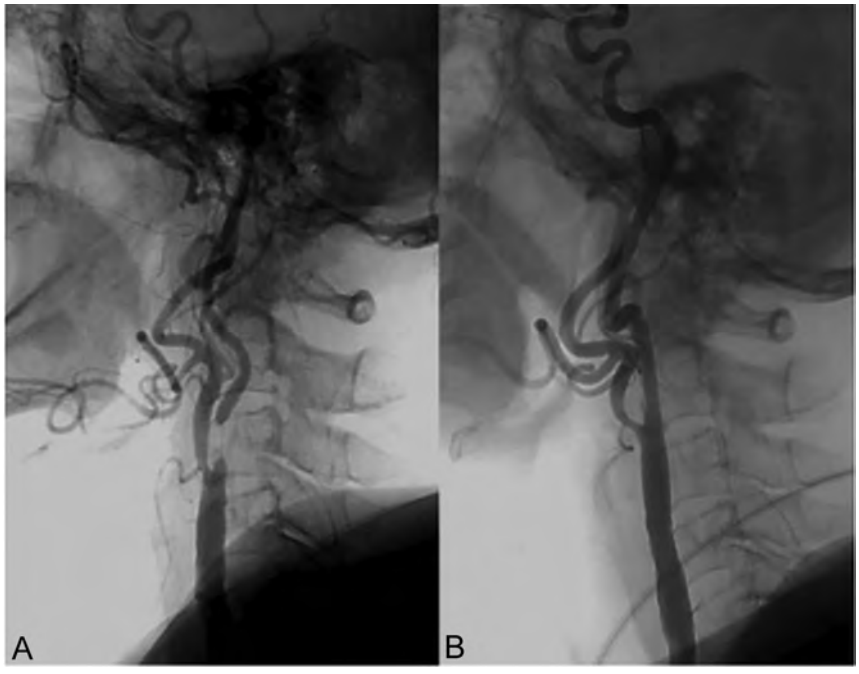

FIG 3. Pre- and postoperative cervical lateral angiograms in patient with near-occlusion without collapse, respectively.

hemiparesis after hyperperfusion syndrome, resulting in a permanent morbidity and mortality rate of 4.9%. In this group, 1 patient complained of headache, and head CT revealed minor intracranial hemorrhage (Fig 4). The patient's initial mRS score was 3 and remained 3 on follow-up.

In 1 patient without collapse, plaque rupture and acute thrombus formation were encountered immediately after predilation. Thrombectomy and stent placement were performed without any clinical adverse outcomes. In 3 patients (2 without collapse and 1 with collapse) following postdilation, antegrade slow flow was encountered proximal to the distal protection device as previously described in the literature.[13] After aspiration of free debris and removal of the distal filter, antegrade flow was restored without clinical outcomes in 2 patients without collapse. In the patient with collapse, intracranial severe stenosis was discovered after postdilation and was unrecognizable before angioplasty. Aspiration of free debris and removal of the distal filter did not restore the optimum antegrade flow in this case. Asymptomatic stent occlusion occurred without clinical outcomes within 1 month after the procedure.

Five patients (8.6%) experienced hyperperfusion syndrome during the perioperative period. Three patients experienced a seizure within 24 hours after the procedure. One patient experienced left upper extremity paresis without any signs of stroke on MR imaging 3 weeks after the procedure, consistent with late hyperperfusion syndrome. There was a decline in the patient's baseline mRS score from 1 to 2. One of the patients who presented with acute ICA occlusion experienced small patchy cortical and subarachnoid hemorrhagic foci without a deterioration in baseline neurologic status (Fig 4). Compared with patients without collapse (2 of 48 patients [4.2%]), those with collapse (3 of 10 stented patients

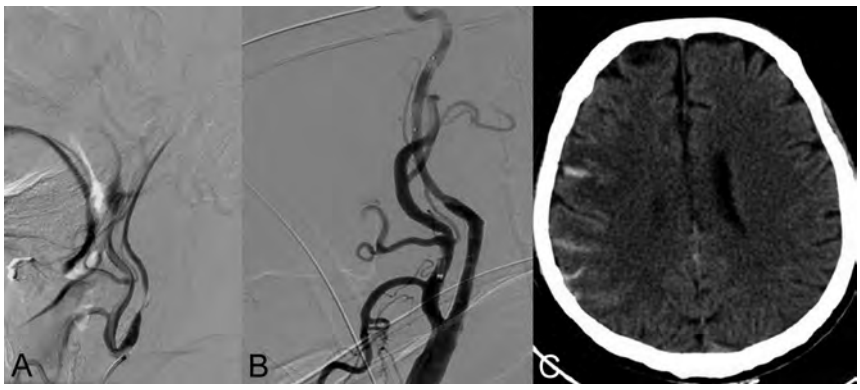

FIG 4. Right carotid angiogram (*A*) before and (*B*) after deployment of a carotid stent. *C*, Postprocedure cranial CT image of the same patient shows right-sided hemorrhage related to hyperperfusion syndrome after carotid artery stent placement.

[30%]) had significantly higher rates of postintervention hyperperfusion syndrome (Fisher exact test, $P = .032$). In 2 of the 3 patients with seizures, seizure control was achieved with antiepileptic drugs. In a patient (without collapse and contralateral occlusion) with intractable seizures, clopidogrel was stopped because of the possibility of an intracranial hemorrhage. The patient was discharged with aspirin and low-molecular-weight heparin after the seizures were controlled. The patient failed to comply with his medication, presented with stent occlusion, and eventually died. One patient (1.7%) developed perioperative minor ischemic stroke without a change in the patient's baseline mRS score (preoperative mRS score, 3). There was no myocardial infarction in either of the groups. In the whole cohort, the overall permanent morbidity and mortality rates were 1.7% and 1.7%, respectively. The ratio of postprocedural ICA diameter divided by preprocedural ICA diameter ranged from 1.16 to 3.69 (mean, 1.76). There was no residual stenosis in the collapse group per NASCET criteria postprocedurally, mainly because the distal artery was small to start with, and it did not expand fully immediately after stent placement (maximum postprocedure carotid artery diameter, 3.69 mm). However, the diameters of all of the stented arteries in the collapse group remained below the nominal size range of the carotid artery immediately after stent placement. There was no difference in the occurrence of hyperperfusion syndrome in patients who had symptomatic carotid near-occlusion versus those who had asymptomatic carotid near-occlusion ($P = 1$).

DISCUSSION

Carotid near-occlusion has been described with the use of various terms in the literature, such as string sign, pseudo-occlusion, slim sign, critical stenosis, and preocclusive stenosis.[14] Carotid near-occlusion was subclassified as near-occlusion with and without string sign in the NASCET.[2] Carotid near-occlusion's definition and its subclassification were revised by Fox et al[11] to include near-occlusion with collapse and the rare subtype[9] of near-occlusion without collapse. Similarly, Johansson et al[14] also advocated the use of near-occlusion with collapse and near-occlusion without collapse in their review. The definition of collapse is described clearly in the literature, yet there may be discrepancies between radiologists as to the presence of collapse, particularly when DSA is used for diagnosis. In the routine clinical setting, patient discomfort and subsequent motion during DSA may add to the degradation of images to an extent that may compromise the validity of measurements. The lack of specific criteria for patients with contralateral carotid occlusion (removing 1 of the 4 diagnostic criteria in this subset of patients) may also lead to discrepancies in the evaluation of the DSA images. Nevertheless, in real-world practice, no angiographic definition is ideal. With relatively clear-cut angiographic criteria[14] and a good-to-excellent interrater agreement of the definition of collapse or near-occlusion,[11] the diagnosis of collapse appears reliable in most patients. Although subclassification has been advocated for near-occlusion, the actual risk of treatment failure and perioperative complication rate related to CAS in the 2 different near-occlusion subgroups are unknown.

The use of invasive treatment in patients with near-occlusion is still controversial. Nevertheless, CAS performed for near-occlusion constitutes 1.72% to 28.9% of all CAS procedures.[10] Many previous CAS studies have reported high technical success with near-occlusion treatment,[15-21] with perioperative complication rates ranging between 3.3% and 17.4%. Interestingly, in studies with low perioperative complication rates, most of the complications were TIA or minor strokes. In contrast, in studies with relatively higher complication rates, the reported complications tended to be major complications, such as major stroke, hyperperfusion syndrome, and death.[16-19,22] Our overall perioperative complication rate was 10.3%. The permanent morbidity and mortality rate was 4.2% in the group without collapse and 0% in the collapsed group. Although the overall complication rate in this study appears to be high, we would like to stress the fact that the permanent morbidity and mortality rate in this cohort is within acceptable range. The overall complication rate is increased by additional inclusion of minor stroke without clinical consequences as well as hyperperfusion syndrome cases discovered by imaging in patients with symptoms such as headache, dizziness, or stiff neck without a clinical sign.

We were unable to find a previous report comparing the outcomes of CAS in the 2 near-occlusion subtypes (with collapse versus without collapse). In our cohort, although there was no significant difference in the composite risk of stroke, death, and myocardial infarction between near-occlusions with and without collapse (Fisher exact test, $P = .682$), we found a significant difference in hyperperfusion syndrome rates between these 2 groups.

In total, 5 of our patients (8.6%) experienced hyperperfusion syndrome perioperatively. Three of the 5 patients were patients with collapse. Compared with patients without collapse, those with collapse had significantly higher rates of postintervention hyperperfusion syndrome ($P = .032$). Previous studies on near-

occlusion treatment with CEA reported a trend toward a higher hyperperfusion syndrome rate in patients with collapse (0% without collapse vs 3.8% to 5.9% with collapse).[9,23] However, studies evaluating CAS in the setting of near-occlusion merged patients both with and without collapse into a single near-occlusion group without comparing these groups.[16-19,22] Hence, the actual perioperative complication rates of near-occlusions with and without collapse are unknown. To the best of our knowledge, Neves et al.[7] are the only authors who reported outcomes of CAS specifically in patients with symptomatic near-occlusion with collapse. They reported no periprocedural complications other than immediate upper limb monoparesis with complete recovery in 19 patients. These authors did not include near-occlusion without collapse in their series, so a comparison was not available.

Hyperperfusion syndrome occurs in 0%–3% of patients with conventional extracranial ICA stenosis treated with carotid intervention.[24] Decreased cerebral autoregulation and postoperative hypertension are the most consistently reported risk factors for hyperperfusion syndrome in the literature, and it is well accepted that the greater extent of ipsilateral stenosis will cause a greater risk of perioperative hyperperfusion syndrome.[24-27] Oka et al[28] demonstrated that patients with near-occlusion were more hemodynamically compromised than those with severe stenosis without near-occlusion. This could be the explanation for the higher perioperative hyperperfusion syndrome rate (8.6%) in our study. Although CAS series with no hyperperfusion syndrome have been reported in patients with near-occlusion,[16,19] in literature defining near-occlusion based on strict angiographic criteria, hyperperfusion syndrome risk was higher. For instance, consistent with our results, Son et al[17] reported an 8.7% perioperative hyperperfusion syndrome risk in patients with near-occlusion treated with CAS. Additionally, Ruiz-Salmeron et al[18] reported a 5.5% perioperative mortality rate related to intracranial hemorrhage secondary to hyperperfusion syndrome in patients with near-occlusion, which was higher than the rate in the group without near-occlusion (perioperative mortality rate related to hyperperfusion syndrome, 0.6%). However, from these studies, it is not possible to extract any data regarding the role of collapse in the near-occlusion group.

Our 8.6% rate of hyperperfusion syndrome is high albeit still within the expected range based on a recent review of the literature.[29] The reported rate of hyperperfusion syndrome actually depends on the proposed definition of the syndrome. For instance, when strict imaging criteria such as TCD imaging criteria are used, the rate of hyperperfusion syndrome is higher compared with the diagnosis of hyperperfusion syndrome based only on clinical symptoms.[12,29] This is why our results, which rely not only on definite symptoms but also on clinical suspicion supported by cross-sectional imaging, are on the higher side of the expected range. Because hyperperfusion syndrome may result in grave consequences, TCD-based detection may allow operators to act earlier, taking additional measures to prevent development of full-blown hyperperfusion syndrome. Aside from vigorous hemodynamic monitoring, these measures include early detection of this syndrome via use of intraprocedural monitoring by TCD as described earlier, prophylactic use of antiepileptics in the perioperative period in high-risk cases, and avoidance of poststent angioplasty. Although the postoperative increase in the diameter of the carotid artery was not related to hyperperfusion syndrome in this study, a possible relation may have been overlooked because of the small number of hyperperfusion syndrome cases. Intuitively, one may put forward that gradual expansion of the ICA with the intrinsic force of a self-expanding stent, without the acute luminal expansion created by poststent angioplasty, may be beneficial in minimizing the risk of hyperperfusion syndrome. This CAS method has been adopted routinely by some authors[30] and may potentially decrease the complications and cost of CAS as well.

After finding an increased rate of hyperperfusion syndrome in the collapsed group, we wanted to determine whether the enlargement of the collapsed artery may be involved in the development of hyperperfusion syndrome. When ICA diameters were calibrated according to the ECA diameter and the proportion of increase in the diameter of the collapsed ICA was calculated after the procedure, we found that the diameter of the ICA consistently increased after the treatment. However, we could not find a significant difference between ICA diameter ratios in the collapse groups with and without hyperperfusion syndrome. This suggests that the higher hyperperfusion syndrome risk in the collapse group may not be related only to luminal diameter, and other factors such as decreased cerebral autoregulation or underlying blood–brain barrier damage may be involved.

The limitations of our study include the retrospective nature of the study and the lack of mid- and long-term follow-up periods for the treated patients. In addition, it would have been ideal to perform routine postprocedure cross-sectional imaging dedicated to hyperperfusion syndrome or perfusion[31] or to obtain postprocedure TCD measurements in all patients.

CONCLUSIONS

Because near-occlusions with and without collapse differ in terms of their natural history, it is imperative that CAS outcomes be discussed separately for these 2 groups. In our series, there was no difference in the overall complication rate, but there was a higher risk of hyperperfusion syndrome in the collapse group than in the noncollapse group, which is likely associated with a lower risk of ipsilateral stroke if left untreated.[7] Thus, there may be a clinical correlate of the subclassification of near-occlusion that needs to be further verified in larger studies or registries. Strict perioperative measures to decrease the likelihood of hyperperfusion syndrome and meticulous performance of the CAS technique may be vital in the collapse group to surpass the natural history in this subgroup.

Disclosures: Ethem Murat Arsava—*UNRELATED: Board Membership:* Boehringer Ingelheim, Pfizer, Abbott, Daiichi Sankyo, Nutricia; *Payment for Lectures including Service on Speakers Bureaus:* Boehringer Ingelheim, Pfizer, Sanofi, Abbott, Nutricia.

REFERENCES

1. Abreu P, Nogueira J, Rodrigues FB, et al. **Intracerebral hemorrhage as a manifestation of cerebral hyperperfusion syndrome after carotid revascularization: systematic review and meta-analysis.** *Acta Neurochir (Wien)* 2017;159:2089–97 CrossRef Medline
2. Morgenstern L, Fox A, Sharpe B, et al. **The risks and benefits of carotid endarterectomy in patients with near occlusion of the carotid artery.** *Neurology* 1997;48:911–15 CrossRef

3. Rothwell P, Gutnikov S, Warlow C. **Reanalysis of the final results of the European Carotid Surgery Trial.** *Stroke* 2003;34:514–23 CrossRef
4. O'Leary DH, Mattle H, Potter JE. **Atheromatous pseudo-occlusion of the internal carotid artery.** *Stroke* 1989;20:1168–73 CrossRef Medline
5. García-Pastor A, Gil-Núñez A, Ramírez-Moreno JM, et al; Stroke Project of the Spanish Cerebrovascular Diseases Study Group. **Early risk of recurrent stroke in patients with symptomatic carotid near-occlusion: results from CAOS, a multicenter registry study.** *Int J Stroke* 2017;12:713–19 CrossRef Medline
6. Johansson E, Öhman K, Wester P. **Symptomatic carotid near-occlusion with full collapse might cause a very high risk of stroke.** *J Intern Med* 2015;277:615–23 CrossRef Medline
7. Neves CRB, Casella IB, da Silva ES, et al. **Medical therapy for asymptomatic patients and stent placement for symptomatic patients presenting with carotid artery near-occlusion with full collapse.** *J Vasc Interv Radiology* 2018;29:998–1005 CrossRef
8. Meershoek A, de Vries E, Veen D, et al. on behalf of the NEON Study Group. **Meta-analysis of the outcomes of treatment of internal carotid artery near occlusion.** *Br J Surg* 2019;106:665–71 CrossRef Medline
9. Meershoek AJA, Vonken EPA, Nederkoorn PJ, et al. **Carotid endarterectomy in patients with recurrent symptoms associated with an ipsilateral carotid artery near occlusion with full collapse.** *J Neurol* 2018;265:1900–05 CrossRef Medline
10. Xue S, Tang X, Zhao G, et al. **A systematic review and updated meta-analysis for carotid near-occlusion.** *Ann Vasc Surg* 2019. [Epub ahead of print] CrossRef Medline
11. Fox AJ, Eliasziw M, Rothwell PM, et al. **Identification, prognosis, and management of patients with carotid artery near occlusion.** *AJNR Am J Neuroradiol* 2005;26:2086–94
12. Pennekamp C, Moll F, Borst DG. **Role of transcranial Doppler in cerebral hyperperfusion syndrome.** *J Cardiovasc Surg (Torino)* 2012;53:765–71
13. Casserly IP, Abou-Chebl A, Fathi RB, et al. **Slow-flow phenomenon during carotid artery intervention with embolic protection devices: predictors and clinical outcome.** *J Am Coll Cardiol* 2005;46:1466–72 CrossRef
14. Johansson E, Fox A. **Carotid near-occlusion: a comprehensive review, part 1—definition, terminology, and diagnosis.** *AJNR Am J Neuroradiol* 2016;37:2–10
15. Koutsoumpelis A, Kouvelos G, Peroulis M, et al. **Surgical and endovascular intervention on internal carotid artery near occlusion.** *Angiology* 2015;34:172–81 CrossRef
16. Gonzalez A, Gil-Peralta A, Mayol A, et al. **Internal carotid artery stenting in patients with near occlusion: 30-day and long-term outcome.** *AJNR Am J Neuroradiol* 2011;32:252–58 CrossRef Medline
17. Son S, Choi DS, Kim SK, et al. **Carotid artery stenting in patients with near occlusion: a single-center experience and comparison with recent studies.** *Clin Neurol Neurosurg* 2013;115:1976–81 CrossRef Medline
18. Ruiz-Salmeron RJ, Gamero MA, Carrascosa C, et al. **Carotid artery stenting: clinical and procedural implications for near-occlusion stenosis.** *Neurologia (Barcelona, Spain)* 2013;28:535–42 CrossRef
19. Akkan K, Ilgit E, Onal B, et al. **Endovascular treatment for near occlusion of the internal carotid artery: 30-day outcome and long-term follow-up.** *Clin Neuroradiol* 2018;28:245–52 CrossRef Medline
20. Barker CM, Gomez J, Grotta JC, et al. **Feasibility of carotid artery stenting in patients with angiographic string sign.** *Catheter Cardiovasc Interv* 2010;75:1104–09 CrossRef Medline
21. Spacek M, Martinkovicova L, Zimolova P, et al. **Mid-term outcomes of carotid artery stenting in patients with angiographic string sign.** *Catheter Cardiovasc Interv* 2012;79:174–79 CrossRef Medline
22. Terada T, Tsuura M, Matsumoto H, et al. **Endovascular treatment for pseudo-occlusion of the internal carotid artery.** *Neurosurgery* 2006;59:301–09, discussion 301–09 CrossRef Medline
23. Fredericks RK, Thomas TD, Lefkowitz DS, et al. **Implications of the angiographic string sign in carotid atherosclerosis.** *Stroke* 1990;21:476–79 CrossRef Medline
24. Lieb M, Shah U, Hines GL. **Cerebral hyperperfusion syndrome after carotid intervention: a review.** *Cardiol Rev* 2012;20:84–89 CrossRef Medline
25. Moulakakis KG, Mylonas SN, Sfyroeras GS, et al. **Hyperperfusion syndrome after carotid revascularization.** *J Vasc Surg* 2009;49:1060–68 CrossRef Medline
26. Galyfos G, Sianou A, Filis K. **Cerebral hyperperfusion syndrome and intracranial hemorrhage after carotid endarterectomy or carotid stenting: A meta-analysis.** *J Neurol Sci* 2017;381:74–82 CrossRef Medline
27. Abou-Chebl A, Yadav JS, Reginelli JP, et al. **Intracranial hemorrhage and hyperperfusion syndrome following carotid artery stenting: risk factors, prevention, and treatment.** *J Am Coll Cardiol* 2004;43:1596–1601 CrossRef Medline
28. Oka F, Ishihara H, Kato S, et al. **Cerebral hemodynamic benefits after carotid artery stenting in patients with near occlusion.** *J Vasc Surg* 2013;58:1512–17 CrossRef Medline
29. Huibers AE, Westerink J, de Vries EE, et al. **Editor's choice—cerebral hyperperfusion syndrome after carotid artery stenting: a systematic review and meta-analysis.** *Eur J Vasc Endovasc Surg* 2018;56:322–33 CrossRef Medline
30. Lownie SP, Pelz DM, Lee DH, et al. **Efficacy of treatment of severe carotid bifurcation stenosis by using self-expanding stents without deliberate use of angioplasty balloons.** *AJNR Am J Neuroradiol* 2005;26:1241–48 Medline
31. Arsava EM, Hansen MB, Kaplan B, et al. **The effect of carotid artery stenting on capillary transit time heterogeneity in patients with carotid artery stenosis.** *Eur Stroke J* 2018;3:263–71 CrossRef

Fully Automated Segmentation of Globes for Volume Quantification in CT Images of Orbits using Deep Learning

L. Umapathy, B. Winegar, L. MacKinnon, M. Hill, M.I. Altbach, J.M. Miller, and A. Bilgin

ABSTRACT

BACKGROUND AND PURPOSE: Fast and accurate quantification of globe volumes in the event of an ocular trauma can provide clinicians with valuable diagnostic information. In this work, an automated workflow using a deep learning-based convolutional neural network is proposed for prediction of globe contours and their subsequent volume quantification in CT images of the orbits.

MATERIALS AND METHODS: An automated workflow using a deep learning -based convolutional neural network is proposed for prediction of globe contours in CT images of the orbits. The network, 2D Modified Residual UNET (MRes-UNET2D), was trained on axial CT images from 80 subjects with no imaging or clinical findings of globe injuries. The predicted globe contours and volume estimates were compared with manual annotations by experienced observers on 2 different test cohorts.

RESULTS: On the first test cohort ($n = 18$), the average Dice, precision, and recall scores were 0.95, 96%, and 95%, respectively. The average 95% Hausdorff distance was only 1.5 mm, with a 5.3% error in globe volume estimates. No statistically significant differences ($P = .72$) were observed in the median globe volume estimates from our model and the ground truth. On the second test cohort ($n = 9$) in which a neuroradiologist and 2 residents independently marked the globe contours, MRes-UNET2D (Dice = 0.95) approached human interobserver variability (Dice = 0.94). We also demonstrated the utility of inter-globe volume difference as a quantitative marker for trauma in 3 subjects with known globe injuries.

CONCLUSIONS: We showed that with fast prediction times, we can reliably detect and quantify globe volumes in CT images of the orbits across a variety of acquisition parameters.

ABBREVIATIONS: ACD = anterior chamber depth; AVD = average volume difference; CNN = convolutional neural network; HD = Hausdorff distance; IGVD = inter-globe volume difference; WL = window level; WW = window width; MRes-UNET2D = 2D Modified Residual UNET architecture; HU = Hounsfield unit

Open-globe injuries are traumatic full-thickness defects of the ocular wall. Although frequently diagnosed on clinical evaluation, open-globe injuries involving the sclera may not be obvious on clinical examination and require surgical exploration for definitive diagnosis and repair.[1,2] When thorough ocular examination of the anterior segment is limited by periorbital edema and hemorrhage, blepharospasm, or hyphema, imaging can be helpful to establish the diagnosis of occult open-globe injury.[3] CT is the preferred imaging technique for assessment of the extent and severity of suspected traumatic injury to the globe.[4,5] Direct CT imaging findings include altered globe contours or volumes, evidence of scleral discontinuity, or intraocular foreign bodies or gas.[6] An additional indirect imaging finding is alteration of anterior chamber depth (ACD), which may either be decreased or increased depending on anterior or posterior segment location of injury, respectively.[7,8] However, CT has been shown to have low sensitivity for the detection of open-globe injury, ranging from 51%–79%, limiting its value as a screening tool.[9-11] In a case series specifically evaluating occult open-globe injuries, CT had similar low sensitivity ranging from 56%–68%.[6]

Accurate and reliable quantification of globe volumes in the event of an ocular trauma can provide clinicians with valuable diagnostic information.[6] Manual segmentation of the globe contours by radiologists, though considered the criterion standard, is a time-consuming and labor-intensive process.[12,13] Furthermore, it is also observer dependent. Automated techniques for globe detection can remedy the pitfalls of manual segmentation.[14]

Previous works have proposed the use of semiautomated and automated techniques to measure ocular volume from CT images

Received November 13, 2019; accepted after revision March 21, 2020.

From the Departments of Electrical and Computer Engineering (L.U., A.B.); Medical Imaging (L.U., B.W., L.M., M.H., M.I.A., A.B.); Ophthalmology and Vision Science (J.M.M.); and Biomedical Engineering (A.B.), University of Arizona, Tucson, Arizona.

Please address correspondence to Ali Bilgin, PhD, Department of Biomedical Engineering, 1657 E Helen St, Keating Building, University of Arizona, Tucson, AZ, 85721; e-mail: bilgin@email.arizona.edu

http://dx.doi.org/10.3174/ajnr.A6538

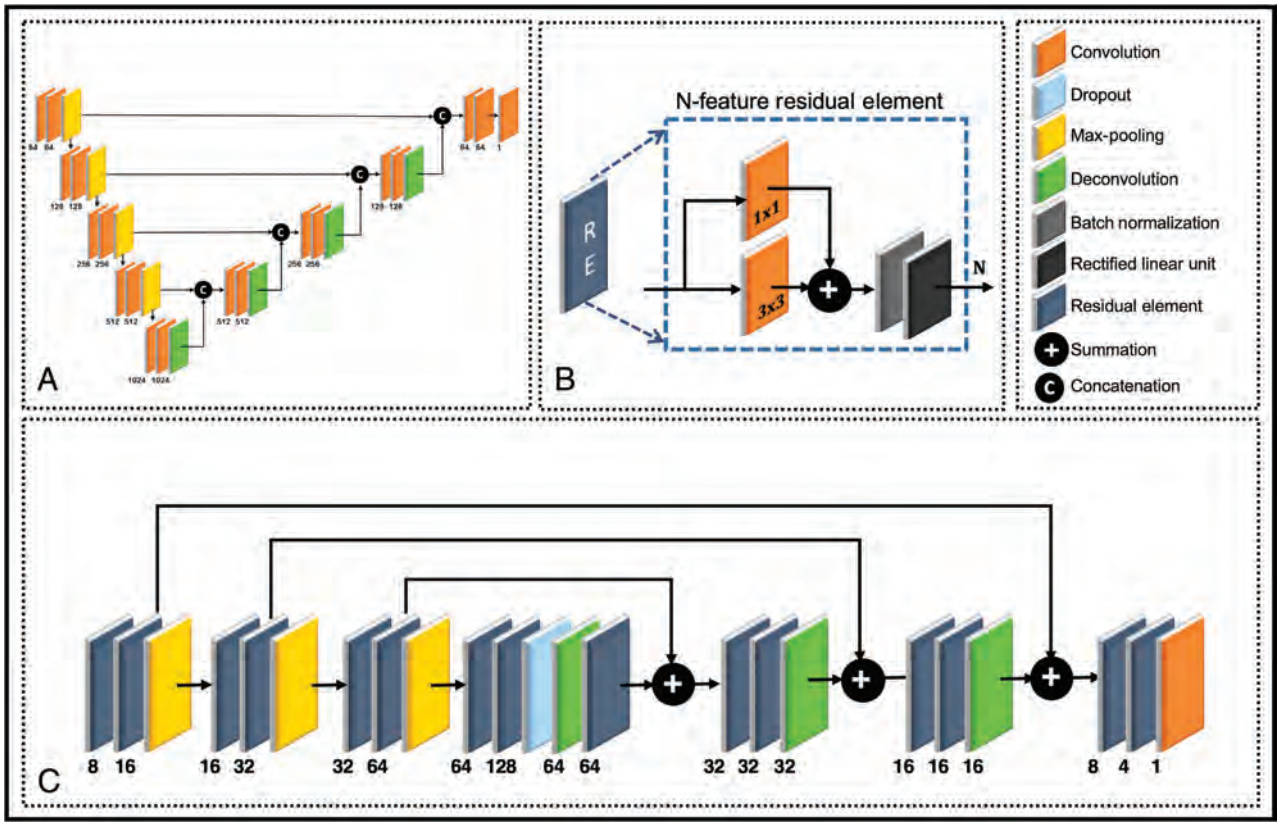

FIG 1. *A*, Architectures for *(A)* a standard 2D UNET and *(C)* a Modified Residual UNET 2D (MRes-UNET2D). *B*, The multiscale architecture in MRes-UNET2D consists of a series of *(B)* residual elements at every resolution level. The contextual information is propagated by using a series of long-and short-range skip connections. The input to the architecture consists of preprocessed axial CT images of the orbits, and the output image contains contours for the left and right globes.

in the context of surgical planning. Bekes et al[12] proposed a geometric model–based segmentation of the globes along with lenses, optic nerves, and optic chiasms in CT images. Because of the lack of a criterion standard, they did not report Dice scores. However, they estimated accuracy using the simultaneous truth and performance-level estimation algorithm published by Warfield et al[15] and reported mean sensitivity values of 97.41% and 98.04% and specificity values of 98.42% and 97.90% for the left and the right globes, respectively. Harrigan et al[13] used optimized registration and fusion methods for a multi-atlas framework[16] for automated detection of optic nerves along with eye globes and muscles on clinically acquired CT images. They reported mean Dice and Hausdorff distance (HD) of 0.84 and 5.27 mm, respectively. Another work by Aghdasi et al[17] segmented the optic nerve, globe, and extraocular muscles for skull-based surgeries in a 2-step process. The approximate boundaries of the globe were first determined followed by 2D shape fitting of the voxels inside the boundary. On 30 publicly available datasets, they reported an average Dice of 0.81 and 0.79 and 95% HD of 3 mm and 2.89 mm for the right and the left globes, respectively.

Convolutional neural networks (CNNs), widely popular in medical image segmentation tasks, are currently the state of the art in several object detection tasks.[18-20] UNET (Fig 1*A*),[21] a fully connected deep learning CNN with its multiscale encoder–decoder type architecture, is a popular choice in many of these semantic segmentation problems. Another popular architecture, ResNet,[22,23] is a single-scale setup that improves gradient back-propagation flow with increased speed of convergence[24] by learning residual features.

In this work, we combine the multiscale framework of UNET with elements that learn residual features and propose a fully automated workflow that allows for fast, accurate, and robust detection of globe contours. The proposed approach uses a deep learning–based CNN, 2D Modified Residual UNET architecture (MRes-UNET2D), and axial CT images of the orbits to predict globe contours, which are then used to quantify globe volumes.

MATERIALS AND METHODS

Convolutional Neural Network

Figure 1*C* shows the MRes-UNET2D used in this work. The network uses high-resolution 2D axial CT images of the orbits as inputs and yields contours for the globes, which are then used to compute globe volumes. The feature analysis path of the architecture uses a series of residual elements to generate multiscale abstract representations of the input images. The residual element used in our work,[25] shown in Fig 1*B*, uses a convolution layer, a short-range skip connection, followed by batch-normalization[26] and a rectified nonlinear activation. A dropout[27] layer is introduced between the analysis and synthesis paths to improve regularization.

The synthesis path of the architecture allows accurate localization by reconstructing high-resolution feature maps while adding contextual information from the corresponding level in the analysis path using long-range skip connections. A final convolution layer combines the feature maps in the native resolution space to yield pixel-wise probability maps for the labels of interest. All convolutions in the main architecture consist of 2D convolution kernels with kernel size of 3 × 3.

Study Population and Imaging Protocol

A cohort of 107 consecutive CT orbit subjects (age, 45 ± 20 years; 63 men and 44 women) older than 18 years of age, imaged over a 3-year period between January 2015 and December 2017, were identified retrospectively with the approval of the local institutional review board. These subjects presented no imaging or clinical evidence of open-globe injuries. CT images from these subjects came from 3 different CT scanners from 2 different manufacturers, Aquilion (Toshiba Medical Systems) (77 subjects), Somatom Definition AS+ (22 subjects), and Somatom Definition Flash (Siemens) (8 subjects). CT images for each subject were acquired according to the following clinical protocol: 120 kVp, 150 mAs, matrix size of 512 × 512, field of view ranging from 125 to 240 mm, and in-plane resolution ranging from 0.25 mm to 0.46 mm. The section thickness used was either 1 or 2 mm.

Three observers, consisting of a neuroradiologist with certificate of added qualification and 2 residents, agreed on a protocol to mark the globe contours on the CT images by using an in-house Matlab (MathWorks)-based graphical user interface. This included manually tracing the boundary pixels of the globes on axial cross-sections while excluding eyelids, insertions of the extraocular muscles, and optic nerves. The observers used the sagittal cross-sections for reference. The graphical user interface provided the observers with tools to adjust the window level (WL), window width (WW), and zoom level, and edit or delete contours to accurately trace the boundaries at a pixel level. No further processing was done on the contours after they were finalized by the observers.

The subjects in our study were randomly split into 3 groups: 80 subjects in the training cohort, 18 subjects in test cohort 1, and 9 subjects in test cohort 2. To measure interobserver variability, each observer annotated the left and the right globe contours for subjects in test cohort 2, blinded to the annotations by others. A consensus observer was generated by using a majority voting scheme on the individual observer contours. The subjects in the training cohort and test cohort 1 were randomly split between the 3 observers.

An overview of the proposed workflow is shown in Fig 2 for the training and test phases. All images undergo an image preprocessing step, which consists of adjusting the WW and WL to enhance soft tissue contrast between the globes, background muscle, and bone, followed by rescaling of image intensities for each subject to have intensities in the range of [0, 1].

From the 80 subjects in the training cohort, 74 subjects, with 2610 images, were used to train the deep learning model; 6 subjects, with 216 images, were used for validation. Data sampling was performed for an equal representation of images with and without globes in the training data. The following 2D augmentation

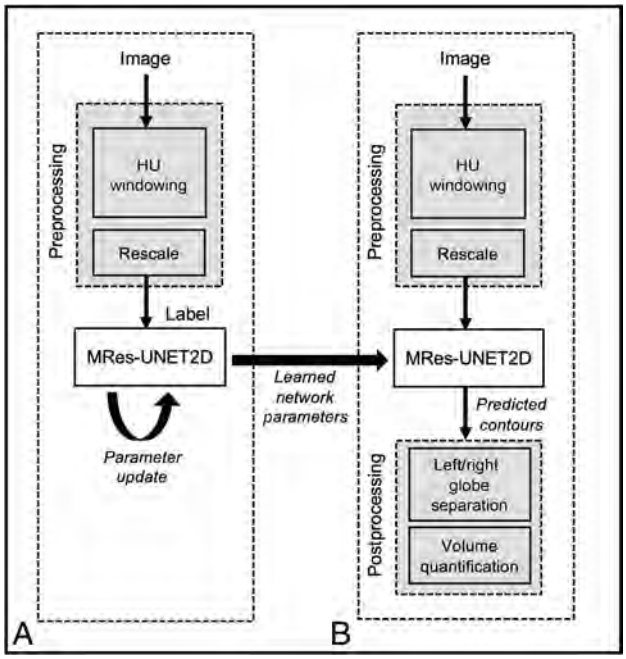

FIG 2. *A*, Train phase and *(B)* test phase of the MRes-UNET2D architecture. The deep learning model's parameters are updated by using image–label pairs in the training set. After the loss converges, the learned network parameters are used to predict the globe contours on test images.

schemes were used: random in-plane translations (±10 pixels in each direction), in-plane rotations selected uniformly from [−15°, 15°], left/right image flips, 2D elastic deformations, and image zoom. During the training process, augmented images were generated in run time on every training image batch. Any 3 of the aforementioned augmentation schemes were randomly selected, and an augmented image was generated by sequentially applying the selected schemes on each image in a training batch.

Network Implementation

A Dice similarity-based loss function was used to maximize the overlap between the predicted globe masks and the ground truth masks. We used the following definition of Dice loss:

$$L_{Dice} = \frac{\sum_n r_n p_n}{\sum_n r_n + \sum_n p_n} + \frac{\sum_n (1 - r_n)(1 - p_n)}{\sum_n (1 - r_n) + \sum_n (1 - p_n)}$$

Here, r_n and p_n refer to the ground truth and the predicted posterior values at the n^{th} pixel, respectively.

Two different window settings were used to study the impact of Hounsfield unit (HU) windowing on model performance. The WL and WW ([WL, WW]) for the 2 experiments were selected to be [50, 200] and [0, 200] HU. In these experiments, the training images retained their original image resolutions, which ranged from 0.25 mm to 0.46 mm in-plane. We also trained an additional model in which all training image volumes were resampled to a common grid by using cubic spline interpolation. This was done to test if resampling the images to a common resolution provides any improvement to the performance of the model. The resolution for the common grid was obtained from the average resolution of the training set: 0.3 mm in-plane and 2-mm section thickness.

All experiments were implemented in Python by using Keras (https://keras.io) with TensorFlow[28] computational backend. The training was performed on a Linux server running Ubuntu, with a Tesla P100 (NVIDIA) and 16-GB VRAM. The MRes-UNET2D architecture, with approximately 133,000 trainable weights, was trained with the following parameters: optimizer = ADAM,[29] maximum epochs = 120, batch size = 5, learning rate = $1e^{-3}$, decay factor = 0.1. The learning rate was optimized for Dice loss by monitoring the training and the validation loss curves for convergence for a range of learning rates along with performance evaluation on the validation images. The MRes-UNET2D model used in this work is also available at https://github.com/spacl-ua/globe-volumes.

We also implemented a standard UNET[21] architecture for comparison. The convolution layers were zero-padded, with 3 × 3 convolution kernels, to yield predictions, which were the same size as input. The cross-entropy loss function used in the original paper was modified to a binary cross-entropy loss for the binary classification problem. The training and the validation images for this UNET were the same as those used for training the MRes-UNET2D model with HU windowing set to [WL = 50, WW = 200]. The training parameters for UNET were as follows: optimizer = ADAM,[29] maximum epochs = 120, batch size = 5, learning rate = $1e^{-3}$, and decay factor = 0.1.

Network Evaluation

The generalizability of the models was evaluated by using the following performance metrics: Dice, precision, recall, 95% HD, and volume difference. These evaluation metrics are defined as follows:

$$Dice = 2 * \frac{|P \cap GT|}{|P| + |GT|}$$

$$Precision\ (\%) = \frac{|P \cap GT|}{|GT|} \times 100$$

$$Recall\ (\%) = \frac{|P \cap GT|}{|P|} \times 100$$

$$\delta_H(G_s, P_s) = \max_{g \in GT} \min_{p \in P} \|g - p\|$$

$$95\%\ HD(G_s, P_s) = \mathrm{P}_{95}\{\delta_H(G_s, P_s), \delta_H(P_s, G_s)\}$$

$$VD = \frac{abs\ (V_P - V_{GT})}{V_{GT}}$$

Here GT refers to the ground truth and P to the predictions from the network. The one-sided HD between point sets $G_s = \{g_1, g_2, \ldots, g_n\}$ and $P_s = \{p_1, p_2, \ldots, p_n\}$ is $\delta_H(G_s, P_s)$. We used the 95th percentile (P_{95}) of HD, referred to as 95% HD, because it is slightly more stable to small outliers compared with taking the maximum value. V_P and V_{GT} refer to the total globe volumes computed from the predicted globe contours and ground truth for a subject, respectively. Higher values of Dice, precision, and recall imply good performance. Lower values of 95% HD imply smaller deviation in the predicted contour compared with the ground truth.

Pair-wise Dice similarity scores were calculated on test cohort 2 between the annotations from the 3 observers, the consensus observer, and the predictions from MRes-UNET2D. For each subject, we also calculated the inter-globe volume difference (IGVD), which is the volume difference in milliliters between the left and the right globe.

$$IGVD = V_L - V_R$$

To test the generalizability of MRes-UNET2D on cases with suspected globe injuries, we also evaluated the model on 3 subjects with varying degrees of globe injuries, with conspicuity on CT imaging ranging from subtle to obvious. These 3 cases were outside of our study cohort and were identified by the radiologists retrospectively as test cases with globe injuries.

Statistical Analysis

A nonparametric Kruskal-Wallis test was performed to determine whether there were any significant differences in the performance of MRes-UNET2D between different image preprocessing settings. This test was repeated to compare for significant differences between the standard UNET and MRes-UNET2D. A 2-sided paired Wilcoxon signed rank test was performed to assess the null hypothesis that the difference in globe volumes predicted by MRes-UNET2D on test cohort 1 and ground truth annotations come from a distribution with zero median. The significance level was selected as .05 for all of these tests. A Bland-Altman analysis was performed to assess the agreement in the computed globe volumes per hemisphere between the human observers, MRes-UNET2D, and the consensus observer. To determine the variation between observers, reproducibility coefficient and coefficient of variation statistics were computed. We also tested for the null hypothesis that the IGVD values from MRes-UNET2D, consensus observer, and the 3 observers come from the same distribution by using the nonparametric Kruskal-Wallis test.

RESULTS

The training of our deep learning model, MRes-UNET2D, took approximately 5 hours. In the test phase, the end-to-end prediction time for a volume (512 × 512 × 40) was approximately 5 seconds on 2 NVIDIA P100 GPUs. The actual prediction time, excluding the pre- and postprocessing times, was approximately 680 ms per volume. Figure 3*A* shows representative axial CT images corresponding to 2 different window settings. The training and the validation loss curves for 1 instance of the MRes-UNET2D are shown in Fig 3*B*.

A comparison of the effect of preprocessing on the performance of the MRes-UNET2D on test cohort 1 is shown in Table 1. The first 2 columns correspond to the different window settings. The third column shows the performance of the network when all images are resampled to a common grid of 0.3-mm resolution in-plane and 2-mm section thickness. Results of the nonparametric Kruskal-Wallis tests indicated that we were unable to reject the null hypothesis that the Dice scores ($P = .39$), average volume difference (AVD) ($P = .57$), or 95% HD ($P = .87$) from MRes-UNET2D for the different image preprocessing schemes come

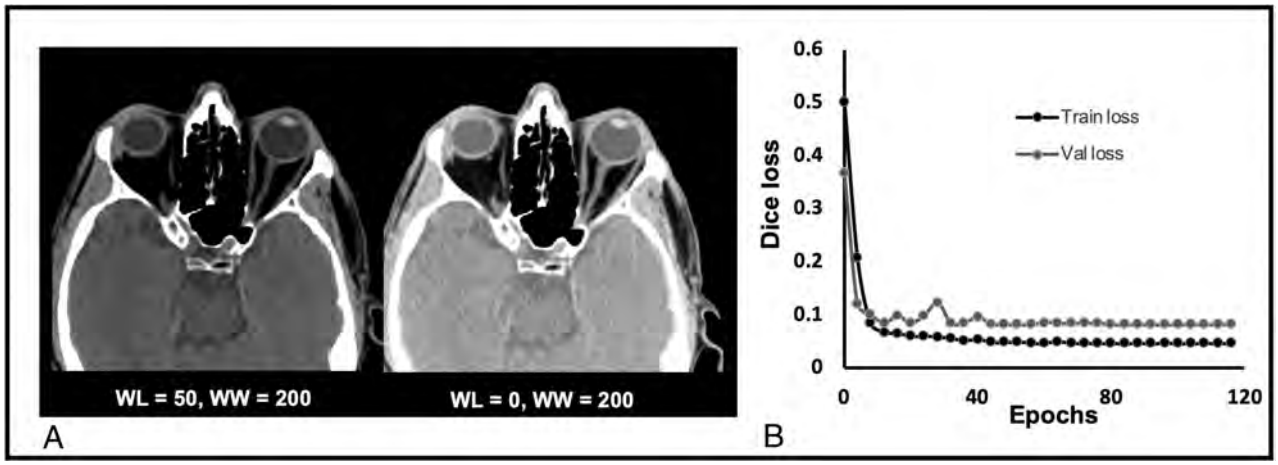

FIG 3. *A*, Representative axial CT images of the orbits with 2 different HU window settings [window level (WL), window width (WW)] = [50,200] *(left)* and [0,200] *(right)*. *B*, Dice loss evolution curves over epochs for 1 of the MRes-UNET2D models.

Table 1: Evaluation of MRes-UNET2D and UNET2D on test cohort 1 ($n = 18$)[a]

	MRes-UNET2D			UNET2D
	WL = 50 WW = 200	WL = 0 WW = 200	Common Grid Resampling	WL = 50 WW = 200
Dice	0.95 (0.02)	0.95 (0.02)	0.94 (0.03)	0.95 (0.02)
Precision (%)	96 (3)	96 (3)	96 (3)	95 (3)
Recall (%)	95 (5)	95 (5)	93 (6)	95 (4)
95% HD (mm)	1.5 (1.3)	1.6 (1.2)	1.6 (1.4)	1.7 (1.2)
AVD (%)	5.3 (5.4)	5.5 (5.1)	6.8 (6.0)	5.8 (4.7)

[a] Values in the table are mean (standard deviation).

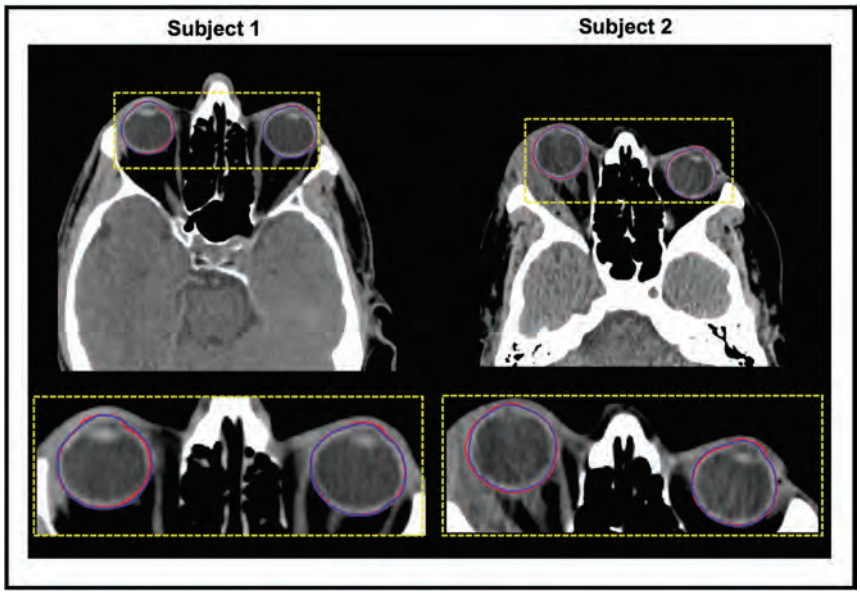

FIG 4. Globe contour predictions from MRes-UNET2D. The predicted contours are overlaid in *blue* on representative axial CT images of the orbits from 2 test subjects. The manual annotations are overlaid in *red* for reference. The *inset* shows a close-up comparison of the predictions.

from the same distribution. Overall, we observe that slight variations in preprocessing did not result in any significant differences in model performance. For subsequent evaluations, we selected the model with windowing [50, 200] because on average, it yielded the smallest HD and AVD with improved Dice overlap scores among the 3 models.

Figure 4 shows the manual annotation (red) and globe contour predictions from MRes-UNET2D (blue) on a few representative CT images. On average, MRes-UNET2D achieved Dice scores of 0.95 with respect to the ground truth, with high precision and recall values of 96% and 95%, respectively. The average 95% HD was only 1.5 mm, with a 5.3% error in the estimation of total globe volume. The 2-sided paired Wilcoxon signed rank test revealed no significant differences ($P = .72$) in the median globe volumes from the ground truth and MRes-UNET2D predictions on test cohort 1.

Table 1 also compares the average performance of MRes-UNET2D to a standard UNET architecture on test cohort 1, where with 10× fewer trainable parameters, MRes-UNET2D obtains lower mean HD and AVD values while also improving on the mean Dice and precision scores (Fig 5). However, we did not find this difference in performance to be significant for Dice ($P = .43$), precision ($P = .22$), recall ($P = .72$), 95% HD ($P = .36$), and AVD ($P = .55$).

Table 2 shows pair-wise Dice overlap metrics for the 3 observers, consensus observer, and our model on test cohort 2. MRes-UNET2D achieved average Dice scores of 0.97 and 0.95 with respect to the consensus observer and the individual observers, respectively. The average Dice between the observers, calculated as an average of

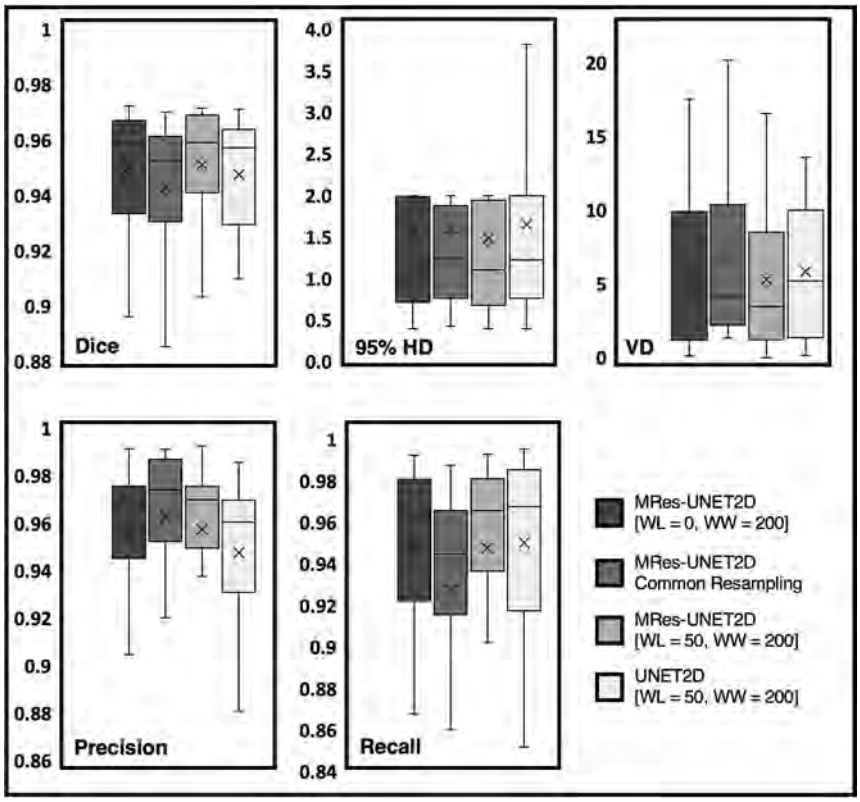

FIG 5. Boxplot comparison of the performances of MRes-UNET2D and UNET2D on test cohort 1. The different panels compare the performances of the deep learning models on Dice, 95% Hausdorff distance (95% HD), volume difference (VD), precision, and recall. Among the 3 MRes-UNET2Ds, we selected [window level (WL), window width (WW)] = [50, 200] because it yielded the best performance across all evaluation metrics.

Table 2: Mean (standard deviation) of pair-wise Dice between the observers, consensus observer, and MRes-UNET2D on test cohort 2 ($n = 9$)

	Observer 1	Observer 2	Observer 3	Consensus	MRes-UNET2D
Observer 1	—	0.95 (0.01)	0.94 (0.01)	0.98 (0.00)	0.96 (0.00)
Observer 2		—	0.93 (0.02)	0.97 (0.01)	0.95 (0.01)
Observer 3			—	0.96 (0.01)	0.94 (0.01)
Consensus				—	0.97 (0.00)
MRes-UNET2D					—

Note:— — indicates the pairwise Dice between Observer 1 and Observer 1 have no meaning.

Dice scores between observer 1 versus observer 2, observer 2 versus observer 3, and observer 1 versus observer 3, was 0.94, whereas this value was 0.97 with respect to the consensus observer.

We also performed Bland-Altman analysis to compare the agreement in globe volumes per hemisphere from the 3 observers and our model, with respect to the consensus observer. We observed tighter limits of agreement (coefficient of variation = 2.1% and reproducibility coefficient = 3.8%) for MRes-UNET2D (Fig 6*A*) compared with the human observers (Fig 6*B–D*).

Figure 7*A* shows the histogram of IGVD values from the entire cohort under study ($n = 98$, -0.01 ± 0.33 mL) excluding test cohort 2. The boxplot in Fig 7*B* compares IGVD values from the consensus observer, MRes-UNET2D, and the human observers on test cohort 2. The mean (± standard deviation) IGVD from the network was 0.05 ± 0.24 mL compared with -0.10 ± 0.25 mL, -0.13 ± 0.23 mL, -0.09 ± 0.5 mL, and 0.20 ± 0.45 mL from the consensus observer and observers 1, 2, and 3, respectively. We were unable to reject the null hypothesis that the IGVD values in test cohort 2 from the consensus, MRes-UNET2D, and the 3 observers come from the same distribution ($P = .3$).

Figure 7*C* shows the globe contours predicted by MRes-UNET2D on the 3 subjects with suspected globe injuries along with the IGVD computed for each case. We also computed a z score, a measure of distance in terms of standard deviation from the population mean, for each of the subjects. For subjects 1, 2, and 3 in Fig 7*C*, the IGVDs were −4.62 mL, 2.32 mL, and 1.22 mL, respectively. The z score values were 14.16, 7.12, and 3.77 for subjects 1, 2, and 3, respectively. The IGVD for subject 1, for instance, is indicative of a smaller left globe compared with the right. Subject 3 highlights a case with subtle globe injury. The z score distance quantifies that the IGVD of 1.22 mL is approximately 3.77 standard deviations away from the mean IGVD from the cohort of normal subjects, depicting abnormality in globe volumes.

DISCUSSION

In this study, we show that our deep learning network, MRes-UNET2D, can provide accurate and reliable detection of globe contours and quantification of globe volumes. With fast prediction times and performance approaching an average human observer, we show that globe contour predictions, as well as volume estimates, can be made available to radiologists in clinically feasible times. We also observe that using the proposed deep learning CNN yields improved Dice scores compared with average Dice scores ranging from 0.80 to 0.85 by using traditional non-deep learning–based schemes described previously in the literature.[12,13,17] The mean 95% HD was also lowered to 1.5 mm compared with approximately 2.89 mm to 3 mm.[17]

We show that MRes-UNET2D works well across images with different fields of view as well as resolutions. The network does not need any special processing in terms of changing image resolution to a common grid; the images can be trained and tested in their native resolution. We observe that minor variations in window level to change contrast between soft tissue and background bones did not result in a significant performance difference between the models. Furthermore, it is important to note that the training and the testing data in this work come from multiple

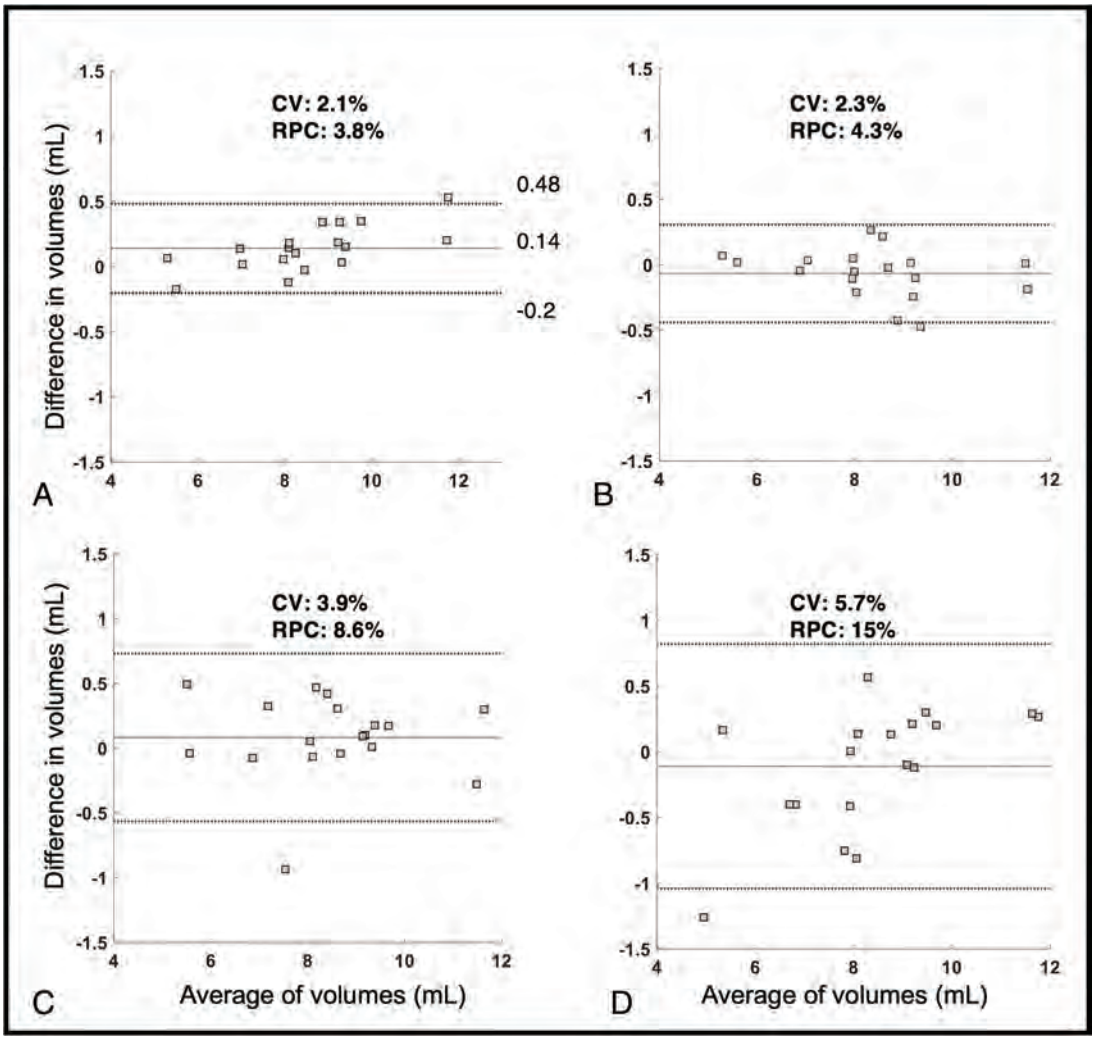

FIG 6. Evaluation on test cohort 2 (cohort used for interobserver variability between the observers). The Bland-Altman plots to depict agreement in globe volume estimates (*left* and *right*) from *(A)* MRes-UNET2D, *(B)* observer 1, *(C)* observer 2, and *(D)* observer 3 with respect to the consensus observer. The consensus observer was created by using a majority voting scheme on the individual observer contours. The coefficient of variation (CV) and reproducibility coefficient (RPC) for each analysis are also shown.

scanners across manufacturers. Therefore, it can be stated that the proposed network is robust to changes in acquisition parameters and scanner hardware variations across manufacturers.

We show that using a deep learning network can provide reliable and consistent contour and volume estimates, thereby, reducing the issues associated with interobserver variability. We observe that the deep learning model's predictions are more in agreement (Dice = 0.95) with the individual observer contours compared with the agreement between observers (Dice = 0.94).

We see that the model, though never trained on images with suspected globe injuries, generalized well to these images on the limited test cases used in this study. The IGVD values and *z* scores from these cases appear to be useful indicators of suspected globe injuries and provide quantitative information regarding the extent of deviation from a normal cohort.

Our proposed technique has limitations. The training cohort entirely consists of subjects with no imaging or clinical findings of globe injury. Although we observe generalizability of the model on a few cases with globe injuries, we currently do not have ground truth annotations to quantitatively validate the performance of our model on these cases. However, this limitation can be overcome by fine-tuning the MRes-UNET2D model using training data that includes these cases.

Although CT provides superior assessment of size and location of intraocular foreign bodies, compared with competing imaging modalities, it has moderate sensitivity for detecting open-globe injuries. This has been reported to be ranging from 51% to 79% and is suboptimal and observer dependent.[6,9-11] Using the IGVD values from the normal study population as a baseline, we can quantitatively compare the IGVD for a given CT image with the population IGVD value and automatically identify globe-related abnormalities if the differences between the globe volumes diverge from the normal population distribution. This comparison could potentially provide additional valuable information to a radiologist, in clinically feasible times, to understand whether any subtle globe injuries exist. We will look at introducing additional parameters such as globe contour distortions, ACD, anterior and posterior segment volumes, and lens thickness along with IGVD to quantitatively predict the

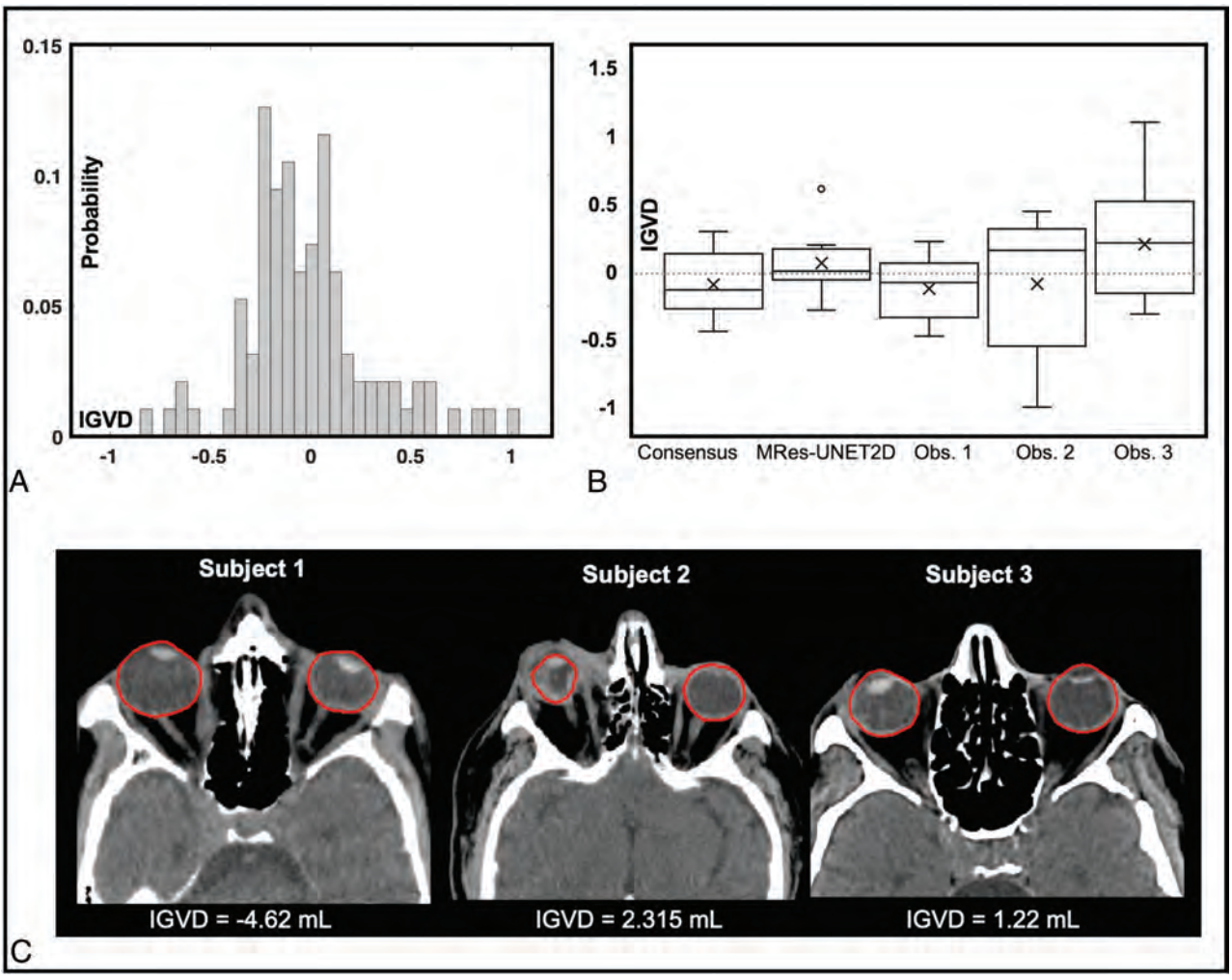

FIG 7. Analysis of inter-globe volume difference (IGVD). *A*, A histogram of IGVD (mL) on the entire study cohort. *B*, The IGVD measured in globe contours on test cohort 2 (cohort used for interobserver variability analysis) from the consensus observer, MRes-UNET2D, and the 3 human observers is shown in the boxplot. *C*, Examples of the utility of IGVD as a quantitative marker for globe trauma. The predicted globe contours are overlaid on representative images from 3 subjects with suspected globe injuries. The IGVD (mL) for each case is depicted in the figure.

presence of globe injuries and measure the degree of injury from a scale of subtle injuries to globe ruptures.

CONCLUSIONS

In this work, we proposed a 2D deep learning architecture, MRes-UNET2D, to detect globe contours in axial CT images of the orbits. We showed that the proposed CNN model, trained and validated on CT images from 80 subjects with no imaging or clinical findings of globe injuries, obtained an average Dice score of 0.95, with less than 5.3% error in globe volume estimates. The performance of MRes-UNET2D approached interobserver variability between 3 human observers. The analysis of images from subjects with known globe injuries demonstrated the utility of IGVD as a quantitative marker for trauma.

ACKNOWLEDGMENTS

The authors would like to acknowledge support from the Technology and Research Initiative Fund (TRIF) Improving Health Initiative.

Disclosures: Maria Altbach—*RELATED: Grant:* University of Arizona, *Comments:* The work was funded by internal grant mechanisms at the University of Arizona as listed in the Acknowledgments. *UNRELATED:* None.

REFERENCES

1. Werner MS, Dana MR, Viana MAG, et al. **Predictors of occult scleral rupture.** *Ophthalmology* 1994;101:1941–44 CrossRef Medline
2. Kylstra JA, Lamkin JC, Runyan DK. **Clinical predictors of scleral rupture after blunt ocular trauma.** *Am J Ophthalmol* 1993;115:530–35 CrossRef Medline
3. Chronopoulos A, Ong JM, Thumann G, et al. **Occult globe rupture: diagnostic and treatment challenge.** *Surv Ophthalmol* 2018;63:694–99 CrossRef Medline
4. Harlan JB, Pieramici DJ. **Evaluation of patients with ocular trauma.** *Ophthalmol Clin North Am* 2002;15:153–61 CrossRef Medline
5. Lee H, Jilani M, Frohman L, et al. **CT of orbital trauma.** *Emerg Radiol* 2004;10:168–72 CrossRef Medline
6. Arey ML, Mootha VV, Whittemore AR, et al. **Computed tomography in the diagnosis of occult open-globe injuries.** *Ophthalmology* 2007;114:1448–52 CrossRef Medline
7. Kubal WS. **Imaging of orbital trauma.** *RadioGraphics* 2008;28:1729–39 CrossRef Medline

8. Kim SY, Lee JH, Lee YJ, et al. **Diagnostic value of the anterior chamber depth of a globe on CT for detecting open-globe injury.** *Eur Radiology* 2010;20:1079–84 CrossRef Medline
9. Crowell EL, Koduri VA, Supsupin EP, et al. **Accuracy of computed tomography imaging criteria in the diagnosis of adult open globe injuries by neuroradiology and ophthalmology.** *Acad Emerg Med* 2017;24:1072–79 CrossRef Medline
10. Yuan W-H, Hsu H-C, Cheng H-C, et al. **CT of globe rupture: analysis and frequency of findings.** *AJR Am J Roentgenol* 2014;202:1100–07 CrossRef
11. Joseph DP, Pieramici DJ, Beauchamp NJ. **Computed tomography in the diagnosis and prognosis of open-globe injuries.** *Ophthalmology* 2000;107:1899–1906 CrossRef
12. Bekes G, Máté E, Nyúl LG, et al. **Geometrical model-based segmentation of the organs of sight on CT images.** *Med Phys* 2008;35:735–43 CrossRef
13. Harrigan RL, Panda S, Asman AJ, et al. **Robust optic nerve segmentation on clinically acquired computed tomography.** *J Med Imaging* 2014;1:034006 CrossRef
14. Sharma N, Aggarwal LM. **Automated medical image segmentation techniques.** *J Med Phys* 2010;35:3–14 CrossRef Medline
15. Warfield SK, Zou KH, Wells WM. **Simultaneous truth and performance level estimation (STAPLE): An algorithm for the validation of image segmentation.** *IEEE Trans Med Imaging* 2004;23:903–21 CrossRef
16. Asman AJ, Landman BA. **Non-local statistical label fusion for multi-atlas segmentation.** *Med Image Anal* 2013;17:194–208 CrossRef
17. Aghdasi N, Li Y, Berens A, et al. **Efficient orbital structures segmentation with prior anatomical knowledge.** *J Med Imaging* 2017;4:034501 CrossRef
18. Kooi T, Litjens G, van Ginneken B, et al. **Large scale deep learning for computer aided detection of mammographic lesions.** *Med Image Anal* 2017;35:303–12 CrossRef
19. Van Grinsven M, Van Ginneken B, Hoyng CB, et al. **Fast convolutional neural network training using selective data sampling: application to hemorrhage detection in color fundus images.** *IEEE Trans Med Imaging* 2016;35:1273–84 CrossRef
20. Litjens G, Kooi T, Bejnordi BE, et al. **A survey on deep learning in medical image analysis.** *Med Image Anal* 2017;42:60–88 CrossRef Medline
21. Ronneberger O, Fischer P, Brox T. **U-Net: convolutional networks for biomedical image segmentation.** May 2015. http://arxiv.org/abs/1505.04597. Accessed July 19, 2019.
22. He K, Zhang X, Ren S, et al. **Deep residual learning for image recognition.** In: *Proceedings of the IEEE Conference on Computer Vision and Pattern Recognition (CVPR),* Las Vegas, NV, June 27–30, 2016 CrossRef
23. He K, Zhang X, Ren S, et al. **Identity mappings in deep residual networks.** *Lect Notes Comput Sci (including Subser Lect Notes Artif Intell Lect Notes Bioinformatics)* 2016;630–45
24. Zagoruyko S, Komodakis N. **Wide residual network** In: *Proceedings of the British Machine Vision Conference 2016*. British Machine Vision Association; 2016:87.1–87.12 CrossRef
25. Guerrero R, Qin C, Oktay O, et al. **White matter hyperintensity and stroke lesion segmentation and differentiation using convolutional neural networks.** *NeuroImage Clin* 2018;17:918–34 CrossRef Medline
26. Ioffe S, Szegedy C. **Batch normalization: accelerating deep network training by reducing internal covariate shift.** 2015. http://arxiv.org/abs/1502.03167
27. Srivastava N, Hinton G, Krizhevsky A, et al. **Dropout: a simple way to prevent neural networks from overfitting.** *J Mach Learn Res* 2014;15:1929–58. http://jmlr.org/papers/v15/srivastava14a.html
28. Abadi M, Agarwal A, Barham P, et al. **TensorFlow: large-scale machine learning on heterogeneous distributed systems.** 2016. https://arxiv.org/abs/1603.04467v2. Accessed April 25, 2020
29. Kingma DP, Ba J. **Adam: a method for stochastic optimization.** 2014. https://arxiv.org/abs/1412.6980v9. Accessed April 25, 2020

Positive Predictive Value of Neck Imaging Reporting and Data System Categories 3 and 4 Posttreatment FDG-PET/CT in Head and Neck Squamous Cell Carcinoma

P. Wangaryattawanich, B.F. Branstetter, J.D. Ly, U. Duvvuri, D.E. Heron, and T.J. Rath

ABSTRACT

BACKGROUND AND PURPOSE: The Neck Imaging Reporting and Data System is a standardized reporting system intended to risk stratify patients treated for head and neck squamous cell carcinoma. The purpose of this study is to investigate the positive predictive value of the Neck Imaging Reporting and Data System categories 3 and 4 on posttreatment PET/CT in patients treated definitively for head and neck squamous cell carcinoma.

MATERIALS AND METHODS: We retrospectively identified patients treated definitively for head and neck squamous cell carcinoma between 2006 and 2018. Patients whose posttreatment PET/CT scans were interpreted as Neck Imaging Reporting and Data System 3 (suspicious) or 4 (definitive recurrence) at the primary site, regional nodes, or at distant sites were included. The reference standard was histopathology or unequivocal imaging or clinical evidence of treatment failure. The positive predictive values of Neck Imaging Reporting and Data System 3 and 4 posttreatment PET/CT were calculated.

RESULTS: Seventy-two of 128 patients with posttreatment PET/CT interpreted as Neck Imaging Reporting and Data System 3 at the primary site, regional nodes, or distant sites were proved to have treatment failure at the suspicious sites, yielding an overall positive predictive value of 56% (95% CI, 48%–65%). The positive predictive values of Neck Imaging Reporting and Data System 3 by subsite were as follows: primary site, 56% (44/79); regional nodes, 65% (34/52); and distant sites, 79% (42/53). All 69 patients with posttreatment PET/CT interpreted as Neck Imaging Reporting and Data System 4 had true treatment failure, yielding a positive predictive value of 100% (95% CI, 96%–100%): primary site, 100% (28/28); regional nodes, 100% (32/32); and distant sites, 100% (29/29).

CONCLUSIONS: The positive predictive value of Neck Imaging Reporting and Data System 3 on posttreatment PET/CT is relatively low. Thus, Neck Imaging Reporting and Data System 3 findings should be confirmed with tissue sampling before instituting new salvage treatment regimens to avoid unnecessary overtreatment and its associated toxicities. Neck Imaging Reporting and Data System 4 reliably indicates recurrent disease.

ABBREVIATIONS: AJCC = American Joint Committee on Cancer; D = distant sites; HNSCC = head and neck squamous cell carcinoma; HPV = human papillomavirus; N = regional nodes; NI-RADS = Neck Imaging Reporting and Data System; P = primary site; PPV = positive predictive value

FDG-PET/CT is a powerful imaging tool and critically important for management of patients with head and neck squamous cell carcinoma (HNSCC). Before treatment, PET/CT can be used for tumor staging, especially in patients with stage III and IV disease, and also for localization of occult primary tumors. After treatment, PET/CT can be used for assessment of treatment response and disease surveillance.[1-3] It has been well-established that posttreatment PET/CT has a high negative predictive value and patients who have complete tumor response on posttreatment PET/CT can avoid an unnecessary operation.[4-6] The clinical impact of positive posttreatment PET/CT findings is less well-studied.

The Neck Imaging Reporting and Data System (NI-RADS) is a standardized report template used for surveillance contrast-enhanced CT with or without concurrent PET. The primary objective of this template is to simplify radiology reports and facilitate communication between radiologists and their clinical colleagues. The results of posttreatment imaging surveillance are classified into 4 numeric categories based on the radiologist's

Received November 29, 2019; accepted after revision April 4, 2020.

From the Departments of Radiology (P.W., B.F.B., J.D.L.), Otolaryngology (B.F.B., U.D., D.E.H.), Biomedical Informatics (B.F.B.), and Radiation Oncology (D.E.H.), School of Medicine, University of Pittsburgh, Pittsburgh, Pennsylvania; and Neuroradiology Section, Department of Radiology (T.J.R.), Mayo Clinic Hospital, Phoenix, Arizona.

Paper previously presented as an oral presentation at: Annual Meeting of the American Society of Neuroradiology, May 18–23, 2019: Boston, Massachusetts.

Please address correspondence to Tanya J. Rath, MD, Neuroradiology Section, Department of Radiology, Mayo Clinic Arizona, 5777 E Mayo Blvd, Phoenix, AZ 8505; e-mail: Rath.Tanya@mayo.edu

http://dx.doi.org/10.3174/ajnr.A6589

suspicion for residual or recurrent tumor (category 1, no evidence of recurrence; category 2, low suspicion; category 3, high suspicion; category 4, definitive disease recurrence).[7-9] High negative predictive values of NI-RADS 1 and 2 on posttreatment PET/CT in HNSCC have been established.[5,10] However, there are inadequate data regarding positive predictive values (PPVs) of NI-RADS 3 and 4 as seen on posttreatment PET/CT.

The purpose of this study was to determine the PPV of NI-RADS categories 3 and 4 on posttreatment PET/CT in patients treated definitively for HNSCC.

MATERIALS AND METHODS

Study Design and Patient Selection

We conducted a retrospective study that was approved by our institutional review board (PRO08120419) and was in compliance with the Health Insurance Portability and Accountability Act. Patient data were obtained from the University of Pittsburgh Medical Center electronic medical record and our Head and Neck oncologic data repository. Data collected on each patient included demographics, diagnosis date, last follow-up date, primary tumor location, molecular profiles, tumor staging, and examination findings, which were compiled into the data base. We included all patients with a diagnosis of HNSCC who underwent definitive surgery, radiation, chemotherapy, or combined therapeutic modalities and had posttreatment PET/CTs performed between 2006 and 2018. Patients who had non-squamous cell malignancies or inadequate clinical or imaging data were excluded. Pretreatment tumor staging was performed on the basis of the American Joint Committee on Cancer (AJCC) *AJCC Cancer Staging Handbook*, 7th edition.[11]

The NI-RADS categories are independently applied to the primary tumor bed (P), the cervical lymph nodes (N), and distant disease (D) so that every examination has 3 NI-RADS values assigned to it. The overall NI-RADS score is considered to be the maximum of the 3 values. We selected patients whose posttreatment PET/CTs were interpreted as NI-RADS 3 (suspicious) or 4 (definitive recurrence) at P, N, or D. The PET/CT features of NI-RADS 3 at the primary site include residual or a new discrete nodule or mass with increased enhancement and/or focal FDG avidity. The features of NI-RADS 3 at the nodal sites include a progressively enlarging soft-tissue mass or lymph node that is worrisome for residual or recurrent tumor. NI-RADS 4 examinations include patients with definite PET/CT evidence of disease progression such as definitive locoregional recurrence or unequivocal metastases in distant organs.

PET/CT Parameters

PET/CT scans were completed by using 1 of several clinical scanners (Discovery; GE Healthcare; and Somatom Emotion; Siemens). Patients were instructed to fast at least 4–6 hours before the examination and were required to have a blood glucose level measuring <200 mg/dL preceding the scan. Patients who did not meet these criteria were rescheduled. Patients were injected with 10–20 mCi of [^{18}F]FDG 60 minutes before obtaining PET emission images. Immediately before PET acquisition, contrast-enhanced (125 mL iopamidol, Isovue-370; Bracco) helical CT (pitch = 1.5–2.0; kV (peak) = 120–140; variable mAs; 3.75-mm collimation) was performed approximately 45 seconds after contrast injection. Images were obtained from the top of the skull through the upper thighs, with PET and CT scans matched and optimized for visualization with CT attenuation-corrected reconstruction. Patients were imaged with arms at their sides. The images of the thorax, abdomen, and pelvis were reconstructed in a 3.75-mm section thickness with a full-body FOV. The images of the head and neck part were reconstructed in a 2.5-mm section thickness with a small FOV. An additional high-resolution chest CT was performed with arms raised to better assess the lung parenchyma.

Image Interpretation

All PET/CT surveillance studies were interpreted by board-certified neuroradiologists within a dedicated head and neck imaging practice. Postprocessing fusion software (Mirada; Mirada Medical, Denver, Colorado) was used to assist in interpretation. Categorization was based on the subjective interpretation of the interpreting radiologist; standard uptake value thresholds were not used.

Treatment and Surveillance Protocols

Patient treatment protocols, including radiation dose and chemotherapy regimen, were determined by the standard practice guidelines of the multidisciplinary head and neck oncology team at our institution. Clinical follow-up was performed at 2-month intervals. The first surveillance PET/CT was performed 2–3 months after the completion of therapy according to established institutional protocols. Subsequent radiologic examinations were performed at 3-month intervals after the first surveillance scan.[5,10] Additional PET/CT and tissue biopsy were performed outside the standard surveillance protocol if patients had any clinical signs and symptoms or radiographic findings suspicious for residual or recurrent tumor. The reference standard for treatment failure was confirmation by histopathology or unequivocal evidence of disease progression on subsequent follow-up imaging and clinical evaluation.

Statistical Methods

Positive predictive value was calculated separately for NI-RADS category 3 and NI-RADS category 4 and was further broken down by primary, nodal, and distant disease. PPV was calculated as the probability of experiencing treatment failure given a NI-RADS category 3 or 4. Ninety-five percent confidence intervals for percentages were calculated using binomial methods, except when the calculated value was 100%, in which case exact methods were used.

RESULTS

In our complete data base, a total of 8768 PET/CT examinations were performed on 3853 patients with head and neck cancer between 2006 and 2018. Of these, 197 patients met the inclusion criteria, with 128 patients classified as NI-RADS 3 and 69 patients classified as NI-RADS 4. Most patients were male ($n = 148$, 75%) with an oropharyngeal primary tumor site ($n = 76$, 39%) and stage IV disease ($n = 149$, 76%). Forty-four of 76 patients with an oropharyngeal tumor were positive for human papillomavirus (HPV) (58%). Patient demographics, tumor characteristics, and Tumor, Node, Metastasis staging of NI-RADS 3 and 4 are summarized in Table 1.

Seventy-two of 128 patients with posttreatment PET/CT interpreted as NI-RADS 3 at P, N, or D were proved to have treatment

Table 1: Patient characteristics ($n = 197$)

	NI-RADS 3 ($n = 128$)	NI-RADS 4 ($n = 69$)
Sex		
Male	97 (76%)	51 (74%)
Female	31 (24%)	18 (26%)
Age (yr)	Range = 27–87, mean = 59, median = 60	Range = 26–87, mean = 62, median = 64
Primary tumor location		
Oropharynx	55 (43%)	21 (30%)
Oral cavity	32 (25%)	26 (38%)
Larynx	29 (23%)	14 (20%)
Hypopharynx	5 (4%)	4 (6%)
Paranasal sinuses/nasal cavity	3 (2%)	3 (4%)
Nasopharynx	2 (1.5%)	1 (2%)
Unknown	2 (1.5%)	0 (0%)
HPV status (oropharynx)		
Positive	32 (58%)	12 (57%)
Negative	18 (33%)	2 (10%)
Unknown	5 (9%)	7 (33%)
TNM stage (7th ed *AJCC*[11])		
Stage I	3 (2%)	4 (6%)
Stage II	12 (10%)	2 (3%)
Stage III	20 (16%)	5 (7%)
Stage IV	91 (71%)	58 (84%)
Unknown primary	2 (1%)	0 (0%)

Note:—TNM indicates Tumor, Node, Metastasis.

Table 2: Timing of posttreatment PET/CT with false-positive NI-RADS 3 results ($n = 56$)

Time Interval between Completion of Therapy and Posttreatment PET/CT with False-Positive NI-RADS 3 Results	No. of Posttreatment PET/CTs with False-Positive NI-RADS 3 Results
0–3 mo	27 (48%)
3–6 mo	10 (18%)
6–12 mo	10 (18%)
1–2 yr	6 (11%)
2–3 yr	0 (0%)
3–4 yr	1 (2%)
4–5 yr	2 (3%)

failure at the suspicious sites, yielding an overall PPV of 56% (95% CI, 48%–65%). The PPVs of NI-RADS 3 by subsite were as follows: P, 56% (44/79); N, 65% (34/52); and D, 79% (42/53). (The denominators do not add up to 128 because some patients were classified as NI-RADS 3 at multiple subsites.) The median time interval between completion of therapy and obtaining PET/CT with NI-RADS 3 was 4 months (range, 2–85 months). Most posttreatment PET/CT with false-positive NI-RADS 3 results was performed within the first 3 months after conclusion of therapy (27/56, 48%; range, 1.5–58 months; median, 3 months). The timing of posttreatment PET/CT with false-positive NI-RADS 3 results is summarized in Table 2.

Thirty-one of 56 patients (55%) with false-positive NI-RADS 3 findings had histopathologic confirmation; 25 patients had no tissue confirmation but had clinical and radiologic follow-up, which demonstrated interval resolution of suspicious findings. With pathologic confirmation, the major causes of false-positives are treatment-related changes (12/31, 39%) and nonspecific infectious/inflammatory processes (10/31, 32%). Five patients with false-positive NI-RADS 3 findings had incidental benign head and neck tumor on surveillance PET/CT (Warthin tumors = 3, pleomorphic adenoma = 1, dermatofibroma = 1). Most patients with false-positive NI-RADS 3 findings had oropharyngeal squamous cell carcinoma (24/56, 43%), with most of these positive for HPV (15/24, 63%). The PPVs of NI-RADS 3 in HPV-related and HPV-unrelated oropharyngeal cancers are not substantially different (HPV-related oropharyngeal cancers: $n = 32$, PPV = 53% [17/32]; HPV-unrelated oropharyngeal cancers: $n = 18$, PPV = 56% [10/18]).

All 69 patients with posttreatment PET/CT interpreted as NI-RADS 4 had true treatment failure, yielding a PPV of 100% (95% CI, 96%–100%). Broken down by subsite, these percentages are the following: P, 100% (28/28); N, 100% (32/32); and D, 100% (29/29). Thirty-eight of 69 patients (55%) with NI-RADS 4 were confirmed with histopathology; 31 patients had no tissue confirmation but had unequivocal treatment failure based on follow-up imaging and clinical examination. The median time interval between completion of therapy and obtaining PET/CT with NI-RADS 4 was 3.4 months (range, 1–158 months).

Representative PET/CT images of the patients with true- and false-positive NI-RADS 3 findings are shown in Figs 1 and 2, respectively. Representative PET/CT images of a patient with NI-RADS 4 are shown in Fig 3.

DISCUSSION

This study demonstrates a very high PPV (100%) of NI-RADS 4 in posttreatment PET/CT surveillance of HNSCC. With appropriate standardization of imaging and reporting practices, this could potentially obviate biopsy confirmation. In contrast, the PPV of NI-RADS 3 in posttreatment PET/CT is relatively low, especially at the primary tumor site. Therefore, patients with "high-suspicion" PET/CT findings should be further investigated with tissue sampling before instituting new treatment regimens to avoid unnecessary overtreatment and its associated toxicities. The results of our study support the current American College of Radiology recommendations for NI-RADS 3 and 4 as well as our recommendations for posttreatment PET/CT surveillance in HNSCC.[9,10] The University of Pittsburgh PET/CT surveillance algorithm for patients with HNSCC is shown in Fig 4. The ultimate goal of the surveillance protocol is to identify recurrences to potentially treat and cure, while maximizing cost-efficiency without increased morbidity and mortality.

The PPV of NI-RADS 3 in our study is similar to that in the previous study of the initial performance of NI-RADS.[12] Krieger et al[12] achieved an overall PPV of NI-RADS 3 of 59.4% (19/32), with a PPV of 54.6% at the primary tumor site (12/22) and a PPV of 70%

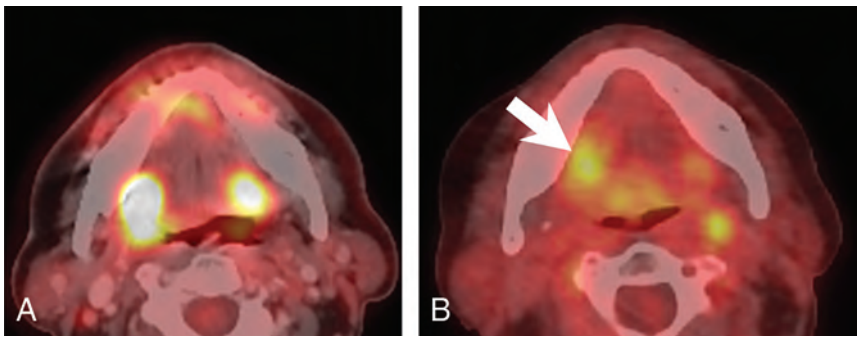

FIG 1. NI-RADS 3 true-positive. A 62-year-old man with advanced HPV-positive oropharyngeal squamous cell carcinoma. *A*, Pretreatment PET/CT shows 2 areas of FDG-avid infiltrative tumor in the oropharynx, one centered in the right faucial tonsil with invasion of the adjacent right tongue base and right-sided floor of mouth and one centered in the left tongue base. *B*, Surveillance PET/CT obtained at 3.5 months after completion of treatment shows interval improvement and a decrease in the size of the primary tumor, but there remains a substantial amount of residual FDG avidity in the right-sided floor of the mouth (*white arrow*), which is suspicious for residual viable tumor. Treatment failure was subsequently confirmed with biopsy.

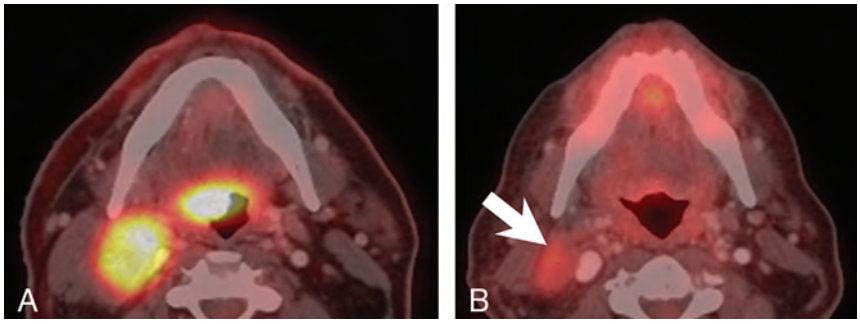

FIG 2. NI-RADS 3 false-positive. A 55-year-old man with metastatic HPV-positive oropharyngeal squamous cell carcinoma. *A*, Pretreatment PET/CT shows a large FDG-avid right oropharyngeal tumor with FDG-avid right level IIa nodal metastasis. *B*, Surveillance PET/CT obtained at 2.5 months after completion of treatment shows complete response of the primary tumor, but there remains a large nodal remnant with moderate FDG-avidity (*white arrow*), which is concerning for residual viable tumor. The patient subsequently underwent right-neck dissection, with final pathology showing treatment-related changes but no viable tumor.

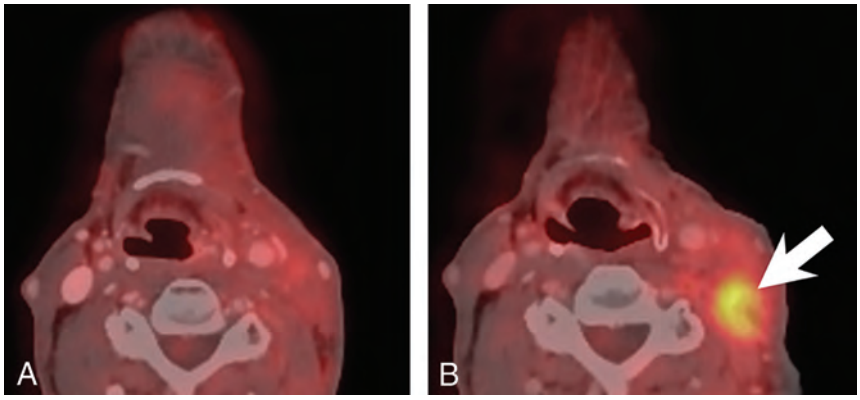

FIG 3. NI-RADS 4 true-positive. A 74-year-old man with squamous cell carcinoma of the oral cavity after tumor resection, left-neck dissection, and adjuvant chemoradiation. *A*, The first surveillance PET/CT obtained at 3.5 months after completion of treatment shows treatment-related changes, with no convincing imaging evidence of viable tumor. *B*, At 8 months after completion of treatment, there is a new FDG-avid soft-tissue mass in the left upper neck (*white arrow*), indicative of locoregional tumor recurrence.

at the nodal site (7/10). Similarly, the PPV for the NI-RADS 3 in primary tumors of our study was also lower than for the lymph nodes (56% versus 65%). A previous study of posttreatment PET/CT in oropharyngeal squamous cell carcinoma likewise demonstrated a low PPV for PET/CT findings of residual FDG uptake suspicious for locoregional recurrence ($n = 30$, overall PPV = 40%, PPV for primary tumor site = 20%, PPV for nodal site = 29%).[13] As expected, treatment-related changes and superimposed infection are the major causes of false-positive NI-RADS 3 results, which account for 71% of patients who had histopathologic confirmation. The primary reason for low PPVs in NI-RADS 3 is likely due to a significant overlap of PET/CT features between viable tumors and inflammatory changes. This may also explain why NI-RADS 3 on posttreatment PET/CT has a slightly higher false-positive rate compared with contrast-enhanced CT alone.[12]

Another cause of false-positive NI-RADS 3 findings is incidental FDG-avid head and neck neoplasms. In our study, 5 patients were found to have incidental benign head and neck neoplasms, with a substantial proportion from major salivary gland tumors. Warthin tumor is one known head and neck tumor that has variable FDG uptakes, one of the pitfalls in the interpretation of head and neck PET/CT.[14-16] These incidental neoplasms can mimic metastases and have an impact on the management of patients with HNSCC. Care should be taken when interpreting posttreatment head and neck PET/CT, with careful evaluation of the contrast-enhanced CT portion. Tissue sampling may also be warranted and used as a problem-solving tool in some cases.

The *AJCC Cancer Staging Handbook*, 8th edition, has classified oropharyngeal cancers into 2 different subtypes based on the HPV profile (p16 overexpression) due to their differences in natural history and prognosis. HPV-related oropharyngeal cancers more commonly occur in younger and healthier individuals, with no history of significant exposure to tobacco, and have better

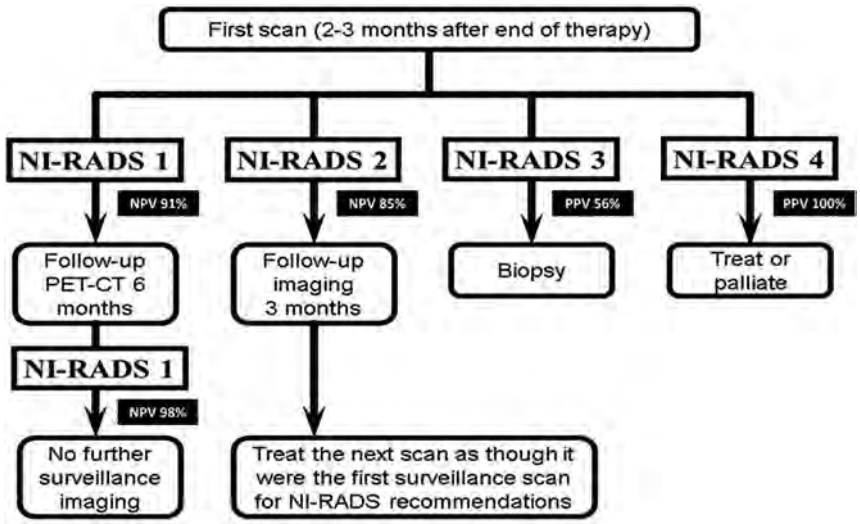

FIG 4. University of Pittsburgh PET/CT Surveillance Flowchart for Head and Neck Squamous Cell Carcinoma. NI-RADS 1, no evidence of recurrence; NI-RADS 2, low suspicion; NI-RADS 3, high suspicion; NI-RADS 4, definitive disease recurrence. Negative predictive values of first NI-RADS 1 PET/CT = 91%; negative predictive values of 2 consecutive NI-RADS 1 PET/CTs = 98%;[5] negative predictive values of the first NI-RADS 2 PET/CT = 85%;[10] PPV of NI-RADS 3 PET/CT = 56%; PPV of NI-RADS 4 PET/CT = 100%.

prognosis compared with HPV-unrelated cancers.[17] Radiologically, HPV-related cancers tend to have more cystic changes in metastatic lymph nodes and distant metastases at unusual sites such as bones or brain.[18] However, the impact of the HPV profile on posttreatment PET/CT results remains unknown. Based on our current data base with a small sample size, the PPVs of NI-RADS 3 in HPV-related and HPV-unrelated oropharyngeal cancers are similar (HPV-related oropharyngeal cancers: $n = 32$, PPV = 53% [17/32]; HPV-unrelated oropharyngeal cancers: $n = 18$, PPV = 56% [10/18]). Further study with a larger sample size is needed for investigation of the potential impact of the new cancer staging system on posttreatment PET/CT results.

This study has several limitations. First, the study is inherently limited due to its retrospective study design. The raw data that we used for retrospective analysis were collected prospectively into a registry conducted at 1 center using institution-specific PET/CT protocols and experienced head and neck neuroradiologists. The results of the data are generated from the head and neck oncologic data repository, which is completed via chart review and dependent on the accuracy of both the repository and the patient chart. The standard uptake value was not used in PET/CT interpretation because there is no standard cutoff standard uptake value threshold that reliably differentiates benign and malignant processes.[19,20] We used the *AJCC Cancer Staging Handbook*, 7th edition, because it was used in the management of the patients during the time of data collection. Last, we included all posttreatment PET/CTs that were obtained at any time after completion of therapy. We did not limit our analysis to the PPV of NI-RADS 3 and 4 on the first posttreatment PET/CT because of the small sample size. Thus, the results are not entirely specific to posttreatment PET/CT at any 1 particular time after treatment. Our subgroup analysis of NI-RADS 3, though insufficiently powered, suggests that most false-positive NI-RADS 3 findings occur within 3 months after the conclusion of treatment, though further study with a larger sample size is required.

CONCLUSIONS

In the setting of PET/CT for surveillance of treated head and neck squamous cell carcinoma, NI-RADS category 4 has a superb positive predictive value and may obviate tissue confirmation. In contrast, the positive predictive value of NI-RADS category 3 on posttreatment PET/CT is relatively low, particularly at the primary tumor site. Therefore, confirmation of NI-RADS category 3 findings should be performed with tissue sampling before instituting new treatment regimens to avoid unnecessary overtreatment and its associated toxicities.

Disclosures: Umamaheswar Duvvuri—*UNRELATED*: *Board Membership*: Activ Surgical; *Consultancy*: Medtronic; *Grants/Grants Pending*: National Institutes of Health R01-DE028343 and Veterans Administration I01-BX003456; *Patents (Planned, Pending or Issued)*: patent pending for robotic surgery instrument.* *Money paid to the institution.

REFERENCES

1. Goel R, Moore W, Sumer B, et al. **Clinical practice in PET/CT for the management of head and neck squamous cell cancer.** *AJR Am J Roentgenol* 2017;209:289–303 CrossRef Medline
2. Tantiwongkosi B, Yu F, Kanard A, et al. **Role of (18)F-FDG PET/CT in pre and post treatment evaluation in head and neck carcinoma.** *World J Radiol* 2014;6:177–91 CrossRef Medline
3. Kale H, Rath TJ. **Chapter 3: the role of PET/CT in squamous cell carcinoma of the head and neck.** *Semin Ultrasound CT MR* 2017;38:479–94 CrossRef Medline
4. Mehanna H, Wong WL, McConkey CC, et al; PET-NECK Trial Management Group. **PET-CT surveillance versus neck dissection in advanced head and neck cancer.** *N Engl J Med* 2016;374:1444–54 CrossRef Medline
5. McDermott M, Hughes M, Rath T, et al. **Negative predictive value of surveillance PET/CT in head and neck squamous cell cancer.** *AJNR Am J Neuroradiol* 2013;34:1632–36 CrossRef Medline
6. Nayak JV, Walvekar RR, Andrade RS, et al. **Deferring planned neck dissection following chemoradiation for stage IV head and neck cancer: the utility of PET-CT.** *Laryngoscope* 2007;117:2129–34 CrossRef Medline
7. Aiken AH, Farley A, Baugnon KL, et al. **Implementation of a novel surveillance template for head and neck cancer: Neck Imaging Reporting and Data System (NI-RADS).** *J Am Coll Radiol* 2016;13:743–46 CrossRef Medline
8. Aiken AH, Hudgins PA. **Neck Imaging Reporting and Data System.** *Magn Reson Imaging Clin N Am* 2018;26:51–62 CrossRef Medline
9. Aiken AH, Rath TJ, Anzai Y, et al. **ACR Neck Imaging Reporting and Data Systems (NI-RADS): a white paper of the ACR NI-RADS Committee.** *J Am Coll Radiol* 2018;15:1097–1108 CrossRef Medline
10. Wangaryattawanich P, Branstetter BFt, Hughes M, et al. **Negative predictive value of NI-RADS category 2 in the first posttreatment FDG-PET/CT in head and neck squamous cell carcinoma.** *AJNR Am J Neuroradiol* 2018;39:1884–88 CrossRef Medline

11. Edge SB, Byrd DR, Compton CC, et al. *AJCC Cancer Staging Handbook: From the AJCC Cancer Staging Manual*. 7th ed. Springer-Verlag 2010;53:39–126
12. Krieger DA, Hudgins PA, Nayak GK, et al. **Initial performance of NI-RADS to predict residual or recurrent head and neck squamous cell carcinoma.** *AJNR Am J Neuroradiol* 2017;38:1193–99 CrossRef Medline
13. Bird T, Barrington S, Thavaraj S, et al. **(18)F-FDG PET/CT to assess response and guide risk-stratified follow-up after chemoradiotherapy for oropharyngeal squamous cell carcinoma.** *Eur J Nucl Med Mol Imaging* 2016;43:1239–47 CrossRef Medline
14. Purohit BS, Ailianou A, Dulguerov N, et al. **FDG-PET/CT pitfalls in oncological head and neck imaging.** *Insights Imaging* 2014;5:585–602 CrossRef Medline
15. Rassekh CH, Cost JL, Hogg JP, et al. **Positron emission tomography in Warthin's tumor mimicking malignancy impacts the evaluation of head and neck patients.** *Am J Otolaryngol* 2015;36:259–63 CrossRef Medline
16. Schwarz E, Hurlimann S, Soyka JD, et al. **FDG-positive Warthin's tumors in cervical lymph nodes mimicking metastases in tongue cancer staging with PET/CT.** *Otolaryngol Head Neck Surg* 2009;140:134–35 CrossRef Medline
17. Huang SH, O'Sullivan B. **Overview of the 8th Edition TNM Classification for Head and Neck Cancer.** *Curr Treat Options Oncol* 2017;18:40 CrossRef Medline
18. Subramaniam RM, Alluri KC, Tahari AK, et al. **PET/CT imaging and human papilloma virus-positive oropharyngeal squamous cell cancer: evolving clinical imaging paradigm.** *J Nucl Med* 2014;55:431–38 CrossRef Medline
19. Manca G, Vanzi E, Rubello D, et al. **(18)F-FDG PET/CT quantification in head and neck squamous cell cancer: principles, technical issues and clinical applications.** *Eur J Nucl Med Mol Imaging* 2016;43:1360–75 CrossRef Medline
20. de Langen AJ, Vincent A, Velasquez LM, et al. **Repeatability of 18F-FDG uptake measurements in tumors: a metaanalysis.** *J Nucl Med* 2012;53:701–08 CrossRef Medline

New Imaging Findings of Incomplete Partition Type III Inner Ear Malformation and Literature Review

R. Hong, Q. Du, and Y. Pan

ABSTRACT

SUMMARY: Incomplete partition type III, also referred to as X-linked deafness, is a rare genetic inner ear malformation. Its characteristic CT findings, including bulbous dilation of the internal auditory canal and absence of the modiolus with the interscalar septa present, have been well-recognized. In this series of 19 cases, we report the abnormalities of the vestibule and semicircular canals and provide a comprehensive description of their CT and MR imaging findings. The inner ear malformations in incomplete partition type III were bilateral and basically symmetric, with involvement of the internal auditory canal, nerve canals in the fundus, cochlea, vestibule, semicircular canals, vestibular aqueduct, otic capsule, round window, oval window, and stapes. An irregular vestibule with a cystic appearance is also a distinctive imaging feature, which could be seen in about 90% of our patients, with a cystic appearance of the semicircular canals present in nearly half of the cases.

ABBREVIATIONS: CN = cochlear nerve; DFNX2 = X-linked deafness type 2; IAC = internal auditory canal; IP-III = incomplete partition type III; SCC = semicircular canal; VA = vestibular aqueduct; VN = vestibular nerve

In 1971, Nance et al[1] described X-linked mixed deafness with congenital fixation of the stapedial footplate and perilymphatic gusher. Based on the classification of sex-linked loci and genes implicated in nonsyndromic deafness, this type of hearing loss has been classified as X-linked deafness type 2 (DFNX2), and the responsible gene is *POU class 3 homeobox 4* (*POU3F4*).[2] Its distinctive CT features were first described by Phelps et al[3] in 1991, and it was named incomplete partition type III (IP-III) by Sennaroglu et al[4] in 2006.

The characteristic CT findings of the cochlea and internal auditory canal (IAC) in IP-III have been described in detail, including absence of the modiolus with interscalar septa present and a bulbous dilated IAC at the lateral end.[3-7] However, there are fewer descriptions of abnormal vestibules and semicircular canals (SCC). By analyzing a case series of 19 patients with IP-III, we aimed to present the newly described imaging findings of the vestibular and SCC abnormalities in IP-III and provide a comprehensive description of its CT and MR imaging features with a literature review.

MATERIALS AND METHODS

This retrospective case series was performed with the approval of the institutional review board and exemption from informed consent. Imaging records of 2075 patients with inner ear malformation (based on the classification of Sennaroğlu and Bajin[8]) between August 2014 and December 2018 were reviewed, and 19 patients (18 males and 1 female, 6 months to 47 years of age) with the IP-III anomaly were finally included. Genetic analyses were not performed.

All 19 patients underwent CT examinations of the temporal bone, and 14 patients underwent MR imaging examinations. The CT scans were performed with a 16- or a 128-section multidetector CT scanner (Somatom Sensation 16 or Definition Edge; Siemens). Image acquisition and reconstruction parameters were as follows: helical acquisition, 120 kV, 240 effective mAs, 0.75 pitch, 0.75- or 0.6- mm thickness, 0.75- or 0.6-mm collimation, 220-mm FOV, and B70 reconstruction kernels. Multiplanar reformatted images were processed on a separate workstation (Carestream RIS 3.1; https://www.carestream.com/en/us/ris-software). The temporal bone MR images were obtained with a 3T MR imaging unit (Magnetom Verio; Siemens) using matched 12-channel phased array coils. The MR imaging protocol included an axial sampling perfection with application-optimized contrasts by using different flip angle evolution (SPACE; Siemens) scan plane (3D-SPACE)

Received December 28, 2019; accepted after revision April 4, 2020.

From the Departments of Radiology (R.H., Y.P.) and Otolaryngology-Head and Neck Surgery (Q.D.), Eye and ENT Hospital of Shanghai Medical School, Fudan University, Shanghai, China.

Please address correspondence to Yucheng Pan, MD, Department of Radiology, Eye and ENT Hospital of Shanghai Medical School, Fudan University, 83 Fenyang Rd, Shanghai 200031, China; e-mail: panyuchengg@sina.com

Indicates article with supplemental on-line tables.

Indicates article with supplemental on-line photo.

http://dx.doi.org/10.3174/ajnr.A6576

sequence with 0.5-mm thickness, oblique sagittal 3D-CISS images perpendicular to IAC with 1-mm thickness, and routine an axial and coronal T1WI and T2WI. Two experienced neuroradiologists and 1 otologist evaluated these CT and MR imaging findings.

The cochlear dimensions, including basal turn length and lumen diameter and upper turn width and height, were measured according to the method of Purcell et al[9] (On-line Figure). Fifteen cases without inner ear malformation were selected as a healthy control group. IP-III and healthy groups were compared using a *t* test.

RESULTS

The prevalence of IP-III among cases of total inner ear anomaly was calculated to be 0.9% (19/2075). The inner ear malformations in IP-III were bilateral and basically symmetric with involvement of the IAC, nerve canals in the IAC fundus, cochlea, vestibule, SCC, vestibular aqueduct (VA), otic capsule, oval and round windows, and stapes. The imaging findings are shown in the Table.

All 19 patients had characteristic cochlear and IAC appearances as follows: bulbous dilation of the lateral end of the IAC, absence of the bony modiolus with the interscalar septa present, hypoplasia at the cochlear base (or enlargement of the cochlear nerve [CN] canal), and thinning of the otic capsule (Fig 1*A*, -*B*). The outline of the cochlea was similar to normal, but the dimensions of the cochlea were slightly smaller than normal (On-line Tables 1 and 2), including basal turn length (7.91-mm versus 8.66-mm, $P = .000$), basal turn lumen diameter (1.78-mm versus 1.93-mm, $P = .004$), and upper turn width (4.59-mm versus 5.87-mm, $P = .000$). However, the upper turn height showed no significant difference between the IP-III and healthy groups (3.45-mm versus 3.51-mm, $P = .258$). The CN and vestibular nerve (VN) were visible in all 14 patients who underwent MR imaging, and there was a hypointense spiral structure extending from the fundus of the IAC to the cochlea in 13 patients (Fig 1*C*, -*D*).

In addition to the markedly widened CN canal, the superior VN canal was enlarged in 16 patients (Fig 2*A*), and the canals of the small branches of the superior VN from the ampulla of the lateral SCC and the utricle were also visible. The labyrinthine facial nerve canal was slightly enlarged in 11 patients (Fig 2*A*), and the singular nerve canal, in 14 ears of 8 patients (Fig 2*B*). The inferior VN canal showed no enlargement. On MR imaging, 14 patients with enlarged superior VN canals and 6 patients with enlarged labyrinthine facial nerve canals demonstrated fluid signal (Fig 2*C*). Twelve patients showed fluid signal in the singular nerve canal (Fig 2*D*), and 6 of them did not show enlargement of the singular nerve canal.

An irregularly shaped vestibule with small cystic bulges in the margin was observed in 17 patients (Fig 3). The small sacs were usually located in the superior margin, between the feet of the superior SCC. A multicystic appearance of SCC was also seen in 9 patients (Fig 4), with a widened lumen of the SCC in 1 patient. Enlargement of the VA at the part close to the vestibule was observed in 13 ears of 7 patients, with a cystic appearance present in 8 ears and a normal VA orifice (Fig 2*A*). No patient showed an enlarged endolymphatic sac on MR imaging.

The oval window was dysplastic in 12 patients, and the round window, in 11 patients, including 1 patient with bilateral oval and round window atresia (Fig 5). A thickened stapedial footplate was observed in 5 patients, with malformed stapes in 1 patient.

Imaging findings of the patients

Imaging Findings	Cases	First Reported, Year
Dilated internal auditory canal	19	Phelps et al,[3] 1991
Hypoplasia at the cochlear base	19	Phelps et al,[3] 1991
Absence of the bony modiolus	19	Talbot and Wilson,[5] 1994
Thin otic capsule	19	Sennaroglu,[13] 2016
Enlarged superior vestibular nerve canal	16	Saylisoy et al,[6] 2014
Enlarged labyrinthine facial nerve canal	11	Phelps et al,[3] 1991
Enlarged singular nerve canal	8	Talbot and Wilson,[5] 1994
Vestibule with cystic appearance	17	Gong et al,[7] 2014
Semicircular canal with cystic appearance	9	Anderson et al,[14] 2020
Dilated vestibular aqueduct	7	Talbot and Wilson,[5] 1994
Dysplasia of oval window	12	Saylisoy et al,[6] 2014
Dysplasia of round window	11	Saylisoy et al,[6] 2014
Abnormal stapes	5	Saylisoy et al,[6] 2014

DISCUSSION

X-linked nonsyndromic deafness has been estimated to contribute only 1%–

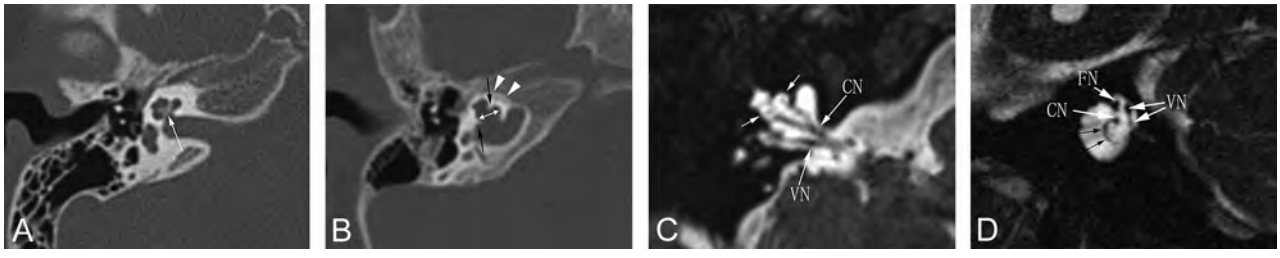

FIG 1. *A*, Axial CT image of a normal inner ear shows the normal shape of the internal auditory canal, cochlea, modiolus (*arrow*), and otic capsule. CT and MR images of a 7-month-old male patient's right ear. *B*, Axial CT image shows a bulbous dilated internal auditory canal and the absence of the modiolus with the interscalar septa present (*black arrows*) and thinning of the otic capsule (*arrowheads*), with mild pericochlear hypodensity. The middle turn width of the cochlea is shorter than normal (*white arrow*). *C*, Axial SPACE image shows the CN, VN, and the hypointense structure in the middle turn of the cochlea (*short arrows*). The branches of the CN are also shown. *D*, Oblique sagittal CISS image perpendicular to the internal auditory canal shows the facial nerve (FN), CN, and VN. There is a spiral structure (*black arrows*) extending from the fundus of internal auditory canal to the cochlea, which is connected to the cochlear nerve.

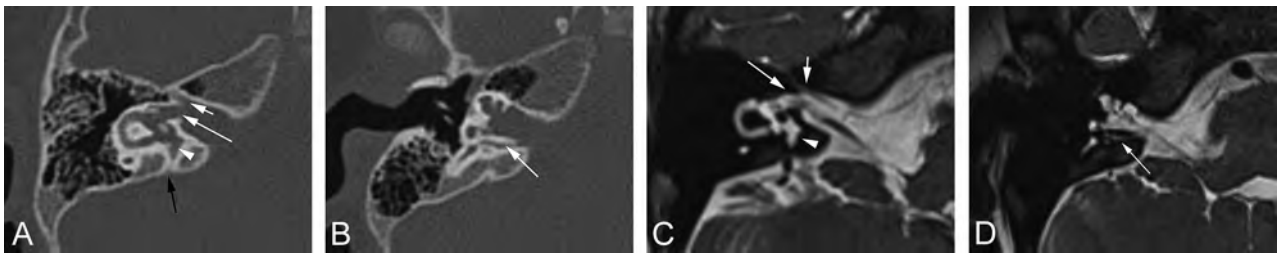

FIG 2. CT and MR images of a 3-year-old male patient's right ear. *A*, Axial CT image shows an enlarged labyrinthine facial nerve canal (*short white arrow*), enlarged superior vestibular nerve canal (*long white arrow*), enlargement of the vestibular aqueduct with a cystic appearance at the part close to the vestibule (*arrowhead*), and the normal vestibular aqueduct orifice (*black arrow*). *B*, Axial CT image shows the enlarged singular nerve canal (*arrow*) and absence of the modiolus. *C*, Axial SPACE image shows fluid signal in the enlarged labyrinthine facial nerve canal (*short white arrow*), superior vestibular nerve canal (*long white arrow*), and the vestibular aqueduct (*arrowhead*). *D*, Axial SPACE image shows fluid signal in the singular nerve canal (*arrow*).

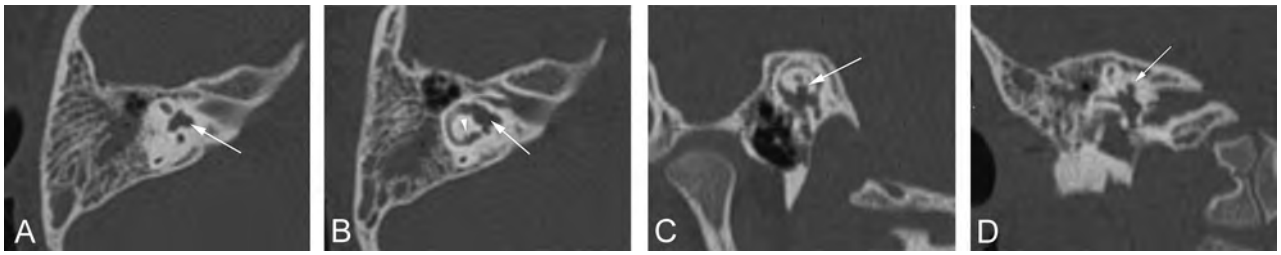

FIG 3. CT images of a 4-year-old male patient's right ear. *A*, Axial CT image shows a cystic bulge between the superior semicircular canal feet (*arrow*). *B*, Axial CT image shows the irregularly shaped vestibule (*arrow*) and small cystic bulges at the lateral semicircular canal (*arrowhead*). *C* and *D*, MPR CT image of the superior semicircular canal and coronal CT image show the cystic bulge of the vestibule protruding upward (*arrow*).

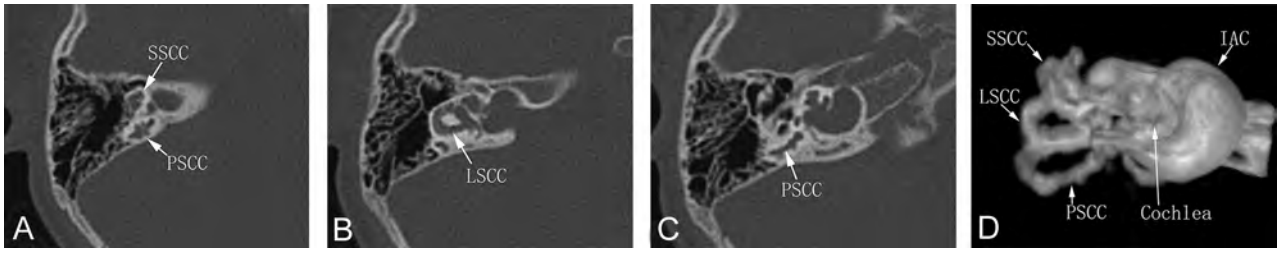

FIG 4. *A–C*, Axial CT images of a 3-year-old male patient's right ear show multicystic appearance at the superior semicircular canal (SSCC), posterior semicircular canal (PSCC), and lateral semicircular canal (LSCC). Bulbous dilation of the IAC and absence of modiolus are also demonstrated. *D*, A 3D MR hydrography image shows the cystic appearance of the semicircular canals and dilation of the IAC.

5% of genetic nonsyndromic deafness.[2] DFNX2 is the most common form of X-linked nonsyndromic deafness, which accounts for approximately 50% of all families with X-linked nonsyndromic deafness.[2] Most interestingly, DFNX2 is the only form of X-linked deafness to show anatomic anomalies on CT of the temporal bone.[2] Sennaroglu et al[4] considered these anomalies as a type between incomplete partition type I (cystic cochleovestibular malformation) and incomplete partition type II (classic Mondini deformity) and called it IP-III. The term IP-III could help radiologists better understand this rare and characteristic type of deformity in the comprehensive classification of inner ear malformations. Choi et al[10] identified IP-III in 10 (4.8%) of 206 patients with inner ear abnormalities in their research. Sennaroğlu and Bajin[8] reported that IP-III constituted 2% of inner ear malformations in their data base. In our case series, it only accounted for 0.9%. IP-III mainly occurs in males, but female carriers may have milder forms of some characteristic findings.[6,11,12]

Phelps et al[3] first reported the following characteristic CT findings: bulbous IACs, incomplete separation of the basal turn of the cochleae from the fundi of the IAC, and wide first and second parts of the intratemporal facial nerve canals. Talbot and Wilson[5] later added absence of the bony modiolus, an abnormal VA, and a dilated singular nerve canal. Sennaroglu[13] noted that the otic capsule around the membranous labyrinth was thinner than normal. Saylisoy et al[6] observed an enlarged VA with a cystic appearance and middle ear anomalies, including dysplasia at the oval and/or round window and stapes abnormalities such as a thickened footplate and single crus. Gong et al[7] reported the stapes abnormalities,

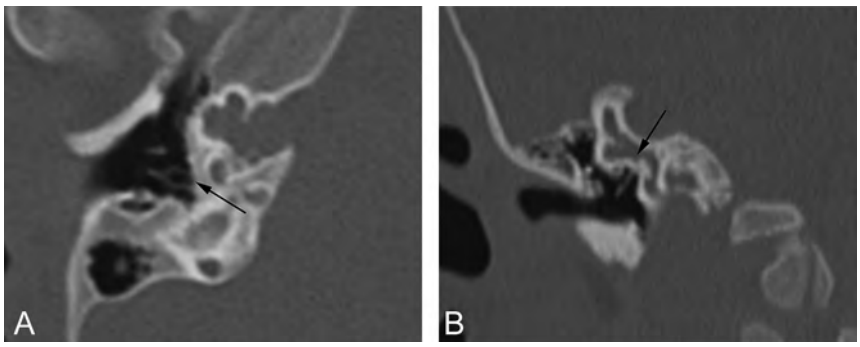

FIG 5. CT images of a 19-month-old male patient's right ear. *A*, Axial CT image shows thickness of the stapedial footplate and atresia of the oval window (*arrow*) and absence of the modiolus. *B*, Coronal CT image shows atresia of the oval window (*arrow*).

enlarged superior VN canal, and the cystic bulge in the superior vestibular margin. Anderson et al[14] described the cystic changes in the SCC and vestibule, and they also reported a potential association between IP-III and hypothalamic hamartoma.

This case series demonstrates that the entire bony labyrinth, otic capsule, and IAC are all involved in IP-III. A dilated IAC at the lateral end and absence of modiolus with interscalar septa present are the most typical imaging findings. The size of the cochlea is slightly smaller, especially in the middle turn width, but the upper turn height is within the normal range. Although the cochlear cavity appears to be empty on CT, a hypointense spiral structure can be observed on MR imaging. This structure probably represents the membranous labyrinth, which extends into the dilated IAC due to the incomplete separation of the cochlear base from the IAC, and correspondingly, the branches of the CN can also be observed in the IAC. The enlarged superior VN canal has some noteworthy details as well. Because the superior VN has several branches from the ampullae of superior and lateral SCC and the utricle, the enlarged bony canals of some of these small branches can also be seen in some cases. An irregular vestibule with a cystic appearance is also a very common imaging finding, which could be seen in about 90% of our cases, and a cystic appearance of the SCC was present in nearly half of our patients. A slightly enlarged VA with a cystic appearance can also be observed in some cases. These cystic bulges show the same signal as the inner ear fluid on MR imaging. Dysplasia of the oval and round windows is also common, and the stapes footplate is sometimes involved.

DFNX2 hearing loss is due to loss of function of the POU3F4 protein.[2] The *POU3F4* gene is expressed in early embryos in the otic capsule, which is involved in mesenchymal-mesenchymal signaling for the development of the inner ear.[2] During the inner ear development of the mouse, the *Brn4/Pou3f4* gene product is initially detected in the ventral aspect of the otic capsule and later throughout the otic capsule in the mesenchyme of both the cochlear and vestibular aspects.[15] The subcellular localization of the *Brn4/Pou3f4* gene product also changes during the differentiation of the otic capsule. It remains nuclear in those regions of the otic capsule that eventually give rise to the mature bony labyrinth. However, the subcellular localization of the product shifts from strictly nuclear to perinuclear in those regions of the otic capsule that will cavitate to form acellular regions in the temporal bone, such as the scala tympani, scala vestibuli, and the internal auditory meatus.[15] *Brn4/Pou3f4*-deficient mice also show very similar anomalies to those in human DFNX2.[16] Most of the phenotypic features of these mutant animals result from the reduction or thinning of the bony compartment of the inner ear, including malformations of the stapes, cochlea, IAC, and superior SCC.[15]

The abnormal development of the otic capsule should be the key factor in these malformations in IP-III. It may lead to a thin otic capsule, absence of the bony modiolus, enlarged nerve canals in the IAC fundus, dysplastic oval and round windows, and an abnormal stapes footplate as well. Sennaroglu[13] reported that the thin otic capsule may be formed by a thick endosteal layer, and probably the second and third layers are either absent or very thin instead of the usual 3 layers. It may not be possible to observe the normal endosteal layer or differentiate these 3 layers on CT with today's level of radiologic precision. However, we still observed hypodense areas in the region of the fissula ante fenestram in the thin otic capsule in most of our young patients, which are prevalent among healthy children.[17] This pericochlear hypodensity suggests that the thin otic capsule may have >1 layer. With respect to the cystic changes of the vestibule, SCC, and VA, we speculate that they might be caused by the abnormal development of the perilymphatic space.

The disadvantage of this case series is that we did not perform genetic analyses. However, the diagnosis of IP-III can be established with typical imaging features. Radiologists should be familiar to these imaging features, thereby preventing harmful interventions and providing proper genetic counseling.

CONCLUSIONS

IP-III is a rare genetic inner ear malformation with distinctive imaging features. It involves not only the cochlea and IAC, but also the whole otic capsule, including the vestibule and SCC.

REFERENCES

1. Nance WE, Setleff R, McLeod A, et al. **X-linked mixed deafness with congenital fixation of the stapedial footplate and perilymphatic gusher.** *Birth Defects Orig Artic Ser* 1971;07:64–69 Medline
2. Petersen MB, Wang Q, Willems PJ. **Sex-linked deafness.** *Clin Genet* 2008;73:14–23 CrossRef Medline
3. Phelps PD, Reardon W, Pembrey M, et al. **X-linked deafness, stapes gushers and a distinctive defect of the inner ear.** *Neuroradiology* 1991;33:326–30 CrossRef Medline
4. Sennaroglu L, Sarac S, Ergin T. **Surgical results of cochlear implantation in malformed cochlea.** *Otol Neurotol* 2006;27:615–23 CrossRef Medline
5. Talbot JM, Wilson DF. **Computed tomographic diagnosis of X-linked congenital mixed deafness, fixation of the stapedial footplate, and perilymphatic gusher.** *Am J Otol* 1994;15:177–82 Medline
6. Saylisoy S, Incesulu A, Gurbuz MK, et al. **Computed tomographic findings of X-linked deafness: a spectrum from child to mother,**

from young to old, from boy to girl, from mixed to sudden hearing loss. *J Comput Assist Tomogr* 2014;38:20–24 CrossRef Medline

7. Gong WX, Gong RZ, Zhao B. **HRCT and MRI findings in X-linked non-syndromic deafness patients with a POU3F4 mutation.** *Int J Pediatr Otorhinolaryngol* 2014;78:1756–62 CrossRef Medline
8. Sennaroğlu L, Bajin MD. **Classification and current management of inner ear malformations.** *Balkan Med J* 2017;34:397–411 CrossRef Medline
9. Purcell D, Johnson J, Fischbein N, et al. **Establishment of normative cochlear and vestibular measurements to aid in the diagnosis of inner ear malformations.** *Otolaryngol Head Neck Surg* 2003;128:78–87 CrossRef Medline
10. Choi JW, Min B, Kim A, et al. **De novo large genomic deletions involving POU3F4 in incomplete partition type III inner ear anomaly in East Asian populations and implications for genetic counseling.** *Otol Neurotol* 2015;36:184–90 CrossRef Medline
11. Marlin S, Moizard MP, David A, et al. **Phenotype and genotype in females with POU3F4 mutations.** *Clin Genet* 2009;76:558–63 CrossRef Medline
12. Papadaki E, Prassopoulos P, Bizakis J, et al. **X-linked deafness with stapes gusher in females.** *Eur J Radiol* 1998;29:71–75 CrossRef Medline
13. Sennaroglu L. **Histopathology of inner ear malformations: do we have enough evidence to explain pathophysiology?** *Cochlear Implants Int* 2016;17:3–20 CrossRef Medline
14. Anderson EA, Ozutemiz C, Miller BS, et al. **Hypothalamic hamartomas and inner ear diverticula with X-linked stapes gusher syndrome: new associations?** *Pediatr Radiol* 2020;50:142–45 CrossRef Medline
15. Phippard D, Heydemann A, Lechner M, et al. **Changes in the subcellular localization of the Brn4 gene product precede mesenchymal remodeling of the otic capsule.** *Hear Res* 1998;120:77–85 CrossRef Medline
16. Phippard D, Lu L, Lee D, et al. **Targeted mutagenesis of the POU-domain gene Brn4/Pou3f4 causes developmental defects in the inner ear.** *J Neurosci* 1999;19:5980–89 CrossRef Medline
17. Pekkola J, Pitkaranta A, Jappel A, et al. **Localized pericochlear hypoattenuating foci at temporal-bone thin-section CT in pediatric patients: nonpathologic differential diagnostic entity?** *Radiology* 2004;230:88–92 CrossRef Medline

Accuracy of MR Imaging for Detection of Sensorineural Hearing Loss in Infants with Bacterial Meningitis

G. Orman, M.K. Kukreja, J.G. Vallejo, N. Desai, T.A.G.M. Huisman, and S.F. Kralik

ABSTRACT

BACKGROUND AND PURPOSE: Bacterial meningitis most commonly affects young children and can result in critical adverse outcomes, including sensorineural hearing loss (SNHL). The purpose of this study is to determine the diagnostic accuracy of MR imaging for predicting the development of SNHL among infants with bacterial meningitis.

MATERIALS AND METHODS: A retrospective review was performed among infants (age <365 days) with bacterial meningitis ($n = 115$). Independent and consensus blinded review of brain MRIs ($n = 239$) performed less than 90 days from presentation were conducted. Abnormal appearance of the inner ear was defined as enhancement on postcontrast T1-weighted (T1-weighted+C) sequence and FLAIR hyperintensity. The consensus MR imaging appearance of the inner ear on FLAIR, T1-weighted+C, and combined evaluation was compared with criterion standard audiometric testing to determine the sensitivity and specificity of MR imaging for detecting SNHL.

RESULTS: The mean age at diagnosis of bacterial meningitis was 50.6 days (range, 0–338 days) and 24.3% had SNHL. Sensitivity and specificity was 0.61/0.96, 0.50/0.94, and 0.61/0.94 for T1-weighted+C, FLAIR hyperintensity, and combined evaluation, respectively, for prediction of SNHL. There was excellent interobserver agreement for both the T1-weighted+C and FLAIR sequences and combined evaluation for presence of abnormal enhancement and hyperintense signal, respectively. Factors associated with abnormal MR imaging findings on T1-weighted+C and/or FLAIR in patients with SNHL included low CSF glucose ($P = .04, .02$) and high CSF protein ($P = .04, .03$).

CONCLUSIONS: Abnormal enhancement and/or FLAIR hyperintensity of the inner ear demonstrate high specificity and average sensitivity for prediction of SNHL among infants with bacterial meningitis.

ABBREVIATIONS: WBC = white blood cell; SNHL = sensorineural hearing loss; GBS = Group B *Streptococcus*; PPV = positive predictive value; NPV = negative predictive value; +C = postcontrast

Meningitis is an inflammation of the meninges affecting the pia, arachnoid, and subarachnoid space in response to infection. Despite advances in antimicrobial therapy and improvements in supportive care, bacterial meningitis remains a devastating disease. Group B *Streptococcus* (GBS) and *Escherichia coli* (*E coli*) remain the most common causes of bacterial meningitis in the first 90 days of life.[1] In the modern era, the mortality of bacterial meningitis in infants is approximately 10%, and survivors remain at high risk for neurologic sequelae.[2,3]

Received November 15, 2019; accepted after revision March 21, 2020.

From the Edward B. Singleton Department of Radiology (G.O., M.K.K., N.D., T.A.G.M.H., S.F.K.); and Department of Pediatrics, Section of Infectious Diseases (J.G.V.), Texas Children's Hospital and Baylor College of Medicine, Houston, Texas.

Please address correspondence to Gunes Orman, MD, Texas Children's Hospital, Edward B. Singleton Department of Radiology, 6701 Fannin St, Suite 470, Houston, TX 77030, e-mail: gxorman@texaschildrens.org

Indicates article with supplemental on-line table.

http://dx.doi.org/10.3174/ajnr.A6539

Sensorineural hearing loss (SNHL) is a serious complication and sequela of bacterial meningitis, occurring in 7%–33% of pediatric patients with bacterial meningitis.[4-7] SNHL in children is more common with *Streptococcus pneumoniae* (*S pneumoniae*) (31%) or *Neisseria meningitidis* (*N meningitidis*) (23.9%) meningitis.[5]

Meningitis leads to SNHL through a presumed mechanism of spread into the inner ear from the CSF through the cochlear aqueduct.[8,9] Three previous studies have specifically investigated MR imaging for detection of inner ear abnormalities in patients with bacterial meningitis.[8-10] These studies showed that MR imaging could detect inner ear abnormalities in patients who developed SNHL. However, these studies only included a small number of patients, included a wide range of patient ages, and did not evaluate the value of the FLAIR sequence, a noncontrast MR imaging sequence routinely performed and useful for detecting abnormal fluid. To date, no large study has evaluated both noncontrast and postcontrast MR imaging techniques for prediction of SNHL among

Table 1: Demographic findings

Age	50.6 Days (0–338 Days)
Sex	67 male/48 female
Pathogens	
SNHL(+)	
CSF culture results	Negative (25%) GBS (21.4%) *E coli* (17.9%) *S pneumoniae* (17.9%) Other pathogens (*H influenza*, *S gallolyticus*, *N meningitidis*, *S infantarius*, and *P mirabilis*) (17.9%)
Blood culture results	*E coli* (29.6%) GBS (22.2%) *S pneumoniae* (14.8%) *H influenza* (7.4%) *K pneumoniae* (7.4%) Other pathogens (*S gallolyticus*, *N meningitidis*, *S infantarius*, *P mirabilis*, and *S hominis*) (18.5%)
SNHL(−)	
CSF culture results	Negative (30%) *E coli* (25%) GBS (21.3%) Other pathogens (Gram-positive cocci, Coccobacilli, Salmonella, Serratia, *S alpha*, *S gallolyticus*, *S gamma*, *S pneumonia*, *S pyogenes*) (23.7%)
Blood culture results	*E coli* (35.4%) GBS (29.1%) Other pathogens (Coagulase negative staphylococcus, Enterobacter, *H influenza*, Klebsiella, Neisseria, *S aureus*, *S bovis*, *S gallolyticus*, *S pneumonia*, *S pyogenes*) (24%) Negative (11.4%)

infants with bacterial meningitis. In addition, only a limited number of studies have evaluated associated factors that may result in detectable MR imaging abnormalities in these patients such as CSF parameters at the diagnosis or timing of MR imaging in the course of meningitis. Early recognition of labyrinthitis in infants with meningitis by neuroimaging can benefit patient care through promoting earlier audiologic consultation and/or intervention in these patients.

The purpose of this study was to determine the diagnostic accuracy of noncontrast and postcontrast MR imaging techniques for prediction of SNHL among a large cohort of infants with a history of meningitis and the factors associated with abnormal MR imaging findings of the inner ear.

MATERIALS AND METHODS

Following institutional review board approval, a retrospective review was performed among neonates and infants (age < 365 days) with confirmed bacterial meningitis imaged between 2011 and 2019. Diagnosis of meningitis was determined by either 1) a positive CSF culture, or 2) positive blood culture combined with elevated CSF white blood cell (WBC) count (>20 WBC/μL for age <30 days, >9 WBC/μL for age 30–90 days, and >6 WBC/μL for age >90 days).[11,12] Patients with immunodeficiency, malignancy, or an intracranial shunt were excluded. The electronic medical records were reviewed to determine patient age at presentation, prematurity (<37 weeks gestation), and audiometric testing results.

MR imaging of the brain was performed using 1.5T and 3T scanners with precontrast axial and sagittal T1-weighted (T1-weighted) turbo spin-echo, axial and/or coronal FLAIR, axial and coronal T2-weighted, axial gradient-echo, axial diffusion-weighted, and postcontrast axial and coronal T1-weighted (T1-weighted+C) turbo spin-echo imaging. Section thickness for all FLAIR and T1-weighted+C sequences was 3–4 mm with zero gap. MR imaging performed within 90 days of presentation was included.The mean time intervals between meningitis presentation to audiometric testing and between first MRI to audiometric testing were calculated (days). Nondiagnostic MRIs were excluded from the study. Forty-nine patients had 1 MR imaging, and 66 patients had more than 1 MR imaging, of which, 10 patients had differences and 56 patients had no differences on follow-up. Therefore, 239 MRIs of 115 patients were included, of which 239/239 MRIs had the FLAIR sequence and 212/239 MRIs had T1-weighted+C sequences. The 27 MRIs without T1-weighted+C sequences were due to a decision to not administer IV contrast in the setting of renal failure.

Retrospective independent reviews of brain MRIs were performed by 2 board-certified pediatric neuroradiologists (S.F.K., M.K.K.) who were blinded to SNHL status, with 7 years and 9 years of experience. Abnormal appearance of the inner ear on MR imaging was defined as presence of abnormal enhancement on T1-weighted+C sequences (yes/no), or presence of hyperintense FLAIR signal (yes/no). The side of abnormal enhancement or hyperintense FLAIR signal (right/left/bilateral), and subjective degree of enhancement (none/mild/moderate/severe) were also recorded. For all patients in whom there was a discordant MR imaging finding, the reviewers performed a combined review, reached a consensus on the MR imaging finding, and this consensus was used as the final diagnosis. Interobserver agreement for individual MR imaging findings was calculated using the κ statistic. A κ value of 0.81–1.0 indicated excellent agreement, 0.61–0.80 indicated good agreement, 0.41–0.60 indicated moderate agreement, 0.21–0.40 indicated fair agreement, and 0–0.20 indicated slight agreement.

Audiometric testing was used as the criterion standard for diagnosis of SNHL in all patients. All audiometric testing was performed by certified audiologists using age-appropriate testing, which included visual reinforcement audiometry, otoacoustic emissions test, auditory brain stem response or auditory steady-state response evaluation. SNHL was graded per hearing levels in decibels (dB) by slight/mild (26–40 dB), moderate (41–60 dB), severe (61–80 dB) and profound (>81 dB) by World Health Organization grades of hearing impairment (https://www.who.int/pbd/deafness/hearing_impairment_grades/en/).

Sensitivity, specificity, positive predictive value (PPV), and negative predictive value (NPV) of enhancement on T1-weighted+C, FLAIR, and combined evaluation were calculated using the results

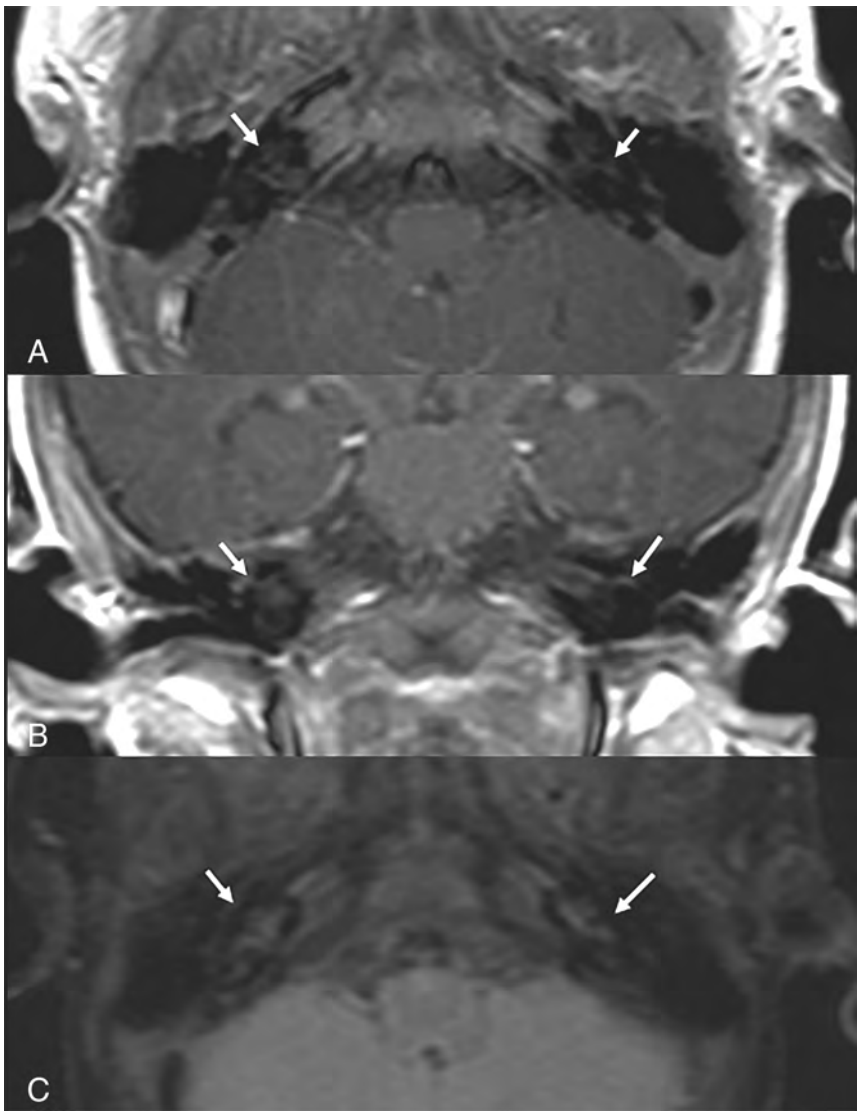

FIG 1. Two-month-old male infant with history of *E coli* meningitis. Magnified MR imaging of the brain with (*A*) axial, (*B*) coronal T1-weighted+C, and (*C*) axial FLAIR reveals normal signal characteristics of the inner ear. The patient did not develop SNHL on follow-up.

of audiometric testing as the reference standard. Binomial exact 95% confidence intervals were calculated to provide an estimate of precision. When a patient had more than 1 MR imaging scan before the audiometric testing, the same audiometric testing result was used for the analysis.

To determine the factors associated with an abnormal MR imaging appearance of the inner ear, an unpaired *t* test was used to compare the age at presentation, time from presentation to MR imaging, CSF WBC count, CSF glucose, and CSF protein. In addition, a Fisher exact test was used to compare positive or negative CSF results between the groups with normal versus abnormal appearance on T1-weighted+C and FLAIR imaging. A *P* value $<.05$ was considered statistically significant.

RESULTS

A total of 115 infants (67 males/48 females) with a mean age of 50.6 days (range, 0–338 days) met the inclusion criteria for the study (Table 1). The mean time from diagnosis of bacterial meningitis to MR imaging was 16.3 days (range 0–79 days). Mean time from diagnosis of bacterial meningitis to audiometric testing was 323.25 days (range, 0–2268 days). Mean time from the first MR imaging to audiometric testing was 311.7 days (range, 0–2234 days). There was no significant difference in time from the first MR imaging to audiometric testing between infants without SNHL (306.01 ± 586.9 days) and infants with SNHL (328.5 ± 469 days) ($P = .85$). CSF culture and blood culture results for patients with and without SNHL are shown in Table 1.

SNHL was present in 24.3% (28/115) of infants. With respect to age at diagnosis of meningitis, SNHL was $n = 12$ (14.6%) for age ≤28 days, $n = 8$ (34.8%) for age 29–90 days, and $n = 8$ (80%) for age 90–365 days. In Figs 1–3, the FLAIR and T1-weighted+C MR imaging findings are shown for patients without and with SNHL. World Health Organization grades of hearing impairment were unilateral slight/mild in 22.2% ($n = 6$), bilateral slight/mild in 37% ($n = 10$), bilateral moderate in 7.4% ($n = 2$), bilateral severe in 7.4% ($n = 2$), unilateral profound in 11.1% ($n = 3$), bilateral profound in 14.8% ($n = 4$) of patients with SNHL. One child had profound SNHL on the right side and slight/mild SNHL on the left side.

A total of 19.8% (42/212) of MR images had consensus interpretation of abnormal enhancement on T1-weighted+C. Sensitivity, specificity, PPV, and NPV of T1-weighted+C MR imaging findings compared with audiometric testing as the reference standard with 95% confidence intervals are shown in the On-line Table. Interobserver agreement between the 2 readers was excellent for the presence of abnormal contrast enhancement ($\kappa = 0.95$). The consensus grade of enhancement was 80.9% mild, 16.7% moderate, and 2.4% severe. There was excellent interobserver agreement for the grading of enhancement ($\kappa = 0.91$). The consensus side of the contrast enhancement on T1-weighted+C was right-sided only 0.9% (2/212), left-sided only 5.7% (12/212), bilateral 12.7% (27/212), and none 80.7% (171/212) for the consensus reading. Interobserver agreement between the 2 readers was excellent for the side of contrast enhancement ($\kappa = 0.94$).

A total of 18.4% (44/239) of MR images had consensus interpretation of hyperintense FLAIR signal. Sensitivity, specificity, PPV, and NPV of FLAIR MR imaging findings compared with audiometric testing as the reference standard with 95% confidence

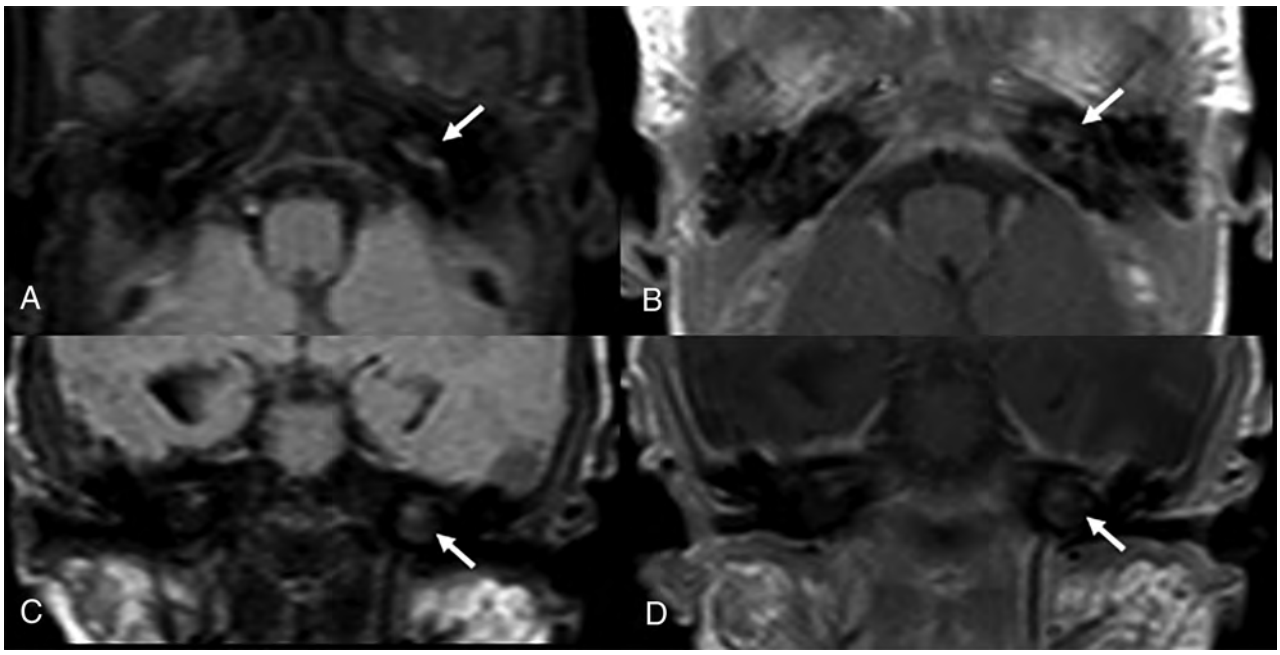

FIG 2. One-month-old male infant with history of late onset GBS meningitis and subsequent cardio-respiratory arrest. Magnified MR imaging of the brain with (*A*) axial FLAIR, (*B*) axial T1-weighted+C, (*C*) coronal FLAIR, and (*D*) coronal T1-weighted+C demonstrates abnormal hyperintense FLAIR signal and enhancement of the left inner ear. The patient developed left-sided SNHL on follow-up.

intervals are shown in the On-line Table. Interobserver agreement between the 2 readers was excellent for presence of FLAIR hyperintensity ($\kappa = 0.93$). Side of the FLAIR hyperintensity was right-sided only 0.4% (1/239), left-sided only 3.3% (8/239), bilateral 14.6% (35/239), and none 81.6% (195/239) for the consensus reading. Interobserver agreement between the 2 readers was excellent for the side of abnormal FLAIR hyperintensity ($\kappa = 0.90$).

Among children with SNHL, the mean CSF glucose was significantly lower for abnormal T1-weighted+C, hyperintense FLAIR signal, and combined evaluation ($P = .04$, .02, and .04, respectively) and the mean CSF protein was significantly higher for abnormal T1-weighted+C, hyperintense FLAIR signal, and combined evaluation in patients with SNHL ($P = .04$, .03, and .04, respectively) (Table 2). The presence of any positive CSF culture demonstrated significant association with abnormal T1-weighted+C, hyperintense FLAIR signal, and combined evaluation ($P = .009$, .007, and .003, respectively). The most common pathogens in patients with SNHL and with abnormal T1-weighted+C or FLAIR hyperintense signal were GBS (38.5%), *E coli* (23.1%), and *S pneumoniae* (23.1%) in our cohort.

DISCUSSION

SNHL is a serious complication and sequela of bacterial meningitis. The pathogenesis of SNHL from bacterial meningitis is from spread of infection into the inner ear through the cochlear aqueduct and subsequent development of labyrinthitis.[8] We believe that the detection of abnormal enhancement within the inner ear on MR imaging is secondary to the inflammation and blood-brain barrier breakdown while the FLAIR hyperintense signal reflects the accumulation of abnormal proteinaceous fluid in the inner ear. Previously reported risk factors for SNHL due to meningitis include *S pneumoniae*, decreased CSF glucose, increased CSF protein, seizure, and a long hospital duration.[5,13]

Twenty-eight patients (24.3%) developed SNHL in our cohort. The most common pathogens in our SNHL cohort were GBS (21.4%) and *E coli* (29.6%). In addition, the most common pathogens in patients with SNHL and with abnormal T1-weighted+C or FLAIR hyperintense signal were GBS (38.5%) and *E coli* (23.1%). GBS and *E coli* are the 2 most common bacteria causing neonatal meningitis.[14] The relatively low mean age of our patient population of 50.6 days likely explains the reason the most common pathogens in our cohort were GBS and *E coli*.

In this large study of infants with bacterial meningitis, we demonstrate high specificity (96% and 94%) but average sensitivity (61% and 50%) for abnormal enhancement and abnormal FLAIR hyperintense signal, respectively, for predicting SNHL among infants with meningitis. Most (81%) inner ear enhancement on postcontrast T1-weighted imaging was subjectively graded as mild indicating the radiologist could miss this finding without direct attention to the inner ear. There was excellent agreement between readers and the individual readings were as high as consensus readings, indicating a high likelihood of the reproducibility of these findings in the clinical setting.

Only a few studies are available in the medical literature for comparison with our results. Kopelovich et al[9] evaluated T1-weighted+C MR imaging sequences in 23 children (3 months–14 years) compared with audiometric testing. Only 35% of their cohort developed SNHL and the authors found 87% sensitivity and 100% specificity for contrast enhancement to predict SNHL.[9] van Loon et al[10] evaluated T1-weighted+C and T2-weighted MRIs of 17 patients (3 months–77 years) with audiometric data and found inner ear enhancement in 87% of the ears affected by SNHL. Enhancement of the labyrinth showed 62% sensitivity and 90% specificity.[10] Differences in the

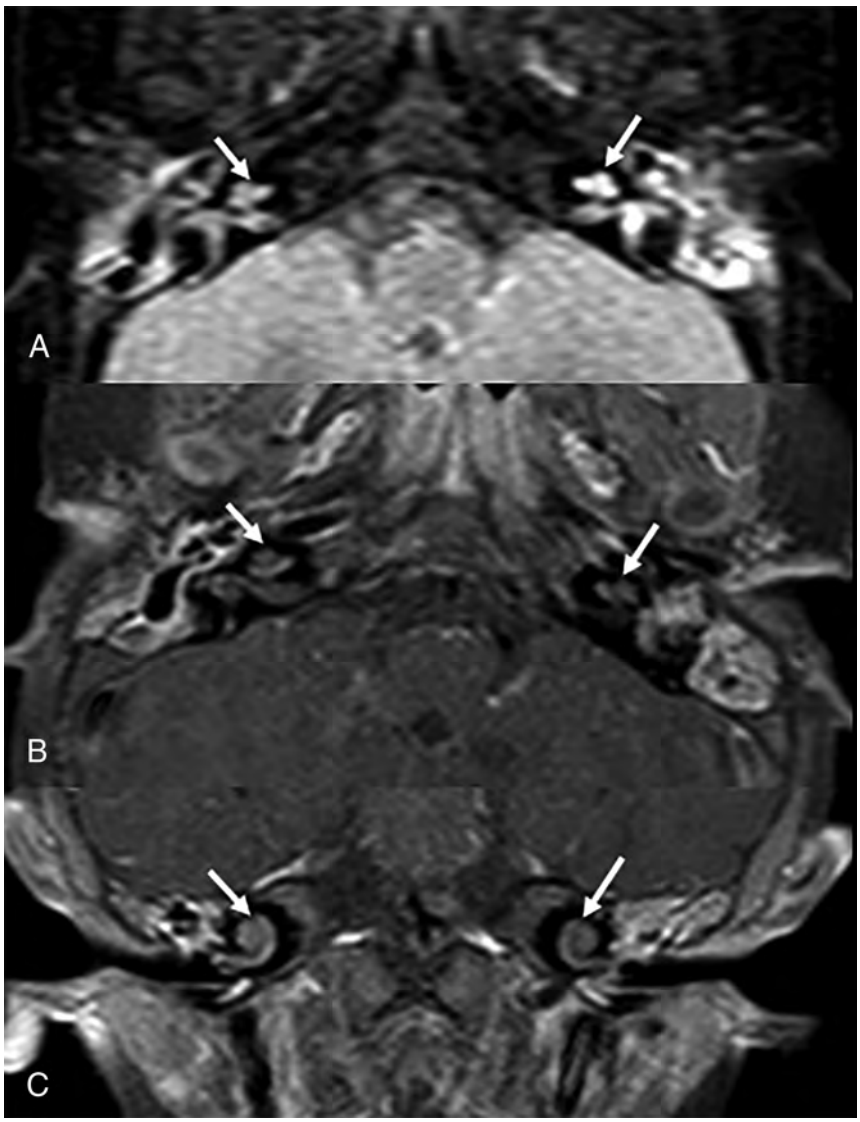

FIG 3. Seven-month-old girl with history of meningitis from *N meningitidis*. (*A*) Magnified axial FLAIR, (*B*) axial T1-weighted+C, and (*C*) coronal T1-weighted+C images demonstrate abnormal hyperintense FLAIR signal and enhancement of both inner ears. There is an increased enhancement on the mastoids bilaterally. The patient developed bilateral SNHL on follow-up.

results of this study and these previous 2 studies may include the patient population (younger age and larger number of patients), and most pathogens being GBS and *E coli*. Our cohort consists of the most homogeneous and largest patient group to date compared with similar studies.[8-10] Last, similar to Kutz et al,[5] we found significantly lower CSF glucose and higher CSF protein in our SNHL cohort to be associated with greater likelihood of abnormal appearance of the inner ear on MR imaging (Table 2).

We did not find any similar studies to compare our abnormal FLAIR hyperintensity results. However, there is 1 report of an adult pneumococcal meningitis patient who developed SNHL and who underwent 3D FLAIR MR imaging that revealed hyperintensity and contrast enhancement in the cochlea and the vestibulum.[15] Another study among adults reported that 3D FLAIR hyperintensity was positively associated with pretreatment SNHL and presence of vertigo in idiopathic sudden SNHL.[16] Due to the low number of postcontrast FLAIR sequences in our data base, we did not include postcontrast FLAIR evaluations in our study design.

Strengths of this study include the large number of patients, a relatively homogeneous age of patients who are most commonly affected by bacterial meningitis, assessment of both a noncontrast and postcontrast sequence for detecting SNHL, and the use of audiometric testing as the criterion standard for diagnosis of SNHL.

Limitations of this study are because of the retrospective nature of the study, and include a discrepancy between number of MRIs and infants, and single-center evaluation of patients with meningitis. Another potential limitation of this study is the subjectivity in the determination of individual MR imaging findings. This subjectivity was mitigated by independent imaging reviews by 2 pediatric neuroradiologists, the consensus diagnosis in discordant findings, and calculation of interobserver agreement. We observed excellent interobserver agreement for both the inner ear enhancement and FLAIR hyperintensity, indicating that the subjectivity in imaging interpretation does not appear to be a significant factor. Because this was a retrospective study, we evaluated the inner ear on whole-brain MR imaging FLAIR and T1-weighted+C sequences, which were available in all patients and had 3–4 mm section thickness. Thinner section thickness imaging through the temporal bones may improve the sensitivity of detection by providing more images and higher resolution of the inner ear. In addition, this limitation affected our ability to perform a more detailed inner ear site-specific analysis of the location of the abnormality, but future studies with thinner and higher resolution imaging may be useful for further differentiation. Regardless, the increased recognition provided from this study regarding the diagnostic accuracy of MR imaging for SNHL in these infants may help radiologists more closely assess the inner ear when routine MRIs of the brain are ordered, routinely report on the status of the inner ear in patients with bacterial meningitis, or modify imaging protocols to provide higher resolution imaging of the inner ear in these patients.

CONCLUSIONS

Abnormal enhancement on T1-weighted+C MR imaging and abnormal FLAIR hyperintense signal of the inner ear are highly specific for predicting SNHL in infants with bacterial meningitis.

Table 2: Associated findings for postcontrast T1, FLAIR, and combined evaluation in patients with SNHL ($P < .05$)

	Normal MR Imaging Findings Mean (SD)	Abnormal MR Imaging Findings Mean (SD)	*P* Value
Inner ear enhancement on T1+C			
Age at presentation (days)	95.2 (116.6)	93.4 (93.5)	.9
Time from presentation to MR imaging (days)	14.1 (11.4)	10.1 (6.4)	.3
CSF WBC count	11692.3 (32,494.4)	2674.8 (5440.94)	.3
CSF glucose	29 (14.3)	18.1 (11)	.04
CSF protein	309.8 (236.9)	505.5 (216.1)	.04
FLAIR hyperintensity			
Age at presentation (days)	74.1 (105.1)	98.2 (95.5)	.5
Time from presentation to MR imaging (days)	12.9 (10.7)	10 (6.6)	.4
CSF WBC count	8613.9 (27,966.7)	2843.62 (5624.81)	.5
CSF glucose	35.5 (22.4)	17.9 (11.4)	.02
CSF protein	301.5 (224.1)	498.54 (223.3)	.03
Combined evaluation			
Age at presentation (days)	95.2 (116.6)	93.4 (93.5)	.9
Time from presentation to MR imaging (days)	14.1 (11.4)	10.1 (6.4)	.3
CSF WBC count	11,692.3 (32,494.4)	2674.8 (5440.94)	.3
CSF glucose	29 (14.3)	18.1 (11)	.04
CSF protein	309.8 (236.9)	505.5 (216.1)	.04

Disclosures: Jesus G. Vallejo—*UNRELATED: Royalties:* Wolters Kluwer – UpToDate.

REFERENCES

1. Ku LC, Boggess KA, Cohen-Wolkowiez M. **Bacterial meningitis in infants.** *Clin Perinatol* 2015;42:29–45 CrossRef Medline
2. Ouchenir L, Renaud C, Khan S, et al. **The epidemiology, management, and outcomes of bacterial meningitis in infants.** *Pediatrics* 2017;140: e20170476 CrossRef
3. de Louvois J, Halket S, Harvey D. **Neonatal meningitis in England and Wales: sequelae at 5 years of age.** *Eur J Pediatr* 2005;164:730–34 CrossRef Medline
4. Koomen I, Grobbee DE, Roord JJ, et al. **Hearing loss at school age in survivors of bacterial meningitis: assessment, incidence, and prediction.** *Pediatrics* 2003;112:1049–53 CrossRef
5. Kutz JW, Simon LM, Chennupati SK, et al. **Clinical predictors for hearing loss in children with bacterial meningitis.** *Arch Otolaryngol Head Neck Surg* 2006;132:941–45 CrossRef Medline
6. Richardson MP, Reid A, Tarlow MJ, et al. **Hearing loss during bacterial meningitis.** *Arch Dis Child* 1997;76:134–38 CrossRef Medline
7. Wellman MB, Sommer DD, McKenna J. **Sensorineural hearing loss in postmeningitic children.** *Otol Neurotol* 2003;24:907–12
8. Beijen J, Casselman J, Joosten F, et al. **Magnetic resonance imaging in patients with meningitis induced hearing loss.** *Eur Arch Otorhinolaryngol* 2009;266:1229–36 CrossRef
9. Kopelovich JC, Germiller JA, Laury AM, et al. **Early prediction of postmeningitic hearing loss in children using magnetic resonance imaging.** *Arch Otolaryngol Head Neck Surg* 2011;137:441–47 CrossRef Medline
10. van Loon MC, Hensen EF, de Foer B, et al. **Magnetic resonance imaging in the evaluation of patients with sensorineural hearing loss caused by meningitis: implications for cochlear implantation.** *Otol Neurotol* 2013;34:845–54 CrossRef Medline
11. Kestenbaum LA, Ebberson J, Zorc JJ, et al. **Defining cerebrospinal fluid white blood cell count reference values in neonates and young infants.** *Pediatrics* 2010;125:257–64 CrossRef
12. Chávez-Bueno S, McCracken GH. Jr. **Bacterial meningitis in children.** *Pediatr Clin North Am* 2005;52:795–810 CrossRef Medline
13. Jaremko JL, Moon AS, Kumbla S. **Patterns of complications of neonatal and infant meningitis on MRI by organism: a 10 year review.** *Eur J Radiology* 2011;80:821–27 CrossRef
14. Kim KS. **Current concepts on the pathogenesis of Escherichia coli meningitis: implications for therapy and prevention.** *Curr Opin Infect Dis* 2012;25:273–78 CrossRef Medline
15. Hara N, Yunoki T, Kubo S, et al. **[Pneumococcal meningitis with accompanying severe hearing loss: 3D-FLAIR imaging of the inner ear and treatment].** *Rinsho Shinkeigaku* 2015;55:119–22 CrossRef Medline
16. Berrettini S, Seccia V, Fortunato S, et al. **Analysis of the 3-dimensional fluid-attenuated inversion-recovery (3D-FLAIR) sequence in idiopathic sudden sensorineural hearing loss.** *JAMA Otolaryngol Head Neck Surg* 2013;139:456–64 CrossRef Medline

A Case Series of X-Linked Deafness-2 with Sensorineural Hearing Loss, Stapes Fixation, and Perilymphatic Gusher: MR Imaging and Clinical Features of Hypothalamic Malformations

J.-A. Prat Matifoll, M. Wilson, R. Goetti, C. Birman, B. Bennett, E. Peadon, A. Prats-Uribe, and K. Prelog

ABSTRACT

SUMMARY: X-linked deafness-2 (DFNX2) is an X-linked recessive disorder characterized by profound sensorineural hearing loss and a pathognomonic temporal bone deformity. Because hypothalamic malformations associated with DFNX2 have been rarely described, we aimed to further describe these lesions and compare them with features of a nonaffected population. All patients diagnosed with DFNX2 between 2006 and 2019 were included and compared with age-matched patients with normal MR imaging findings and without hypothalamic dysfunction. MR imaging features differing between groups were selected to help identify DFNX2. Sensitivity and specificity were calculated for these features. Agreement among 3 radiologists was quantified using the index κ. Information on the presence or absence of gelastic seizures, precocious puberty, or delayed puberty was also gathered. We selected distinctive MR imaging features of hypothalamic malformations in DFNX2. The feature selected on axial T2 images was the folded appearance of the ventromedial hypothalamus (sensitivity, 100%; specificity, 95.8%) characterized by an abnormal internal/external cleft (sensitivity, 100%; specificity, 95.7%). On coronal T2, the first distinctive feature was a concave morphology of the medial eminence (sensitivity, 100%; specificity, 97.1%), the second feature was at least 1 hypothalamic-septum angle $\geq$90° (sensitivity, 90%; specificity, 72.5%), and the third feature was a forebrain-hypothalamic craniocaudal length of $\geq$6 mm (sensitivity, 70%; specificity, 79.7%). Clinical features were also distinctive because 9 patients with DFNX2 did not present with gelastic seizures or precocious puberty. One patient had delayed puberty. The κ index and intraclass correlation coefficient ranged between 0.78 and 0.95. Imaging and clinical features of the hypothalamus suggest that there is a hypothalamic malformation associated with DFNX2. Early assessment for pubertal delay is proposed.

ABBREVIATIONS: CMA = chromosomal microarray; DFNX2 = X-linked deafness-2; ICC = intraclass correlation coefficient; SE = sensitivity; SP = specificity

X-linked deafness-2 (DFNX2) is an X-linked recessive disorder (Online Mendelian Inheritance in Man No. 304400; https://www.omim.org/) characterized by profound sensorineural hearing loss with or without a conductive component[1] and a pathognomonic temporal bone deformity.[2,3] The pathognomonic inner ear abnormalities include dilation of the inner auditory canal, absence of a lamina cribrosa between the base of the cochlea and the internal auditory canal,[4] and an absent bony modiolus.[5] The bony interscalar septa are partially present, and the external dimensions of the cochlea do not differ from normal.[6-9] The absence of a bone partition between the inner ear and the internal auditory canal results in a perilymphatic fluid "gusher" during stapes surgery.[10,11] The disorder is caused by a mutation in the *POU domain, class 3, transcription factor 4* (*POU3F4*) gene (Online Mendelian Inheritance in Man No. 300039) located in chromosome band Xq21. Furthermore, *POU3F4* gene malfunction can be caused by inversions and duplications upstream of this gene region.[12]

Because hypothalamic malformations associated with DFNX2 have been rarely described, we aimed to further describe these lesions and compare them with a nonaffected population.[13]

MATERIALS AND METHODS

This retrospective study included patients with sensorineural hearing loss who underwent MR imaging at a tertiary pediatric hospital (Children's Hospital at Westmead, Sydney) between 2006 and 2019 and demonstrated a pathognomonic DFNX2 inner ear abnormality (Fig 1). A second comparison group of age-matched patients with or without hearing loss and normal MR imaging brain findings was extracted from the same hospital. None of the controls had hypothalamic dysfunction.

Received December 18, 2019; accepted after revision March 20, 2020.

From the Departments of Radiology (J.-A.P.M., K.P.); Clinical Genetics (M.W.) and Ear Nose Throat (C.B.); Child Development Unit (B.B.); and Deafness Centre (E.P.); Children's Hospital at Westmead (Sydney), Westmead, New South Wales, Australia; Radiology Department (R.G.), University of Sydney, Children's Hospital at Westmead (Sydney), Westmead, New South Wales, Australia; and Nuffield Department of Orthopaedics, Rheumatology and Musculoskeletal Sciences (A.P.-U.), Centre for Statistics in Medicine, Botnar Research Centre, University of Oxford, Oxford, UK.

Please address correspondence to Joan-Albert Prat Matifoll, MD, The Children's Hospital at Westmead, Radiology Department, Hawkesbury Rd and Hainsworth St, Westmead New South Wales, Australia 2145; e-mail: j.prat@vhebron.net
http://dx.doi.org/10.3174/ajnr.A6541

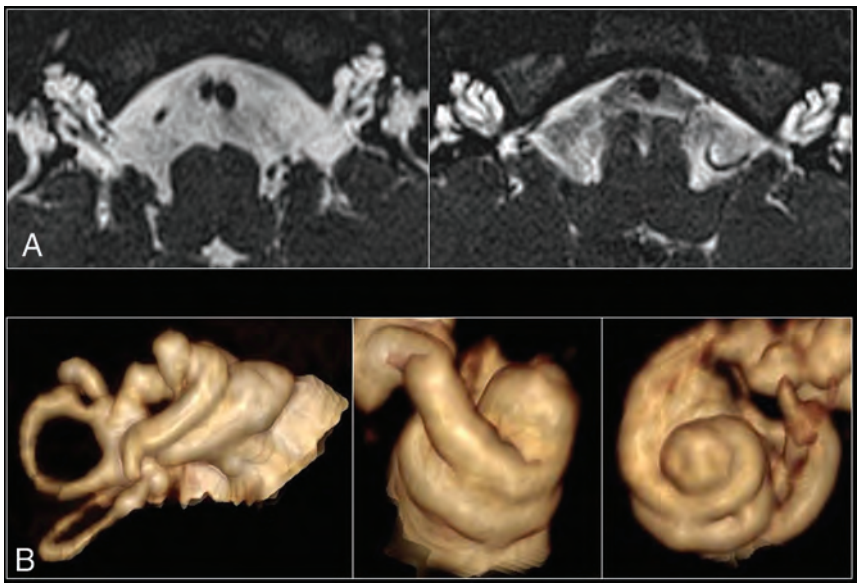

FIG 1. *A*, High-resolution axial T2 images of both inner ears in a patient with incomplete partition type III. The 3 main features include a dilated internal auditory canal, incomplete separation of the basal turn of the cochlea from the internal auditory canal, with an absent lamina cribrosa and modiolus. *B*, 3D reconstructions of several cochleae with incomplete partition type III, which demonstrate the presence of interscalar septa and cochlear turns.

Ethical approval for this study was obtained by the institutional ethics review board (2019/ETH08734).

MR Imaging Protocol

MR imaging was performed using a 1.5T (Gyroscan Intera and Ingenia; Philips Healthcare) or a 3T scanner (Verio; Siemens). While the acquired MR imaging pulse sequences varied during the course of the included studies, at a minimum, the inner ear/auditory canal MR imaging protocol consisted of the following pulse sequences encompassing the inner acoustic canal and inner ear: axial T2 and fast (turbo) spin-echo techniques with special modifications optimizing them for isotropic 3D imaging (T2 sampling perfection with application-optimized contrasts by using different flip angle evolution [SPACE sequence; Siemens]). Other sequences acquired included axial T1 FLAIR, DWI/ADC, gradient-echo, coronal T2/T2 FLAIR, sagittal T1 FLAIR, and sagittal T1 MPRAGE. The matrix size was 320 with voxel size of 0.5 mm, resulting in an FOV of 16 cm on axial, coronal, and sagittal T2 SPACE sequences.

MR Imaging Analysis

MR imaging features of the inner ear and hypothalamus were read by 2 pediatric neuroradiologists with 15 and 5 years of experience in pediatric radiology, respectively, and a pediatric radiology fellow; all of them were blinded to the patient group category. We reviewed the following variables:

1) Inner ear: presence of vestibulocochlear and facial nerves and a lamina cribrosa between the basal turn and internal auditory canal; presence of the modiolus and interscalar septa, dysplastic vestibule, and dilated endolymphatic duct.
2) Hypothalamus: axial T2—folded appearance, abnormal cleft side, internal or external cleft, signal intensity on T2WI/T1WI/T2 FLAIR compared with the orbito-frontal cortex, presence of cystic spaces. Coronal T2: shape of the medial eminence, a low-lying ventromedial hypothalamus in relation to the medial eminence, an angle between the tip of the ventromedial hypothalamus and septum pellucidum, presence of a round lesion, craniocaudal length of the ventromedial hypothalamus tip to the forebrain. Sagittal T2/T1: midline tuber cinereum thickness, infundibular recess morphology, and mammillary body or lamina terminalis involvement.

Genetic Test Data

Genetic test results from medical records were reviewed by a clinical geneticist. The available genetic tests included chromosomal karyotypes, chromosomal microarrays (CMAs), and single-gene tests (*gap junction protein beta 2* [GJB2] gene sequencing ± *gap junction protein beta 6* [*GJB6*] gene-deletion testing, and *POU3F4* gene sequencing).

Clinical Features

Information about the presence or absence of gelastic seizures, precocious puberty, or delayed puberty at the time of the first MR imaging or during follow-up was gathered.

Statistical Methods

Quantitative data were described for each group, using mean and SD when normally distributed or median and interquartile range when not. Qualitative data were described using the number of patients and proportions. We compared measurements for the DFNX2 group with the ones in the nonaffected group. We used conditional logistic regression for qualitative measurements and a clustered linear regression for the continuous ones.

We assessed the quality and robustness of our measurements of the inner ear and hypothalamus. For this assessment, we quantified the agreement between observers' measurements and the ones taken by the 2 certified pediatric radiologists and the fellow. We used the intraclass correlation coefficient (ICC) for continuous measures and the κ index for qualitative variables. Disagreements between the readers were resolved by consensus. There were no missing data because measures were taken on the available MR imaging scans. No prospective data were analyzed.

RESULTS

Participants

There were 11 patients with image-diagnosed DFNX2 between 2006 and 2019 in our population. One patient was

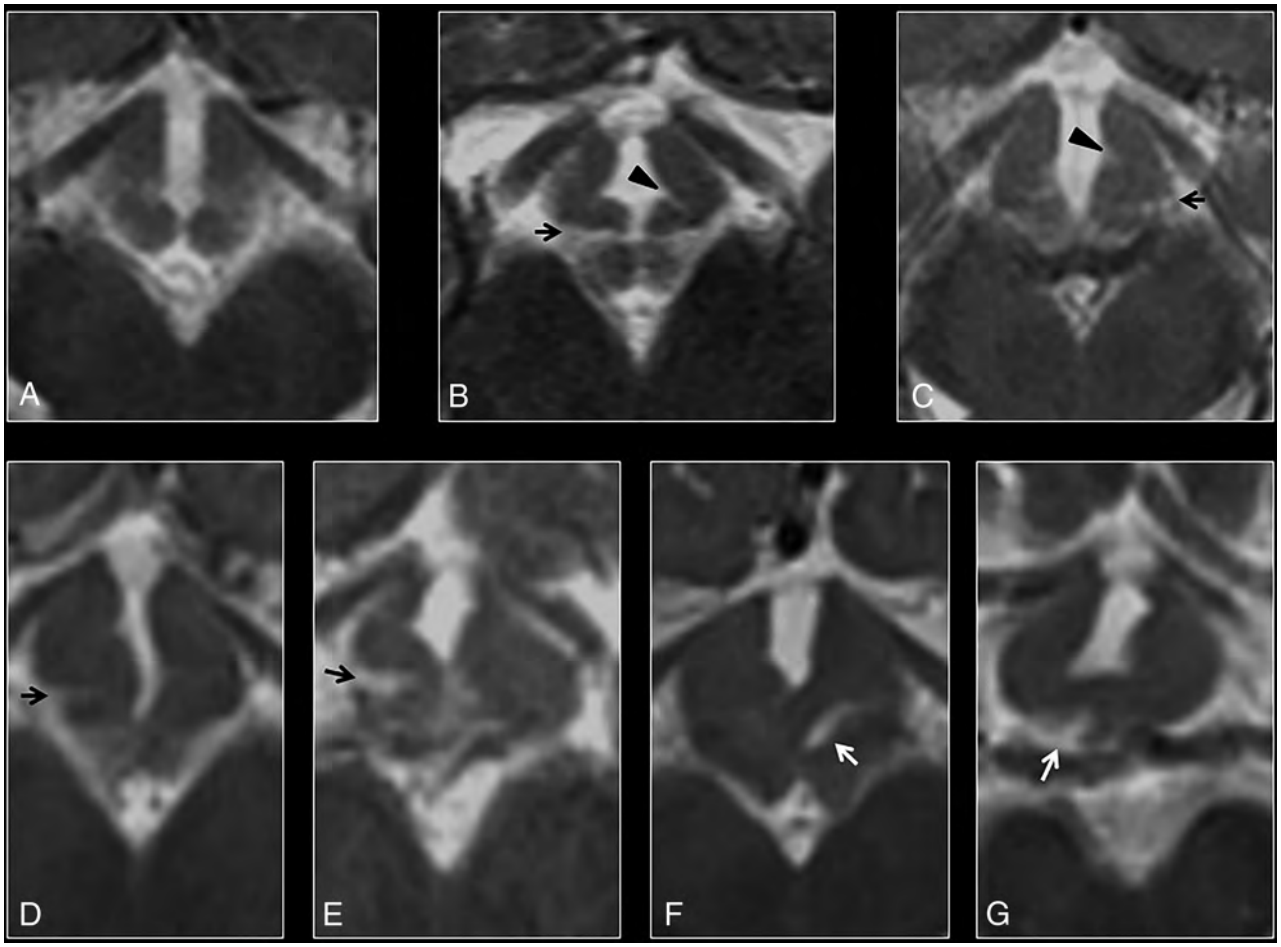

FIG 2. *A*, Axial T2 image of a normal hypothalamus at the level of the optic radiations. *B–G*, Axial T2 images of the hypothalamus in a patient with DFNX2, which demonstrate progressive folding of the ventromedial hypothalamus. Note the presence of bilateral clefts in most cases, with external clefts being more easily recognizable (*arrows*). Internal clefts are also noted on *B* and *C* (*arrowheads*).

excluded due to the lack of MR images available. The remaining 10 patients with DFNX2 were all males and had the pathognomonic temporal bone deformity (Fig 1) with absence of the lamina cribrosa between the basal turn of the cochlea and the internal auditory meatus (IAM) ($\kappa = 1$). Eight patients with DFNX2 had a dysplastic vestibule ($\kappa = 0.86$), and 6 showed a dilated endolymphatic duct ($\kappa = 0.61$). The mean age at the time of performing the first MR imaging was 78.6 months, with a median value of 22 months (range, 6–270 months).

The age-matched control group included 69 age-matched patients (younger than 10 years ± 4 months, 10–18 years ±10 months, older than 18 years + 28 years). Each patient with DFNX2 younger than 10 years of age had an age-matched control with an age difference of ±4 months. Patients with DFNX2 between 10 and 18 years of age had an age-matched control with an age difference of ±10 months. The third group of patients older than 18 years of age had age-matched controls with up to 28 years' difference. Furthermore, each patient with DFNX2 had at least 3 age-matched controls with available MR imaging of the internal auditory canal. All patients had normal labyrinth structures.

Hypothalamic Malformations on MR Imaging

DFNX2 Group versus Age-Matched Control Group

Axial T2 morphology. Morphology of the ventromedial hypothalamus was assessed at the level of the optic radiations. While none of the controls showed hypothalamic overfolding (Fig 2*A*), 7 patients with DFNX2 demonstrated a folded appearance of the ventromedial hypothalamus ($P < .001$). This hypothalamic overfolding was characterized by an abnormal external or internal cleft in the ventromedial hypothalamus in 7 patients; most (n = 6) showed bilateral abnormal clefts on axial images rather than unilateral ones (Fig 2*B–G*). All 7 patients showed external clefts compared with internal clefts (pointing toward the third ventricle), which were only present in 5 patients with DFNX2. None of the controls (67 patients) showed hypothalamic clefts ($P < .001$), and 2 controls had suboptimal axial images. The κ index ranged between 0.76 and 0.95.

Coronal T2 morphology. Six patients with DFNX2 showed concave morphology of the medial eminence in relation to the pituitary gland, with the lowest point of the ventromedial hypothalamus below the medial eminence ($\kappa = 0.78$). Two patients with DFNX2 showed convex morphology, and 2 had suboptimal images of the hypothalamus on the coronal plane (Fig 3*A–C*). None of the

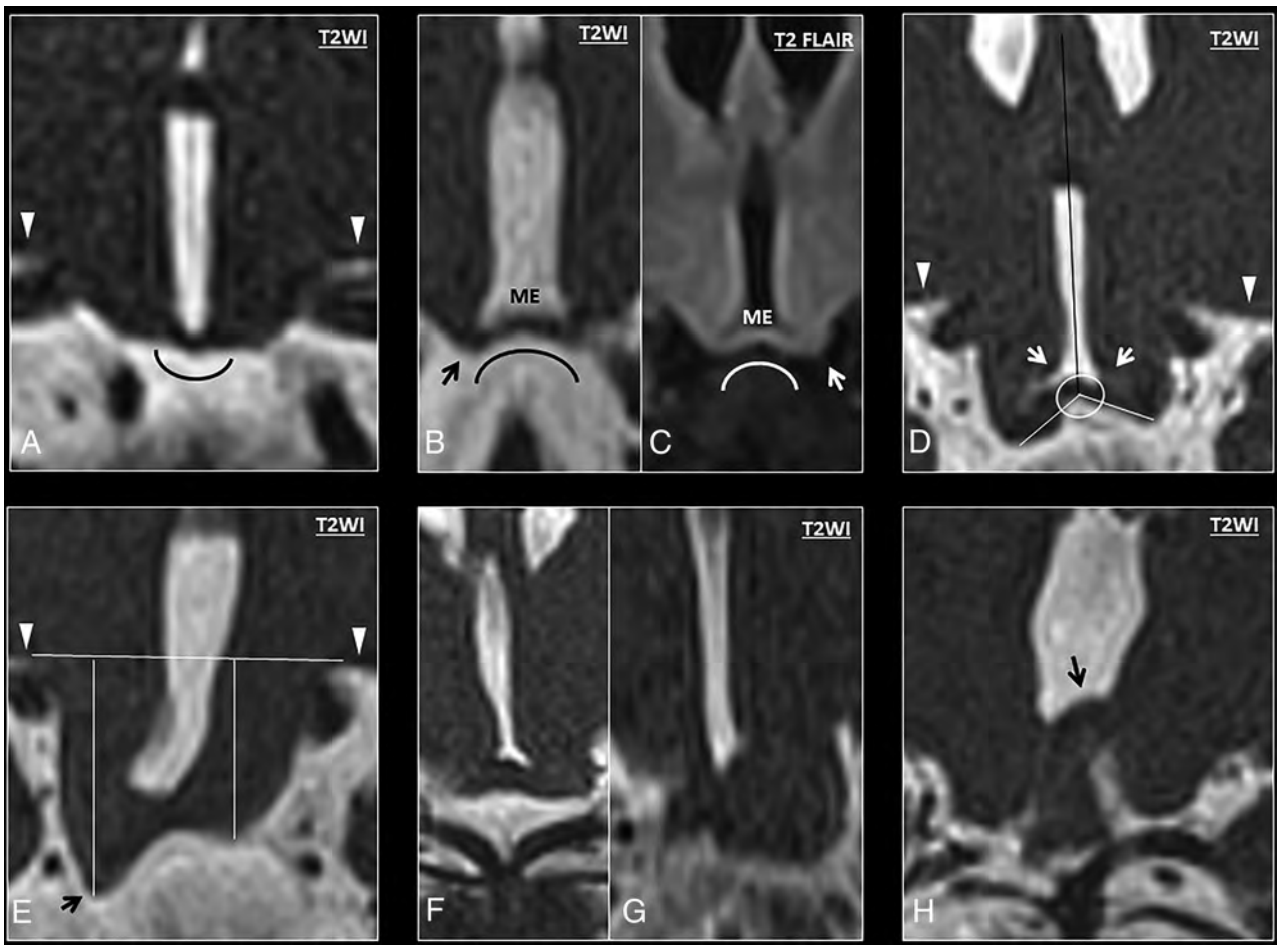

FIG 3. *A*, Coronal T2 anatomy of a normal hypothalamus showing the classic convex morphology of the medial eminence. *B–H*, High-resolution coronal T2 images show progressive bending of the ventromedial hypothalamus (from mild to severe). *B*, High-resolution coronal T2 image shows abnormal concavity at the junction between the ventromedial hypothalamus and the medial eminence, with a low-lying ventromedial hypothalamus (*black arrow*) in relation to the medial eminence (ME). These findings show an abnormal concave morphology of the hypothalamus in relation to the pituitary gland. *C*, Coronal T2 FLAIR image of another patient with DFNX2, which demonstrates isointense signal compared with the adjacent globus pallidus. Note again the characteristic bending of the ventromedial hypothalamus and its caudal location in relation to the medial eminence (*white arrow*). *D*, Measurement of the angle between the tip of the ventromedial hypothalamus and the septum pellucidum (*white arrows*). *E*, Measurement of the craniocaudal length of the ventromedial hypothalamus at the lowest point (*black arrow*) in relation to the basal forebrain (*horizontal line*). The basal forebrain (*white arrowheads*) is also indicated on images *A* and *D*. *F* and *G*, In some cases, the low-lying hypothalamus and the folding are so severe that some hypothalamic segments appear masslike, though the overall appearance is in keeping with diffuse folding. *H*, Severe hypothalamic bending in a patient with DFNX2, which shows cranial folding of the hypothalamus (*black arrow*) apart from the typical low-lying or hanging infundibular nucleus (not shown in this image).

controls showed concave medial eminence morphology ($P < .001$). To further characterize the abnormal hypothalamic concavity on the coronal plane, we measured the coronal hypothalamic–septum pellucidum angle. The first component of this angle was a straight craniocaudal line along the septum pellucidum that crossed the vertex of the concave or convex medial eminence (Fig 3*D*, black line). The second component was another straight line originating from the previously mentioned vertex of the medial eminence to the most caudal end of the ventromedial hypothalamus; the angle between these 2 lines on either side was named the right and left coronal hypothalamic–septum angle, respectively. The right coronal hypothalamic–septum angle of patients with DFNX2 measured 115.5° ± 17.34°, while it measured 79° ± 8.05° in age-matched controls ($P < .001$). The left coronal hypothalamic–septum angle of patients with DFNX2 measured 113.87° ± 16.87°, while it measured 81.87° ± 9.32° in age-matched controls ($P < .001$). The individual intraclass correlation coefficient was 0.88 and 0.77 on the right and left sides, respectively.

Another measurement was proposed to further characterize the hypothalamic concavity and low-lying ventromedial hypothalamus: the craniocaudal length between the basal forebrain and the lowest point of the ventromedial hypothalamus. The first component of this measurement was a straight line over the inferior edge of the basal forebrain (Fig 3*E*, white arrowheads), and the second component was a perpendicular line linking this line with the lowest point of the ventromedial hypothalamus on either side (Fig 3*E*, black arrow). The right forebrain-hypothalamus length in DFNX2 was 7.15 ± 3.02 mm, while it was 4.26 ± 0.7 mm in age-matched controls ($P < .001$). The left forebrain-hypothalamus length in DFNX2 measured 6.9 ± 2.1 mm, while it was 4.21 ± 0.73 mm in controls ($P < .001$). The individual intraclass correlation coefficient was 0.92 and 0.87 on the right and left sides, respectively.

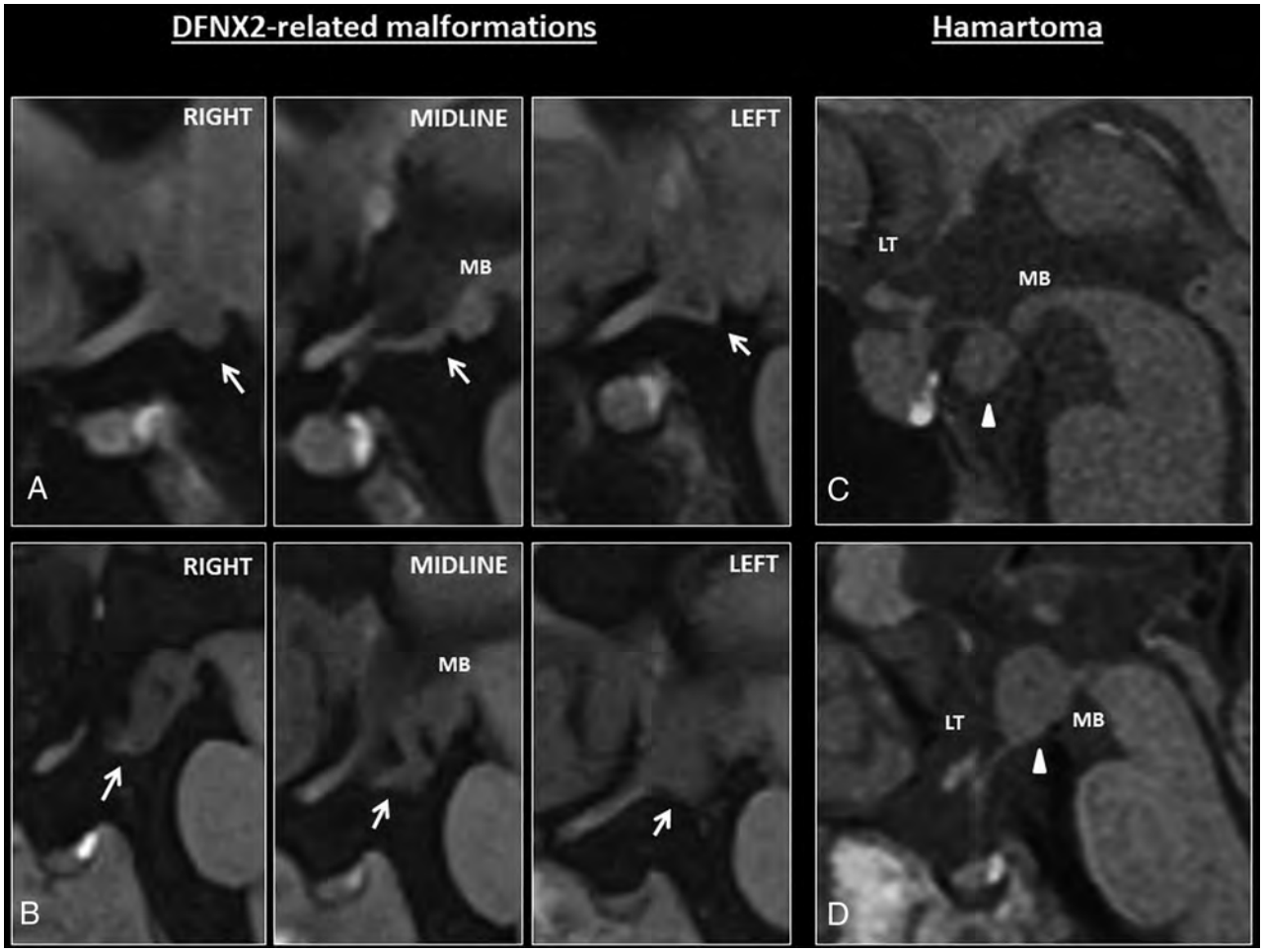

FIG 4. *A*, Sagittal T1 images show mild hypothalamic folding in a patient with DFNX2 (*white arrows*). This is usually apparent on one of the sagittal slices, such as the left/right one on these series; however, coronal images are better to depict subtle hypothalamic folding. Note the T1-isointense signal of the hypothalamic folding. *B*, The folding is apparent on all the sagittal images through the hypothalamus. Note again the T1-isointense signal compared with the adjacent brain parenchyma. *C–D*, Hypothalamic hamartomas tend to be masslike rather than cause hypothalamic folding. They usually arise from the tuber cinereum protruding caudally toward the suprasellar cistern or grow within the third ventricle (*white arrowheads*) and tend to involve adjacent structures such as the mamillary bodies. MB indicates mamillary bodies; LT, lamina terminalis.

Sagittal T1/T2 morphology. None of DFNX2 hypothalamic malformations showed infundibular, mammillary body, or lamina terminalis involvement (Fig 4*A*, *-B*).

Signal intensity. The hypothalamic overfolding was isointense on T2 FLAIR in all patients with available T2 FLAIR sequences ($P = .44$), isointense on T2 compared with the adjacent orbitofrontal cortex in all cases, and isointense on T1. The κ index ranged between 0.72 and 0.82. Only 3 patients had available magnetic susceptibility sequences, none showed blooming artifacts, and only 1 was administered contrast, without identifying contrast enhancement.

Incidental findings in patients with DFNX2: Two patients with DFNX2 had a retrocerebellar cyst, 2 had a Meckel cave cyst, 2 had temporal arachnoid cysts, another patient had a cavum septum vergae, and 1 had a cavum velum interpositum.

Proposed MR Imaging Features of Hypothalamic Malformation in DFNX2

On axial T2 images. The folded appearance of the ventromedial hypothalamus (sensitivity [SE], 100%; specificity [SP], 95.8%) characterized by an abnormal internal/external cleft (SE 100% SP 95.7%) showed high specificity and sensitivity as well as interobserver agreement for patients with DFNX2 (Fig 2).

On coronal T2 images. A concave morphology of the medial eminence in relation to the pituitary gland with the lowest point of the ventromedial hypothalamus below the medial eminence (Fig 3) also showed high specificity and sensitivity (SE, 100%; SP, 97.1%). Furthermore, 2 measurements could help distinguish DFNX2 hypothalamic malformations from features in healthy patients: at least 1 hypothalamic-septum angle of $\geq 90°$ (SE, 90%; SP, 72.5%) as well as 1 forebrain-hypothalamic craniocaudal length of ≥ 6 mm (SE 70%; SP 79.7%). The presence of at least 3 abnormal variables was sufficient to rule out a normal hypothalamus (Table).

Clinical Results

There was no clinical history of gelastic seizures or precocious puberty in 9 patients with DFNX2. One patient had delayed puberty, and no clinical information was available for 1 patient.

Proposed MR imaging features of hypothalamic malformations in patients with DFNX2 compared with age-matched controls[a]

	Patients with DFNX2 ($n = 10$)	Age-Matched Controls ($n = 69$)
Axial T2		
Folded appearance	70% ($P < .001$; $\kappa = 0.95$)	0%
Bilateral abnormal internal or external cleft	60% ($P < .001$; $\kappa = 0.83$)	0%
Coronal T2		
Concave medial eminence	75% ($P < .001$; $\kappa = 0.78$)	0%
Right hypothalamic-septum angle	115.5° ± 17.34° ($P < .001$) ICC = 0.88 (95% CI, 0.75–0.95)	79° ± 8.05°
Left hypothalamic-septum angle	113.87° ± 16.87° ($P < .001$) ICC = 0.77 (95% CI, 0.58–0.89)	81.87° ± 9.32°
Right forebrain-hypothalamus length (mm)	7.15 ± 3.02 ($P < .001$) ICC = 0.92 (95% CI, 0.70–0.97)	4.26 ± 0.7
Left forebrain-hypothalamus length (mm)	6.9 ± 2.1 ($P < .001$) ICC = 0.87 (95% CI, 0.70–0.95)	4.21 ± 0.73

Note:—κ indicates the Cohen κ coefficient.

[a] Data are mean values ± standard deviation. *P* values correspond to Wilcoxon/Mann-Withney test for differences in means of DFNX2 versus age-matched controls.

Genetic Test Results. Eight of 10 patients with DFNX2 had some genetic testing recorded. Two patients (brothers) had a *POU3F4* gene mutation (X:82763940:AAAG>A, NM_000307.4:c.614_616delGAA, p.Arg205del) detected by targeted sequencing. One also had a CMA-detected duplication variant of unknown significance in 14q24.3, considered clinically insignificant. Two other patients (brothers) had a CMA-detected Xq21.1 deletion ~600 to ~1700 Kilobase (kb) upstream of *POU3F4,* considered causative because deletions located ~10 to ~970 kb upstream of *POU3F4* are reported in some patients with DFNX2, suggesting that they contain regulatory elements of the structural gene itself.[14] All 4 patients had normal sequencing of *GJB2*. Four additional patients had *GJB2* sequencing ± *GJB6* deletion testing, with normal findings. One of a pair of brothers had a CMA-detected 1q21.1–1q21.2a duplication variant, involving a known neurodevelopmental susceptibility locus, not known to be associated with hearing loss; this was not present in his brother. The 2 others did not have CMA testing, but 1 had a normal karyotype. The last 2 patients had not undergone any genetic testing. Thus, of the 6 patients not yet confirmed by genetic testing, 4 have not yet had CMA testing and none have had *POU3F4* sequencing. The lack of genetic confirmation was a limitation in our study, though all patients without genetic confirmation presented with the pathognomonic temporal bone deformity described in DFNX2.

DISCUSSION

Hypothalamic malformations in our patients with DFNX2 demonstrate the aforementioned folded appearance on axial images and concave morphology on coronal images without signal abnormalities. To date, there are 2 case reports and 1 case series in the literature describing hypothalamic malformations or hamartomatous-like lesions in patients with DFNX2. Whitehead et al[15] described a ventrolateral tuber cinereum diverticulum associated with other midline abnormalities in a patient with Xq21 deletion involving the *POU3F4* gene. Anderson et al[16] described a 4-year-old boy with sensorineural hearing loss, autism, and a hypothalamic mass just anterior to the mammillary bodies that was isointense on both T1- and T2-weighted sequences, without restricted diffusion, susceptibility artifacts, or enhancement, which was labeled as an asymptomatic hypothalamic hamartoma. No hormonal disturbance was identified before 10 years of age. Whole-exome sequencing revealed a mutation of the *POU3F4* gene (p.G216E, hemizygous). Siddiqui et al[17] reported a series of 12 patients with DFNX2 and mild-to-severe but characteristic dysmorphism of the hypothalamus. These malformations ranged from a thickened and irregular hypothalamus to hamartoma-like hypothalamic enlargement. They were isointense to gray matter on T1WI and iso- or slightly hyperintense on T2WI and showed no contrast enhancement. None of the patients had seizures or endocrinologic abnormalities.

The possible mechanism linking the pathognomonic inner ear deformity and hypothalamic malformations was described by Andersen and Rosenfeld,[18] who stated that a DNA transcription factor involved in the development of the nervous system, hypothalamus, pituitary gland, and inner ears was encoded by *POU3F4*. This gene also plays a role in the formation of hypothalamic nuclei and regulation of the proglucagon promoter.

Our case series is the second largest available and the largest case series from a single institution. Our clinical results confirm the association described by Siddiqui et al[17] between DFNX2 and hypothalamic malformations. Moreover, we pinpoint specific MR imaging features and measurements that could help further describe these malformations to identify subtle malformations that could otherwise be overlooked. Our proposed features and measurements to describe DFNX2-related hypothalamic malformations are as follows: On axial T2 images, the folded appearance of the ventromedial hypothalamus is characterized by an abnormal cleft (predominantly external and bilateral). On coronal T2 images, the first distinctive feature would be a concave morphology of the medial eminence in relation to the pituitary gland, the second feature would include at least 1 hypothalamic-septum angle above 90°, and the third feature would consist of at least 1 forebrain-hypothalamic craniocaudal length above 6 mm. On sagittal T1 images, the lack of infundibular, mamillary body, or lamina terminalis involvement could be helpful because it was not identified in any DFNX2 case. Furthermore, our population of patients with DFNX2 also appeared to show variable cystic dilations of subarachnoid spaces (retrocerebellar cysts, Meckel cave cysts, and temporal arachnoid cysts). The presence of these cystic dilations might be associated with a broad spectrum of hypothalamic anomalies because

arachnoid cysts have also been described in patients with hypothalamic hamartoma by Booth et al.[19]

Clinically, none of patients with DFNX2 with available clinical information ($n = 9$) presented with gelastic seizures or precocious puberty, while patients with hypothalamic hamartomas usually present with gelastic seizures, precocious puberty, or both.[20] One of our cohort had delayed puberty without any evidence of hormonal disturbance, and his brother was lost to follow-up. The remaining patients are prepubescent; therefore, clinical follow-up to assess for pubertal delay may be helpful.

Limitations

There were 3 main limitations to our study: First, the small number of patients affected by this rare pathology; and second, the presence of 3 pairs of brothers in our sample. Third, although all had the DFNX2 clinical phenotype, only 4 of our patients (2 pairs of brothers) have had confirmatory genetic testing. Of the other 6 patients, 4 have not yet had a CMA and none have had *POU3F4* sequencing.

CONCLUSIONS

MR imaging and clinical features of the hypothalamus in patients with DFNX2 suggest that there is a hypothalamic malformation associated with DFNX2 that does not behave clinically like a typical hypothalamic hamartoma. We expect our research to help differentiate DFNX2-related hypothalamic malformations and their clinical behavior from a normal hypothalamus and classic hypothalamic hamartoma because DFNX2-related hypothalamic malformations may be misinterpreted as a neoplasm or hamartoma and therefore lead to unnecessary further investigations. Early assessment for pubertal delay is proposed.

Disclosures: Catherine Birman—*UNRELATED*: *Board Membership*: The Royal Institute for Deaf and Blind Children (RIDBC), *Comments*: only on an unpaid board; *Payment for Lectures Including Service on Speakers Bureaus*: lectures for Cochlear Investments Pty Ltd; *Travel/Accommodations/Meeting Expenses Unrelated to Activities Listed*: for some conferences supported by Cochlear Investments Pty Ltd or MED-EL, *Comments*: support for attendance at some conferences such as accommodations or registration or travel if an invited speaker.* *Money paid to the institution.

REFERENCES

1. Bitner-Glindzicz M, Turnpenny P, Höglund P, et al. **Further mutations in Brain 4 (pou3f4) clarify the phenotype in the x-linked deafness, dfn3.** *Hum Mol Genet* 1995;4:1467–69 CrossRef Medline
2. Nance WE, Setleff R, McLeod A, et al. **X-linked mixed deafness with congenital fixation of the stapedial footplate and perilymphatic gusher.** *Birth Defects Orig Artic Ser* 1971;07:64–69 Medline
3. Sennaroğlu L, Bajin MD. **Incomplete partition type III: a rare and difficult cochlear implant surgical indication.** *Auris Nasus Larynx* 2018;45:26–32 CrossRef Medline
4. Phelps PD, Reardon W, Pembrey M, et al. **X-linked deafness, stapes gushers and a distinctive defect of the inner ear.** *Neuroradiology* 1991;33:326–30 CrossRef Medline
5. Talbot JM, Wilson DF. **Computed tomographic diagnosis of X-linked congenital mixed deafness, fixation of the stapedial footplate, and perilymphatic gusher.** *Am J Otol* 1994;15:177–82 Medline
6. Huang BY, Zdanski C, Castillo M. **Pediatric sensorineural hearing loss, Part 1: practical aspects for neuroradiologists.** *AJNR Am J Neuroradiol* 2012;33:211–17 CrossRef Medline
7. Sennaroglu L, Saatci I. **A new classification for cochleovestibular malformations.** *Laryngoscope* 2002;112:2230–41 CrossRef Medline
8. Huang BY, Zdanski C, Castillo M. **Pediatric sensorineural hearing loss, Part 2: syndromic and acquired causes.** *AJNR Am J Neuroradiol* 2012;33:399–406 CrossRef Medline
9. Özbal Batuk M, Çınar BÇ, Özgen B, et al. **Audiological and radiological characteristics in incomplete partition malformations.** *Int Adv Otol* 2017;13:233–38 CrossRef Medline
10. Pembrey M, Ropers H, Monaco A, et al. **Association between X-linked mixed deafness and mutations in the POU domain gene POU3F4.** *Science* 1995;267:685–88 CrossRef Medline
11. Lee H, Choi J, Kim S, et al. **Clinical evaluation of DFN3 patients with deletions in the POU3F4 locus and detection of carrier female using MLPA.** *Clin Genet* 2010;78:524–32 CrossRef Medline
12. Haaf T, Hofrichter MA, Vona B, et al. **Non-syndromic hearing loss gene identification: A brief history and glimpse into the future.** *Mol Cell Probes* 2015;29:260–70 CrossRef Medline
13. Baroncini M, Jissendi P, Balland E, et al. **MRI atlas of the human hypothalamus.** *Neuroimage* 2012;59:168–80 CrossRef Medline
14. Naranjo S, Voesenek K, de la Calle-Mustienes E, et al. **Multiple enhancers located in a 1-Mb region upstream of POU3F4 promote expression during inner ear development and may be required for hearing.** *Hum Genet* 2010;128:411–19 CrossRef Medline
15. Whitehead MT, Vezina G. **Tuber cinereum diverticula in a 28-month-old with Xq21 deletion syndrome.** *Case Rep Radiol* 2014;2014:1–4 CrossRef
16. Anderson EA, Özütemiz C, Miller BS, et al. **Hypothalamic hamartomas and inner ear diverticula with X-linked stapes gusher syndrome: new associations?** *Pediatr Radiol* 2020;50:142–45 CrossRef Medline
17. Siddiqui A, D'Amico A, Colafati GS, et al. **Hypothalamic malformations in patients with X-linked deafness and incomplete partition type 3.** *Neuroradiology* 2019;61:949–52 CrossRef Medline
18. Andersen B, Rosenfeld MG. **POU domain factors in the neuroendocrine system: lessons from developmental biology provide insights into human disease.** *Endocr Rev* 2001;22:2–35 CrossRef Medline
19. Booth TN, Timmons C, Shapiro K, et al. **Pre- and postnatal MR imaging of hypothalamic hamartomas associated with arachnoid cysts.** *AJNR Am J Neuroradiol* 2004;25:1283–85 Medline
20. Harrison VS, Oatman O, Kerrigan JF. **Hypothalamic hamartoma with epilepsy: review of endocrine comorbidity.** *Epilepsia* 2017;58: (Suppl 2):50–59 CrossRef

New MRI Findings in Fukuyama Congenital Muscular Dystrophy: Brain Stem and Venous System Anomalies

A. Hirasawa-Inoue, N. Sato, Y. Shigemoto, Y. Kimura, A. Ishiyama, E. Takeshita, M. Mori-Yoshimura, Y. Oya, Y. Takahashi, H. Komaki, H. Matsuda, and M. Sasaki

ABSTRACT

BACKGROUND AND PURPOSE: Leptomeningeal glioneuronal heterotopia of the brain stem and cerebral migration abnormality were pathologically reported in Fukuyama congenital muscular dystrophy, but the radiologic assessments of the brain stem and cerebral venous system (which may be involved in the development of the anomaly) were insufficient. Here, we evaluated the brain stem and cerebral veins on MR imaging in patients with Fukuyama congenital muscular dystrophy.

MATERIALS AND METHODS: We retrospectively reviewed the MR imaging findings of 27 patients with Fukuyama congenital muscular dystrophy. We visually assessed the hypoplasia, superficial structures, and signal intensity of the brain stem on T2WI, FLAIR, and double inversion recovery images and the cerebral, superficial, and deep veins with and without hemorrhage on T2WI and SWI.

RESULTS: Brain stem fluffy structures were seen in 96.3% of the cases on T2WI. Superficial high signal intensity on T2WI and FLAIR images was seen in 96.3% and 92.6%, respectively. Abnormally located superficial vessels beneath the cortex were seen in 11.1% on T2WI. Hypoplasia of the superficial cerebral veins was noted in all patients who underwent SWI. Dilated and tortuous subependymal veins were seen in 40.0% on SWI. Hemorrhages were seen in 11.1% on T2WI and in 60.0% on SWI.

CONCLUSIONS: Superficial brain stem structural and signal abnormalities would be useful MR imaging findings to diagnose Fukuyama congenital muscular dystrophy as well as venous system abnormalities. Clinicians must keep in mind that this disease has a high risk of hemorrhage.

ABBREVIATIONS: DIR = double inversion recovery; FCMD = Fukuyama congenital muscular dystrophy

Patients with Fukuyama congenital muscular dystrophy (FCMD) have generalized muscle weakness, hypotonia, and developmental delay beginning in early infancy. Characteristic brain MR imaging findings and high serum creatine kinase levels facilitate a clinical diagnosis of FCMD. The characteristics of FCMD as shown by brain MR imaging are cortical dysplasia (polymicrogyria or pachygyria), cerebellar cysts, cerebellar cortical dysplasia, white matter abnormality, and brain stem hypoplasia.[1-3]

We recently noticed that many cases of FCMD showed abnormal signals along the brain stem surface on T2WI and FLAIR images. Pathologic studies disclosed leptomeningeal glioneuronal heterotopia, abnormal courses of the corticospinal tracts, and neuronal loss and degeneration in the brain stem.[4,5] However, radiologic assessments of the brain stem have not been published, and we have treated patients with FCMD who showed cerebral vascular abnormalities in both deep and superficial vessels with and without hemorrhage on T2WI or SWI. Cortical dysplasia is known to be caused by an overmigration of neurons into the subarachnoid space through breaches in the glia limitans,[6] and abnormal changes of the vascular endothelial cells have been observed in biopsied muscle samples.[7,8] Abnormal vessels running beneath the cerebral cortex of patients with FCMD were observed on T2WI.[1] To the best of our knowledge, there is no published report of the venous system anomalies or hemorrhages in FCMD that are most detectable by SWI. We conducted the present study to evaluate brain MR imaging findings in patients with FCMD, including the findings of the brain stem and cerebral venous system.

Received January 6, 2020; accepted after revision April 3.

From the Departments of Child Neurology (A.H.-I., A.I., E.T., H.K., M.S.), Radiology (N.S., Y.S., Y.K.), and Neurology (M.M.-Y., Y.O., Y.T.), National Center Hospital, Translational Medical Center (H.K.), and Integrative Brain Imaging Center (H.M.), National Center of Neurology and Psychiatry, Tokyo, Japan.

Please address correspondence to Noriko Sato, MD, PhD, Department of Radiology, National Center Hospital, National Center of Neurology and Psychiatry, 4-1-1 Ogawahigashi-cho, Kodaira-shi, Tokyo, Japan; e-mail: snoriko@ncnp.go.jp

Indicates article with supplemental on-line table.

http://dx.doi.org/10.3174/ajnr.A6577

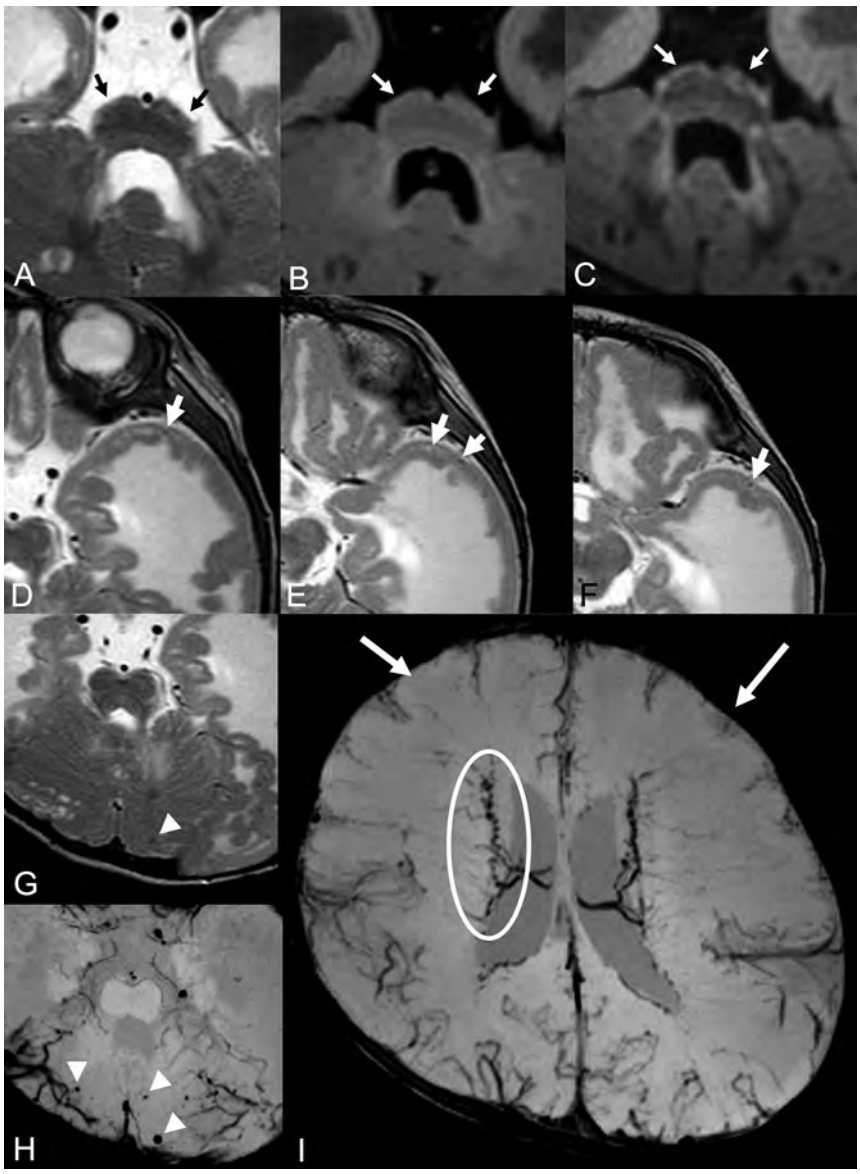

FIG 1. Brain MR imaging of patient 15. Brain stem images on T2WI (*A*), FLAIR (*B*), and DIR (*C*). There is a fluffy structure on T2WI (*A*, *black arrows*) and high intensity of the hypoplastic pontine surface on the FLAIR image (*B*, *white arrows*). High signal intensity along the brain stem surface on the DIR image is recognized more clearly than on the T2WI or FLAIR image (*C*, *white arrows*). T2WIs of the left temporal lobe (*D–F*) show lissencephalic and the abnormally located cortical superficial vessels running through the superficial layer of the lissencephalic cortex (*white arrows*). Microhemorrhages were seen in the cerebellar cyst on T2WI (*G*) and SWI (*H*). More microhemorrhages are recognizable on the SWI than on T2WI (*white arrowheads*). Cerebral SWI (*I*) shows hypoplasia of a superficial cerebral vein in both frontal lobes (*white arrows*) and dilated and tortuous subependymal veins (*white circle*).

MATERIALS AND METHODS

We retrospectively reviewed the MR imaging findings of the 53 patients who were clinically and genetically diagnosed with FCMD at our hospital from 2006 through 2018. We excluded 26 patients who did not have both axial T2WI and FLAIR images as brain MR imaging because axial T2WI and FLAIR images are required for the evaluation of the brain stem. We examined a final total of 27 patients: 17 males and 10 females (age range, 5 months to 23 years; median, 18 months; mean, 6 years). Axial 2D- or 3D-T1WI, axial T2WI, and FLAIR images were obtained for all 27 patients. Six patients also had 3D double inversion recovery (DIR) images, and 5 patients had SWI findings. This retrospective study was approved by the institutional review board of our hospital, and the need for patient informed consent was waived.

We evaluated the presence/absence of brain stem hypoplasia (ie, a small and flattened ventral portion at the level of the middle cerebellar peduncle, a fluffy brain stem surface on T2WI, and high signals of the brain stem surface on T2WI, FLAIR, and DIR images). We also evaluated the presence or absence of abnormal vessels running just beneath the cortical surface on T2WI, hemorrhage on T2WI and SWI, and whether the cerebral superficial and deep veins are hypoplastic or dilated on SWI. We assessed other MR imaging findings: cerebellar cysts, cerebral cortical dysplasia (polymicrogyria or pachygyria), and white matter abnormal high signals (patchy/spotty or diffuse) on T1WI, T2WI, and FLAIR images. Two neuroradiologists (Y.K. and N.S. with 14 and 30 years of experience in neuroradiology, respectively) independently evaluated all images. The differences were resolved by consensus.

RESULTS

The clinical and MR imaging findings for all 27 patients are summarized in the On-line Table. All patients showed brain stem hypoplasia (Figs 1 and 2). We observed a fluffy brain stem surface and mild high signal intensity along the surface of a hypoplastic pons on T2WI in 26 patients (96.3%) and FLAIR images in 25 patients (92.6%) (Figs 1*A*, -*B* and 2*A*, -*B*). The DIR images of all 6 patients showed high signal intensity along the brain stem surface (Fig 1*C*), and the high signal intensity was recognized more clearly on the DIR images than on the T2WI and FLAIR images.

Abnormally located superficial vessels beneath the cortex were observed in 3 patients (11.1%). The vessels ran through, inside, or beneath the lissencephalic cortex, and they were recognizable especially in the temporal lobes (Figs 1*D–F* and 2*C–E*). Hypoplasia of superficial cerebral veins around the frontal lobes was noted in all 5 patients who had SWI findings (Figs 1*I* and 3*C*, -*D*). Dilated and tortuous subependymal veins were identified in 2 of these 5 patients (40.0%) on SWI (Figs 1*I* and 3*C*, -*D*).

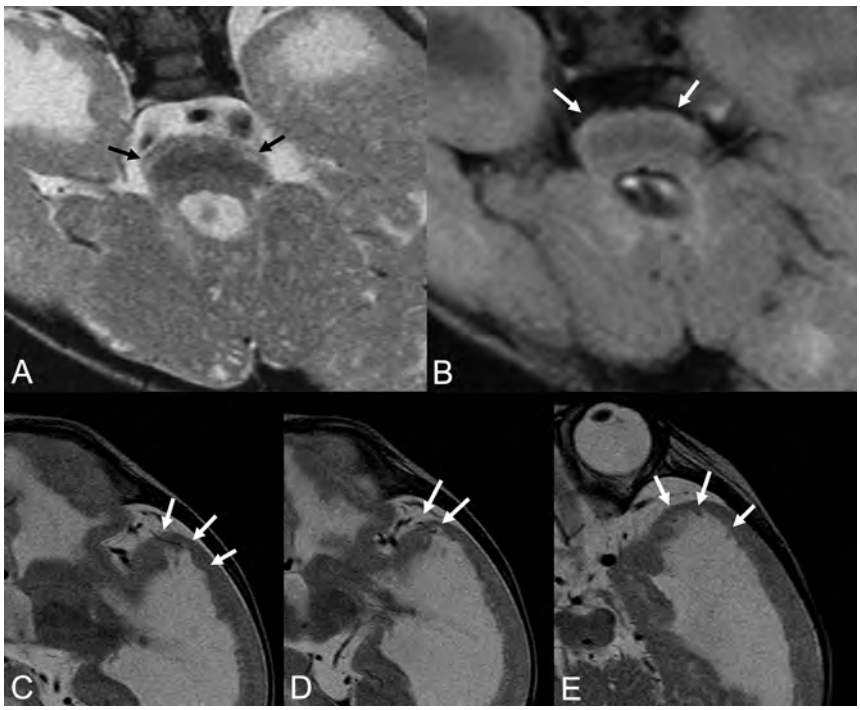

FIG 2. Brain stem (*A* and *B*) and left temporal (*C–E*) MRIs of patient 20. A brain stem T2WI (*A*) shows a fluffy structure and high intensity of the hypoplastic pontine surface (*black arrows*). The FLAIR image (*B*) detects high intensity of the pontine surface (*white arrows*). Left temporal T2WIs (*C–E*) show lissencephaly, which contains abnormally located superficial cortical vessels running through and beneath the cortex (*white arrows*).

Hemorrhages were detected on T2WI in 3 of the 27 patients (11.1%) and on SWI in 3 of the 5 patients (60.0%). Patient 7 showed microhemorrhages in the cerebral and cerebellar cysts on SWI. Numerous microhemorrhages were seen in the cerebellar cysts in patient 15 on T2WI and SWI (Fig 1*G*, *-H*). Patient 23 exhibited a hemorrhage in the white matter around the occipital horn of the left lateral ventricle on T2WI and SWI. Patient 25 showed a hemorrhage in the white matter of the frontal lobe on T2WI (Fig 4).

All 27 patients had a degree of cerebral dysplasia; the degrees varied among the patients. Polymicrogyria was recognized in all 27 patients. The frontal lobe was involved in all patients, and the temporoparietal lobes were affected in some patients. Pachygyria that involved mainly the temporo-occipital lobes was also seen in 4 patients. All 27 patients had T1 low signal and T2 high signal in the white matter (Figs 1, 2, and 4). The signal extent varied among the patients. Cerebellar intraparenchymal cysts located in the peripheral hemispheres were identified in 26 patients.

DISCUSSION

We assessed the brain stem and cerebral venal abnormalities and hemorrhage in patients with FCMD on brain MR imaging, including DIR and SWI. Fluffy structures around the pons and high signal intensity along the surface of hypoplastic pons were confirmed in 96.3% of the patients on T2WI. On SWI, hypoplasia of superficial cerebral veins around the frontal lobes was noted in all patients, and dilated and tortuous subependymal veins were seen in 40.0%. Hemorrhages were seen in 11.1% on T2WI and 60% on SWI. Thus, the identification of brain stem marginal abnormal findings and venous system anomalies could help diagnose FCMD. Our findings also indicate that FCMD presents a high risk of hemorrhage as a complication.

Cerebral cortical developmental abnormalities are well-known in FCMD. Cortical dysplasia is caused by the overmigration of neurons into the subarachnoid space through breaches in the glia limitans.[6] FCMD belongs to a group of α-dystroglycanopathies; α-dystroglycan is important for normal basement membrane formation and neuronal migration. It was suggested that a dystroglycan-null brain loses its high-affinity binding to the extracellular matrix protein laminin and shows discontinuities in the pial surface basal lamina.[9] In addition, a *FKTN* gene defect may result in functional disruption through the hypoglycosylation of both neuronal and glial α-dystroglycan.[10]

Similar pathology is observed in the brain stem as well as the cerebral cortex in FCMD. Leptomeningeal glioneuronal heterotopia and an aberrant pyramidal tract in the brain stem of patients with FCMD have been described.[11] In another study, the cases of FCMD had a band of gliotic tissue along the surface of the brain stem, and this made the glia limitans thicker than in healthy control subjects. Pontine nuclei exhibiting some neuronal clusters that protruded into the subarachnoid space at the ventrolateral pontine surface were also observed; this parenchymal protrusion extended ventromedially, tangential to the pontine surface.[5] We speculate that the fluffy structures and high signal intensity along the brain stem surface on T2WI, FLAIR, and DIR images reflect leptomeningeal glioneuronal heterotopia, a thick glia limitans, or an extrapial protrusion of glial tissue.

DIR images suppress signals from both white matter and CSF and may enhance visualization of abnormal features at the gray-white matter interface; then, we could see brain stem abnormality more clearly.

We also observed both abnormally located cortical superficial vessels running through, inside, or beneath the lissencephalic cortex and hypoplasia of superficial cerebral veins around the frontal lobes. Abnormal vessels running beneath the cerebral cortex on T2WI were reported,[1] and it was confirmed pathologically that there were many small vessels that entered the cortex through the breaches in the glia limitans.[6] However, the dilated and tortuous subependymal veins revealed in the present study had not been reported previously. Hypoplasia of superficial cerebral veins around frontal lobes would be a secondary consequence of overmigration. As a result, a subependymal vein may be dilated.

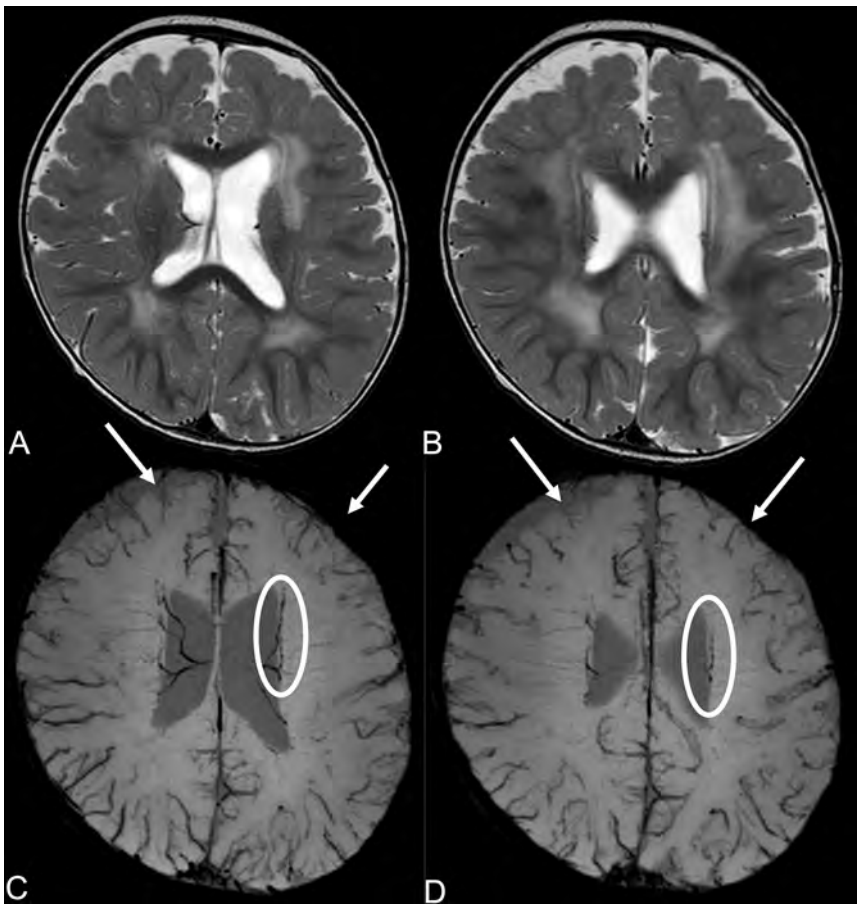

FIG 3. Cerebral MRIs of patient 13. T2WIs (*A* and *B*) show polymicrogyria and diffuse high signal in the white matter. SWIs (*C* and *D*) reveal hypoplasia of superficial cerebral veins in the frontal lobe (*white arrows*) and meandering subependymal veins (*white circles*).

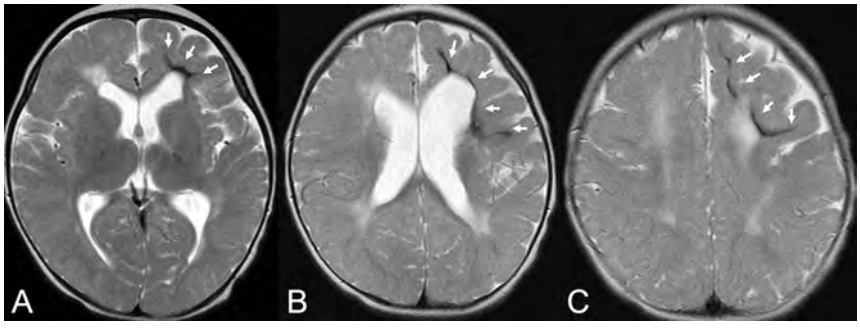

FIG 4. Cerebral MRIs of patient 25. There are hemorrhages in the deep and subcortical white matter of the atrophic left frontal lobe (*white arrows*) on T2WIs. The location of the hemorrhage in this patient is different from that of the subependymal hemorrhage in a premature neonate.

On the other hand, it is possible that venous abnormalities can be a primary result of a dysfunction of α-dystroglycan. In a muscle pathology study of patients with FCMD, vascular changes, including replication of the basement membrane, blister-like swelling of endothelial cells, and platelet adhesion and aggregation on small blood vessels, were observed.[8] It was reported that dystroglycan was expressed in vascular endothelial cells in the human brain and that endothelial dystroglycan plays a role in angiogenesis.[12,13] In addition, intersegmental vessels and distorted eye vasculature were seen in a *FKTN* morphant. It is suspected that the disruption of angiogenesis was a primary result caused directly by the knockdown of *FKTN* and dystroglycan.[7] We speculated that not only would hypoplasia of superficial cerebral veins result in the enlargement of subependymal veins but vulnerable brain vessels would also be related to dilated subependymal veins.

Hemorrhages can occur as a result of the vulnerability of brain vessels and congestion due to hypoplasia of superficial cerebral veins. Assessment of brain vessel abnormalities and the presence/absence of hemorrhage will contribute to the management of patients with FCMD.

There are a few limitations to this study. Although an earlier study indicated a relationship between motor function and brain stem abnormality,[14] we were not able to evaluate the relationship between the maximum motor function and brain stem dysplasia or venous abnormalities in our patient series because some of the 27 patients came to our hospital only for the diagnosis and we could not follow them to the age at which they reached the maximum motor function. In addition, there were only 5 patients who had SWI findings, and SWI is the most suitable sequence to precisely assess the presence and severity of vessel anomalies and hemorrhages. Evaluations of SWI of patients with FCMD would provide more information.

CONCLUSIONS

The results of our retrospective analyses of the imaging of 27 patients with FCMD demonstrated the fluffy structure around the pons and high signal intensity along the surface of a hypoplastic brain stem on T2WI/FLAIR/DIR images. These findings can be useful in the diagnosis of FCMD. Hemorrhage and abnormalities of cerebral superficial and subependymal veins were also highly meaningful MR imaging findings. Clinicians must keep in mind that patients with FCMD are at risk of incurring a hemorrhage, and follow-up MR imaging would be useful to manage these patients.

REFERENCES

1. Aida N, Tamagawa K, Takada K, et al. **Brain MR in Fukuyama congenital muscular dystrophy.** *AJNR Am J Neuroradiol* 1996;17:605–13 Medline
2. Aida N. **Fukuyama congenital muscular dystrophy: a neuroradiologic review.** *J Magn Reson Imaging* 1998;8:317–26 CrossRef Medline
3. Clement E, Mercuri E, Godfrey C, et al. **Brain involvement in muscular dystrophies with defective dystroglycan glycosylation.** *Ann Neurol* 2008;64:573–82 CrossRef Medline
4. Itoh M, Houdou S, Kawahara H, et al. **Morphological study of the brainstem in Fukuyama type congenital muscular dystrophy.** *Pediatr Neurol* 1996;15:327–31 CrossRef Medline
5. Saito Y, Kobayashi M, Itoh M, et al. **Aberrant neuronal migration in the brainstem of Fukuyama-type congenital muscular dystrophy.** *J Neuropathol Exp Neurol* 2003;62:497–508 CrossRef Medline
6. Nakano I, Funahashi M, Takada K, et al. **Are breaches in the glia limitans the primary cause of the micropolygyria in Fukuyama-type congenital muscular dystrophy (FCMD)? Pathological study of the cerebral cortex of an FCMD fetus.** *Acta Neuropathol* 1996; 91:313–21 CrossRef Medline
7. Wood AJ, Muller JS, Jepson CD, et al. **Abnormal vascular development in zebrafish models for fukutin and FKRP deficiency.** *Hum Mol Genet* 2011;20:4879–90 CrossRef Medline
8. Sugino S, Miyatake M, Ohtani Y, et al. **Vascular alterations in Fukuyama type congenital muscular dystrophy.** *Brain Dev* 1991; 13:77–81 CrossRef Medline
9. Moore SA, Saito F, Chen J, et al. **Deletion of brain dystroglycan recapitulates aspects of congenital muscular dystrophy.** *Nature* 2002;418:422–25 CrossRef Medline
10. Saito Y, Yamamoto T, Mizuguchi M, et al. **Altered glycosylation of alpha-dystroglycan in neurons of Fukuyama congenital muscular dystrophy brains.** *Brain Res* 2006;1075:223–28 CrossRef Medline
11. Fukuyama Y, Osawa M, Suzuki H. **Congenital progressive muscular dystrophy of the Fukuyama type: clinical, genetic and pathological considerations.** *Brain Dev* 1981;3:1–29 CrossRef Medline
12. Yamamoto T, Shibata N, Kanazawa M, et al. **Localization of laminin subunits in the central nervous system in Fukuyama congenital muscular dystrophy: an immunohistochemical investigation.** *Acta Neuropathol* 1997;94:173–79 CrossRef Medline
13. Hosokawa H, Ninomiya H, Kitamura Y, et al. **Vascular endothelial cells that express dystroglycan are involved in angiogenesis.** *J Cell Sci* 2002;115:1487–96 Medline
14. Kato I, Osawa M, Murasugi S, et al. **Neuroimaging morphological study of brain stem and cerebellum in cases of Fukuyama type congenital muscular dystrophy.** *Journal of Tokyo Women's Medical University* 1998;68:772–78

Effect of Age on GABA+ and Glutathione in a Pediatric Sample

M.G. Saleh, A. Papantoni, M. Mikkelsen, S.C.N. Hui, G. Oeltzschner, N.A. Puts, R.A.E. Edden, and S. Carnell

ABSTRACT

BACKGROUND AND PURPOSE: Gamma-aminobutyric acid (GABA) is the primary inhibitory neurotransmitter in the human brain and is implicated in several neuropathologies. Glutathione is a major antioxidant in the brain and is considered a marker of oxidative stress. Several studies have reported age-related declines in GABA levels in adulthood, but the trajectory of both GABA and glutathione during childhood has not been well explored. The aim of this study is to establish how GABA and glutathione vary with age during early development.

MATERIALS AND METHODS: Twenty-three healthy children (5.6–13.9 years of age) were recruited for this study. MR imaging/MR spectroscopy experiments were conducted on a 3T MR scanner. A 27-mL MR spectroscopy voxel was positioned in the frontal lobe. J-difference edited MR spectroscopy was used to spectrally edit GABA and glutathione. Data were analyzed using the Gannet software, and GABA+ (GABA + macromolecules/homocarnosine) and glutathione were quantified using water ($GABA+_{H2O}$ and $Glutathione_{H2O}$) and Cr (GABA+/Cr and glutathione/Cr) as concentration references. Also, the relative gray matter contribution to the voxel volume (GM_{ratio}) was estimated from structural images. Pearson correlation coefficients were used to examine the association between age and $GABA+_{H2O}$ (and $glutathione_{H2O}$), between age and GABA+/Cr (and glutathione/Cr), and between age and GM_{ratio}.

RESULTS: Both $GABA+_{H2O}$ ($r = 0.63$, $P = .002$) and GABA+/Cr ($r = 0.48$, $P = .026$) significantly correlated with age, whereas glutathione measurements and GM_{ratio} did not.

CONCLUSIONS: We demonstrate increases in GABA and no differences in glutathione with age in a healthy pediatric sample. This study provides insight into neuronal maturation in children and may facilitate better understanding of normative behavioral development and the pathophysiology of developmental disorders.

ABBREVIATIONS: f_{GM} = gray matter voxel tissue fraction; f_{WM} = white matter voxel tissue fraction; GABA = gamma-aminobutyric acid; GSH = glutathione; HERMES = Hadamard Encoding and Reconstruction of MEGA-Edited Spectroscopy; MEGA-PRESS = MEscher-GArwood point-resolved spectroscopy sequence; i.u. = institutional units; GM_{ratio} = relative GM contribution to voxel volume; GABA+ = GABA with macromolecules/homocarnosine

In vivo MR spectroscopy is a noninvasive tool for measuring brain metabolite levels to investigate both healthy and pathologic physiology.[1,2] The main inhibitory neurotransmitter gamma-aminobutyric acid (GABA) and the primary antioxidant glutathione (GSH) are of considerable interest due to their critical roles in governing neuronal activity and protection against oxidative stress. However, in vivo measurement of GABA and GSH is challenging due to substantial signal overlap with creatine (Cr).[3] Hadamard Encoding and Reconstruction of MEGA-Edited Spectroscopy (HERMES)[4] is a novel J-difference editing method that selectively detects multiple metabolites simultaneously and removes overlapping signals, offering substantial scan time reductions over previously used MEscher-GArwood point-resolved spectroscopy sequence (MEGA-PRESS),[5] which is limited to single-metabolite editing. In the present study, we use J-difference editing methods

Received January 27, 2020; accepted after revision March 23.

From the Russell H. Morgan Department of Radiology and Radiological Science (M.G.S., M.M., S.C.N.H., G.O., N.A.P., R.A.E.E.); and Department of Psychiatry and Behavioral Sciences, Division of Child and Adolescent Psychiatry (A.P., S.C.), The Johns Hopkins University School of Medicine, Baltimore, Maryland; F.M. Kirby Research Center for Functional Brain Imaging (M.G.S., M.M., S.C.N.H., G.O., N.A.P., R.A.E.E.), Kennedy Krieger Institute, Baltimore, Maryland; and Department of Forensic and Neurodevelopmental Sciences (N.A.P.), Institute of Psychiatry, Psychology and Neuroscience, King's College, London, UK.

This work was supported by National Institutes of Health grants P41 EB015909 R01 016089 R01 EB023693, K99AG062230, R01DK113286, UG3OD023313, R00DK088360, and a Johns Hopkins Discovery Award.

Please address correspondence to Muhammad G. Saleh, PhD, Russell H. Morgan Department of Radiology and Radiological Science, The Johns Hopkins University School of Medicine, 600 N Wolfe St, Baltimore, MD 21287; e-mail: msaleh10@jhmi.edu

http://dx.doi.org/10.3174/ajnr.A6543

to measure age-related changes in GABA and GSH in vivo in a healthy pediatric sample.

GABA is critical to brain function throughout the life span,[2] playing a vital role in inhibitory control. However, studies of age-related differences are limited. Most studies examining the relationship between GABA and age have focused on late development to adulthood. Some studies have demonstrated increases in GABA with age from late childhood to late adulthood,[6-8] and others observed decreases in GABA from late adolescence to late adulthood.[9-11] Also, a small number of cross-sectional studies have compared GABA between 2 age groups. Silveri et al[12] found lower GABA levels in adolescents relative to emerging adults; Simmonite et al[13] demonstrated higher GABA levels in younger participants relative to older participants. Thus, prior work seems to suggest an increase in GABA through development, followed by a period of relative stability, and then a decline. However, we have limited understanding of how GABA levels vary in early life. This information is of particular interest given the important role of GABA in cortical pruning and plasticity in early development.[14]

GSH is a critical element in the natural defense of the cell against damaging reactive oxygen species. Oxidative stress and GSH have been implicated in a range of neurologic and psychiatric conditions, including neurodevelopmental and neurodegenerative disorders.[15] It has previously been shown in healthy individuals that plasma levels of GSH decline with age.[16] However, plasma measurements do not directly reflect brain levels of GSH, which are most relevant to psychiatric and neurologic pathologies.[17] Only 1 study reported a relationship between MR spectroscopy measures of GSH and age; GSH levels in the occipital cortex in healthy young participants were higher compared with healthy elderly participants.[18]

Because an understanding of normative neuronal maturation is essential to understand the biologic basis of normative behavioral development (eg, development of inhibitory control) as well as to investigate neurodevelopmental disorders, the aim of this study was to use MR spectroscopy to establish how GABA and GSH vary with age during early development. Prior work suggests that GABA increases in early adolescence and decreases in late adulthood, whereas plasma measurements of GSH do not significantly vary from childhood to adulthood (0–40 years of age). We therefore hypothesized that GABA increases and that GSH does not change from early childhood to early adolescence.

Sample distribution of the pediatric cohort, voxel tissue composition, and metabolite concentrations[a]

Parameters	
No.	23
Sex (male/female)	12/11
Age (yr)	5.6–13.9; 10.2 ± 2.5
Male	5.6–13.9; 9.81 ± 3.01
Female	8.1–13.1; 10.61 ± 1.76
Race (No.)	
Black/African-American	4
White	16
>1 race	3
Voxel tissue composition	
Gray matter (%)	51.7 ± 4.8
White matter (%)	31.0 ± 3.5
GM_{ratio} (%)	62.5 ± 3.8
Metabolite levels	
$GABA+_{H2O}$ (i.u.)	2.70–4.37; 3.35 ± 0.48
GABA+/Cr	0.073–0.120; 0.102 ± 0.011
GSH_{H2O} (i.u.)	1.07–1.92; 1.50 ± 0.24
GSH/Cr	0.036–0.058; 0.05 ± 0.006

[a] Data are minimum–maximum; mean ± SD.

MATERIALS AND METHODS

Subjects

A total of 23 children were recruited for this study (Table). The study protocol and consent forms were approved by the local institutional review board (Johns Hopkins Medicine). Written parental consent was obtained for all participants. Additionally, written assent was obtained from children able to make an independent decision to participate (older than 8 years of age).

Acquisition Protocol

MR imaging/MR spectroscopy experiments were conducted on a Philips 3T MR imaging scanner (Philips Healthcare, Eindhoven, Netherlands) using a 32-channel head coil. After a high-resolution (1 mm^3) whole-brain 3D MPRAGE acquisition, the MR spectroscopy voxel was positioned in the frontal lobe on the midline above the genu of the corpus callosum, to include the anterior cingulate cortex, as shown in Fig 1. Subjects were scanned using the HERMES sequence for the simultaneous measurement of GABA with macromolecules and homocarnosine (GABA+) at 3.0 ppm and GSH at 2.95 ppm. Briefly, the HERMES sequence consists of 4 subexperiments: A) a dual-lobe editing pulse (ON_{GABA} at 1.9 ppm; ON_{GSH} at 4.56 ppm); B) a single-lobe editing pulse (ON_{GABA}); C) a single-lobe editing pulse (ON_{GSH}); and D) a single-lobe editing pulse at 7.5 ppm ($OFF_{GABA/GSH}$). GABA+- and GSH-edited spectra were generated using the Hadamard combinations A + B–C–D and A–B + C–D, respectively. Due to technical error, HERMES was not run for 3 subjects in whom the MEGA-PRESS sequence for detection of GABA+ was performed instead (ON_{GABA} at 1.9 ppm and OFF_{GABA} at 7.5 ppm). MR spectroscopy data were acquired with the following acquisition parameters: $30 \times 30 \times 30$ mm^3 voxel size, TE/TR = 80/2000 ms, 20-ms editing pulse duration, 2048 data points, 2-

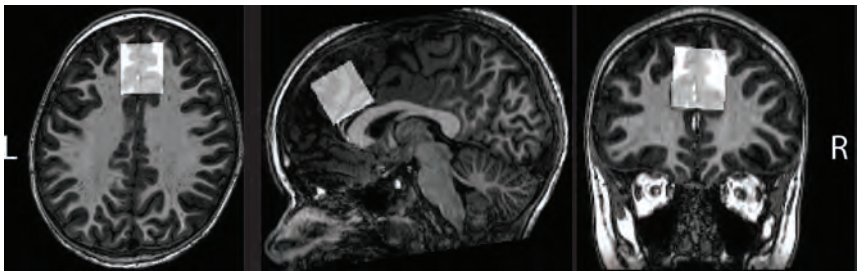

FIG 1. Structural images showing voxel localized in the frontal lobe on the midline above the genu of the corpus callosum, to include the anterior cingulate cortex.

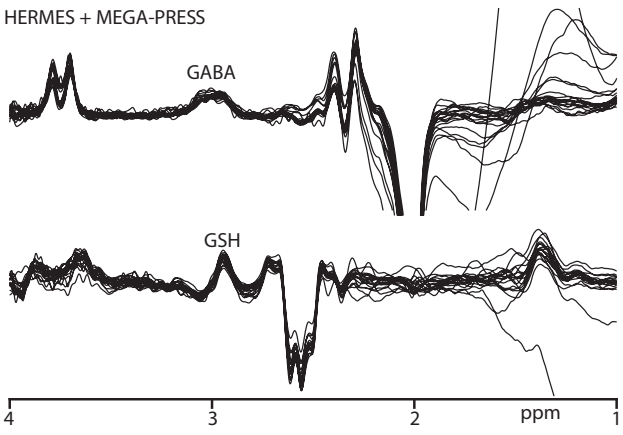

FIG 2. GABA+- and GSH-edited spectra from participants with a fit error of <15%. GABA+-edited spectra are acquired using both HERMES and MEGA-PRESS sequences.

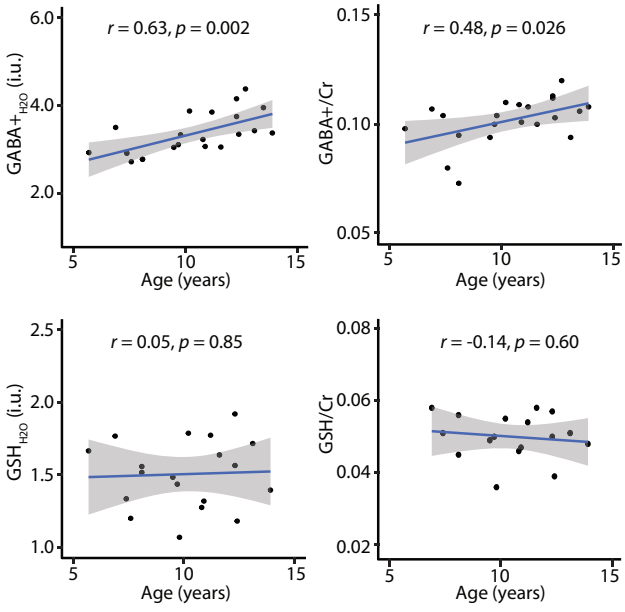

FIG 3. GABA+ and GSH correlations with age. Significant correlations are observed between GABA+ and age, whereas GSH does not significantly correlate with age. *r* indicates the Pearson correlation coefficient.

kHz spectral width, 304 transients, and variable power and optimized relaxation delays (VAPOR) water suppression.[19] Inter-leaved water referencing was applied to minimize the effects of magnetic field (B_0) drift during data acquisition[20] and as concentration reference data for each subject.

Data Processing

Data were analyzed using Gannet software (Version 3.1).[21] A modified multistep frequency-and-phase correction was applied to the data to reduce subtraction artifacts,[22] followed by a 3-Hz exponential filter and zero-padding by a factor of 16. Finally, the fully-processed HERMES and MEGA-PRESS subspectra were combined to generate GABA+- and GSH-edited spectra (HERMES only). Hankel Singular Value Decomposition water filtering was applied to remove the residual water signal.[23] The GABA+, GSH, and 3.0-ppm Cr (from $OFF_{GABA/GSH}$ and OFF_{GABA}, respectively) signals were modeled to calculate GABA+/Cr and GSH/Cr integral ratios. MPRAGE images were segmented by using SPM12 (http://www.fil.ion.ucl.ac.uk/spm/software/spm12)[24] to calculate gray matter (f_{GM}), white matter (f_{WM}), and CSF voxel tissue fractions. Absolute concentrations ($GABA+_{H2O}$ and GSH_{H2O}) were also calculated in institutional units (i.u.), correcting for tissue-dependent signal attenuation.[25] The gray matter ratio ($GM_{ratio} = f_{GM} / f_{GM} + f_{WM}$) was calculated using the tissue fractions for correlational analysis, as described below. To assess data quality, we used B_0 drift and water signal linewidth at full width at half maximum. The Cr signal at 3 ppm and the water signal at 4.68 ppm were used to estimate B_0 drift in the in vivo HERMES and MEGA-PRESS data, respectively, before frequency/phase alignment. Also, the GABA+ and GSH fit errors (defined as the ratio of the SD of the fit residual to the amplitude of the modeled peak) from Gannet were used for assessing modeling errors.[21]

Analysis

The mean and SD of all fit errors (combining GABA and GSH fit errors) were calculated, and subsequently determined that a value of 15% was approximately the 95th percentile (ie, ~2 SDs above the mean); therefore, we used this as a threshold for data rejection before statistical analysis. Pearson correlation coefficients (*r*) were calculated to examine the association between age and GABA and between age and GSH, with separate analyses for water- ($GABA+_{H2O}$ and GSH_{H2O}) and Cr-referenced (GABA+/Cr and GSH/Cr) measurements, and between age and the GM_{ratio}. Subsequently, correlations of $GABA+_{H2O}$ (and GABA+/Cr) with age were calculated in male and female participants separately. Outliers were identified using the Cook[26] distance estimates, excluding values higher than $4/(n - 2)$, where *n* is the sample size. A *P* value < .05 was considered statistically significant. Statistical analyses were conducted in R statistical and computing software (http://www.r-project.org).[27] Unless otherwise stated, values are presented as mean or mean ± SD.

RESULTS

All participants recruited for the study successfully completed scanning. B_0 drift during the 10-minute edited MR spectroscopy acquisitions was 2.41 ± 0.91 Hz, and the water linewidth was 8.22 ± 0.49 Hz, respectively, indicating good frequency stability and B_0 homogeneity. One GABA+ and 2 GSH measurements were removed due to fit errors exceeding 15%. The remaining data yielded low fit errors (GABA+/GSH: 6.03 ± 1.85/8.80 ± 1.51%). Figure 2 shows the edited difference spectra for subjects with fit errors <15%.

GM_{ratio}, GABA+, and GSH measurements are reported in the Table. Correlations between $GABA+_{H2O}$ (and GSH_{H2O}) and age, and GABA+/Cr (and GSH/Cr) with age are shown in Fig 3. Significant correlations were observed between $GABA+_{H2O}$ and age ($r = 0.63$, $P = .002$), and between GABA+/Cr and age ($r = 0.48$, $P = .026$). Neither GSH measurements nor GM_{ratio} significantly correlated with age.

When we separated results by sex, correlations of $GABA+_{H2O}$ to age were observed in both male and female participants (male/female ratio: $r = 0.60/0.71$, $P = .07/.01$); however, only the

correlation in female participants was significant. Also, nonsignificant correlations of GABA+/Cr to age were observed in both male and female participants (male/female ratio: $r = 0.50/0.58$, $P = .15/.06$).

DISCUSSION

Inhibitory dysfunction and oxidative stress are widely implicated disease mechanisms in young children and adolescents, including in autism,[28,29] depression,[30] and Tourette syndrome.[31,32] To understand the involvement of GABA and GSH in inhibitory dysfunction and oxidative stress with respect to normal and pathologic development, one must establish baseline distributions of these metabolites in typically developing children. To our knowledge, this is the first study investigating age-related effects on GABA and GSH levels in a healthy young pediatric sample (ranging from ~5 to ~14 years of age). Our findings demonstrate significant increases in GABA+ with increasing age, whereas GSH measurements show no association with age.

The age-related increase in GABA+ we report in this study is consistent with previous studies that used MEGA-PRESS to assess GABA+ in healthy adolescents.[6,12] Studies have linked GABA with important functions in the developing brain, including myelination and synaptic pruning.[33,34] Myelination begins during gestation and extends beyond adolescence, progressing from parietal to frontal regions.[35,36] Besides de novo myelination, existing myelin can undergo remodeling—such as a change in myelin sheath length/thickness or internode length—to restore myelination patterns or facilitate neuronal activity during development or learning.[37,38] Oligodendrocyte precursor cells have the potential to proliferate, differentiate, and form new myelin-forming oligodendrocytes.[38] Hamilton et al[39] recently demonstrated in mice that endogenous release of GABA, which acts on $GABA_A$ receptors of oligodendrocyte precursor cells, reduces the number of oligodendrocyte precursor cells and oligodendrocytes produced, thus, the control of myelination and myelin internode length. Because our study shows insignificant correlation of GM_{ratio} with age, it is possible that increasing GABA+ levels with age may support remodeling or regulation of existing myelin. Synaptic pruning is an important process that eliminates unnecessary synaptic connections to increase the efficiency of neuronal transmission. $GABA_A$ receptors in the dendritic spines of mice trigger synaptic pruning at puberty, improving spatial relearning.[34] Thus, increases in GABA+ with age may facilitate synaptic pruning to allow the development of new cognitive abilities during adolescence. Both myelin remodeling and synaptic pruning may have structural and functional implications. Structural implications take place at the neuronal level and cannot be detected using macroscopic morphometry measurements, whereas functional implications can be inferred by correlations with relevant measures of cognition (eg, impulsivity, response inhibition, working memory).[7,12]

In this study, the overall positive correlation of GABA+ with age was not sex-specific, with both males and females showing a positive correlation between GABA+ and age (albeit with a loss of power associated with splitting the data). In the present study, female participants' ages overlapped with the postpubertal period, which may impact GABA+,[40] and were not controlled for in our analyses. The absence of consistently significant correlation values is likely due to the small sample size. The present findings would ideally be replicated in a larger sample, controlling for menstrual status in female participants.

There were no GSH differences with age, consistent with a large study involving 176 healthy subjects that demonstrated no statistical differences in plasma GSH among 3 age groups (age: 2–11, 12–24, and 25–40 years).[16] These findings suggest that GSH synthesis remains stable in young children and early adolescents, providing effective protection against reactive oxygen species. Furthermore, our results suggest that the trajectory of GSH is consistent between brain and plasma. Glutathione also exists in an oxidized form, which is 40–100 times lower than the reduced form (GSH) in a healthy brain.[15,16] Although levels of GSH represent the ability of the brain to defend against reactive oxygen species, the ratio of GSH/oxidized glutathione would be a useful indicator of age-related cellular redox status. However, the current state of MR spectroscopy lacks the sensitivity to detect oxidized glutathione in vivo.[41]

The acquisition protocol for this study has limitations. First, GABA and GSH have low signal amplitudes, necessitating the use of a large volume of interest. Enhancements in hardware and pulse sequences[42,43] might enable the use of smaller VOIs and more efficient region-specific analyses of brain GABA and GSH changes. Second, the detected GABA+ signal contains a significant contribution from macromolecules and homocarnosine.[44] It is possible that the presence of a correlation was due to an increase in the concentration of macromolecules or homocarnosine as a function of age, as suggested by a number of studies.[45-49] Further studies applying metabolite nulling[47] or macromolecule-suppressed editing[44,50] are required to directly address this question. Third, subject motion is a concern when scanning children, causing data acquisition at an unintended location and reduced data quality,[51] and additional concerns for edited measurements. Thus, macromolecule-suppressed editing (the most motion-sensitive technique) was not applied in this cohort. This study did apply real-time frequency correction,[20] resulting in relatively good B_0 stability (~3 Hz) and postprocessing frequency corrections to minimize subtraction artifacts. Incorporation of motion-and-shim-correction methods[52-55] would ensure improved robustness of measurements to motion. Fourth, the present study focused on 1 brain region. Results may not be uniform across all brain regions, as demonstrated in adults.[56] Finally, the study uses a cross-sectional design, and future studies should use longitudinal data to explicitly investigate age-related changes in GABA and GSH across the brain.

CONCLUSIONS

To our knowledge, this is the first study to demonstrate that $GABA+_{H2O}$ and GABA+/Cr increases with age, while GSH does not in a healthy pediatric sample. Given the increasing use of MR spectroscopy to measure both GABA and GSH to investigate both normal and abnormal brain physiology, normative studies of age-related differences in GABA and GSH are needed.

Disclosures: Afroditi Papantoni—*UNRELATED: Employment*: Johns Hopkins University. Georg Oeltzschner—*RELATED: Grant*: National Institute on Aging, *Comments*: K99AG062230.* Nicolaas A. Puts—*RELATED: Grant*: National Institute of Mental Health, *Comments*: Salary paid from this grant.* Richard A. E. Edden—*RELATED: Grant*: National Institutes of Health, *Comments*: P41 EB015909 R01 016089 R01 EB023693.* Susan Carnell—*RELATED: Grant*: National Institutes

of Health, *Comments*: R00DK088360, R01DK113286 UG3OD023313 and the Johns Hopkins Discovery award.* *Money paid to the institution.

REFERENCES

1. Currie S, Hadjivassiliou M, Craven IJ, et al. **Magnetic resonance spectroscopy of the brain.** *Postgrad Med J* 2013;89:94–106 CrossRef Medline
2. Rae CD. **A guide to the metabolic pathways and function of metabolites observed in human brain 1H magnetic resonance spectra.** *Neurochem Res* 2014;39:1–36 CrossRef Medline
3. Harris AD, Saleh MG, Edden RA. **Edited 1H magnetic resonance spectroscopy in vivo: methods and metabolites.** *Magn Reson Med* 2017;77:1377–89 CrossRef Medline
4. Saleh MG, Oeltzschner G, Chan KL, et al. **Simultaneous edited MRS of GABA and glutathione.** *Neuroimage* 2016;15:576–82 CrossRef Medline
5. Mescher M, Merkle H, Kirsch J, et al. **Simultaneous in vivo spectral editing and water suppression.** *NMR Biomed* 1998;11:266–72 CrossRef Medline
6. Gaetz W, Bloy L, Wang D, et al. **GABA estimation in the brains of children on the autism spectrum: measurement precision and regional cortical variation.** *Neuroimage* 2014;86:1–9 CrossRef Medline
7. Ghisleni C, Bollmann S, Poil S-S, et al. **Subcortical glutamate mediates the reduction of short-range functional connectivity with age in a developmental cohort.** *J Neurosci* 2015;35:8433–41 CrossRef Medline
8. Port RG, Gaetz W, Bloy L, et al. **Exploring the relationship between cortical GABA concentrations, auditory gamma-band responses and development in ASD: evidence for an altered maturational trajectory in ASD.** *Autism Res* 2017;10:593–607 CrossRef Medline
9. Gao F, Edden RA, Li M, et al. **Edited magnetic resonance spectroscopy detects an age-related decline in brain GABA levels.** *Neuroimage* 2013;78:75–82 CrossRef Medline
10. Porges EC, Woods AJ, Edden RA, et al. **Frontal gamma-aminobutyric acid concentrations are associated with cognitive performance in older adults.** *Biol Psychiatry Cogn Neurosci Neuroimaging* 2017;2:38–44 CrossRef Medline
11. Marenco S, Savostyanova AA, van der Veen JW, et al. **Genetic modulation of GABA levels in the anterior cingulate cortex by GAD1 and COMT.** *Neuropsychopharmacology* 2010;35:1708–17 CrossRef Medline
12. Silveri MM, Sneider JT, Crowley DJ, et al. **Frontal lobe γ-aminobutyric acid levels during adolescence: associations with impulsivity and response inhibition.** *Biol Psychiatry* 2013;74:296–304 CrossRef Medline
13. Simmonite M, Carp J, Foerster BR, et al. **Age-related declines in occipital GABA are associated with reduced fluid processing ability.** *Acad Radiol* 2019;26:1053–61 CrossRef Medline
14. Wu X, Fu Y, Knott G, et al. **GABA signaling promotes synapse elimination and axon pruning in developing cortical inhibitory interneurons.** *J Neurosci* 2012;32:331–43 CrossRef Medline
15. Rae CD, Williams SR. **Glutathione in the human brain: review of its roles and measurement by magnetic resonance spectroscopy.** *Anal Biochem* 2017;529:127–43 CrossRef Medline
16. Erden-Inal M, Sunal E, Kanbak G. **Age-related changes in the glutathione redox system.** *Cell Biochem Funct* 2002;20:61–66 CrossRef Medline
17. Smaga I, Niedzielska E, Gawlik M, et al. **Oxidative stress as an etiological factor and a potential treatment target of psychiatric disorders, Part 2: depression, anxiety, schizophrenia and autism.** *Pharmacol Rep* 2015;67:569–80 CrossRef Medline
18. Emir UE, Raatz S, McPherson S, et al. **Noninvasive quantification of ascorbate and glutathione concentration in the elderly human brain.** *NMR Biomed* 2011;24:888–94 CrossRef Medline
19. Tkác I, Starcuk Z, Choi IY, et al. **In vivo 1H NMR spectroscopy of rat brain at 1 ms echo time.** *Magn Reson Med* 1999;41:649–56 CrossRef Medline
20. Edden RA, Oeltzschner G, Harris AD, et al. **Prospective frequency correction for macromolecule-suppressed GABA editing at 3T.** *J Magn Reson Imaging* 2016;44:1474–82 CrossRef Medline
21. Edden RA, Puts NA, Harris AD, et al. **Gannet: a batch-processing tool for the quantitative analysis of gamma-aminobutyric acid–edited MR spectroscopy spectra.** *J Magn Reson Imaging* 2014;40:1445–52 CrossRef Medline
22. Mikkelsen M, Saleh MG, Near J, et al. **Frequency and phase correction for multiplexed edited MRS of GABA and glutathione.** *Magn Reson Med* 2018;80:21–28 CrossRef Medline
23. Barkhuijsen H, De Beer R, van Ormondt D. **Improved algorithm for noniterative time-domain model fitting to exponentially damped magnetic resonance signals.** *Journal of Magnetic Resonance (1969)* 1987;73:553–57 CrossRef
24. Ashburner J, Friston KJ. **Unified segmentation.** *Neuroimage* 2005;26:839–51 CrossRef Medline
25. Gasparovic C, Song T, Devier D, et al. **Use of tissue water as a concentration reference for proton spectroscopic imaging.** *Magn Reson Med* 2006;55:1219–26 CrossRef Medline
26. Cook RD. **Influential observations in linear regression.** *Journal of the American Statistical Association* 1979;74:169–74 CrossRef
27. R Project for Statistical Computing. https://www.R-project.org. Accessed July 19, 2019
28. Drenthen GS, Barendse EM, Aldenkamp AP, et al. **Altered neurotransmitter metabolism in adolescents with high-functioning autism.** *Psychiatry Res Neuroimaging* 2016;256:44–49 CrossRef Medline
29. Puts NA, Wodka EL, Harris AD, et al. **Reduced GABA and altered somatosensory function in children with autism spectrum disorder.** *Autism Res* 2017;10:608–69 CrossRef Medline
30. Freed RD, Hollenhorst CN, Weiduschat N, et al. **A pilot study of cortical glutathione in youth with depression.** *Psychiatry Res Neuroimaging* 2017;270:54–60 CrossRef Medline
31. Puts NA, Harris AD, Crocetti D, et al. **Reduced GABAergic inhibition and abnormal sensory symptoms in children with Tourette syndrome.** *J Neurophysiol* 2015;114:808–17 CrossRef Medline
32. Frustaci A, Neri M, Cesario A, et al. **Oxidative stress-related biomarkers in autism: systematic review and meta-analyses.** *Free Radic Biol Med* 2012;52:2128–41 CrossRef Medline
33. Vélez-Fort M, Audinat E, Angulo MC. **Central role of GABA in neuron–glia interactions.** *Neuroscientist* 2012;18:237–50 CrossRef Medline
34. Afroz S, Parato J, Shen H, et al. **Synaptic pruning in the female hippocampus is triggered at puberty by extrasynaptic GABAA receptors on dendritic spines.** *Elife* 2016;5 CrossRef Medline
35. Sowell ER, Thompson PM, Toga AW. **Mapping changes in the human cortex throughout the span of life.** *Neuroscientist* 2004;10:372–92 CrossRef Medline
36. Gogtay N, Giedd JN, Lusk L, et al. **Dynamic mapping of human cortical development during childhood through early adulthood.** *Proc Natl Acad Sci U S A* 2004;101:8174–79 CrossRef Medline
37. Williamson JM, Lyons DA. **Myelin dynamics throughout life: an ever-changing landscape?** *Front Cell Neurosci* 2018;12:424 CrossRef Medline
38. Sampaio-Baptista C, Johansen-Berg H. **White matter plasticity in the adult brain.** *Neuron* 2017;96:1239–51 CrossRef Medline
39. Hamilton NB, Clarke LE, Arancibia-Carcamo IL, et al. **Endogenous GABA controls oligodendrocyte lineage cell number, myelination, and CNS internode length.** *Glia* 2017;65:309–21 CrossRef Medline
40. Epperson CN, Haga K, Mason GF, et al. **Cortical γ-aminobutyric acid levels across the menstrual cycle in healthy women and those with premenstrual dysphoric disorder: a proton magnetic resonance spectroscopy study.** *Arch Gen Psychiatry* 2002;59:851–58 CrossRef Medline
41. Satoh T, Yoshioka Y. **Contribution of reduced and oxidized glutathione to signals detected by magnetic resonance spectroscopy as indicators of local brain redox state.** *Neurosci Res* 2006;55:34–39 CrossRef Medline

42. Bogner W, Hangel G, Esmaeili M, et al. **1D-spectral editing and 2D multispectral in vivo^{1}H-MRS and ^{1}H-MRSI: methods and applications.** *Anal Biochem* 2017;529:48–64 CrossRef Medline
43. Saleh MG, Mikkelsen M, Oeltzschner G, et al. **Simultaneous editing of GABA and glutathione at 7T using semi-LASER localization.** *Magn Reson Med* 2018;80:474–77 CrossRef Medline
44. Deelchand DK, Marjańska M, Henry PG, et al. **MEGA-PRESS of GABA+: influences of acquisition parameters**. *NMR Biomed* 2019 Oct 28. [Epub ahead of print] CrossRef Medline
45. Aufhaus E, Weber-Fahr W, Sack M, et al. **Absence of changes in GABA concentrations with age and gender in the human anterior cingulate cortex: a MEGA-PRESS study with symmetric editing pulse frequencies for macromolecule suppression.** *Magn Reson Med* 2013;69:317–20 CrossRef Medline
46. Rowland LM, Krause BW, Wijtenburg SA, et al. **Medial frontal GABA is lower in older schizophrenia: a MEGA-PRESS with macromolecule suppression study.** *Mol Psychiatry* 2016;21:198–204 CrossRef Medline
47. Hofmann L, Slotboom J, Boesch C, et al. **Characterization of the macromolecule baseline in localized 1H-MR spectra of human brain.** *Magn Reson Med* 2001;46:855–63 CrossRef Medline
48. Tkácõ I, Rao R, Georgieff MK, et al. **Developmental and regional changes in the neurochemical profile of the rat brain determined by in vivo 1H NMR spectroscopy.** *Magn Reson Med* 2003;50:24–32 CrossRef Medline
49. Kreis R, Hofmann L, Kuhlmann B, et al. **Brain metabolite composition during early human brain development as measured by quantitative in vivo 1H magnetic resonance spectroscopy.** *Magn Reson Med* 2002;48:949–58 CrossRef Medline
50. Henry PG, Dautry C, Hantraye P, et al. **Brain GABA editing without macromolecule contamination.** *Magn Reson Med* 2001;45:517–20 CrossRef Medline
51. Hess AT, van der Kouwe AJ, Mbugua KK, et al. **Quality of 186 child brain spectra using motion and B0 shim navigated single voxel spectroscopy.** *J Magn Reson Imaging* 2014;40:958–65 CrossRef Medline
52. Saleh MG, Alhamud A, Near J, et al. **Volumetric navigated MEGA-SPECIAL for real-time motion and shim corrected GABA editing.** *NMR Biomed* 2016;29:248–55 CrossRef Medline
53. Saleh MG, Near J, Alhamud A, et al. **Reproducibility of macromolecule suppressed GABA measurement using motion and shim navigated MEGA-SPECIAL with LCModel, jMRUI and GANNET.** *MAGMA* 2016;29:863–74 CrossRef Medline
54. Bogner W, Gagoski B, Hess AT, et al. **3D GABA imaging with real-time motion correction, shim update and reacquisition of adiabatic spiral MRSI.** *Neuroimage* 2014;103:290–302 CrossRef Medline
55. Hnilicová P, Povazõan M, Strasser B, et al. **Spatial variability and reproducibility of GABA-edited MEGA-LASER 3D-MRSI in the brain at 3 T.** *NMR Biomed* 2016;29:1656–65 CrossRef Medline
56. Hermans L, Leunissen I, Maes C, et al. **The aging brain and changes in GABA concentrations.** In: *Proceedings of the 12th National Congress of the Belgian Society for Neuroscience*, Brussels, Belgium. May 24, 2019

Fetal and Neonatal MRI Predictors of Aggressive Early Clinical Course in Vein of Galen Malformation

L. Arko, M. Lambrych, A. Montaser, D Zurakowski, and D.B. Orbach

ABSTRACT

BACKGROUND AND PURPOSE: Neonates with vein of Galen malformations are split into 2 cohorts: one needing urgent neonatal embolization, with relatively high mortality and morbidity even with expert care, and a cohort in which embolization can be deferred until infancy, with far better prognosis. We aimed to identify brain MR imaging characteristics obtained from fetal and early neonatal scans that can predict the clinical presentation.

MATERIALS AND METHODS: Patients with vein of Galen malformations were stratified into a neonatal at-risk cohort if the patient needed urgent neonatal intervention or if neonatal death occurred; or an infantile treatment cohort if they were stable enough not to require treatment until >1 month of age. Twelve vascular MR imaging parameters, measured by 2 independent observers, were systematically correlated with the need for early neonatal intervention and/or neonatal mortality.

RESULTS: A total of 32 neonatal patients (21 patients in the neonatal at-risk cohort, 11 in the infantile treatment cohort) were identified. Maximal mediolateral diameter (area under the curve = 0.866, $P < .001$) and cross-sectional area (area under the curve = 0.836, $P = .002$) at the narrowest point of the straight or falcine sinus were most predictive of clinical evolution into the neonatal at-risk cohort. There were 15 patients who had fetal MRIs (10 in the neonatal at-risk cohort and 5 in the infantile treatment cohort). Here too, maximal mediolateral diameter (area under the curve = 0.980, $P = .003$) and cross-sectional area (area under the curve = 0.941, $P = .007$) at the narrowest point of the straight or falcine sinus were highly predictive of the neonatal at-risk cohort.

CONCLUSIONS: Early neonatal and fetal MR imaging can be readily used for accurate early risk stratification, assisting in directing resources, timing treatment decisions, and identifying appropriate cohorts for novel interventions.

ABBREVIATIONS: AUC = area under the curve; BA-MD = basilar artery maximal diameter; CC = craniocaudal diameter; ICA-MD = internal carotid artery maximal diameter; IT infantile treatment cohort; NAR = neonatal at-risk cohort; ROC = receiver operating characteristic; Sig-MD = sigmoid sinus maximal diameter; SS-A = straight sinus cross-sectional area at the narrowest point of the straight or falcine sinus; SS-MD = straight sinus maximal diameter at the narrowest point of the straight or falcine sinus; SS-P = straight sinus outer perimeter at the narrowest point of the straight or falcine sinus; VOGM = vein of Galen malformations

Vein of Galen malformations (VOGM) are rare congenital cerebral arteriovenous lesions that represent approximately 30% of all pediatric vascular anomalies.[1] The condition is characterized by presumed persistence of direct arteriovenous communications between the embryonic choroidal arteries and the median prosencephalic vein of Markowski.[2,3] The latter normally involutes by 11 weeks' gestation.

The development of endovascular embolization techniques for VOGM in the 1990s transformed the condition from near-universal mortality or severe morbidity to a potentially manageable condition, as demonstrated by multiple institutional cohorts and 2 recent meta-analyses.[4,5] However, mortality and severe neurocognitive morbidity remain daunting challenges for patients with vein of Galen malformations. A recent literature review of all published prenatally diagnosed cases reported a 54% mortality rate, a 14% rate of survival with severe neurocognitive compromise, and only an approximately one-third chance of survival without severe neurologic impairment.[6] In this study, approximately two-thirds of patients with VOGM presented in the first few days of life with aggressive high-

Received March 5, 2020; accepted after revision April 3.

From the Departments of Neurosurgery (L.A., M.L., A.M., D.B.O.); Anesthesiology and Surgery (D.Z.); and Neurointerventional Radiology (D.B.O.), Boston Children's Hospital, Harvard Medical School, Boston, Massachusetts.

This work was supported by the Sage Schermerhorn Fund for Image-Guided Therapy.

Please address correspondence to Darren B. Orbach, MD, PhD, Neurointerventional Radiology, Boston Children's Hospital, 300 Longwood Avenue Boston, MA 02115; e-mail: darren.orbach@childrens.harvard.edu

Indicates article with supplemental on-line photo.

http://dx.doi.org/10.3174/ajnr.A6585

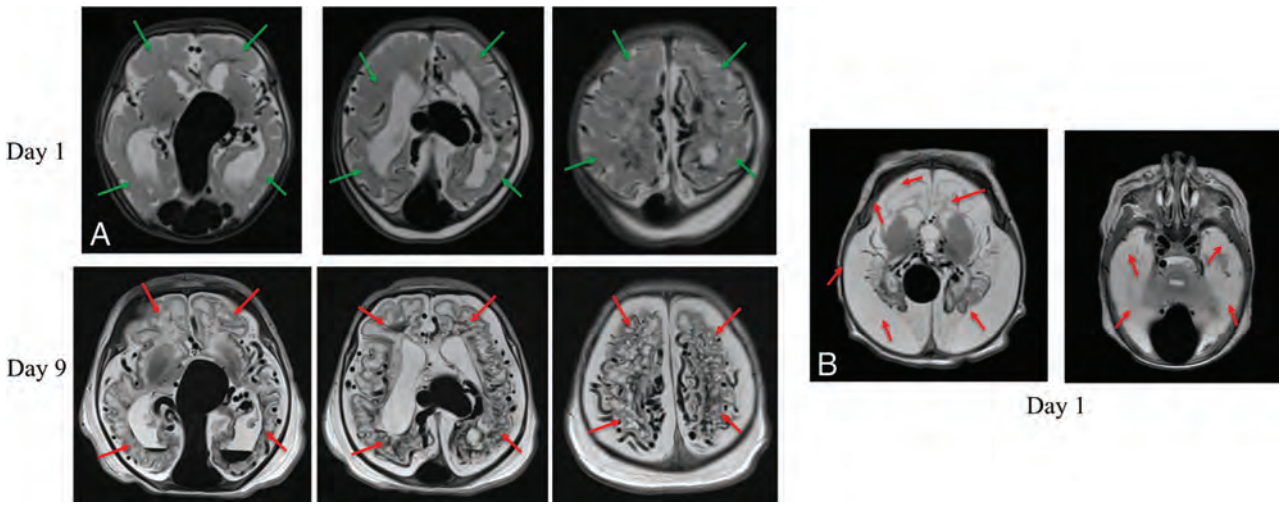

FIG 1. Aggressive early evolution of a vein of Galen malformation (NAR cohort) (*A*, *left panels*). After med-flighting this neonate with VOGM to our center for urgent treatment, the MR imaging obtained on day-of-life 9 showed diffuse bihemispheric brain injuries (*red arrows*) not seen on the initial on day-of-life 1 MR imaging (*green arrows* showing analogous regions). Increased soft-tissue edema in the neck and scalp on day 0 is secondary to overwhelming heart failure (*B*, right panels). Another patient, a one-day-old neonate with VOGM presents with complete liquefactive gliosis of both cerebral hemispheres (white brain signal resembles white CSF signal on T2-weighted imaging).

output cardiopulmonary failure, requiring several rounds of high-risk urgent embolization; we refer to these patients as the neonatal at-risk cohort (NAR). A report with nationwide population data from the United Kingdom reported, in this NAR cohort with aggressive neonatal presentation, a 40% mortality with 50% of the survivors having severe neurocognitive compromise and an overall 30% likelihood of survival to adulthood without significant neurologic injury.[7] Several examples of the kind of global parenchyma brain injuries seen in such patients are shown in Fig 1.

Note that at our center, if diffuse parenchymal brain injury or hemorrhage is seen on fetal imaging, comfort care rather than embolization is recommended. Fortunately, such cases are extremely rare, because the brain parenchymal findings in most cases appear postnatally. However, such patients invariably manifest severe cardiopulmonary decompensation at birth and are thus included in the NAR cohort. The remaining approximately one-third of patients with VOGM present after the neonatal period, often with macrocephaly, ventriculomegaly, or seizures; we refer to these patients as the infantile treatment cohort (IT). These patients are typically embolized at several months of age, and the same UK national population data found a 90% survival rate in this more stable IT cohort.[8] An example of the response to embolization in an infant with this presentation is shown in the On-line Figure.

Clinical presentation based on prenatal imaging has been difficult to predict, with no particular marker being found to correlate with a benign course. Thus, at most expert centers, including our own, every neonate with VOGM is admitted to the neonatal intensive care unit and carefully observed for clinical deterioration, with the team prepared for urgent embolization as needed. The wide range of possible outcomes, from normal neurocognitive development and life span to death within days or severe neurologic compromise, is unnerving to families and providers and stymies efforts to triage care. Thus, we first sought to determine whether vascular anatomic differences based on an early neonatal MR imaging measurement could differentiate the NAR and IT and thus aid in risk stratification. If so, as a second step, we sought to ascertain whether the same would hold for fetal MR imaging. Identification of prenatal and early neonatal predictors would allow advance preparation for the likely clinical evolution, offer potential guidance in parental consideration of possible termination of pregnancy, and allow identification of appropriate patient cohorts for the development of novel therapeutic approaches.

Finally, it has been hypothesized that 1 particular morphologic subtype of vein of Galen malformation, the choroidal subtype (consisting of multiple, often innumerable bilateral arteriovenous fistulas investing the walls of the prosencephalic varix), is associated with NAR compared with the mural subtype (consisting of a single arteriovenous fistula). Thus, along with anatomic measurements, we sought to determine whether, in fact, morphology was such a predictor.

MATERIALS AND METHODS

After obtaining approval of our institutional review board, a prospective data base of patients who presented with a VOGM from 2007 through 2018 was used to identify the cohort of interest. For the initial analysis, inclusion criteria consisted of all patients with VOGM who had brain MR imaging within the first 10 days of life, before the initiation of any treatment; all patients with only posttreatment scans available were excluded. Note that for nearly the entire neonatal cohort, the neonatal scan was obtained on day-of-life 1 after birth. For the fetal cohort, we included all patients with fetal MR images obtained as part of consultation at our Maternal Fetal Care Center where neonatal clinical follow-up was also available. Demographic information was collected.

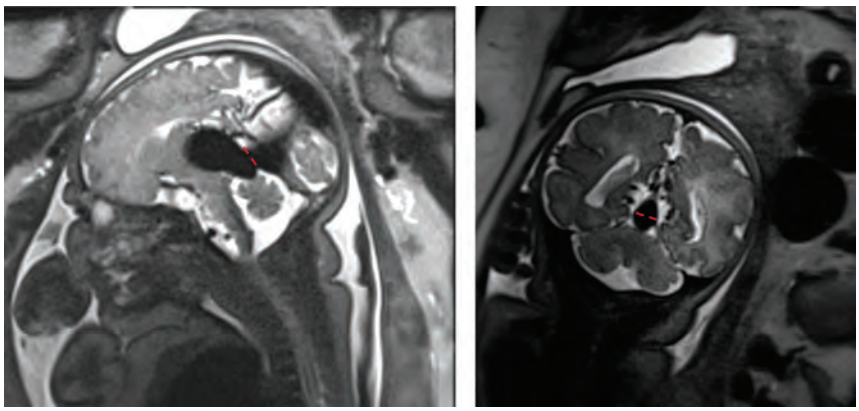

FIG 2. Measurement of the mediolateral diameter of the falcine sinus at its shortest point. The *left image* shows a sagittal view of a fetal MR imaging, with the *dashed red line* at the section of shortest height of the falcine sinus. The *right image* shows a coronal view with the mediolateral diameter of the sinus demonstrated with *red dashes*, measured at this same shortest section. This diameter efficiently differentiated the IT from the NAR cohort, as did the cross-sectional area of the sinus, measured at this same section.

All images were viewed using a PACS system by 2 independent readers, a neuroendovascular fellow (reader 1) and the senior author (reader 2). The readers were blinded to the patient's clinical outcome. Twelve cerebrovascular anatomic parameters were measured manually in the PACS in the entire neonatal cohort. Neonatal subjects for whom all measurements could not be obtained due to image quality and/or lack of relevant sequences were excluded from the study. Attempts were made to obtain all measurements in the fetal cohort as well, but given the variability intrinsic to fetal imaging secondary to fetal movements, fetal subjects were not excluded from the study if it was not possible to obtain all measurements. Parameters included the following: the maximal diameter of the prosencephalic varix (anterior-posterior, craniocaudal [CC], and mediolateral); maximal diameter of the basilar artery (BA-MD) and the internal carotid arteries bilaterally (ICA-MD); maximal diameter of the sigmoid sinuses (Sig-MD) bilaterally; and the maximal mediolateral diameter of the straight or falcine sinus at its narrowest point in the craniocaudal axis (ie, its shortest point, along the course from the prosencephalic varix to the torcular [SS-MD]) (Fig 2). This last measurement was designed to assess the degree of constraint on outflow by assessing the caliber of the point of maximal constriction.

In addition, as potentially even more precise assessments of flow constraint, the perimeter of the straight or falcine sinus at this narrowest point (SS-P) was also measured by reader 1, while reader 2 measured the cross-sectional area at this point (SS-A). Each malformation was independently categorized morphologically as mural or choroidal by reader 2. In addition, the presence or absence of an occipital sinus was also noted (by both readers), because the nonregression of this fetal venous sinus might potentially correlate with markedly increased flow return to the systemic circulation.

Patients were categorized as either NAR, those who either continued to decline despite maximal medical management of their severe cardiopulmonary failure and who thus underwent urgent neonatal embolization as a potential life-saving intervention or those who died before such intervention could be given; or as IT, those who were successfully managed medically in the neonatal intensive care unit, extubated, and discharged home. These patients underwent elective embolization in infancy (typically at 3–6 months of age).

Statistical Analysis

Univariate analysis comparing cohorts was conducted using the nonparametric Mann-Whitney *U* test. Statistical significance was set at 2-tailed $P < .01$, using the Holm test to account for multiple variables being tested to protect against type I false-positive errors.[9] The Mann-Whitney *U* test was calculated for both independent readers. To assess interrater reliability, we calculated a 2-way mixed intraclass correlation coefficient between readers for continuous variables.

For categoric variables, VOGM morphology, and occipital sinus presence, a Pearson χ^2 analysis was used. Interrater chance-corrected reliability was measured by the Cohen κ. Imaging variables chosen for multivariable logistic regression analysis were based on a level of significance from univariate analysis.

On the basis of the measurements of reader 2, multivariable logistic regression using backward-selection stepwise modeling was used to identify independent imaging parameters that differentiate the NAR and IT cohorts and to determine the probability of NAR. For model selection, we chose a *P* value criterion of $<.05$ for entry and a less stringent value of .10 for retaining a variable in the model to avoid missing important imaging parameters, and we obtained the same results with a backward and forward selection, which we interpreted as a sign of a robust multivariable model. A receiver operating characteristic (ROC) curve was created to assess differentiation of the 2 cohorts using SS-MD and SS-A with an area under the curve (AUC) to assess predictive accuracy. The Youden J index was used to identify the best cutoff value for SS-MD and SS-A, to maximize the combination of sensitivity and specificity.

Univariate and multivariable analyses were performed separately for the early neonatal and fetal MR image sets. Both a paired-samples *t* test and a Pearson correlation (*r*) coefficient were used to compare continuous variables of patients who had both fetal and corresponding early neonatal MR imaging. All statistical analyses were performed using SPSS statistical software, Version 25.0 (IBM).

RESULTS

In the early neonatal MR imaging cohort, there was a total of 32 patients, with 21 patients in the NAR cohort and 11 in the IT cohort. Mean gestational age was 38 ± 2.3 weeks, with no significant age difference between the NAR (37.7 ± 2.8 weeks) and IT (38.5 ± 1.3 weeks) cohorts ($P = .453$). Univariate analysis (Table 1)

Table 1: Fetal MR imaging scan univariate data

	Reader 1							Reader 2							
	NAR			Infant Treatment			*P*	NAR			Infant Treatment			*P*	
Region	No.	Median	IQR	No.	Median	IQR	Value	No.	Median	IQR	No.	Median	IQR	Value	ICC
Varix ML (mm)	10	18	13–22	4	19	11–25	1.00	10	18	13–24	5	20	12–23	1.00	0.98
Varix AP (mm)	10	30	28–33	4	19	12–25	<.01	9	30	21–34	5	20	16–27	.15	0.75
Varix CC (mm)	10	20	18–21	4	16	8–25	.64	10	18	12–21	5	18	11–23	.77	0.89
Varix V (CM^3)	10	5	2–5	4	3	1–5	.73	9	5	2–6	5	5	2–6	1.00	0.93
SS-MD (mm)	10	10	8–12	4	6	4–6	<.01	10	8	5–11	5	3	3–5	<.001	0.95
SS-P (mm)	9	43	39–49	4	28	22–34	<.001	10	39	28–41	5	20	17–31	<.01	0.87
SS-A (mm^2)								10	85	56–112	5	20	18–45	<.01	
BA-MD (mm)	5	3	3–4	3	3	2–0	.57								
R ICA-MD (mm)	5	4	3–5	3	3	2-0	.57								
L ICA-MD (mm)	5	3	3–5	3	3	2-0	.39								
R Sig-MD (mm)	8	10	9–12	4	6	4–8	<.001	10	7	6–8	5	5	4–6	<.001	0.72
L Sig-MD (mm)	8	11	7–12	4	6	5–7	.05	10	9	7–9	5	6	4–6	<.01	0.94

Note:—AP indicates anterior-posterior diameter; IQR, interquartile range; L, left; ML, mediolateral diameter; R, right; V, volume; ICC, intraclass correlation coefficient. Statistical significance was set using a conservative criterion of $P < .01$ to account for multiple testing.

Table 2: Early MR imaging scan data for neonatal at-risk and infant treatment cohorts

	Reader 1							Reader 2							
	NAR			Infant Treatment				NAR			Infant Treatment				
Region	No.	Med	IQR	No.	Med	IQR	*P*	No.	Med	IQR	No.	Med	IQR	*P*	ICC
Varix ML (mm)	21	24	18–27	11	21	19–25	.46	21	23	17–27	11	21	18–26	.97	0.921
Varix AP (mm)	21	30	19–35	11	20	20–27	.22	21	30	25–35	11	22	20–29	.05	0.633
Varix CC (mm)	20	24	20–27	11	19	16–24	.16	21	21	16–29	11	18	15–24	.14	0.875
Varix V (CM^3)	21	6	4–10	11	4	3–8	.24	20	9	4–13	11	4	3–8	.15	0.961
SS-MD (mm)	17	10	8–14	11	6	5–8	.00	21	9	7–11	11	3	2–6	<.001	0.983
SS-A (mm^2)	21	6	4–8	11	3	3–4	.00	20	85	65–123	11	28	18–55	<.001	
SS-P (mm)	17	40	36–48	11	29	21–37	.00	20	35	32–43	11	27	21–35	.03	0.969
BA-MD (mm)	21	4	3–5	11	4	3–4	.03	21	4	3–4	11	3	2–3	<.01	0.877
R ICA-MD (mm)	21	4	4–5	11	3	2–4	.00	21	4	3–4	11	3	2–3	<.001	0.851
L ICA-MD (mm)	21	4	3–5	11	3	3–3	.00	21	4	3–4	11	3	2–3	<.01	0.655
R Sig-MD (mm)	21	9	7–10	11	7	4–9	.04	21	6	5–8	11	5	2–6	.02	0.642
L Sig-MD (mm)	21	8	8–11	11	7	6–9	.10	21	7	6–8	11	4	3–6	<.001	0.775

Note:—Med indicates median; AP, anterior-posterior diameter; IQR, interquartile range; L, left; ML, mediolateral diameter; R, right; V, volume; ICC, intraclass correlation coefficient. Statistical significance was set using a conservative criterion of $P < .01$ to account for mutliple testing.

showed that varix caliber measurements (varix mediolateral diameter, varix anterior-posterior, varix CC), varix volume, and right Sig-MD were not significant between the 2 cohorts, as measured by both readers. The 2 readers differed in their assessment of whether the left Sig-MD, SS-P, and BA-MD measurements differed significantly. Significant differences between cohorts were found and were consistent between both readers for SS-MD, right ICA-MD, and left ICA-MD. Interrater reliability, as measured by the intraclass correlation coefficient, was >0.80 for most caliber measurements (varix mediolateral diameter, varix CC, varix volume, SS-MD, SS-P, BA-MD, and right ICA-MD (Table 2).

VOGM morphology was of the choroidal type, in most cases for both readers. There was a significant difference in VOGM morphology between cohorts based on the observations of reader 2 ($P < .01$), but this was not reproduced by reader 1; thus, the interrater reliability was moderate ($\kappa = 0.48$, $P = .05$) (Table 3). The occipital sinus was present in all of the NAR cohort as observed by both readers, and its presence was significantly different between cohorts (Table 4). Thus, absence of an occipital sinus in a neonatal MR imaging strongly implies belonging to the IT cohort. The interrater reliability for observation of the occipital sinus was high ($\kappa = 0.819$, $P < .001$) (Table 4).

After performing multivariable analysis using the measurements that significantly differed between the cohorts and had a high interrater reliability, the most predictive parameters were SS-MD (AUC = 0.866, $P < .001$) and SS-A (AUC = 0.836,

$P = .002$) (Table 5 and Fig 3*A*). ROC curves showed that an SS-MD of >6.2 mm and an SS-A of >58 mm^2 strongly predicted clinical evolution to the NAR cohort based on early MR imaging (Fig 3*A*).

There were considerably fewer patients with fetal MR imaging ($n = 15$), but the fraction of fetal patients in the NAR cohort ($n = 10$) was nearly identical to the fraction of neonatal patients in the NAR cohort (67% and 66%, respectively). Mean gestational age was comparable in the NAR (34 ± 3 weeks) and IT (33 ± 5 weeks) cohorts. Both readers found a significant difference between cohorts in measurements of SS-MD, SS-P, and right Sig-MD. There was no significant difference in measurements between cohorts for most varix measurements (varix mediolateral diameter, varix CC, and varix volume) for both readers. Here too, the interrater reliability was high (>0.80) for most caliber measurements: varix mediolateral diameter, varix CC, varix volume, SS-MD, SS-P, and left Sig-MD.

There were notably several missing parameters on fetal MR imaging, including BA, ICA bilaterally, and the sigmoid sinuses bilaterally. In most cases, the missing variables could not be measured due to suboptimal fetal positioning in all relevant slices. Only 1 fetal MR imaging had a missing SS-P value, due to the lack of a coronal sequence. Similarly, the presence of the occipital sinus and VOGM morphology was difficult to fully assess on the fetal MR imaging on a consistent basis.

Multivariable analysis again demonstrated that SS-MD (AUC = 0.980, $P = .003$) and SS-A (AUC = 0.941, $P = .007$) were most predictive of clinical evolution to NAR (Table 5). By means of an ROC curve, the most predictive cutoff values for SS-MD and SS-A were >5.2 and >33 mm^2, respectively (Fig 3*B*).

Eleven patients had both an early neonatal and a fetal MR imaging, with an average time difference between these scans of 3.3 ± 2.7 weeks. If one compared the fetal with the neonatal scan in these cases, there was no significant difference in mean measurements of either the SS-MD ($P = .837$) or SS-A ($P = .794$) and the fetal and neonatal measurements were highly correlated for both SS-MD ($r = 0.90$, $P < .001$) and SS-A ($r = 0.91$, $P < .001$). High correlation between fetal and neonatal scans within the same patients suggests that there was a minimal differential change in the size of the SS-MD and SS-A measurements with time. Thus, data from the larger neonatal cohort could potentially be used to confirm the results in the much smaller fetal cohort.

As an illustration of the sharp increase in the likelihood of evolution to NAR with an increasing mediolateral diameter of the straight or falcine sinus, we calculated this probability, along with 95% confidence intervals, for a single reader (reader 2), as illustrated in Table 6.

Table 3: Presence of VOGM morphology in early MR imaging scan data for neonatal at-risk and infant treatment cohorts

VOGM Morphology	Choroidal	Mural	Total
Reviewer 1			
Cohort			
NAR	19	2	21
IT	9	2	11
Total	28	4	32
$\chi^2(1, n = 32) = 0.495$, $P = .48$			
Reviewer 2			
Cohort			
NAR	21	0	21
IT	4	7	11
Total	25	7	32
$\chi^2(1, n = 32) = 17.105$, $P < .001$			
$\kappa = 0.48$, $P = .05$			

Table 4: Presence of occipital sinus morphology in early MR imaging scan data for neonatal at-risk and infant treatment cohorts

Presence of Occipital Sinus	No	Yes	Total
Reviewer 1			
Cohort			
NAR	0	21	21
IT	6	5	11
Total	6	26	32
$\chi^2(1, n = 32) = 14.1$, $P < .001$			
Reviewer 2			
Cohort			
NAR	0	21	21
IT	4	7	11
Total	4	28	32
$\chi^2(1, n = 32) = 8.3$, $P < .01$			
$\kappa = 0.819$, $P < .001$			

Table 5: Cutoff values for NAR on fetal and neonatal MR imaging[a]

	AUC	95% CI	*P* Value	Cutoff Value	Sensitivity	Specificity
Neonatal						
SS-MD	0.866	0.736–0.996	<.001	>6.2 mm	86%	82%
SS-A	0.836	0.690–0.983	.002	>58 mm^2	80%	82%
Fetal scans						
SS-MD	0.980	0.919–1.000	.003	>5.2 mm	90%	100%
SS-A	0.941	0.823–1.000	.007	>33 mm^2	90%	80%

[a] Probabilities determined by logistic regression, where straight or falcine sinus diameter on MR imaging was identified as a multivariable predictor of clinical outcome (AUC = 0.89, $P < .001$).

DISCUSSION

Vein of Galen malformation is a rare congenital vascular anomaly with a complex and potentially devastating outcome. The presence of a cerebral arteriovenous shunt with resultant high cardiac output leads to multiple possible morbidities: severe pulmonary hypertension, increased cardiac preload, holodiastolic reversal of flow in the descending aorta with concomitant organ hypoperfusion, cerebral venous congestion and hypertension, and so forth. In severe cases, the persistent arteriovenous shunting may lead to multiorgan failure and progressive destruction of hemispheric white matter and cortical parenchyma.[10] This severely affected cohort (NAR), representing approximately two-thirds of neonates with VOGM, continues to have a high mortality rate and a high rate of severe neurodevelopmental morbidity among survivors, despite advances in neuroendovascular management.[7] However, other patients with VOGM of similar overall caliber do not decompensate physiologically, do not require intubation or cardiac

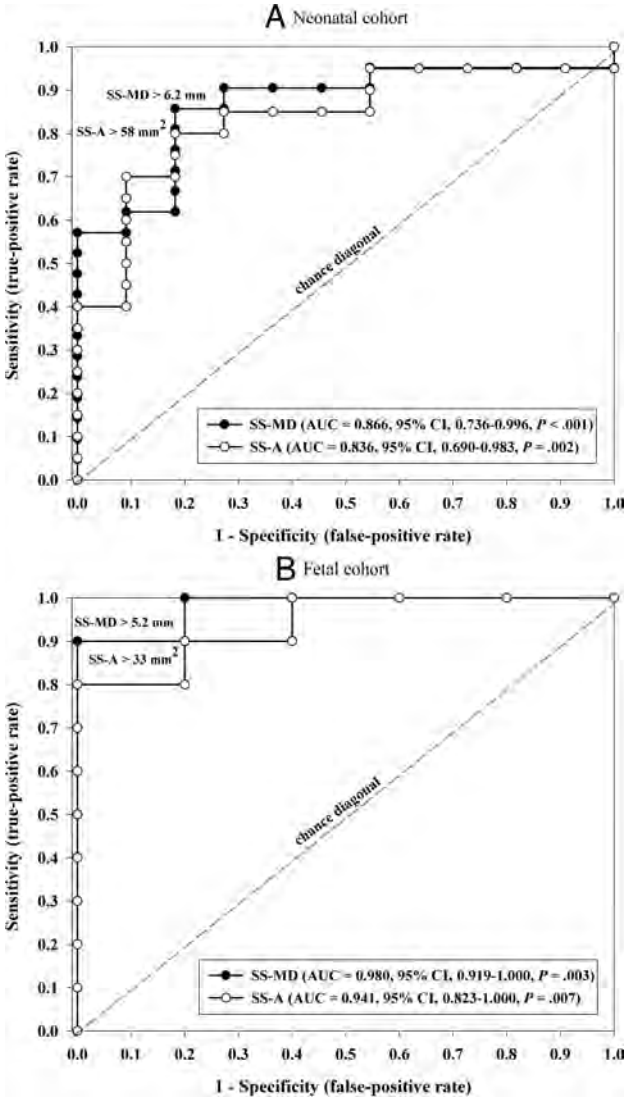

FIG 3. ROC curves showing measurements of the straight or falcine sinus area (SS-A) and the straight or falcine sinus maximal mediolateral diameter (SS-MD) at the shortest point of the sinus. Measurements from neonatal MR imaging (*A*) and from fetal MR imaging (*B*).

support, are discharged home from the neonatal intensive care unit, and are treated electively at several months of age. This latter group (IT) has a mortality rate of ~10%.

For the past 2 decades, the most widely used clinical scale for grading VOGM severity at presentation has been the Bicêtre neonatal evaluation score.[11] Low scores on this scale (<8), consistent with multiorgan presentation, have been used in many centers as a rationale for withholding all treatment efforts; high scores (>12) have been used as a rationale for watchful waiting; and midrange scores (8–12), as an indicator of the need for urgent embolization. However, it has become clear that with expert treatment, some neonates scoring in the <8 range can have good outcomes and most referral centers no longer use strict score cutoffs for assignation of care. Moreover, the Bicêtre score is based on clinical criteria and is, thus, post hoc. It cannot be calculated during the antenatal period; and even at birth, it is impossible to predict how a given patient will evolve. Thus, to direct clinical resources appropriately, to offer families a realistic assessment of likely clinical outcome, and to identify an appropriate cohort to whom novel therapies should be directed, a need for a mechanism for prognosticating fetal outcomes exists. The present study was conducted to assess whether select vascular parameters on fetal MR imaging could play this role.

Measurements can be reliably obtained on MR imaging of most relevant fetal and neonatal vascular architecture. We found that vascular parameters on neonatal MR imaging revealed widespread dilation of both arterial and venous structures in patients in the NAR cohort compared with those in the IT cohort; to the best of our knowledge, these measurements have not been systematically evaluated previously.

However, we reasoned that the point of greatest constriction to flow return from the malformation to the systemic circulation might serve as the single most efficient predictor of neonatal outcome. Indeed, we found that in both fetal and neonatal MR imaging, patients with lesser constriction at this critical point (ie, those with a large mediolateral diameter or cross-sectional area of the straight or falcine sinus at its shortest section) were at significantly greater risk of evolving to NAR; thus, dilation at this point was sharply predictive of mortality and the need for neonatal intervention. The rationale behind choosing the mediolateral axis for diameter measurement was because the falcine and straight sinuses are tightly tacked by the dural reflection on the rostral and caudal edges of the sinus (thus the choice of the section with the shortest height as the section of interest), while the lateral walls of the sinus are free and unattached. This degree of freedom allows the sinus to expand or contract in the lateral plane as a function of flow; thus, the mediolateral diameter serves as an anatomic marker of flow. These measurements were readily obtained from both fetal and neonatal MR imaging and can be reliably quantified in either the axial or coronal plane, as long as a cross-referenced sagittal sequence is available to identify the shortest section of the sinus. While other studies have suggested broadly that a dilated straight sinus was a poor prognosticator for patients with VOGM on both MR imaging and sonography, none of these studies detailed where or how to measure dilation, and no quantitative or systematic analysis was performed.[12,13] The specific measurement we put forward here has not been previously described. The utility of this technique in terms of readily differentiating cohorts with very low likelihood versus very high likelihood of evolution to NAR is illustrated in Table 6, even for a single MR imaging reader.

Most interesting, median prosencephalic varix size itself was not a predictor of clinical evolution to NAR versus IT, a finding in conflict with some earlier reports. Paladini et al[12] found that a VOGM varix volume of >20,000 mm^3 was predictive of poor outcome and parenchymal injury. On the other hand, Saliou et al[14] found that the size of the varix on prenatal MR imaging was not predictive of poor outcome, as others had reported.[11] We would note that Paladini et al grouped patients with VOGM who had neurologic sequelae, neonatal death, and termination of pregnancy into a single cohort, while in the present study, NAR assignation was determined by neonatal death or need for urgent neonatal embolization. In the same study, Saliou et al reported on middle cerebral artery "pseudofeeders" on fetal MR imaging as a

Table 6: Likelihood of clinical evolution to NAR as a function of the mediolateral diameter of the straight or falcine sinus at its shortest point[a]

Straight or Falcine Sinus Diameter (mm)	Probability of NAR	95% CI
0	4%	1%–30%
1	8%	2%–38%
2	14%	3%–44%
3	24%	8%–52%
4	38%	18%–60%
5	53%	33%–72%
6	68%	49%–83%
7	80%	60%–92%
8	88%	69%–96%
9	93%	75%–98%
10	96%	80%–99%
11	98%	84%–99%
12	99%	87%–99%
13	100%	90%–100%

[a] Probabilities determined by logistic regression, where straight or falcine sinus diameter on MR imaging was identified as a multivariable predictor of clinical outcome (AUC = 0.89, $P < .001$).

risk factor for poor clinical prognosis, but we found making standardized assessments of middle cerebral artery branches in the Sylvian fissure to be very challenging, largely due to variable fetal positioning.

Quisling and Mickle[15] performed transtorcular venous pressure measurements on a small cohort of patients. They found that patients with an enlarged straight or falcine sinus trended toward increased venous pressures. Additionally, 1 patient presented with a normal straight sinus and normal pressure; but across time, the straight sinus dilated and repeat measurement found elevated pressure. The relationship between straight or falcine sinus dilation and venous pressure is difficult to prove on the basis of that small study but does represent an interesting direction for further research.

The major limitation in this study is the small sample size (in keeping with the rarity of VOGM), along with incomplete measurements in some cases due to either image quality or lack of relevant MR imaging sequences. Even with these limitations, our central finding was quite robust.

CONCLUSIONS

We identified vascular anatomic characteristics on neonatal and fetal MR imaging that strongly predicted clinical outcome. Specifically, while the caliber of many arterial and venous structures statistically differed between the NAR and IT cohorts, the most robust differentiator was the width (mediolateral) and area of the straight or falcine sinus measured at the point of its shortest height (ie, the point of greatest constriction to flow return to the systemic circulation). This measurement clearly and unambiguously differentiated between high- and low-risk cohorts. The ability to accurately predict clinical evolution after birth based on fetal MR imaging can be of help for both caregivers and families, enabling better preparedness for urgent treatment and better planning for allocation of resources. Additionally, fetal patients who are very likely to evolve to NAR represent an appropriate cohort for novel therapeutic approaches.

REFERENCES

1. Recinos PF, Rahmathulla G, Pearl M, et al. **Vein of Galen malformations: epidemiology, clinical presentations, management.** *Neurosurg Clin N Am* 2012;23:165–77 CrossRef Medline
2. Raybaud CA, Strother CM, Hald JK. **Aneurysms of the vein of Galen: embryonic considerations and anatomical features relating to the pathogenesis of the malformation.** *Neuroradiology* 1989;31:109–28 CrossRef Medline
3. Bhattacharya JJ, Thammaroj J. **Vein of Galen malformations.** *J Neurol Neurosurg Psychiatry* 2003;74(Suppl 1):i42–44 CrossRef Medline
4. Brinjikji W, Krings T, Murad MH, et al. **Endovascular treatment of vein of Galen malformations: a systematic review and meta-analysis.** *AJNR Am J Neuroradiol* 2017;38:2308–14 CrossRef Medline
5. Yan J, Wen J, Gopaul R, et al. **Outcome and complications of endovascular embolization for vein of Galen malformations: a systematic review and meta-analysis.** *J Neurosurg* 2015;123:872–90 CrossRef Medline
6. Deloison B, Chalouhi GE, Sonigo P, et al. **Hidden mortality of prenatally diagnosed vein of Galen aneurysmal malformation: retrospective study and review of the literature.** *Ultrasound Obstet Gynecol* 2012;40:652–58 CrossRef Medline
7. Lecce F, Robertson F, Rennie A, et al. **Cross-sectional study of a United Kingdom cohort of neonatal vein of Galen malformation.** *Ann Neurol* 2018;84:547–55 CrossRef Medline
8. Gopalan V, Rennie A, Robertson F, et al. **Presentation, course, and outcome of postneonatal presentations of vein of Galen malformation: a large, single-institution case series.** *Dev Med Child Neurol* 2018;60:424–29 CrossRef Medline
9. Staffa SJ, Zurakowski D. **Strategies in adjusting for multiple comparisons: a primer for pediatric surgeons.** *J Pediatr Surg* 2020 Jan 23. [Epub ahead of print] CrossRef Medline
10. Alvarez H, Garcia Monaco R, Rodesch G, et al. **Vein of Galen aneurysmal malformations.** *Neuroimaging Clin N Am* 2007;17:189–206 CrossRef Medline
11. Lasjaunias PL, Chng SM, Sachet M, et al. **The management of vein of Galen aneurysmal malformations.** *Neurosurgery* 2006;59:(Suppl 3)S184–94; discussion S3–13 CrossRef Medline
12. Paladini D, Deloison B, Rossi A, et al. **Vein of Galen aneurysmal malformation (VGAM) in the fetus: retrospective analysis of perinatal prognostic indicators in a two-center series of 49 cases.** *Ultrasound Obstet Gynecol* 2017;50:192–99 CrossRef Medline
13. Yuval Y, Lerner A, Lipitz S, et al. **Prenatal diagnosis of vein of Galen aneurysmal malformation: report of two cases with proposal for prognostic indices.** *Prenat Diagn* 1997;17:972–77 Medline
14. Saliou G, Vraka I, Teglas JP, et al. **Pseudofeeders on fetal magnetic resonance imaging predict outcome in vein of Galen malformations.** *Ann Neurol* 2017;81:278–86 CrossRef Medline
15. Quisling RG, Mickle JP. **Venous pressure measurements in vein of Galen aneurysms.** *AJNR Am J Neuroradiol* 1989;10:411–17 Medline

Counterpoint: Conventional Fluoroscopy-Guided Selective Cervical Nerve Root Block—A Safe, Effective, and Efficient Modality in the Hands of an Experienced Proceduralist

F.W. Ott, R. Pluhm, K. Ozturk, A.M. McKinney, and J.B. Rykken

ABSTRACT

BACKGROUND AND PURPOSE: The conventional fluoroscopy-guided (CF) selective cervical nerve root block (SCNRB) is being used commonly as a treatment for cervical radicular pain as well as a diagnostic tool. This study aimed to identify any major complications and determine the safety and clinical utility of CF-SCNRB performed in a university hospital and associated outpatient clinics.

MATERIALS AND METHODS: Two-hundred fifty-four conventional fluoroscopy-guided selective cervical nerve root blocks were retrospectively identified from 2011 to 2018 using a radiology report search tool. Each procedure was performed by an experienced neuroradiologist performing spinal injections on a full-time basis in clinical practice. A 10-point pain scale was used for pre- and postprocedural pain-level assessment. Successful conventional, fluoroscopy-guided, selective cervical nerve root block was defined as a patient-reported pain scale reduction of at least 50% and/or alleviation of numbness or paresthesia at ≥2 weeks postinjection. All clinically important immediate and delayed complications were also recorded.

RESULTS: Two-hundred fifty-four conventional fluoroscopy-guided selective cervical nerve root blocks were performed via an anterolateral approach with an average fluoroscopy time of 24.3 seconds for all cases. There were no aborted procedures and no major or permanent complications. There were 14 minor complications; 12 of these were periprocedural and resolved by the 2-week follow-up visit. One-hundred eighty-five patients (75.2%) reported pain improvement of >50% from baseline at 15 minutes postinjection. Overall, 172 patients (67.7%) reported >50% pain scale reduction or alleviation from paresthesia at least 2 weeks postinjection.

CONCLUSIONS: Conventional fluoroscopy-guided selective cervical nerve root block is an efficacious, efficient, and safe outpatient procedure when performed by a skilled and experienced proceduralist.

ABBREVIATIONS: CF = conventional fluoroscopy; CT/F = CT fluoroscopy; SCNRB = selective cervical nerve root block

Patients experiencing cervical and radicular arm pain, numbness, and paresthesia secondary to foraminal narrowing or impingement and resultant inflammation of the cervical nerve root may be treated with a transforaminal steroid cervical nerve root block.[1,2] Selective cervical nerve root block (SCNRB) with imaging guidance, with either conventional fluoroscopy (CF) or CT, is an intervention that has been proved effective for many patients by alleviating pain, increasing activity, improving tolerance of physical therapy, and delaying or preventing surgical intervention.[1,3,4] This procedure involves the introduction of a needle near or into the neural foraminal perineural space, inherently carrying the risk of arterial, nerve root, and spinal cord injury.[1,4-7]

Currently, CF and CT-guided SCNRBs are the most commonly available and established methods, with a trend in recent literature suggesting that CT-guided nerve blocks allow improved safety and efficacy by way of better needle tip awareness, direct visualization of the perineural space, and visualization of the vertebral and radicular arteries when using a transforaminal approach.[2,7,8] However, CT-guided SCNRB may deliver a larger radiation dose to both the patient and proceduralist,[9] with CT fluoroscopy (CT/F) reported to have an increase in the incurred radiation dose over CF by 19-fold in the cervical region (an increase of the incremental dose of 49 uSv).[10] CT guidance is also more costly,[11] may have longer procedural times,[2] and limits real-time assessment of intravascular invasion.[3,4,8] Although sparse, current literature on SCNRB reports various differences in techniques via imaging medium, approach,

Received January 30, 2020; accepted after revision April 7.

From the Department of Radiology, University of Minnesota, Minneapolis, Minnesota.

Please address correspondence to Frederick W. Ott, MD, University of Minnesota Medical School, M Health Fairview, M Health Fairview Maple Grove Medical Center, 420 Delaware St SE B226, Mayo Memorial Building MMC 292, Minneapolis, MN 55455; e-mail: ottxx014@umn.edu

http://dx.doi.org/10.3174/ajnr.A6580

and needle placement. While there are proponents of different techniques and modalities, most proceduralists have developed small variations that make their approach consistent and what they believe will be efficacious and safe. The authors propose that a meticulous and consistently reproducible technique and proceduralist experience are major contributors to safe and effective SCNRB.

Although relatively rare, numerous reports of complications secondary to CF and CT-guided SCNRB exist, ranging from transient arm numbness to spinal cord infarction, nerve palsies and injury, arterial injury, respiratory arrest, and death.[1,4-8,12-14] While these complications have been reported in both CF- and CT-guided cases, a direct comparison of complication rates between the modalities has not been performed in a single study, to our knowledge. While injection success criteria vary from study to study, rates of patient-reported efficacy appear to be similar between CT and CF, with CT-guided efficacy rates ranging from 60% to 70.3%,[15-17] and CF-guided efficacy rates of 47%–63%.[3,18,19] Thus, the authors posit that the safety of either methodology is based on the use of a meticulous technique by an experienced proceduralist, and both imaging modalities are equally safe and effective in multiple settings on a rather consistent basis with reports of severe complications being scattered among both CT and CF-guided cases. The above warrants weighing the perceived advantages of CT against its pitfalls versus our experience of the safety and efficacy using CF. The purpose of this study was to assess the efficacy, identify any major complications, and evaluate the rate of minor complications from CF-guided SCNRB performed in a tertiary care university hospital and associated outpatient clinics.

MATERIALS AND METHODS

Data Source

Institutional review board approval was obtained from the University of Minnesota for this study. A retrospective analysis using the radiology information system/PACS, the electronic medical record, and the Vitrea Intelligence search tool (Vital Images, a subsidiary of Canon Group) allowed searching selected imaging reports using desired keywords. All procedures performed were in accordance with the ethical standards of the institutional research committee and with the 2013 revised Helsinki declaration and its later amendments or comparable ethical standards.

Inclusion and Exclusion Criteria

After searching the data base using the radiology information system/PACS search tool for cervical nerve root injection cases, all patients who received a CF-SCNRB from 2011 to 2018 were collected. All patients with a procedural report and postprocedural follow-up clinic visit of >2 weeks postinjection were included. Each procedure was performed by a single experienced neuroradiologist actively performing spinal injections on a full-time basis in clinical practice. Patients with injections lacking a comparative pre- and postprocedural patient-reported pain scale or postprocedural clinical follow-up at >2 weeks after SCNRB indicating nerve root block efficacy were excluded. For this study, a successful SCNRB was defined as a patient-reported pain scale reduction of at least 50% and/or alleviation of numbness or paresthesia at ≥2 weeks postinjection. The definition of pain reduction was selected as an objective metric to reflect a cutoff for what is thought to constitute adequate pain relief, and this pain reduction metric has been used previously.[16]

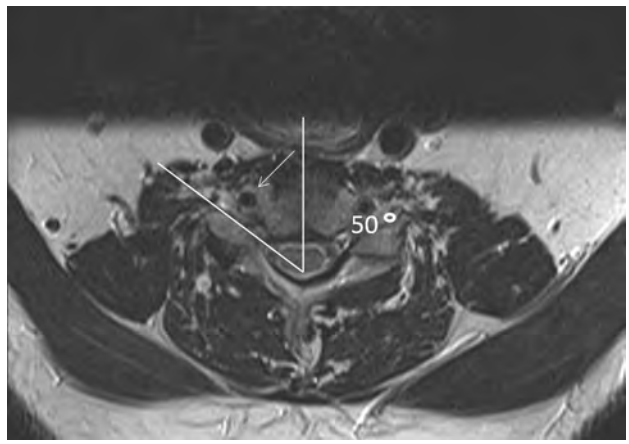

FIG 1. The foraminal angle is 50°. *White arrow* demonstrates the vertebral artery.

Author Technique

There are many ways to perform SCNRB. The technique described herein is naturally based on the premise of safety first, but also with a requirement of efficiency, given our busy spine injection service with procedural time slots scheduled for 30 minutes. As a word of caution, SCNRBs should not be performed until the proceduralist has performed a large number of lumbar transforaminal epidural/nerve root injections and is confident and comfortable steering a spinal needle into a 1- to 2-mm space. At the participating institution, all patients undergoing SCNRB must have undergone either cervical spine MR imaging, a CT angiogram of the neck, or contrast-enhanced CT of the neck within 2 years before the procedure so that the location of the vertebral artery within the neural foramen can be identified. The vertebral artery should be located in an anterior position in the neural foramen so that the spinal needle can be safely placed posteroinferiorly. The exact angle of the neural foramen is then measured at the desired level (Fig 1) on the available cross-sectional study. Verbal and written consent is obtained from the patient, including statements of the risks of bleeding, infection, nerve root injury, vertebral or carotid artery injury, cord infarct, and stroke. The patient is then positioned at approximately a 45° angle with a wedge-shaped sponge behind the back on the fluoroscopy table with the desired side of the neck for the planned injection facing upward (Fig 2*A*). This position requires maintaining the patient's spine in a relatively straight line so that the measured angle can be accurately reproduced at the desired level. In some cases, the patient may be positioned supine. While the supine position arguably eases the ability to maintain the spine in a straight line, it is somewhat more challenging for the proceduralist because the image intensifier will be partially in the path of access to the patient's neck, thus necessitating a table and C-arm that can be raised in unison to get the patient positioned so the proceduralist can comfortably stand (or sit on a stool) with the patient's neck at about eye level (Fig 2*B*).

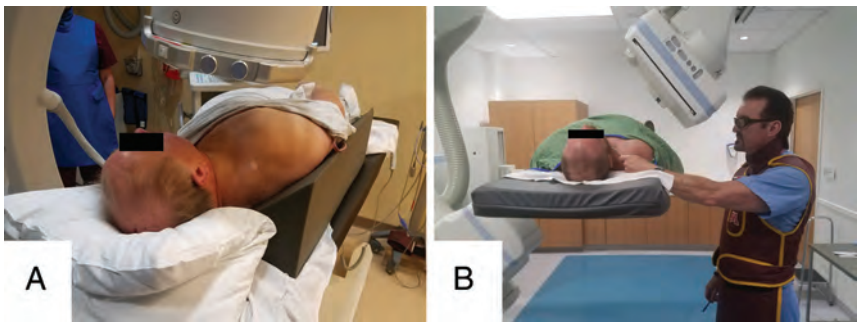

FIG 2. *A*, Patient positioned obliquely on a 45° wedge for right-sided injection. *B*, The patient positioned supine for right-sided injection with the proceduralist using fluoroscopy to position the clamp before marking the skin. Table and C-arm are raised to eye-level to facilitate proceduralist visualization during the procedure.

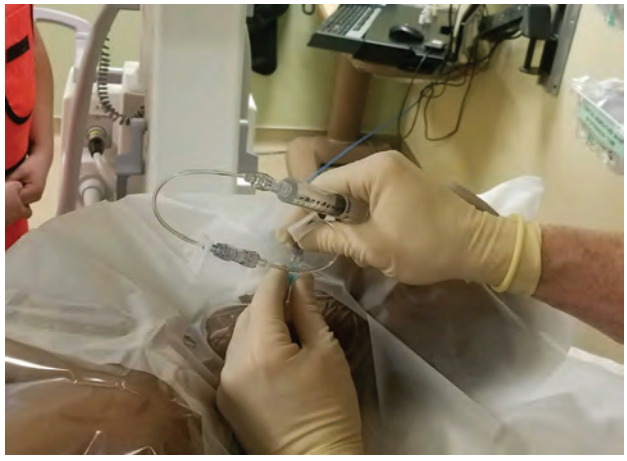

FIG 3. Contrast syringe connected via 2 short, low-volume tubing to the hub of the 25-ga spinal needle. The patient is positioned for a left-sided injection.

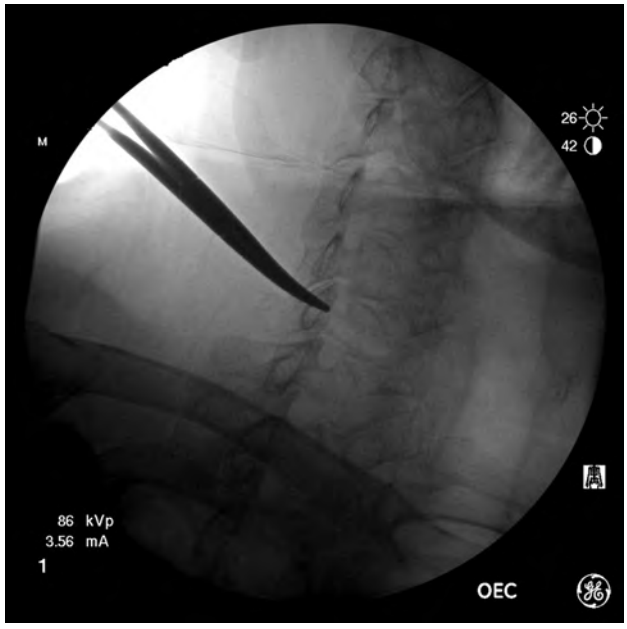

FIG 4. Curved clamp tip placed gently on the skin overlying the posterior-inferior aspect of neural foramen for optimal location, taking care to avoid indenting the skin surface.

For either approach, the straight anterior-posterior position should first be obtained with the image intensifier. If the patient is positioned on a wedge-shaped sponge, the C-arm would be positioned at approximately 45° and then adjusted so that the spinous processes are centered between the lateral masses. The anterior-posterior position in the supine position should be at about 0°. From this position, the C-arm is then rotated to the measured angle of the foramen. When the 45° sponge position is used, the proceduralist should stand behind the patient. With the supine position, the patient should be positioned so that the affected side can be visualized with the C-arm rotated toward the proceduralist and the range of motion adequate for the C-arm to reproduce the desired foraminal angle from the anterior-posterior position. For either method, the patient will be positioned on the table 180° in a different direction for a right- versus left-sided injection (Figs 2 and 3, respectively).

The level of the desired neural foramen is then determined by counting down from C2. A curved Kelly clamp is then lightly positioned on the skin so that the tip is at the posterior-inferior aspect of the neural foramen (Fig 4). Notably, if the clamp is pressed too firmly against the skin, then the mark will not be representative of the desired location once the skin has recoiled. The skin is then marked with a felt tip writing instrument. The neck is then sterilely prepped and draped. The skin and deeper tissues are then anesthetized with 1% lidocaine using a 5-mL syringe and a 1.5-inch 25-ga needle. The 2-inch needle is not used because with many patients, the tip of the needle could reach the neural foramen and potentially the vertebral artery. The syringe is aligned parallel to the x-ray beam, and the needle is advanced all the way in. After test aspiration, the needle is slowly withdrawn and 1% lidocaine is infiltrated as the needle is backed out, leaving a small wheal on the skin. After rechecking the skin mark with a sterile clamp, either a 2- or a 3.5-inch 25-ga spinal needle with the stylet in place is advanced, while checking the needle position along the way with fluoroscopy (Fig 5). The 2-inch needle is preferred for improved control during the approach, but patients with a thicker neck require the 3.5-inch needle. The neural foramina are not very deep to the skin in the cervical spine in most patients of normal body mass index, so it is prudent to check the anterior-posterior position fairly soon to judge the distance to the lateral mass.

Some proceduralists may aim at the superior articular facet, and once the bone is hit, the needle is moved anteriorly into the posterior aspect of the neural foramen. We prefer to not use this method because hitting the nonanesthetized periosteum is painful and can cause the patient to startle and move, potentially advancing the needle inadvertently. Additionally, the needle may skim along the anterior surface of the superior articular facet and enter and even pass through the neural foramen, potentially causing injury to the cord. The needle should be advanced to the edge

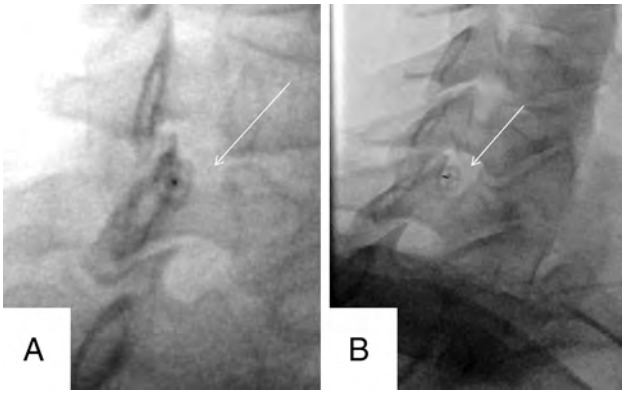

FIG 5. Ideal needle position in the posterior-inferior corner of the neural foramen (*A*, *arrow*) and acceptable needle position (*B*, *arrow*).

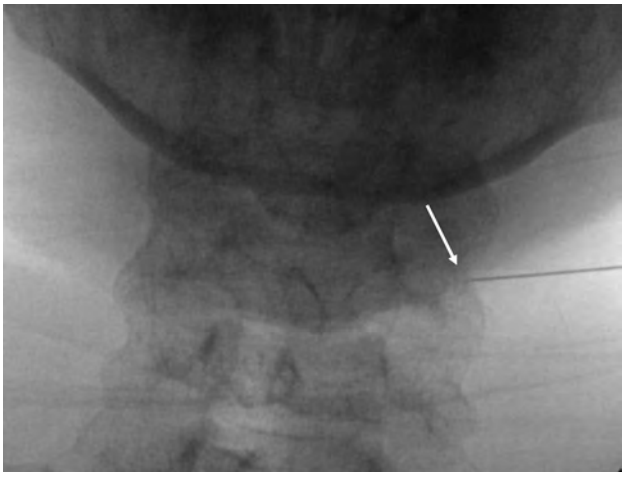

FIG 6. Needle tip advanced to the edge of the lateral mass on the anterior-posterior projection (*arrow*).

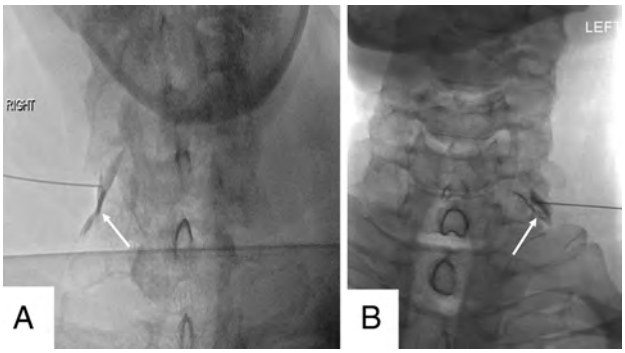

FIG 7. Contrast in the perineural space along the right C6 nerve root (*A*, *arrow*) and clearly outlining the left C7 nerve root (*B*, *arrow*). Either result is acceptable.

of the lateral mass (on the anterior-posterior image) and no deeper than a few millimeters past this point (Fig 6). At this point, after removing the stylet, 2 short low-volume extension tubing (approximately 0.15 mL each) connected in tandem and connected to the syringe containing nonionic contrast are then attached to the hub of the 25-ga spinal needle (Fig 3). While the operator steps on the fluoroscopy pedal, a small amount of

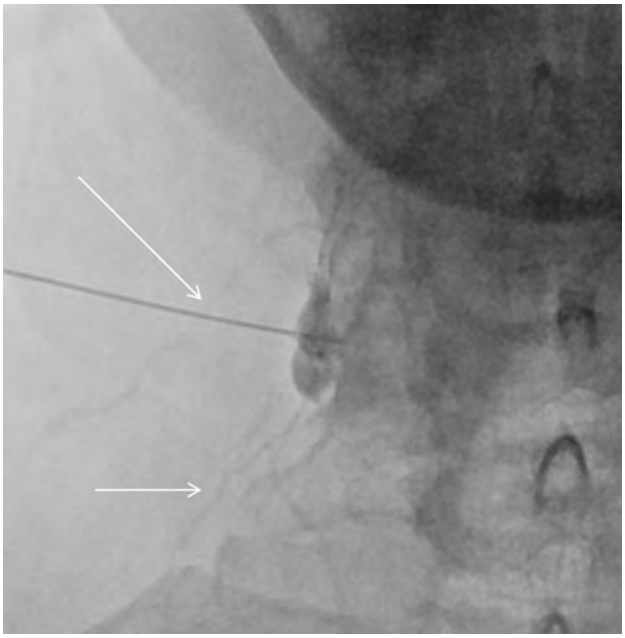

FIG 8. Vascular filling demonstrated during live injection (*arrows*) requiring needle repositioning.

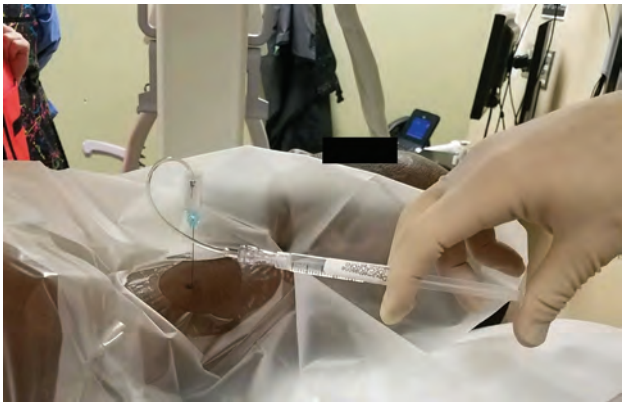

FIG 9. Syringe containing 1 mL of dexamethasone, 10 mg/mL; 1 mL of 1% lidocaine; and a small amount of air connected to the remaining tubing segment closest to the hub. The syringe should be held so that the air floats anti-dependently during the injection, not horizontally as shown in this picture, which was taken before injection.

contrast is injected to outline the nerve root (Fig 7). The injection should be performed under "live" fluoroscopy to assess possible vascular filling (Fig 8). This could be missed if the contrast is injected and then the fluoroscopy activated. This is a distinct advantage of using CF over CT, permitting a large FOV while observing a live or real-time injection. This same degree of visualization is not readily achievable with CT or CT/F, particularly of import above and below the FOV with CT.

From this author's experience, advancing the needle further into the foramen only increases the chance of encountering a vessel, which requires repositioning the needle and is unnecessary to improve efficacy. Once the nerve root is outlined with contrast and there is no vascular filling, the tandem tubing is separated in the middle leaving 1 segment of tubing connected to the hub of

Table 1: Patient demographics

Study Population	Male	Female
Average age (yr)	51.5	50.2
No.	123	131
Percentage	48.4%	51.6%

Table 2: Levels of SCNRBs

Level of Injection	No. of Patients
C4	9
C5	25
C6	115
C7	76
C8	29

the needle (rather than disconnecting the tubing from the hub of the needle, which could potentially change the needle tip position during manipulation). A syringe containing 1 mL of 10 mg/mL dexamethasone, 1 mL of 1% lidocaine, and a small amount of air is connected to the tubing segment that remains attached to the needle hub (Fig 9). After a brief test aspiration, the dexamethasone and lidocaine mixture is slowly injected. The tandem tubing is used in this fashion to minimize the chance of needle displacement when changing syringes, which could be disastrous. In addition, using 2 tubing portions connected in tandem allows an increased distance between the proceduralist's hand and the x-ray beam during the live contrast injection. A small amount of air is kept in the syringe with the medication, held such that the air floats anti-dependently as the medication is injected. As the final amount of medication enters the tubing, it is followed by the air kept anti-dependently in the syringe until the medication gets to the hub of the needle. At this point, the injection is completed, and the needle, still connected to the tubing and syringe, is removed. With this technique, no air is injected into the patient. Even then, if it were injected, it would merely be deposited in the perineural space and eventually resorbed. Dexamethasone is used as the steroid of choice because it is a solution rather than a suspension of particles, decreasing the chance of occluding end capillaries in the brain and spinal cord. It has been shown that direct injection of dexamethasone solution into the vertebral artery of pigs produced no serious sequelae, whereas injecting particulate corticosteroids produced serious neurologic changes and infarction requiring ventilator support.[20]

After the procedure, the patient is assessed for any adverse reactions and then observed for 15 minutes before discharge. A 10-point pain scale is used for pre- and postprocedural pain-level assessment. Notably, these procedures are performed without the patient under conscious sedation. This helps minimize the patient's time at the facility, avoids the risk of sedation, permits quick feedback during the procedure, and allows more rapid identification of any complications.

RESULTS

All 254 injections were technically successful and without permanent adverse sequelae. Of the 254 cases, 131 patients were women and 123 men (Table 1). The average ages of men and women included in the study were 51.5 and 50.2 years, respectively (Table 1).

There were 9 injections at C4, twenty-five at C5, one hundred fifteen at C6, seventy-six at C7, and 29 at C8 (Table 2). The average fluoroscopy time for all cases was 24.3 seconds. Three patients reported a brief vasovagal reaction following the injection, all of whom achieved resolution of symptoms within a few minutes postinjection with conservative measures such as flat positioning and oral fluids. Another patient (right C6 nerve root blockade) had transient pseudo-Horner syndrome with self-reported right-sided blurry vision as well as right-sided ptosis and a constricted pupil. This patient's symptoms resolved within 30 minutes of injection, and with clinical evaluation, she was diagnosed with anesthetic-related sympathetic blockade due to inadvertent epidural extension of the injection with resultant anesthetization of the C8–T2 nerve roots as they traversed the epidural space on their way to the neural foramina. Two more patients reported diffuse headaches days after the procedure that each attributed to the cervical nerve root blockade. Both patients reported resolution at their next follow-up.

There were no aborted procedures and no major or permanent complications, which would include cerebral, cerebellar, brain stem, or spinal cord infarction, permanent nerve injury, and death. Of note, transient arm numbness was not included as an untoward effect because it is expected when exposing cervical nerve roots to a lidocaine-containing mixture.

There were 14 events reflecting minor complications, potential complications, or adverse effects (Table 3). Twelve (4.7%) patients had transient minor adverse reactions to the injection, while 2 (0.8%) reported delayed minor adverse reactions, which also resolved by 2 weeks at follow-up. Of the 254 patients questioned at the 15-minute interval, 8 reported a mild increase from their usual pain in a familiar distribution. Of these, all 8 had resolution of that pain at the 2-week follow-up.

One hundred eighty-five patients (75.2%) reported pain improvement of >50% from baseline at 15 minutes postinjection, while 61 patients (24.8%) reported a reduction of <50% from baseline pain at 15 minutes. For the improved-pain group, the average pain score preinjection was 4.7/10 before injection and 0.7/10 at 15 minutes postinjection, while the nonimproved group averaged a preinjection pain score of 5.2/10 and a postinjection score of 4.4/10.

Of the 185 patients with >50% pain reduction reported at 15 minutes postinjection, 139 (75.1%) reported maintenance of meaningful pain reduction below their baseline at the 2-week follow-up. Forty-six (24.9%) of the 185 patients with an adequate response at 15 minutes postinjection reported that their pain had returned to baseline at 2 weeks.

Of the 61 patients with <50% pain reduction reported at 15 minutes postinjection, 26 (42.6%) reported meaningful pain reduction below their baseline at the 2-week follow-up. Thirty-five (57.4%) of the 61 patients with an inadequate response at 15 minutes postinjection reported that their pain had remained unimproved at 2 weeks. Seven of the 8 patients (87.5%) with radiculopathy without pain also reported resolution of their symptoms 2 weeks postinjection (Table 3 and Fig 10). Overall, 172 of the 254 patients (67.7%) reported >50% pain scale reduction or alleviation from paresthesia at least 2 weeks postinjection.

Table 3: Pre- and postprocedural pain level assessment[a]

	No. of Patients
Primary outcomes	
>50% pain relief at 15 min	185 (75.2%)
<50% pain relief at 15 min	61 (24.8%)
>50% pain reduction from baseline at 2 wk	165 (67.1%)
<50% pain reduction from baseline at 2 wk	81 (32.9%)
No preprocedural pain (patient-reported numbness or paresthesia)	8 (3.1%)
Alleviation of preprocedural numbness or paresthesia at 2 wk	7 of 8 (87.5%)
Minor adverse reactions or events	
Vasovagal reaction	3 (1.2%)
Transient pseudo-Horner syndrome (sympathetic blockade)	1 (0.4%)
New onset of diffuse headache	2 (0.8%)
Increase in usual pain in a familiar distribution	8 (3.1%)

[a] Transient arm numbness postinjection was not included as an untoward effect because it is expected when exposing cervical nerve roots to a lidocaine containing mixture.

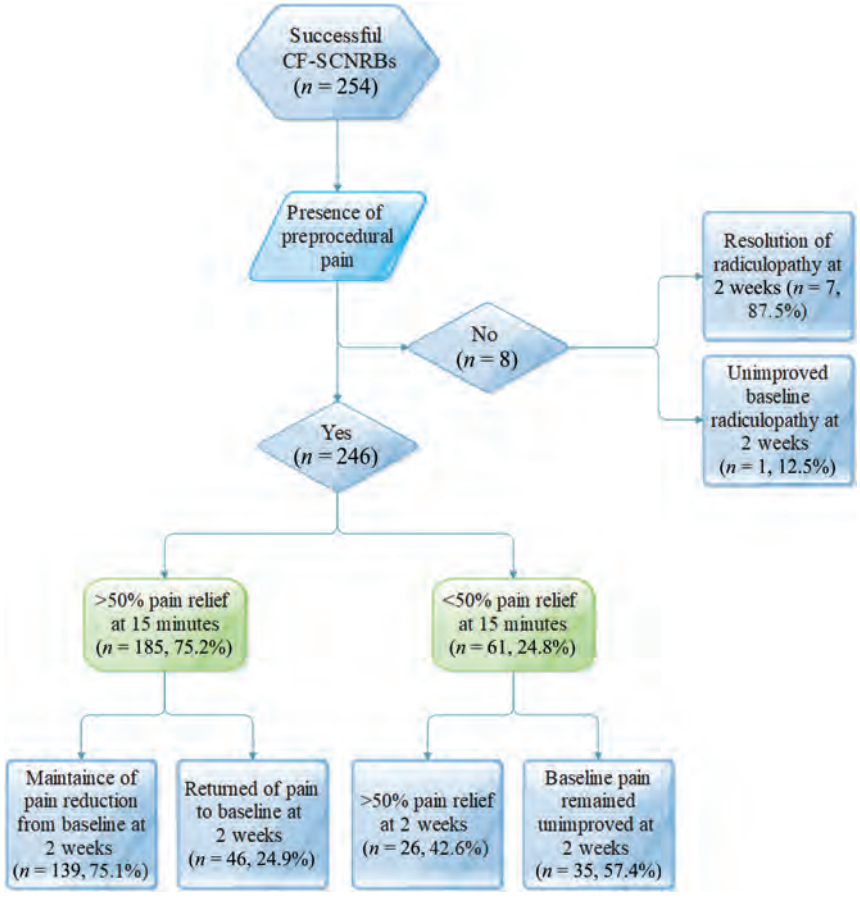

FIG 10. Flow chart demonstrates the effectiveness of CF-SCNRB with regard to postprocedural pain assessment at 15 minutes and 2 weeks.

Table 4: Radiation exposure based on time[a]

Approximate Corresponding Radiation Incurred	
CT-guided average effective dose	0.36 ± 0.41 mSv
CF average fluoroscopy time of 24.3 sec	0.17 mSv

[a] Average CT-guided effective dose was calculated from dose-length product values reported by Lazarus et al[11] over 228 SCNRB cases using a conversion factor of 5.4 uSv/mGy × cm for cervical spine examinations developed by Huda et al.[21] CF radiation dose is referenced and extrapolated from a direct comparison by Schmid et al[27] using an Alderson Rando phantom.

All fluoroscopy times for CF-SCNRB were recorded at under 2 minutes, with a range of 7–78 seconds. The fluoroscopy time averaged 24.3 seconds per procedure, and radiation exposure based on the time is shown in Table 4 and compared with an average effective dose for CT-guided interventions in a study by Lazarus et al[11] using a conversion factor developed by Huda et al.[21]

DISCUSSION

This investigation supports the supposition that CF-SCNRBs, when performed by an experienced provider and with meticulous technique, are equivalent in safety and efficacy compared with existing CT-SCNRB publications. First, no major complications occurred, and there was a minor complication rate (5.5%) comparable with the CF rate (5.3%) of Pobiel et al[3] and with a CT-guided series (4%).[22] Slight variations of postinjection minor complication rates between our study and existing publications could be explained by different definitions of what is considered an expected or adverse reaction (eg, including-versus-excluding increased radicular pain).[23] Our expected symptoms including mild injection site pain, lightheadedness on standing, and transient numbness in an expected distribution, are similar to those in other publications with minor adverse event rates.[3,15,22,23] Hence, the authors of this study opine that the lack of major complications and comparative minor adverse event rates in this study are products of meticulous adherence to a proved technique performed by an experienced neuroradiologist.

The use of a nonparticulate steroid likely also plays a role in the safety of our technique. A review of complications during cervical nerve root injections by Scanlon et al[5] supports an embolic mechanism possibly being the most common cause of major complications, with an inadvertent intra-arterial injection of particulate steroid causing a distal infarct. The ability to fully assess real-time intravascular invasion paired with the use of a nonparticulate steroid, in our experience, renders CF guidance along with a dexamethasone-based injection mixture the safest and most efficient option. Bartleson and Maus[24] reported that with the acquisition of a

preprocedural imaging study such as MR imaging or CT angiography, appropriate anatomic understanding of each patient could be achieved, especially the location of the vertebral artery in the neural foramen. Pobiel et al[3] also discussed how real-time visualization of the contrast injection with CF is more advantageous in preventing accidental arterial injection than increased anatomic visualization during needle tip guidance via CT. This is also recommended by others including Palmer[25] and accentuated by the presentation by Hodler et al[4] of 2 cases with the disastrous complication of tetraplegia secondary to ischemic myelopathy during procedures performed under CT guidance. We do not use DSA to assess vascular filling, and it has been recently reported that the detection rate of intravascular injection during real-time fluoroscopy shows no statistical difference compared with the detection rate during DSA when performing SCNRB.[26]

This study demonstrated that CF-SCNRB could be as effective as CT-SCNRB if performed correctly. We believe our criteria for adequate pain reduction were stringent, with a minimum of 50% patient-reported decrease in usual pain or continued alleviation of radiculopathy and paresthesia at a follow-up clinic visit after at least 2 weeks to be considered successful. This metric has been used as a fair indication of significant pain relief previously,[16] potentially aiding rehabilitation and hopefully avoiding the need for surgical intervention. At ≥2 weeks, 172 of 254 patients (67.7%) reported a >50% reduction in usual pain or complete alleviation of paresthesia in this study. In comparison with the success rates found in the existing CT-SCNRB series, our efficacy rate was favorable.[15-17]

A study in 2014 found that CT/F-guided SCNRB increased the incurred radiation dose up to 19-fold in the cervical region and 8.0-fold in the lumbar region (incremental doses of 49 and 140 mSv, respectively) relative to CF.[10] Another disadvantage of CT guidance is added cost to the patient.[11,25] CT guidance has been reported as approximately 0.9 relative value units higher than CF (3.32 for CT for therapy guidance versus 2.41 for CF-guided spinal injection).[11] With safety and efficacy equivalence, this study suggests that CF is the more practical technique by way of potentially reduced procedural times and radiation exposure for both the patient and the proceduralist.[11,21,25,27]

Nevertheless, there is a recent publication by Dietrich et al[28] that suggests that radiation exposure for the proceduralist may be higher with CF than with CT/F-guided lumbar procedures. However, the authors indicated that during most CT/F acquisitions, the proceduralist is positioned behind the side of the gantry, while during most acquisitions with CF guidance, the operator is directly adjacent to the patient. The authors state that "fluroscopy-guided lumbar spine injections necessitate real-time manual guidance and manipulation of the needles; thus, the body, wrist, and hand of the interventionalist is[sic] exposed to scattered radiation due to the proximity of the primary x-ray beam."[28] That seems to indicate that the proceduralist was actively using fluoroscopy while guiding the needle and a "plastic forceps" was used to keep his or her hand out of the beam. With our technique, we do not use live fluoroscopy while steering the needle; rather, we triangulate, advance the needle, and then check the needle position by tapping the fluroscopy pedal. As a consequence, we are uncertain as to whether their study design applies to our technique. The only real-time exposure in our technique would be during contrast injection, which we strongly recommend. This study also reports a higher dose to the patient during CT versus CF guidance for lumbar transforaminal injections, at 0.33 ± 0.1 and 0.24 ± 0.22 mSv, respectively. Although these data are from lumbar injections and cervical injections may yield higher differential exposures, this is a significantly smaller difference than had been previously stated, which is likely due to use of newer low-dose CT applications.

Although a procedural time advantage with CF has been reported, to our knowledge, there is no study that directly compares CT-guided procedural times with CF procedural times. With the wide availability of CT/F, especially for the highly skilled proceduralists frequently performing these injections, and presuming conservative use of fluoroscopy, a significant procedural time advantage using CF guidance seems unlikely, though this may be worthy of further investigation.

There are certain limitations to our study design. The retrospective nature of this study relies heavily on the accuracy of consultation and procedural notes, as well as appropriate patient reporting of events surrounding and at the time of injection. Although we are confident that a major complication as a result of an injection would be made known to our department, it is conceivable that additional minor complications occurred that were not properly reported by patients or recorded in consultation or procedural notes. Notably, the injection levels in this patient population are generally in the mid and lower cervical spine. Thus, applying the same generalization regarding safety to upper cervical nerve root injections should be made with caution. Also, the efficacy of our injections did not account for a vertebral level or classification of the severity of foraminal stenosis, which may be a useful area of study in the future. Last, because the injections in this study were performed by a single proceduralist, further evaluation of safety using data from injections performed by multiple proceduralists using the same technique would be of interest.

The efficacy rate in this study is similar to that of CT-guided SCNRB. This finding combined with the small percentage of minor adverse events and the efficiency of our methodology render CF a viable option for SCNRB. Recent reports in the literature suggest that CT guidance provides better visualization of anatomic landmarks relative to the needle tip, which arguably reduces the risk of major complications; however, catastrophic neurovascular complications during CT-guided SCNRB injections have occurred. In any event, the reports of major neurovascular complications for either CF or CT guidance are extremely rare and a sufficiently powered prospective study comparing major complication rates between modalities would likely not be possible. To date, using this technique, which has been routinely repeated by 2 additional neuroradiologists in our group, we have yet to encounter a major complication in our own practice.

CONCLUSIONS

Whether using CF or CT guidance for cervical nerve root injections, there is a low incidence of minor complications (4%–6%) and serious complications are exceedingly rare, given the large number of these procedures performed annually. This study confirms that CF is as safe and effective as CT for the guidance of SCNRB when

using a meticulous technique and a nonparticulate steroid and performed by an experienced and skilled proceduralist. The lack of meaningful superiority in these areas by existing CT-guided datasets in conjunction with the increased patient radiation exposure and cost to the patient inherent in CT makes CF the favorable technique in our practice.

REFERENCES

1. Rozin L, Rozin R, Koehler SA, et al. **Death during transforaminal epidural steroid nerve root block (C7) due to perforation of the left vertebral artery.** *Am J Forensic Med Pathol* 2003;24:351–55 CrossRef Medline
2. Wolter T, Mohadjer M, Berlis A, et al. **Cervical CT-guided, selective nerve root blocks: improved safety by a dorsal approach.** *AJNR Am J Neuroradiol* 2009;30:336–37 CrossRef Medline
3. Pobiel RS, Schellhas KP, Eklund JA, et al. **Selective cervical nerve root blockade: prospective study of immediate and longer term complications.** *AJNR Am J Neuroradiol* 2009;30:507–11 CrossRef Medline
4. Hodler J, Boos N, Schubert M. **Must we discontinue selective cervical nerve root blocks? Report of two cases and review of the literature.** *Eur Spine J* 2013;22(Suppl 3):466–70 CrossRef Medline
5. Scanlon GC, Moeller-Bertram T, Romanowsky SM, et al. **Cervical transforaminal epidural steroid injections: more dangerous than we think?** *Spine (Phila Pa 1976)* 2007;32:1249–56 CrossRef Medline
6. Brouwers PJ, Kottink EJ, Simon MA, et al. **A cervical anterior spinal artery syndrome after diagnostic blockade of the right C6-nerve root.** *Pain* 2001;91:397–99 CrossRef Medline
7. Chang MC. **Spinal cord injury by direct damage during CT-guided C7 transforaminal epidural steroid injection.** *Am J Phys Med Rehabil* 2018;97:e62–64 CrossRef Medline
8. Keir A, Pandey UC, Cheri T, et al. **Respiratory arrest following CT guided selective cervical nerve root injection.** *Crit Care Shock* 2018;21:99–102
9. Nawfel RD, Judy PF, Silverman SG, et al. **Patient and personnel exposure during CT fluoroscopy-guided interventional procedures.** *Radiology* 2000;216:180–84 CrossRef Medline
10. Maus T, Schueler BA, Leng S, et al. **Radiation dose incurred in the exclusion of vascular filling in transforaminal epidural steroid injections: fluoroscopy, digital subtraction angiography, and CT/fluoroscopy.** *Pain Med* 2014;15:1328–33 CrossRef Medline
11. Lazarus MS, Forman RB, Brook AL, et al. **Radiation dose and procedure time for 994 CT-guided spine pain control procedures.** *Pain Physician* 2017;20:E585–91 CrossRef Medline
12. Suresh S, Berman J, Connell A. **Cerebellar and brainstem infarction as a complication of CT-guided transforaminal cervical nerve root block.** *Skeletal Radiol* 2007;36:449–52 CrossRef Medline
13. Park GY, Kwon DR, Kwon DG. **Complex regional pain syndrome type II after cervical transforaminal epidural injection: a case report.** *Medicine (Baltimore)* 2018;97:e10784 CrossRef Medline
14. Bogduk N, Dreyfuss P, Baker R, et al. **Complications of spinal diagnostic and treatment procedures.** *Pain Med* 2008;9(Suppl 1):S11–34 CrossRef
15. Cyteval C, Thomas E, Decoux E, et al. **Cervical radiculopathy: open study on percutaneous periradicular foraminal steroid infiltration performed under CT control in 30 patients.** *AJNR Am J Neuroradiol* 2004;25:441–45 Medline
16. Kim MS, Lee DG, Chang MC. **Outcome of transforaminal epidural steroid injection according to severity of cervical foraminal stenosis.** *World Neurosurg* 2018;110:e398–403 CrossRef Medline
17. Costandi SJ, Azer G, Eshraghi Y, et al. **Cervical transforaminal epidural steroid injections: diagnostic and therapeutic value.** *Reg Anesth Pain Med* 2015;40:674–80 CrossRef Medline
18. Slipman CW, Lipetz JS, Jackson HB, et al. **Therapeutic selective nerve root block in the nonsurgical treatment of atraumatic cervical spondylotic radicular pain: a retrospective analysis with independent clinical review.** *Arch Phys Med Rehabil* 2000;81:741–46 CrossRef Medline
19. Vallée JN, Feydy A, Carlier RY, et al. **Chronic cervical radiculopathy: lateral-approach periradicular corticosteroid injection.** *Radiology* 2001;218:886–92 CrossRef Medline
20. Okubadejo GO, Talcott MR, Schmidt RE, et al. **Perils of intravascular methylprednisolone injection into the vertebral artery: an animal study.** *J Bone Joint Surg Am* 2008;90:1932–38 CrossRef Medline
21. Huda W, Ogden KM, Khorasani MR. **Converting dose-length product to effective dose at CT.** *Radiology* 2008;248:995–1003 CrossRef Medline
22. Lukies MW, Teoh WW, Clements W. **Safety of CT-guided cervical nerve root corticosteroid injections.** *J Med Imaging Radiat Oncol* 2019;63:300–06 CrossRef Medline
23. Depriester C, Setbon S, Larde A, et al. **CT-guided transforaminal cervical and lumbar epidural injections.** *Diagn Interv Imaging* 2012;93:704–10 CrossRef Medline
24. Bartleson JD, Maus TP. **Diagnostic and therapeutic spinal interventions: epidural injections.** *Neurol Clin Pract* 2014;4:347–52 CrossRef Medline
25. Palmer W. **Spinal injections for pain management.** *Radiology* 2016;281:669–88 CrossRef Medline
26. Jeon Y, Kim S. **Detection of intravascular injection during cervical transforaminal epidural injection: a comparison of digital subtraction angiography and real time fluoroscopy.** *Pain Physician* 2018;21:E181–86 CrossRef Medline
27. Schmid G, Schmitz A, Borchardt D, et al. **Effective dose of CT- and fluoroscopy-guided perineural/epidural injections of the lumbar spine: a comparative study.** *Cardiovasc Intervent Radiol* 2006;29:84–91 CrossRef Medline
28. Dietrich TJ, Peterson CK, Zeimpekis KG, et al. **Fluoroscopy-guided versus CT-guided lumbar steroid injections: comparison of radiation exposure and outcomes.** *Radiology* 2019;290:752–59 CrossRef Medline

Major Radiologic and Clinical Outcomes of Total Spine MRI Performed in the Emergency Department at a Major Academic Medical Center

C.W.C. Huang, A. Ali, Y.-M. Chang, A.F. Bezuidenhout, D.B. Hackney, J.A. Edlow, and R.A. Bhadelia

ABSTRACT

BACKGROUND AND PURPOSE: Total spine MRIs are requested by the emergency department when focused imaging can not be ordered on the basis of history or clinical findings. However, their efficacy is not known. We assessed the following: 1) major radiologic and clinical outcomes of total spine MR imaging performed by the emergency department, and 2) whether the presence of a high-risk clinical profile and/or neurologic findings impacts the clinical outcomes.

MATERIALS AND METHODS: Total spine MRIs requested by the emergency department during a 28-month period were evaluated for major radiologic (cord compression, cauda equina compression, and other significant findings) and major clinical outcomes (hospital admission during the visit followed by an operation, radiation therapy, or intravenous antibiotics or steroids). Associations between a high-risk clinical profile (cancer, infection, coagulopathy) and/or the presence of neurologic findings and outcomes were assessed.

RESULTS: After we excluded trauma or nondiagnostic studies, 321/2047 (15.7%) MRIs ordered during study period were total spine MR imaging; 117/321 (36.4%) had major radiologic and 60/321 (18.6%) had major clinical outcomes (34/60 in <24 hours); and 58/117 (49.6%) with major radiologic outcome were treated compared with 2/205 (1.0%) without (OR = 99, $P < .001$). The presence of both a high-risk clinical profile and neurologic findings concurrently in a patient (142/321) increased the likelihood of major clinical outcomes during the same visit (OR = 3.1, $P < .001$) and in <24-hours (OR = 2.6, $P = .01$) compared with those with either a high-risk clinical profile or neurologic findings alone (179/321).

CONCLUSIONS: Total spine MR imaging ordered by our emergency department has a high radiologic and significant clinical yield. When a high-risk clinical profile and neurologic findings are both present in a patient, they should be prioritized for emergent total spine MR imaging, given the increased likelihood of clinical impact.

ABBREVIATIONS: CEC = cauda equina compression; ED = emergency department; HRCP = high-risk clinical profile; SCC spinal cord compression; TS = total spine

Twenty-four-hour availability of MR imaging in the United States has significantly increased its use in spine imaging.[1-6] Although this may be beneficial in many instances, overuse of imaging has become a concern of both hospital administrators and health care policy makers.[1,7] This concern is based on previous studies that have shown that emergent MR imaging of the spine rarely results in an immediate clinical intervention.[1] Furthermore, it has also been shown that MR imaging of the lumbar spine does not improve overall clinical outcome compared with standard clinical care in patients without "red flags" indicating underlying conditions such as cancer, infection, or cauda equina syndrome.[8]

Because clinical symptoms and physical examination are often inconsistent and inadequate in identifying and localizing spinal pathology in patients presenting with neck or back pain and neurologic deficits,[4,9-11] MR imaging is frequently ordered for patients in the emergency department (ED). Despite increasing regulatory scrutiny from governmental and private insurers, over-reliance on expensive imaging studies in this clinical scenario is often justified because delayed diagnosis and treatment of spinal cord or cauda equina compression (CEC) may result in permanent morbidity or even mortality.[10-13]

While most major radiology departments with 24/7 MR imaging service are able to accommodate unscheduled emergent single-segment spine MR imaging ordered by the ED, an unscheduled

Received January 20, 2020; accepted after revision March 24.

From the Departments of Radiology (C.W.C.H., A.A., Y.-M.C., A.F.B., D.B.H., R.A.B.) and Emergency Medicine (J.A.E.), Beth Israel Deaconess Medical Center, Harvard Medical School, Boston, Massachusetts; Department of Radiology (C.W.C.H.), Wan Fang Hospital, Taipei Medical University, Taipei, Taiwan; and Department of Radiology (C.W.C.H.), School of Medicine, College of Medicine, Taipei Medical University, Taipei, Taiwan.

Please address correspondence to Rafeeque A. Bhadelia, MD, Department of Radiology, Beth Israel Deaconess Medical Center, WCB90, 330 Brookline Ave, Boston, MA, 02215; e-mail: rbhadeli@bidmc.harvard.edu; @rbhadeliaMD

http://dx.doi.org/10.3174/ajnr.A6578

total spine (TS) MR imaging can disrupt the normal workflow due to longer scan and interpretation times compared with a single-level study and would likely reduce its use.[14] It is generally understood that TS-MR imaging is ordered by the ED when patients have a high-risk clinical profile (HRCP) such as a history of cancer and clinical suspicion of infection or coagulopathy and when distinction between spinal cord and cauda equina compression could not be made clinically.[11,14] Except for a single study showing extremely low radiologic and clinical outcomes of TS-MR imaging for spinal cord compression,[14] there are insufficient data about the clinical impact of emergent TS-MR imaging examinations ordered by the ED to assess the appropriateness of these studies or implement change in use. Therefore, our purpose was to assess the major radiologic and clinical outcomes of TS-MR imaging performed by the ED and whether HRCP and/or neurologic findings impact the clinical outcome.

MATERIALS AND METHODS

Patient Population

The patient population was drawn from a major academic medical center (Beth Israel Deaconess Medical Center, Boston, Massachusetts) serving a large metropolitan city and surrounding area, with 704 hospital beds. The hospital is a level 1 trauma and comprehensive cancer, stroke, neurosurgical, and spine center with approximately 56,000 ED visits per year.

Institutional review board approval was obtained for this retrospective study of adult (18 years of age or older) patients with a waiver of informed consent. This study was based on imaging data collected for a quality-assurance project designed to assess use of emergent spinal MRIs obtained by the ED at our institution between March 1, 2016, and June 30, 2018. The inclusion criterion was a TS-MR imaging examination ordered by the ED. Exclusion criteria were a history of major trauma or a nondiagnostic examination. Repeat examinations performed on the same day for either additional contrast-enhanced images or a nondiagnostic, inconclusive, or incomplete initial study were considered 1 examination.

During the study period, 384 consecutive TS-MR imaging examinations were performed of 2047 spine MRIs ordered from the ED. We excluded 63/384 TS-MRIs: 46/384 for a history of major trauma and 17/384 for examinations being nondiagnostic either due to severe motion artifacts or pain or claustrophobia (that were not repeated later). Examinations performed for major trauma were excluded because most of those studies were performed for evaluation of abnormalities seen on an initial CT examination or due to severe neurologic findings and thus would have a bias for an increased pretest probability of major clinical outcomes. Thus, 321 TS-MR imaging examinations were included in the study.

MR Imaging

The MR imaging examinations were performed on either a 1.5T or 3T Signa HDx scanner (GE Healthcare) or a 1.5T Magnetom Espree scanner (Siemens). All MR imaging was performed with a standard protocol, including sagittal T1-weighted, T2-weighted, and inversion recovery and axial T2 images through the entire spine. The sagittal images (3-mm thickness; FOV = 34 cm; matrix = 384–512 × 256) covered the entire spine in 2 acquisitions (posterior fossa to T6–7 and T5–6 to S2–3 levels) and axial contiguous images (5-mm thickness; FOV = 20 cm; matrix = 256 × 256) in 4 acquisitions (cervical, upper thoracic, lower thoracic, and lumbar). If gadolinium was administered, then T1-weighted sagittal and axial postcontrast images were also obtained (230/321 patients undergoing TS-MR imaging received gadolinium). Pregadolinium T1-weighted axial images through the spine were not obtained, to limit the imaging time, which was 45–50 minutes without and 65–70 minutes with gadolinium for a TS-MR imaging examination.

Radiologic Outcomes

TS-MR imaging was considered to have a major radiologic outcome with ≥1 of the following findings:

- Spinal cord compression (SCC): severe spinal canal narrowing with compression of the spinal cord and a lack of surrounding CSF (Fig 1).[15]
- Cauda equina compression: severe narrowing of the lumbar spinal canal on axial images and lack of CSF within the thecal sac (Fig 2).[16]
- Other significant findings: findings without spinal cord or cauda equina compression that may affect clinical management (Fig 3), such as an intramedullary spinal cord lesion (other than myelomalacia), spinal and extraspinal manifestations of infection (discitis/osteomyelitis and abscess), bone or soft-tissue abnormalities (fracture, hematoma, lymphadenopathy, mass), or vascular abnormalities.

Degenerative spinal stenosis or disc herniation without SCC or CEC and the presence of neural foraminal narrowing were not considered major radiologic outcomes for TS-MR imaging.

Clinical Outcomes

TS-MR imaging was considered to have a major clinical outcome if the patient was admitted and treated with an operation, radiation, intravenous antibiotics, or steroid therapy or image-guided abscess drainage during the same visit on the basis of the radiologic findings. If a patient received empiric IV antibiotics or steroid therapy while in the ED but these treatments were not performed on the inpatient service, it was not considered a major clinical outcome. The clinical outcomes were further refined to identify those who received treatment within the first 24 hours of arrival to the ED.

History and Neurologic Findings

Electronic medical records of patients including ED and specialist consultation notes (if available) were reviewed and stratified as having the presence or absence of HRCP and neurologic findings accordingly.

Patients were considered to have a HRCP when a history of cancer, predisposing factors, or evidence for infection (back pain with fever, intravenous drug use, bacteremia, or laboratory markers of infection), coagulopathy, prior spinal intervention, or demyelinating disease was noted in their history.

Patients were considered to have positive neurologic findings if there was ≥1 of the following present: bilateral extremity pain or weakness, sensory deficits, abnormal reflexes, urinary or stool incontinence, decreased anal tone, and/or saddle anesthesia.

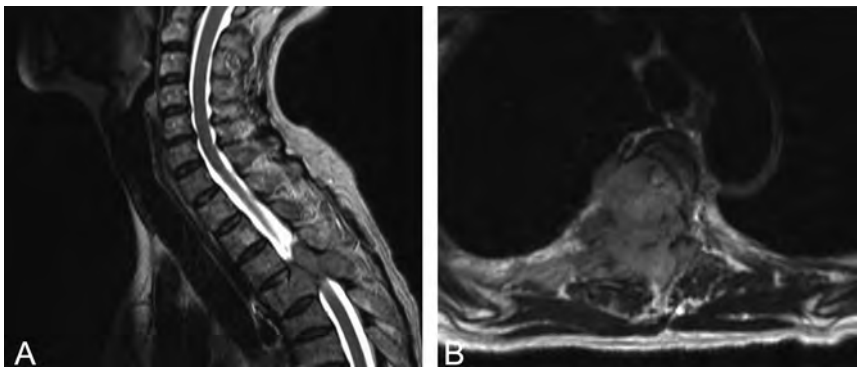

FIG 1. A 67-year-old woman with a history of breast cancer presented with bilateral lower extremity and right upper extremity weakness. The upper portion of total spine MR imaging with T2-weighted sagittal (*A*) and axial (*B*) images shows severe compression of the spinal cord at the T4 level with no CSF visualized within the spinal canal at that level.

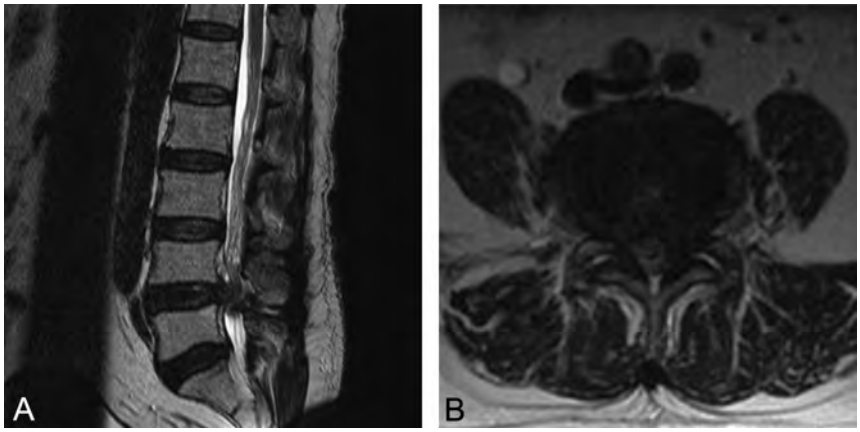

FIG 2. An 83-year-old man presenting with lower back pain, leg numbness, leg weakness, and urinary retention. T2-weighted sagittal (*A*) and axial (*B*) images from total spine MR imaging show a herniated L4–L5 intervertebral disc causing severe spinal canal stenosis with a lack of CSF within the thecal sac, suggesting cauda equina compression.

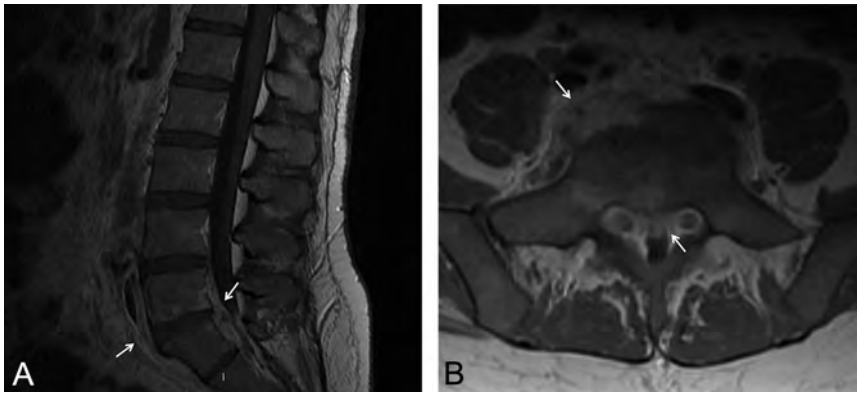

FIG 3. A 41-year-old man with a history of intravenous drug use presenting with fever, severe diffuse back pain, and right lower quadrant abdominal pain. The lower portion of total spine MR imaging with T1-weighted postcontrast sagittal (*A*) and axial (*B*) images shows discitis and osteomyelitis, with epidural and right paraspinal phlegmon.

Data Analysis

The presence and absence of radiologic and clinical outcomes were recorded. Patients who had major radiologic outcome at >1 spinal segment (cervical, thoracic, or lumbar spine) were considered to have multisegment disease. The radiologic outcomes among SCC, CEC, or other significant findings that were treated or considered most clinically symptomatic (from medical records review) were included in the analysis.

Odds ratios were determined to assess the strength of association between the following:

- Major clinical outcomes between patients with and without major radiologic outcomes.
- Major clinical outcomes between patients who had both HRCP and neurologic findings and those who had either HRCP or neurologic findings alone.

A radiologic or clinical outcome ≥5% was considered a significant outcome. An on-line calculator (https://www.medcalc.org/calc/odds_ratio.php) was used to determine OR, 95% CI, and significance. $P < .05$ was considered significant.

RESULTS

After exclusions for trauma or nondiagnostic studies, 321/2047 (15.7%) MR imaging examinations ordered during the study period by the ED were TS-MR imaging. The mean age of 321 patients was 52 ± 17 years; 171/321 (53%) were women (52 ± 17 years) and 150/321 (47%) were men (51 ± 17 years).

Radiologic Outcomes

Table 1 shows radiologic outcomes of 321 TS-MR imaging examinations; 117/321 (36%) had a major radiologic outcome, and 204/321 (64%) had no major radiologic outcome. Forty-eight of 117 (41%) patients with radiologic outcomes had major findings at multiple spinal segments, and 69/117 (59%) had major findings at single spinal segment.

SCC or CEC was noted in 72/321 (22.4%) TS-MR imaging examinations. The most common cause for SCC or CEC was degenerative disease

Table 1: Radiologic and clinical outcomes of TS-MR imaging[a]

Radiologic Outcomes of TS-MR Imaging with Major Radiologic Outcome	(*N* = 321) 117/321 (36.4%)	Major Clinical Outcome in Patients, (*n* = 60/321) (18.6%) During Visit 58/117 (49.6%)[b]	<24 Hours 33/117 (28.2%)[c]
SCC or CEC	72	36	20
Degenerative disease	41	12	3
Neoplasm	16	12	5
Infection	10	10	10
Hematoma	2	2	2
Iatrogenic	1	0	0
Traumatic findings	2	0	0
Other significant findings	45	22	13
Neoplasm	19	8	1
Infection	8	8	8
Iatrogenic	1	1	1
Spinal cord lesion	7	3	3
Traumatic findings	3	0	0
Extraspinal findings[d]	7	2	0
Without major radiologic outcome	204/321 (63.6%)	2/204 (1.0%)[b]	1/204 (0.5%)[c]

Note:—Bold indicates total of subsequent raws respectively.
[a] Clinical Outcome: hospital admission followed by an operation, radiation, IV therapy (antibiotics or steroids), or abscess drainage during same visit as well as in <24 hours and >24 hours after arrival to ED.
[b] Odds Ratio = 99 (95% CI, 23.5–419; *P* value < .001) between patients with and without major radiologic outcomes.
[c] Odds Ratio = 80 (95% CI, 10.7–593; *P* value < .001) between patients with and without major radiologic outcomes.
[d] Psoas muscle abscess and lymphoma.

Table 2: Impact of HRCP and neurologic findings on major clinical outcomes[a]

Variable	No. of Patients (*N* = 321)	During Visit	Odds Ratio (95% CI)	*P* Value	<24 Hours	Odds Ratio (95% CI)	*P* Value
HRCP + NF	142/321 (44%)	40/142 (28%)	3.1 (1.7–5.6)	<.001	22/142 (15%)	2.6 (1.2–5.4)	.01
HRCP or NF alone	179/321 (56%)	20/179 (11%)			12/179 (7%)		

Note:—NF indicates neurologic findings.
[a] Major clinical outcomes of patients who had both HRCP + NF were compared with patients who had either HRCP or NF alone.

(57%), followed by neoplasm (22%) and infection (14%). Other significant findings were noted in 45/321 (14%) TS-MR imaging examinations. The most common cause of other significant findings was neoplasm (42%), followed by infection (18%), spinal cord lesion (15%), and extraspinal findings (15%).

Clinical Outcomes

Table 1 shows major clinical outcomes of 321 TS-MR imaging examinations; 60/321 (19%) had major clinical outcome, and 34/321 (11%) were treated within 24 hours of arrival in the ED. Patients with a major radiologic outcome were more likely to have a major clinical outcome (58/117) compared with those without a major radiologic outcome (2/204, OR = 99; 95% CI, 23.5–419; $P < .001$). The patients with a major radiologic outcome were also more likely to have a < 24-hour clinical outcome compared with those without one (OR = 80; 95% CI, 10.7–593; $P < .001$).

Of the 16/72 patients with SCC/CEC due to tumor, 12/16 (75%) had a major clinical outcome, 9/12 patients underwent an operation (4 in <24 hours), and 3/12 underwent radiation (1 in <24 hours). Of the 41 patients with SCC/CEC due to degenerative disease, 12/41 (29%) had major clinical outcome (3 in <24 hours), and they underwent an operation. Of the 19 patients with other significant findings (without SCC/CEC) for neoplasm, 2/19 underwent an operation (1 in <24-hours) and 6/19 underwent radiation therapy within the same visit.

All 18/18 patients with major radiologic findings for infection (SCC/CEC or other significant findings) had a major clinical outcome. All received IV antibiotic treatment. Seven underwent an operation (6 in <24 hours), and 2 had image-guided drainage of an associated abscess.

Two of 204 patients without a major radiologic finding underwent an operation. One patient underwent anterior cervical fusion for cervical radiculopathy with severe foraminal narrowing at the C5–C6 level with moderate spinal stenosis without cord compression or cord signal abnormality. The second patient underwent revision laminectomy with far lateral decompression and spinal fusion at the L3–L4 levels for radiculopathy.

Impact of HRCP and/or Neurologic Findings on Clinical Outcomes

Table 2 shows the impact of HRCP and neurologic findings on major clinical outcomes.

One hundred forty-two of 321 (44%) patients presented with both HRCP and neurologic findings compared with 179/321 (56%) patients who had either HRCP or neurologic findings alone (80/179 with HRCP alone and 99/179 with neurologic findings alone). There were no patients without HRCP or neurologic findings who underwent TS-MR imaging.

The likelihood of a major clinical outcome during an ED visit (admission followed by an operation, radiation, intravenous antibiotics or steroids therapy, or image-guided abscess drainage) was significantly higher in patients with both HRCP and neurologic findings than in those with either HRCP or neurologic findings alone (OR = 3.1; 95% CI , 1.7–5.6; $P < .001$). Finally, the likelihood

of <24-hour clinical outcome after an ED visit was also increased in those with both HRCP and neurologic findings compared with those with either HRCP or neurologic findings alone (OR = 2.6; 95% CI , 1.2–5.4; $P = .01$).

DISCUSSION

Our results suggest that TS-MR imaging performed by the ED at a tertiary care academic medical center has a high radiologic yield, with major findings seen in 1 of 3 patients despite using stringent criteria for a radiologic outcome with positive findings. Furthermore, although major clinical outcomes of these studies were lower than radiologic outcomes, they were not insignificant. Nearly 1 of 6 patients imaged were treated during the same hospital visit, and nearly 1 of 10 imaged was treated within the first 24 hours of arrival in the ED. We also observed that the clinical yield of TS-MR imaging was much higher in patients who had both HRCP and neurologic findings simultaneously than in either of them alone. Moreover, those with SCC/CEC due to tumor/infection were more likely to be treated than those with degenerative disease. Finally, an interesting additional finding of the study was that the use of strict radiologic criteria improves the clinical impact of radiologic observation, with nearly half of the patients with positive radiologic outcomes receiving treatment during the hospital visit. On the basis of these results, we recommend that for interpretation of TS-MR imaging studies, strict diagnostic criteria be used to improve their clinical impact.[17,18]

American College of Radiology recommendations suggest that performing emergent MR imaging of the spine is appropriate in the setting of back pain associated with red flags such as cancer, infection, coagulopathy, or cauda equina syndrome.[5] Similarly, many previous studies have also used signs and symptoms in the patient's history and clinical examination in combination as red flags.[6,8] In this study, we took a slightly different approach and used a patient's high-risk clinical profile (such as history of cancer, predisposing factors, or evidence of infection and coagulopathy) and neurologic findings (neurologic signs and symptoms such as bilateral extremity pain or weakness, sensory deficits, abnormal reflexes, urinary or stool incontinence, decreased anal tone, and/or saddle anesthesia) as separate variables to assess their impact on clinical outcomes of TS-MR imaging ordered by the ED. We were able to quantitatively demonstrate that the simultaneous presence of both HRCP and neurologic findings in a patient significantly increased the likelihood of positive clinical outcomes compared with those who had HRCP or neurologic findings alone. Our results thus provide a practical guideline: A patient who has both HRCP and neurologic findings should be prioritized in the ED setting for an emergent TS-MR imaging.

Previous studies evaluating the radiologic and clinical outcomes of spine MR imaging have generally focused on a single-segment spine study such as cervical or lumbar spine MR imaging.[1,19] Black et al[1] looked at the radiologic and clinical outcomes of 179 emergent spine MRIs during a 13-year period. There were 77 cervical, 87 thoracic, and 101 lumbar spine MR imaging studies, in combination or in isolation, without providing a specific number for TS-MR imaging. A significant radiologic finding was seen in 104/179 (58%), and 66/179 (36.8%) were treated within 48 hours.[1] Another study by Gardner et al[19] looking only at the lumbar spine for patients with cauda equina syndrome found that 33% of patients with suspected cauda equina syndrome had positive radiologic findings but only 7% received treatment. Both of these studies used different radiologic outcome criteria and different patient populations such as those with mixed single- and multiple-segment MR imaging scans as in the study by Black et al and lumbar spine studies in case of Gardner et al compared with all TS-MR imaging in our study, making it difficult to compare the results. Nevertheless, our results are similar to those previous studies when accounting for these differences.

However, our results are quite dissimilar to those by Potigailo et al,[14] who found a very low 1.4% radiologic outcome of total spine MR imaging performed by the ED for acute spinal cord compression, which increased to 4.4.% after an institutional change in policy of ordering spine MR imaging for spinal cord compression. Unlike their study, in our study, 22.4% (72/321) of TS-MR imaging was positive for spinal cord or cauda equina compression despite using a rather restrictive definition for both the entities. The reason for the high radiologic outcomes in our study appears to be that our ED ordered TS-MR imaging only when spine-related symptoms were associated with a high-risk clinical profile or neurologic findings, and none of the studies were ordered for vague symptoms.

An emergent TS-MR imaging is challenging to a radiology department both for performance and interpretative purposes and from the health care policy perspective due to its added cost. A TS-MR imaging takes between 60 and 75 minutes of MR imaging scan time (total MR imaging table time) compared with 25–35 minutes for a single-segment spine MR imaging or brain MR imaging. Furthermore, most of these studies ordered from the ED are emergent and need to be performed immediately to avoid delays in diagnosis and treatment. Because MR imaging scanners at most major academic hospitals are in constant use, a TS-MR imaging is difficult to accommodate, given the time required. There is also a concern about their interpretations around the clock because large numbers of images have to be reviewed, with decreased spatial resolution given the larger FOV per a given matrix size, and these may increase the potential for interpretation errors. Additionally, the cost of obtaining a TS-MR imaging is more than twice that of a single-segment spine MR imaging. In light of the aforementioned, it is important to find ways to optimize the use of TS-MR imaging by developing guidelines for its use, which are currently lacking.

Our data are hypothesis-generating. They have provided a roadmap for a prospective study in collaboration with the ED that may help in reducing the use of TS-MR imaging. First, how successful ED physicians are in restricting the TS-MR imaging orders to a single level using their clinical judgment even in the presence of equivocal findings should be assessed. A prospective study would allow a physician to record the most likely pathologic level while ordering a TS-MR imaging (when they are unable to restrict it to a single level) so that their localizing accuracy can be subsequently assessed. Such a study we believe would be much superior to a retrospective attempt of comparing results of TS-MR imaging and single-level MR imaging and can be done without putting patients at risk of missing a clinically important finding such spinal cord or cauda equina compression. Second, while a history of cancer may not have a quick laboratory test to exclude its presence, infection can be

detected with a rapid laboratory test such as C-reactive protein. Thus, a prospective study should use estimation of an objective laboratory finding such as C-reactive protein (as opposed to clinical suspicion of infection) to provide an independent proof of the presence of infection before an MR imaging is performed.[20–22] While a high C-reactive protein level does not always indicate that a spinal infection is present because it is nonspecific and could be positive for infection anywhere in the body, a low level may eliminate the need for an emergent TS-MR imaging study.

There are a few limitations to our study. First, our hospital is a tertiary care center with 24-hour MR imaging availability. Therefore, many patients may have been referred here specifically for further treatment for a process noted on other imaging techniques at an outside institution. This situation may increase the number of positive outcomes. However, as noted previously, this effect was likely minimal because our results are comparable with those of previous studies. Second, our study was a retrospective one, and the clinical information about risk profile and neurologic findings was obtained from the electronic records, which could be missing some important observations made by the clinicians. While TS-MR imaging constituted a small percentage (one-sixth) of all emergent spine MR imaging ordered by the ED during the study period, we were unable to consistently determine from the medical records why a particular patient underwent TS-MR imaging in place of a focused MR imaging study. Likewise, we were not always able to determine the exact time of onset of the patient's symptoms that brought them to the ED and whether their symptoms were a recent exacerbation of chronic symptoms. Therefore, a prospective study is required before an attempt is made to decrease/optimize TS-MR imaging use based on this information. Third, in several cases, documentation of the timing of treatment was unclear and may have affected our results for therapy under 24 hours. Last, it was not possible to assess long-term outcomes of patients after they underwent TS-MR imaging because many patients likely received follow-up assessment elsewhere.

CONCLUSIONS

We observed a high radiologic yield for TS-MR imaging performed by the ED with clinical outcomes lower but not insignificant. The presence of both a high-risk clinical profile and neurologic findings in a patient increases the likelihood of positive clinical outcomes. We propose that a patient who simultaneously has both a high-risk clinical profile and neurologic findings should be prioritized for emergent TS-MR imaging, given the significantly increased likelihood of a clinical outcome.

Disclosures: David B. Hackney—*UNRELATED*: *Grants/Grants Pending*: National Institutes of Health–National Institute of Arthritis and Musculoskeletal and Skin Diseases, *Comments*: grant to study the risk of vertebral fracture in patients treated with stereotactic body radiosurgery for spinal metastases.* Jonathan A. Edlow—*UNRELATED*: *Expert Testimony*: CRICO, Boston, MA. *Comments*: review of medico-legal cases for both plaintiff and defense firms. *Money paid to the institution.

REFERENCES

1. Black DF, Wood CP, Wells ML, et al. **Emergent, after hours magnetic resonance imaging of the spine.** *J Neuroimaging* 2015;25:590–94 CrossRef Medline
2. Pakpoor J, Saylor D, Izbudak I, et al. **Emergency department MRI scanning of patients with multiple sclerosis: worthwhile or wasteful?** *AJNR Am J Neuroradiol* 2017;38:12–17 CrossRef Medline
3. Rankey D, Leach JL, Leach SD. **Emergency MRI utilization trends at a tertiary care academic medical center: baseline data.** *Acad Radiol* 2008;15:438–43 CrossRef Medline
4. Ahad A, Elsayed M, Tohid H. **The accuracy of clinical symptoms in detecting cauda equina syndrome in patients undergoing acute MRI of the spine.** *Neuroradiol J* 2015;28:438–42 CrossRef Medline
5. Lavi ES, Pal A, Bleicher D, et al. **MR imaging of the spine: urgent and emergent indications.** *Semin Ultrasound CT MR* 2018;39:551–69 CrossRef Medline
6. Sizer PS Jr, Brismee JM, Cook C. **Medical screening for red flags in the diagnosis and management of musculoskeletal spine pain.** *Pain Pract* 2007;7:53–71 CrossRef Medline
7. Iglehart JK. **Health insurers and medical-imaging policy: a work in progress.** *N Engl J Med* 2009;360:1030–37 CrossRef Medline
8. Chou R, Fu R, Carrino JA, et al. **Imaging strategies for low-back pain: systematic review and meta-analysis.** *Lancet* 2009;373:463–72 CrossRef Medline
9. Rooney A, Statham PF, Stone J. **Cauda equina syndrome with normal MR imaging.** *J Neurol* 2009;256:721–25 CrossRef Medline
10. Gitelman A, Hishmeh S, Morelli BN, et al. **Cauda equina syndrome: a comprehensive review.** *Am J Orthop (Belle Mead NJ)* 2008;37:556–62 Medline
11. Ropper AE, Ropper AH. **Acute spinal cord compression.** *N Engl J Med* 2017;376:1358–69 CrossRef Medline
12. Davis JW, Phreaner DL, Hoyt DB, et al. **The etiology of missed cervical spine injuries.** *J Trauma* 1993;34:342–46 CrossRef Medline
13. Ahn UM, Ahn NU, Buchowski JM, et al. **Cauda equina syndrome secondary to lumbar disc herniation: a meta-analysis of surgical outcomes.** *Spine (Phila Pa 1976)* 2000;25:1515–22 CrossRef Medline
14. Potigailo VL, Christoforidis GA, Katzman GL. **Acute spinal cord compression: CQI framework increases resource efficiency while promoting delivery of high-quality care.** *J Am Coll Radiol* 2015;12:90–94 CrossRef Medline
15. Bilsky MH, Laufer I, Fourney DR, et al. **Reliability analysis of the epidural spinal cord compression scale.** *J Neurosurg Spine* 2010;13:324–28 CrossRef Medline
16. Huang CWC, Ali A, Chang YM, et al. **Performance of on-call radiology residents in interpreting total spine MRI studies for the detection of spinal cord compression or cauda equina compression.** *AJR Am J Roentgenol* 2019;213:1341–47 CrossRef Medline
17. Stafira JS, Sonnad JR, Yuh WT, et al. **Qualitative assessment of cervical spinal stenosis: observer variability on CT and MR images.** *AJNR Am J Neuroradiol* 2003;24:766–69 Medline
18. Weber C, Rao V, Gulati S, et al. **Inter- and intraobserver agreement of morphological grading for central lumbar spinal stenosis on magnetic resonance imaging.** *Global Spine J* 2015;5:406–10 CrossRef Medline
19. Gardner A, Gardner E, Morley T. **Cauda equina syndrome: a review of the current clinical and medico-legal position.** *Eur Spine J* 2011;20:690–97 CrossRef Medline
20. Davis DP, Salazar A, Chan TC, et al. **Prospective evaluation of a clinical decision guideline to diagnose spinal epidural abscess in patients who present to the emergency department with spine pain.** *Neurosurg Spine* 2011;14:765–70 CrossRef Medline
21. Davis DP, Wold RM, Patel RJ, et al. **The clinical presentation and impact of diagnostic delays on emergency department patients with spinal epidural abscess.** *J Emerg Med* 2004;26:285–91 CrossRef Medline
22. Davis WT, April MD, Mehta S, et al. **High risk clinical characteristics for pyogenic spinal infection in acute neck or back pain: prospective cohort study.** *Am J Emerg Med* 2019 May 17. [Epub ahead of print] CrossRef Medline

High Prevalence of Spinal Cord Cavernous Malformations in the Familial Cerebral Cavernous Malformations Type 1 Cohort

M.C. Mabray, J. Starcevich, J. Hallstrom, M. Robinson, M. Bartlett, J. Nelson, A. Zafar, H. Kim, L. Morrison, and B.L. Hart

ABSTRACT

BACKGROUND AND PURPOSE: Cavernous malformations occur most often in the brain but can occur in the spinal cord. Small studies of patients with familial cerebral cavernous malformations suggested a prevalence of spinal cord cavernous malformations of 20%–42%. We aimed to review our familial cohort and prospectively estimate the prevalence of spinal cord cavernous malformations.

MATERIALS AND METHODS: We initially reviewed our familial cerebral cavernous malformations cohort for spinal cord cavernous malformations and reviewed clinical spine MR imaging examinations for sequence sensitivity. We then prospectively performed research MR imaging of the spinal cord in 29 patients from the familial cohort to estimate the prevalence.

RESULTS: Gradient-based sequences identified the most spinal cord cavernous malformations on clinical MR images, forming the basis for developing our screening MR imaging. Screening spinal cord MR imaging demonstrated a prevalence of 72.4%, and a positive correlation with patient age and number of cerebral cavernous malformations.

CONCLUSIONS: Spinal cord cavernous malformations occur commonly in the familial cerebral cavernous malformation population. Gradient-based sequences are the most sensitive and should be used when spinal cord cavernous malformations are suspected. This study establishes the prevalence in the familial population at around 70% and supports the idea that this condition is a progressive systemic disease that affects the entire central nervous system.

ABBREVIATIONS: CM = cavernous malformation; CCM = cerebral cavernous malformation; SCCM = spinal cord cavernous malformation; MEDIC = Multi-Echo Data Image Combination

Cavernous malformations (CMs) are dilated capillary-type low-flow vascular malformations, which are prone to repeated hemorrhage and growth over time.[1-5] Cerebral cavernous malformations (CCMs) occur with a prevalence of about 0.5% in the general population.[1,2,6] About 80% of CCMs are sporadic, solitary, and often closely associated with a developmental venous anomaly, and about 20% of CCMs are familial/syndromic.[1,2] Mutations that lead to familial CCM syndrome can occur in 3 genes (*CCM1* or *KRIT1*, *CCM2*, and *CCM3* or *PDCD10*) with an autosomal dominant transmission.[2,4,7-9] There is a particularly high prevalence of familial CCM syndrome (*CCM1*-common Hispanic mutation) in southwest North America due to a founder effect in early Hispanic settlers.[1,2,4,9] Spinal cord cavernous malformations (SCCMs) are less common than CCMs and have been considered rare, with relatively less attention in the CCM literature and most reported cases being sporadic nonfamilial SCCMs.[10-19] A 2009 report on a single Italian family with familial CCM found SCCMs in 5 of 12 patients (41.7%), 2 of which were discovered clinically and 3 of which were discovered with screening MR imaging (3 of 6 screened patients had SCCMs).[20] An additional 2017 report on 13 patients with familial CCM found upper SCCMs in 3 patients (23.1%).[21] Given these estimates of SCCM prevalence in small sample sizes, and what we

Received February 27, 2020; accepted after revision March 19.

From the Departments of Radiology (M.C.M., J.S., J.H., B.L.H.) and Neurology (M.R., M.B., A.Z., L.M.), University of New Mexico Health Sciences Center, University of New Mexico, Albuquerque, New Mexico; and Departments of Anesthesia and Perioperative Care, Center for Cerebrovascular Research (J.N., H.K.), and Epidemiology and Biostatistics (H.K.), University of California San Francisco, San Francisco, California.

Grant funding from the National Institute of Health-National Institute of Neurological Disorders and Stroke (grant number U54 NS065705), Radiology Department Seed Grant, and the Cody Unser First Step Foundation.

Portions of this research previously presented at: Annual Meetings of the American Society of Neuroradiology Annual Meeting, May 23–26, 2016, Washington, DC; American Society of Spine Radiology Annual Symposium, February 18–21, 2016, Bonita Springs, Florida; Western Neuroradiological Society Annual Meeting October 11–14, 2018, Dana Point, California; and Annual Angioma Alliance Cerebral Cavernous Malformations Scientific Meeting, November 8–9, 2018, Silver Spring, Maryland.

Please address correspondence to Marc C. Mabray, MD, Department of Radiology, University of New Mexico, MSC 10 5530, 1 University of New Mexico, Albuquerque, NM, 87131; email: mamabray@salud.unm.edu

Indicates open access to non-subscribers at www.ajnr.org

http://dx.doi.org/10.3174/ajnr.A6584

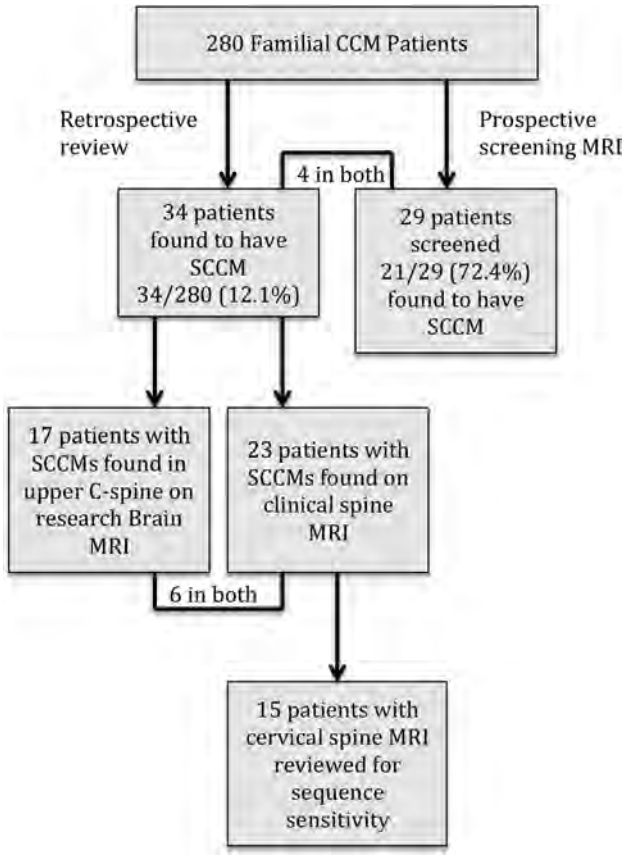

FIG 1. Flow chart of the study.

had been encountering in our cohort, we aimed to systematically study SCCMs in our familial *CCM1* cohort. We initially reviewed our familial CCM cohort retrospectively and evaluated the sensitivity of various MR imaging sequences for detecting SCCMs; we then prospectively imaged the spinal cord in 29 patients to estimate the prevalence of SCCMs in familial CCM. We expected to find a high prevalence of SCCMs in this patient population and that the number of SCCMs would positively correlate with the number of brain CCMs and age, supporting the idea of familial CCM as a progressive systemic disease that affects the entire central nervous system.

MATERIALS AND METHODS

The study was institutional review board compliant, and all subjects gave informed consent to participate. An overall outline of the study is demonstrated in Fig 1.

Initial Retrospective Review

Our research cohort consisted of 280 patients with familial CCM syndrome participating in a prospective longitudinal study. This cohort consists of patients with the *CCM1* common Hispanic mutation. Patients must have a genetic diagnosis of CCM, or meet 2 of the 3 criteria of a clinical diagnosis of CCM, have evidence of multiple CMs on MR imaging, or a family member with a diagnosis of *CCM1*. We initially retrospectively reviewed the records of patients in this research cohort to identify patients with known SCCMs as an estimate of the lower bound of prevalence in our cohort.

MR Imaging Sequence Sensitivity

Based on this initial retrospective analysis, we set out to determine the sensitivity of sequences to determine our protocol for screening the spinal cord for SCCMs. Fifteen of the patients had clinically performed cervical spine MR images available, for which the number of SCCMs visible on each sequence was analyzed. Sequences consisted of sagittal T1 TSE, sagittal T2 TSE, and axial T2 Multi-Echo Data Image Combination (MEDIC; Siemens). A sagittal 3D MEDIC was also performed in 8 of the patients. SWI was performed in 2 cases, but proved significantly limited by artifact and was not analyzed for sequence sensitivity. Anonymized and randomized MR imaging sequences were presented to 2 attending neuroradiologists, who separately recorded the number of SCCMs seen on each individual sequence. This was followed by a consensus review to agree upon the number of SCCMs detected for each sequence. The proportion of SCCMs detected for each sequence was calculated compared with the total number detected across all sequences, and the sensitivity of detecting SCCMs was calculated relative to the total number of SCCMs.

Screening Spinal Cord MR Imaging

After the initial review of our cohort and using what we had learned about sequence sensitivity, we prospectively screened the spinal cord with MR imaging in 29 of the patients in the study. We offered research MR imaging of the cervical and thoracic spine to consecutive patients who were returning for research brain MR imaging; 30 patients were scheduled for cervical and thoracic spine MR imaging and 29 patients completed the MR imaging. Four patients in the prospective screening group were also in the group of 34 patients found to have SCCMs on retrospective review. Research MR imaging was performed on a 3T Skyra scanner (Siemens) and was set up as sagittal T1 TSE (TE, 10 ms; TR, 647), sagittal T2 TSE (TE, 110 ms; TR, 2500 ms), and sagittal 3D MEDIC (TE, 11 ms; TR, 28 ms) performed in 2 segments (cervical spine through upper thoracic spine with a field of view of 280 mm, and upper thoracic spine through the conus with a field of view of 340 mm) (Fig 2). The 3D MEDIC sequence was reformatted into 1-mm axial images for review.

An attending neuroradiologist reviewed the research MR imaging examinations, and SCCMs were characterized by number, size, and imaging appearance. We also recorded and characterized any vertebral intraosseous vascular malformations on screening MR imaging as these have recently been reported to be of high prevalence in patients with CCM.[22] We tested whether SCCM counts were associated with age and total brain CCM count by using the Spearman rank correlation.

RESULTS

In the overall cohort study of 280 patients, 61.4% of the patients enrolled were female, and 72.4% of the spine MR imaging screened patients were female, which was not statistically significantly different ($P = .14$). The mean age for the 280 patients enrolled in the overall cohort study was 39.0 years (SD 19.7); the mean age for the 29 patients prospectively screened with spine MR imaging was higher at 47.4 years (SD 18.4) ($P = .009$).

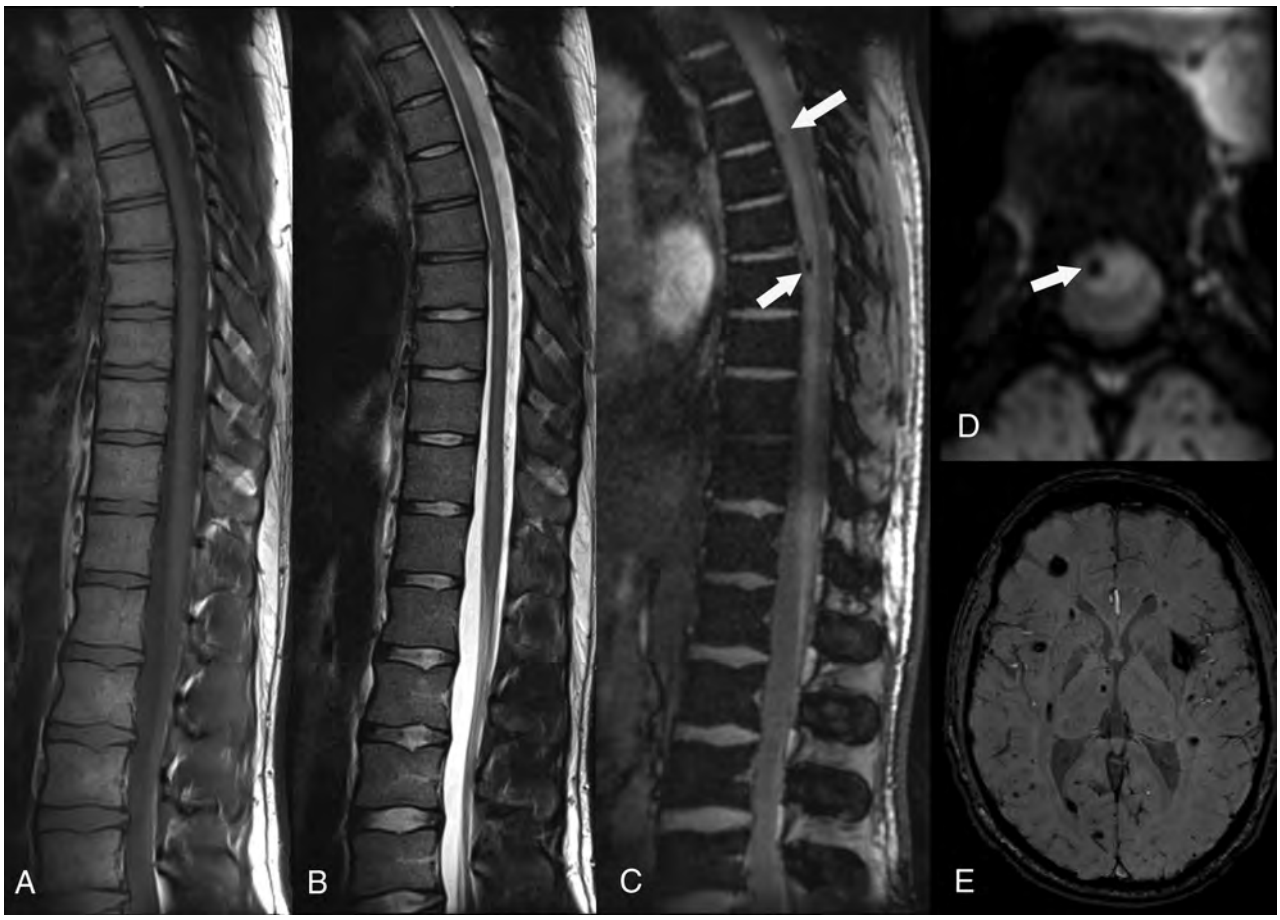

FIG 2. Sagittal T1 TSE (*A*), sagittal T2 TSE (*B*), sagittal 3D MEDIC (*C*), and axial reformat of the 3D MEDIC (*D*), from spinal cord screening research MR imaging and corresponding SWI from brain research MR imaging done on the same day (*E*). On sagittal 3D MEDIC (*C*), arrowsdenote small SCCM. *D*, Axial reformat shows small CM in the right aspect of the spinal cord (*arrow*), corresponding to the more inferior of the 2 lesions. *E*, SWI of the brain shows multiple CMs which are typical of familial CCM syndrome.

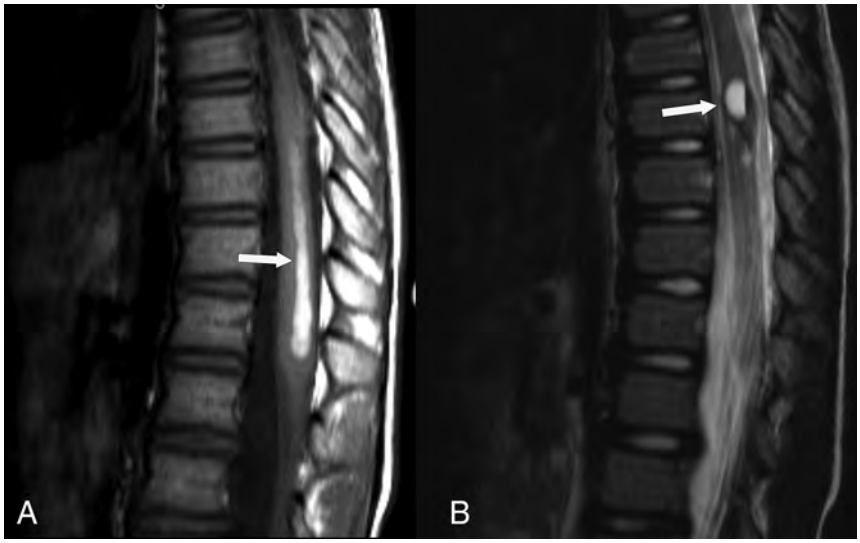

FIG 3. *A*, Sagittal T1 TSE and sagittal T2 TSE (*B*), from clinical MR imaging of the thoracic spine demonstrates spinal cord hemorrhage from a SCCM. On sagittal T1 TSE (*A*), there are T1 hyperintense blood products tracking down the thoracic spinal cord (*arrow*) toward the conus medullaris. On sagittal T2 TSE (*B*), there are mixed-signal blood products (*arrow*) at the site of the spinal cord cavernous malformation.

Initial Retrospective Review

On retrospective review of the familial CCM cohort, we found that 34 patients (12.1%; 95% CI, 8.6%–16.6%) had SCCMs: 17 were identified in the upper cervical spinal cord on research brain MR imaging, and 23 were found on clinical spine MR imaging (6 in both groups). Seven of the 23 showed findings of acute spinal cord hemorrhage on MR imaging (Fig 3). Seven patients had surgery to remove the SCCM, 4 of whom had spinal cord hemorrhage. Nineteen patients were deemed to have clinical symptoms referable to the SCCM.

MR Imaging Sequence Sensitivity on Clinical Cervical Spine MRI

Some SCCMs were visible on routine TSE sequences, but gradient-based techniques were more sensitive for

Table 1: Analysis of sequence sensitivity for SCCM, retrospectively performed on 15 clinically performed cervical spine MR imaging studies

	Number of SCCMs Detected	Sensitivity Relative to Total Number of SCCMs
Sagittal T1 TSE	3 of 21	14.3% (95% CI, 3.0%–36.3%)
Sagittal T2 TSE	6 of 21	28.6% (95% CI, 11.2%–52.2%)
Axial T2 TSE	5 of 21	23.8% (95% CI, 8.2%–47.2%)
Axial T2 MEDIC	17 of 21	81.0% (95% CI, 58.1%–94.6%)
3D MEDIC	8 of 8[a]	100% (95% CI, 68.8%–100%)

[a] 3D MEDIC sequence was performed on a subset of patients.

Table 2: Results of prospective screening MR imaging of the spinal cord

	Prevalence	Lesions per Patient
Spinal cord cavernous malformations	21/29 72.4% (95% CI, 52.8%–87.3%)	Mean = 3.2 (SD 3.9) Median = 2 Range = 0–17
Cerebral cavernous malformations	29/29 100% (95% CI, 90.2%–100%)	Mean = 105.7 (SD 128.0) Median = 53 Range = 4–584
Vertebral osseous vascular malformations	20/29 69.0% (95% CI, 49.2%–84.7%)	Mean = 1.6 (SD 1.7) Median = 1 Range = 0–7

detecting SCCMs (Table 1). Of the 15 patients with cervical spine MR imaging, we detected more of the 21 total SCCMs with the gradient-based MEDIC sequences than traditional T1 and T2 sequences (Table 1). Sagittal T1 TSE detected 14.3% (of total SCCMs), sagittal T2 TSE detected 28.6%, axial T2 TSE detected 23.8%, and axial T2 MEDIC detected 81.0% (including 4 of 8 SCCMs seen by 3D MEDIC) of the total SCCMs. 3D MEDIC, when performed, had detected the most SCCMs and had an advantage over 2D MEDIC in spatial resolution and permitted multiplanar reconstruction. Thus, 3D MEDIC was selected for use in our screening MR imaging of the spinal cord.

Screening MR Imaging of the Spinal Cord

In the prospective group of 29, the mean age was 46.3 (SD 18.8) and 21 (72.4%) were female. We found SCCMs in 21 of 29 patients (72.4%; 95% CI, 52.8%–87.3%) screened with the dedicated research spinal cord MR imaging (Table 2). The mean number of SCCMs per patient was 3.2 (SD 3.9, median 2, range 0–17). SCCMs were small with a mean axial diameter of 2.5 mm (SD 1.3, median 2, range 1–8 mm) (Fig 2) on the axial reformat of the 3D MEDIC. Only 2 of the larger SCCMs showed mixed T2 signal intensity (type II CMs), the rest showed only dark hemosiderin signal (type IV CMs).[3] Only 20 of the 29 patients (69.0%; 95% CI, 49.2%–84.7%) had any vertebral intraosseous vascular malformation; while 11 of the 29 (37.9%; 95% CI, 20.7%–57.7%) had an atypical (T1 hypointense) intraosseous vascular malformation, and 16 of the 29 (55.2%; 95% CI, 35.7%–73.6%) had a typical (T1 hyperintense) intraosseous vascular malformation (Table 2). There was a strong, positive correlation between number of SCCMs and age ($\rho = 0.748$, $P < .001$) and between number of SCCMs and number of brain CMs ($\rho = 0.649$, $P < .001$). There was not a statistically significant correlation between the number of SCCMs and intraosseous vascular malformations.

DISCUSSION

With prospective imaging to screen the spinal cord, we found SCCMs in 21 of 29 patients with familial *CCM1*, a prevalence of 72.4% (95% CI, 52.8%–87.3%). Prior reports of 5 of 12 patients (41.7%, 3 discovered with screening MRI), and 3 of 13 patients (23.1%) were higher than what was initially known in our cohort, but lower than what we found with screening MR imaging.[20,21] Our study establishes an estimated prevalence of SCCMs in the familial *CCM1* population of approximately 70%.

Our study demonstrates that SCCMs are indeed a common finding in patients with familial CCM and supports the idea of familial CCM syndrome as a progressive systemic disease that affects the entire central nervous system. We found an expected positive correlation of number of SCCMs with both patient age and number of intracranial CCMs. We also found a high prevalence of vertebral intraosseous vascular malformations (69%), including atypical (T1 hypointense) intraosseous vascular malformation in approximately 38% of the patients who underwent MR imaging screening, supporting the recent finding that these are common in patients with familial CCM.[22]

Many of the SCCMs that we found with screening were quite small (mean diameter of 2.52 mm) and we would not expect them to currently alter patient management. SCCMs were not commonly clinically discovered in our larger cohort (23/280 patients, 8.2%), and presenting with spinal cord hemorrhage ($n = 7$) and being operated on for SCCM ($n = 7$) were even rarer in our cohort. Currently, there are no guidelines to suggest screening the spinal cord for SCCMs in patients with familial CCM; if that were performed, we would expect that many, mostly small, SCCMs would be found as was the case in this study.[2]

Gradient-based MEDIC sequences were found to be more sensitive to the detection of SCCMs compared with T1 and T2 sequences (which detected only 14.3–28.6% of the SCCMs compared with the MEDIC sequences). Additionally, 3D MEDIC was more sensitive for SCCM detection compared with 2D MEDIC, which detected only 4/8 SCCMs in patients with both 2D and 3D imaging. Many SCCMs were visible only as small foci of susceptibility, accounting for the limited visibility on T2 and T1 sequences. SWI, of proved superiority for detection of CMs in the brain as compared with T2 or GRE sequences, was limited in the spine by artifact.[23,24] 3D MEDIC is an isotropic, high-resolution gradient-based technique that can quickly image a long section of the spine in a single, narrow, sagittal acquisition with multiplanar reconstructions, which we found to be ideal for identifying SCCMs, and thus we utilized this sequence in our screening spinal cord research MR imaging. When there is suspicion for CMs, using sensitive sequences in the spine and brain is necessary because the identification of a second CM changes the presumptive diagnosis from

sporadic to genetic disease. This distinction has important implications for the individual, their family, and for genetic counseling.

Limitations of this study include the mix of clinically and incidentally discovered SCCMs in the baseline part of the study, the varied imaging techniques used for clinical and research imaging, and the limited collected clinical data. Also, because our cohort is patients with *CCM1* and does not include patients with *CCM2* and *CCM3*, we are thus unable to extrapolate our results to patients with *CCM2* and *CCM3* familial CCM. Screening of the spinal cord as we did with our spinal cord research MR imaging by using only sagittal imaging would potentially be impractical in clinical practice where other spinal pathology may also be important to adequately image. However, if imaging is performed primarily to identify SCCMs, then performing a sequence sensitive to small foci of susceptibility as we did with our 3D MEDIC sequence, provides a highly sensitive evaluation.

CONCLUSIONS

SCCMs are a common feature of familial CCM syndrome. We have established an estimate of the prevalence of SCCMs in the familial *CCM1* cohort at approximately 70%. SCCMs can present clinically, including with hemorrhage, or can be found incidentally in these patients. Optimal technique, including gradient-based sequences such as 3D MEDIC, should be used for spinal cord imaging if SCCMs are suspected. This study supports the idea of familial CCM as progressive systemic disease that affects the entire central nervous system.

Disclosures: Marc Mabray—*RELATED: Grant:* NIH NINDS.* Jeffrey Nelson—*RELATED: Grant:* NIH.* Atif Zafar—*RELATED: Grant:* National Institute of Health–National Institute of Neurological Disorders and Stroke, *Comments:* National Institute of Health–National Institute of Neurological Disorders and Stroke (grant number U54 NS065705), Radiology Department Seed Grant, and the Cody Unser First Step Foundation. *UNRELATED: Employment:* UNM Hospital. Helen Kim—*RELATED: Grant:* NIH*; *UNRELATED: Consultancy:* Recursion Pharmaceuticals, *Comments:* Consulting services for clinical advisory board; *Grants/Grants Pending:* NIH.* Leslie Morrison—*RELATED: Grant:* NINDS. Blaine Hart—*RELATED: Grant:* NIH.* *Money paid to institution.

REFERENCES

1. Zafar A, Quadri SA, Farooqui M, et al. **Familial cerebral cavernous malformations.** *Stroke* 2019;50:1294–301 CrossRef Medline
2. Akers A, Al-Shahi Salman R, Awad IA, et al. **Synopsis of guidelines for the clinical management of cerebral cavernous malformations: Consensus recommendations based on systematic literature review by the Angioma Alliance Scientific Advisory Board Clinical Experts Panel.** *Neurosurgery* 2017;80:665–80 CrossRef Medline
3. Zabramski JM, Wascher TM, Spetzler RF, et al. **The natural history of familial cavernous malformations: results of an ongoing study.** *J Neurosurg* 1994;80:422–32 CrossRef Medline
4. Morrison L, Akers A, et al. Cerebral Cavernous Malformation, Familial. In: Adam MP, Ardinger HH, Pagon RA, eds. *GeneReviews®*. University of Washington, Seattle. 1993.
5. Al-Shahi Salman R, Berg MJ, Morrison L, et al. **Hemorrhage from cavernous malformations of the brain: definition and reporting standards. Angioma Alliance Scientific Advisory Board.** *Stroke* 2008;39:3222–30 CrossRef Medline
6. Flemming KD, Graff-Radford J, Aakre J, et al. **Population-based prevalence of cerebral cavernous malformations in older adults: Mayo Clinic Study of Aging.** *JAMA Neurol* 2017;74:801–05 CrossRef Medline
7. Choquet H, Pawlikowska L, Lawton MT, et al. **Genetics of cerebral cavernous malformations: current status and future prospects.** *J Neurosurg Sci* 2015;59:211–20 Medline
8. Plummer NW, Zawistowski JS, Marchuk DA. **Genetics of cerebral cavernous malformations.** *Curr Neurol Neurosci Rep* 2005;5:391–96 CrossRef Medline
9. Gunel M, Awad IA, Finberg K, et al. **A founder mutation as a cause of cerebral cavernous malformation in hispanic Americans.** *N Engl J Med* 1996;334:946–51 CrossRef Medline
10. Babu R, Owens TR, Karikari IO, et al. **Spinal cavernous and capillary hemangiomas in adults.** *Spine* 2013;38:E423–30 CrossRef Medline
11. Badhiwala JH, Farrokhyar F, Alhazzani W, et al. **Surgical outcomes and natural history of intramedullary spinal cord cavernous malformations: a single-center series and meta-analysis of individual patient data: Clinic article.** *J Neurosurg Spine* 2014;21:662–76 CrossRef Medline
12. Canavero S, Pagni CA, Duca S, et al. **Spinal intramedullary cavernous angiomas: a literature meta-analysis.** *Surg Neurol* 1994;41:381–88 CrossRef Medline
13. Choi GH, Kim KN, Lee S, et al. **The clinical features and surgical outcomes of patients with intramedullary spinal cord cavernous malformations.** *Acta Neurochir (Wien)* 2011;153:1677–84 CrossRef Medline
14. Gross BA, Du R, Popp AJ, et al. **Intramedullary spinal cord cavernous malformations.** *Neurosurg Focus* 2010;29:E14 CrossRef Medline
15. Goyal A, Rinaldo L, Alkhataybeh R, et al. **Clinical presentation, natural history and outcomes of intramedullary spinal cord cavernous malformations.** *J Neurol Neurosurg Psychiatry* 2019;90:695–703 CrossRef Medline
16. Nagoshi N, Tsuji O, Nakashima D, et al. **Clinical outcomes and prognostic factors for cavernous hemangiomas of the spinal cord: a retrospective cohort study.** *J Neurosurg Spine* 2019;31:271–78 CrossRef
17. Ren J, Hong T, He C, et al. **Surgical approaches and long-term outcomes of intramedullary spinal cord cavernous malformations: a single-center consecutive series of 219 patients.** *J Neurosurg Spine* 2019;31:123–32 CrossRef
18. Ren J, Hong T, Zeng G, et al. **Characteristics and long-term outcome of 20 children with intramedullary spinal cord cavernous malformations.** *Neurosurgery* 2019;nyz381 CrossRef
19. Ren J, Hong T, He C, et al. **Coexistence of intracranial and spinal cord cavernous malformations predict aggressive clinical presentation.** *Front Neurol* 2019;10:618 CrossRef Medline
20. Toldo I, Drigo P, Mammi I, et al. **Vertebral and spinal cavernous angiomas associated with familial cerebral cavernous malformation.** *Surg Neurol* 2009;71:167–71 CrossRef Medline
21. de Vos I, Vreeburg M, Koek GH, et al. **Review of familial cerebral cavernous malformations and report of seven additional families.** *Am J Med Genet A* 2017;173:338–51 CrossRef Medline
22. Tandberg SR, Bocklage T, Bartlett MR, et al. **Vertebral intraosseous vascular malformations in a familial cerebral cavernous malformation population: prevalence, histologic features, and associations with CNS disease.** *AJR Am J Roentgenol* 2020;214:428–36 CrossRef Medline
23. de Souza JM, Domingues RC, Cruz LCH, et al. **Susceptibility-weighted imaging for the evaluation of patients with familial cerebral cavernous malformations: a comparison with T2-weighted fast spin-echo and gradient-echo sequences.** *AJNR Am J Neuroradiol* 2008;29:154–58 CrossRef Medline
24. Sparacia G, Speciale C, Banco A, et al. **Accuracy of SWI sequences compared to T2*-weighted gradient echo sequences in the detection of cerebral cavernous malformations in the familial form.** *Neuroradiol J* 2016;29:326–35 CrossRef

Improved Cervical Cord Lesion Detection with 3D-MP2RAGE Sequence in Patients with Multiple Sclerosis

S. Demortière, P. Lehmann, J. Pelletier, B. Audoin, and V. Callot

ABSTRACT

SUMMARY: Spinal cord lesions have a real diagnostic and prognostic role in multiple sclerosis. Thus, optimizing their detection on MR imaging has become a central issue with direct therapeutic impact. In this study, we compared the 3D-MP2RAGE sequence with the conventional Magnetic Resonance Imaging in Multiple Sclerosis (MAGNIMS) set for cervical cord lesion detection in 28 patients with multiple sclerosis. 3D-MP2RAGE allowed better detection of cervical lesions (+62%) in this population, with better confidence, due to optimized contrast and high spatial resolution.

ABBREVIATION: MAGNIMS = Magnetic Resonance Imaging in Multiple Sclerosis

Since the last revision of the Magnetic Resonance Imaging in Multiple Sclerosis (MAGNIMS) guidelines[1] and the McDonald criteria of 2017,[2] all spinal cord lesions must be counted to increase the sensitivity and specificity of the MS diagnosis.[3] In this context, standardized acquisition protocols have been proposed.[1] For spinal cord MR imaging, at least 2 sagittal sequences among T2WI, STIR, double inversion recovery, T1WI with gadolinium injection, and/or T2WI axial acquisitions[1] are recommended. Nonetheless, different sequences are often necessary because of motion and flux artifacts,[4] which is time-consuming.

The MP2RAGE sequence[5] has been shown to improve the detection of cerebral lesions that are difficult to visualize on conventional sequences, such as cortical lesions.[6] This T1WI MR imaging sequence, which creates a composite image, limiting field inhomogeneity bias while providing a quantitative T1 map, has recently been optimized for the spinal cord[7] but has not yet been evaluated in the context of MS.

The aim of this study was to compare the MP2RAGE sequence with the conventional set of routine sequences for detecting spinal cord lesions in patients with MS.

MATERIALS AND METHODS

Patients

This retrospective study, approved by the local Aix-Marseille University ethics committee with written informed consent, included 28 patients with MS from January 2017 to January 2019. Inclusion criteria were a diagnosis of MS according to the revised McDonald criteria,[2] older than 18 years of age, clinical symptoms suggesting spinal cord involvement, and MR imaging examination performed at least 3 months after steroid infusion.

Image Acquisition

Sequences were acquired on a 3T system (Magnetom Verio; Siemens) during the same examination. The protocol was as follows (see Table for MR imaging parameters):

- One sagittal 3D-MP2RAGE sequence, providing 2 contrasted images, from which a uniform image free of B_1 inhomogeneities and a T1 map were derived.[5]
- A conventional set with sagittal 2D-T2WI, STIR-weighted, and T1WI postgadolinium sequences, with axial 2D-T2*-WI MRI for confirmation of suspicious lesions on a sagittal set.

Received October 29, 2019; accepted after revision March 23, 2020.

From the Centre d'exploration métabolique par résonance magnétique (S.D., P.L., J.P., B.A., V.C.); Departments of Neurology (S.D., J.P., B.A.); and Neuroradiology (P.L.), Assistance Publique–Hôpitaux de Marseille, Hôpital Universitaire Timone, Marseille, France; and Center for Magnetic Resonance in Biology and Medicine (V. C.), Aix-Marseille University, National Centre for Scientific Research, Marseille, France.

This work was performed in a laboratory member of the France Life Imaging network (grant ANR-11-INBS-0006) and was supported by the Fondation pour l'Aide à la Recherche sur la Sclérose en Plaques and Centre National de la Recherche Scientifique.

Paper previously presented, in part, at: Annual Meeting of the European Research Committee for Treatment and Research in Multiple Sclerosis, October 18–22; 2019; Berlin, Germany (poster p1265), for which S. Demortière held a European Research Committee for Treatment and Research in Multiple Sclerosis fellowship grant.

Please address correspondence to Virginie Callot, PhD, CRMBM-Centre d'exploration métabolique par résonance magnétique, UMR 7339, CNRS, Aix-Marseille Université, Faculté de Médecine, 27, bd Jean Moulin, 13385 Marseille Cedex 5, France; e-mail: virginie.callot@univ-amu.fr

Indicates open access to non-subscribers at www.ajnr.org
Indicates article with supplemental on-line table.

http://dx.doi.org/10.3174/ajnr.A6567

Main sequence parameters

	MP2RAGE	STIR-Weighted	T2WI	TIWI Postgadolinium
Orientation/readout	3D sagittal/GRE	2D sagittal/TSE	2D sagittal/TSE	2D sagittal/TSE
TE/TR	2.48/4000 ms	53/4000 ms	113/3200 ms	10/700 ms
FOV	300 mm	320 mm	280 mm	220 mm
Voxel size	$0.9 \times 0.9 \times 1\ mm^3$	$0.9 \times 0.7 \times 3\ mm^3$	$1.1 \times 0.9 \times 2\ mm^3$	$0.8 \times 0.6 \times 3\ mm^3$
T_{acq}	7 min 18 sec	2 min 18 sec	1 min 54 sec	4 min 31 sec
Spatial coverage	Brain + C1–C7	C1–C7	C1–C7	C1–C7
Phase-encoding direction	A>>P	H>>F	H>>F	H>>F
Other parameters	TI1/TI2 = 650/2000 ms; $\alpha 1/\alpha 2 = 4/5$			
Reconstruction image	T1 quantitative map and UNI			

Note:—GRE indicates gradient recalled-echo; T_{acq}, acquisition time; A, anterior; P, posterior; H, head; F, feet; UNI, uniform image; TI1/TI2, inversion times 1 and 2; $\alpha 1/\alpha 2$, flip angles 1/2.

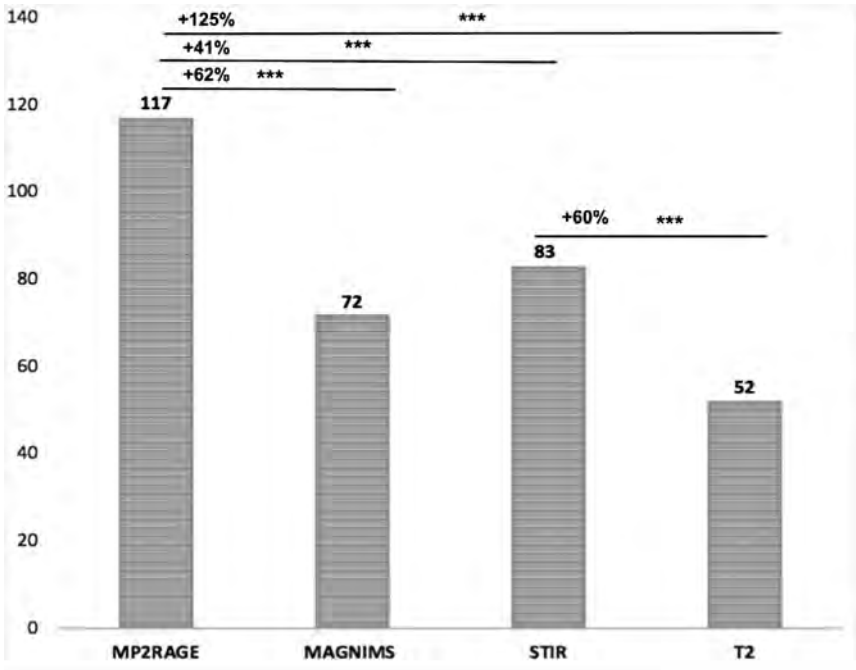

FIG 1. Number of lesions detected by sequence (Wilcoxon test; *triple asterisks* indicate $P < .0001$). The MP2RAGE sequence detected significatively more lesions than using the MAGNIMS criteria (117 vs 72, $P < .0001$), than STIR (117 vs 83, $P < .0001$) and T2 (117 vs 52, $P < .0001$) sequences (according to the MAGNIMS criteria, a lesion was validated if visible on at least two sequences of the conventional set). This corresponds to a +62%, + 41% and +125% increase in the lesion detection using MP2RAGE as compared to MAGNIMS, STIR and T2, respectively.

Lesion Detection and Scoring Confidence

The cervical spinal cord from C1 to C7 was evaluated. Two operators, a senior neuroradiologist and a neurologist who were blinded to patient data, read the results of the conventional set and the 3D-MP2RAGE sequence (T1 map and uniform image). Identification took place during a consensus session,[8] on a high-resolution monitor, using syngo.via (Siemens) image-analysis software. MS lesions were detected on the basis of hyperintensity on T2WI, STIR, MP2RAGE T1 map, and T1-weighted postgadolinium images in case of inflammatory lesions or hypointensity seen on MP2RAGE uniform images compared with normal cord signals. The lesion had to be visible on at least 2 slices in a row for the millimetric MP2RAGE sequence. According to the MAGNIMS criteria, a lesion was validated if visible on at least 2 sequences of the conventional set. Lesion detection was re-evaluated (reproducibility assessment) 3 weeks later, to minimize recall bias.

Confidence in detection was defined during the consensus session by use of a qualitative scale:[9] 0, no lesion detected; 1, low detection confidence; 2, moderate-to-high detection confidence; and 3, very high detection confidence.

Statistical Analysis

Wilcoxon tests (JMP 9; SAS Institute) were used to compare the number of detected lesions between conventional and MP2RAGE datasets, as well as the reader's confidence between sequences. $P < .05$ was considered statistically significant.

RESULTS

Demographic and Clinical Characteristics

We included 28 patients with MS (19 women; median age, 34.5 years; interquartile range, 28–41 years); 23 had relapsing-remitting MS, 4 had secondary-progressive MS, and 1 patient had primary-progressive MS. The mean Expanded Disability Status Scale score was 1.5 ± 1.4 (range, 0–6.5). The median disease duration was 4.8 years (interquartile range, 1.7–10.1 years).

Spinal Cord Lesions

In total, 27 patients had at least 1 identifiable spinal cord lesion, and 2 patients had an active enhancing lesion. A total of 117 lesions were detected. All lesions identified during the first image-analysis session were found during the second session (100% reproducibility). MP2RAGE significantly revealed more lesions than the conventional set ($P < .001$) (Fig 1). All lesions seen by the conventional sagittal set were detected on MP2RAGE.

Conversely, 13 lesions (7 patients) were detected only by MP2RAGE. These lesions had an average (minimum/maximum) diameter of 2.6 mm (1.9/4.1 mm). They all fulfilled the characteristics of MS lesions[10] in terms of size and location (54% posterior, 31%

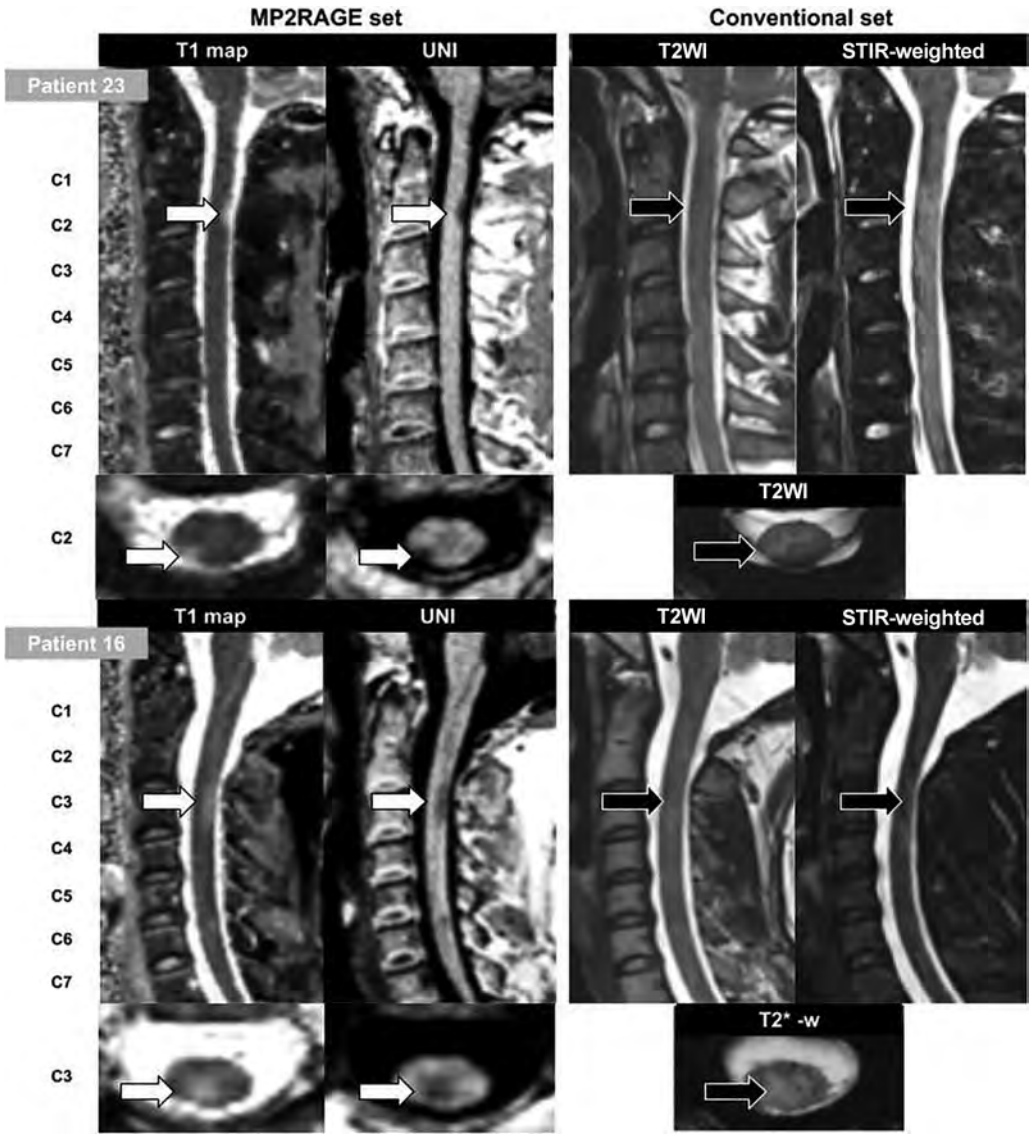

FIG 2. Illustration of MR imaging with the different investigated sequences for patient 23 (a 33-year-old man with relapsing-remitting MS) and patient 16 (a 27-year-old woman with relapsing-remitting MS). *White arrows* indicate good confidence in the lesion; *black arrows*, moderate confidence or no lesion seen; UNI, uniform image.

lateral, and 15% anterior), and their presence was carefully double-checked in the axial/coronal plane. The image quality of the conventional set for the corresponding slices was carefully re-evaluated and was satisfactory. Among these 7 patients, 3 had no visible lesions at all on conventional set detection (On-line Table and Fig 2).

Detection Confidence

Mean reading confidence was significantly higher with MP2RAGE than with STIR (2.1 ± 0.7 versus 1.5 ± 1.2, $P = .001$) and T2 (2.1 ± 0.7 versus 0.7 ± 0.9, $P < .001$) sequences. Confidence did not differ between lesions detected by MP2RAGE alone and those seen jointly by MP2RAGE and the conventional set (2.0 ± 0.6 versus 2.2 ± 0.8, $P = .11$).

DISCUSSION

The present study reveals, for the first time in MS, that the 3D-MP2RAGE method can detect cervical cord lesions with higher confidence and higher sensitivity than the recommended conventional MAGNIMS set. Given the essential diagnostic and prognostic significance of spinal cord lesions in MS, these results could have some critical added value for clinical practice, as previously demonstrated using phase-sensitive inversion recovery or double inversion recovery contrast.[9-11] In this work, 3D-MP2RAGE detected significantly more lesions than STIR, T2WI, and MAGNIMS set sequences. Most important, it also allowed detection of lesions in patients classified as not having cord lesions with the conventional set (11%). Of note, the validation of these undetected lesions was achieved by consensus between 2 experienced operators, repeated once with blinding to the previous assessment. Furthermore, the detection confidence for all the lesions visualized by MP2RAGE alone (2.0 ± 0.6, $n = 13$ lesions) was as high as that for those visualized by both MP2RAGE and the conventional set; this finding consolidates our findings. Finally, the characteristics of these lesions were typical for MS,[10] showing, for the first time in the

cord, similar detection capability than previously reporter in MS brain.[12-14] A recent study also demonstrated good correlation between cerebral lesions detected with MP2RAGE and histologic findings;[6] however, such data were not available in the present study and similar work remains to be done.

The present study has some additional limitations. First, the sample size was small and did not include patients with clinically isolated syndrome, for whom it will be necessary to assess the potential value of MP2RAGE diagnosis. Second, the respective contrast-to-noise ratios of the different sequences were not compared because of different spatial resolutions and partial volume effects. According to the present study design, we cannot exclude the possibility that the better sensitivity of MP2RAGE is mostly related to its 3D isotropic nature rather than its better ability to visualize lesions regardless of their size. Indeed, some authors reported a gain in sensitivity in 3D sequences[15,16] from 28% to 65% for cervical lesion detection.[9,11,17] Comparison among 3D-MP2RAGE, 3D-STIR, and 3D-T2WI is left for future specific studies. Concerning the 3 patients in whom no lesions were detected by the conventional set, missed lesions were mainly due to their small size and sequence spatial resolutions. However, 8/13 lesions detected only with the MP2RAGE sequence exceeded the spatial resolution of the conventional set; this feature suggests that the better sensitivity of MP2RAGE may be related more to its better contrast than its 3D isotropic resolution.

Finally, the MP2RAGE acquisition time (7 minutes) may seem relatively long compared with the 2D individual sequences. However, the volume acquired here covered the whole brain and the entire cervical spinal cord with isotropic submillimeter resolution. This feature offers promising opportunities for global assessment of the upper part of the central nervous system (brain and upper cervical cord). Brain evaluation was beyond the scope of this study. Finally, a compressed-sensing version of the sequence is now proposed,[18] which may further improve the added clinical value of the MP2RAGE sequence.

Further assessment and multicentric studies must now be promoted to improve lesion-detection capabilities and clinical evaluation and bring additional proof of specificity.

CONCLUSIONS

In this study, an optimized 3D-MP2RAGE sequence was demonstrated to allow a significant gain in the detection of MS cervical lesions (including in patients otherwise presenting with no lesions on conventional MR imaging), with assessment with high reader confidence compared with the conventional set. This MP2RAGE protocol, allowing brain and cervical cord coverage in 7 minutes, could be promising to improve clinical practice. Future studies using larger samples are necessary to confirm these preliminary results.

ACKNOWLEDGMENTS

The authors thank V. Gimenez, L. Pini, C. Costes, and M.P. Ranjeva for study logistics; A. Rico for patient recruitment; A. Massire, J.P. Ranjeva, and A. Maarouf for helpful discussions; and T. Kober (Siemens) for MP2RAGE sequence provision.

Disclosures: Sarah Demortière—*RELATED*: *Grant*: France Life Imaging Network.* Jean Pelletier—*UNRELATED*: *Board Membership*: Roche, Merck, Biogen, Novartis*; *Consultancy*: Roche, Merck, Biogen, Novartis*; *Grants/Grants Pending*: Fondation pour l'Aide à la recherche sur la Sclérose en Plaques Roche, Merck*; *Payment for Lectures Including Service on Speakers Bureaus*: Novartis, Biogen, Roche, Merck.* Virginie Callot—*RELATED*: *Grant*: Accueil–Fondation Sclérose en plaques, *Comments*: grant support for MRI exams. *Money paid to the institution.

REFERENCES

1. Filippi M, Rocca MA, Ciccarelli O, et al. **MRI criteria for the diagnosis of multiple-sclerosis: MAGNIMS consensus guidelines.** *Lancet Neurol* 2016;15:292–303 CrossRef Medline
2. Thompson AJ, Banwell BL, Barkhof F, et al. **Diagnosis of multiple sclerosis: 2017 Revisions of the McDonald Criteria.** *Lancet Neurol* 2018;17:162–73 CrossRef Medline
3. Filippi M, Preziosa P, Meani A, et al. **Prediction of a multiple-sclerosis diagnosis in patients with clinically isolated syndrome using the 2016 MAGNIMS and 2010 McDonald criteria: a retrospective study.** *Lancet Neurol* 2018;17:133–42 CrossRef Medline
4. Vargas MI, Delavelle J, Kohler R, et al. **Brain and spine MRI artifacts at 3 Tesla.** *J Neuroradiol* 2009;36:74–81 CrossRef Medline
5. Marques JP, Kober T, Krueger G, et al. **MP2RAGE, a self bias-field corrected sequence for improved segmentation and T1-mapping at high field.** *Neuroimage* 2010;49:1271–81 CrossRef Medline
6. Beck ES, Sati P, Sethi V, et al. **Improved visualization of cortical lesions in multiple-sclerosis using 7T MP2RAGE.** *AJNR Am J Neuroradiol* 2018;39:459–66 CrossRef Medline
7. Rasoanandrianina H, Massire A, Taso M, et al. **Regional T1 mapping of the whole cervical spinal cord using an optimized MP2RAGE sequence.** *NMR.Biomed* 2019;32:e4142 CrossRef Medline
8. Poonawalla AH, Hou P, Nelson FA, et al. **Cervical spinal cord lesions in multiple-sclerosis: T1-weighted inversion-recovery MR imaging with phase-sensitive reconstruction.** *Radiology* 2008;246:258–64 CrossRef Medline
9. Fechner A, Savatovsky J, El Methni J, et al. **A 3T phase-sensitive inversion recovery MRI sequence improves detection of cervical spinal-cord lesions and shows active lesions in patients with multiple-sclerosis**. *AJNR Am J Neuroradiol* 2019;40:370–75 CrossRef Medline
10. Moccia M, Ruggieri S, Ianniello A, et al. **Advances in spinal-cord imaging in multiple-sclerosis.** *Ther Adv Neurol Disord* 2019;12:1756286419840593 CrossRef Medline
11. Mirafzal S, Goujon A, Deschamps R, et al. **3D PSIR MRI at 3 Tesla improves detection of spinal-cord lesions in multiple-sclerosis.** *J Neurol* 2020;267:406–14 CrossRef
12. Kober T, Granziera C, Ribes D, et al. **MP2RAGE multiple-sclerosis magnetic resonance imaging at 3 T.** *Invest Radiol* 2012;47:346–52 CrossRef Medline
13. Fartaria MJ, Bonnier G, Roche A, et al. **Automated detection of white matter and cortical lesions in early stages of multiple-sclerosis.** *J Magn Reson Imaging* 2016;43:1445–54 CrossRef Medline
14. Fartaria MJ, Sati P, Todea A, et al. **Automated detection and segmentation of multiple–sclerosis lesions using ultra-high-field MP2RAGE.** *Invest Radiol* 2019;54:356–64 CrossRef Medline
15. Nayak NB, Salah R, Huang JC, et al. **A comparison of sagittal short T1 inversion recovery and T2-weighted FSE sequences for detection of multiple-sclerosis spinal cord lesions.** *Acta Neurol Scand* 2014;129:198–203 CrossRef Medline
16. Chong AL, Chandra RV, Chuah KC, et al. **Proton density MRI increases detection of cervical spinal-cord multiple-sclerosis lesions compared with T2-weighted fast spin-echo.** *AJNR Am J Neuroradiol* 2016;37:180–84 CrossRef Medline
17. Riederer I, Karampinos DC, Settles M, et al. **Double inversion recovery sequence of the cervical spinal-cord in multiple sclerosis and related inflammatory diseases.** *AJNR Am J Neuroradiol* 2015;36:219–25 CrossRef Medline
18. Mussard E, Hilbert T, Forman C, et al. **Accelerated MP2RAGE imaging using Cartesian phyllotaxis readout and compressed sensing reconstruction.** *Magn Reson Med* 2020 CrossRef Medline

How the Lives of Neuroradiologists and Neurosurgeons Have Been Changed by COVID-19

Two months ago, European neuroradiologists and neurosurgeons were planning their respective annual congresses in spring and summer, the best time of year in Europe and the United States. Suddenly an "earthquake" from Asia hit our shores. Italy was one of the first countries to be affected and went on to become one of those paying the highest toll alongside Spain. Country borders were closed, and in Europe, people were ordered to self-isolate at home. In the United States, the mythical McCormick Place, associated with teaching, meeting, and friendship and where the biggest radiology congress in the world has taken place for many years, was turned into a hospital.

Hospitals all over Europe drastically modified their activities. However, leaders of clinical services reacted differently; some, more distant from "the floor," tended to be "behind the curve" as the pandemic quickly evolved and issued orders disconnected from the real situation and, depending on the material capacities, quite similar to what played out at national levels. On the other hand, professional societies like the European Association for Neurosurgical Societies (EANS) provided direction on how to triage nonemergent neurosurgical procedures,[1] and the EANS President created a dedicated Web page to provide a discussion forum for European neurosurgeons where they could share their experiences about the impact of this on our professional lives, our hospitals, and our work and how we are coping with it.[2]

At our hospital, Geneva University Hospital and Faculty of Medicine in Switzerland, the neuroradiology and neurosurgery services were instructed to only attend to emergencies and patients in oncology. In everyday practice, patients were separated into those with the disease and those without or who were asymptomatic. In certain larger hospitals, the infrastructure permitted dedication of CT or MR imaging machines to patients positive for coronavirus disease 2019 (COVID-19). Given the strict constraints of resources, the neurosurgeons faced a drastic decrease in operations that could be performed, and residents were reassigned to newly established COVID wards. All multidisciplinary conferences were cancelled, except for oncology boards. In the administrative part, teleworking had to be organized. It was recommended that all hospital staff wear masks and use only dedicated hospital clothes, including shoes, as well as practice social distancing and hand washing.

The university was closed; the researchers and students were sent home, and the courses were taught with the help of distance-learning applications. The private lives of doctors and paramedical staff were also disrupted. Many feared that their professional activities were putting their own families at risk, and some colleagues took extreme precautions to avoid contamination. For many colleagues, childcare had to be reorganized because all schools and daycare centers were closed and grandparents were instructed to self-isolate.

Finally, our thoughts are with those colleagues who are absorbing the biggest burden at any moment and colleagues who have perished in this COVID-19 epidemic.

REFERENCES

1. **EANS advice: triaging non-emergent neurosurgical procedures during the COVID-19 outbreak.** https://cdn.ymaws.com/www.eans.org/resource/resmgr/documents/corona/eans_advice2020_corona.pdf
2. European Association of Neurosurgical Societies. **COVID-19 in Neurosurgery, News, Guidelines and Discussion Forum.** https://www.eans.org/page/covid-19

M.I. Vargas
Division of Neuroradiology

T.R. Meling
Division of Neurosurgery
Geneva University Hospital and Faculty of Medicine
Geneva, Switzerland

Indicates open access to non-subscribers at www.ajnr.org
http://dx.doi.org/10.3174/ajnr.A6562

Stroke Health Care Use and COVID-19

The patterns of health care use change in emerging infectious disease outbreaks. During an outbreak, resources are scarce and the focus is appropriately on the urgent needs of reducing the spread of disease and providing supportive care to victims.[1]

Similarly, the coronavirus disease 2019 (COVID-19) pandemic has placed an enormous strain on the health care systems of the nations where it has spread widely. Hence, care streams have been rapidly reprogrammed when trying to contain the COVID-19 and to rationalize the use of resources.

A serious increase in patients with COVID-19 should be anticipated. At the same time, provisions for general health services for acute and severe chronic illnesses must be maintained.

Several countries implemented stringent infection-control measures starting in early March 2020, including, but not limited to, social distancing measures, use of telemedicine, emergency infection protocols instituted in hospitals to contain COVID-19, suspension of all nonessential visits, and adjustment of clinical inpatient and outpatient services.

Although these protocols are essential for containing COVID-19 infections, these may impact health care systems in unexpected ways. Therefore, the response to COVID-19 and the large number of infected people requiring care can compromise rapid triage and may impact optimal treatment delivery to patients with acute cerebrovascular conditions. Delays in seeking care, transferring patients, and evaluating patients after hospital arrival could have a detrimental impact on outcomes if health care systems are not prepared. For instance, preliminary available data showed that the number of thrombectomies in Shanghai decreased by 50% in the first month after the Spring Festival compared with the same period in 2019.[2]

Adverse health outcomes resulting from accessibility barriers posed by the fear of COVID-19 should not be overlooked. Thus, it is necessary to encourage patients to continue seeking emergency care if experiencing acute stroke symptoms. Furthermore, all stroke teams should endeavor to adhere to all published guidelines regarding patient selection for therapies, treatment times, and posttreatment monitoring, and all staff engaged in acute stroke care should receive training for COVID-19 infection control to strictly prevent cross-infection.[3]

Finally, information on the most up-to-date evidence surrounding COVID-19 management should be widely disseminated. In our current digital world, on-line platforms are perhaps the most accessible source of health-related information for the public.[4] Hence, government agencies and national and international health agencies should consider increasing their on-line presence and consider on-line platforms and social media as a popular source for dissemination of reliable information to get to an optimal adherence to preventative measures population-wide and improve the education of the public.

REFERENCES

1. Chang HJ, Huang N, Lee CH, et al. **The impact of the SARS epidemic on the utilization of medical services: SARS and the fear of SARS.** *Am J Public Health* 2004;94:562–64 CrossRef Medline
2. Jing Z, Anthony R, Renyu L. **Challenges and potential solutions of stroke care during the coronavirus disease 2019 (COVID-19) outbreak.** *Stroke* 2020 Mar 31. [Epub ahead of print] CrossRef Medline
3. **Temporary emergency guidance to US stroke centers during the COVID-19 pandemic.** *Stroke* 2020 Apr 1. [Epub ahead of print] CrossRef Medline
4. Hernández-García I, Giménez-Júlvez T. **Assessment of health information about the prevention of COVID-19 on the Internet.** *JMIR Public Health Surveill* 2020;6:e18717 CrossRef Medline

I. Derraz
Department of Diagnostic and Interventional Neuroradiology
Gui de Chauliac Hospital, Montpellier University Medical Center
Montpellier, France

http://dx.doi.org/10.3174/ajnr.A6563

Neuroradiologists, Be Mindful of the Neuroinvasive Potential of COVID-19

The COVID-19 pandemic continues to have a far-reaching impact on nearly all aspects of society. First identified in December 2019 in Wuhan, the capital city of Hubei, China, COVID-19 is disseminated primarily via respiratory droplets and has the potential to cause severe respiratory distress in vulnerable patients, resulting in pneumonia, acute respiratory distress syndrome (ARDS), multiorgan dysfunction, and death.[1] Although recent literature on the virus has centered on the respiratory manifestations of the disease, a multitude of studies during the past few decades have shown that several respiratory viruses, including coronaviruses (CoVs), have neuroinvasive potential, demonstrating the ability to spread from the respiratory tract to the CNS to trigger or exacerbate neurologic pathology as a result of direct viral replication in the CNS or overactive host immune response.[2,3] This information is of interest to neuroradiologists, given that as the pandemic rages on, they may encounter sequelae of disease in the brain and spinal cord as these patients are imaged for neurologic symptoms.

First isolated in the mid-1960s, 6 types of CoVs, large-enveloped nonsegment positive-sense RNA viruses, are known to infect humans: HCoV-229E, HCoV-OC43, HCoV-NL63, HCoV-HKU1, Severe Acute Respiratory Syndrome-CoV (SARS), Middle East Respiratory Syndrome-CoV (MERS), and now, SARS-CoV-2 (COVID-19), a close relative of SARS. Most of these CoVs result in mild disease, with the exception of SARS and MERS, and most recently COVID-19, which may be lethal. Moreover, HCoV-229E, HCoV-OC43, SARS, and MERS have demonstrated neurotropism, or the ability to infect resident cells of the CNS (neuronal and glial).[4] MERS and SARS have demonstrated the ability to invade human neuronal cells in vitro. Moreover, SARS, among numerous other CoV strains, has been found in the CSF of patients, as well as in neurons in situ per postmortem studies.[5-7] It is known that both SARS and COVID-19 leverage the angiotensin-converting enzyme 2 (ACE-2) receptor for entry into host cells, though there is debate as to whether there are sufficient concentrations of this receptor in the CNS to explain their neurotropic nature.[8,9]

There are 2 main candidate mechanisms by which respiratory viruses may infect the CNS: hematogenous or neuronal retrograde. In the hematogenous route, the virus may pass through the BBB by transcytosis across brain microvascular endothelial cells and pericytes by endocytic vesicles or, rather, directly infect endothelial or epithelial cells to pass across the BBB or blood-CSF barrier in the choroid plexus of the ventricular system, respectively. Alternatively, the virus could be transported intracellularly in a concealed manner by leukocytes. There is mixed evidence regarding the viability of the hematogenous route in the neuroinvasiveness of CoVs. On the one hand, it has been reported that SARS has the ability to directly infect the BBB epithelium, representing 1 avenue of hematogenous spread.[3] Additionally, several strains of CoVs, including SARS, have shown the ability to infect multiple types of leukocytes both in vitro and in vivo.[5,10,11] This feature represents a potential second avenue of hematogenous spread, akin to the "Trojan Horse" model exhibited by HIV, by which the virus is covertly introduced to the CNS by a host's infected immune cells. However, evidence against the hematogenous route revolves around human postmortem in situ studies demonstrating the presence of SARS only in neurons and not other cell types of the brain, as was recently argued by Li et al.[9]

In the neuronal retrograde route of CNS entry, the virus invades neurons in the periphery, such as olfactory receptor neurons, those of the trigeminal nerve that reside in the nasal cavity, or sensory fibers of the vagus nerve in the brain stem, and leverages active transport mechanisms to gain access to the CNS.[12] The ability of SARS, MERS, and other CoVs to leverage this mechanism has been demonstrated in mouse models, via intranasal inoculation and subsequent infection of the olfactory bulb, as in Fig 1.[13-16] Once in the CNS, some strains of CoVs have been shown to be able to propagate between neurons, possibly through synaptic transmission.[3]

Several CoVs have demonstrated the potential for neurovirulence in both children and adults.[2,17] While no direct causal link has been established, multiple strains of CoVs have been associated with chronic CNS diseases, such as multiple sclerosis and neurodegeneration,[2,3] in addition to acute processes, such as encephalitis,[6] acute flaccid paralysis,[18] Guillan-Barre syndrome,[19] acute disseminated encephalomyelitis (ADEM),[20] focal seizures,[21] and other neurologic syndromes, including hemorrhage and stroke.[22-24] Clinical studies have begun to elucidate physiologic changes associated with acute CoV CNS infection, such as unique cytokine profiles;[7,25] moreover, malfunction of the cardiorespiratory center in

http://dx.doi.org/10.3174/ajnr.A6551

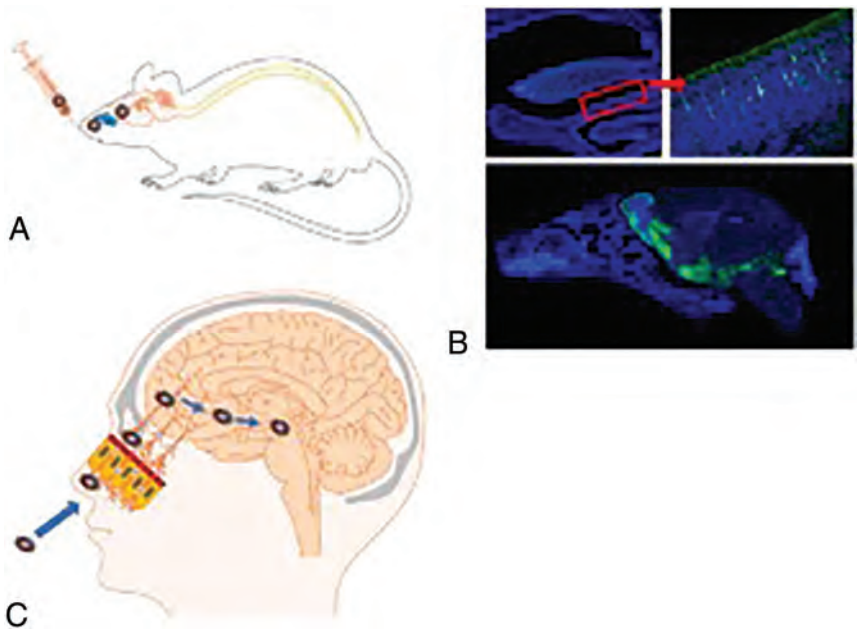

FIGURE. Representation of the neuronal retrograde method of CoV entry into the CNS. *A*, Upper left depicts a schematic of the experimental design allowing CoV infection in mouse experiments. The virus is introduced into the nasal cavity, traveling from the olfactory receptor neurons (ORN) to the olfactory bulb in the brain, and from there, to various areas in the brain stem. *C*, Lower left depicts the schematic for the same route in humans. *B*, Upper right depicts a decalcified murine nasal cavity from one such experiment. A close-up image denoted by a *red arrow* shows infected ORNs in green. The lower half of the panel shows dissemination of the virus through infected neurons, from the olfactory bulb to various areas of the brain stem. Reprinted with permission from Desforges et al.[2]

the brain stem has been hypothesized to play a potential role in respiratory distress in both humans[9] and mouse models.[15]

Although it is still fairly early in the COVID-19 pandemic, there are already reports of neurologic symptoms. In a study published in February this year in hospitalized patients with COVID-19 in Wuhan, China, the authors found that around one-third of patients had neurologic manifestations, most commonly dizziness and headache, though peripheral nervous system symptoms, primarily hypogeusia and hyposmia, were also seen.[26] A small number of patients experienced acute cerebrovascular injury (ischemic stroke, cerebral hemorrhage), loss of consciousness, and muscle injury. It is interesting that some patients developed hypogeusia or hyposmia, perhaps in support of the retrograde neuronal route of CNS invasion in COVID-19 via the olfactory bulb or other sensory branches of cranial nerves.

Several older reports have incorporated imaging in the neurologic work-up of patients with CoV infections. In a 15-year-old previously healthy boy, CoV-OC43 was detected in the CSF and nasopharyngeal secretions by polymerase chain reaction, while MR imaging of the brain and spinal cord demonstrated findings characteristic of ADEM, with T2-weighted hyperintensities in white matter tracts of the brain, some of which enhanced after intravenous gadolinium administration, as well as some in the spinal cord, which were nonenhancing, with follow-up imaging demonstrating improvement in these lesions.[20] In a study of hospitalized children with CoV and acute encephalitis-like syndrome, half of patients who underwent MRI or CT showed abnormalities, such as in the temporal lobes in patients with seizures, in the periventricular regions in patients with headaches, and in the basal ganglia and thalami in patients with fever and/or vomiting.[7] Moreover, in a study that incorporated imaging in 3 patients with MERS, brain MRI revealed widespread, bilateral T2-weighted hyperintense lesions in white matter and subcortical areas of the frontal, temporal, and parietal lobes; the basal ganglia; and corpus callosum, none of which showed gadolinium enhancement, which investigators attributed to ADEM, anoxic injury, and encephalitis, respectively.[22,24] Most interestingly, meningeal enhancement has not been shown in brain MRI of patients with CoV infection, arguing against a hematogenous method of entry into the CNS.[22,24]

Neuroradiologists will undoubtedly encounter increasing numbers of patients with COVID-19 in the course of daily practice. Therefore, they should be cognizant of the potential for CNS injury, either directly as the virus replicates in cells, or indirectly as host immune responses wage an all-out war. Furthermore, neuroradiologists should be wary of secondary impacts of COVID-19 on the CNS in severely ill patients, such as anoxic brain injury as a result of ARDS, cerebral hemorrhage as a result of thrombocytopenia, and disseminated intravascular coagulation, and air and fat emboli in patients with sepsis. As COVID-19 continues to spread across the globe, neuroradiologists should entertain this virus as a possible etiologic agent in patients with progressive or worsening CNS symptoms.

The possible imaging manifestations of CoV disease in the brain and spinal cord are varied, as shown by the aforementioned studies, and include injuries to both gray and white matter. In reading rooms, neuroimaging should be tailored to the clinical question while evaluating for complications such as ADEM, encephalitis, and Guillain-Barre syndrome, as reported in prior case series, whenever the clinical scenario can support such etiologies. Just as important, imaging should be reasonable and not excessive, keeping in mind that hospitalized patients with COVID-19 tend to be quite ill, so as to provide optimal patient care, preserve hospital resources, and minimize exposure of radiology staff, such as technologists and nurses, to the virus. With time and large-scale and rigorous investigations, hopefully the full spectrum of neuropathologies and exact mechanisms of injury in patients with COVID-19 will be uncovered.

REFERENCES

1. Guan WJ, Ni ZY, Hu Y, et al; China Medical Treatment Expert Group for Covid-19. **Clinical characteristics of coronavirus disease 2019 in China.** *N Engl J Med* 2020 Feb 28. [Epub ahead of print] CrossRef Medline

2. Desforges M, Le Coupanec A, Dubeau P, et al. **Human coronaviruses and other respiratory viruses: underestimated opportunistic pathogens of the central nervous system?** *Viruses* 2019;12:14 CrossRef Medline
3. Desforges M, Le Coupanec A, Brison E, et al. **Neuroinvasive and neurotropic human respiratory coronaviruses: potential neurovirulent agents in humans.** *Adv Exp Med Biol* 2014;807:75–96 CrossRef Medline
4. Arbour N, Day R, Newcombe J, et al. **Neuroinvasion by human respiratory coronaviruses.** *J Virol* 2000;74:8913–21 CrossRef Medline
5. Gu J, Gong E, Zhang B, et al. **Multiple organ infection and the pathogenesis of SARS.** *J Exp Med* 2005;202:415–24 CrossRef Medline
6. Morfopoulou S, Brown JR, Davies EG, et al. **Human coronavirus OC43 associated with fatal encephalitis.** *N Engl J Med* 2016;375:497–98 CrossRef Medline
7. Li Y, Li H, Fan R, et al. **Coronavirus infections in the central nervous system and respiratory tract show distinct features in hospitalized children.** *Intervirology* 2016;59:163–69 CrossRef Medline
8. Baig AM, Khaleeq A, Ali U, et al. **Evidence of the COVID-19 virus targeting the CNS: tissue distribution, host-virus interaction, and proposed neurotropic mechanisms.** *ACS Chem Neurosci* 2020. https://doi.org/10.1021/acschemneuro.0c00122. Accessed March 25, 2020
9. Li YC, Bai WZ, Hashikawa T. **The neuroinvasive potential of SARS-CoV2 may play a role in the respiratory failure of COVID-19 patients.** *J Med Virol* 2020 https://https://doi.org/10.1002/jmv.25728. Accessed March 25, 2020
10. Collins AR. **In vitro detection of apoptosis in monocytes/macrophages infected with human coronavirus.** *Clin Diagn Lab Immunol* 2002;9:1392–95 CrossRef Medline
11. Nicholls JM, Butany J, Poon LM, et al. **Time course and cellular localization of SARS-CoV nucleoprotein and RNA in lungs from fatal cases of SARS.** *PLoS Med* 2006;3:e27 CrossRef Medline
12. Swanson II PA, McGavern D. **Portals of Viral Entry into the Central Nervous System.** In: Dorovine-Zis K, ed. *The Blood-Brain Barrier in Health and Disease Volume 2: Pathophysiology and Pathology*, 1st ed., Boca Raton, FL: CRC Press; 2016:23–47
13. McCray PB Jr, Pewe L, Wohlford-Lenane C, et al. **Lethal infection of K18-hACE2 mice infected with severe acute respiratory syndrome coronavirus.** *J Virol* 2007;81:813–21 CrossRef Medline
14. St-Jean JR, Jacomy H, Desforges M, et al. **Human respiratory coronavirus OC43: genetic stability and neuroinvasion.** *J Virol* 2004;78:8824–34 CrossRef Medline
15. Netland J, Meyerholz DK, Moore S, et al. **Severe acute respiratory syndrome coronavirus infection causes neuronal death in the absence of encephalitis in mice transgenic for human ACE2.** *J Virol* 2008;82:7264–75 CrossRef Medline
16. Li K, Wohlford-Lenane C, Perlman S, et al. **Middle East Respiratory Syndrome coronavirus causes multiple organ damage and lethal disease in mice transgenic for human dipeptidyl peptidase 4.** *J Infect Dis* 2016;213:712–22 CrossRef Medline
17. Principi N, Bosis S, Esposito S. **Effects of coronavirus infections in children.** *Emerging Infect Dis* 2010;16:183–88 CrossRef Medline
18. Turgay C, Emine T, Ozlem K, et al. **A rare cause of acute flaccid paralysis: human coronaviruses.** *J Pediatr Neurosci* 2015;10:280–01 CrossRef Medline
19. Sharma K, Tengsupakul S, Sanchez O, et al. **Guillain–Barré syndrome with unilateral peripheral facial and bulbar palsy in a child: a case report.** *SAGE Open Med Case Rep* 2019;7:2050313X1983875 CrossRef Medline
20. Yeh EA, Collins A, Cohen ME, et al. **Detection of coronavirus in the central nervous system of a child with acute disseminated encephalomyelitis.** *Pediatrics* 2004;113:e73–76 CrossRef Medline
21. Lau KK, Yu WC, Chu CM, et al. **Possible central nervous system infection by SARS coronavirus.** *Emerging Infect Dis* 2004;10:342–44 CrossRef Medline
22. Algahtani H, Subahi A, Shirah B. **Neurological complications of Middle East Respiratory Syndrome coronavirus: a report of two cases and review of the literature.** *Case Rep Neurol Med* 2016;2016:3502683 CrossRef Medline
23. Bohmwald K, Gálvez NM, Ríos M, et al. **Neurologic alterations due to respiratory virus infections.** *Front Cell Neurosci* 2018;12:386 CrossRef Medline
24. Arabi YM, Harthi A, Hussein J, et al. **Severe neurologic syndrome associated with Middle East Respiratory Syndrome corona virus (MERS-CoV).** *Infection* 2015;43:495–501 CrossRef Medline
25. Xu J, Zhong S, Liu J, et al. **Detection of severe acute respiratory syndrome coronavirus in the brain: potential role of the chemokine mig in pathogenesis.** *Clin Infect Dis* 2005;41:1089–96 CrossRef Medline
26. Mao L, Wang M, Chen S, et al. **Neurological manifestations of hospitalized patients with COVID-19 in Wuhan, China: a retrospective case series study.** *MedRXiv* 2020. https://doi.org/10.1101/2020.02.22.20026500. Accessed March 25, 2020

M. Morris
V.M. Zohrabian
Department of Radiology and Biomedical Imaging
Yale School of Medicine
New Haven, Connecticut

"No Man is an Island"

John Donne

We read with great interest the recent Editorial by Mahajan and Hirsch[1] in the *American Journal of Neuroradiology (AJNR)*. At a time when the coronavirus disease 2019 (COVID-19) pandemic is raging, it provides a helpful and succinct summary and reminds us to play our part as good citizens as an informed and steadying influence on our colleagues, nurses, technologists, patients, families, and community.

As neuroradiologists, readers of the *AJNR* might also be concerned about the possible CNS manifestations or complications in this novel disease. Outbreaks of zoonotic viral diseases affecting the CNS have happened previously: The Nipah virus outbreak in 1998 was spread from bats via pigs to humans and caused respiratory and encephalopathic symptoms. MR imaging patterns included either extensive involvement of the cortex, temporal lobe, and pons, or multiple small (<1 cm in maximum diameter) abnormalities involving the subcortical and deep white matter, corpus callosum, and brain stem, especially visible on diffusion-weighted images.[2] In a case report of a patient with sequential organ failure, including meningoencephalitis from the Ebola virus, MR imaging showed multiple punctate lesions in the corpus callosum, cerebral white matter, and spinal cord, some with restricted diffusion, consistent with microvascular occlusion and ischemia.[3] However, the literature on imaging of CNS involvement in the Coronaviridae family, which also includes the Severe Acute Respiratory Syndrome (SARS) and the Middle East Respiratory Syndrome (MERS), is more limited. In the previous SARS outbreak in 2003, CT findings in 5 patients who developed large-artery ischemic stroke were reported, with the recommendation to be vigilant in future outbreaks for thrombotic complications in critically ill patients, especially if intravenous immunoglobulin is being used for treatment.[4]

Similarly, neurologic symptoms have been observed in a preprint report on severely ill patients in Wuhan during the current COVID-19 outbreak, including acute cerebrovascular diseases, consciousness impairment, and skeletal muscle symptoms; unfortunately, no CT or MR imaging has been described thus far.[5] Case reports of encephalitis and meningitis have also appeared in the lay press in both Beijing, China,[6] and Yamanashi, Japan.[7] We await the full publication of these results, to respond appropriately.

Unlike previous, localized outbreaks among smaller clusters of patients, this current COVID-19 epidemic affects us all personally: Neuroradiologists are responding to a constant barrage of official directives, planning for potential disruptions, and adjusting to patient case mixes as they occur. We urge good citizen neuroradiologists to learn as much as we can, report and share accurate data on patients undergoing CNS imaging, keep up with fast-moving developments, and help one another. In a worldwide pandemic, we are all in this together and we are all citizens of the world. Therefore, we would be wise to heed the famous quotation from John Donne, "No man is an island...Any man's death diminishes me, because I am involved in mankind. And therefore, never send to know for whom the bell tolls; It tolls for thee."

REFERENCES

1. Mahajan A, Hirsch JA. **Novel coronavirus: what neuroradiologists as citizens of the world need to know.** *AJNR Am J Neuroradiol* 2020 Mar 20. [Epub ahead of print] CrossRef Medline
2. Lim C, Sitoh YY, Hui F, et al. **Nipah viral encephalitis or Japanese encephalitis? MR findings in a new zoonotic disease.** *AJNR Am J Neuroradiol* 2000;21:455–61 Medline
3. Chertow DS, Nath A, Suffredini AF, et al. **Severe meningoencephalitis in a case of Ebola virus disease: a case report.** *Ann Intern Med* 2016;165:301–04 CrossRef Medline
4. Umapathi T, Kor AC, Venketasubramanian N, et al. **Large artery ischaemic stroke in severe acute respiratory syndrome (SARS).** *J Neurol* 2004;251:1227–31 CrossRef Medline
5. Mao L, Wang M, Chen S, et al. **Neurological manifestations of hospitalized patients with COVID-19 in Wuhan, China: a retrospective case series study.** *medRxiv* 2020 CrossRef https://www.medrxiv.org/content/10.1101/2020.02.22.20026500v1. Accessed March 21, 2020
6. **New research sparks debate over whether Coronavirus can infect the nervous system.** *Caixin* https://www.caixinglobal.com/2020-03-06/new-research-sparks-debate-over-whether-coronavirus-can-infect-the-nervous-system-101524986.html. Accessed March 21, 2020
7. Shah S. **Can novel Coronavirus cause meningitis? Japan has the answer.** *International Business Times* March 8, 2020. https://www.ibtimes.sg/can-novel-coronavirus-cause-meningitis-japan-has-answer-40647. Accessed March 21, 2020

C.C.T. Lim
Department of Neuroradiology
National Neuroscience Institute
Duke-NUS Graduate Medical School
Singapore

K. Tsuchiya
Department of Radiology
Saitama Medical Center, Saitama Medical University
Kawagoe City, Saitama, Japan

http://dx.doi.org/10.3174/ajnr.A6544

The Significance of Natural Anastomoses among Intracranial Vessels in Moyamoya Disease

We read with great interest the article by Bonasia et al[1] regarding the angiographic analysis of natural anastomoses between the posterior cerebral arteries (PCAs) and anterior cerebral arteries (ACAs) in Moyamoya disease (MMD) and syndrome. The authors observed 3 different types of anastomoses between the anterior and posterior circulations, with different abilities to compensate the anterior circulation. We really appreciate the interesting observations in their Conclusions. Meanwhile, after reading this article, we would like to highlight 2 important questions that it raises.

First, the authors found a wide anastomoses among intracranial vessels, especially between the PCAs and ACAs, in patients with MMD. This finding is consistent with our latest observations.[2] We observed different hemodynamic sources of the recipient parasylvian cortical arteries (PSCAs) among the frontal, temporal, and parietal PSCAs in MMD hemispheres. PSCAs from the PCAs accounted for 25.3%. The extensive anastomosis between PCAs and ACAs provides new evidence to explain the various hemodynamic sources of PSCAs observed in MMD hemispheres. More interesting, in the current study, the degree of posterior collaterals among Suzuki scores was positively correlated. We observed the same phenomenon. This suggests that although the posterior circulation is less affected in MMD, the compensatory effect of the posterior circulation on the anterior ischemic and hypoperfusion areas becomes more and more important as the disease progresses.

Second, the broad anastomosis of intracranial blood vessels in patients with MMD reminds neurosurgeons that the hemodynamics in PSCAs are complex. Previous studies[3,4] have also mentioned the different types of collaterals that naturally develop in MMD. These collaterals can not only provide blood flow support for the ischemic area but also are risk factors for hemorrhagic stroke. During direct bypass surgery, surgeons should pay more attention to DSA, rather than relying solely on anatomy, to determine the hemodynamic source of the recipient vessel. Recipient vessels of different hemodynamic sources have different effects on postoperative perfusion recovery in different cerebral regions. We have found that the hemodynamic source of the recipient vessel is closely related to postoperative hyperperfusion syndrome.

REFERENCES

1. Bonasia S, Ciccio G, Smajda S, et al. **Angiographic analysis of natural anastomoses between the posterior and anterior cerebral arteries in Moyamoya disease and syndrome.** *AJNR Am J Neuroradiol* 2019;40:2066–72 CrossRef Medline
2. Zhang J, Li S, Fujimura M, et al. **Hemodynamic analysis of the recipient parasylvian cortical arteries for predicting postoperative hyperperfusion during STA-MCA bypass in adult patients with Moyamoya disease.** *J Neurosurg* 2019 Dec 27:1–8. [Epub ahead of print] CrossRef Medline
3. Baltsavias G, Khan N, Valavanis A. **The collateral circulation in pediatric Moyamoya disease.** *Childs Nerv Syst* 2015;31:389–98 CrossRef Medline
4. Robert T, Ciccio G, Sylvestre P, et al. **Anatomic and angiographic analyses of ophthalmic artery collaterals in Moyamoya disease.** *AJNR Am J Neuroradiol* 2018;39:1121–26 CrossRef Medline

J. Yu
J. Zhang
J. Chen
Department of Neurosurgery
Zhongnan Hospital of Wuhan University
Wuhan, China

http://dx.doi.org/10.3174/ajnr.A6502

REPLY:

We were pleased to read the letter written by our colleagues from Wuhan about our recent article, "Angiographic Analysis of Natural Anastomoses between the Posterior and Anterior Cerebral Arteries in Moyamoya Disease and Syndrome."[1] Their comments focused mainly on 2 issues analyzed in our article: on the one hand, the importance of the posterior circulation in the development of collateral circles that allow compensation of the anterior hypoperfused regions; on the other hand, the hemodynamic complexity of the cerebral circulation in patients with Moyamoya disease. The studies conducted by our 2 groups analyzed the compensatory, collateral circles present in Moyamoya disease from 2 different points of view: In our study, we focused on an angiographic description of the posterior cerebral artery–anterior cerebral artery (PCA-ACA) collaterals. The Wuhan group instead correlated some particular types of collaterals to the post–superficial temporal artery (STA)-MCA bypass hypoperfusion syndrome. The conclusions we both came to, even if from different points of view, are the same: In patients with more advanced stages of the disease, the contribution of PCA-ACA anastomoses becomes more and more consistent, though the posterior circulation is less affected by the disease. Although the posterior circle makes an important contribution in the reperfusion of ischemic areas, to have a more global picture, we must also consider the other collateral circles described by Baltsavias et al,[2,3] in 2014 and 2015, the superficial meningeal systems (pio-pial and duro-pial connections) and the deep parenchymal systems (subependymal or periventricular and thalamic connections).

http://dx.doi.org/10.3174/ajnr.A6503

Considering the lack of a detailed description of the collateral circles in Moyamoya disease in the literature, the intention of our group is to analyze in the future, after the analyses performed for collaterals between the ophthalmic artery and anterior cerebral artery, the contribution of the other systems to reperfusion. Since this pathology is very rare and often occurs in young patients and with emergency presentation, the possibility to analize the different collaterals involved into the riperfusion through selective microcatheterization is limited.

REFERENCES

1. Bonasia S, Ciccio G, Smajda S, et al. **Angiographic analysis of natural anastomoses between the posterior and anterior cerebral arteries in Moyamoya disease and syndrome.** *AJNR Am J Neuroradiol* 2019;40:2066–72 CrossRef Medline
2. Baltsavias G, Valavanis A, Filipce V, et al. **Selective and superselective angiography of pediatric moyamoya disease angioarchitecture: the anterior circulation.** *Interv Neuroradiol* 2014;20:403–12 CrossRef Medline
3. Baltsavias G, Khan N, Valavanis A. **The collateral circulation in pediatric moyamoya disease.** *Child nervous system* 2015;31:389–398 CrossRef Medline

S. Bonasia
Department of Neurosurgery
Neurocenter of Southern Switzerland
Regional Hospital of Lugano
Lugano, Switzerland
T. Robert
Department of Neurosurgery
Neurocenter of Southern Switzerland
Regional Hospital of Lugano
University of the Southern Switzerland
Lugano, Switzerland

Myelin Imaging Can Be Affected by a Number of Factors

We read with great interest the article by Yu et al,[1] which investigated the utility of myelin volume fraction, axon volume fraction, and G-ratio, which is the ratio of the inner-to-outer diameter of a nerve fiber, in the evaluation of WM in patients with MS. They used macromolecular tissue volume imaging to calculate myelin volume fraction and revealed that myelin volume fraction was lower in the normal-appearing WM of patients with MS compared with the WM of healthy controls. Furthermore, they also revealed that disability, as measured by the Expanded Disability Status Scale, was significantly associated with myelin volume fraction in the normal-appearing WM of patients with MS. We believe that this study is an important step toward the introduction of myelin imaging into clinical practice.

We thank Yu et al[1] for referring to our article entitled, "Analysis of White Matter Damage in Patients with Multiple Sclerosis via a Novel In Vivo MR Method for Measuring Myelin, Axons, and G-Ratio."[2] The myelin volume fraction used in our study was calculated from the R1 and R2 relaxation rates and proton density measured by synthetic MR imaging, by simulating a 4-compartment model: myelin volume fraction, cellular volume fraction, excess parenchymal water volume fraction, and free water volume fraction.[3] Myelin volume fraction in the MS lesions in our study was lower than in their study, and they discussed this discrepancy possibly being because the 4-compartment model used in our study did not incorporate the partial volume pool to account for magnetization transfer effects. Even though magnetization transfer effects may have resulted in small changes in the measured R2 estimations, myelin is estimated from combinations of the measured R1, R2, and proton density values by the model used in our study, and the effect of a potential offset in R2 is expected to be small.

Here, we should also consider the fact that magnetization transfer imaging, which detects macromolecules, is known to be sensitive to not only intact myelin but also other macromolecules, including myelin debris.[4] Hence, macromolecular tissue volume may also be affected by myelin debris, which may have led to the higher myelin volume fraction in the study by Yu et al[1] than in our study. Because myelin debris is assumed to have much lower R2 than the tightly packed myelin, the contribution of myelin debris to the estimated myelin by synthetic MR imaging is expected to be small. Because myelin imaging can be affected by a number of factors, the interpretation of the results is not straightforward. A histologic study comparing macromolecular tissue volume and synthetic myelin imaging is awaited to further disentangle the mechanism underlying the discrepancy in the results between the study by Yu et al[1] and our study.

This work was supported by Japan Society for the Promotion of Science KAKENHI grant No. 16K19852 and grant No. JP16H06280, Grant-in-Aid for Scientific Research on Innovative Areas-Resource and technical support platforms for promoting research "Advanced Bioimaging Support." This work was also supported by the program for Brain Mapping by Integrated Neurotechnologies for Disease Studies (Brain/MINDS) from the Japan Agency for Medical Research and Development, AMED.

http://dx.doi.org/10.3174/ajnr.A6525

Disclosures: Akifumi Hagiwara—*RELATED*: *Grant*: Japan Society for the Promotion of Science KAKENHI, Grant-in-Aid for Scientific Research on Innovative Areas-Resource and technical support platforms for promoting research "Advanced Bioimaging Support," and Japan Agency for Medical Research and Development, *Comments*: Japan Society for the Promotion of Science KAKENHI grant No. 16K19852, grant No. JP16H06280, Grant-in-Aid for Scientific Research on Innovative Areas-Resource and technical support platforms for promoting research "Advanced Bioimaging Support," the program for Brain Mapping by Integrated Neurotechnologies for Disease Studies from Japan Agency for Medical Research and Development. Osamu Abe—*UNRELATED*: *Grants/Grants Pending*: Canon Medical Systems, Daiichi Sankyo Company Ltd, Eisai Co Ltd, Bayer Yakuhin Ltd, Nihon Medi-Physics Co Ltd, Fujifilm, Toyama Chemical Co Ltd, Guerbet Japan, Siemens Healthcare Diagnostics KK, and Fuji Pharma Co Ltd*; *Payment for Lectures Including Service on Speakers Bureaus*: Canon Medical Systems, Daiichi Sankyo Company Ltd, Eisai Co Ltd, Bayer Yakuhin Ltd, GE Healthcare, Hitachi HealthCare, Philips Healthcare, Fujifilm, Toyama Chemical Co Ltd, Guerbet Japan, Nippon Zoki Pharmaceuticals Co Ltd, AZE, Siemens Healthcare Diagnostics KK, and Fuji Pharma Co Ltd. Shigeki Aoki—*RELATED*: *Grant*: Japan Society for the Promotion of Science KAKENHI 18H02772, "Advanced Bioimaging Support," *Comments*: Japan Society for the Promotion of Science KAKENHI grant No.18H02772, Grant-in-Aid for Scientific Research on Innovative Areas-Resource and technical support platforms for promoting research "Advanced Bioimaging Support"*; *UNRELATED: Board Membership:* Bayer Yakuhin Ltd, Canon Medical Systems; *Grants/Grants Pending*: Bayer Yakuhin Ltd, Daiichi Sankyo Co Ltd, Eisai, Fuji-Toyamakagaku, Nihon Medi-Physics Co Ltd, Guerbet Japan; *Payment for Lectures Including Service on Speakers Bureaus*: GE Healthcare, Canon Medical Systems, AZE, Siemens Healthineers, Bayer Yakuhin Ltd, Daiichi Sankyo Co Ltd, Eisai, Fuji-Toyamakagaku, Mediphysics, Guerbet Japan. *Money paid to the institution.

REFERENCES

1. Yu F, Fan Q, Tian Q, et al. **Imaging G-ratio in multiple sclerosis using high-gradient diffusion MRI and macromolecular tissue volume.** *AJNR Am J Neuroradiol* 2019;40:1871–77 CrossRef Medline
2. Hagiwara A, Hori M, Yokoyama K, et al. **Analysis of white matter damage in patients with multiple sclerosis via a novel in vivo MR method for measuring myelin, axons, and G-ratio.** *AJNR Am J Neuroradiol* 2017;38:1934–40 CrossRef Medline
3. Hagiwara A, Warntjes M, Hori M, et al. **SyMRI of the brain: rapid quantification of relaxation rates and proton density, with synthetic MRI, automatic brain segmentation, and myelin measurement.** *Invest Radiol* 2017;52:647–57 CrossRef Medline

4. Vavasour IM, Laule C, Li DK, et al. **Is the magnetization transfer ratio a marker for myelin in multiple sclerosis?** *J Magn Reson Imaging* 2011;33:713–78 CrossRef Medline

A. Hagiwara
Department of Radiology
Juntendo University School of Medicine
Tokyo, Japan

M. Hori
Department of Radiology
Juntendo University School of Medicine
Tokyo, Japan

Department of Diagnostic Radiology
Toho University Omori Medical Center
Tokyo, Japan

C. Andica
Department of Radiology
Juntendo University School of Medicine
Tokyo, Japan

O. Abe
Department of Radiology, Graduate School of Medicine
The University of Tokyo
Tokyo, Japan

S. Aoki
Department of Radiology
Juntendo University School of Medicine
Tokyo, Japan

The Ubiquitous Use of Resting State as a Control Task for Language Mapping in Task-Based Functional MRI

We read with great interest the article entitled, "Lesion-Specific Language Network Alterations in Temporal Lobe Epilepsy," by Foesleitner et al.[1] Functional connectivity, often synonymously used in reference to "resting-state functional connectivity," offers a unique insight into brain connections and has shown some promise in better understanding of normal and abnormal brain function, which complements information that can be ascertained from task-based fMRI studies. Indeed, the authors found distinct functional connectivity profiles in these different epilepsy cohorts that were not ascertainable by task-based fMRI analysis, which may lead to a better understanding of how epilepsy affects language organization. However, we have concerns about the study design and assertions by the authors.

First, the use of a "rest" control block is relatively ubiquitous in clinical task-based fMRI for language mapping, despite its well-known effects on calculated "activation."[2,3] Binder et al[2] have previously shown considerable overlap in activation patterns when contrasting a resting state with a tone-decision task and a semantic-decision task with the same tone control task. Critically, when one contrasts the semantic decision task with rest, expected areas of language activation are no longer observed.[2] Using rest as a control condition can result in false-negative activation maps and erroneous calculation in the laterality index. Most important, the strongest validation for the laterality index compared with Wada and verbal memory outcomes is by use of such an active control task (semantic-decision versus tone-decision task).

Multiple factors likely contribute to the apparent loss of activation when using rest as the language control compared with an active control task. Because the resting state is not truly devoid of synchronized neuronal activity, it is a false assumption that rest is somewhat of a "blank canvas" with which cognitive functions can be compared. So-called task-negative networks (eg, default mode network [DMN]) show greater activity during the rest state and are relatively suppressed at the onset of a cognitive task. Thus, during a block design (as performed by the authors), one can model these task-negative networks as "off" during the language task block and "on" during the rest block, resulting in its own "block design," which is anticorrelated to the task of interest. Therefore, these areas of task-negative network activation will be subtracted from the language task activation, giving an erroneous calculation of task activation. Most important, this adds an additional source of subject-specific variability because the degree of deactivation of these networks has been shown to be dependent on the perceived difficulty of the task.[4] While there is debate on whether the DMN functions in the semantic network,[4] the effect of task-negative network activation is critical, nevertheless, because it shares similar anatomic overlap with areas of semantic processing; therefore, rest is generally an inappropriate control for language mapping.

Second, we also have concerns about the use of resting blocks in a task-based acquisition for functional connectivity because these are known not to be entirely representative of true dedicated resting acquisitions.[5] The authors do not clearly discuss this point, making extrapolation to more widely used dedicated resting-state scans problematic. Our greater concern is the suggestion by the authors that the strategy of using resting blocks from a task acquisition is advantageous because it adds no additional scan time. The encouragement to use rest as a control block for task-based language fMRI may potentially have profound adverse effects on decision-making in epilepsy surgery with regard to risks of verbal memory decline and should be discouraged.

Last, while their results raise interesting questions about the pathophysiology of language function and organization in the setting of various epilepsy cohorts, it is critical to remember that we use laterality index with task-based fMRI to assess surgical risks. Because no such outcome data are presented in this study, one must exercise caution in assuming that these functional connectivity findings have any role in assessing risks for epilepsy surgery and cannot replace task-based fMRI until such validation has occurred.

http://dx.doi.org/10.3174/ajnr.A6464

Disclosures: Erik Middlebrooks—*UNRELATED*: *Grants/Grants Pending*: Varian Medical Systems and Boston Scientific Corp, *Comments*: Both entities provided research support unrelated to this work.* *Money Paid to the Institution.

REFERENCES

1. Foesleitner O, Nenning KH, Bartha-Doering L, et al. **Lesion-specific language network alterations in temporal lobe epilepsy.** *AJNR Am J Neuroradiol* 2020;41:147–54 CrossRef Medline
2. Binder JR, Swanson SJ, Hammeke TA, et al. **A comparison of five fMRI protocols for mapping speech comprehension systems.** *Epilepsia* 2008; 49:1980–97 CrossRef Medline
3. Middlebrooks EH, Yagmurlu K, Szaflarski JP, et al. **A contemporary framework of language processing in the human brain in**

the context of preoperative and intraoperative language mapping. *Neuroradiology* 2017;59:69–87 CrossRef Medline
4. Humphreys GF, Hoffman P, Visser M, et al. **Establishing task- and modality-dependent dissociations between the semantic and default mode networks.** *Proc Natl Acad Sci U S A* 2015;112:7857–62 CrossRef Medline
5. Ganger S, Hahn A, Kublbock M, et al. **Comparison of continuously acquired resting state and extracted analogues from active tasks.** *Hum Brain Mapp* 2015;36:4053–63 CrossRef Medline

E.H. Middlebrooks
Departments of Radiology and Neurosurgery
Mayo Clinic
Jacksonville, Florida

D.S. Sabsevitz
Department of Neuropsychology
Mayo Clinic
Jacksonville, Florida

REPLY:

We would like to thank Drs Middlebrooks and Sabsevitz for their interesting comment on our recent publication, "Lesion-Specific Language Network Alterations in Temporal Lobe Epilepsy."[1] In this group analysis of patients with temporal lobe epilepsy (TLE) due to different underlying pathologies, we targeted the main question: Can distinct lesion-specific language network changes be identified using functional connectivity (FC) analysis? Indeed, we showed that different etiologies (ie, hippocampal sclerosis, nonlesional temporal lobe epilepsy, and mesiotemporal low-grade glioma) of TLE cause distinct patterns of language network changes.

We agree with the authors that a critical appraisal of the paradigm design is extremely important in presurgical fMRI. However, we would like to emphasize that due the robustness of our FC group analysis results, the main results are very unlikely to change, even after choosing a different paradigm approach. We would like to further comment on the points mentioned.

As outlined in the authors' comment, Binder et al[2] found a significant difference between auditory semantic language tasks with rest versus active, nonlinguistic tasks as a baseline condition.[2] Auditory tasks, as exclusively used in the study by Binder et al, cannot be simply extrapolated to our visually presented language paradigms using cross-fixation (with/without alternating hashtags) as a baseline task. The use of cross-fixation as a baseline is common[3] and recommended by the American Society of Functional Neuroradiology in their recently published guideline article (see, for instance, the "Antonym Generation" paradigm).[4] As expected, cross-fixation typically results in bilateral activations in the primary visual cortex,[4] which need to be considered when interpreting the results. Furthermore, we would like to stress that using a homogeneous protocol (ie, the same scanner, same task design, systematic prescanning patient training, quality assessment by on-line processing during fMRI acquisition, the same processing, and the same analysis parameters), we could reduce the risk of a systematic bias. However, we do agree that potential intersubject differences in the ability to "rest" during cross-fixation could have translated into subtle differences of network characteristics.

To our knowledge, the examined etiologies were never proved to differ in the patients' ability to optimally adhere to the baseline task. Moreover, many of the included patients scored low on verbal fluency and naming tests (36.8% and 69.1%, respectively). Although no group differences were found in their actual language abilities, these facts strongly suggest that the observed lesion-specific changes can be explained by functional connectivity changes in the language domain and not, as otherwise assumed, by differences in baseline task completion.

We do agree that task-based fMRI, regardless of whether active or cross-fixation is used as baseline condition, is not equivalent to pure resting-state fMRI. We absolutely do not and did not recommend to either replace task-based fMRI by resting-state fMRI or vice versa. For the investigation of specific cognitive networks, such as language in our case, task-based fMRI may be superior to resting-state fMRI due to its higher reliability and robustness.[5] As outlined in our Materials and Methods section,[1] we included all acquired time points ($n = 100$ per run) into our FC analysis in order not to introduce artificial fluctuations into the frequency spectrum by cutting and concatenating task and resting blocks.[6] Moreover, this approach should maximize the available number of time points, which is known to critically influence the reliability of connectivity measures.[7] In our opinion, activation analysis and FC are complementary approaches. However, before the full transition of functional connectivity from research to clinics, further studies on the reproducibility and interpretation of these correlation values on a single-subject level are needed. One such promising approach could be connectivity fingerprints, in which individual network features are compared with normative values derived from a large pool of healthy subjects, as recently attempted.[8-10]

REFERENCES

1. Foesleitner O, Nenning KH, Bartha-Doering L, et al. **Lesion-specific language network alterations in temporal lobe epilepsy.** *AJNR Am J Neuroradiol* 2020;41:147–54 CrossRef Medline
2. Binder JR, Swanson SJ, Hammeke TA, et al. **A comparison of five fMRI protocols for mapping speech comprehension systems.** *Epilepsia* 2008;49:1980–97 CrossRef Medline
3. Benjamin CF, Dhingra I, Li AX, et al. **Presurgical language fMRI: technical practices in epilepsy surgical planning.** *Hum Brain Mapp* 2018;39:4032–42 CrossRef Medline
4. Black DF, Vachha B, Mian A, et al. **American Society of Functional Neuroradiology-Recommended fMRI paradigm algorithms for presurgical language assessment.** *AJNR Am J Neuroradiol* 2017;38:E65–73 CrossRef Medline
5. Kristo G, Rutten GJ, Raemaekers M, et al. **Task and task-free FMRI reproducibility comparison for motor network identification.** *Hum Brain Mapp* 2014;35:340–52 CrossRef Medline
6. Ganger S, Hahn A, Kublbock M, et al. **Comparison of continuously acquired resting state and extracted analogues from active tasks.** *Hum Brain Mapp* 2015;36:4053–63 CrossRef Medline
7. Shah LM, Cramer JA, Ferguson MA, et al. **Reliability and reproducibility of individual differences in functional connectivity acquired during task and resting state.** *Brain Behav* 2016;6:e00456 CrossRef Medline
8. Finn ES, Shen X, Scheinost D, et al. **Functional connectome fingerprinting: identifying individuals using patterns of brain connectivity.** *Nat Neurosci* 2015;18:1664–71 CrossRef Medline
9. Amico E, Goni J. **The quest for identifiability in human functional connectomes.** *Sci Rep* 2018;8:8254 CrossRef Medline
10. Voets NL, Parker Jones O, Mars RB, et al. **Characterising neural plasticity at the single patient level using connectivity fingerprints.** *Neuroimage Clin* 2019;24:101952 CrossRef Medline

O. Foesleitner
K.-H. Nenning
Departments of Biomedical Imaging and Image-Guided Therapy
L. Bartha-Doering
Department of Pediatrics and Adolescent Medicine
C. Baumgartner
General Hospital Hietzing with Neurological Center Rosenhuegel
Vienna, Austria
E. Pataraia
D. Moser
Department of Neurology
M. Schwarz
V. Schmidbauer
Departments of Biomedical Imaging and Image-Guided Therapy

http://dx.doi.org/10.3174/ajnr.A6597

S. Bonelli
Department of Neurology
G. Kasprian
Departments of Biomedical Imaging and Image-Guided Therapy
Medical University of Vienna
Vienna, Austria

J.A. Hainfellner
Institute of Neurology
T. Czech
C. Dorfer
Department of Neurosurgery
G. Langs
D. Prayer
Departments of Biomedical Imaging and Image-Guided Therapy